3D modelling of star-forming regions. The contribution of the graphical interface GASS to radiative transfer codes.

David D. Quénard

To cite this version:

David D. Quénard. 3D modelling of star-forming regions. The contribution of the graphical interface GASS to radiative transfer codes. . Solar and Stellar Astrophysics [astro-ph.SR]. Université Toulouse 3 - Paul Sabatier, 2016. English. NNT : . tel-01402482v1

HAL Id: tel-01402482
https://theses.hal.science/tel-01402482v1

Submitted on 24 Nov 2016 (v1), last revised 20 Dec 2016 (v2)

THÈSE

En vue de l'obtention du

DOCTORAT DE L'UNIVERSITÉ DE TOULOUSE

Délivré par : *l'Université Toulouse 3 Paul Sabatier (UT3 Paul Sabatier)*

Présentée et soutenue le *20/09/2016* **par :**

David QUÉNARD

Modélisation 3D de régions de formation d'étoiles
La contribution de l'interface graphique GASS aux codes de transfert radiatif

---

JURY

Peter VON BALLMOOS	Professeur d'Université	Président du Jury
Serena VITI	Professeur d'Université	Membre du Jury
Fabrice HERPIN	Astronome	Membre du Jury
Claudine KAHANE	Professeur d'Université	Membre du Jury
Laurent LOINARD	Professeur d'Université	Membre du Jury
Sandrine BOTTINELLI	Maître de Conférence	Directrice de thèse
Emmanuel CAUX	Directeur de Recherche	Co-directeur de thèse

École doctorale et spécialité :
SDU2E : Astrophysique, Sciences de l'Espace, Planétologie
Unité de Recherche :
Institut de Recherche en Astrophysique et Planétologie (UMR 5277)
Directeur(s) de Thèse :
Sandrine BOTTINELLI et *Emmanuel CAUX*
Rapporteurs :
Serena VITI et *Fabrice HERPIN*

“*Depuis l’espace, quand on suit la course de la nuit sur notre planète,*
on voit des points lumineux qui s’allument.
Cela semble bien peu de choses dans l’immensité de l’Univers
qui brille de tous ses feux.
Et pourtant, cela représente une nouvelle étape de la matière;
Les hommes dans les ténèbres qui cherchent sans fin la lumière.”

Extrait de “Univers, l’inimaginable naissance” – David Biau

RÉSUMÉ

L'ère des observations interférométriques mène à la nécessité d'une description de plus en plus précise de la structure physique et dynamique des régions de formation d'étoiles, des cœurs pré-stellaires aux disques proto-planétaires. L'émission du continuum de la poussière et des raies moléculaires peut être décrite grâce à plusieurs composantes physiques. Afin de comparer avec les observations, une modélisation de transfert radiatif précise et complexe de ces régions est nécessaire.

Dans ce but, j'ai développé au cours de ma thèse une application autonome appelée GASS (Generator of Astrophysical Sources Structures, Quénard et al., in prep.). Grâce à son interface, GASS permet de créer, manipuler et mélanger plusieurs composantes physiques différentes, telles que des sources sphériques, des disques et des outflows. Le code est divisé en différentes parties: l'interface, la génération de la grille, la création du modèle, ainsi que les options de post-traitement. Une analyse comparative entre la combinaison de GASS et LIME (un code non-ETL de transfert radiatif 3D, Brinch and Hogerheijde, 2010) et RATRAN (une contre-partie 1D, Hogerheijde and van der Tak, 2000) a été effectuée.

Dans cette thèse, j'ai utilisé GASS pour travailler sur différents cas astrophysiques et, parmi eux, j'ai étudié en détail l'émission de l'eau et de l'eau deutérée dans le cœur pré-stellaire L1544 et l'émission des ions dans la proto-étoile de faible masse IRAS16293-2422.

J'ai analysé l'émission de l'eau dans le cœur pré-stellaire L1544 (Quénard et al., 2016) en utilisant la combinaison de GASS et LIME. Contrairement aux études précédentes, ce nouveau travail donne un profil d'abondance de l'eau différent ainsi qu'une nouvelle estimation de l'opacité de la poussière dans le cœur. Sur la base de ce résultat, j'ai utilisé un code astrochimique gaz-grain pour reproduire le nouveau profil de l'abondance de l'eau. Le rapport HDO/H_2O a été estimé à partir de cette modélisation chimique, ce qui a permis de prédire l'émission de la raie de HDO dans ce cœur. À partir de cette estimation, j'ai montré qu'il est impossible avec les instruments et les télescopes actuels (en considérant un temps d'observation réaliste) de détecter HDO dans les cœurs pré-stellaires.

Le deuxième travail que j'ai réalisé vise à étudier l'émission des ions dans IRAS16293-2422 (Quénard et al., submitted) en utilisant également GASS et LIME. Je me suis concentré sur HCO^+ et N_2H^+, ainsi que leurs isotopologues (fractionnés et deutérés) car ce sont les ions les plus abondants dans cette source, De plus, beaucoup de données en provenance des différents relevés spectraux sont disponibles pour ces espèces. L'émission de HCO^+ résulte principalement d'un jeune outflow, mais également de l'enveloppe tandis que l'émission de N_2H^+ provient seulement de cette dernière. Le code astrochimique gaz-grain Nautilus a été utilisé pour prédire le profil d'abondance de ces deux ions dans l'enveloppe et un taux d'ionisation cosmique élevé ($\geqslant 5 \times 10^{-17}\,\mathrm{s}^{-1}$) est nécessaire pour reproduire correctement l'émission des raies. Un nuage en avant-plan est également nécessaire pour reproduire correctement l'absorption et/ou l'émission de certaines transitions.

ABSTRACT

The era of interferometric observations leads to the need of a more and more precise description of the physical structure and dynamics of star-forming regions, from pre-stellar cores to proto-planetary disks. The molecular and dust continuum emission can be described with multiple physical components. To perform a meaningful comparison with the observations, a precise and complex radiative transfer modelling of these regions is required.

I have developed during this thesis a standalone application called GASS (Generator of Astrophysical Sources Structures, Quénard et al., in prep.) for this purpose. Thanks to its interface, GASS allows to create, manipulate, and mix several different physical components such as spherical sources, disks, and outflows. The code is divided into different parts: the interface, the grid generation, the model creation, and the post-treatment options. A benchmarking between the combination of GASS and LIME (a 3D non-LTE radiative transfer code, Brinch and Hogerheijde, 2010) and RATRAN (a 1D counter-part, Hogerheijde and van der Tak, 2000) has been performed.

In this thesis, I used GASS to work on different astrophysical cases and, among them, I studied in details the water and deuterated water emission in the pre-stellar core L1544 and the emission of ions in the low-mass proto-star IRAS16293-2422.

I analysed the water emission in the pre-stellar core L1544 (Quénard et al., 2016) using the combination of GASS and LIME. This work shows that the water abundance profile and the dust opacity estimation in the core are different from the values obtained with previous works. Based on this result, I used an astrochemical gas-grain code to reproduce the new water abundance profile. The HDO/H_2O ratio has also been estimated from this chemical modelling, allowing to predict the line emission of HDO in this core. From this estimate, I showed that it is not possible with current instruments and telescopes (considering a realistic observing time) to detect HDO in pre-stellar cores.

The second work I carried out aims at studying the emission of ions in IRAS16293-2422 (Quénard et al., submitted) also using GASS and LIME. I focused on HCO^+, N_2H^+, and their (fractionated and deuterated) isotopologues since they are the most abundant ions in this source. Moreover, a lot of data are available from the spectral surveys for these species. The HCO^+ emission arises mainly from a young outflow but also from the envelope whereas the N_2H^+ emission is only resulting from the latter. The Nautilus gas-grain chemical code was used to predict the abundance profile of these two ions in the envelope. The results of this work show that a high cosmic ionisation rate ($\geqslant 5 \times 10^{-17}\,\mathrm{s}^{-1}$) is needed to reproduce correctly the line emission and that the presence of a foreground cloud is required to correctly reproduce the absorption and/or emission of some transitions.

ACKNOWLEDGMENT

Premièrement, j'aimerais remercier Emmanuel Caux et Sandrine Bottinelli de m'avoir encadré pendant ces trois années de thèse mais aussi les stages lors du M1 et M2. Ces cinq années passées à apprendre à vos côtés ont été enrichissantes, que ce soit d'un point de vue de travail ou humain. Vous avez été là pour moi quand il le fallait, en étant disponibles et à l'écoute. Le temps que j'ai passé au sein du groupe MICMAC est inoubliable et toutes les personnes de ce couloir vont me manquer. Je pense particulièrement à toi Charlotte, tu as toujours été là pour m'écouter quand ça n'allait pas et je tiens à t'en remercier chaleureusement. C'était super de travailler avec toi, tu m'as fait découvrir les observations au 30m de l'IRAM et les cours de M1 Astrochimie ensemble vont beaucoup me manquer ! Olivier, tu es le meilleur co-bureau qu'on puisse espérer, garde-moi la place avec toi au chaud !

La recherche c'est avant tout une grande famille, et je tiens à remercier toutes les personnes avec qui j'ai pu collaborer et travailler durant ma thèse. Merci à Cecilia Ceccarelli et Paola Caselli pour leur enthousiasme lors de nos échanges, j'espère vraiment continuer à interagir avec vous. Je pense bien évidemment à Laurent Loinard et Antonio Hernandez et même si la vie mexicaine n'est pas faite pour moi, j'ai beaucoup appris grâce à vous et c'est avec joie que je continuerai ce que nous avons commencé ensemble. Je remercie Valentine Wakelam qui a suivi la progression de ma thèse depuis son commencement (et même avant) et pour nos échanges qui ont toujours été fructueux. Enfin, merci à tous les membres de mon jury de thèse: les deux examinateurs Claudine Kahane et Laurent Loinard ainsi que les deux rapporteurs Serena Viti et Fabrice Herpin, sans oublier Peter von Ballmoos, le président.

Je remercie tous les doctorants de l'IRAP et plus particulièrement toute l'équipe d'Astro-Jeunes. L'ambiance des préparatifs et de la semaine du Festival est irremplaçable. Un grand merci particulièrement à Jason pour nos séances de tennis-papier et baseball-papier dans le couloir MICMAC, merci à toi Gabriel pour ta gentillesse et ta bonne humeur inébranlable. Philippe, tu es quelqu'un que j'admire beaucoup, et préparer le ballon stratosphérique avec toi et William était mon activité favorite pendant l'été !

Une thèse c'est des hauts et des bas, et ces trois années auraient été différentes sans mes proches. Merci tout d'abord à tous mes amis, Arnaud tu as été là sur Skype, tous les jours, et nos discussions sont indispensables à mon environnement de travail désormais. Tout comme celles que j'ai avec Nicolas, avec qui j'ai pu partager tant de choses, y compris Astro-jeunes, mais bien plus encore (merci pour le maté). Tu m'as soutenu tout au long de cette thèse et tes conseils m'ont toujours beaucoup aidé. Merci à toi Kévin, tu m'as toujours dit que je ferai ce que tu n'avais pas pu faire et ça m'a toujours touché. Mon aventure à l'IRAP a commencé grâce à toi, lorsque tu m'as présenté à Sandrine. Avec Arnaud vous avez toujours su être là pour moi depuis 9 ans, et je vous considère comme les frères que je n'ai pas eu. Merci à Hélène et Isabelle pour nos innombrables fous rires et votre soutien. Nous avons vécu une sacrée expédition ensemble (plus jamais comme Tulum !) qui restera gravée dans ma mémoire.

Merci à ma famille, Maman tu m'as toujours dit de faire ce que j'avais envie de faire, et maintenant c'est fait ! Enfant, tu m'as toujours emmené à la bibliothèque à chaque fois que je le désirais pour passer des heures à lire des livres sur l'Univers. C'est sûrement ainsi que mon aventure Astronomique à commencé. Valérie, Aurore, vous avez toujours été là pour me changer les idées quand ça n'allait pas. J'ai pu voir la fierté dans vos yeux quand je vous parlais de mon travail et c'est la plus belle chose qu'un petit frère puisse recevoir de ses soeurs. Merci à vous trois pour votre soutien tout au long de cette thèse.

Enfin, je tiens à remercier celle qui a su être là pour moi à chaque instant. Isabelle, ma femme, tel un phare en plein milieu de la tempête, tu as éclairé ma vie depuis le jour où l'on s'est rencontré. Tu as partagé avec moi l'aventure de cette thèse et tu m'as apporté réconfort et soutien dans tous les aspects de ma vie. Tu as toujours cru en moi, tu m'as toujours pousser à donner le meilleur et rien de tout ça n'aurait été pareil sans toi.

Du fond du coeur, je vous remercie tous !

CONTENTS

Introduction

L'ère des observations interférométriques mène à la nécessité d'une description de plus en plus précise de la structure physique et dynamique des régions de formation d'étoiles, des cœurs pré-stellaires aux disques proto-planétaires.

Cette thèse a permis de développer GASS (Generator of Astrophysical Sources Structures, Quénard et al., in prep.), une application autonome (codée sous MatLab) qui permet de créer des structures physiques complexes en 3D pour les codes de transfert radiatif. GASS est empaqueté dans une interface graphique, ce qui simplifie la visualisation des modèles 3D générés. GASS est capable de mélanger plusieurs structures astrophysiques, comme des sources sphériques, des outflows ou des disques. GASS est capable de générer des modèles physiques pour LIME (Brinch and Hogerheijde, 2010), un code de transfert radiatif 3D hors équilibre thermodynamique local (non-ETL). Des outils de post-traitement sont également implémentés afin de permettre l'analyse des cubes hyper-spectraux fournis par les codes de transfert radiatifs. Ces différents outils permettent par exemple d'afficher des spectres ou des cartes intégrées de l'émission moléculaire ou encore d'effectuer des simulations d'observation.

GASS est disponible à la communauté sur demande (site en construction) et il fonctionne sur différents types de systèmes d'exploitation (Mac OS X et Windows pour la version application et Linux pour la version scriptée).

Le premier Chapitre donne le contexte astrophysique général de la thèse. J'évoque dans cette partie les différentes étapes du processus de formation des étoiles de faible masse, en partant du nuage moléculaire jusqu'au système planétaire. Je mentionne également la chimie qui se produit dans l'environnement de ces objets, et plus généralement la chimie dans le milieu interstellaire. Je décris les processus chimiques à la fois de la phase gazeuse mais également ceux qui se produisent à la surface des grains de poussière. Cette partie est suivie d'une brève introduction à la spectroscopie moléculaire, nécessaire à la compréhension du travail effectué dans cette thèse. Je donne également un aperçu du processus d'observation en radio-astronomie, à la fois avec les télescopes à antenne unique mais aussi avec les interféromètres. Ce chapitre se termine par une description des différents modèles de transfert radiatif utilisés dans cette thèse, en partant de la modélisation à l'ETL jusqu'au traitement complet du transfert radiatif 3D non-ETL. Je développerai alors la théorie liée à ces modèles ainsi que les différents outils d'analyse permettant de les utiliser.

Dans le Chapitre 2, je donne une présentation détaillée du fonctionnement du code GASS. Cela commence par l'explication du processus de génération de la grille, inspiré du processus implémenté dans LIME : il s'agit d'un découpage en cellules 3D de l'espace qui définit la "zone de travail" dans laquelle les différentes structures physiques vont être construites par GASS. Ces différentes structures physiques générées sont des sources sphériques, des outflows, et des disques. Il n'y a pas de limites sur le nombre d'objets que GASS est capable de gérer à la fois, ainsi il est possible de modéliser un cluster de proto-étoiles si on le désire. Je présente également dans ce chapitre les différentes options de LIME qui sont disponibles à partir de l'interface graphique de GASS. En effet, ce dernier est capable de créer directement et automatiquement tout le contenu nécessaire à l'utilisation de LIME, ce qui simplifie grandement l'utilisation de celui-ci. Une partie de ce chapitre est consacrée à la description des divers outils de post-traitement de cubes hyper-spectraux (ne venant pas forcément que de LIME) qu'offre GASS. Ce chapitre se clôture sur une analyse comparative ("benchmarking") approfondie entre LIME et RATRAN (l'équivalent de LIME mais 1D, Hogerheijde and van der Tak, 2000) et, enfin, je présente deux exemples astrophysiques pertinents montrant les capacités de GASS.

Grâce à la combinaison de GASS et de LIME, j'ai pu étudier différents types d'objets astrophysiques mais je me suis intéressé plus particulièrement à l'étude de deux d'entre eux: l'émission de l'eau et de l'eau deutérée dans le cœur pré-stellaire L1544 et l'émission des ions dans la proto-étoile de faible masse IRAS16293-2422.

L'eau est une molécule importante non seulement sur Terre, mais aussi dans l'espace. En effet, étant donné qu'elle est formée par deux des éléments les plus abondants dans l'Univers, l'eau régit la composition chimique et l'équilibre thermique du gaz moléculaire interstellaire dense. Ce dernier est également le gaz à partir duquel se forment les étoiles, de sorte que l'eau influe sur l'ensemble du processus de formation des étoiles à différents niveaux selon les phases (e.g. Caselli and Ceccarelli, 2012). Dans les nuages moléculaires, l'eau sous forme de glace est présente en grande quantité, jusqu'à la moitié de l'abondance élémentaire de l'oxygène, et est synthétisée sur les grains interstellaires (e.g. Boogert et al., 2015). Dans les régions plus denses à l'intérieur des nuages moléculaires, où les cœurs pré-stellaires sont présents, l'eau est encore principalement sous forme de glace (Caselli and Ceccarelli, 2012). Plus tard, lorsque l'environnement proto-stellaire devient assez chaud ($\geq$100 K), les grains de poussière se réchauffent et cette eau est alors libérée dans la phase gazeuse. Ce phénomène se produit dans les coeurs chauds (*hot cores* ou *hot corinos*) et dans les chocs moléculaires proto-stellaires (par exemple van Dishoeck et al., 2014). Pour reconstruire l'histoire de l'origine de l'eau, l'étude de sa deutération est cruciale car celle-ci est très sensible aux conditions physiques au moment où la molécule est formée. Dans les cœurs pré-stellaires, aucune tentative pour mesurer l'abondance de l'eau deutérée n'a été faite jusqu'à présent.

Le Chapitre 3 présente l'analyse de l'eau (H_2O) et de l'eau deutérée (HDO) que j'ai réalisée dans le cœur pré-stellaire L1544. C'est la première fois que de l'eau est détectée en direction d'un cœur pré-stellaire, observation rendue possible grâce à l'observatoire spatial *Herschel*. De plus, le profil spectral de la raie montre un profil appelé "P-Cygni inversé", signe d'effondrement gravitationnel. Cet objet est donc sur le point de s'effondrer gravitationnellement sur lui-même pour former une étoile.

L'émission de l'eau dans ce cœur a déjà été abordée dans de précédentes études (Caselli and Ceccarelli, 2012; Keto et al., 2014) mais contrairement à celles-ci, la nouvelle étude que j'ai réalisée utilise un traitement radiatif complet (non-ETL). La prédiction de l'émission des raies dépend grandement de la méthode de transfert radiatif utilisée, ainsi j'effectue dans ce chapitre une nouvelle analyse complète de l'eau dans cette source. La structure physique de la source étant déjà connue grâce à de précédentes études (Keto and Rybicki, 2010; Caselli and Ceccarelli, 2012), je n'ai modifié que l'abondance de l'eau dans la source en fonction du rayon ainsi que l'opacité de la poussière pour reproduire le profil de la transition de l'eau détectée.

Ce travail a été couplé à un code astrochimique gaz-grain afin de prédire le profil de l'abondance de l'eau et de le comparer à celui obtenu par l'analyse avec GASS et LIME. En partant de cette modélisation chimique, le profil de l'abondance de l'eau deutérée a été obtenu, permettant ainsi de prédire l'émission de HDO dans ce cœur pré-stellaire. Le but étant d'étudier, en se basant sur les observations faites dans L1544, la détectabilité de HDO dans ce type d'objet en prenant en compte les différents instruments et télescopes disponibles actuellement.

Le second cas auquel je me suis intéressé pendant cette thèse est l'étude des ions dans la proto-étoile de faible masse IRAS16293-2422, présentée au Chapitre 4. En effet, les ions et les électrons sont chargés électriquement, ils suivent donc le champ magnétique de l'étoile naissante et vont de ce fait interagir par collision avec les espèces neutres qui se trouvent sur le passage, ralentissant l'accrétion du matériel proto-stellaire sur l'objet central. Ainsi, l'étude des ions permet de comprendre l'échelle de temps de l'effondrement gravitationnel d'une proto-étoile et donc de mieux comprendre son évolution dans le temps. De plus, les espèces ionisées peuvent aussi aider à créer et détruire de plus grandes molécules telles que les molécules organiques complexes (COMs). Les ions sont donc activement impliqués dans la chimie et la dynamique de la source (Bergin and Langer, 1997).

L'étude de ces ions est axée sur l'émission de l'ion formyl HCO^+ et de l'ion diazénylium N_2H^+ au regard des deux relevés spectraux (TIMASSS et CHESS) qui ont observé de nombreuses transitions de ces deux espèces dans IRAS16293-2422, couvrant de surcroît une large gamme d'énergie. Ces observations ont permis de détecter une quarantaine de transitions de HCO^+, de N_2H^+ et de leur isotopologues (fractionnés et deutérés), contraignant plus fortement les résultats obtenus dans ce travail. Le but de cette étude est de donner de meilleures contraintes sur les structures physiques responsables de l'émission des raies moléculaires. Une analyse a montré que ces structures sont au nombre de trois: un outflow jeune (responsable de la majorité de l'émission des raies de HCO^+), l'enveloppe proto-stellaire (responsable de l'émission des raies de N_2H^+), et un nuage en avant plan, responsable de l'absorption et/ou de l'émission de certaines transitions moléculaires. Ces trois structures ont été modélisées grâce à GASS.

Ces deux études ne sont pas les seules auxquelles j'ai participé pendant cette thèse (cf. Conclusion). Je participe, par exemple, à une étude sur la structure physique à petite échelle ($< 2''$) de la source IRAS16293-2422 B, à deux études concernant des disques proto-planétaires (le disque massique et évolué "Hamburger de Gomez" et le proplyd 203–506), mais aussi à des études du continuum de la poussière dans les premières galaxies.

SUMMARY

The era of interferometric observations leads to the need of a more and more precise description of physical structures and dynamics of star-forming regions, from pre-stellar cores to proto-planetary disks. This thesis allowed to develop GASS (Generator of Astrophysical Sources Structures), a standalone application that helps to create complex 3D physical structures for radiative transfer codes. GASS is wrapped into a graphical interface, simplifying the visualisation of the generated 3D models. GASS is able to mix several astrophysical structures such as spherical sources, outflows, or disks. GASS is able to generate physical models for LIME, a 3D non-LTE radiative transfer code. Post-treatment tools are also implemented to analyse hyper-spectral data cubes (e.g. spectra and integrated maps plotting or observation simulation). This tool is available to the community upon request (website under construction) for different operating systems.

The first Chapter gives the general astrophysical context of the thesis. I will evoke the different steps of the low-mass star formation process as well as the chemistry involved in their environment (and more generally in the interstellar medium) from both the gas phase and the grain surfaces. This is followed by a short introduction to molecular spectroscopy and an insight of the observation process in radio-astronomy, with both single-dish and interferometers telescopes. This chapter ends with a description of the different radiative transfer models used in this thesis, from LTE modelling to 3D full radiative transfer treatment.

In Chapter 2, I give an extensive presentation of the functioning of the GASS code. Starting with the explanation of the grid generation process, it is followed by a description of the different physical structures implemented in GASS (spherical sources, outflows, disks). I also present in this chapter the different LIME options available within GASS and the content of the various post-treatment options. An extensive benchmarking between LIME and RATRAN (a 1D non-LTE radiative transfer code) has been performed and, finally, I present two relevant astrophysical examples of the use of GASS.

The next chapter concerns the first scientific case performed during this thesis using the combination of GASS and LIME. I present the analysis of water (H_2O) and deuterated water (HDO) in the pre-stellar core L1544. Unlike previous studies of the water emission in this core, a new study was carried out using a non-LTE treatment, coupled with a gas-grain astrochemical code to predict the water abundance profile. Based on this chemical result, the deuterated water abundance profile has been derived, allowing to predict the detectability of HDO in pre-stellar cores.

The second scientific case is the study of ions in the low-mass proto-star IRAS16293-2422, presented in Chapter 4. This work is focused on the HCO^+ and N_2H^+ emission since two spectral surveys (TIMASSS and CHESS) observed many transitions in this source, covering a large range of energies. The aim of this study is to give better constraints on the physical properties of the outflow (responsible for a majority of the emission of HCO^+), the envelope (responsible for the emission of N_2H^+), and the foreground cloud. These three structures have been modelled with GASS. This work also includes several fractionated and deuterated isotopologues of these two species, helping to better constrain the physical properties of the aforementioned structures.

The last chapter gives the conclusions and the ongoing work related to this thesis.

“Le silence éternel de ces espaces infinis m’effraie.”

Blaise Pascal

This image from the Hubble Space Telescope shows the galaxy cluster MACSJ0717.5+3745. Almost everything in this image is a galaxy. Credit: NASA/ESA/HST Frontier Fields team.

FOREWORD

Archeoastronomy

For thousands of years, astronomy has been a subject of interest for erudites and scientists all over the world. Looking at the sky, stargazing has fascinated everyone at least once in their life. The lights from stars have always reached us and since the beginning of the human race, we wonder what is going on up there, in the darkness of the night. Our ancestors already thought about it when they draw paintings in their caves, showing the premises of constellations. Archeoastronomy (or paleoastronomy) is the subject that is trying to link the study of astronomy with the study of ancient civilisations. Astronomy is believed to have influenced them in the past.

The study of the sky has been a common subject for many civilisations around the world and they left clues about it behind them. The link between religions and astronomy is very tight when looking at the position of places of worship. Megaliths have been built in Great-Britain as ancient "observatories". The oldest one is $\sim$7,000 years old and it was used as an astronomical calendar for summer solstices. Alexander Thom studied very deeply the origin of megaliths during the 1960s in Great-Britain. He published a book[1] showing that many megalithic monuments are used as calendars and built for this on purpose. These monuments mark the sunset and the sunrise of multiple object such as the Moon, the Sun, or even the brightest stars in the sky at particular moment of the year: solstices and equinoxes. One of the most popular megalithic monument is the site of Stonehenge that is covered with mysteries. It has been built around 3,100 BC and its function is still discussed nowadays. Like any other megaliths, it is aligned very particularly well with the Moon or the Sun during solstices and equinoxes. Megaliths have not been found only in Great-Britain but also in France ("Cromlech du Petit-Saint-Bernard", frontier with Italy), Brazil ("Calçoene" site), Germany ("Harhoog" site), Israel, The Netherlands, Ireland,... and many other countries all around the world.

An other example of astronomical monuments are the Giza pyramid complex in Egypt. They have been built in 2,560 BC by Cheops (IVth dynasty) and are composed of three pyramids: Khufu (the Great Pyramid), Khafra, and Menkaure. The "Orion correlation theory" claims that there is a correlation between the location of the three pyramids and the constellation Orion. This theory has been developed by Robert Bauval in 1994, when he realised that the position of the three stars of the Orion's Belt (δ Orionis, ϵ Orionis, and ζ Orionis) matched the position of the three pyramids. He even went further, claiming that the slope of the king chamber is directly pointed to the Orion's Belt when the constellation is at the meridian, as well as the North corridor is pointed to α Draconis (celestial North pole at this epoch) and the South corridor directed to Sirius (α Canis Majoris). The pyramids would have been built by the ancient Egyptians with respect to their main gods Osiris (associated to Orion) and Isis (associated with Sirius).

If we look at the American continent, the Maya, Inca, and Aztecs have also been influenced by astronomy. One of the most famous Maya civilisation's site is the city of Chichen Itza (Yucatán, Mexico). A step-pyramid called the "Temple of Kukulcan" (or El Castillo) lies in the centre of the

---

[1] Thom, Alexander; *Megalithic Sites in Britain.* Oxford: OUP, 1967

city. The shape, position, size, and overall characteristics of the pyramid are highly influenced by astronomical and mathematical references. For instance, the total number of steps which is equal to the number of days in their calendar. The position of the pyramid and its shape were studied to produce light and shade effects on solstices and equinoxes in offer to their god Kukulcan.

A closer example in time are Christian's edifices that are often oriented with the sunset or the sunrise. Some of them are even built as a function of summer solstices in order to enlighten a specific relic in a precise period of the year (e.g the cathedral of Chartres in France).

Other examples exist in other places, built by many other civilisations (e.g. Nazca Lines). But what remains is the alignment of monuments with astronomical objects as a kind of "tradition", dating back to Prehistory, Celtic epoch, Middle Ages, and even further. It is a beautiful example of how our ancestors associated their respective religions with the study of the sky to predict the seasons and understand their environment.

History of astronomy

In the History, astronomy not always inspired mankind to build the ceremonial monuments described previously. As civilisations developed, mostly in Mesopotamia, Greece, India, China, Egypt and Central America, the observation of the sky begun, trying to understand the nature of the Universe. First, the observations were done with the naked eyes and only dealt with the motion of the Sun, the Moon, planets, and bright stars. The Earth was believed to be at the centre of the Universe: it is the geocentric model or the Ptolemaic system (named after the Greek scientist Ptolemy).

Many technological and astronomical discoveries were done first by the Greek civilisations around the 2nd and 3rd centuries BC. Philosophers, mathematician, and astronomers were interested in the study of the sky. Among them we can cite Aristarchus of Samos (size of and distance to the Moon and the Sun, first to claim heliocentric model) or Hipparchus (astrolabe, precession effect). During the Middle Ages, the main discoveries were made in the Muslim and Chinese worlds. The study of galaxies and precise measurement of star motions are attributed to Persian and Arab astronomers between the 9th and 13th centuries.

The Renaissance and mainly the Enlightenment was for the european civilisations a great epoch of discoveries and major advances in astronomy. The proven heliocentric model by Nicolaus Copernicus, accepted and corrected by Galileo Galilei and Johannes Kepler was the biggest leap forward. The evolution of techniques (optic telescopes) helped astronomers such as Galileo to observe and understand our nearest celestial objects (the Moon, Jupiter's satellites). Kepler was the first to develop a theory behind the motion of planets but Isaac Newton was the one who put a law behind it: the law of gravitation. William Herschel developed a catalog of bright objects visible in the sky and he discovered the planet Uranus. Scientists such as Lagrange, Euler, Laplace, or D'Alembert have also contributed to the study of planets during the 18th and 19th centuries.

Later, the development of techniques (spectroscopy, photometry, interferometry) allowed to learn more about our own galaxy, the Milky Way, but not only. Edwin Hubble and his law gave a better understanding of the expanding Universe, Albert Einstein and his theory of relativity was a revolution. Modern astronomy is composed of various fields of research, classified by a specific kind of objects or energies in the electromagnetic spectrum. The development of numerous observatories on Earth but also space telescopes allows now to perform accurate observations of astrophysical objects. The 20th and now the 21th centuries are the era of the new astronomy: it is not only the study of moving objects but it is now the complete understanding of the dynamical and physical properties of the whole Universe and its complexity.

The origin of life

The development of astronomy and observational techniques led to a greater number of questions, and most of them are still unanswered. The most common question is of course: are we alone in the Universe? It is a question that has been the focus of mankind for ages and it is related to two other ones: how does life form? Why is there life on Earth? These are the first questions to answer in the search of our origin and it is partially responsible for the interest one can have in astronomy.

What is “life”?

In order to search for life, one must first understand the definition of it (Lovelock, 1965; McKay, 2004; Mautner, 2009). In the early 1960s, the chemist James Lovelock proposed the “Gaia hypothesis”, a definition which suggests to see life as a single organism on Earth. This idea has been criticised initially for being more philosophical rather than scientific. Later, this idea has been developed in the subject of geo-physiology and aims at studying the self-regulation of the Earth as a complex system: the regulation of the biosphere, of the atmosphere, of the surface temperature,... This idea of life is for sure not the common definition of it. It is the American biologist James Grier Miller who first defines life as we imagine it in his living system theory in 1978 (Sullivan and Baross, 2007). His theory sees life as an assembly of complex functions that are a part of a whole system which organises and develops itself. This system has been further developed by Koshland (2002) who characterised seven fundamentals traits called “*The Seven Pillar of Life*”:

- *Program*: reflects the fact that any living system is somewhat organised by a plan which describes its development. It is the role of the DNA.
- *Improvisation*: the ability to adapt in a sustainable manner over time in order to survive. *Improvisation* modifies the *Program* in response to environmental changes: it is the natural selection which leads to Darwin’s evolution theory.
- *Compartmentalisation*: any organism possesses multiple functions that are distributed within a unique system. Each function has an interaction with the others and they are confined in a limited volume.
- *Energy*: in order to exist, life needs energy. It is required not only to build it but also to maintain the different functions over time. For instance, energy can be found through the Sun, the heat of volcanoes or the environment in general.
- *Regeneration*: because nothing is eternal, even the simplest metabolism needs to regenerate its cells at some point. It is the biggest difference between a “living” machine and life. Every second, our body is recreating what it has already created. This idea is associated with the reproduction process: we start over and a new living system is built from scratch.
- *Adaptability*: this is different from *Improvisation* since *Adaptability* reflects the ability to survive in the environment with a behavioural response (answer to pain, reflexes,...) rather than a mutation of the *Program*.
- *Seclusion*: even a single cell is subjected to an incredible number of chemical and dynamical processes that occurs at the same time. *Seclusion* prevents all these reactions to dramatically interact with chaos thus each function has a role and it does not interfere with other functions if it is not supposed to. It is a role played by enzymes in a living system.

Gathered together, these seven pillars form what Daniel R. Koshland called the “PICERAS” principles (see Fig. 1). This definition of life as a complex living system has been widely spread for a few decades and has been a solid help for NASA to define their search for extraterrestrial life. This

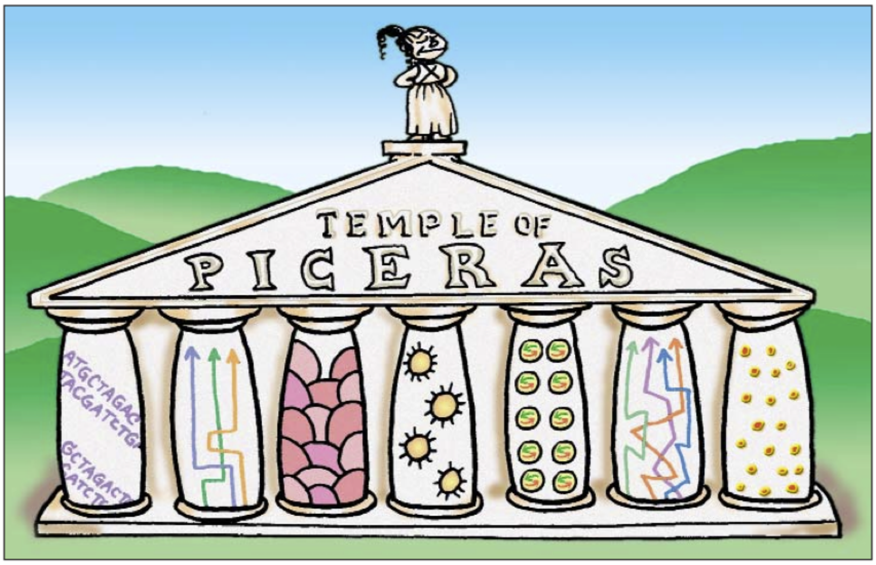

Figure 1 – Representation of "*The Seven Pillar of Life*" as seen by Daniel E. Koshland. Taken from Koshland (2002).

goal requires a more compact and conceptual vision of it and NASA proposed a shorter version of the definition of life as "a living chemical autonomous system able to survive and interact with its environment and led by a Darwinian open-ended evolution" (Ruiz-Mirazo et al., 2004).

The first bricks

We can now go back to the questions: how does life form and why is there life on Earth? We have set the definition of life thus we can now think about its origin. What is the common ancestor of life on Earth? Two theories are trying to explain it: the "genes-first" and the "metabolism-first" theories. Their goal is to find a path to form life from the simplest organic molecules to proto-cells. The first theory suggests that DNA was formed first since it encodes and synthesises proteins with polymers of amino acids. The other theory is that proteins formed first and led to the formation of RNA and DNA polymers. A more general theory suggests that they have both appeared separately. In this case, RNA would be the common ancestors (Gilbert, 1986; Szostak, 2009) since it shares many properties with DNA ("genes-first" theory) but is synthesised thanks to proteins ("metabolism-first" theory).

Therefore, DNA and mostly RNA are believed to be the first bricks of life in the primitive Earth. These nucleic acids are both formed from five different nucleo-bases: Adenine (A), Thymine (T), Cytosine (C), Guanine (G), and Uracil (U). DNA is composed of A, T, C, and G whereas RNA is formed from the combination of A, U, C, and G. They are basically nucleic acids macro-molecules of nucleo-bases. Experiments have shown that it is possible to form these nucleo-bases under the chemical and physical conditions of the early Earth. Such an experiment has been conducted for the first time by Stanley Miller and Harold Urey in 1952 (Miller-Urey experiment, Miller, 1953; Miller and Urey, 1959). As seen in Fig. 2, their experiment contains different parts:

- A heat source to reproduce the early Earth's high volcanic activities. It plays the role of the energy source, fundamental in order to create life as seen above (PICERAS theory).
- Water in a 500 ml flask close to the heat source to micmic oceans, where life supposedly arose from. This allows the water to evaporate and reach other chemicals.
- A 5 l flask filled with the molecular components of the primitive Earth's atmosphere: water (H_2O), methane (CH_4), ammonia (NH_3), and hydrogen (molecular form, H_2). Electrical sparks are produced inside the flask to simulate lightning in the gas.

- A condenser in order to recycle the water mixed with the molecular components. A sampling probe is located before the smallest flask to retrieve the newly formed molecules.

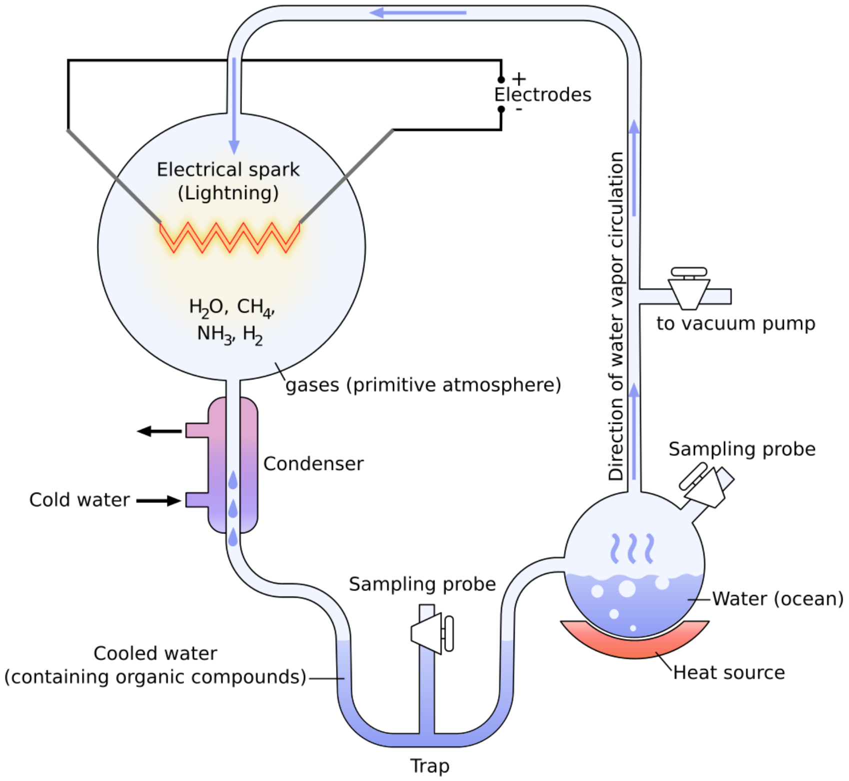

Figure 2 – The Miller-Urey experiment.

After one week, the solution contained the 20 known amino acids (Miller and Urey, 1959) contained in any living system such as glycine and the α- and β- forms of alanine (Miller, 1953). Other species were created during this experiment including hydrogen cyanide (HCN), cyanoacetylene (HC_3N), formaldehyde (H_2CO), and acetylene (C_2H_2). No nucleo-bases were formed during this experiment. Later, multiple experiments based on the Miller-Urey one were performed with various initial molecular gas mixtures, according to the possible compositions of the primitive Earth's atmosphere (Bada, 2013; Ruiz-Mirazo et al., 2014). In March 2015, NASA scientists have led a similar experiment under outer space conditions using pyrimidine initially. Pyrimidine is a Polycyclic Aromatic Hydrocarbons (PAHs) and has been already found in meteorites (Callahan et al., 2011). PAHs have been found in many different astrophysical objects and are the most carbon-rich chemicals found in space. Pyrimidine is also a fundamental component of uracil, cytosine, and thymine (see Fig. 3). For the first time they managed to build these nucleo-bases from ices containing pyrimidine exposed to UV radiations in high vacuum and low temperature (~ 10 K) conditions to reproduce interstellar conditions[2]. By freezing onto icy dust grains contained in interstellar clouds, pyrimidine shields itself from the destructive radiation field of the interstellar medium (ISM). Thus, pyrimidine can react with other molecules contained in the ice such as water but also methane, ammonia, methanol, or methane to form RNA and DNA nucleo-bases.

These experiments showed that it is possible, with the addition of energy, to build the first blocks of proteins and other macro-molecules comprised in any living organism from the chemical composition found both in the early phases of Earth and in interstellar clouds. The needed molecular (e.g. HCN, H_2CO) and complex organic compounds (e.g. pyrimidine, PAHs) are already observed in various stages of star and planet formation.

---

[2] `http://www.nasa.gov/content/nasa-ames-reproduces-the-building-blocks-of-life-in-laboratory`

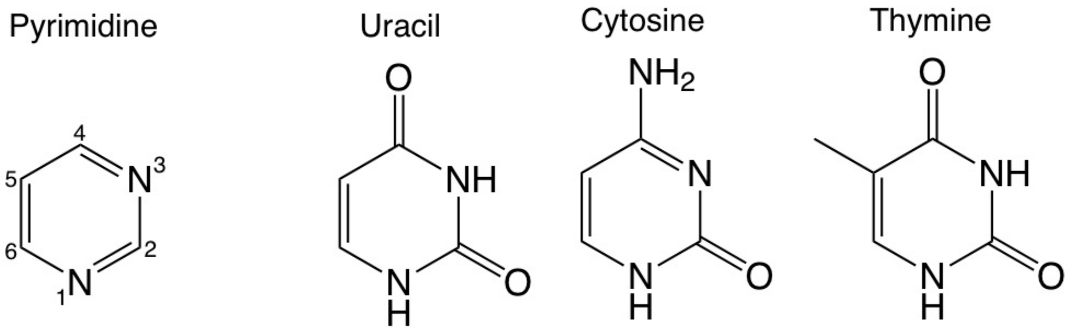

Figure 3 – Pyrimidine is the basis of uracil, cytosine, and thymine (nucleo-bases of RNA and DNA). Credits: NASA.

From dust to planets

The goal of astrochemistry is to study the chemical elements and molecules in space, as well as their formation, interactions, and destruction. Almost 200 molecules have been detected in the interstellar medium or circumstellar shells as of February 2016 (see Table 1). These molecules are composed of two to more than 12 atoms. The molecules used in the Miller-Urey experience for their primitive Earth's atmosphere (H_2, CO, H_2O, NH_3, and CH_4) have been detected as well as some output molecules (HCN, H_2CO, C_2H_2, and HC_3N).

One can note from this table that the number of detected molecules with five or more atoms is relatively large with respect to the number of diatomic molecules. This shows the incredible richness of the interstellar medium and the complex chemistry that occurs in it. These carbon-chain molecules are called Complex Organic Molecules (COMs) and are composed of more than two carbons, and other atoms such as hydrogen, nitrogen or oxygen: acetylene (C_2H_2), methyl formate ($HCOOCH_3$), acrylonitrile (C_2H_3CN), cyanoacetylene (HC_3N)... Note that the definition of "organic molecule" is different if we consider the chemical, rather than the astrophysical point of view: for the chemist, an organic molecule is a macro-molecule such as proteins or nucleo-bases. COMs help to form bigger organic molecules: the pre-biotic molecules. Molecules such as hydrogen cyanide (HCN) or formaldehyde (H_2CO) are important precursors of COMs thus they are at the base of the formation of pre-biotic molecules.

No amino acids nor nucleo-bases have been found in space until now, even if several attempts have been made to detect them in different star-forming regions. The search for glycine (NH_2CH_2COOH), the simplest amino acid, is still today one of the major goal of astrochemistry and astrobiology (Ceccarelli et al., 2000b; Kuan et al., 2003; Jiménez-Serra et al., 2014) but its detection has always been convincingly questioned (Hollis et al., 2003; Snyder et al., 2005) thus it is considered as not detected yet.

2 atoms	H_2	AlF	AlCl	C_2^{**}	CH	CH^+	CN	CO	CO^+	CP
	SiC	HCl	KCl	NH	NO	NS	NaCl	OH	PN	SO
	SO^+	SiN	SiO	SiS	CS	HF	$NO^{+?}$	$FeO^?$	O_2	CF^+
	$SiH^?$	PO	AlO	OH^+	CN^-	SH^+	SH	HCl^+	TiO	ArH^+
3 atoms	C_3^*	C_2H	C_2O	C_2S	CH_2	HCN	HCO	HCO^+	HCS^+	HOC^+
	H_2O	H_2S	HNC	HNO	MgCN	MgNC	N_2H^+	N_2O	NaCN	OCS
	SO_2	l-SiC_2	CO_2^*	NH_2	$H_3^{+(*)}$	SiCN	AlNC	SiNC	HCP	CCP
	AlOH	H_2O^+	H_2Cl^+	KCN	FeCN	HO_2	TiO_2	C_2N	Si_2C	
4 atoms	l-C_3H	l-C_3H	C_3N	C_3O	C_3S	$C_2H_2^*$	NH_3	HCCN	$HCNH^+$	HNCO
	HNCS	$HOCO^+$	H_2CO	H_2CN	H_2CS	H_3O^+	l-SiC_3	CH_3^*	C_3N^-	PH_3
	HCNO	HOCN	HSCN	H_2O_2	C_3H^+	HMgNC	HCCO			
5 atoms	C_5^*	C_4H	C_4Si	l-C_3H_2	l-C_3H_2	H_2CCN	CH_4^*	HC_3N		
	H_2CNH	H_2C_2O	H_2NCN	HNC_3	SiH_4^*	H_2COH^+	C_4H^-	HC(O)CN		
	NH_4^+	$H_2NCO^{+?}$	$NCCNH^+$	CH_3O	HCOOH	HC_2NC	HNCNH			
6 atoms	C_5H	l-H_2C_4	$C_2H_4^*$	CH_3CN	CH_3NC	CH_3OH	CH_3SH	HC_3NH^+	HC_2CHO	
	C_5N	l-HC_4H^*	l-HC_4N	l-H_2C_3O	$H_2CCNH^?$	C_5N^-	HNCHCN	NH_2CHO		
7 atoms	C_6H		CH_2CHCN		CH_3C_2H		HC_5N		CH_3CHO	
	CH_3NH_2		l-C_2H_4O		H_2CCHOH		C_6H^-		CH_3NCO	
8 atoms	CH_3C_3N		$HC(O)OCH_3$		CH_3COOH		H_2NCH_2CN		CH_3CHNH	
	CH_2OHCHO		l-HC_6H^*		$CH_2CHCHO^?$		CH_2CCHCN		C_7H	C_6H_2
9 atoms	CH_3C_4H		CH_3CH_2CN		$(CH_3)_2O$		CH_3CH_2OH		HC_7N	
	C_8H		$CH_3C(O)NH_2$		C_8H^-		C_3H_6		$CH_3CH_2SH^?$	
10 atoms	CH_3C_5N		$(CH_3)_2CO$		$(CH_2OH)_2$		CH_3CH_2CHO			
11 atoms	HC_9N		CH_3C_6H		C_2H_5OCHO		$CH_3OC(O)CH_3$			
12 atoms	l-$C_6H_6^*$		l-C_3H_7CN		l-C_3H_7CN		$C_2H_5OCH_3^?$			
>12 atoms	$HC_{11}N$		C_{60}^*		C_{70}^*		C_{60}^{+*}			

Table 1 – Molecules in the Interstellar Medium or Circumstellar Shells as of February 2016. Deuterated and fractionated species are not given in this table. * indicates molecules that have been detected by their rotation-vibration spectrum and ** those detected by electronic spectroscopy only. ? stands for tentative detections, weak line intensity, or (partially) overlapping lines. Source: CDMS website.

CHAPTER 1

ASTROPHYSICAL FRAME

Contents

1.1 Star formation

The formation of stars may be different between the low-mass ($\lesssim 8\,M_\odot$) and high-mass stars ($\gtrsim 8\,M_\odot$). The high-mass star formation is still not very well understood, involving different mechanisms than the low-mass star formation. However, some theories state that the formation process is the same, but scaled up for high-mass stars (Zinnecker and Yorke, 2007). One can distinguish several stages during the formation of a Sun-like star, shown in Fig. 1.1 and detailed below.

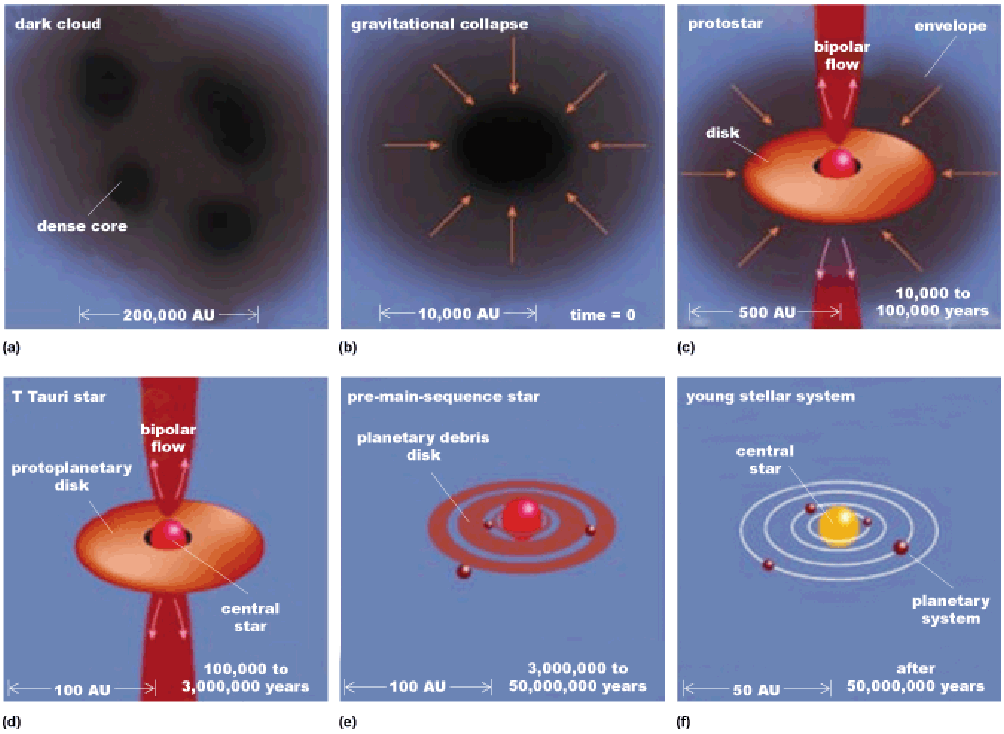

Figure 1.1 – Low-mass star formation stages. Credits: Spitzer Science Center.

Everything begins with a molecular cloud (a few parsec[1] wide), essentially composed of hydrogen (in the molecular form of H_2) and small dust grains (see panel (a)). The latter absorb the visible and UV radiation coming from neighbouring stars and re-emit it in radio frequencies. Therefore, such clouds are dark in the visible range, this is why they are call *dark clouds*. Under the effect of gravitational forces, the molecular cloud splits into several dense zones called *pre-stellar cores*. Each of theses cores has a high H_2 density ($\geq 10^5$ particles cm^{-3}, hereafter cm^{-3}) and a low temperature ($\sim 10\,$K). They are smaller than the original cloud, with a size of a few 10 000 AU (Astronomical Units; distance between the Earth and the Sun *i.e.* 1.496×10^{11} m). The pre-stellar core phase is considered as the start ($t = 0$) of the star formation process.

With the gravitational collapse, the density at the centre of the fragment rises, increasing the temperature: it is the *Class 0 proto-stellar* stage. From this step, the proto-star is surrounded by an envelope of gas and dust, remnants of the initial pre-stellar core, which will be the main source of accreting material from which the central object will grow, slowly increasing its mass (see panel (b)). The increasing energy coming from the angular momentum of the proto-star will lead to the emission of strong (bipolar) jets of matter, outflowing from the central object. Such objects emit in the millimetre and sub-millimetre range because the energy radiated by the central object is absorbed by the dust envelope. This cocoon of dust makes this object invisible to visible wavelengths and produces a strong emission at infrared wavelengths. No clue of disk formation has

---

[1] 1 parsec $\simeq 3.26$ ly

been detected yet in such young object due to the thick surrounding envelope. This phase lasts a few 10 000 yr.

With time, the envelope becomes thinner due to the mass accretion and the outflowing material, pushing the envelope away from the proto-star. When the mass of the envelope is smaller than the mass of the central object, the object becomes a *Class I proto-star*. The accretion of mass decreases and the forming disk can now be observed around the central proto-star. Outflowing material is still ejected, but the jet is less collimated and weaker than in the Class 0 stage (see panel (c)). The heated dust of the disk now emits at infrared wavelengths, dominating the spectral energy distribution (SED) of this kind of object. This phase lasts between a few 10 000 and 100 000 yr.

The total loss of the envelope marks the beginning of the *Class II proto-star* phase, also known as *classical T Tauri stars (CTTS)*, in reference of the T Tauri star located in the Taurus constellation. They are identified by the proto-planetary disk surrounding the central object. This is the reservoir of the future material from which planets will be formed. A weak outflow of material can still occur in this stage (see panel (d)). The emission of such objects is dominated by the strong infrared excess of the disk and the visible light coming from the central star. The size of these objects is only a few hundreds of AU. This phase lasts roughly between 1 to 10 millions years. Fig. 1.2 shows 4 different proto-planetary disks observed in the Orion nebula. The dust only composes 1% of the total mass of the disks (and 99% of gas) but it is enough to make them opaque and dark at visible wavelengths with respect to the bright background emission of the Orion molecular cloud. The red glows at the center is the young T Tauri star.

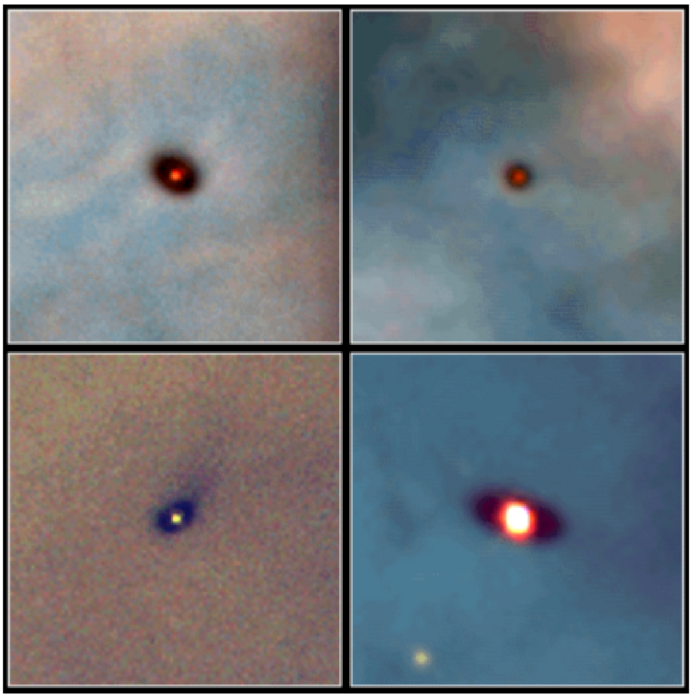

Figure 1.2 – Disks observed in absorption with the Hubble Space Telescope (HST) in the Orion constellation. Credits: NASA and the Space Telescope Science Institute.

With the formation of planetesimals, the proto-planetary disk becomes thinner and the infrared emission of the object decreases, marking the *Class III proto-stellar* phase. The spectral energy distribution of the source is now dominated by the black-body emission of the young star, also called *weak-line T Tauri stars (WTTS)* because of the fainter disk or even *naked T Tauri stars (NTTS)* if there is no proto-planetary disk at all.

Finally, planets are growing (during tens of millions years) while the central young star is contracting, increasing the temperature until it is hot enough to initiate the nuclear fusion reactions in its core. The star enters now the *pre-main sequence* phase. A debris disk is still rotating around the star (see panel (e)). Slowly, the stellar wind will blow the remnants of the disk away. The young stellar system now looks like our Solar System during its formation, 5 billions years ago (Evans, 1999; McKee and Ostriker, 2007).

Fig. 1.3 shows the classification of proto-stars as a function of the spectral energy distribution of the dust continuum emission (Adams et al., 1987; Andre et al., 1993; Andre and Montmerle, 1994; Andre, 1994).

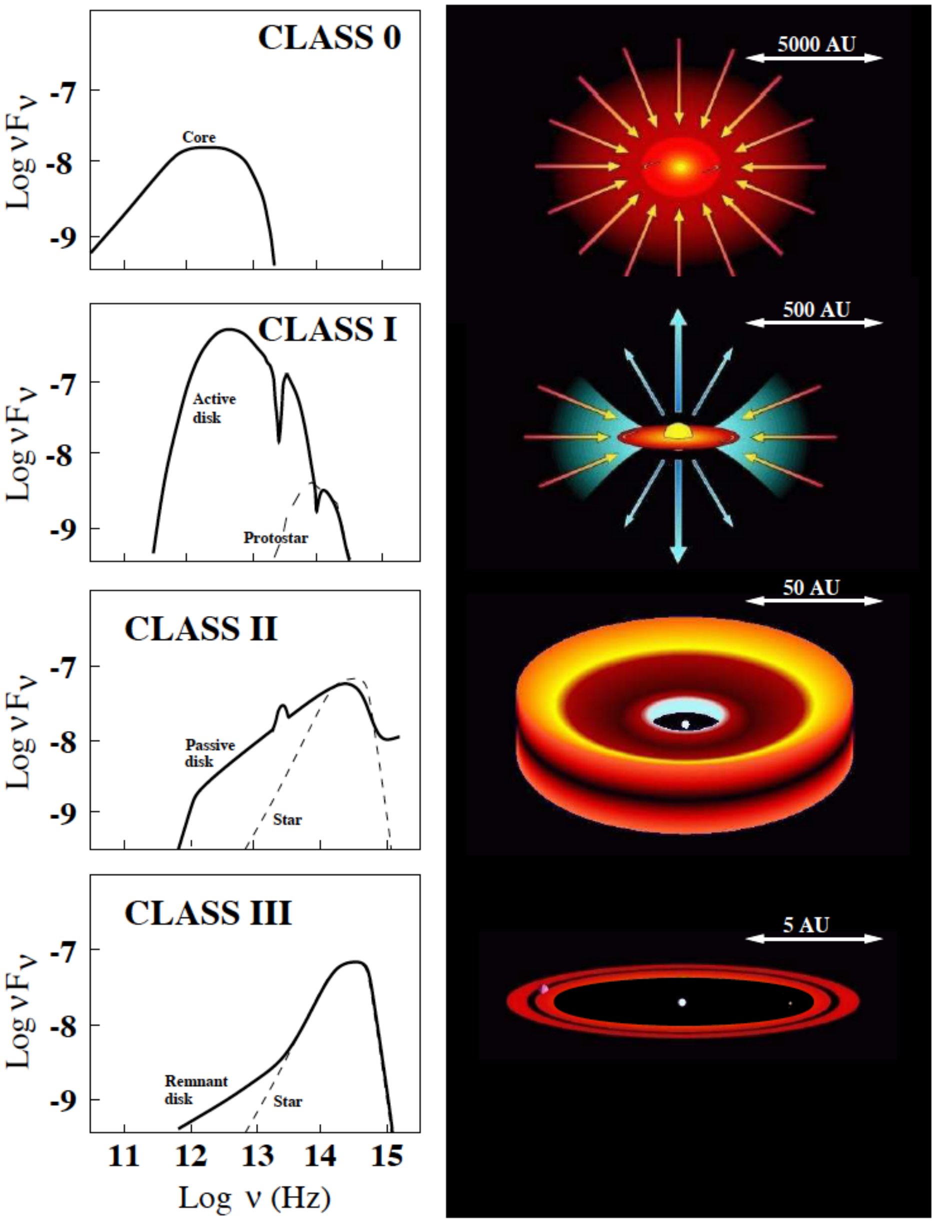

Figure 1.3 – A graphical overview of the four stages of proto-star evolution taken from Andrea Isella's PhD thesis (2006). A typical SED of each class is shown in the left column and a cartoon of the corresponding geometry is shown in the right column.

1.2 Chemistry in the Interstellar Medium

1.2.1 Processes and mechanisms

Molecules in the Interstellar Medium can be formed following different processes: chemical reactions in the gas phase, on the dust grain surfaces but also in the dust grain mantles. The physical conditions (temperature, density,…) have profound implications because they determine whether a reaction is possible or not. Both exothermic (but with an energy barrier: "activation barrier") and endothermic reactions can occur in space.

The different processes that govern the gas phase chemical reactions are organised in different categories (X, Y, and Z are atoms or molecules):

- **Formation processes:**
  - *Radiative association*: $\mathrm{X + Y \rightarrow XY + h\nu}$ or $\mathrm{X^+ + Y \rightarrow XY^+ + h\nu}$, slow process but highly efficient if one of the reactant is abundant (e.g. $\mathrm{H_2}$).
  - *Associative detachment*: $\mathrm{X^- + Y \rightarrow XY + e^-}$.
- **Destruction processes:**
  - *Photo-dissociation*: $\mathrm{XY + h\nu \rightarrow X + Y}$, mechanism responsible for the destruction of molecules in the external region of molecular cloud, where the UV radiation field is strong.
  - *Dissociation by cosmic rays (CR)*: $\mathrm{XY + CR \rightarrow X + Y}$. Cosmic rays are highly energetic particles (e.g. protons and atomic nuclei), coming from supernovae of massive stars in our galaxy.
  - *Photo-ionisation*: $\mathrm{X + h\nu \rightarrow X^+ + e^-}$.
  - *Ionisation by cosmic rays*: $\mathrm{X + CR \rightarrow X^+ + e^-}$. In dense cores, where UV radiation does not penetrate, cosmic rays are responsible for the formation of key ions such as $\mathrm{H_3^+}$ or $\mathrm{C^+}$.
  - *Dissociative electronic recombination*: $\mathrm{XY^+ + e^- \rightarrow X + Y}$, fast reactions at low temperature. They drive the ionisation level and so the reaction rates.
  - *Radiative electronic recombination*: $\mathrm{XY^+ + e^- \rightarrow XY + h\nu}$ or $\mathrm{X^+ + e^- \rightarrow X + h\nu}$, same as above but slow reactions.
  - *Electronic attachment*: $\mathrm{X + e^- \rightarrow X^- + h\nu}$.
- **Rearrangement processes:**
  - *Neutral-neutral reactions*: $\mathrm{X + YZ \rightarrow XY + Z}$, weak long range interaction (van der Waals interaction). These reactions can play a role at low temperature, but they are fundamental at higher temperature, such as reached in shocks, photo-dissociation regions or hot cores of proto-stars.
  - *Ion-neutral reactions*: $\mathrm{X^+ + YZ \rightarrow XY^+ + Z}$, these reactions often lack an activation barrier thus they are favoured in cold media. They allow to form molecules with increasing complexity.
  - *Ion-ion reactions*: $\mathrm{X^+ + YZ^- \rightarrow XY + Z}$.
  - *Charge-transfer reactions*: $\mathrm{X^+ + YZ \rightarrow X + YZ^+}$ or $\mathrm{X^+ + YZ^- \rightarrow X + YZ}$.

The 4 most important gas phase reactions are ion–molecule reactions, neutral–neutral reactions, photo-dissociation, and dissociative recombination.

The grain surface chemistry is fundamental in the chemistry of the interstellar medium. Two different formation mechanisms exist: the Langmuir-Hinshelwood formation by diffusion or the Eley-Rideal direct formation. The Langmuir-Hinshelwood formation by diffusion is the process described by:

1. *The adsorption*: it is a surface phenomenon in which species in the gas phase stick on a specific site onto the solid surface of dust grains, forming a mantle around the carbonaceous and silicate grain core. It can be a *physisorption* if the adsorbed species is linked to the surface with van der Waals forces or *chemisorption* if the adsorbed species is linked to the surface with covalent or ionic bonds. The adsorption depends on the collision rate r_c between a gaseous species and a dust grain:

   $$r_c = \sigma_g \, \langle v_{\rm mol} \rangle \, n_g \, n_{\rm mol}, \tag{1.1}$$

   with n_g the grains density, $n_{\rm mol}$ the molecular density, σ_g the geometric cross section (assuming a spherical grain, $\sigma_g = \pi a^2$, with a the grain size), and $\langle v_{\rm mol} \rangle$ the mean velocity of the molecular species, defined as:

   $$\langle v_{\rm mol} \rangle = \sqrt{\frac{8 k_B T}{\pi \mu_{\rm mol}}}, \tag{1.2}$$

   with k_B the Boltzmann constant, T the gas temperature, and $\mu_{\rm mol}$ the reduced mass of the molecule. By looking at previous equations, one can note that a higher molecular density will increase the collision rate, increasing adsorption. When adsorption occurs, atomic and molecular species are less abundant in the gas phase: it is the *depletion*. This effect is important in the inner regions of pre-stellar cores where the temperature is low (around 10 K) and the density is high. Particularly, the carbon monoxide CO and the molecular nitrogen N_2 deplete from the gas phase to stick into the grain surfaces. They will react with other species (e.g. H_2) to form more complex molecules such as the formaldehyde H_2CO and the methanol CH_3OH (hydrogenation of CO, Shalabiea and Greenberg, 1994; Watanabe and Kouchi, 2002). Depletion occurs at different temperatures depending on the molecule (for instance CO depletes at ~ 27 K and H_2O at ~ 100 K).

2. *The diffusion*: atoms and molecules can move from one site to another by thermal hopping or by quantum tunnelling. The mean distance between two sites is ~ 1.5 Å (1.5×10^{-10} m), travelled during a "hopping time" of $\sim 10^{-9}$ s. However, not all sites are fulfilled, thus several thermal hopping are required to encounter another atom or molecule. The total migration time between two occupied sites is $\sim 10^{-3}$ s (corresponds to a few millions of thermal hopping).

3. *The reaction*: when the reactants are on the same site, they will react following for instance atom-atom (e.g. $N + O \rightarrow NO$), radical-atom (e.g. $NO + H \rightarrow HNO$), radical-radical (e.g. $CH_3 + OH \rightarrow CH_3OH$), molecule-atom (e.g. $CO + O \rightarrow CO_2$), or radical-H_2 (e.g. $OH + H_2 \rightarrow H_2O + H$) reactions.

4. *The desorption*: finally, newly formed molecules can leave the surface to go back to the gas phase: it is the *desorption*. When the temperature increases, the thermal excitation of grains allows these molecules to desorb from the dust surface. This effect depends on the sublimation temperature of molecules, currently badly known for many species, and precise measurements in laboratories through temperature-programmed desorption (TPD) experiments are needed (e.g. Fraser et al., 2001; Collings et al., 2004; Burke et al., 2015; Fayolle et al., 2016). Thermal desorption is not the only desorbing mechanism: shocks and jets, eroding the grain surface, also desorb molecular species in the gas phase, populating cold regions with complex molecules. The exothermicity of a chemical reaction is also responsible of desorption, especially in cold regions (e.g. inner part of pre-stellar cores).

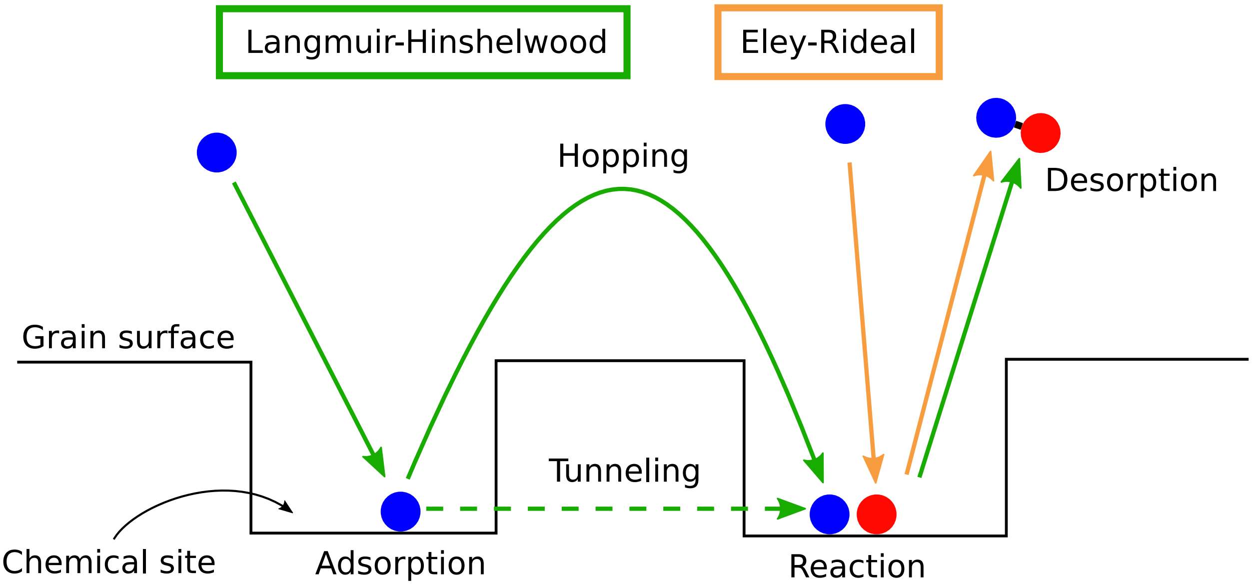

Figure 1.4 – Sketch showing the two different chemical mechanisms that occur onto the grain surface. Blue and red disks represent atoms and/or molecules.

These different steps are shown as a sketch in Fig. 1.4.

The Eley-Rideal direct formation mechanism uses the same processes as the Langmuir-Hinshelwood formation by diffusion except that the adsorption occurs on the same site as the reaction, and there is no diffusion (see Fig. 1.4). This mechanism requires the grain surface to be fulfilled of adsorbed species. This mechanism is more effective at high temperature.

Molecules such as CO_2, detected in the inner regions of molecular clouds, and the icy mantles (*i.e.* water) covering dust grains are perfect examples of the significance of grain chemistry, since these two molecules are weakly produced in the gas phase. Moreover, the high density of H_2, the most abundant molecule in the ISM, can only be explained thanks to the grain surface chemistry.

1.2.2 Chemical modelling

Let us consider the reaction between two bodies:

$$\mathrm{X} + \mathrm{Y} \xrightarrow{k} \mathrm{XY}, \tag{1.3}$$

where k is the constant rate of the reaction, defined as $k = \sigma\, v$ with σ and v the cross section and the mean velocity of reactants, respectively. The reaction rate at which the species XY is formed is given by the following equation:

$$\frac{\mathrm{d}\, n_{\mathrm{XY}}}{\mathrm{dt}} = k\, n_{\mathrm{X}}\, n_{\mathrm{Y}}. \tag{1.4}$$

with n the molecular densities of species X, Y, and XY. Most of these reactions have a constant rate given by the Arrhenius law:

$$k = \alpha \left(\frac{T}{300}\right)^{\beta} e^{-\gamma/T}, \tag{1.5}$$

with T the gas or the dust grain temperature. The coefficient α, β, and γ are gathered in chemical databases such as KIDA[2] (KInetic Database for Astrochemistry). For a reaction between one body and a cosmic ray, such as:

$$\mathrm{XY} + \mathrm{CR} \xrightarrow{k} \mathrm{X} + \mathrm{Y}, \tag{1.6}$$

---

[2] `http://kida.obs.u-bordeaux1.fr`

the constant rate is defined as $k = \alpha\,\zeta$ with ζ the cosmic ionisation rate. The standard value of the cosmic ionisation rate in molecular clouds is $\zeta \simeq 3 \times 10^{-17}$. This value can be higher by a factor of 50 in diffuse clouds. For a reaction between one body and a photon, such as:

$$\mathrm{XY} + \mathrm{h}\nu \xrightarrow{k} \mathrm{X} + \mathrm{Y}, \tag{1.7}$$

the constant rate is defined as $k = \alpha\, e^{-\gamma\, A_V}$ with A_V the visual extinction.

A chemical modelling always aims at predicting the density of one or several species, solving multiple reaction rate equations (such as Eq. (1.4)) at the same time. The complexity of a chemical modelling depends on the number of species and reactions involved as well as the physical properties of the studied object (static or dynamic description). Chemical networks gathering the previously described chemical processes for different species are needed. These networks can be built from databases such as KIDA, and so can gather thousands of gas phase and grain surface reactions, including hundreds of molecules and atoms. For instance, the latest update of the KIDA database (Wakelam et al., 2015) contains 489 different species composed of 13 elements and 7509 reactions, both in the gas phase and on grain surfaces.

1.3 Observations

1.3.1 What do we observe?

1.3.1.1 Molecular spectroscopy: basics

The only information an astronomer receives from space is the light emitted by the different objects. The light can be described either as a particle (a *photon*) or as an electro-magnetic wave. This particular concept, the *wave-particle duality*, exists because the properties of light cannot be fully explained by one or the other theory separately, but together they do. This electro-magnetic wave propagates in space carrying a certain amount of energy E determined by its wavelength λ (or its frequency ν) following:

$$E = \frac{hc}{\lambda} = h\nu, \tag{1.8}$$

with $h = 6.6260 \times 10^{-34}\,\mathrm{m^2\,kg\,s^{-1}}$, the Planck constant and $c = 299\,792\,458\,\mathrm{m\,s^{-1}}$, the speed of light. The full spectrum of light (shown in Fig. 1.5) ranges from radio frequencies to gamma (γ) rays, the lowest and highest energetic photons respectively.

One can note from this figure that the visible spectrum of light takes up just a narrow band of the full spectrum. The energy of a photon can also be expressed as a temperature:

$$E = k_B T, \tag{1.9}$$

where T is the absolute temperature (in Kelvin, K) and $k_B = 1.3806 \times 10^{-23}\,\mathrm{m^2\,kg\,s^{-2}\,K^{-1}}$ is the Boltzmann constant. A highly energetic photon is “hot” whereas a poorly energetic one is “cold”.

In the interstellar medium, molecules will interact with photons coming from everywhere. **These interactions only occur if the energy (or wavelength, or frequency) of a given photon corresponds to the energy of a molecule**. It is the golden rule of molecular spectroscopy.

1.3.1.2 Energy levels

The energy of a molecule is characterised by different processes, such as the excitation of its electrons or the different motions this molecule can adopt. It can be rotations around different axes, vibrations (stretching, bending, scissoring, rocking, wagging, twisting,...), or translations (see Fig. 1.6)

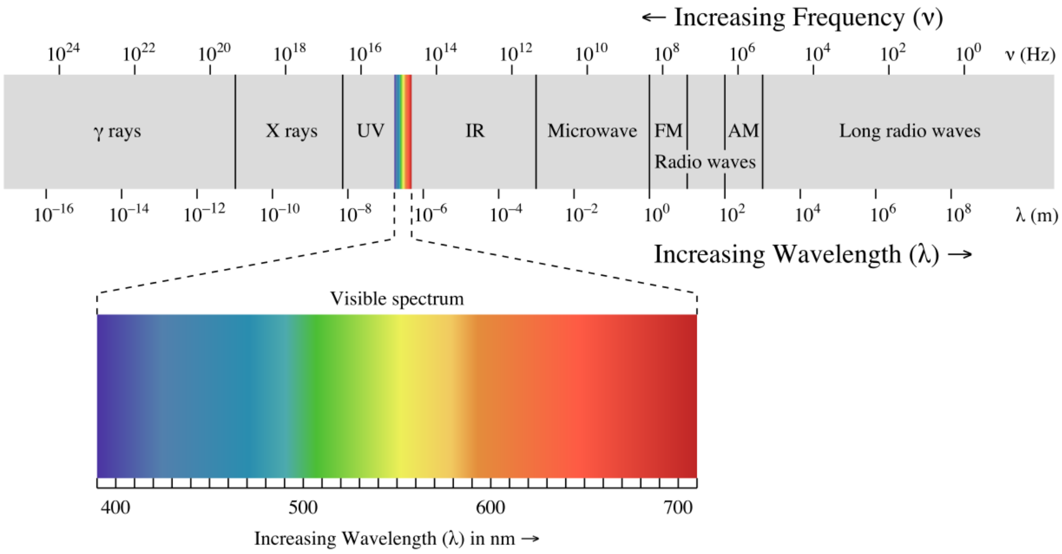

Figure 1.5 – Light electro-magnetic spectrum. Credits: Wikipedia/Philip Ronan.

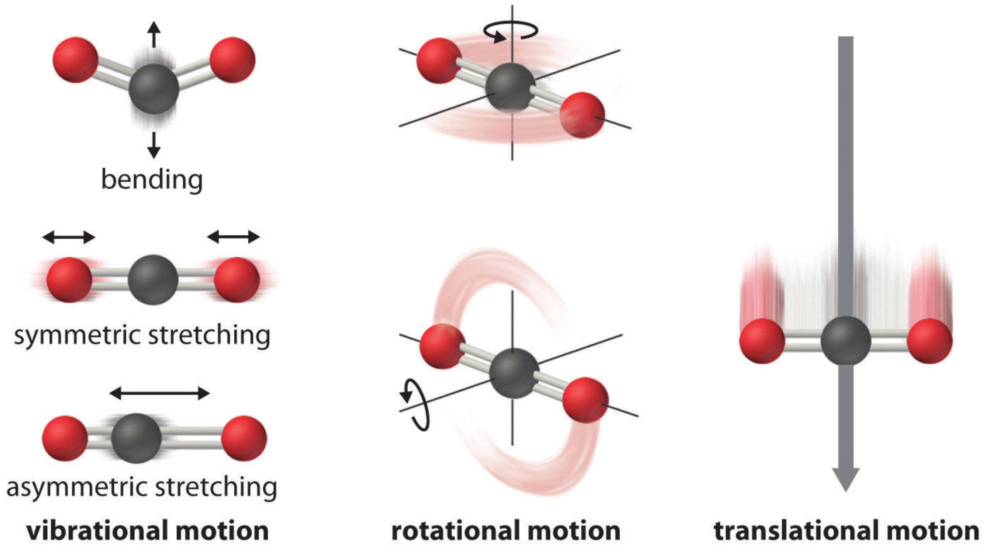

Figure 1.6 – Representation of the different movements a molecule can adopt. Taken from *Principles of general chemistry* (Martin Silberberg).

Energies associated to these different processes (electronic excitation, vibrations, rotations, translations) are **quantified** and define the different energy levels of a molecule (see Fig. 1.7). Each electronic level possesses several vibrational levels, in which are located several rotational levels.

A molecule at rest is in the *ground state* (level S_0 in Fig. 1.7) and the energy of this level is defined as E_0. This molecule can reach, for instance, the excited electronic level S_1, having an energy E_1, if it absorbs a photon having a specific energy $\Delta E = E_1 - E_0$ (see Fig. 1.7). The energy of the electronic transition between the level S_0 and the level S_1 is also ΔE. Vibrational, rotational, and translational transitions are defined the same way. Electronic transitions are more energetic than vibrational transitions ($\Delta E_{el} \gg \Delta E_{vib}$) because electronic energy levels are more spaced than vibrational levels, thus ΔE is larger. Similarly, vibrational transitions are more energetic than rotational ones ($\Delta E_{vib} \gg \Delta E_{rot}$).

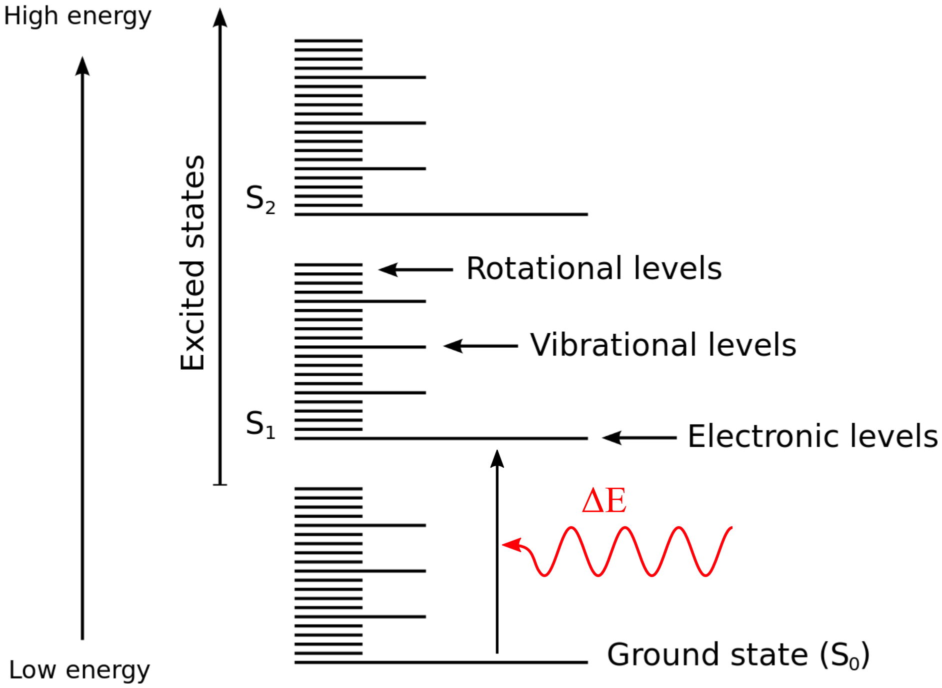

Figure 1.7 – Representation of the different types of transitions and their nesting. This molecule is absorbing a photon (in red) having an energy ΔE.

In the interstellar medium, where the temperature is low (ranging from less than 10 K to a few 100 K), only rotational transitions can occur because the energy required to go from a level to another is low enough. As a consequence, given Eqs. 1.8 and 1.9, molecules will only emit radio frequencies, within the millimetre/sub-millimetre wavelength range:

$$\lambda[\mathrm{mm}] = \frac{14.388}{\mathrm{T}}, \tag{1.10}$$

with T the absolute temperature of the photon and λ its wavelength. Nonetheless, in some environments where the temperature is higher, molecules may also emit in the infra-red range.

Rotational transitions are identified by the quantum number J. The $J = 0$ level is the ground state and rotational transitions are only permitted if $\Delta J = \pm 1$. Thus, when a molecule absorbs the right photon, it will go from the rotational level J (of energy E_J) to the level $J + 1$ (of energy E_{J+1}). Oppositely, when a molecule emits a photon, it will go from the rotational level J (of energy E_J) to the level $J - 1$ (of energy E_{J-1}).

These energetic levels can be calculated by solving the Schrödinger equation (quantum mechanics theory) or they can be determined with laboratories experiments. Properties of molecules are gathered in spectroscopic databases such as the Cologne Database for Molecular Spectroscopy[3] (CDMS; Müller et al., 2001, 2005), the Jet Propulsion Laboratory[4] (JPL; Pickett et al., 1998), or the National Institute of Standards and Technology[5] (NIST).

As an example, Fig. 1.8 shows the spectrum of the 46 first rotational transitions of the formyl ion (HCO^+) as a function of the frequency. These spectra are the signatures of molecules in space.

---

[3] `http://www.astro.uni-koeln.de/cdms/`

[4] `http://spec.jpl.nasa.gov`

[5] `http://www.nist.gov/pml/data/asd.cfm`

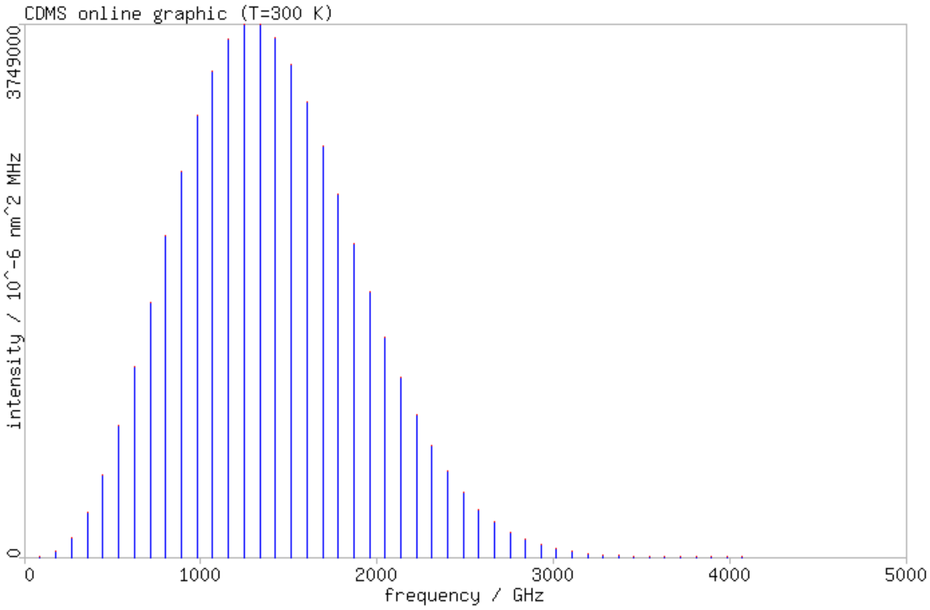

Figure 1.8 – Spectrum of the first 46 rotational transitions of HCO^+. The intensities of the transitions depend on the temperature, taken to be 300 K in this example. Taken from the CDMS website.

1.3.2 How do we observe?

1.3.2.1 Presentation of radio-telescopes

To observe these spectra in the sub-millimetre/millimetre radio band, astronomers uses two different kind of telescopes:

- *single-dish* telescopes, with only one antenna (e.g. the IRAM-30m, see Fig. 1.9),
- *interferometers*, composed of multiple antennas (e.g. ALMA, see Fig. 1.10).

Interferometers are powerful telescopes since they combine the observations by interfering the light coming from multiple antennas. They can produce an image that looks like as if it was taken from one large single-dish telescope.

Figure 1.9 – The IRAM 30 m single-dish telescope located on the Pico Veleta in the Spanish Sierra Nevada.

Figure 1.10 – The ALMA interferometer composed of 66 antennas, located on the Chajnantor plateau (Chile).

Dozens of radio-telescopes are spread around the world and three characteristics are important to determine which telescope best suits the needs of an astronomer, depending on the physical case studied: the location of the telescope, the observable frequencies available from the instruments (both spectral bandwidth and resolution to detect the signature of a targeted molecule), and the size of the antenna.

The latter will determine the angular resolution, *i.e.* the minimum spatial scale the telescope can resolve. For a single-dish telescope with an antenna diameter D, the angular resolution θ_B (in rad) is given by the general equation:

$$\theta_B = 1.22\,\frac{\lambda}{D}, \tag{1.11}$$

where λ is the observed wavelength. This formula depends on the apodisation and, in practice, it is recommanded to use the formula given by the telescopes' documentation. The higher the wavelength is, the poorer the angular resolution is and the observed object is badly resolved. A bigger antenna improves the angular resolution. For an interferometer, the angular resolution θ_I is determined by the baseline distance between the two most distant antennas B_{max}:

$$\theta_I \approx \frac{\lambda}{B_{max}}. \tag{1.12}$$

Ideally, observing with bigger antennas is always better, even for an interferometer, because more photons are collected, increasing the sensitivity of the signal received. The angular resolution of single-dish telescopes ranges commonly between $\sim 5 - 50''$ whereas for interferometers it can be as low as only a few milliarcseconds, depending on the frequency. With their poor spatial resolution, single-dish telescopes can recover extended emission whereas interferometers are better at studying the small scale structures of objects. However, interferometers cannot recover extended emission larger than

$$\theta_{LAS} \approx 0.6\,\frac{\lambda}{B_{min}}, \tag{1.13}$$

where θ_{LAS} is the angular resolution of the largest angular structure and B_{min} is the baseline distance between the two closest antennas.

During this thesis I have mostly used single-dish telescopes:

- The 30-metre single-dish telescope (presented in Fig. 1.9) of the Institut de Radio-astronomie millimétrique (IRAM) is located at an altitude of 2850 m. I went twice (2 × 1 week) to the telescope site to perform a spectral survey of different sources, including a survey of the pre-stellar core L1544 (presented in Chapter 3).
- The James Clerk Maxwell Telescope (JCMT). It is a 15-metre single-dish telescope on the summit of Maunakea, Hawaii, at an altitude of 4092 m.
- The Atacama Pathfinder EXperiment (APEX). It is a 12-metre single-dish telescope located at an altitude of 5105 m on the Chajnantor plateau in Chile.
- The *Herschel Space Observatory* (HSO). It is a ESA 3.5-metre telescope launched on the 14th of May 2009 by an Ariane 5 ECA rocket (shared with the Planck telescope). *Herschel* was orbiting around the Earth-Sun Lagrange point number 2 (L_2, a gravitational unstable point), located at about 1.5 millions km from the Earth. Science observing started in autumn 2009 and continued until the end of the mission on 29 April 2013. *Herschel* was sent to a "graveyard" heliocentric orbit around the Sun (see Fig. 1.11 for a goodbye photo of the telescope).

I have also used observations coming from interferometers:

- The Sub-Millimetre Array (SMA). It is composed of 8 antennas (6 metres each) located atop Maunakea in Hawaii at 4080 m. The 6 m dishes may be arranged to reach a maximum baseline of 509 m.

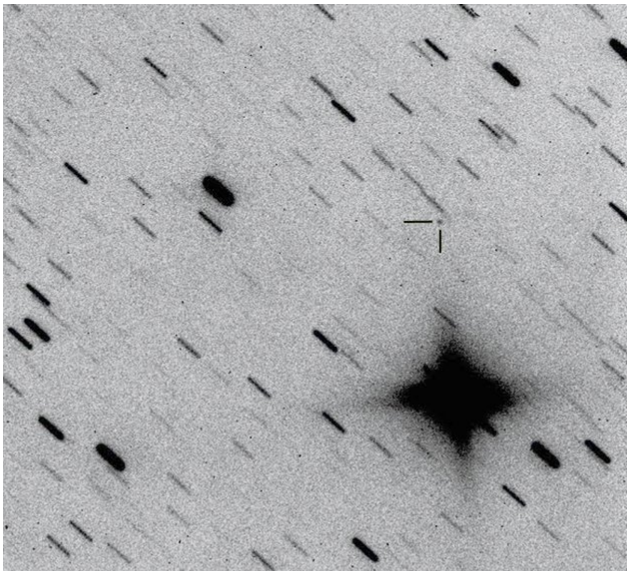

Figure 1.11 – Last picture of *Herschel*, the tiny dot located at the tip of the two lines, in contrast with stars in the background. This photo was taken by Nick Howes and Ernesto Guido with the 2-metre Faulkes North telescope (Hawaii).

- The Very Large Array (VLA). Located at 2124 m on the Plains of San Agustin (New Mexico, USA), it is one of the first radio interferometer. Composed of 27 antennas (25 metres each) distributed in a Y-shaped configuration, the maximum baseline of the VLA is 36 km.
- the Atacama Large Millimetre/sub-millimetre Array (ALMA), presented in Fig. 1.10, located at 5058 m on the Chajnantor plateau (Chile). The most powerful interferometer of its kind, composed of 66 antennas among which 54 are 12-metre dishes and the other 12 are 7-metre dishes. The maximum baseline of ALMA is 16 km.

1.3.2.2 Functioning of a radio-telescope

The distant signal is first collected by the primary parabolic reflector surface (the primary mirror) of the antenna, and reflected back to the sub-reflector (secondary mirror). The latter collimates the signal to the feed horn from which it is carried by cables (optic fibre) to the control room for processing (see Fig. 1.12).

The signal collected by the antenna is in reality a mix of several signals coming from different objects along the direction of the targeted source. These non-desired emissions are coming from the cosmic microwave background, the Earth atmosphere, or any astrophysical object located between the antenna and the object of interest. To get rid of most of these “disruptives”, during an observation, the antenna will alternatively observe the targeted position (ON spectra) and get a reference spectra (OFF spectra). To do so, several techniques exist:

- The Position Switching (PSW) technique: the whole antenna moves to be pointed alternatively to the targeted source (ON position) and to a nearby position (OFF position), a few tens of arc seconds away from the ON position.
- The Wobbler Switching (WSW) technique: the secondary mirror moves regularly to receive alternatively the signal from the ON and OFF positions. This technique can be used if the targeted source is not too extended (generally between a few tens arc seconds to a few arc minutes).
- The Dual Beam Switching (DSB) technique: used for the Herschel/HIFI instrument, an internal chopper mirror is used to move the beam to the OFF position, $3'$ away from the ON

position in the case of HIFI (de Graauw et al., 2010).

- The Frequency Switching (FSW) technique: the observing frequency (of the Local Oscillator) is changed. The antenna and the mirror do not move. Recommended technique if the source is too extended but one must be sure that the OFF position does not contain any spectral line from the ON position, hence not recommended if the spectrum is very line rich.

The remaining measured signal will be (taken from the IRAM-30m data-sheet):

$$T_{mes} = \mathrm{ON} - \mathrm{OFF} = \left(T'_A \exp\left(-\frac{\tau_0}{\sin(el)} \right) + T_{bg} \right) - T_{bg} \tag{1.14}$$

with el the elevation of the source, T_{bg} the background emission, T'_A the antenna temperature corrected from the atmosphere, and τ_0 the opacity of the atmosphere at the zenith. The antenna temperature corrected from both the atmosphere and the antenna losses is:

$$T^*_A = \frac{T'_A}{F_{eff}} \tag{1.15}$$

where F_{eff} is the forward efficiency of the telescope, defined as the fraction of the received power that enters the front lobe of the antenna.

Antenna temperatures cannot be compared directly to the brightness temperature T_b (emitted intensity by the object) predicted by theoretical models because they depend on the telescope used. It is necessary to convert them first into the main beam temperature T_{mb}:

$$T_{mb} = T^*_A \times \frac{F_{eff}}{B_{eff}} = \frac{T'_A}{B_{eff}} \tag{1.16}$$

where B_{eff} is the beam efficiency of the telescope, sort of effectiveness of the main lobe, defined as the fraction of the received power entering the main lobe.

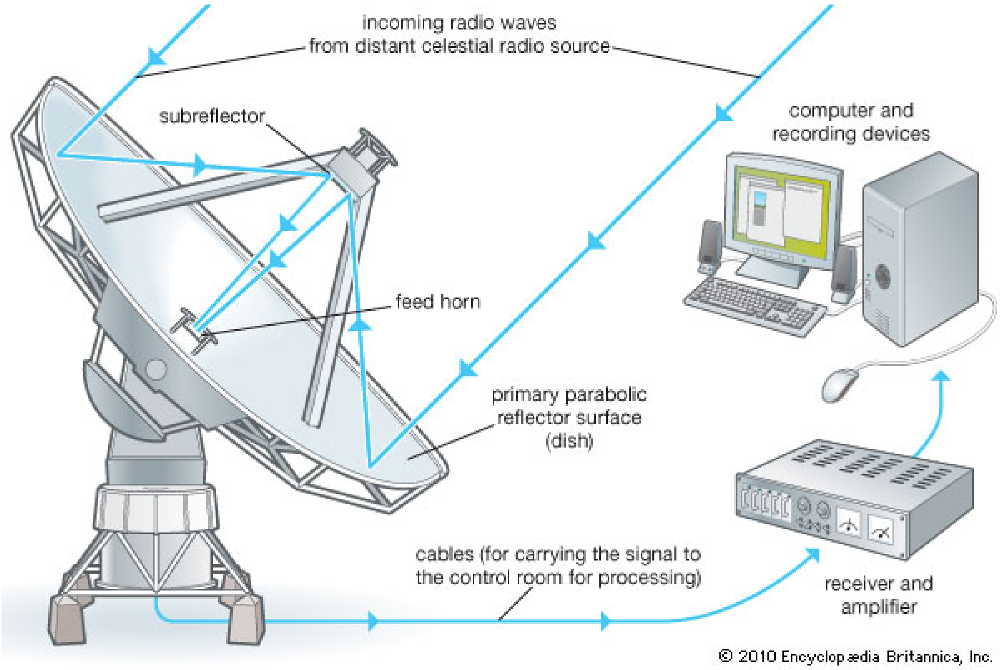

Figure 1.12 – Sketch showing the different components of the antenna of a single-dish telescope and its data processing pipeline.

Finally, the total power received from a source depends on the size of the telescope. To take into account this effect, the brightness temperature of the source is converted to the main beam temperature of a given antenna by:

$$T_{mb} = T_b \times \eta_{BD} \tag{1.17}$$

with η_{BD} the beam dilution defined as:

$$\eta_{BD} = \frac{\theta_S^2}{\theta_S^2 + \theta_B^2} \tag{1.18}$$

where θ_S is the source size and θ_B is the beam size.

1.3.2.3 Radio interferometry

Interferometers are composed of multiple single-dish antennas, thus the data processing is more complicated because it is necessary first to combine the signal coming from multiple antennas. Fig. 1.13 displays an example of an interferometer with only two antennas.

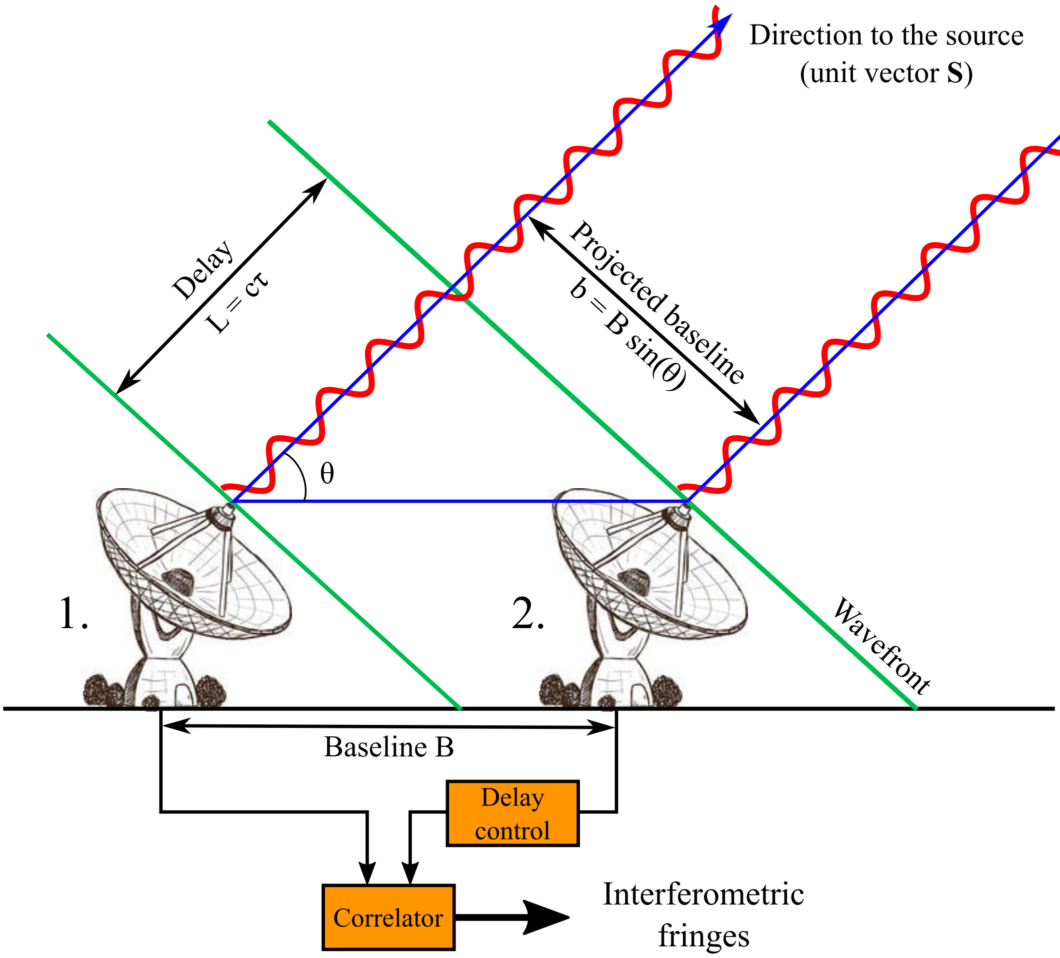

Figure 1.13 – Sketch showing the functioning of an interferometer with two antennas.

Two antennas are separated by a baseline distance B. These antennas are observing the same object, located so far away that the wavefront of the signal coming to the antennas can be considered as flat. In other words, the signal coming to the first antenna is parallel to the second one. As can be seen in Fig. 1.13, antenna 2 receives the signal before antenna 1. The phase shift in time between these two antennas is τ. The distance travelled by the light during this time is the spatial delay $L = c\tau$. Knowing the baseline distance B, it can also be expressed as:

$$L = B\,\cos(\theta) = c\tau, \tag{1.19}$$

where the angle θ is defined as the angle between the direction to the source and the baseline. The phase shift τ is taken into account to bring back the signal in phase for the radio correlator. In practice, antennas collect information coming from not just a single point but from an area of the sky. Therefore, a reference point known as the *phase tracking centre* $\vec{s_0}$ is defined. All other observed points are offset from this centre by a vector $\vec{\alpha}$, thus $\vec{s} = \vec{s_0} + \vec{\alpha}$ (see Fig. 1.14). To achieve that, an instrumental time delay is introduced so that the phase shift of $\vec{s_0}$ is 0. Therefore, all time delays in the signals are due to the positional offset $\vec{\alpha}$.

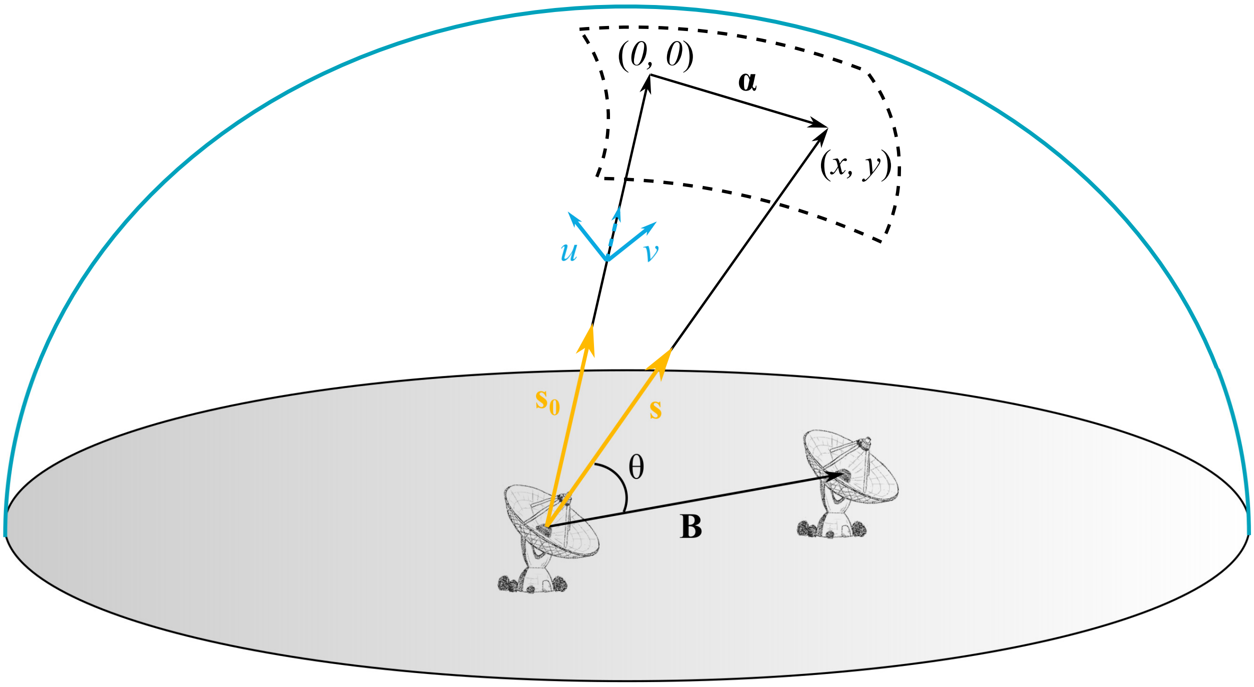

Figure 1.14 – Coordinates systems and vectors defined in this section. Bold letters indicate vectors.

From Eq. (1.19), one can write:

$$\tau = \frac{B\,\cos(\theta)}{c} = \frac{\vec{B}\cdot\vec{s}}{c} = \frac{\vec{B_\lambda}\cdot\vec{s}}{\nu}, \tag{1.20}$$

where $\vec{B_\lambda}$ is the baseline length measured in wavelengths of the observations (*i.e.* B divided by λ, both in metres). $\vec{B_\lambda}$ can be decomposed on the plane of sky into a set of components: u in the E–W direction and v in the N–S direction.

Let us consider a concrete example with $E_1(t)$ and $E_2(t)$, the electro-magnetic field coming to antenna 1 and 2 respectively:

$$E_1(t) = e_1 e^{2\pi i\nu(t+\tau)} \quad \text{and} \quad E_2(t) = e_2 e^{2\pi i\nu t} \tag{1.21}$$

where e_1 and e_2 are the intensities of the signal for each antenna, ν the observing frequency and t the time. The output of the correlator, the cross-correlation ($\otimes$) of the two signals, is the complex function $\Gamma_{1,2}$ given by:

$$\Gamma_{1,2}(\tau) = E_1 \otimes E_2 = \lim_{T\to\infty} \frac{1}{2T}\int_{-T}^{T} E_1(t)E_2^*(t)dt. \tag{1.22}$$

Using Eq. (1.21), the previous equation becomes:

$$\Gamma_{1,2}(\tau) = \lim_{T\to\infty} \frac{1}{2T} \int_{-T}^{T} e_1 e_2 e^{2i\pi\nu\tau} dt = e_1 e_2 e^{2\pi i\nu\tau}. \tag{1.23}$$

The real part of this function is thus a cosine wave as a function of θ, considering Eq. (1.20). One can re-write the previous equation:

$$\Gamma_{1,2}(\tau) = e_1 e_2 e^{2i\pi\vec{B_\lambda}\cdot\vec{s}} \tag{1.24}$$

The Van Cittert–Zernike theorem (van Cittert, 1934; Zernike, 1938), stands that the brightness temperature I of an astronomical object is linked to the cross-correlation of the signals received by all the antennas (and not only two):

$$\boxed{\Gamma(u,v) = \int_{-\infty}^{+\infty}\int_{-\infty}^{+\infty} I(x,y)e^{-2\pi i(ux+vy)}\,dx\,dy.} \tag{1.25}$$

It is assumed that Γ has been calibrated and scaled so that its units are in Jansky (Jy) thus ensuring that the units of the sky brightness I are in Jansky per beam area (Jy/beam). $\Gamma(u,v)$ is the Fourier transform of the brightness temperature $I(x,y)$, where x and y are the displacement in angle from the field centre $\vec{s_0}$, *i.e.* the coordinates of $\vec{\alpha}$. In astronomy, x and y are expressed in the equatorial coordinates therefore the couple (x,y) corresponds to a displacement in right ascension (ΔRA) and declination (ΔD) from the field centre:

$$x = -\Delta RA\cos(D) \quad \text{and} \quad y = \Delta D. \tag{1.26}$$

The (u,v) plane is also called the *resolution plane*. While observing, the Earth rotates and each pair of telescopes will give a portion of an ellipse on the (u,v) plane, even though antennas are not moving. Some part of the ellipse will be missing due to the source having set below the horizon (or because of a too low declination) or due to right ascension limitations of the telescopes. N telescopes in an array will give $N(N-1)/2$ baselines and hence $N(N-1)/2$ tracks in the (u,v) plane. Thus the data are sampled by a set of partial ellipses, with a data point taken every integrations period. Eq. (1.25) can be inverted to obtain the sky brightness temperature of the source from the cross-correlation function:

$$I(x,y) = \int_{-\infty}^{\infty}\int_{-\infty}^{\infty} \Gamma(u,v)e^{2\pi i(ux+vy)}\,dx\,dy. \tag{1.27}$$

The previous equation requires an infinite number of telescopes to fill the (u,v) plane so in practice a discrete transform is made to obtain the true sky brightness I_{true}:

$$I^{true}(x,y) = \sum_{j=1}^{M} \Gamma(u_j,v_j)e^{2\pi i(u_j x+v_j y)} \tag{1.28}$$

The quality of the image, *i.e.* the ability to recover $I^{true}(x,y)$, depends on the amount M of (u,v) plane data available. Generally, antennas of interferometers are arranged to browse the (u,v) plane in an optimum manner but there is a common rule that the more antennas in an array, the better the image will be.

1.3.3 Data analysis with CASSIS

During this thesis, I have used the CASSIS software[6] (Vastel et al., 2015) to analyse the properties of observation spectra. I have mostly used CASSIS for its line identification tool. To do

---

[6] `http://cassis.irap.omp.eu`

so, one selects a molecule from the spectroscopic database (implemented in CASSIS and based on JPL, CDMS, etc…) and the software indicates the frequency of all the possible transitions of this molecule. If several transitions match with several lines of the spectra, then the molecule is considered as detected. To use this technique, one needs to test all the molecules one after the other. It is possible with CASSIS to display all the transitions of several molecules at the same time (or even all the molecules of the database) but it is time-consuming to do so. Displaying several molecules at the same time is useful in order to disentangle whether a line is blended with another one or not. From the spectroscopic database, CASSIS displays several spectroscopic parameters of a given molecular transition, such as its frequency (ν), quantum numbers ($J, K_a, K_b, F \ldots$), Einstein coefficient (A_{ij}), upper energy level (E_{up}),…

When a line is identified, it is possible with CASSIS to perform a Gaussian fit of the line profile, varying the parameters of the following formula:

$$T(v) = I_0 \exp\left(-\frac{(v - v_0)}{2\sigma^2}\right). \tag{1.29}$$

I_0 is the peak intensity of the Gaussian (in K), v_0 is the velocity at the peak (in $\mathrm{km\,s^{-1}}$), and σ is related to the *Full Width at Half Maximum* ($FWHM$) by:

$$\sigma = \frac{FWHM}{2\sqrt{2\ln 2}}. \tag{1.30}$$

v_0 is the velocity of the source with respect to the Local Standard of Rest, denoted as V_{LSR}. This velocity can be calculated from the central frequency ν of a detected transition (*sky frequency*) by:

$$V_{LSR} = c\,\frac{\Delta\nu}{\nu_0} = c\,\frac{\nu_0 - \nu}{\nu_0}, \tag{1.31}$$

with c the speed of light in the vacuum ($\mathrm{c} = 299\,792\,458\,\mathrm{m\,s^{-1}}$) and ν_0 the frequency of the molecule at rest (*rest frequency*).

From the Gaussian fit, the total flux (or integrated intensity) of the line is also calculated by CASSIS, which is simply:

$$\int T(v)\,dv = I_0 \times \sqrt{2\pi\sigma^2}, \tag{1.32}$$

combined with Eq. (1.30):

$$\int T(v)\,dv = I_0 \times FWHM \times \sqrt{\frac{\pi}{4\ln 2}} \approx 1.065 \times I_0 \times FWHM. \tag{1.33}$$

In addition, a baseline fitting is also possible to obtain the *rms* (*root mean square*) of the spectra. This is determined in CASSIS thanks to the following equation:

$$rms = \sqrt{\frac{1}{N}\sum_{i=1}^{N}(T_i - \langle T_i \rangle)^2}. \tag{1.34}$$

where N is the number of data points of the spectra and T_i their intensity. For a single-dish telescope, the *rms* can also be expressed as a function of the system temperature T_{sys} which is the measured antenna temperature corrected from the atmosphere opacity:

$$rms \approx \frac{T_{sys}}{\sqrt{2\Delta\nu\, t_{int}}}, \tag{1.35}$$

with $\Delta\nu$ and t_{int} the spectral resolution and the integration time (on-source) of the observations. For an interferometer with N antennas, the equation is similar to the previous one:

$$rms \approx \frac{T_{sys}}{\sqrt{N(N-1)\Delta\nu\, t_{int}}}. \tag{1.36}$$

Multiplying the on-source time by a factor of 2 only decreases the noise by a factor of $\sqrt{2}$. The noise is also anti-correlated with the spectral resolution of the spectra hence smoothing the spectra also reduces the noise level. I consider a line as detected in the spectra, if the total flux of the line is greater than at least 3 times the uncertainty σ of its integrated intensity:

$$\sigma = \sqrt{\Big((1+x)\, rms\ \sqrt{2\,\Delta v\, FWHM}\Big)^2 + \Big(x\int T(v)\, dv\Big)^2}, \tag{1.37}$$

with Δv the spectral resolution in the velocity frame (units of $\mathrm{m\,s^{-1}}$) and x the calibration uncertainty.

The previously calculated parameters, alongside with the spectroscopic parameters of the desired molecular transitions, can be stored into a file and later used to perform rotational diagram analysis within CASSIS for instance.

Finally, it is possible with CASSIS to perform line modellings under the assumption of Local Thermodynamical Equilibrium (LTE, see Sect. 1.4.3) or Large Velocity Gradient (LVG, see Sect. 1.4.4.1). The LTE method is directly implemented in CASSIS whereas the LVG method is performed with the RADEX[7] code (van der Tak et al., 2007). To do so, CASSIS needs the column density of the molecule (N_{mol}), the excitation temperature (T_{ex}) for LTE modelling or the kinetic temperature (T_{kin}) for LVG modelling, the $FWHM$ of the line, and the source size (θ_S). It is possible to vary the different parameters of the LTE models, in order to derive the best fit model of the line profiles, by calculating a regular grid of models or using the *Monte–Carlo Markov Chain* (MCMC) method. The latter is the most performant one since it scans all the parameters at the same time (with a random walk), browsing the solution space by calculating an acceptance rate determined for each solution (which is either retained or rejected) until a final solution.

I widely used this CASSIS tool during a Master's degree internship to carry out an LTE and LVG analysis of the HCO^+ and N_2H^+ emission on the low-mass proto-star IRAS16293-2422. This work has been the starting point of the study described in Chapter 4.

1.4 Radiative transfer models

1.4.1 The radiative transfer equation

The radiative transfer aims to study the transport of photons through one or several different media. The principle is rather simple: how does the light emitted by a source reach a telescope? (see Fig. 1.15).

The answer to this question is found by solving the radiative transfer equation:

$$\boxed{\frac{dI_\nu}{ds} = j_\nu - \alpha_\nu I_\nu,} \tag{1.38}$$

with j_ν the emission coefficient and α_ν the absorption coefficient. By dividing the previous equation by α_ν, one obtains:

$$\frac{dI_\nu}{d\tau_\nu} = S_\nu - I_\nu, \tag{1.39}$$

---

[7] `http://home.strw.leidenuniv.nl/~moldata/radex.html`

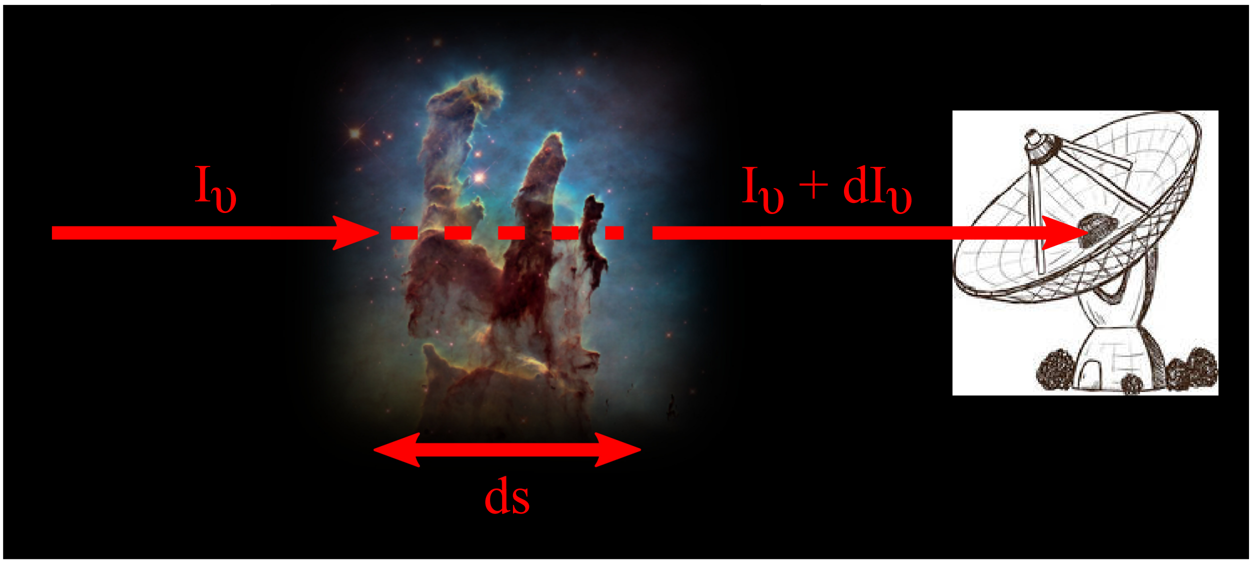

Figure 1.15 – The radiation I_ν coming from the left is modified by the interstellar cloud (of size ds), and becomes $I_\nu + \mathrm{d}I_\nu$ when received by the telescope.

where τ_ν is the optical depth (opacity) and S_ν is the source function (from the Kirchhoff's law of thermal radiation):

$$S_\nu = \frac{j_\nu}{\alpha_\nu}. \tag{1.40}$$

The optical depth is defined by:

$$\tau_\nu = \int_0^L \alpha_\nu ds, \tag{1.41}$$

with L the size of the object along the line-of-sight. If S_ν is constant, solving the differential equation (1.38) is rather simple and one obtains:

$$I_\nu(\tau_\nu) = I_\nu(0)e^{-\tau_\nu} + S_\nu(1 - e^{-\tau_\nu}), \tag{1.42}$$

where $I_\nu(0)$ is the background radiation, *i.e.* the Cosmic Microwave Background (CMB). From this equation, one can consider two cases depending on the optical depth of the source:

- the source is optically thin ($\tau \ll 1$), $e^{-\tau_\nu} \rightarrow 1$ hence $I_\nu(\tau_\nu) = I_\nu(0)$, the total emission is equal to the background emission,
- the source is optically thick ($\tau \gg 1$), $e^{-\tau_\nu} \rightarrow 0$ hence $I_\nu(\tau_\nu) = S_\nu$, the total emission is equal to the source function.

In Eq. (1.42), I_ν also contains this background emission, so to derive the source emission, $I_\nu^{src}(\tau_\nu)$, one needs to subtract it:

$$\begin{aligned} I_\nu^{src}(\tau_\nu) = I_\nu(\tau_\nu) - I_\nu(0) &= I_\nu(0)(e^{-\tau_\nu} - 1) + S_\nu(1 - e^{-\tau_\nu}), & (1.43) \\ &= (S_\nu - I_\nu(0))(1 - e^{-\tau_\nu}). & (1.44) \end{aligned}$$

If we are under the assumption of Local Thermodynamical Equilibrium (LTE), one can write:

$$\boxed{S_\nu = B_\nu(T_{ex}),} \tag{1.45}$$

where $B_\nu(T_{ex})$ is the Planck's function taken at the excitation temperature T_{ex}:

$$B_\nu(T_{ex}) = \frac{2h\nu^3}{c^2}\frac{1}{\exp(h\nu/k_B T_{ex}) - 1}, \tag{1.46}$$

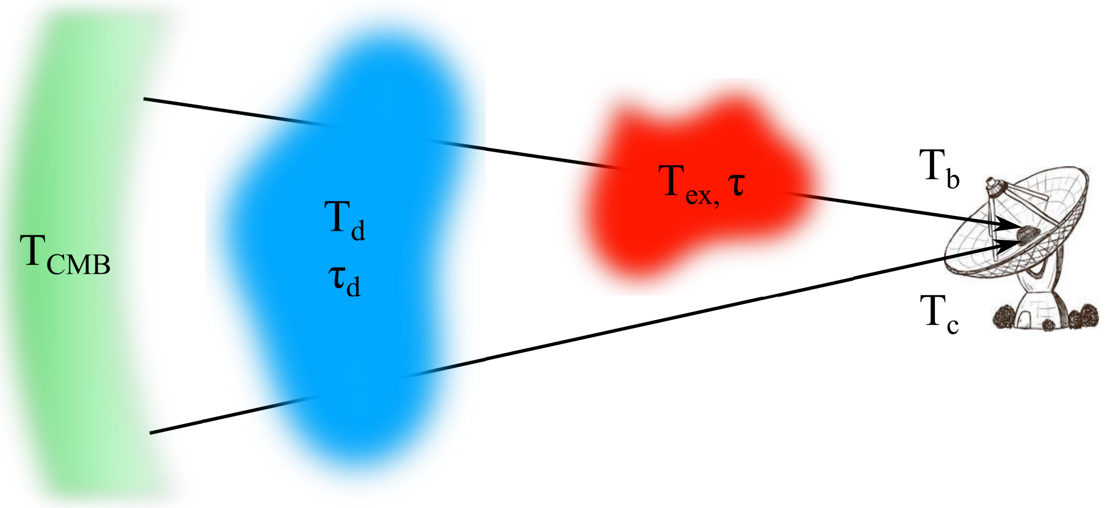

Figure 1.16 – Sketch showing the emission from a dust continuum source and a cloud. The brightness temperature of the continuum is T_c whereas the one of the cloud is T_b.

with h the Planck's constant, k_B the Boltzmann's constant, c the speed of light in the vacuum, and ν the frequency. Gathering Eqs. (1.45) and (1.46) into Eq. (1.43) one gets:

$$\begin{aligned} I_\nu^{src}(\tau_\nu) &= (B_\nu(T_{ex}) - B_\nu(T_{\text{CMB}}))(1 - e^{-\tau_\nu}) && (1.47) \\ &= \frac{2h\nu^3}{c^2}\left(\frac{1}{\exp(h\nu/k_B T_{ex}) - 1} - \frac{1}{\exp(h\nu/k_B T_{\text{CMB}}) - 1}\right)(1 - e^{-\tau_\nu}), && (1.48) \end{aligned}$$

where $T_{\text{CMB}} = 2.73\,\text{K}$ is the CMB temperature. The radiation I_ν^{src} coming from the source is defined by the Planck's function taken at T_b, the brightness temperature of the source (in K). Taking into account the latter and the Rayleigh–Jeans approximation, defined as the intensity of the Planck's function for $\lambda \gg \frac{hc}{k_B T}$ (or $h\nu \ll k_B T$):

$$I_\nu^{src} = B_\nu(T_b) = \frac{2k_B\nu^2}{c^2} T_b, \tag{1.49}$$

Eq. (1.47) becomes:

$$\boxed{T_b(\nu) = \frac{h\nu}{k_B}\left(\frac{1}{\exp(h\nu/k_B T_{ex}) - 1} - \frac{1}{\exp(h\nu/k_B T_{\text{CMB}}) - 1}\right)(1 - e^{-\tau_\nu}).} \tag{1.50}$$

To simplify the previous equation, one can define:

$$J_\nu(T) = \frac{h\nu}{k_B}\left(\frac{1}{\exp(h\nu/k_B T) - 1}\right), \tag{1.51}$$

so that Eq. (1.50) is finally written:

$$T_b(\nu) = (J_\nu(T_{ex}) - J_\nu(T_{\text{CMB}}))(1 - e^{-\tau_\nu}). \tag{1.52}$$

One can now consider a more general case, described in Fig. 1.16, with a background dusty cloud emitting a radio continuum (temperature T_d and opacity τ_d) coupled with a foreground cloud (temperature T_{ex} and opacity τ) along the line-of-sight.

The brightness temperature of the continuum is the following:

$$\begin{aligned} T_c &= J_\nu(T_{\text{CMB}})e^{-\tau_d} + J_\nu(T_d)(1 - e^{-\tau_d}) - J_\nu(T_{\text{CMB}}) && (1.53) \\ &= (J_\nu(T_d) - J_\nu(T_{\text{CMB}}))(1 - e^{-\tau_d}). && (1.54) \end{aligned}$$

For the foreground cloud, the brightness temperature is described by:

$$\begin{aligned} T_b &= J_\nu(T_{\text{CMB}})\, e^{-\tau_d}\, e^{-\tau} + J_\nu(T_d)(1-e^{-\tau_d})\, e^{-\tau} + J_\nu(T_{ex})(1-e^{-\tau}) - J_\nu(T_{\text{CMB}}) && (1.55)\\ &= (J_\nu(T_d) - J_\nu(T_{\text{CMB}}))(1-e^{-\tau_d})\, e^{-\tau} + (J_\nu(T_{ex}) - J_\nu(T_{\text{CMB}}))(1-e^{-\tau}). && (1.56) \end{aligned}$$

Combining Eqs. (1.53) and (1.55), one can obtain:

$$T_b = T_c\, e^{-\tau} + (J_\nu(T_{ex}) - J_\nu(T_{\text{CMB}}))(1-e^{-\tau}). \tag{1.57}$$

The intensity of line emission of the foreground T^{em}_{cloud} is then defined as:

$$\begin{aligned} T^{em}_{cloud} &= T_b - T_c && (1.58)\\ &= (J_\nu(T_{ex}) - J_\nu(T_{\text{CMB}}) - T_c)(1-e^{-\tau}), && (1.59) \end{aligned}$$

whereas the depth of an absorption line T^{abs}_{cloud} is:

$$\begin{aligned} T^{abs}_{cloud} &= T_c - T_b && (1.60)\\ &= (T_c - J_\nu(T_{ex}) + J_\nu(T_{\text{CMB}}))(1-e^{-\tau}). && (1.61) \end{aligned}$$

1.4.2 Two-levels radiative equilibrium

The emission coefficient j_ν used in Eq. (1.38) is defined by:

$$j_\nu = \frac{h\nu}{4\pi} n_u A_{ul} \Phi(\nu), \tag{1.62}$$

whereas the absorption coefficient α_ν is given by:

$$\alpha_\nu = \frac{h\nu}{c}\left(n_l B_{lu} - n_u B_{ul}\right)\Phi(\nu), \tag{1.63}$$

where u and l are two energy levels (see Sect. 1.3.1.2), respectively the upper and lower ones, having a population density n_u and n_l. A_{ul} is the Einstein coefficient for spontaneous emission, B_{ul} is the Einstein coefficient for stimulated emission, and B_{lu} is the Einstein coefficient for absorption. ν_0 is the frequency corresponding to the transition between the two levels ($E_{ul} = h\nu_0$). The Gaussian function $\Phi(\nu)$ reflects the probability that the emission may occur around the frequency ν_0 due to thermal excitation:

$$\Phi(\nu) = \sqrt{\frac{4\ln 2}{\pi(\Delta\nu)^2}}\, \exp\left(-4\ln 2 \frac{(\nu-\nu_0)^2}{(\Delta\nu)^2}\right). \tag{1.64}$$

This profile is normalised so that:

$$\int_{-\infty}^{+\infty} \Phi(\nu) d\nu = 1. \tag{1.65}$$

The spontaneous emission A_{ul} represents the probability (in s^{-1}) that a spontaneous de-excitation occurs between the upper and lower levels. It is defined by:

$$A_{ul} = \frac{16\pi^3}{3\epsilon_0 h c^3}\, \nu_0^3\, |\mu_{ul}|^2 \tag{1.66}$$

with μ_{ul} the dipolar moment matrix of the molecule, ϵ_0 the vacuum permittivity constant, and ν_0 the frequency of the transition. The different Einstein coefficients are linked by the following equations:

$$A_{ul} = \frac{8\pi h \nu_0^3}{c^3} B_{ul}, \tag{1.67}$$

and:

$$g_u B_{ul} = g_l B_{lu}, \tag{1.68}$$

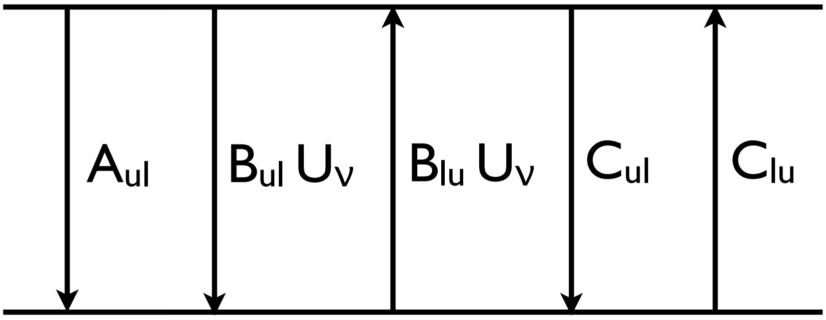

Figure 1.17 – Statistical radiative equilibrium between two energy levels.

where g_u and g_l are respectively the statistical weight of the upper and lower levels, expressed as $g_J = 2J + 1$ for the rotational transition of a linear molecule (e.g. CO, HCO$^+$, N$_2$H$^+$).

The upper and lower population densities, n_u and n_l are determined considering the statistical equilibrium between the different radiation and collision processes:

$$n_u(R_{ul} + C_{ul}) = n_l(R_{lu} + C_{lu}), \tag{1.69}$$

with C_{ul} and C_{lu} are probabilities for collisional de-excitations and excitations. These collisional rates are defined by:

$$C_{ul} = n\langle\sigma_{ul}v\rangle = n\gamma_{ul} \quad \text{and} \quad C_{lu} = n\langle\sigma_{lu}v\rangle = n\gamma_{lu}, \tag{1.70}$$

with n the number density of the particles responsible for the collisions (e.g. H$_2$, He, e$^-$), v their velocity and σ their cross-section. $\gamma = \langle\sigma v\rangle$ is gathered in molecular databases such as the Leiden Atomic and Molecular Database[8] (LAMDA, Schöier et al., 2005). R_{ul} and R_{lu} are probabilities for radiative de-excitations and excitations, respectively. In a radiation field a with monochromatic energy density U_ν, these upward and downward probabilities are respectively:

$$R_{lu} = B_{lu}U_\nu \quad \text{and} \quad R_{lu} = A_{ul} + B_{ul}U_\nu. \tag{1.71}$$

In the ISM, the radiation is isotropic hence one can write:

$$U_\nu = \frac{4\pi}{c}J_\nu, \tag{1.72}$$

with J_ν the local mean intensity of the radiation field:

$$J_\nu = \frac{1}{4\pi}\int I_\nu d\Omega. \tag{1.73}$$

Injecting Eqs. (1.71) in Eq. (1.69), one gets:

$$n_u(A_{ul} + B_{ul}U_\nu + C_{ul}) = n_l(B_{lu}U_\nu + C_{lu}) \tag{1.74}$$

The different emission and absorption processes are displayed in Fig. 1.17.

For a system with multiple levels, the previous equation becomes:

$$\boxed{n_l\left(\sum_{k<l} A_{lk} + \sum_{k\neq l}(B_{lk}U_\nu + C_{lk})\right)} = \boxed{\sum_{k>l} n_k A_{kl} + \sum_{k\neq l} n_k(B_{kl}U_\nu + C_{kl}),} \tag{1.75}$$

---

[8] `http://home.strw.leidenuniv.nl/~moldata/`

with:

$$\sum_i n_i = n_{tot}. \tag{1.76}$$

In Eq. (1.75), the part of the equation framed in blue corresponds to the spontaneous de-excitation, the spontaneous and stimulated emission, and the exciting and de-exciting collisions taken from the level l. On the other hand, the part of the equation framed in red corresponds to the same rates but directed to the level l.

This is a complex problem since U_ν is related to I_ν and n_k are related to the radiative transfer equation. To solve this, assumptions are made to reduce the difficulty of the problem (see Sect. 1.4.3 or 1.4.4.1) or the problem is numerically solved (see Sect. 1.4.4.2 and 1.4.4.3).

1.4.3 LTE modelling

1.4.3.1 Solution of the equation

Under the assumption of Local Thermodynamic Equilibrium (LTE), collisions govern the statistical equilibrium and $C_{ul} \gg A_{ul}, B_{ul}, B_{lu}$:

$$n_u C_{ul} = n_l C_{lu} \tag{1.77}$$

LTE happens when the temperature is really high or the collision partner density n is largely greater than the critical density n_{cr}, defined by:

$$n_{cr} = \frac{A_{ul}}{\gamma_{ul}} = \frac{n A_{ul}}{C_{ul}}. \tag{1.78}$$

Since population densities follow the Boltzmann distribution, one can write:

$$\frac{n_u}{n_l} = \frac{g_u}{g_l} \exp\left(-\frac{h\nu_0}{k_B T_{ex}}\right). \tag{1.79}$$

where T_{ex} is the excitation temperature of the transition. Moreover, collisional rates are defined by:

$$g_u C_{ul} = g_l C_{lu} \exp\left(\frac{h\nu_0}{k_B T_{kin}}\right), \tag{1.80}$$

with T_{kin} the kinetic temperature of the medium. Combining Eqs. (1.77) and (1.80), one gets:

$$\frac{n_u}{n_l} = \frac{g_u}{g_l} \exp\left(-\frac{h\nu_0}{k_B T_{kin}}\right). \tag{1.81}$$

Comparing Eqs. (1.81) and (1.79), one finally obtains:

$$\boxed{T_{ex} = T_{kin},} \tag{1.82}$$

The medium is said **thermalised**, excitation and kinetic temperatures are the same.

1.4.3.2 The Boltzmann diagram

The Boltzmann diagram or rotational diagram (because only involving rotational transitions) has been introduced first by Goldsmith and Langer (1999). This diagram is a graphical representation of the column density N_u of each level, divided by the statistical weight of this level, g_u as a function of this level's energy E_u. This diagram allows to know if the populations levels are at LTE and if the emission is optically thin or not. The column density of a level i is defined as:

$$N_i = \int_0^L n_i ds \tag{1.83}$$

with n_i the volumetric number density of the level i, L the size of the source along the line-of-sight, and ds the infinitesimal element of length along the line-of-sight. Considering the partition function (given by spectroscopic databases):

$$Q(T_{ex}) = \sum_i g_i \exp\left(-\frac{E_i}{k_B T_{ex}}\right), \tag{1.84}$$

in LTE and from Eqs. (1.79) and (1.83), one can write that the total column density N_{tot} is:

$$\begin{aligned} N_{tot} &= \sum_i N_i && (1.85) \\ &= \sum_i \frac{N_0}{g_0} g_i \exp\left(-\frac{h\nu_i}{k_B T_{ex}}\right) = \frac{N_0}{g_0} Q(T_{ex}), && (1.86) \end{aligned}$$

where N_0 and g_0 are respectively the column density and the statistical weight of the $J = 0$ transition whereas $h\nu_i = E_i - E_0 = E_i$ since $E_0 = 0$. Combining the previous equation with Eq. (1.84):

$$\begin{aligned} \frac{N_u}{g_u} &= \frac{N_0}{g_0} \exp\left(-\frac{E_u}{k_B T_{ex}}\right) && (1.87) \\ &= \frac{N_{tot}}{Q(T_{ex})} \exp\left(-\frac{E_u}{k_B T_{ex}}\right). && (1.88) \end{aligned}$$

Then passing to logarithmic scale:

$$\boxed{\ln\left(\frac{N_u}{g_u}\right) = \ln\left(\frac{N_{tot}}{Q(T_{ex})}\right) - \frac{E_u}{k_B T_{ex}}.} \tag{1.89}$$

Thanks to this equation, it is possible to plot the Boltzmann diagram. Plotting $\ln(N_u/g_u)$ as a function of E_u/k_B, one can write:

$$\ln\left(\frac{N_u}{g_u}\right) = a \times \frac{E_u}{k_B} + b. \tag{1.90}$$

which is the equation of a line with slope a and intercept b, defined by:

$$b = \ln\left(\frac{N_{tot}}{Q(T_{ex})}\right) \quad \text{and} \quad a = -\frac{1}{T_{ex}}. \tag{1.91}$$

From a and b (determined graphically) it is possible to derive the physical properties N_{tot} and T_{ex} of the molecule.

The previous equation does not take into account the effect of the opacity of the line. To do so, let us start with the definition of the opacity (see Eq. (1.41)):

$$\tau_\nu = \int_0^L \alpha_\nu ds, \tag{1.92}$$

Injecting Eq (1.63) in the previous equation, one gets:

$$\tau_\nu = \int_0^L \frac{h\nu}{c} \left(n_l B_{lu} - n_u B_{ul}\right) \Phi(\nu) ds, \tag{1.93}$$

One integrates the previous equation over dv knowing that $dv = c d\nu/\nu$:

$$\begin{aligned} \tau = \int \tau_\nu dv &= \int \left(\int_0^L \frac{h\nu}{c} \left(n_l B_{lu} - n_u B_{ul}\right) \Phi(\nu) ds\right) c\frac{d\nu}{\nu} && (1.94) \\ &= \int \left(\int_0^L h \left(n_l B_{lu} - n_u B_{ul}\right) \Phi(\nu) ds\right) d\nu. && (1.95) \end{aligned}$$

Since B_{lu} and B_{ul} do not depend on ν and taking into account Eq. (1.65), one can simplify:

$$\tau = h \int_0^L (n_l B_{lu} - n_u B_{ul}) ds. \tag{1.96}$$

With the definition of the column density given in Eq. (1.83) and Eq. (1.68):

$$\tau = h\,(N_l B_{lu} - N_u B_{ul}) = h\,B_{ul}\left(N_l \frac{g_u}{g_l} - N_u\right). \tag{1.97}$$

Combining with the Boltzmann distribution of Eq. (1.79) applied to column densities:

$$\tau = h\,B_{ul}\,N_u \left[\exp\left(\frac{h\nu_0}{k_B T_{ex}}\right) - 1\right]. \tag{1.98}$$

B_{ul} is related to A_{ul} by Eq. (1.67)

$$\tau = \frac{c^3}{8\pi\nu_0^3} A_{ul}\,N_u \left[\exp\left(\frac{h\nu_0}{k_B T_{ex}}\right) - 1\right]. \tag{1.99}$$

On the other hand, the opacity can be described as a Gaussian function (see Eqs. 1.41 and 1.64):

$$\tau_v = \tau_0 \exp\left(-\frac{(v - v_0)^2}{2\sigma^2}\right). \tag{1.100}$$

The summation over dv leads to:

$$\tau = \int \tau_0 \exp\left(-\frac{(v - v_0)^2}{2\sigma^2}\right) dv = \tau_0 \sqrt{2\pi\sigma^2} = \tau_0 \frac{FWHM\,\sqrt{\pi}}{2\sqrt{\ln 2}}. \tag{1.101}$$

By equalising the previous equation with Eq. (1.99), one finally gets:

$$\boxed{\tau_0 = \frac{c^3 A_{ul} N_u}{8\pi\nu_0^3 \frac{FWHM\,\sqrt{\pi}}{2\sqrt{\ln 2}}} \left[\exp\left(\frac{h\nu_0}{k_B T_{ex}}\right) - 1\right].} \tag{1.102}$$

From Eq. (1.50), with the assumption that $h\nu_0/k_B \gg T_{\text{CMB}}$, one can write the brightness temperature at the line centre:

$$T_b(\nu_0) = \frac{h\nu_0}{k_B}\left(\frac{1}{\exp(h\nu_0/k_B T_{ex}) - 1}\right)(1 - e^{-\tau_0}). \tag{1.103}$$

By artificially injecting τ_0 in the previous equation, one obtains:

$$T_b(\nu_0) = \frac{h\nu_0}{k_B}\left(\frac{1}{\exp(h\nu_0/k_B T_{ex}) - 1}\right)\left(\frac{1 - e^{-\tau_0}}{\tau_0}\right) \times \tau_0. \tag{1.104}$$

As for τ_ν, $T_b(\nu)$ can be described as a Gaussian function, hence:

$$\int T_b(v) dv = \int T_b(\nu_0) \exp\left(-\frac{(v - v_0)^2}{2\sigma^2}\right) dv = T_b(\nu_0)\,\frac{FWHM\,\sqrt{\pi}}{2\sqrt{\ln 2}} \tag{1.105}$$

Combining the previous equation with Eqs. (1.102) and (1.104):

$$W = \int T_b(v) dv = \frac{h\nu_0}{k_B}\frac{c^3 A_{ul} N_u}{8\pi\nu_0^3}\left(\frac{1 - e^{-\tau_0}}{\tau_0}\right), \tag{1.106}$$

where W is the integrated flux of the line. From the previous equation one derives:

$$N_u = W \times \frac{8\pi k_B \nu_0^2}{hA_{ul}c^3} \times C_\tau \tag{1.107}$$

with:

$$C_\tau = \frac{\tau_0}{1 - e^{-\tau_0}} \tag{1.108}$$

the opacity correction factor. If the line is optically thin ($\tau \ll 1$), $C_\tau = 1$ and one can easily calculate N_u using spectroscopic databases. If the line is optically thick ($\tau \gg 1$), C_τ cannot be neglected and the Boltzmann diagram is not a line anymore. With this new definition of N_u, Eq. (1.89) is now written in a general way:

$$\boxed{\ln\left(W\frac{8\pi k_B \nu_0^2}{hA_{ul}c^3 g_u}\right) = \ln\left(\frac{N_{tot}}{Q(T_{ex})}\right) - \ln(C_\tau) - \frac{E_u}{k_B T_{ex}}.} \tag{1.109}$$

While doing an analysis with the rotational diagram, a change in the slop of the line may occur in the plot, indicating one or a combination of the following causes:

1. the LTE assumption is not verified,
2. several sources (or components) are responsible for the total emission of the line,
3. lines are optically thick.

1.4.4 Non-LTE modelling

1.4.4.1 The “Large Velocity Gradient” method

The LTE method is the simplest one but it does not describe the majority of the studied physical cases. The LVG method (Large Velocity Gradient) or *escape probability* allows to decouple the population level calculation from the radiative transfer equation. This method has been introduced for the first time by Sobolev (1960) for an expanding sphere. This method works as follows: a factor $\beta(\tau)$ is added in the statistical equilibrium equation for population densities. This factor corresponds to the probability a photon produced locally at the optical depth τ can escape the studied system. The Sobolev approximation is only valid if the conditions of the gas do not change over the Sobolev length L_S, defined as:

$$L_S = \frac{v_{th}}{dv/dr}, \tag{1.110}$$

with v_{th} the thermal broadening of the line and dv/dr the velocity gradient. The Sobolev approximation applies if the size of the LVG cells L are smaller than the Sobolev length:

$$L < L_S. \tag{1.111}$$

This assumption is valid if the turbulence dominates the natural width of the line. Under the Sobolev approximation, photons emitted in the cloud can only interact with the closest molecules, reducing the problem of global transport of photons to a local problem. To do so, the probability β that a photon escapes is calculated: a fraction $1 - \beta$ of emitted photons stay in the medium whereas the other fraction β leaves. The local mean radiation is now expressed as:

$$J_\nu^{loc} = (1 - \beta)S_\nu + \beta\, J_\nu(T_{bg}). \tag{1.112}$$

If $\beta = 0$, $J_\nu^{loc} = S_\nu$ (ETL case) and if $\beta = 1$, $J_\nu^{loc} = J_\nu(T_{bg})$ corresponding to the optically thin case. As a consequence, locally, the equilibrium is defined by: net absorption = emitted photons that do not escape; putting this into an equation yields:

$$(n_l B_{lu} - n_u B_{ul})\, U_\nu = n_u A_{ul}\, (1 - \beta(\tau)). \tag{1.113}$$

Considering that, the equilibrium between the population levels (see Eq. (1.74)) is now written:

$$n_l C_{lu} - n_u C_{ul} - \beta(\tau) n_u A_{ul} = 0. \tag{1.114}$$

In this new form, the energy density U_ν does not in interfere in the population density calculation, which makes it much simpler.

This parameter $\beta(\tau)$ depends on the source geometry:

- For an expanding sphere:

$$\beta(\tau) = \frac{1 - e^{-\tau}}{\tau}, \tag{1.115}$$

- For a homogeneous slab:

$$\beta(\tau) = \frac{1 - e^{-3\tau}}{3\,\tau}, \tag{1.116}$$

- For an uniform sphere (determined by Osterbrock, 1974):

$$\beta(\tau) = \frac{1.5}{\tau}\left[1 - \frac{2}{\tau^2} + \left(\frac{2}{\tau} + \frac{2}{\tau^2}\right) e^{-\tau}\right]. \tag{1.117}$$

When the gas becomes optically thick ($\tau \gg 1$), the probability for a photon to escape the medium is considerably reduced, because of the "trapping" of emitted photons. In this case, the effective rate of spontaneous emission has to be reduced by the number of photons leaving the system:

$$A_{ul}^{eff} = A_{ul}\,\beta(\tau). \tag{1.118}$$

Hence the critical density n_{cr} is now described by:

$$n_{cr}^{eff} = \frac{A_{ul}\,\beta(\tau)}{\gamma_{ul}}. \tag{1.119}$$

This situation leads to more easily thermalised molecular levels since the critical density leading to thermalisation is reduced ($\beta(\tau) < 1$). The resolution of the LVG method is quite similar to the LTE method described in the previous Sect. 1.4.3, except that the term A_{ul} is replaced by $A_{ul}\,\beta(\tau)$ and the term U_ν is replaced by $(1 - \beta)S_\nu$ in the equations.

Starting from Eq. (1.114), one can write:

$$n_l\, n\, \gamma_{lu} = n_u\,(n\,\gamma_{ul} + \beta\, A_{ul}). \tag{1.120}$$

Combined with Eq. (1.80):

$$n_l\, n\, \gamma_{ul} \frac{g_u}{g_l}\, e^{-\frac{h\nu_0}{k_B T_{kin}}} = n_u\,(n\,\gamma_{ul} + \beta\, A_{ul}), \tag{1.121}$$

after some manipulations, it leads to:

$$\frac{n_u}{n_l} = \frac{g_u}{g_l}\, e^{-\frac{h\nu_0}{k_B T_{kin}}} \left[\frac{\beta\, A_{ul}}{n\gamma_{ul}} + 1\right]^{-1}. \tag{1.122}$$

Taking in account the Eq. (1.119):

$$\frac{n_u}{n_l} = \frac{g_u}{g_l}\, e^{-\frac{h\nu_0}{k_B T_{kin}}} \left[\frac{n_{cr}^{eff}}{n} + 1\right]^{-1}. \tag{1.123}$$

Moreover, if one equalises the previous equation with Eq. (1.79):

$$\begin{aligned}
\frac{g_u}{g_l}\, e^{-\frac{h\nu_0}{k_B T_{ex}}} &= \frac{g_u}{g_l}\, e^{-\frac{h\nu_0}{k_B T_{kin}}} \left[\frac{n_{cr}^{eff}}{n}+1\right]^{-1}, && (1.124)\\
\Leftrightarrow \quad \frac{h\nu_0}{k_B T_{ex}} &= \frac{h\nu_0}{k_B T_{kin}} \ln\left(\frac{n_{cr}^{eff}}{n}+1\right). && (1.125)
\end{aligned}$$

With some arrangement, one obtains:

$$\boxed{T_{ex} = \frac{T_{kin}}{1+\frac{k_B T_{kin}}{h\nu_0}\ln\left(\frac{n_{cr}^{eff}}{n}+1\right)}.} \qquad (1.126)$$

If $n \gg n_{cr}^{eff}$, hence $T_{ex} = T_{kin}$ and the line are thermalised (LTE case).

The RADEX (see Sect. 1.3.3) and LVG_GRE (Ceccarelli et al., private communication) codes both use the *escape probability* method. These two codes need in input the kinetic temperature T_{kin}, the collision partner density n, the molecular total column density N_{tot} and they give in output several pieces of information such as the integrated flux of the line $\int T_b dv$, the excitation temperature T_{ex}, or the opacity at the centre of the line τ_0. Both codes use molecular data files from the LAMDA database, in which they can find the spectroscopic parameters of the molecule ($\nu_{ul}, A_{ul}, g_u, g_l, E_l \dots$) and collisional rates (γ_{ul}) for one or several collision partner. These codes are limited by very high opacities and they do not treat correctly maser effects. Moreover, as seen previously, it is necessary to choose *a priori* a geometry to calculate β since the excitation depends on it: the shape and the size of this geometry can change the needed input total column density N_{tot}.

The drawback of RADEX and LVG_GRE is that they cannot directly treat efficiently the comparison between modellings and observations. Between the end of the Master's internship and the beginning of this thesis, I have developed a Graphical User Interface (GUI) that allows to generate LVG modellings from RADEX or LVG_GRE and then to compare them with observations. It is possible, thanks to the interface, to calculate a grid of models for several geometries and for several isotopologues of the same species at the same time and it is also possible to set a grid of isotopic ratio as well. The interface allows to directly compare the predicted and observed integrated fluxes as a function of upper energy levels. It is also possible to perform a χ^2 minimisation and to plot contour plots to determine error bars.

This interface has been entirely converted into a web-service application as part of the STOP[9] project led at the institute by Sandrine Bottinelli and Ivan Zolotukhin, also involving Emmanuel Caux and myself. The website is still under construction but it is already available for the community from the World Wide Web[10].

1.4.4.2 From 1D radiative transfer...

RATRAN[11] (Hogerheijde and van der Tak, 2000) is a non-LTE radiative transfer code based on the Monte–Carlo method. It only takes into account spherical symmetries, thus it is a 1-dimensional (1D) code. This code takes the point of view of cells and not the point of view of photons. This helps to separate local and external contributions of the radiation field. The advantage of this code is that it takes into consideration the source structure for the different physical parameters in input. Indeed, in general, it is important to define a precise physical structure of the source since

---

[9] Spectral TOols Platform - STOP duplicating work

[10] `http://stop-dev.irap.omp.eu/lvg`

[11] `http://www.sron.rug.nl/~vdtak/ratran/`

many gradients (e.g. in collision partner density and kinetic temperature) are present, depending on the radius. It is therefore necessary to give the values of these parameters for each layer of the spherical shell modelled from this 1D structure. These parameters are the collision partner density, the gas and dust temperature, the radial velocity, the b-doppler parameter, and the density of the studied molecule (linked to its abundance $[\mathrm{X}] = n_\mathrm{X}/n(\mathrm{H_2})$).

This code calculates the line profile and the dust continuum from the dust opacities given in input as a function of the wavelength. These dust opacities can be taken, for instance, from the tabulated files of Ossenkopf and Henning (1994). This code is suitable for optical opacities up to $10^3 - 10^4$.

From Hogerheijde and van der Tak (2000), the combination of radiative transfer and statistical equilibrium can be written as:

$$J_\nu = \Lambda \left[S_{ul}(J_\nu) \right], \tag{1.127}$$

where the operator Λ acts on the source function S_{ul}, which depends on level populations and hence J_ν. S_{ul} is defined as:

$$S_{ul} \equiv \frac{j_{\nu_0}(dust) + \int j_\nu^{ul}(gas)d\nu}{\alpha_{\nu_0}(dust) + \int \alpha_\nu^{ul}(gas)d\nu}. \tag{1.128}$$

This equation can be solved iteratively, and the following J_ν value is obtained from the previous population densities:

$$J_\nu = \Lambda \left[S_{ul}^\dagger(J_\nu) \right], \tag{1.129}$$

where the sign "†" refers to the adjoint matrix. Because of the notation presented in the previous equation, iterative schemes for non-LTE radiative transfer codes are commonly referred to as Λ-iteration, even if no Λ-operator is actually created. J_ν is estimated in a cell from the different contribution coming from all the different directions. The contribution of the different cells to the radiation field J_ν are summed along the propagation of the photon. Generally, the Monte–Carlo method allows to choose the random direction of these photons in the model (see Fig. 1.18), but it is not the method implemented in RATRAN. Indeed, the radiation field is calculated from the cell point of view, *i.e.* for each cell, only incoming rays are traced back to their origin at the edge of the cloud, where the boundaries conditions are met (considered to be the CMB, see Fig. 1.18).

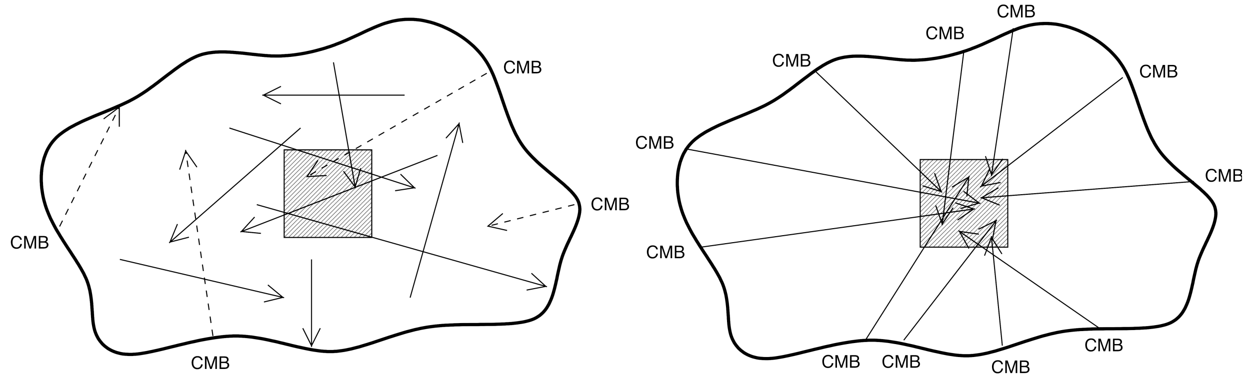

a) Monte Carlo method, taking photon point of view.

b) Monte Carlo method, taking cell point of view.

Figure 1.18 – Monte–Carlo method as seen from the photon points of view (top panel) and from the cell point of view (bottom panel). Figure adapted from Hogerheijde and van der Tak (2000).

The Monte–Carlo method used in RATRAN randomly choose the origin of this photon from the edge of the model. This process is coupled with the *Accelerated Lambda Iteration* (ALI, Rybicki and Hummer, 1991) defined by:

$$J_\nu = (\Lambda - \Lambda^\star) \left[S_{ul}^\dagger(J_\nu) \right] + \Lambda^\star \left[S_{ul}(J_\nu) \right], \tag{1.130}$$

with $\Lambda^\star$ an approximate operator. This methods allows to efficiently separate the local contribution to the radiation field from the global radiative transfer, reducing the calculation time, especially at high opacities. More details on the ALI method are given in Hogerheijde and van der Tak (2000).

RATRAN works in two stages called *amc* and *sky*. The first step (*amc*) calculates the population levels densities using the previously described method. The second stage (*sky*) calculates the distribution of emission for transitions defined by the user with the method called *ray-tracing*. This gives a hyper-spectral cube (3D data cube), two spatial dimensions and one dimension in velocity (giving the line profiles). This cube is convolved with the beam of the telescope taken at the frequency of the transition to obtain the line profile (T_{mb} as a function of the velocity), which can be compared to observations. The functioning of RATRAN is summarised in Fig. 1.19.

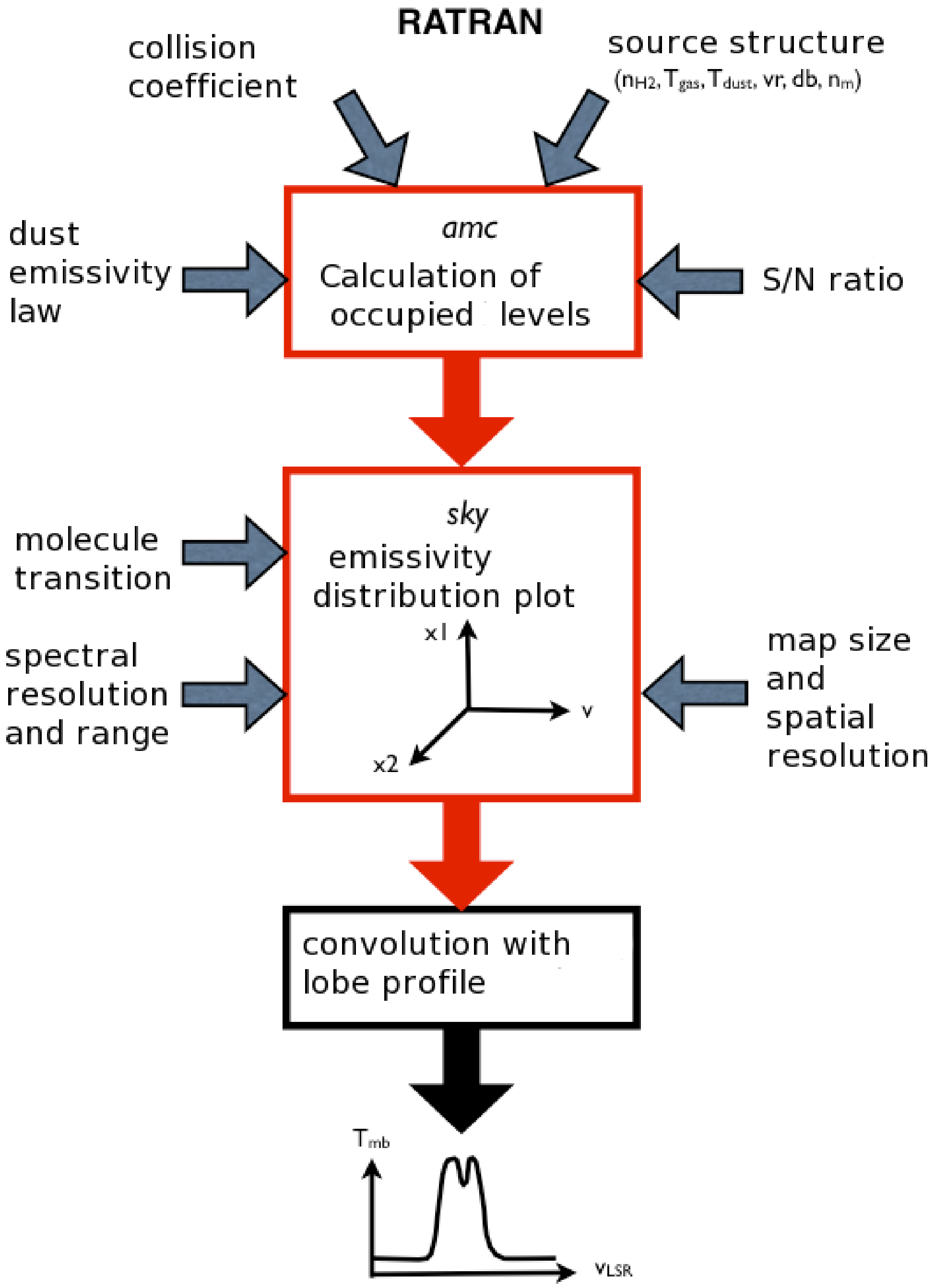

Figure 1.19 – Schematic view of the non-LTE radiative transfer code RATRAN. Adapted from (Coutens et al., 2012).

1.4.4.3 . . . To 3D radiative transfer

With the rising of interferometric observations, more and more precise details of the small scale structures of a source are resolved. The spherical symmetry is not sufficient to describe most of the observed source structure, and even if a different version of RATRAN allows to use a (2D) cylindrical symmetry, it is only available on a collaborative basis with the authors.

LIME[12] (Line Modelling Engine, Brinch and Hogerheijde, 2010) is a 3D non-LTE radiative transfer code based on the Monte-Carlo method coupled with an ALI treatment. It is mostly based on the structure of RATRAN, although rewritten from scratch, adapted to a 3-dimensional problem. It shares with RATRAN most of the code base and the solution method.

Nonetheless, there are differences between LIME and RATRAN and a benchmarking between the two codes is done in Sect. 2.6. The main difference between the two codes is the photon propagation method which considerably reduces the calculation time, making 3D models feasible to solve in a reasonable time, and allows for flexible model inputs. LIME is suitable to study various objects such as proto-planetary disks, envelopes, outflows, cluster of proto-stars,. . . As for RATRAN, one needs a good description of the input physical structure of the studied source.

Unfortunately, it can be extremely difficult to describe a complex 3D physical structures in the current version of LIME (v1.5). Indeed, in input, it is required to describe the physical structure of the source as a function of the Cartesian coordinates (x, y, z). For a complex 3D structure, for instance a cluster of proto-stars, it is practically impossible to describe the physical structure with mathematical functions, limiting the description one can made in input, restraining the 3D capabilities of LIME.

To circumvent the problem, I have developed during this thesis a code (GASS, Generator of Astrophysical Sources Structures, see the following Chapter) that allows to easily describe and generate complex 3D physical structures for LIME. I have used the combination of GASS and LIME to study different scientific cases, belonging to different star-formation stages (see Chapters 3 and 4). Throughout the next chapter, I describe the GASS code alongside some descriptions of the functioning of LIME.

---

[12] `http://www.nbi.dk/~brinch/index.php?page=lime`

"Il ne sert de rien à l'homme de gagner la Lune s'il vient à perdre la Terre."

François de Mauriac

This picture has been taken by the stratospheric balloon made by the children of the Astro-Jeunes Festival 2016. The (tiny) Moon is visible on the upper left corner of the picture.

CHAPTER 2

Modelling the 3D physical structure of astrophysical sources with GASS

Contents

2.1 Introduction

The ability to predict line emission is crucial in order to make a comparison with observations. Different modelling approximations and hypothesis can be considered depending on the complexity of the problem. From LTE to full radiative transfer codes, the goal is always to predict the physical properties of the source the most accurately possible. Non-LTE calculations can be very time consuming but are needed in most of the cases since many studied regions are far from LTE. A few freely usable codes are available such as RATRAN[1] (Hogerheijde and van der Tak, 2000) a 1D radiative transfer code, LIME (Brinch and Hogerheijde, 2010) a 3D one, MC3D[2], and RADMC-3D[3], both also 3D codes (see below).

Among the choice of 3D radiative transfer codes available to date, LIME is the only one doing a full non-LTE ALI (*Accelerated Lambda Iteration*) continuum and gas line radiative transfer treatment. Other available codes only offer a LTE or LVG gas line radiative transfer (RADMC-3D) or a dust continuum radiative transfer (MC3D and RADMC-3D). LIME is based on RATRAN and a benchmarking of the two codes has been made by Brinch and Hogerheijde (2010). LIME is well-suited for the treatment of most physical problems due to its performance and its flexible use: proper treatment of line blending, multiple species input, multi-line raytracing, and multi-core parallelisation.

I have developed a user-friendly interface, GASS (Generator of Astrophysical Sources Structure), in order to easily define the physical structure of a star-forming region and create input models for LIME. Thanks to its interface (see Appendix A), GASS allows to create, manipulate, and mix one or several different physical components such as spherical sources (see Section 2.3.1), disks (see Section 2.3.2), and outflows (see Section 2.3.3). Fig. 2.1 displays the organisational chart of GASS coupled with LIME. The functioning of GASS follows three distinct parts: *(1)* the grid generation, where GASS generates its “working zone” (region where the points of the grid are generated); *(2)* the creation of the physical models from the grid; and *(3)* the post-treatment analysis options, created to deal with output hyper-spectral data cubes (created by LIME for instance). As seen in Fig. 2.1, GASS is fully coupled to LIME but it can be easily adapted to any existing (or future) radiative transfer code. Once again, the main goal of GASS is the generation of 3D physical structures and the easy post-treatment of hyper-spectral data cubes. GASS is freely available for the community upon request (website in construction) as a standalone application for Mac OS X, Windows, and any Unix-based operating systems. A scripted MatLab version is also available.

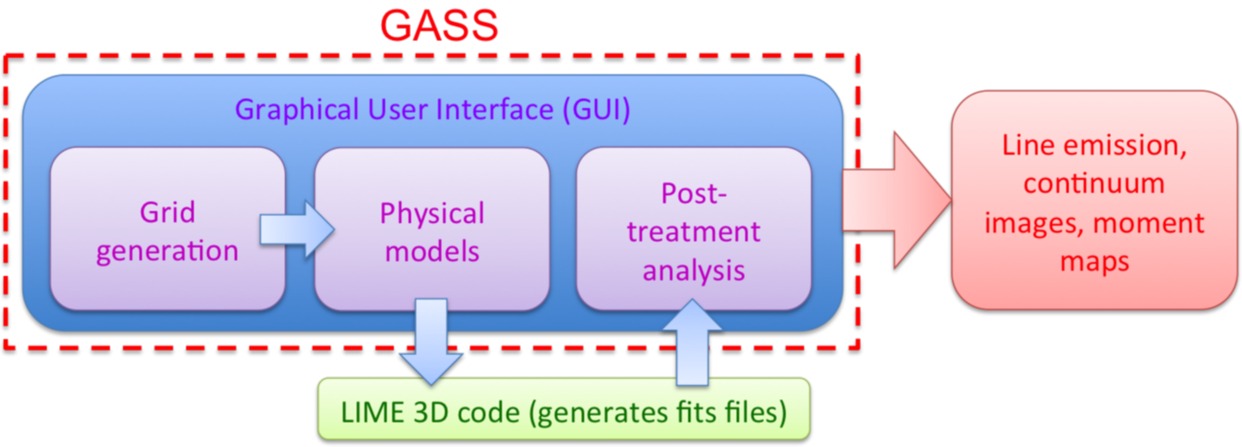

Figure 2.1 – Organisational chart of GASS coupled with LIME

---

[1] http://www.sron.rug.nl/~vdtak/ratran/

[2] http://www.astrophysik.uni-kiel.de/~star/index.php?seite=mc3d

[3] http://www.ita.uni-heidelberg.de/~dullemond/software/radmc-3d/

2.2 Grid generation

LIME requires models to be set in a cartesian grid that can be defined by two means: (a) from a script called `model.c` included directly in the LIME code that allows to define the physical properties very basically, for instance as a function of the radius without any complex 3D structure; (b) from an input model parameter file of the source in which the physical parameters (temperature, density, abundance,. . .) are described at each point of the cartesian grid. It is important to keep in mind that an input file is a huge gain in time since the model is created before giving it to LIME. Otherwise, LIME will generate its own grid as a function of the desired number of points and this step can be very time-consuming.

The model generation is entirely managed by GASS and the procedure is the following:

1. Creation of the random grid as a function of the number of points. In order to have a good convergence of the calculations, the advice is to use at least a few thousands points for the grid (Brinch and Hogerheijde, 2010). Each point is randomly distributed on the grid, depending on the desired structure. Points are always generated within the desired inner and outer radii of the grid. In the spherical source case, the distribution of grid points follows the density profile. Such a distribution leads to an increasing number of grid points per unit volume toward the centre to follow the distribution of the volume density across the spherical source. In the disk and outflow cases, considering their specific geometries, I decided to distribute the points equally all over their structure.

2. From this random grid, a Delaunay triangulation (Delaunay, 1934) is generated by connecting three neighbouring points. These points define the Delaunay circle and no other point of the grid lies in the circle.

3. From the Delaunay grid I can construct the Voronoï cells (Voronoï, 1908). Fig. 2.2 shows a sketch of how the Voronoï diagram is built from the Delaunay triangulation of the black dots. The three bisectors (in blue) of each Delaunay triangle (in red) define the centre of the circumcircle (in brown) of each triangle. This centre defines a vertex (green points) of the Voronoï diagram. Thus, each bisector of a Delaunay triangle is an edge of a Voronoï cell. By construction, two given points of the grid can thus be created much closer or further apart than desired. This leads to a very irregular Delaunay grid and an insufficient number of points in the grid will produce non-homogenous effects induced by the different sizes and shapes of the Voronoï cells. A few thousands points is the minimum required to avoid this effect.

4. The final step consists in smoothing the grid to reduce even more the previous effect. I based the smoothing on the Lloyd algorithm (Lloyd, 1982; Springel, 2010), which consists in moving every point in the centre of mass of its Voronoï cell. From the new points positions, the Delaunay grid is re-created and the process is repeated (items 3. and 4.). The number of iterations is limited to 10 to keep the randomness of the distribution. A great number of iterations will tend to completely smooth the grid and form a regular grid.

Fig. 2.3 displays the Delaunay triangulation and the Voronoï diagram before and after smoothing of a 2D grid. The points of the grid are plotted in red. The comparison between the two figures shows the impact of the smoothing algorithm after 10 iterations: the sizes of the Voronoï cells are more homogeneous at a given radius but the grid points are still distributed randomly.

As said above, GASS can generate three different structures (spherical sources, outflows, and disks). To illustrate the different point distribution and smoothing effect according to these different structures, I simulated them and the results are shown in Fig. 2.4 where the cumulated number of points in the grid as a function of the radius in arcsec are plotted. The blue and red

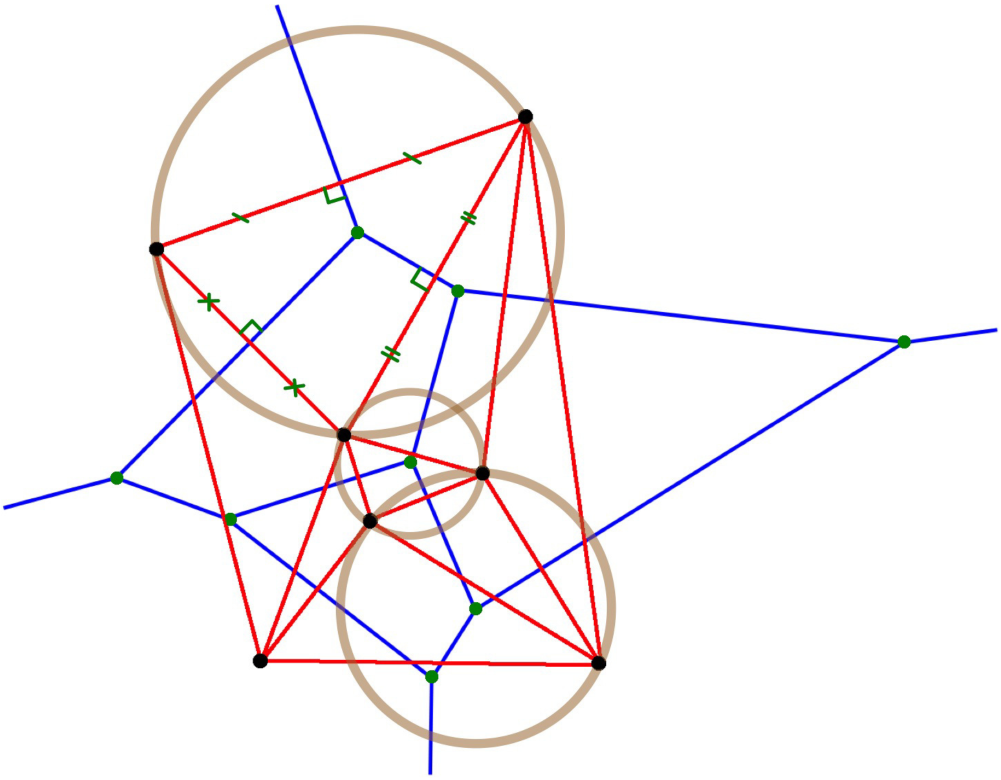

Figure 2.2 – Example of the Voronoï cells building. The black dots are the grid points and the red lines show the Delaunay triangulation from which the Voronoï cells are derived in blue. Three examples of the Delaunay triangle circumcircle are plotted in brown. One example of the three bisector construction in one Delaunay triangle is also displayed.

curves are the distribution of points before and after smoothing respectively. In the top panel, a spherical source located at 120 pc generated with 10 000 points distributed over a 50″ grid was considered. In this plot, one can notice that the smoothing process only moves the points in the 3D grid without affecting the distribution as a function of the radius. During the smoothing process, some of the points will be moved inside and outside of the inner and outer edges of the grid (in this example: 0.1″ for the inner edge and 50″ for the outer one), and these points are not included in the model anymore. To be sure that the minimum number of points will be at least around 10 000 points after rejection, 2.5% more points are arbitrary added (total of 10 250 points) during the creation of the grid. In this example, 239 points have been rejected after the smoothing process.

The spherical source grid generation is rather simple since I only need to consider the inner r_{in}^{sphere} and outer r_{out}^{sphere} radii of the sphere. These radii will be the boundaries in which the grid points will be generated following the previous description.

The case of the disk grid generation is slightly different since I also have to consider the inner cylindrical and outer spherical radii (ρ_{in} and r_{max}) and the maximum height (h_{max}) of the disk (see Fig. 2.5 and Section 2.3.2). This results in a different distribution of points compared to the spherical source. Indeed, grid points are generated over the entire volume of the cube defining the size of the modelled region, whereas the disk is a flattened structure, resulting in many points being generated outside of the edges. The Lloyd algorithm will then reject more points outside of the grid. To avoid this effect the number of iterations is limited to five and 5% more points are added in this case. The middle panel of Fig. 2.4 displays a simulation of a disk grid generation by setting a total number of 5,000 points, an inner and outer radii of 1″ and 10″ respectively. The maximum height of the disk is set to 2″. One can note from this figure that the Lloyd algorithm moves many

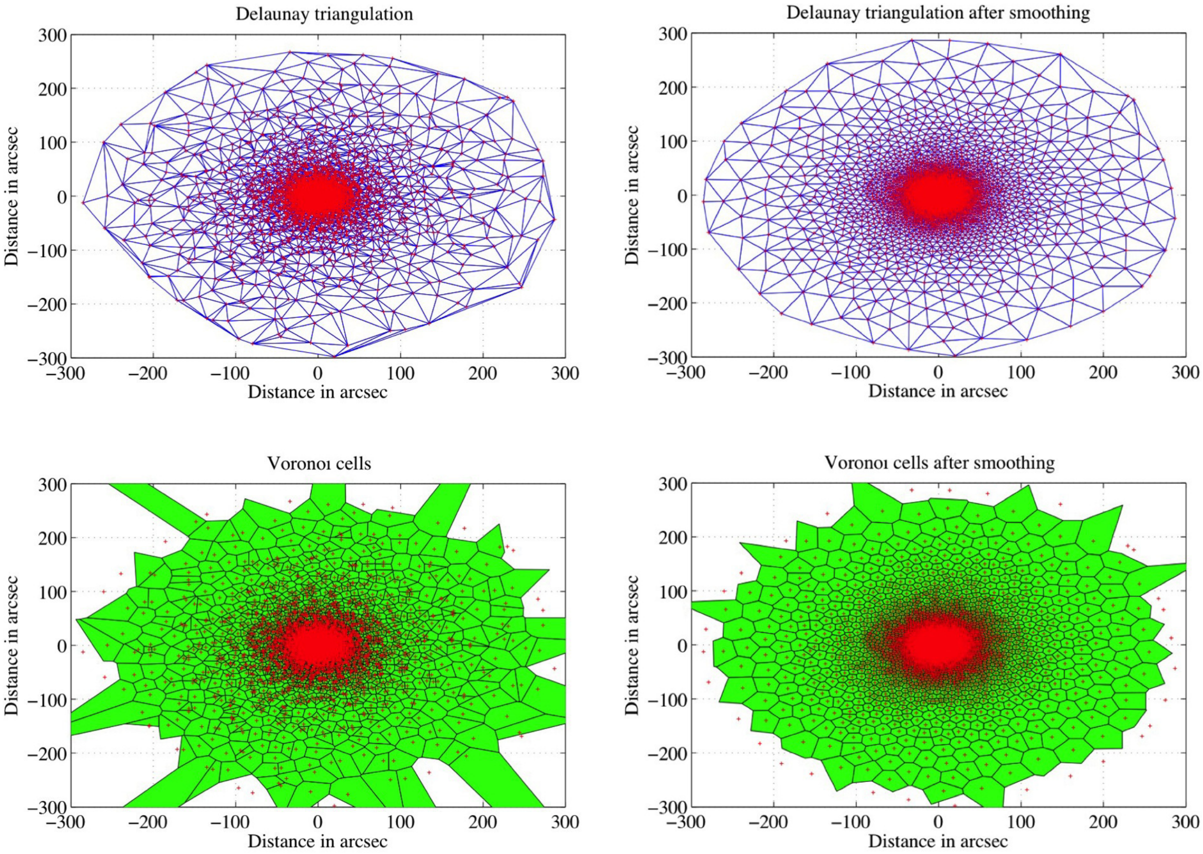

Figure 2.3 – The Delaunay triangulation (top panels) and Voronoï cells (bottom panels) before (left) and after (right) the smoothing process with the Lloyd algorithm. The grid points are shown in red.

points according to the different shape of the distribution before and after the smoothing process.

The outflow model is always considered attached either to a spherical source or a disk and cannot be created alone. Nonetheless, for the outflow the points generation is performed as it is done for the disk (see bottom panel of Fig. 2.4). In the outflow case I consider the inner cylindrical radius ρ_{in} and the maximum height z_{out} of the outflow (see Fig. 2.6). The cavity angle $\tan\gamma_{cav} = z_{outflow}/\rho_{outflow}$ is defined as the angle between the points and the mid-plane (see Fig. 2.6). Each point of the grid is generated between γ_{cav} and $\gamma_{cav} + \Delta\gamma$ where $\Delta\gamma$ is set by the user and defines the width of the cavity wall (see Section 2.3.3 for more details about the cavity walls). The smoothing process is here also limited to five iterations to avoid a great number of points to be moved outside of the model and 5% more points are added as in the disk generation process. The bottom panel of Fig. 2.4 displays a simulation of an outflow cavity grid generation by setting a total number of 5,000 points, inner and outer radii of $1''$ and $15''$ respectively with $a_{outflow} = 150''$, $b_{outflow} = 15''$, and $\Delta\gamma = 5°$. $a_{outflow}$ and $b_{outflow}$ are respectively the major and minor axis of the outflow, assimilated to be an ellipse (see Sect. 2.3.3). The shape and the clear limit of the maximum height $z_{out} = 15''$ of the outflow can be identified in this plot. Visser et al. (2012) have used the same kind of outflow cavity walls gridding process.

It is also important to note that in the case where multiple structures are modelled at the same time, the total number of points will be equally distributed for each structure. For instance, for a total number of points of 15 000 and if one wants to model one spherical source, one disk, and one outflow, GASS will distribute 5 000 points for each structure.

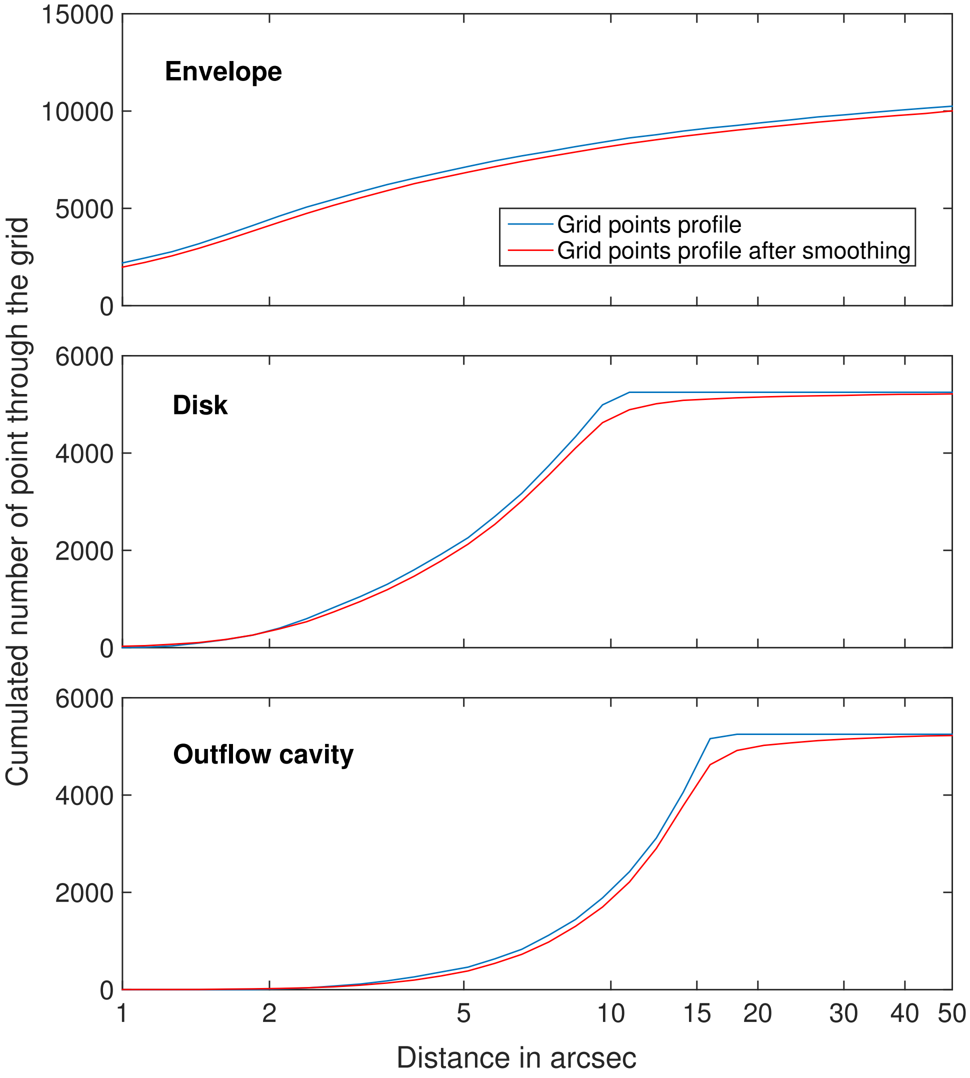

Figure 2.4 – Cumulated number of points through the grid as a function of the radial distance in arcsec for the three different types of structure. The distribution of points is shown before (in blue) and after (in red) the smoothing process.

2.3 Creation of the physical model

2.3.1 Spherical sources generation

Each Voronoï cell created will be defined by a constant value for each of the physical parameters I consider: gas temperature, dust temperature, H_2 density, molecular abundance, velocity field and doppler parameter. The given value for each cell is determined through an interpolation of the physical profile defined in input for each of these parameters. Since the grid is distributed randomly, each one of the Voronoï cells is situated at a different radius, thus it is uniquely defined by its physical properties. Both the density and temperature profiles can be defined with a variable number of regions N_{dens} and N_{temp} respectively as a function of the radial distance from the central object by:

1. Multiple power law profiles: for each temperature region i, a power law coefficient α_i and a temperature $T_{env,i}$ value is set for a given radius $r_{0,i}^{temp}$ and for each density region j a power law coefficient β_j and a density $n(H_2)_{env,j}$ value is set for a given radius $r_{0,j}^{dens}$. The total

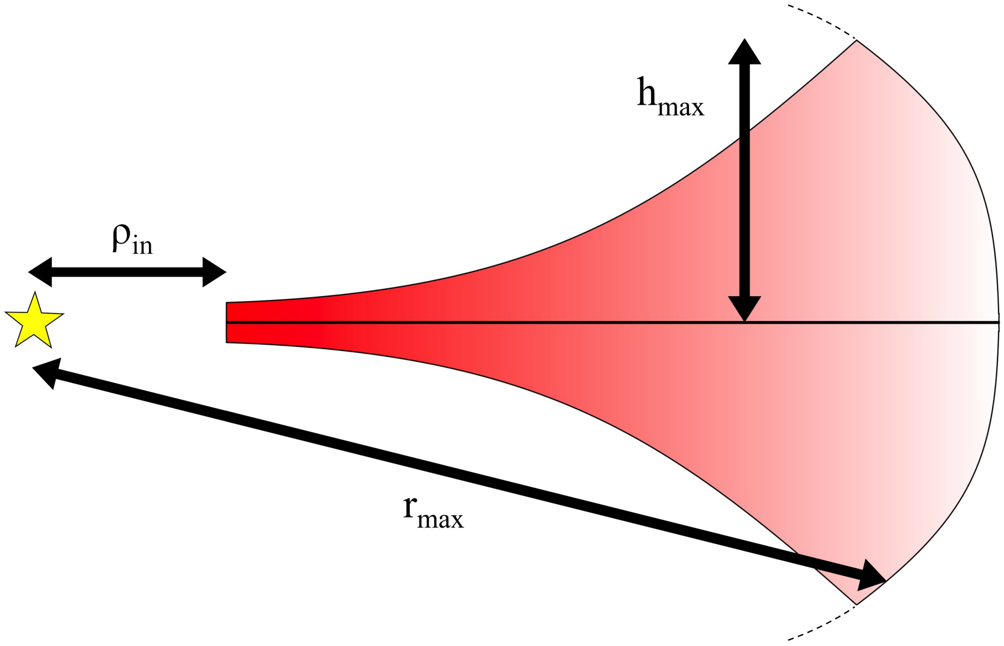

Figure 2.5 – Sketch showing the different parameters that define the structure of the disk. ρ_{in} is the inner cylindrical radius of the disk while r_{max} is its outer spherical radius, shown by the dotted lines. h_{max} is taken from the mid-plane of the disk.

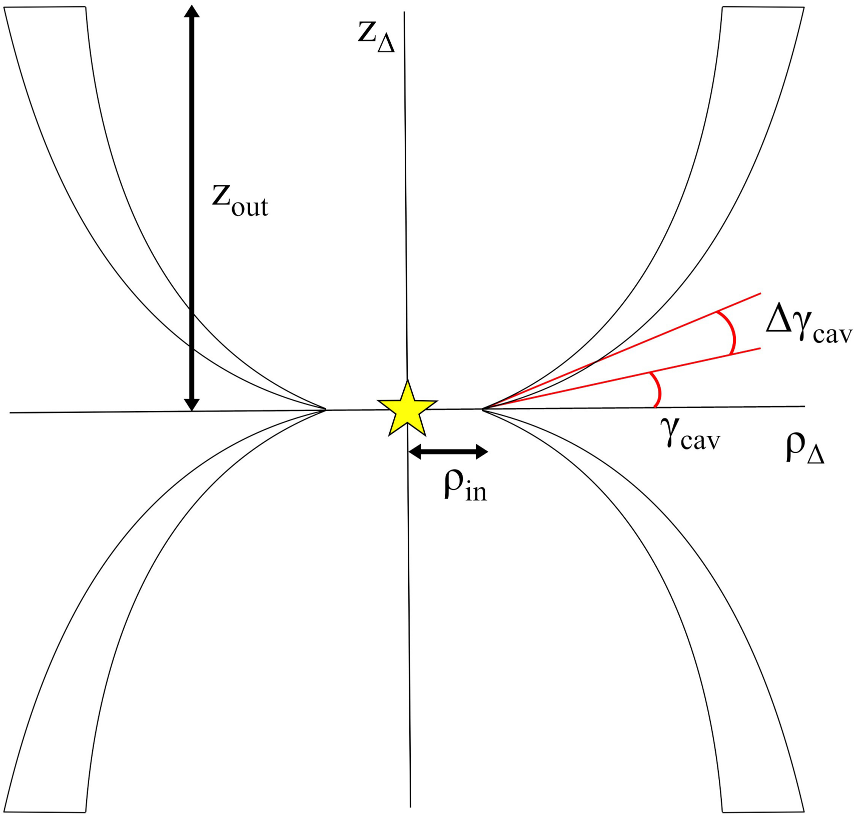

Figure 2.6 – Sketch showing the different parameters that define the structure of the outflow. ρ_{in} is the inner cylindrical radius of the outflow while z_{out} is the maximum height that the outflow can reach. ρ_Δ and z_Δ define the cylindrical axes of the outflow. $\Delta\gamma_{cav}$ defines the width of the cavity walls.

physical profile is then defined as

$$T_{env} = \sum_{i}^{N_{temp}} T_{env,i} \left(\frac{r_i}{r_{0,i}^{temp}} \right)^{\alpha_i}, \tag{2.1}$$

$$n(H_2)_{env} = \sum_{j}^{N_{dens}} n(H_2)_{env,j} \left(\frac{r_j}{r_{0,j}^{dens}} \right)^{\beta_j}. \tag{2.2}$$

where r_i and r_j are all the radii that define the regions i and j respectively. Thus, the final temperature or density value of a region becomes the first temperature or density value of the following regions, ensuring the continuity of the physical profile.

2. Multiple temperature or density steps: for each region, a temperature or a density is set for a given radius. The code interpolates the temperature linearly and the density logarithmically between the two points. As above, different radii can be set for the temperature and the density profile.

The abundance profile can be defined in multiple regions N_{abund} as a function of the radius or the temperature (once the temperature profile is defined). This option can be used, for instance, to describe the freeze out or the desorption of a specific molecular species at a given temperature (e.g. CO at ~27 K). The interpolation process is the same as for the temperature or the density profile but the user can choose a constant or a logarithmic variation of the abundance within the region. Each abundance value in each region can be gridded to calculate multiple models at the same time.

In the case that more than one structure (spherical source or disk) is used, the problem is to take into account their different contribution over the entire grid. This is only done for the spherical sources whereas outflows and disks impose their own physical properties in the region where they are defined, without considering the presence of the spherical sources (see Section 2.3.3). In any case, the outflow structure always prevails over other structures. For each point of the grid, the density of each spherical source is added following the equation:

$$n_{cell} = \sum_{i}^{N} n_i, \tag{2.3}$$

where n_{cell} is the total H_2 density of the cell, n_i the H_2 density contribution of the spherical structure i and N the number of different spherical structures. At the current development stage of GASS, the gas-to-dust mass ratio cannot be defined and is left to the default value of 100 set by LIME (see Sect. 2.5.4).

For the gas temperature I consider the ideal gas law equation of state $P = nk_BT$, where P is the pressure of the gas, n the number density, k_B the Boltzmann constant, and T the absolute temperature. Since I consider polyatomic species, each cell contains a total energy of

$$U_{cell} = \frac{5}{2} k_B T_{cell} n_{cell} = \sum_{i}^{N} \frac{5}{2} k_B T_i n_i, \tag{2.4}$$

where U_{cell} is the internal energy of the cell, T_{cell} the total temperature and n_{cell} the total number density. The previous equation combined with Eq. (2.3) leads to

$$T_{cell} = \frac{1}{\sum_i^N n_i} \times \sum_{i}^{N} T_i n_i. \tag{2.5}$$

By default, the dust temperature is considered to be equal to the gas temperature except if the user defines its value in a separate file and give it as an input for GASS.

The molecular abundance $[X]$ is defined as

$$[X] = \frac{n_X}{n}, \tag{2.6}$$

where n_X is the number density of the species. Considering the contribution of all the spherical sources, the abundance in each cell is

$$[X_{cell}] = \frac{n_{X,cell}}{n_{cell}} = \frac{1}{\sum_i^N n_i} \times \sum_i^N [X]_i n_i, \tag{2.7}$$

where $[X_{cell}]$ is the total molecular abundance in the cell and $n_{X,cell}$ is the total number density of the species.

To calculate the radiative transfer one needs to define the total Doppler broadening, often called the $b-$doppler parameter:

$$b = v_D = \sqrt{v_{th}^2 + v_{turb}^2}, \tag{2.8}$$

where v_{turb} is the (micro-)turbulence velocity which operates on length scales shorter than the photon mean free path. The thermal velocity, v_{th}, is the random motion of the molecules due to the kinetic temperature of the gas:

$$v_{th} = \sqrt{\frac{2\, k_B\, T}{\mu\, m_H}}, \tag{2.9}$$

Considering a Gaussian profile, the FWHM due to the Doppler broadening is:

$$\mathrm{FWHM}_D = 2\,\sqrt{\ln(2)} \times v_D, \tag{2.10}$$

where FWHM_D is the spectral line full width at half maximum. Eq. 2.10 can also be written as

$$b = \frac{1}{2\,\sqrt{\ln(2)}} \times \mathrm{FWHM}_D = 0.60\ \times\ \mathrm{FWHM}_D. \tag{2.11}$$

In the current GASS version, the $b-$doppler parameter can be considered either constant throughout the grid or variable as a function of the grid radius. Its value is defined by the user in the interface (see top panel of Fig. A.1).

The velocity field of the spherical source is determined by adding the different projections on the cartesian coordinates (X, Y, Z) of each velocity field induced by each structure included in the model. The intensity of the velocity field for each point of the grid for the spherical model is defined as an infall model (Shu, 1977) by:

$$V_{inf}(r) = \sqrt{\frac{2\, G\, M_\star}{r}}, \tag{2.12}$$

where V_{inf} is the infall velocity, G the gravitational constant, $M_\star$ the mass of the central object, and r the distance from the central object. The projections on each cartesian coordinates are calculated by:

$$r \;=\; \sqrt{(X - X_\star)^2 + (Y - Y_\star)^2 + (Z - Z_\star)^2}, \tag{2.13}$$

$$\theta \;=\; \arctan\left(\frac{\sqrt{(X - X_\star)^2 + (Y - Y_\star)^2}}{Z - Z_\star}\right), \tag{2.14}$$

$$\phi \;=\; \arctan\left(\frac{(Y - Y_\star)}{(X - X_\star)}\right), \tag{2.15}$$

where $X_\star$, $Y_\star$, and $Z_\star$ are the coordinates of the central object. This leads to the following equations for the projection of the velocity vector:

$$\left\{\begin{array}{lcl} \vec{V_x} & = & -r\sin\theta\cos\phi\ \vec{e}_x, \\ \vec{V_y} & = & -r\sin\theta\sin\phi\ \vec{e}_y, \\ \vec{V_z} & = & -r\cos\theta\ \vec{e}_z, \end{array}\right. \tag{2.16}$$

where $\vec{e}_x$, $\vec{e}_y$, and $\vec{e}_z$ are the unit vectors. The velocity vector for each cell is then defined from the velocity of each structure i by:

$$\left\{\begin{array}{lcl} \vec{V}_{x,cell} & = & \sum_i^N \vec{V}_{x,i}, \\ \vec{V}_{y,cell} & = & \sum_i^N \vec{V}_{y,i}, \\ \vec{V}_{z,cell} & = & \sum_i^N \vec{V}_{z,i}. \end{array}\right. \tag{2.17}$$

2.3.2 Disk generation

The main difference between the spherical source model and the disk model is the number of symmetries. In the spherical case, every physical parameter can be defined as a function of the radius. In the disk model there is only one symmetry around the rotational axis of the disk. The physical properties are therefore defined as a function of both the radii ρ and the height z. One must take care of the difference between r and ρ: r is the spherical radial distance and ρ is the cylindrical radial distance. The link between the two radii is given by $r = \sqrt{\rho^2 + z^2}$. As said above, I have to consider the inner and outer radius (ρ_{in} and r_{max}) and the maximum height (h_{max}) of a disk. Every point of the grid must be included between these values and they must also be at a smaller height than the pressure scale height h_0, which is defined as follow (Brinch and Hogerheijde, 2010):

$$h_0 = \sqrt{\frac{2\,T_{mid}\,k_B\,\rho^3}{G\,M_\star\,m_H}}, \tag{2.18}$$

with T_{mid} the mid-plane temperature of the disk, k_B the Boltzmann constant, G the gravitational constant, $M_\star$ the mass of the central object, and m_H the hydrogen atom mass. To calculate this value, one needs to define the mid-plane temperature gradient across the disk. This temperature can be defined by a power law (Williams and Best, 2014):

$$T_{mid} = T_{mid,0}\left(\frac{\rho}{\rho_{in}}\right)^{\gamma}, \tag{2.19}$$

where $T_{mid,0}$ is the mid-plane temperature at the radius ρ_{in}. The atmosphere temperature profile of a disk is also defined as the temperature profile at a specific height $z = 4\,h_0$ of the disk (see Williams and Best, 2014). The atmosphere temperature is set the same way the mid-plane temperature is defined, by a power law:

$$T_{atm} = T_{atm,0}\left(\frac{\rho}{\rho_{in}}\right)^{\gamma}, \tag{2.20}$$

with $T_{atm,0}$ is the atmosphere temperature at the radius ρ_{in}. All the characteristic values ($T_{mid,0}$, $T_{atm,0}$, ρ_{in}, and γ) can be set in the GASS user interface (see bottom panel of Fig. A.2) and plots are made to visualise the structure of the results. The resulting temperature $T(\rho, z)$ in each cell of the disk as a function of ρ and z is (Williams and Best, 2014):

$$T(\rho, z) = \begin{cases} T_{mid} + (T_{atm} - T_{mid})\left[\sin\left(\frac{\pi z}{4\,h_0}\right)\right]^4 & \text{if } z < 4\,h_0 \\ T_{atm} & \text{if } z \geq 4\,h_0 \end{cases}. \tag{2.21}$$

The density distribution is based on the profile from Brinch and Hogerheijde (2010) and defined by

$$n_{\mathrm{H_2}}(\rho, z) = n_0\left(\frac{\rho}{\rho_{in}}\right)^{\delta}\exp\left[-\left(\frac{z}{h_0}\right)^2\right], \tag{2.22}$$

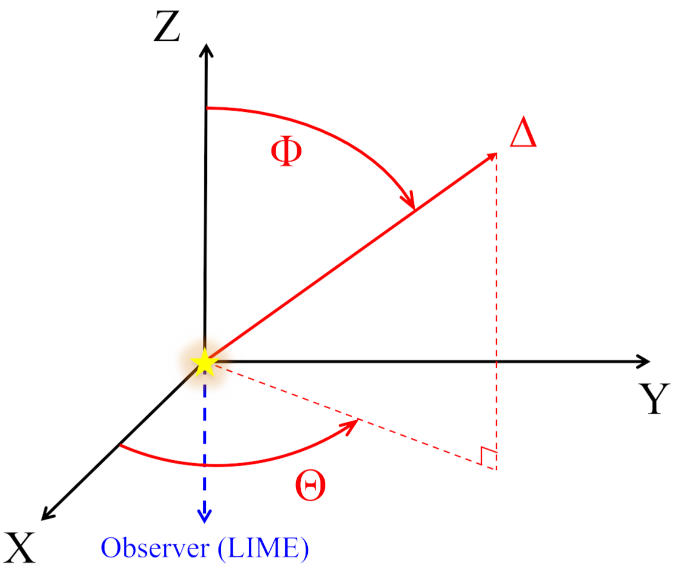

Figure 2.7 – Sketch showing the different angles that are used by the code to rotate the disk and the outflow models. Δ represents the axis on which the model is constructed. The blue dashed line shows the position of the observer in LIME.

with n_0 the H_2 density at ρ_0. As for the temperature profile, n_0 and δ can be set in the interface. The way GASS deals with the abundance profile generation is the same as for the spherical source. The abundance profile can be defined as a function of the cylindrical radial distance ρ or as a function of the total temperature profile $T(\rho, z)$ of the disk. Thus, if only the second option is chosen, the abundance profile will depend on the disk height z.

The cylindrical axis Δ of the disk model can be rotated as a function of two angles, Θ and Φ, thanks to the rotation matrix

$$R_{(\Theta,\Phi)} = \begin{pmatrix} \cos(\Phi) & 0 & -\sin(\Phi) \\ \sin(\Theta)\sin(\Phi) & \cos(\Theta) & \sin(\Theta)\cos(\Phi) \\ \cos(\Theta)\sin(\Phi) & -\sin(\Theta) & \cos(\Theta)\cos(\Phi) \end{pmatrix}, \tag{2.23}$$

where Θ is the angle between the axis Δ and the z-axis and Φ is the angle between the x-axis and projection of the axis Δ in the (X, Y) plane (see Fig. 2.7).

Fig. 2.8 shows a disk located at 300 pc generated with 10 000 points, $\rho_{in} = 0.7''$, $r_{max} = 7''$, $\Theta = 45°$, and $\Phi = 45°$. In this figure is also displayed the velocity field, supposed to follow the Keplerian rotation with the equation

$$V_{rot}(\rho, z) = \sqrt{\frac{G\,M_\star}{(\rho^2 + z^2)^{1/2}}}. \tag{2.24}$$

Fig. 2.9 shows the resulting positions of the grid points in cylindrical coordinates plotted with the pressure scale height h_0. This plot checks that the program correctly rejects as disk points any point higher than the pressure scale height.

GASS also computes the total gas mass of the disk by adding the mass contribution of every cell i identified to belong to the disk model. Considering the total number of disk points N_{disk}, one can write

$$M_{disk}^{gas} = \frac{m_{H_2}}{M_\odot} \times \sum_{i}^{N_{disk}} 2\pi\,\rho_i\,d\rho_i\,dz_i\,n(H_2)_i, \tag{2.25}$$

with m_{H_2} the mass of H_2, ρ_i the cylindrical distance of the cell i, $d\rho_i$ and dz_i its size, and $n(H_2)_i$ its H_2 density.

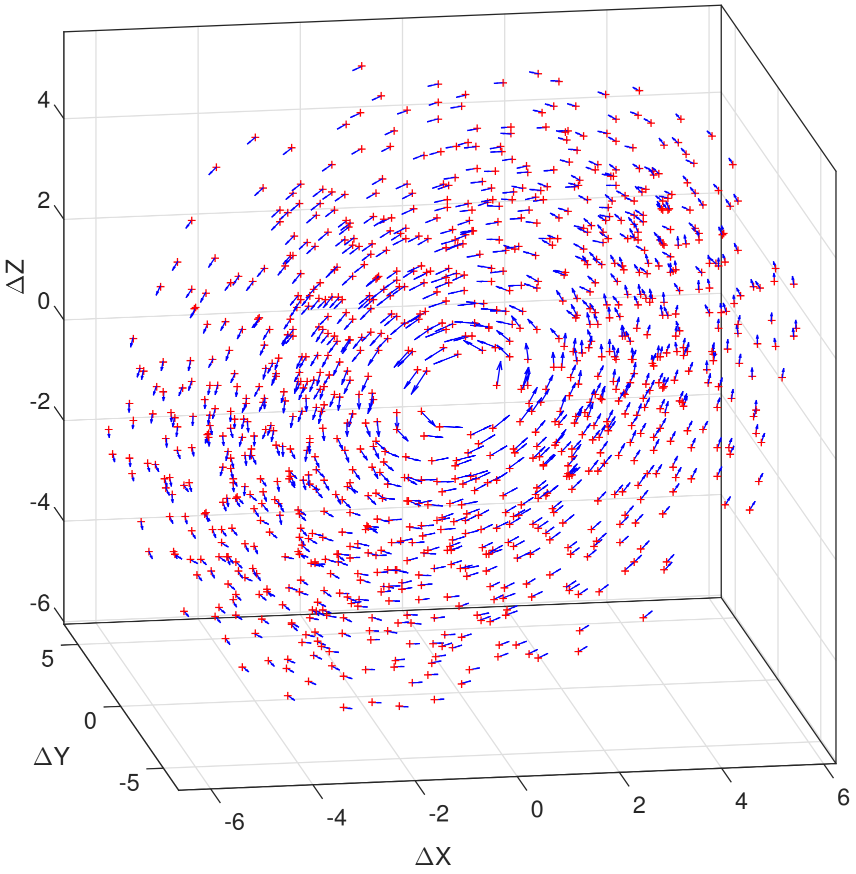

Figure 2.8 – Grid points distribution (red crosses) of the disk model described in Sect. 2.3.2. The inner radius ρ_{in} is clearly visible as well as the two rotation angles Θ and Φ. The velocity vectors are plotted in blue and show the Keplerian rotation of the disk.

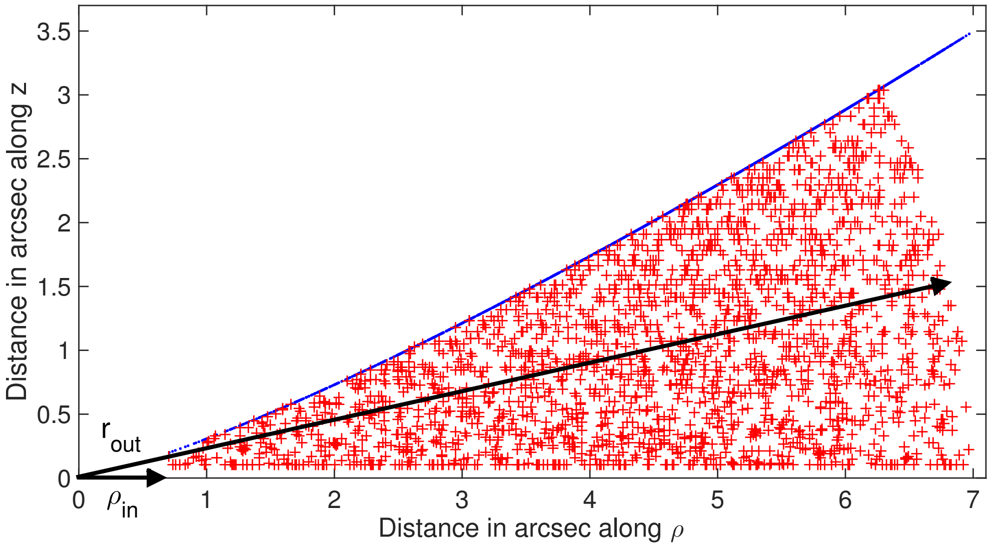

Figure 2.9 – Disk profile in cylindrical coordinates (ρ, z). Grid points are shown in red whereas the specific pressure scale height h_0 is plotted in blue. GASS automatically rejects any point above this height. The inner cylindrical and outer spherical radii (ρ_{in} and r_{out}) can be identified as well.

2.3.3 Outflow generation

To date, one can consider three distinct types of outflows driven by jets or winds and a summary of their properties has been given in Arce et al. (2007):

1. The jet bow-shock model with a highly collimated jet blowing the envelope away and creating a thin outflow shell (cavity walls) around the jet.
2. The wind-driven shell model, with a wide-angle radial wind and a thin shell interacting with the envelope.
3. The turbulent jet model, with Kelvin-Helmholtz instabilities along the jet/environment boundary leading to a turbulent viscous layer.

Arce and Sargent (2006) and Arce et al. (2007) have shown that in reality these different kinds of outflows are probing different outflow ages, thus probing different proto-stellar stages as shown in Fig. 2.10 (Cantó et al., 2008). Young outflows tend to be associated to the outflow type *(1)* with highly collimated jets and a faint wind, around Class 0 objects. As the proto-star evolves, the loss of surrounding materials leads to a less dense environment around the jet. The outflow becomes wider and the wind stronger, now associated to the type *(2)* of outflows, observed in Class I proto-stars. This trend can be used to estimate the age of a low-mass proto-star (see Arce and Sargent (2006), especially their discussion section).

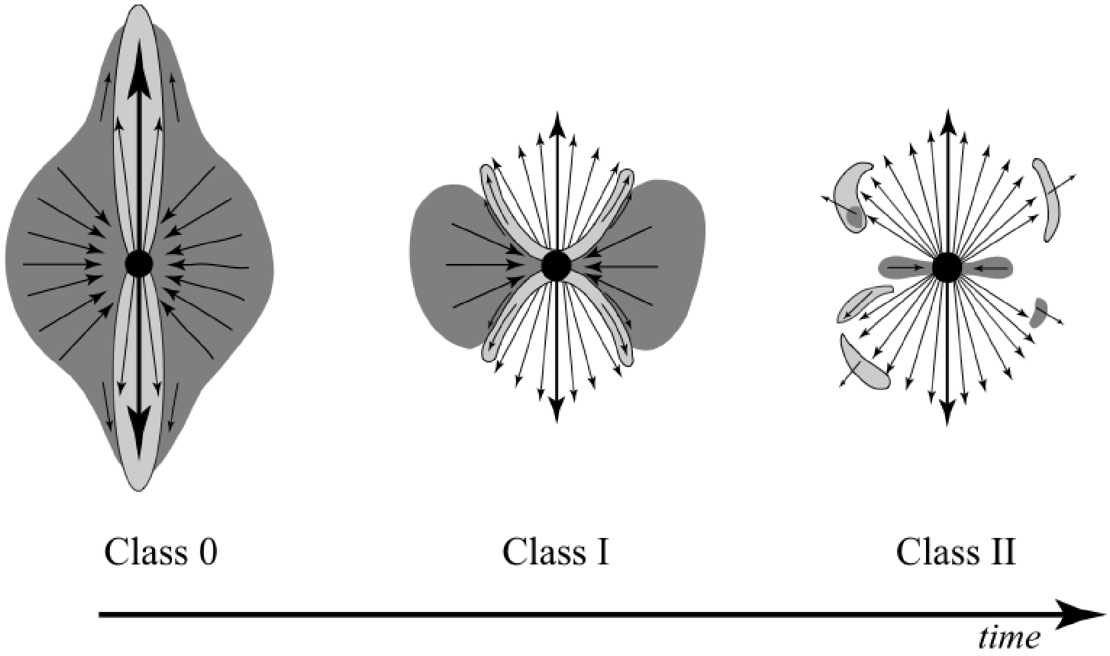

Figure 2.10 – Image showing the evolution of the outflowing material coming from a forming star during its different evolutionary stages. Source: Arce and Sargent (2006).

GASS can deal with both the jet bow-shock outflow model *(3)* and the wind-driven shell model *(1)* by setting the appropriate value of the parameters $a_{outflow}$, $b_{outflow}$, and $\Delta\gamma$ (see Fig. 2.6).

As mentioned in Sect. 2.2, the outflow model is based on the mathematical definition given by Visser et al. (2012) and assimilated to an ellipse (or a part of an ellipse) centred on a central object with $a_{outflow}$ and $b_{outflow}$ the ellipse parameters. The outflow is modelled around an axis Δ (first superimposed to the z-axis) and the height of the outflow z_Δ is defined as a function of the

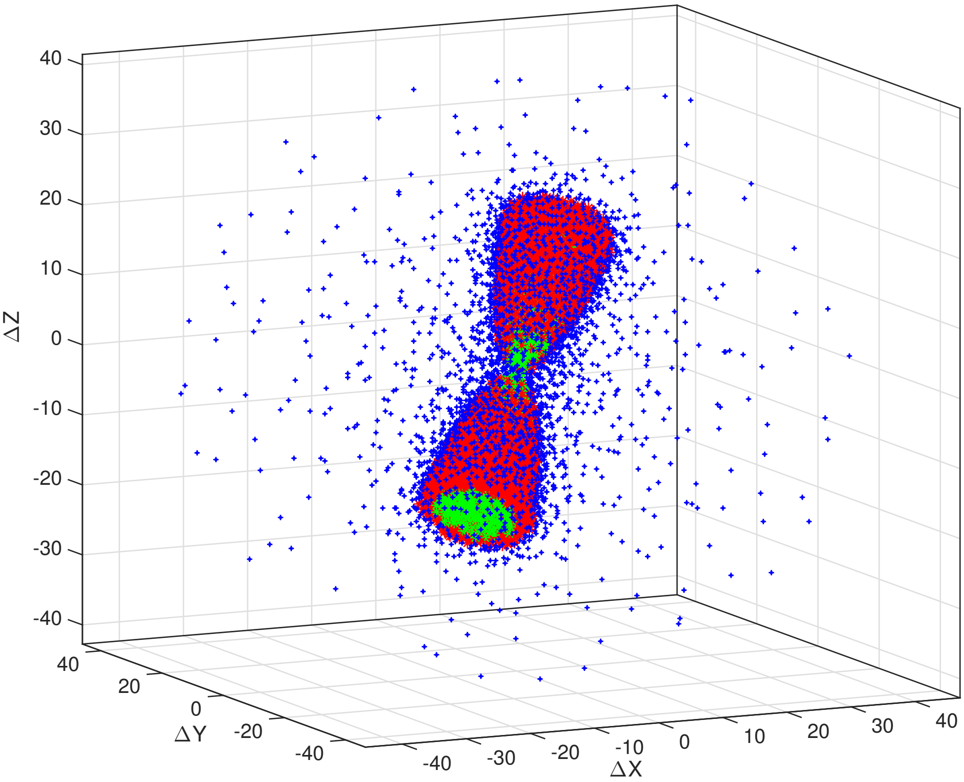

Figure 2.11 – Example of points generated by the outflow grid process (see text for the outflow parameters). The red points have been identified among these points as the outflow cavity structure and now belongs to its model. All the other points have been rejected, the blue and green ones are respectively outside and inside the cavity walls of the outflow.

cylindrical radial distance ρ_Δ from Δ by:

$$z_\Delta = b_{outflow}\sqrt{1-\left(\frac{\rho_\Delta}{a_{outflow}}-1\right)^2}. \tag{2.26}$$

The model is considered to be bipolar and symmetric with respect to the (X, Y) plane but the user can choose only one part of the outflow in the interface if needed (see top panel of Fig. A.3). In GASS, outflows are always associated to a spherical structure or a proto-planetary disk and cannot be modelled alone. Thus, there is always a central object which defines the centre coordinates of the outflow. The axis Δ can be rotated in the model as a function of the two angles Θ and Φ thanks to the rotation matrix described in the previous section. The size of the outflow is limited by an inner radius r_{in} and a maximum height z_{out} determined by the user in the interface. The code will then identify which points belong to the outflow structure, thus no points are added to the model.

In its region of influence, the outflow imposes its physical parameters as if its gas blows away the spherical envelope when it forms. The H_2 density n_{H_2}, the gas temperature T_{gas}, and the abundance $[X]$ are defined using a power law as a function of the cylindrical radial distance ρ from the central object:

$$\{n_{H_2}, T_{gas}, [X]\} = \{n_0, T_0, [X]_0\}\left(\frac{\rho}{\rho_{in}}\right)^{\{\epsilon,\zeta,\eta\}}, \tag{2.27}$$

where n_0, T_0, and $[X]_0$ are respectively the density, temperature, and abundance value at ρ_{in}. ϵ, ζ, and η are the power-law indices associated to each of these parameters respectively. The velocity field is defined along the shape of the outflow with a constant value, taking into account that the velocity vector is always parallel to the Δ axis. Since the outflow gas is still subject to the gravitational field of the central object, the velocity vector of the outflow is added to the spherical model one. Fig. 2.11 shows the grid points that are assimilated to an outflow model located at 120 pc. The outflow parameters are: $\rho_{in} = 1''$, $\rho_{out} = 15''$, $a_{outflow} = 150''$, $b_{outflow} = 15''$, $\Theta = 45°$, and $\Phi = -45°$.

2.4 LIME options implemented in GASS

Several useful options of LIME normally defined in the input `model.c` file can be directly set in the GASS interface (see bottom panel of Fig. A.3). GASS will then simply creates the `model.c` file, taking into account all the LIME parameters set by the user. GASS produces a directory containing all the files required by LIME. The user just needs to launch LIME within this directory to obtain the output fits files. The user can directly describe the parameters of the output data cubes produced by LIME by giving the central frequency, the channel resolution, the bandwidth, the number of pixels per dimension, the pixel size, and the name of the output fits files. The unit of these fits files can also be selected here, choosing between Kelvin, Jansky/pixel, or S.I. units. Finally, the GASS interface also allows the user to select a dust opacity and a collision file (if needed).

LIME does not necessarily calculate line emissions and it is possible to only choose to calculate the dust continuum emission. If so, the channel resolution, the bandwidth, and the collision file are not required and the output fits is simply a continuum image.

GASS can also set the LTE mode of LIME. If it is the case, the population levels are directly calculated and no iterations are made, the output fits is then generated. This is very useful for molecules with no existing collisional rates or if non-LTE calculations are not required. However, one must be careful because in any case, the “collision” file (even if it does not contain collisional rates) is still required by LIME, since it is from this file that the code retrieves the spectroscopic parameters of the studied molecule, *i.e.* the Einstein coefficient $\mathrm{A_{i,j}}$, the frequency, or the upper energy level $\mathrm{E_{up}}$ of the transitions.

A useful option coded in GASS is to consider the ortho-to-para ratio of the $\mathrm{H_2}$ molecule. The dihydrogen molecule is composed by two H atoms linked by a covalent bond. Each ${}^1_1\mathrm{H}$ atom consists in one proton and one electron. The proton has a nuclear spin angular momentum which is a vector that can be described by a magnitude L:

$$L = \hbar\sqrt{I(I+1)}. \tag{2.28}$$

where I is the spin angular momentum quantum number. Each fermion (e.g. proton or neutron) has $I = \frac{1}{2}$. The projection of this vector on the z axis (arbitrarily chosen) gives the degeneracy of I, given by the magnetic quantum number m_I:

$$m_I = -I, -I+1, -I+2, \ldots, +I. \tag{2.29}$$

The angular moment along the z axis is now:

$$I_z = m_I \hbar. \tag{2.30}$$

For a proton alone, the spin quantum number is $I = \frac{1}{2}$ ($L = \frac{\sqrt{3}}{2}\hbar$) and the magnetic quantum number m_I can be either $+\frac{1}{2}$ (spin up, $\uparrow$) or $-\frac{1}{2}$ (spin down, $\downarrow$). In the case of the dihydrogen molecule $\mathrm{H_2}$, the nuclear spin angular momentum is composed by two protons. Each particle can be either spin up ($\uparrow$) or spin down ($\downarrow$), so the system has four basis states:

$$\uparrow\uparrow,\ \uparrow\downarrow,\ \downarrow\uparrow,\ \downarrow\downarrow, \tag{2.31}$$

Three of the previous states lead to a total spin angular momentum of 1 (thus $m_I = -1, 0, 1$):

$$\left\{\begin{matrix} m_I = 1 & \text{for } \uparrow\uparrow \\ m_I = 0 & \text{for } (\uparrow\downarrow + \downarrow\uparrow)\frac{1}{\sqrt{2}} \\ m_I = -1 & \text{for } \downarrow\downarrow \end{matrix}\right\} \rightarrow I = 1 \quad \text{(triplet)}, \tag{2.32}$$

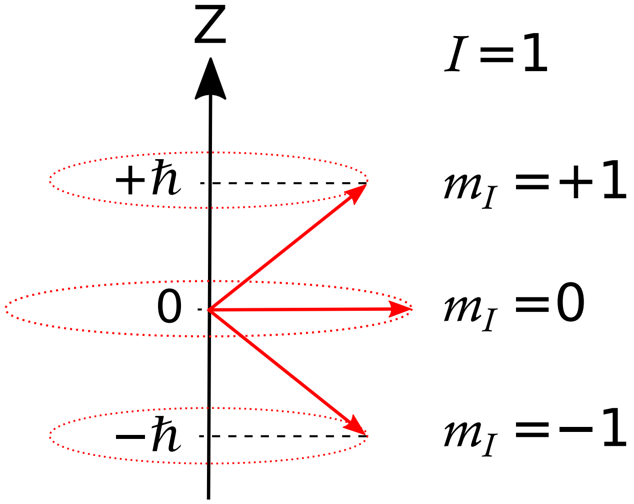

Figure 2.12 – The quantised angular momentum values for $I = 1$. The magnitude ($L = \hbar\sqrt{2}$) is denoted by red arrows while the projection along the z axis is denoted by the red circles.

and one leads to a total spin angular momentum of 0 (thus $m_I = 0$):

$$m_I = 0 \text{ for } (\uparrow\downarrow - \downarrow\uparrow)\frac{1}{\sqrt{2}} \quad \rightarrow I = 0 \quad \text{(singlet)}. \tag{2.33}$$

The triplet is associated to ortho–H_2 (parallel nuclear spins) the singlet to para–H_2 (anti-parallel nuclear spins). A sketch depicting the spin angular momentum for a $I = 1$ case is shown in Fig. 2.12.

The quantum mechanical (Pauli exclusion) principle for the molecular wave function in the permutation of fermions imposes restrictions on the possible rotational states the two forms of H_2 can adopt. Ortho–H_2, with symmetric nuclear spins, can only have antisymmetric rotational wave functions, corresponding to odd values of the rotational quantum number J (1, 3, ...). On the contrary, para–H_2, with an antisymmetric nuclear spin, can only have symmetric rotational wave functions, corresponding to even J (0, 2, ...). H_2 is a linear diatomic molecule that can be assimilated to a rigid rotor therefore energies E_J and degeneracies g_J of the rotational states can be obtained by solving the Schrödinger equation:

$$E_J = \frac{J(J+1)\,\hbar^2}{2M} \quad \text{and} \quad g_J = 2J+1, \tag{2.34}$$

where M is the moment of inertia of the dihydrogen molecule:

$$M = \mu\, r_0^2 \tag{2.35}$$

where $r_0 = 74.14\,\mathrm{pm}$ is the length of the covalent bond in the H_2 molecule and μ its reduced mass:

$$\frac{1}{\mu} = \frac{1}{m_\mathrm{H}} + \frac{1}{m_\mathrm{H}}. \tag{2.36}$$

Here $m_\mathrm{H} \simeq m_p = 1.67262 \times 10^{-24}\,\mathrm{g}$. The rotational constant B (in Kelvin unit) is defined as:

$$B = \frac{\hbar^2}{2Mk_B}. \tag{2.37}$$

For the H_2 molecule $B = 87.61\,\mathrm{K}$. From the Boltzmann distribution, the LTE value of the ortho-to-para ratio of H_2 can be written:

$$\left(\frac{n_{ortho}}{n_{para}}\right)_\mathrm{LTE} = \frac{3\sum_{ortho} g_{ortho}\, e^{-E_{ortho}/k_B T_L}}{\sum_{para} g_{para}\, e^{-E_{para}/k_B T_L}}, \tag{2.38}$$

as a function of T_L, the local gas temperature. The factor of 3 is here to take into account the spin degeneracies of the $I = 1$ spin state. With Eq. (2.34) and Eq. (2.37):

$$\left(\frac{n_{ortho}}{n_{para}}\right)_{\rm LTE} = \frac{3\sum_{odd\ J}(2J+1)e^{-BJ(J+1)/T_L}}{\sum_{even\ J}(2J+1)e^{-BJ(J+1)/T_L}}. \tag{2.39}$$

Fig. 2.13 displays the LTE ortho/para ratio of H_2 as a function of the local temperature. The ratio of 3, based on the nuclear spin statistics, is clearly reached for temperature of $\sim 250\,$K. At 20 K this ratio is below 0.002 meaning that more than 99.8% of H_2 is in the para form.

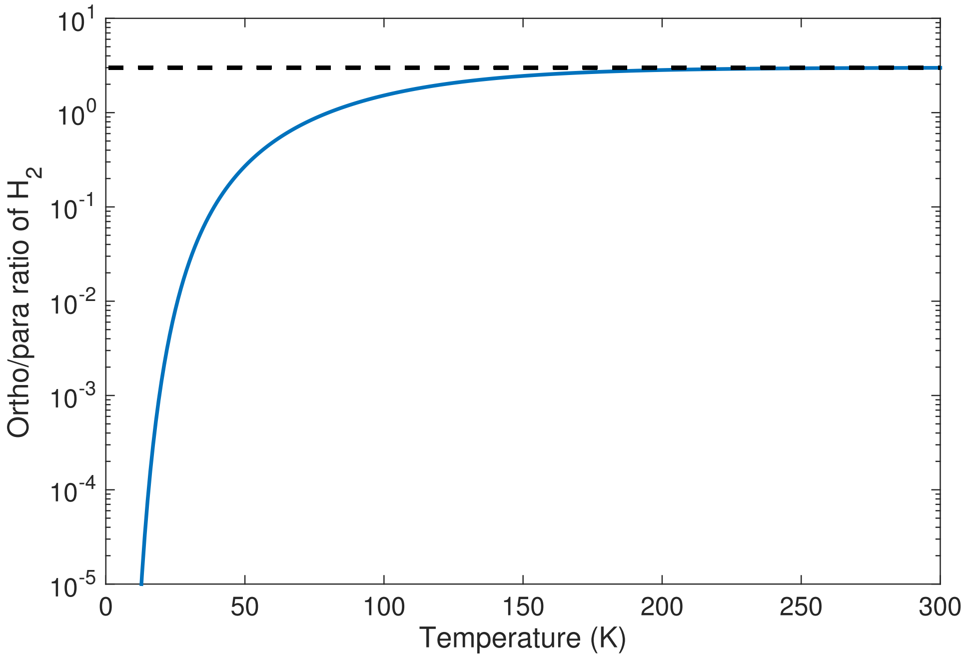

Figure 2.13 – LTE ortho-to-para ratio of H_2 as a function of the local temperature (blue curve). The black dashed line indicates a ratio of 3.

Regarding other molecules, it is up to the user to correctly describe the ortho-to-para ratio of the studied molecule. Since frequencies of ortho and para species are not the same, their spectroscopic parameters are usually gathered in separated collision files[4]. Thus, from the point of view of LIME, they are treated as two completely different molecules and two radiative transfer calculations are required to get the result of both ortho and para forms.

All available LIME options are not yet implemented in GASS (antialias, line blending, polarisation,...) mainly because I need more time to include them into the code. Another reason is that some options have not yet been revised by the LIME development team since the release of the version 1.5, and they may cause issues or wrong results. It is the case of the line blending option for instance. As a consequence, I chose not to implement them yet in GASS.

2.5 Post-treatment analysis options

To analyse hyper-spectral data cubes (generated by LIME for instance), GASS offers several functionalities to deal with the output fits files, depending on the observations in the hands of the user or depending on the processing s/he wants to perform with the models (see Fig. A.4).

---

[4] It is the case of the LAMDA database

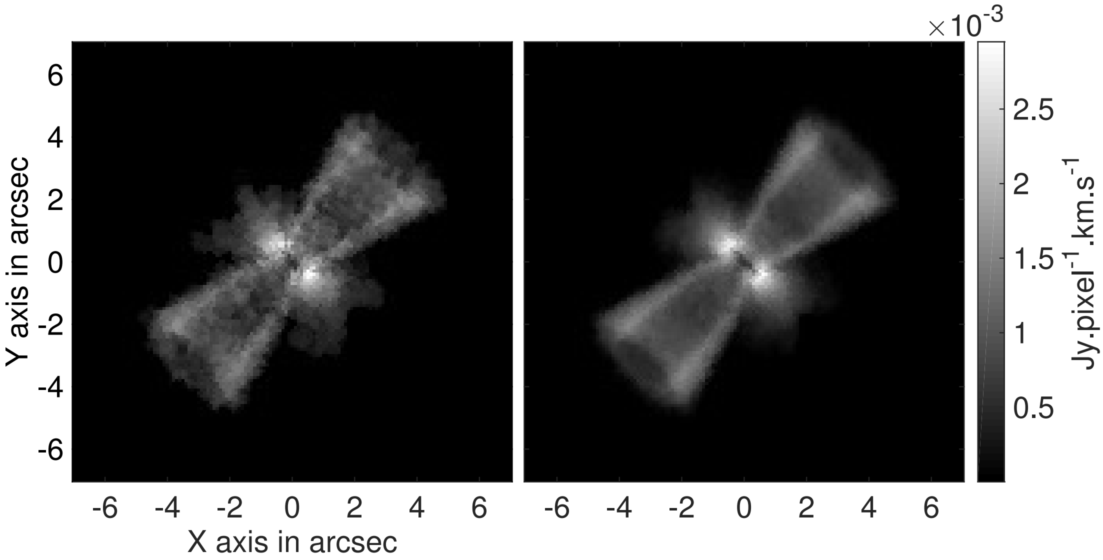

Figure 2.14 – Integrated intensity map over all channels for one model only (left panel) and ten models averaged with the "smoothing tool".

2.5.1 "Smoothing tool"

A "smoothing tool" allows the user to average a certain number of hyper-spectral cubes. Artefacts can appear in the data cube images, produced by the *ray-tracing* step in LIME. This is mainly due to a lack of points in the outermost part of the grid, even if a smoothing process is already done through the Lloyd algorithm (see Section 2.2) in order to homogenise the distribution of points. Since each model is built with a different grid in GASS, averaging several runs reduces the artefacts due to the grid. Moreover, it allows to reduce the initial number of points in the grid and the total execution time of a run in LIME depends a lot on this initial number of points. Therefore it is faster and more efficient to run ten models with 10 000 points at the same time and average them rather than doing a single run with 100 000 points. The smooth option implemented in GASS does this procedure automatically and creates a resulting smoothed fits file for each transition of a given model. I want to point out that an updated version of the *ray-tracing* process coming soon will drastically reduce the appearance of artefacts in data cubes. An example of the averaging process is shown in Fig. 2.14 where the integrated intensity over all channels is plotted for one model only compared to the smoothed one.

2.5.2 Integrated maps

Integrated maps (moment 0, M_0, and 1, M_1) of a given data cube can be calculated by the program, considering the following equations:

$$M_0 = \int I(v)\,dv, \tag{2.40}$$

$$M_1 = \frac{\int I(v)\,v\,dv}{\int I(v)\,dv} = \frac{\int I(v)\,v\,dv}{M_0}, \tag{2.41}$$

where I is the pixel intensity and v the velocity. The integral is calculated over the desired number of channels. The graphical interface allows the user to choose the channels over which s/he wants to calculate the moments and plot the results.

2.5.3 Plots of best modelled vs observed spectra

Another tool allows to plot the resulting spectra of each transition in order to compare them to single-dish observations. The user gives in input a formatted file containing the information about

Frequency (GHz)	HPBW ($''$)
150	28
230	21
345	14
690	8
870	6

Table 2.1 – Beam sizes for the JCMT telescope (taken from the website) at given frequencies.

the observations such as the name of the telescope (or the size of the antenna), the rms and a table gathering the frequencies and intensities for each spectra. GASS can directly read CASSIS line files (`.lis` format) and convert them in the GASS format. If several modelling directories exist in the current working directory, GASS reads all data cubes (fits files) produced by LIME in all these different modelling directories. Thanks to the graphical interface, the user can choose to display a specific data cube of a selected modelling. From this interface, it is possible to span the different channels of the data cube and the user can select the desired pointing position of the telescope with a cursor or directly choose the centre of the map.

Once the pointing position is set, GASS will produce a spectrum for each data cube by convolving the model with the different antenna beam sizes. I have taken these beam sizes from the different telescopes' respective websites and implemented them in GASS. For the IRAM-30m[5], beam sizes are calculated following:

$$\theta^{('')}_{\text{IRAM-30m}} = \frac{2460}{\nu}, \tag{2.42}$$

where ν is the frequency in GHz. I have derived the JCMT telescope beam size equation from a power law fitting of beam values given at some frequencies on the JCMT website[6] (see Table 2.1):

$$\theta^{('')}_{\text{JCMT}} = 801.6 \times \nu^{-0.6377} - 4.65, \tag{2.43}$$

where ν is the frequency in GHz. For APEX, I directly took the equation on the telescope's website[7]:

$$\theta^{('')}_{\text{APEX}} = 7.8 \times \left(\frac{800}{\nu}\right), \tag{2.44}$$

where ν is the frequency in GHz. Finally, for the Herschel/HIFI telescope, the HIFI beam release note of September 2014[8] gives a general law to calculate beam sizes, depending on the HIFI band:

$$\theta^{('')}_{\text{HIFI}} = \theta_0 \times \left(\frac{\nu_0}{\nu}\right), \tag{2.45}$$

with θ_0 and ν_0 gathered in Table 2.2. A summary of beam sizes used by GASS for these telescopes as well as the frequency range currently available (with both PI and non-PI instruments) is plotted in Fig. 2.15. If the user is using any other telescope, GASS only needs the diameter D (in m) of the dish to calculate the beam following the theoretical equation:

$$\theta^{('')}_{B} = 1.22 \times \left(\frac{\lambda}{D}\right) \times \frac{3600 \times 180}{\pi} \simeq \frac{7.54 \times 10^4}{(\nu/\text{GHz}) \times D}, \tag{2.46}$$

where λ is the wavelength and ν is the frequency.

---

[5] `http://www.iram.es/IRAMES/mainWiki/Iram30mEfficiencies`

[6] `http://www.eaobservatory.org/jcmt/instrumentation/heterodyne/`

[7] `http://www.apex-telescope.org/telescope/`

[8] The HIFI Beam: Release #1

Frequency ν_0 (GHz)	HPBW θ_0 ($''$)
480	43.30
640	32.85
800	26.05
960	21.80
1120	19.50
1410	14.80
1910	11.10

Table 2.2 – Beam sizes for the Herschel/HIFI telescope (taken from the HIFI beam release note of September 2014) at given frequencies.

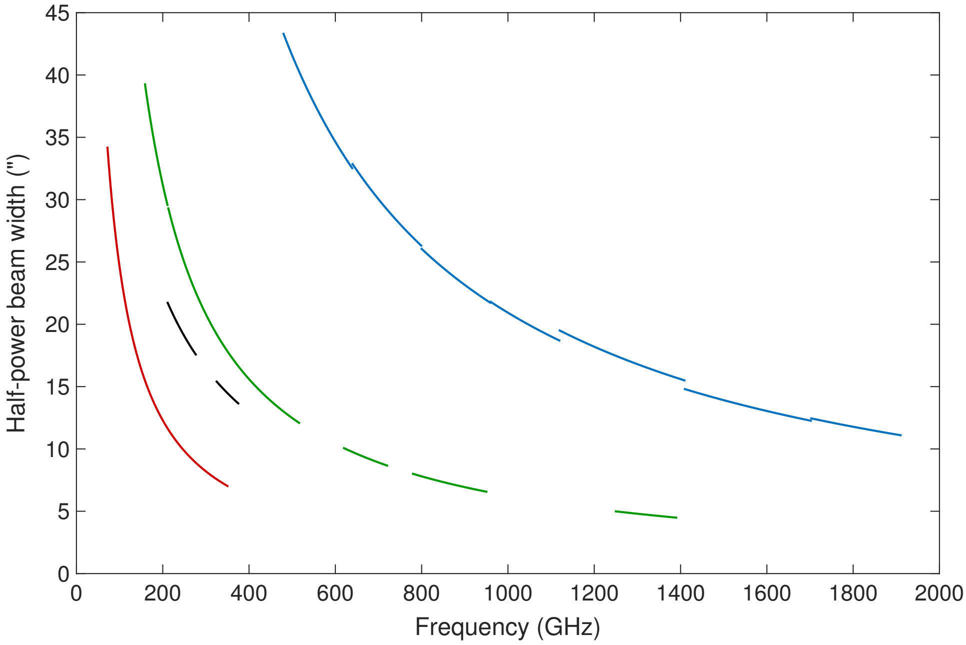

Figure 2.15 – Half-power beam width (HPBW) as a function of the frequency for the IRAM-30m telescope (in red), JCMT (in black), APEX (in green), and Herschel/HIFI (in blue).

The calculated beam sizes can be wrong by a few percents with respect to the real beam size of the telescope (which depends on the shape of the dish) but it is always an insignificant source of error in modelling results.

Once all the data cubes have been read and correctly convolved with GASS, the best fit model is calculated over all the models, following the standard χ^2 minimisation value for N_{spec} spectra i of N_i points, given by the equation (Lampton et al., 1976):

$$\chi^2_{red} = \frac{1}{\sum_i^{N_{spec}} N_i} \sum_{i=1}^{N_{spec}} \chi^2_i \quad \text{and} \quad \chi^2_i = \sum_{j=1}^{N_i} \frac{(I_{obs,ij} - I_{model,ij})^2}{rms_i^2 + (cal_i \times I_{obs,ij})^2}, \tag{2.47}$$

where $I_{obs,ij}$ and $I_{model,ij}$ are respectively the observed and the modelled intensity in the channel j of the transition i, rms_i is the rms of the spectrum i, cal_i its calibration error. The method described in Lampton et al. (1976) uses a different formulae for the reduced χ^2:

$$\chi^2_{red} = \frac{1}{N_p - p} \sum_{i=1}^{N_{spec}} \chi^2_i, \tag{2.48}$$

with N_p equals $\sum_i^{N_{spec}} N_i$ and p is the degree of freedom of the minimisation *i.e.* the number of adjustable parameters. It is difficult to trace this number since grid of models can be created by varying different parameters at the same time and not always the same ones. Nonetheless, I have verified that $p \ll N_p$ thus $1/N_p \simeq 1/(N_p - p)$. For instance, fitting 5 transitions of 50 channels each by varying 5 different parameters leads to $N_p = 250$ and $p = 5$, which is much less than N_p.

This tool is useful to constrain results when combined with grid of models, for instance grid of abundance profiles. An example of this tool is given in Sect. 2.7.

2.5.4 Plots of best continuum model vs observations

The same analysis as for spectra can be done in GASS for continuum only models, using the same beam sizes. Rather than plotting spectra, this tool presents the continuum fluxes as a function of the frequency compared to the observations. Nonetheless, the minimisation is different and the χ^2 is calculated for N_{cont} continuum measurements with:

$$\chi^2_{red} = \frac{1}{N_{cont}} \sum_{i=1}^{N_{cont}} \chi^2_i \text{ and } \chi^2_i = \frac{(F_{obs,i} - F_{model,i})^2}{(cal_i \times F_{obs,i})^2}, \tag{2.49}$$

where $F_{obs,i}$ and $F_{model,i}$ are respectively the observed and the modelled intensity at the frequency i, and cal_i the calibration error.

It is not possible at the moment to perform spectral energy distribution (SED) fitting due to the thermal emission of dust in GASS but I plan to incorporate it to the code by varying the different parameters of the following equation (Hildebrand, 1983), especially $T_{\rm dust}$ and β:

$$S_\nu = \Omega N \kappa_0 \left(\frac{\nu}{\nu_0}\right)^\beta B_\nu(T_{\rm dust}). \tag{2.50}$$

This equation follows the Planck function, $B_\nu(T)$, calculated at the dust temperature $T_{\rm dust}$. N is the column density of dust, Ω is the solid angle of the observing beam, and $\kappa_0\,(\nu/\nu_0)^\beta$ is the opacity of the emitting dust. This equation is valid at far-IR wavelengths ($\lambda \gtrsim 60\,\mu$m) and to use it the dust emission has to be optically thin, *i.e.* $\tau(\nu) \ll 1$. The optical depth τ of dust is calculated with:

$$\tau(\nu) = \int \kappa(\nu) \frac{\rho(\mathrm{H_2})}{gas/dust} dl, \tag{2.51}$$

where $\kappa(\nu) = \kappa_0\,(\nu/\nu_0)^\beta$, $\rho(\mathrm{H_2})$ is the volumetric mass density of $\mathrm{H_2}$, and *gas/dust* is the gas-to-dust mass ratio (~ 100). It is currently not possible to define the gas-to-dust mass ratio in GASS (the default value set in LIME is 100) but it will be added in a future release of the code. The previous equation can be also written as:

$$\tau(\nu) = \kappa_0 \left(\frac{\nu}{\nu_0}\right)^\beta \frac{m(\mathrm{H_2})}{gas/dust} \int n(\mathrm{H_2}) dl = \kappa_0 \left(\frac{\nu}{\nu_0}\right)^\beta \frac{2m_p}{gas/dust} N(\mathrm{H_2}). \tag{2.52}$$

with m_p the mass of the proton and $N(\mathrm{H_2})$ the column density of $\mathrm{H_2}$. Kelly et al. (2012, and references therein) have shown that there is a $T_{\rm dust} - \beta$ degeneracy (producing an anti-correlation between the two) when doing χ^2 minimisation of SED fitting, leading to erroneous estimates of $T_{\rm dust}$ and/or β. Hierarchical Bayesian techniques (Kelly et al., 2012) can be used to solve the problem but I delayed its implementation in GASS due to a lack of time and because it was not a priority. I expect to implement it in a future version of GASS.

2.5.5 Simulation of interferometric observations

In the case of interferometric observations, the analysis is more complicated. GASS possesses a tool that helps the comparison between the observations and the models.

A 2D Gaussian tool allows to convolve the data cube with the observed beam of the interferometric data by giving the major and minor axes ($X_{\rm FWHM}$ and $Y_{\rm FWHM}$) of the beam and its position angle θ. It is possible to directly compare the convolved predicted model with the observed data in a case where the $(u, v)-$coverage of the plane of sky is good and no flux is filtered out during the process. Therefore this tool can be used to compare models with observations but it cannot be used to predict interferometric observations since it does not take into account the position and the number of antennas for instance. To do the convolution, first the beam area is calculated using:

$$X^{(pix)}_{\mathrm{FWHM}} = \frac{X^{('')}_{\mathrm{FWHM}}}{pix_x} \quad \text{and} \quad Y^{(pix)}_{\mathrm{FWHM}} = \frac{Y^{('')}_{\mathrm{FWHM}}}{pix_y}, \tag{2.53}$$

where $X^{(pix)}_{\mathrm{FWHM}}$ and $Y^{(pix)}_{\mathrm{FWHM}}$ are respectively the x–axis and y–axis pixel size of the beam and pix_x, pix_y are respectively the x–axis and y–axis pixel size in arcsec. The beam area in pixel/beam can be then calculated following:

$$\Theta_{beam} = \frac{\pi X^{(pix)}_{\mathrm{FWHM}} Y^{(pix)}_{\mathrm{FWHM}}}{4\ln 2}. \tag{2.54}$$

Then the standard deviations σ_x and σ_y are calculated:

$$\sigma_x = \frac{X^{(pix)}_{\mathrm{FWHM}}}{2\sqrt{2\ln 2}} \quad \text{and} \quad \sigma_y = \frac{Y^{(pix)}_{\mathrm{FWHM}}}{2\sqrt{2\ln 2}}. \tag{2.55}$$

A 2D Gaussian can be defined as:

$$f(x,y) = f_0 \, \exp\left[-\left(\frac{(x-x_0)^2}{2\sigma_x^2} + \frac{(y-y_0)^2}{2\sigma_y^2} \right) \right], \tag{2.56}$$

where f_0 is the amplitude and (x_0, y_0) the centre. Generally, a 2D Gaussian can also be defined using:

$$f(x,y) = f_0 \, \exp\left[-\left(a(x-x_0)^2 + 2b(x-x_0)(y-y_0) + c(y-y_0)^2 \right) \right], \tag{2.57}$$

with:

$$a = \frac{\cos^2\theta}{2\sigma_x^2} + \frac{\sin^2\theta}{2\sigma_y^2}, \tag{2.58}$$

$$b = \frac{\sin(2\theta)}{4\sigma_x^2} - \frac{\sin(2\theta)}{4\sigma_y^2}, \tag{2.59}$$

$$c = \frac{\sin^2\theta}{2\sigma_x^2} + \frac{\cos^2\theta}{2\sigma_y^2}. \tag{2.60}$$

The signs in the b coefficient determine the rotation of the Gaussian, defined as clockwise from the +y–axis here. For a counter-clockwise rotation, one needs to invert the signs in b. An example of the clockwise rotation is shown in Fig. 2.16 for several position angles θ.

This 2D Gaussian is normalised using the volume V under the Gaussian:

$$V = \int_{-\infty}^{\infty} \int_{-\infty}^{\infty} f(x,y) \, dxdy = 2\pi f_0 \sigma_x \sigma_y. \tag{2.61}$$

In GASS, $f_0 = 1$ and the final beam function $F(x, y)$ used to be convolved with the predicted model is:

$$F(x,y) = \frac{f(x,y)}{V}. \tag{2.62}$$

It is also possible to add a white Gaussian noise to the data cube before the convolution to reproduce the observed *rms*. The input data cube must be in Jy/pixel and GASS can write an output fits file with the final results in Jy/beam using the beam area Θ_{beam} to perform the conversion from Jy/pixel to Jy/beam. An example of this tool is shown in Fig. 2.17 where the input

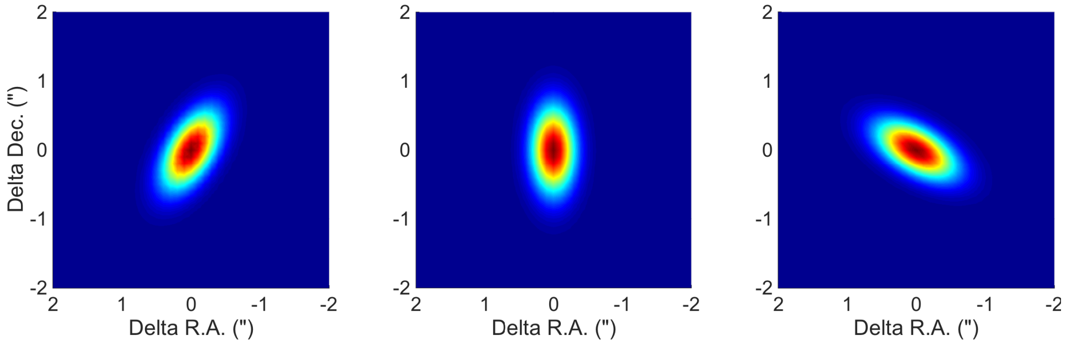

Figure 2.16 – Final beam $F(x, y)$ shape for $X_{\mathrm{FWHM}} = 0.5''$ and $Y_{\mathrm{FWHM}} = 1''$ and $\theta = -30°$ (left panel), $\theta = 0°$ (middle panel), and $\theta = 60°$ (right panel) with respect to the +y–axis.

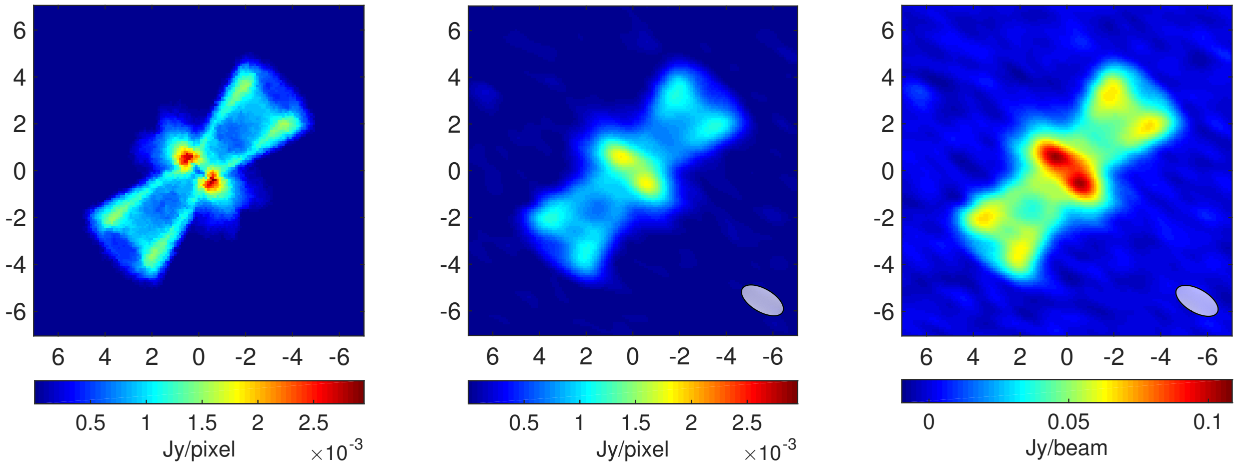

Figure 2.17 – *Left panel:* Moment 0 map (in Jy/pixel units) over all channels for the smooth model presented in the right panel of Fig. 2.14. *Middle panel:* Moment 0 map (in Jy/pixel units) resulting from the convolution between the data cube and a beam of $X_{\mathrm{FWHM}} = 0.5''$, $Y_{\mathrm{FWHM}} = 1''$, $\theta = 60°$, and a white Gaussian noise of $rms = 0.03$ Jy/beam per channel. The full ellipse in the right corner shows the shape of the beam. *Right panel:* Same as the middle panel but in Jy/beam units.

fits file is the smoothed data cube shown in Fig. 2.14. The beam is defined with $X_{\mathrm{FWHM}} = 0.5''$, $Y_{\mathrm{FWHM}} = 1''$, $\theta = 60°$ (see right panel of Fig. 2.16) for a beam area $\Theta_{beam} \simeq 56.65$ pixel/beam.

It is possible with GASS to create output fits files with the convolved data cube with the beam shape written in the header. These files can be read with data cube analysis packages (CASA, GILDAS, DS9, etc.) to proceed with any further analysis. For instance, with the Common Astronomy Software Applications package (CASA), one can perform simulations of observations using directly the output hyper-spectral cube created by LIME, with the help of the *simobserve* and *simanalyze* CASA tasks.

2.6 Benchmarking

Considering a 1D collapse model of HCO^+, Brinch and Hogerheijde (2010) performed a benchmarking between LIME and RATRAN, and only focused on the convergence of the population level between the two codes. In this section I extended this benchmarking to test different critical physical output parameters between the two codes:

1. The population density of the energy levels as a function of the radius.
2. The shape and intensity of the line profile from different beam positions and sizes in the map.

3. The value of the predicted continuum level.

This benchmarking is thus more complete than the one presented in Brinch and Hogerheijde (2010). Moreover, it has been performed with the newest LIME version 1.5. The RATRAN version used is that of March 2013. I have run about 30 different models to compare the results between LIME and RATRAN, varying the different input parameters and using different options of the two codes. In this section I only show two of them: the first benchmarking is a non-LTE model with continuum emission; the second one is an LTE model without continuum.

2.6.1 Model 1 - Variable physical parameters with continuum

To perform this benchmarking, since RATRAN is a 1D code, I can only consider structures with a spherical symmetry centred at the origin of the grid. The model is based on the physical structure of the low-mass proto-star IRAS16293-2422 (see Chapter 4) as derived by Crimier et al. (2010): a collapsing spherical source around a central object located at 120 pc. The emission of HCO^+ from $J = 1 \rightarrow 0$ to $J = 13 \rightarrow 12$ is computed. LIME and RATRAN have different input parameters needed to be set. For this benchmarking, these parameters are defined in Table 2.3. Variable gas and dust temperatures as well as H_2 density profiles are used as a function of the radius (see Fig. 2.18) and set a constant abundance and $b-$doppler value all over the model of 5×10^{-12} and 200 $\mathrm{m\,s^{-1}}$, respectively.

Table 2.3 – Benchmarking model properties.

Number of channels	71
Channel resolution	$100\,\mathrm{m\,s^{-1}}$
Image size	171 × 171
Pixel size	$0.2''$
Outer radius	6000 AU ($50''$ at 120 pc)
Gas-to-dust ratio	100
RATRAN shell numbers	191
LIME number of points	101992

By construction, in the two codes, the velocity field plays an important role in the resulting data cubes. Since RATRAN is built with spherical shells, the total velocity field is considered radial and its value is the same between two given radii. In LIME, every cell is located at a different radius and thus possesses a different value of the total velocity field, not always considered radial (depending on the 3D structure of the model). This effect strongly affects the calculated opacity since a larger column density of gas has the same velocity in RATRAN. Therefore, in order to avoid any difference between the two calculations, the velocity field was set to zero in this benchmarking. The only line broadening process considered is the $b-$doppler parameter.

RATRAN and LIME are both doing first the calculation of the population density of the different energy levels of the molecule. Fig. 2.19 shows a good agreement between RATRAN and LIME for the calculation of the population density of the first five levels of HCO^+. One can note that the LIME curves become a bit ratty at large radii, this is due to the cell density becoming smaller in the outer part of the model. This effect does not affect the resulting images since the mean values stay very close to the RATRAN ones.

An illustration of the comparison between the outputs of RATRAN and LIME is shown in Fig. 2.20 and Fig. 2.21 for three transitions among all the calculated ones. Figures 2.20a, 2.20b, and 2.21c display the $J = 1 \rightarrow 0$, $J = 6 \rightarrow 5$, and $J = 13 \rightarrow 12$ transitions respectively. These transitions span a wide range of upper energy levels, E_{up} ($\sim 4\,\mathrm{K}$ to $\sim 400\,\mathrm{K}$), and give a good sample to trace the differences between the two codes. Figures 2.21d shows the results for the $J = 13 \rightarrow 12$ transition, but with a different pixel size than the one written in Table 2.3. In each of

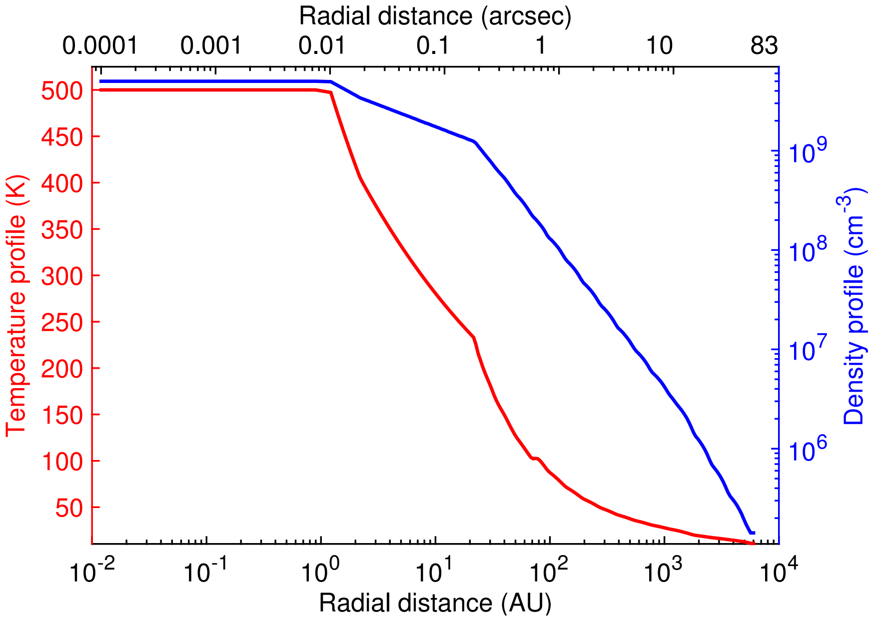

Figure 2.18 – Gas and dust temperatures (in red) and H_2 density (in blue) as a function of the radius.

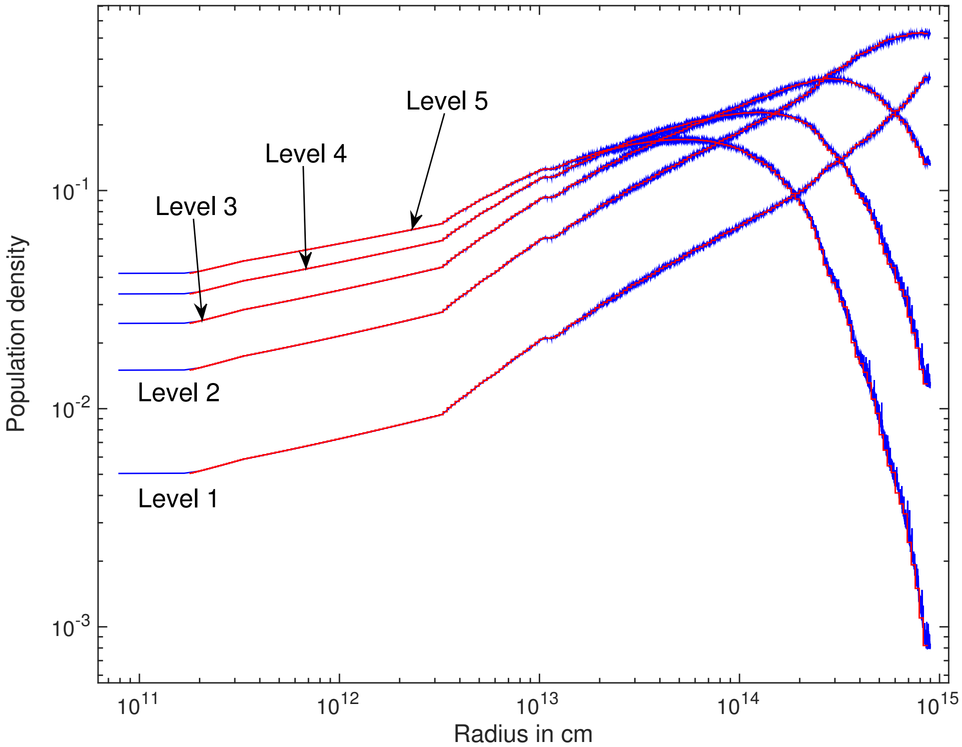

Figure 2.19 – Population density of the first 5 levels of HCO^+ as a function of the radius. The blue curves correspond to LIME and the red ones to RATRAN.

the four figures, the left panel shows the resulting image of the difference $Diff$ in percent between the run of RATRAN and the run of LIME, calculated by:

$$Diff[\%] = 100 \times \frac{\mathrm{RATRAN} - \mathrm{LIME}}{\mathrm{RATRAN}}. \tag{2.63}$$

For each beam drawn on these images, a spectrum is computed as the mean value of all the pixels

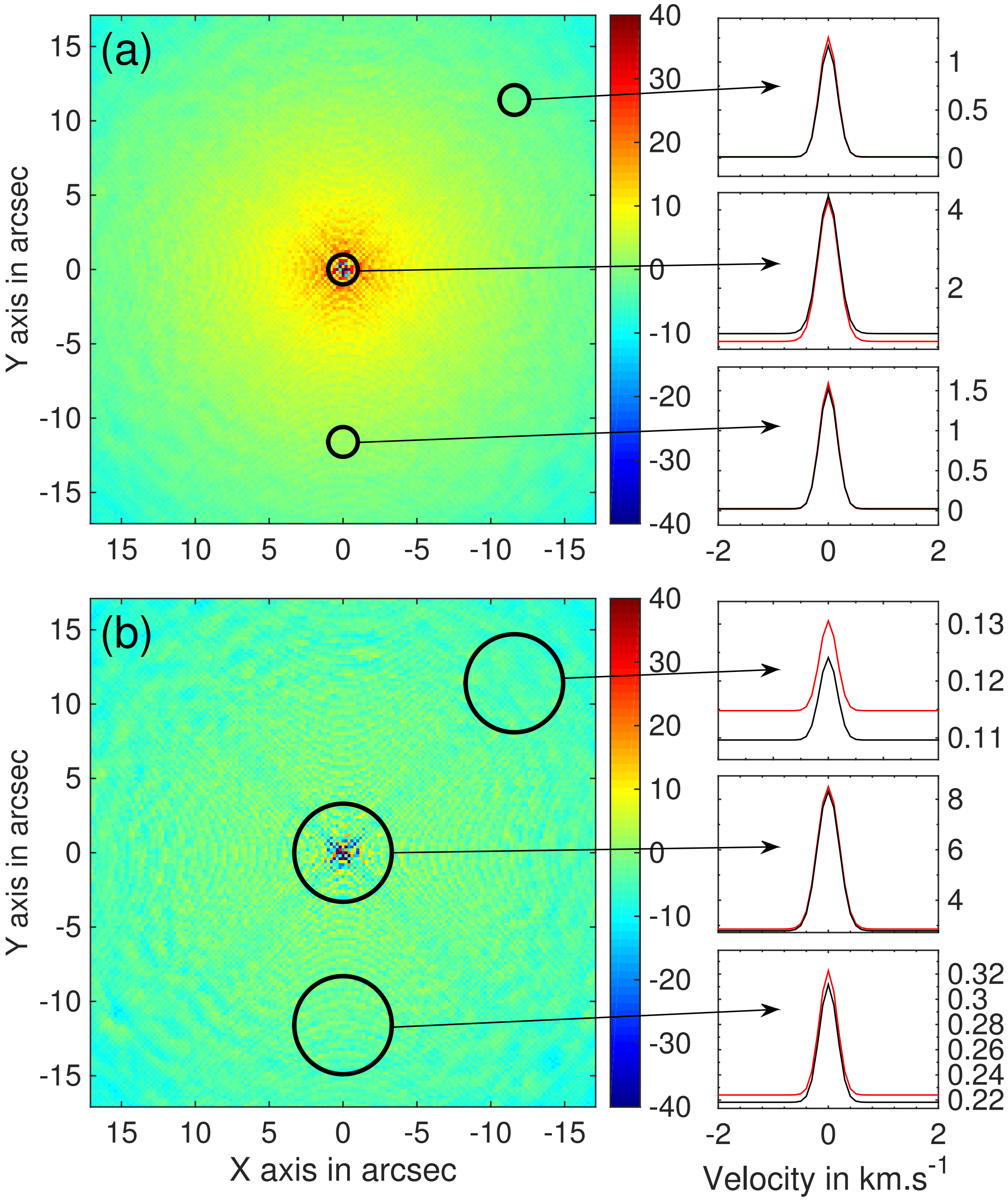

Figure 2.20 – *Left panels:* Comparison in % (see Eq. 2.63) between the output cubes of RATRAN and LIME for the HCO$^+$ J = 1 → 0 (panel a) and J = 6 → 5 (panel b) transitions. The white circles show the positions and the size of the beams used to compute the spectra. Panel (a): $[0,0]''$, $[0,-11.6]''$, $[-11.6,11.4]''$ and $\theta = 1''$ and panel (b): same positions, $\theta = 3.3''$. *Right panels:* Resulting spectra (in K) are plotted in black for RATRAN and in red for LIME.

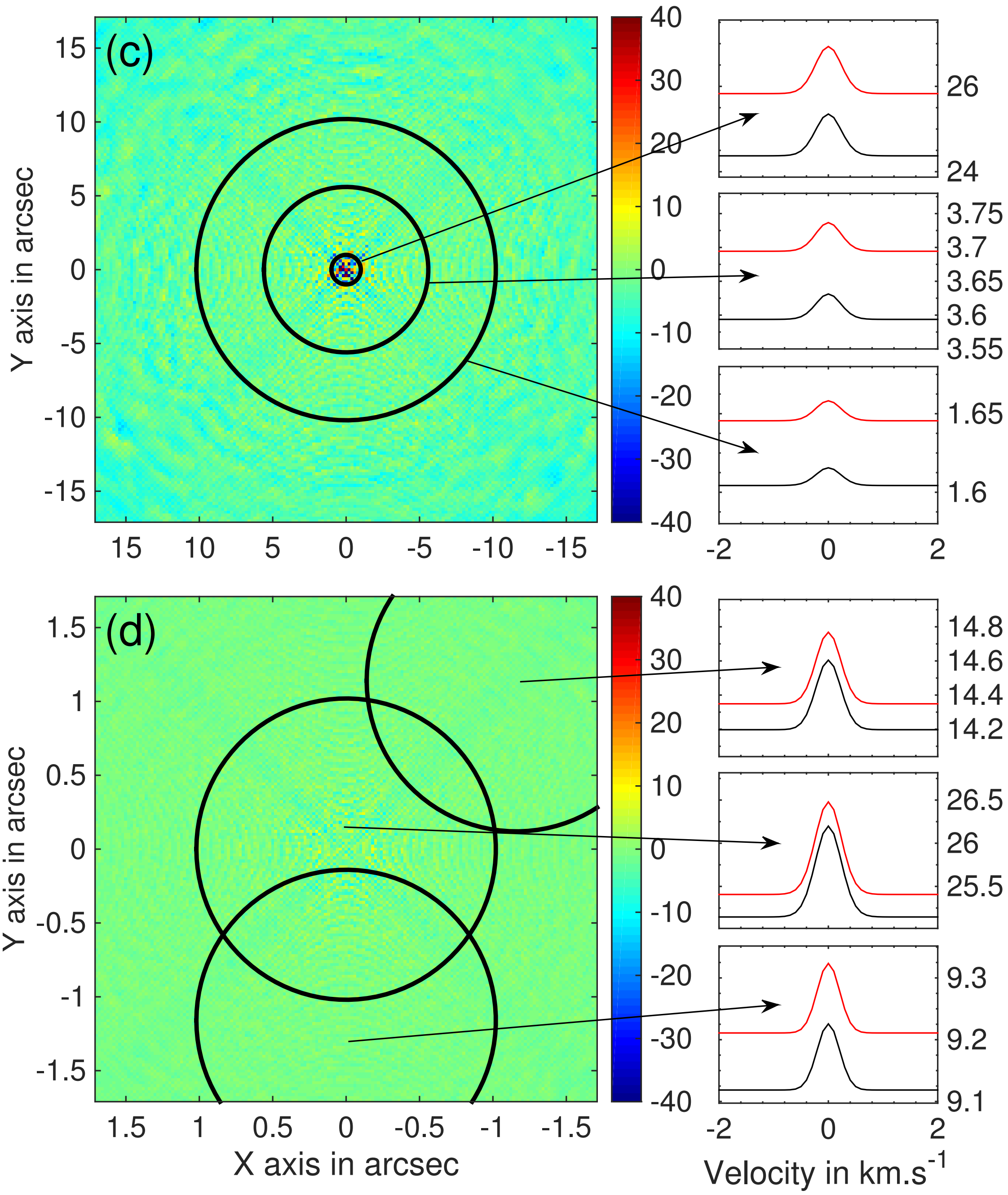

Figure 2.21 – Same as Fig. 2.20 for the J = 13 → 12 (both panels). Panel (c): $[0,0]''$ and $\theta = 1''$, $5.6''$ and $10.2''$, panel (d): $[0,0]''$, $[0,-1.16]''$, $[-1.16,1.14]''$ and $\theta = 1.02''$. *Right panels:* Resulting spectra (in K) are plotted in black for RATRAN and in red for LIME.

contained in that beam. All computed spectra of a given transition are plotted in the right panels of the corresponding figure.

The total flux of a given transition is also caculated by integrating the map over **all channels and all pixels**. The absolute difference between RATRAN and LIME on this total flux is about ±3% for all the transitions calculated. Examining the maps in details (see Fig. 2.20a, b, and Fig. 2.21c), one can note that the innermost part of the image ($\theta \sim 3''$) shows a pixel-to-pixel difference larger than those of the outer part of the image. In this region the difference can reach a value up to ±40% in contrast to the average absolute value $\lesssim$6% obtained anywhere else (see explanation below). This effect is filtered out when looking at the spectrum averaged over a certain number of pixels.

Figure 2.22 shows the impact on the flux differences (see Eq. 2.63) for each transition and each beam as a function of the beam position in the map or as a function of the beam radius. The left panel shows a clear trend depending on the distance from the centre of the map. This is in direct correlation with the difference seen in the innermost part of the image. In the right panel, the size of the beam also affects the difference between the maps, the more pixels are averaged, the more the differences are filtered out between the spectra, especially when the beam is on the centre of the map. One can also note that the difference is larger for the $\mathrm{J} = 1 \rightarrow 0$ transition compared to other transitions, which is also noticeable on the map (left panel of Fig. 2.20a). This may be explained by:

- The different continuum level calculated by RATRAN and LIME, visible in the spectra plotted in the right panel of Fig. 2.20a (one must take care of the different y–axis scales between the spectra). This is due to opacity effects resulting from the *ray-tracing* process between the two codes. Since the $\mathrm{J} = 1 \rightarrow 0$ transition of HCO^+ is the most optically thick line among the others, this trend is therefore enhanced for this line. This effect is also seen in the spectra plotted in the right panels of Fig. 2.20a, b, and Fig. 2.21c.
- The emission of the $\mathrm{J} = 1 \rightarrow 0$ transition is much more extended than the other transitions. With smaller beam sizes, a greater fraction of the signal will not be received leading to a greater error.

The difference in the calculation of the continuum is induced by the pixel size used ($0.2''$). The physical properties of the described model are varying a lot in a region that corresponds to the size of only one pixel ($n(\mathrm{H}_2)$ decreases by about a factor of 10), and particularly the temperature profile ($\Delta T \sim 300$). Since the dust emission is strongly dependent on this temperature profile, the pixel-to-pixel difference is larger with a larger pixel size. In fact, to determine the pixel intensity, LIME ray-traces photons in straight lines, considering a certain number of line-of-sights per pixel. Only one is considered, located at the centre of the pixel, if the *antialias* option of LIME is set to 1 (which is the case here). The *antialias* option controls the number of line-of-sights taken to determine the intensity of each pixel. LIME uniformly distributes these line-of-sights over the pixel surface, as it can be seen in the Fig. 2.23. If the pixel size is greater than the mean dimension of cells located behind, only the physical properties of cells located at the pixel centre will be taken into account, distorting the final results. To avoid this issue, one must decrease the pixel size or increase the value of the *antialias* option but in any case, it will increase (almost in a similar way) the executing time of LIME.

Fig. 2.21d displays the $\mathrm{J} = 13 \rightarrow 12$ transition modelled with a pixel size of $0.02''$. The number of pixels is the same, thus only an inner map of the previous $\mathrm{J} = 13 \rightarrow 12$ map (shown in Fig. 2.21c) is output. In this zoomed map, the previous difference seen in the centre of the map does not appear anymore. The resulting spectra (right panel of Fig. 2.20 and Fig. 2.21) show a better agreement for the continuum level (1% vs 6% previously) considering the same beam size and position.

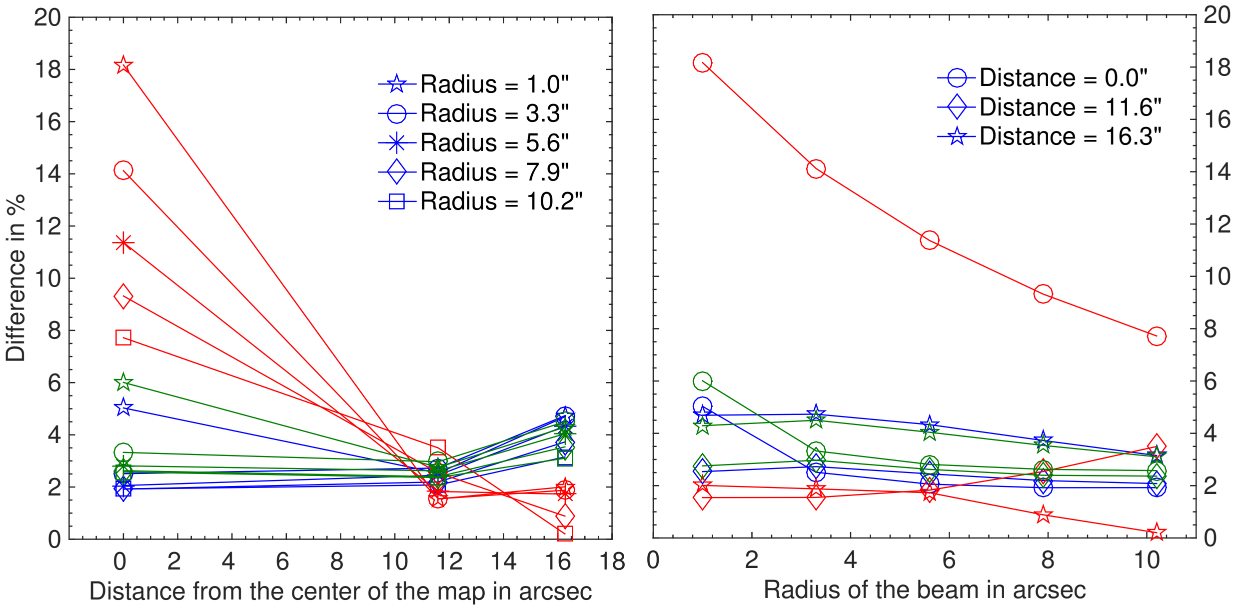

Figure 2.22 – For both panels, the red line refers to the J = 1 → 0 transition, the blue line refers to the J = 6 → 5 transition, and the green line refers to the J = 13 → 12 transition. *Left panel:* Absolute difference in % (see Eq. 2.63) between the LIME and RATRAN maps as a function of the distance of the beam from the centre of the map in arcsec. Different marker styles refer to different beam sizes. *Right panel:* Absolute difference in % (see Eq. 2.63) between the LIME and RATRAN map as a function of the beam size in arcsec. Different marker styles refer to different beam distances from the centre of the map.

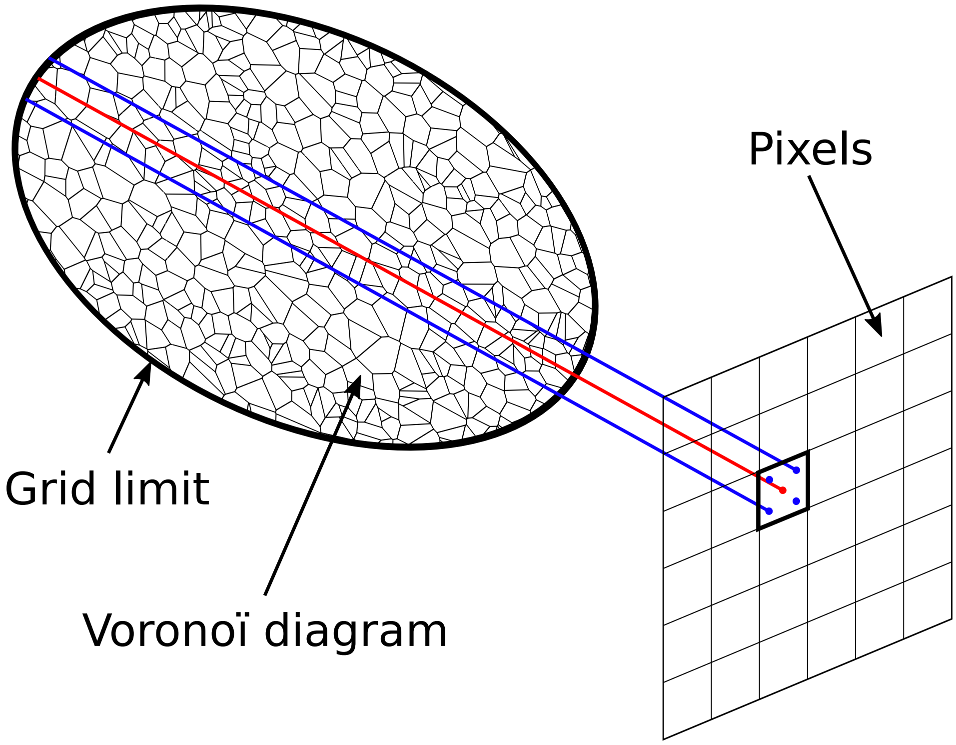

Figure 2.23 – Sketch explaining the *ray-tracing* of LIME. The pixel intensity is only determined with cells crossing the different line-of-sights. The red line is the line-of-sight located at the centre of a pixel, for *antialias* = 1. Blue ones shows the distribution of line-of-sights for *antialias* = 4.

The importance of the point distribution on the difference has also been tested. The exact same model has been used considering a linear distribution of points as a function of the radius instead of a distribution following the density as a function of the radius (see Sect. 2.2). A linear distribution produces more points in the external part of the model compared to the density distribution, considering the density profile shown in Fig. 2.18. With this new distribution, the difference is reduced by a factor of up to 2, depending on the beam radius and position. The gain is greater on the outer part of the image and for the smaller beam radii. This trend shows that the point distribution, as well as the number of points, are both important parameters to consider while comparing RATRAN to LIME. This new distribution does not change much the final result given by LIME because the difference was already small ($\lesssim 5\%$) for the previous distribution; but it explains why the difference is greater on the outer part of the model.

To summarise, depending on the physical problem treated, one must take care of some input properties that can be set in LIME and leads to wrong results compared to RATRAN:

1. If too few points are set in the model, the population density will not be calculated correctly and the spatial coverage of the model will not be smooth enough. This will result in visible and non-desired structure in the output image.

2. A pixel size much larger (or an *antialias* value too low) than the mean scale of variation of the physical properties set in the model will lead to a wrong continuum calculation. Since the pixel is too large, it will not probe correctly the physics occurring in the region it covers and the pixel intensity will only reflect an average value of what is going on on a smaller scale.

Finally, one can note that if the size of the data cube is too large (large number of pixels and/or channels), LIME will take a long time to create it, leading to a long calculation time while running a grid of models.

2.6.2 Model 2 - Constant physical parameters without continuum to reach LTE

This model was made in order to intentionally reach the LTE, in order to compare the maximum peak intensity reached by the two codes and compare the results with a LTE and LVG method. I used CASSIS to calculate the model in LTE and RADEX Online[9] to calculate it in LVG. The velocity field is removed in this model as well in order to avoid any difference between the two calculations. The only remaining line broadening process is defined by the $b-$doppler parameter.

I have run 10 times the same LIME model with approximately 10 000 points but with a different grid to get rid off the fluctuations due to the randomness of the gridding process. All these models are then averaged together to obtain a smoother map, thanks to the GASS tool presented in Sect. 2.5.1. The benchmarking model properties are the same as the previous model (see Table 2.3) and the physical parameters for this model are gathered in Table 2.4. The same analysis as for the previous model has been done.

T_{kin}, T_{dust}	70 K
$n(H_2)$	1×10^{9} cm^{-3}
$N(H_2)$	8.976×10^{25} cm^{-2}
$N(HCO^+)$	8.976×10^{16} cm^{-2}
$X(HCO^+)$	1×10^{-9}
$b-$doppler	1000 m s^{-1}

Table 2.4 – Physical parameters of the LTE model.

---

[9] `http://var.sron.nl/radex/radex.php`

Fig. 2.24 shows a perfect agreement of the population density between the two codes, since the first five levels calculated by LIME or RATRAN are completely superimposed. Thus, a very good agreement of the line profiles between LIME and RATRAN is expected.

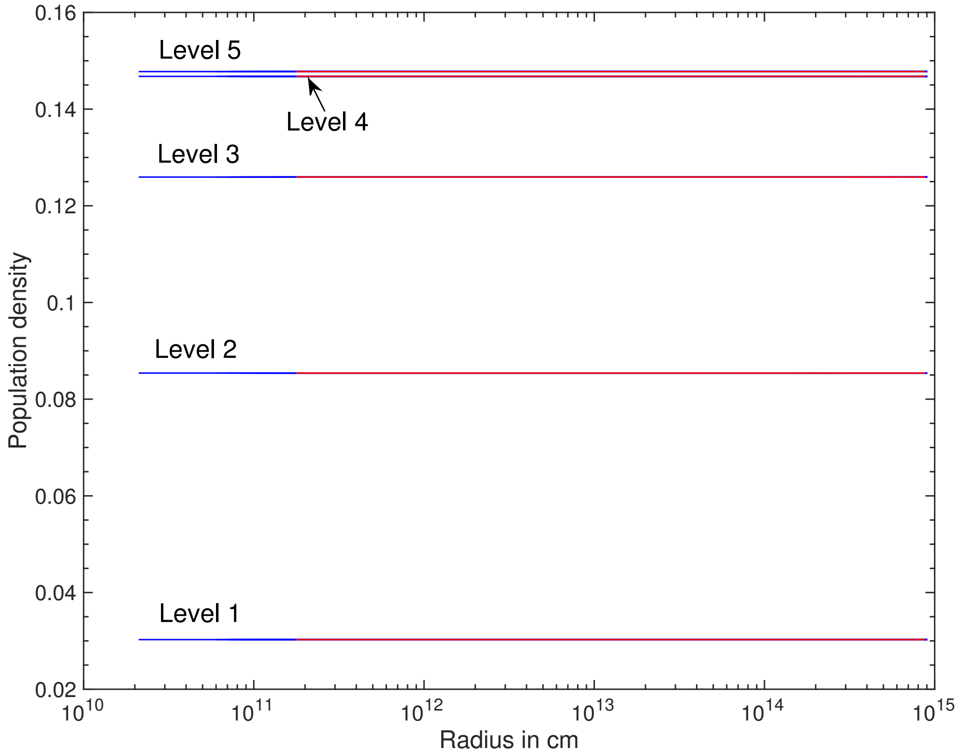

Figure 2.24 – Population density of the first 5 levels of HCO^+ as a function of the radius. The blue curves correspond to LIME and the red ones to RATRAN.

Figures 2.25a, 2.25b, and 2.25c display the $J = 1 \rightarrow 0$, $J = 6 \rightarrow 5$, and $J = 13 \rightarrow 12$ HCO^+ transitions respectively. In each of the four figures, the left panel shows the resulting image of the difference in percent (see Eq. 2.63) between the run of RATRAN and the run of LIME. For each beam drawn on these images, a spectrum is computed as the mean value of all the pixels contained in that beam. All computed spectra of a given transition are plotted in the right panels of the corresponding figure.

The total flux of a given transition is also calculated by integrating the map over **all channels and all pixels**. The difference between RATRAN and LIME on this total flux is about -2% for all the transitions calculated, suggesting that LIME calculates a slightly higher total flux than RATRAN. For this case, I have also compared the peak value with both LTE and LVG models for three different transitions (see Table 2.5). For all codes it has been checked that the LTE is reached since $T_{\mathrm{kin}} = T_{\mathrm{ex}}$. LIME and RATRAN always give the same peak intensity (differences $\leq 0.05\%$) as the LVG and LTE models from RADEX and CASSIS respectively.

	LIME	RATRAN	LTE (CASSIS)	LVG (RADEX Online)
$J = 1 \rightarrow 0$	66.76	66.75	66.75	66.75
$J = 6 \rightarrow 5$	57.94	57.94	57.94	57.94
$J = 13 \rightarrow 12$	45.84	45.82	45.83	45.83

Table 2.5 – Intensity in K at the centre of different transitions, compared for different codes.

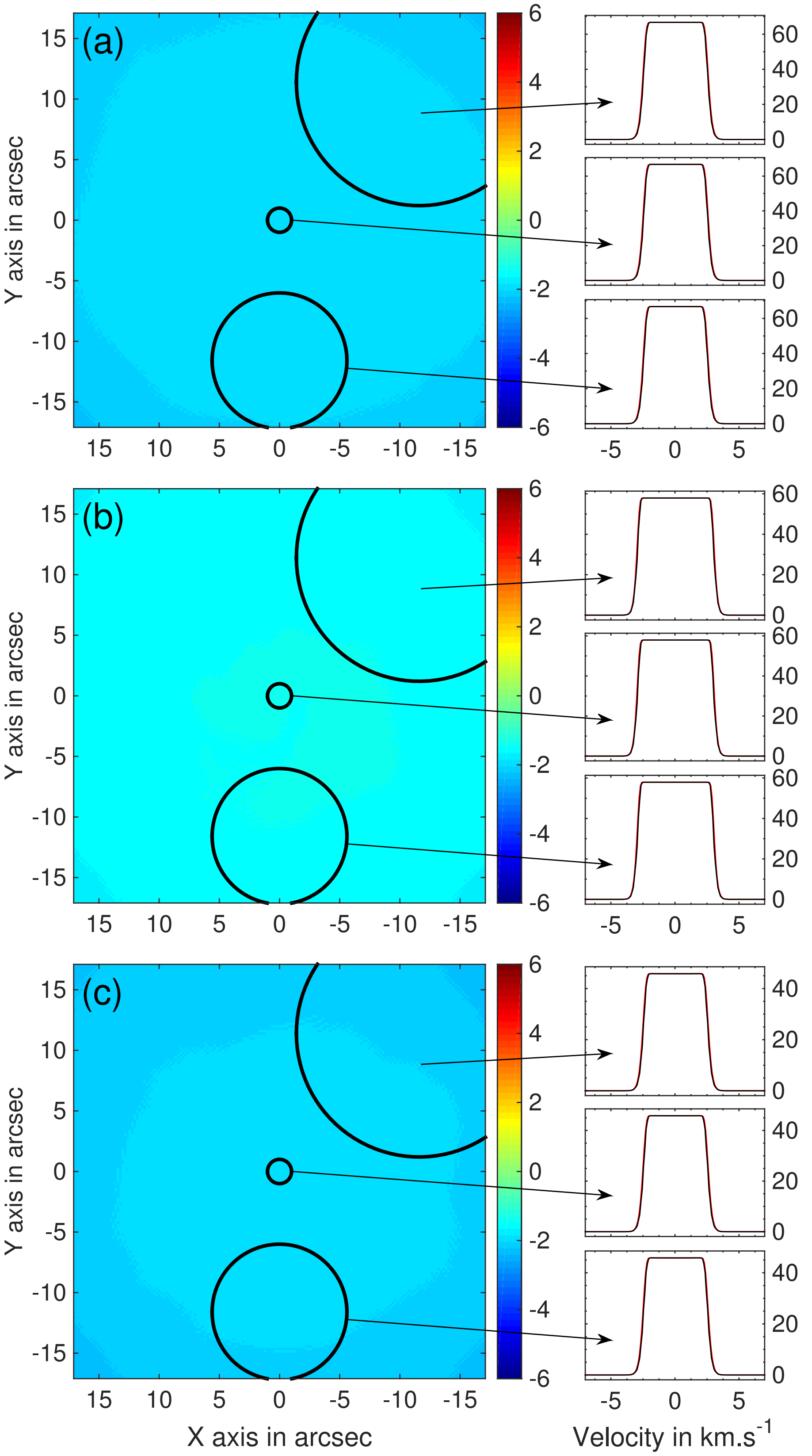

Figure 2.25 – *Left panels:* Comparison in % (see Eq. 2.63) between the output cubes of RATRAN and LIME for the HCO$^+$ J = 1 → 0 (panel a), J = 6 → 5 (panel b), and J = 13 → 12 (panel c) transitions. The black circles show the positions and the size of the beams used to compute the spectra: $[0,0]''$, $[0,-11.6]''$, $[-11.6,11.4]''$ and $\theta = 1''$, $\theta = 5.6''$, $\theta = 10.2''$ respectively. *Right panels:* Resulting spectra (in K) are plotted in black for RATRAN and in red for LIME.

Figure 2.26 shows the impact on the flux differences (see Eq. 2.63) for each transition and each beam as a function of the beam position in the map or as a function of the beam radius. The left panel shows no clear trend and the absolute difference is $\lesssim 2\%$. Same conclusion for the right panel, the size of the beam does not affect the difference between the two codes. I note that the absolute difference seems to drop slightly for the J = 6 → 5, from $\sim 2\%$ to $\sim 1.5\%$, maybe due to the higher opacity ($\tau \simeq 3600$) of this line compared to the other two ($\tau \simeq 300$).

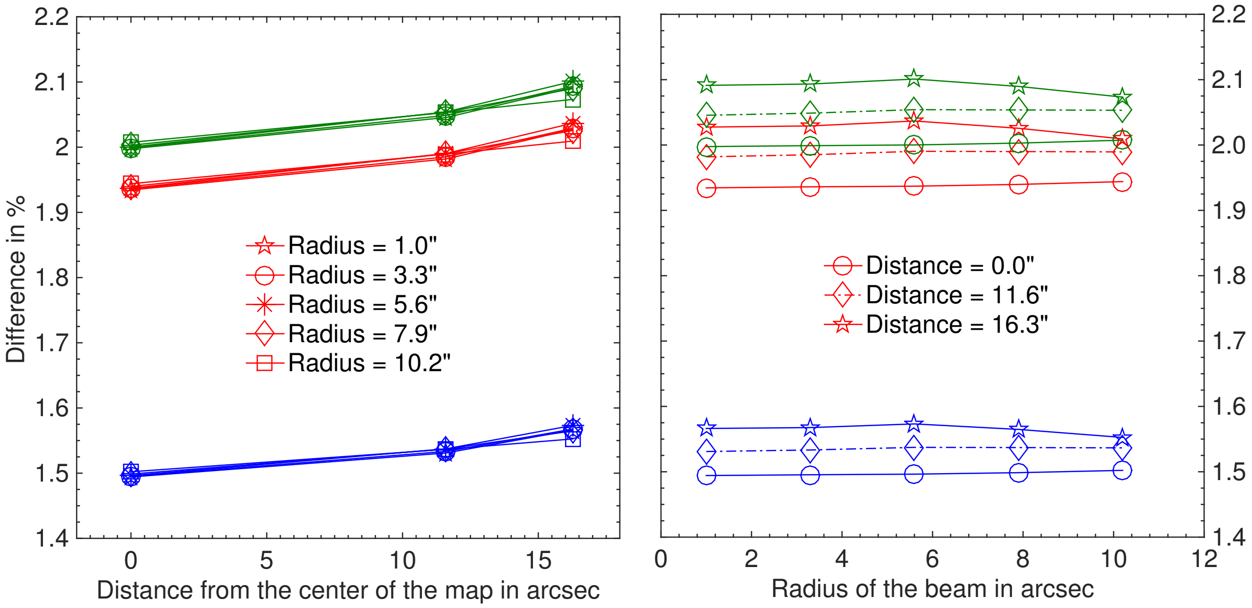

Figure 2.26 – For both panels, the red line refers to the J = 1 → 0 transition, the blue line refers to the J = 6 → 5 transition, and the green line refers to the J = 13 → 12 transition. *Left panel:* Absolute difference in % (see Eq. 2.63) between the LIME and RATRAN maps as a function of the distance of the beam from the centre of the map in arcsec. Different marker styles refer to different beam sizes. *Right panel:* Absolute difference in % (see Eq. 2.63) between the LIME and RATRAN map as a function of the beam size in arcsec. Different marker styles refer to different beam distances from the centre of the map.

2.7 Examples

In this section I will show different examples of the GASS capabilities. The first example demonstrates the 3D structures that can be created in GASS and the second one intends to reproduce an already existing model published in de Gregorio-Monsalvo et al. (2013).

2.7.1 Example 1 - 3D demonstration

The ^{13}CO J $= 2 \rightarrow 1$ emission of an object composed of a spherical source (similar to a proto-stellar envelope), a proto-planetary disk, and a bipolar outflow is modelled in this example. Table 2.6 summarises the physical properties set in this example, which does not correspond to any already observed case. All the structures are located in the centre (0, 0, 0) of the model and the resulting complete velocity field given by these structures is taken into account. I have chosen ^{13}CO as an example because its transitions are not too optically thick compared to ^{12}CO. For the disk model, the abundance drops a lot when the temperature is below 27 K, to reproduce the freeze-out of ^{13}CO onto dust grains. This will highlight clearly the emission regions of the disk for this example.

Table 2.6 – Physical properties of the model set for the first example.

Physical properties	Value
General properties	
Grid min, max radius	$0.1''$, $7''$
N° points	10 000
Distance	300 pc
$b-$doppler	200 $\mathrm{m\,s^{-1}}$
V_{LSR}	0 $\mathrm{km\,s^{-1}}$
Central object mass	3 $M_\odot$
Envelope properties	
$T_{env,max}$	200 K ($\alpha = -0.5$)
$n(H_2)_{env,max}$	1×10^9 cm^{-3} ($\beta = -1.5$)
$X_{in}(^{13}CO)$, $X_{out}(^{13}CO)$	1.5×10^{-13}, 7.5×10^{-11}
Proto-planetary disk properties	
ρ_{in}, r_{max}, h_{max}	$0.7''$, $4.5''$, $5''$
Θ, Φ	$(0, 45, 90)^\circ$, $(0, 45, 90)^\circ$
T_{atm}, T_{mid}	500 K, 50 K ($\gamma = -0.5$)
$n(H_2)_{disk}$	6.5×10^7 cm^{-3} ($\delta = -1.0$)
$X_{in}(^{13}CO)$ for T < 27 K	1.5×10^{-6}
$X_{out}(^{13}CO)$ for T > 27 K	1.5×10^{-17}
Outflow properties	
$a_{outflow}$, $b_{outflow}$, ρ_{in}, z_{out}	$150''$, $8''$, $0.5''$, $5''$
$V_{outflow}$	10 $\mathrm{km\,s^{-1}}$
Θ, Φ, $\Delta\gamma$	$(0, 45, 90)^\circ$, $(0, 45, 90)^\circ$, 15°
$T_{outflow}$	100 K
$n(H_2)_{outflow}$	5×10^6 cm^{-3}
$X(^{13}CO)$	1.5×10^{-8}

The output data cube was set with 151 channels and a spectral resolution of 100 $\mathrm{m\,s^{-1}}$ to cover a 15 $\mathrm{km\,s^{-1}}$ bandwidth. The spatial resolution is $0.1''$ with 141 pixels to cover the radial size of $7''$ of the model. From the previous section, one can note that the pixel size is small enough to cover the physical variation of the example since no dust continuum emission is set. The same physical case considering the dust continuum would have required a pixel size of $0.01''$.

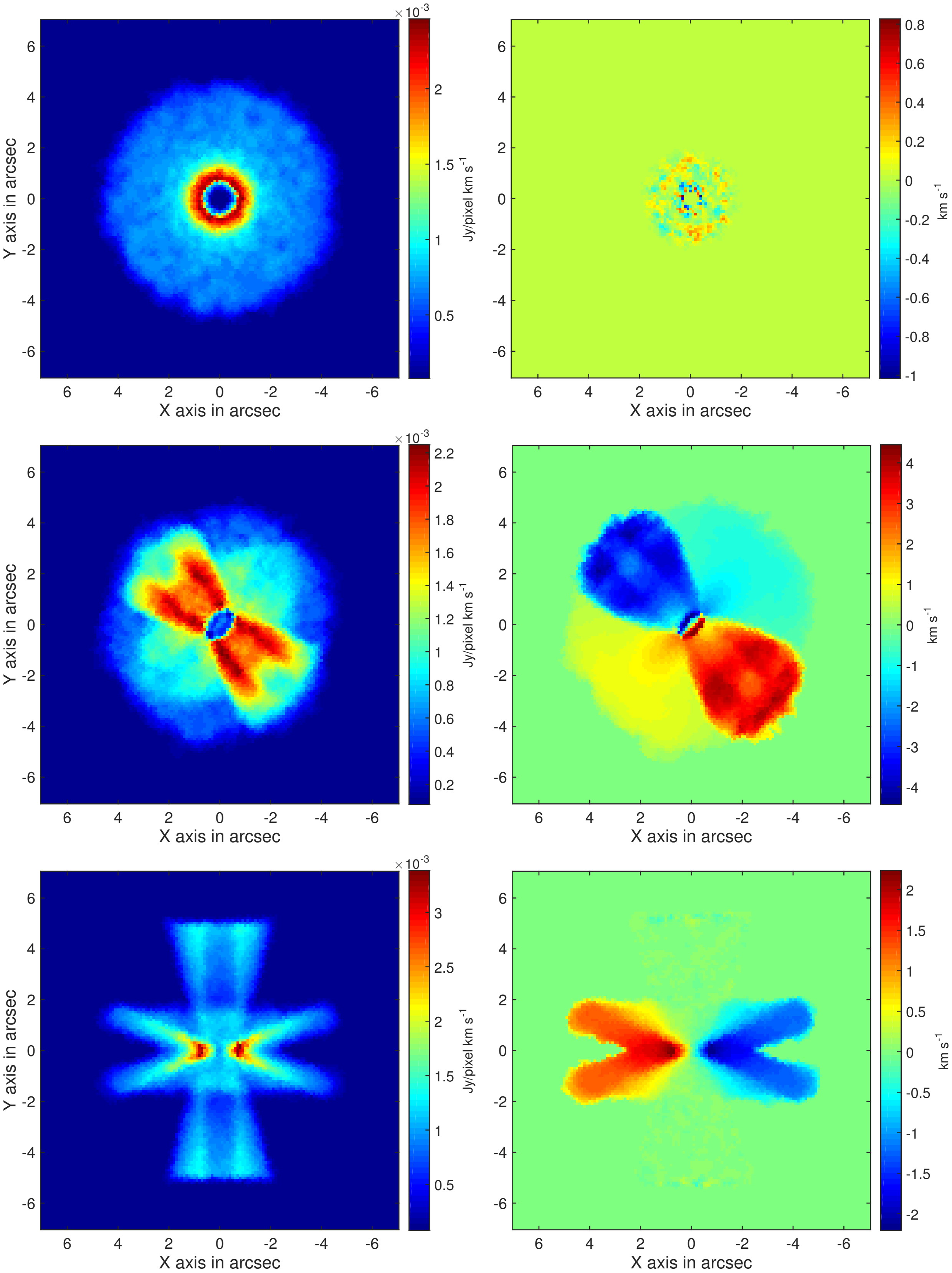

Figure 2.27 – Moment 0 (left) and moment 1 (right) maps calculated over all channels of the data cubes for the ^{13}CO J $= 2 \rightarrow 1$ transition. The model has been rotated by different angles: $\theta = 0°, \phi = 0°$ (top panels); $\theta = 45°, \phi = 45°$ (middle panels); $\theta = 90°, \phi = 90°$ (bottom panels).

Thanks to GASS, I ran 10 times the same model and averaged them as described in Section 2.5.1 in order to completely blur out the artefacts due to the gridding process. From the fits file of the smoothed data cubes, Fig. 2.27 shows the resulting moment 0 and moment 1 maps over all channels for different sets of the (θ, ϕ) angles. In the moment 0 map, the outflow cavity emission is plainly identifiable with the $\theta = 0°, \phi = 0°$ (top-left panel, face-on) and $\theta = 90°, \phi = 90°$ (bottom-left panel, edge-on) models. The disk emission is also well identifiable at the centre of the image, especially in the $\theta = 90°, \phi = 90°$ (bottom panels), where the disk is completely seen edge-on. The depletion of ^{13}CO is well marked as expected. In the moment 1 map, the outflow is clearly identified in the middle-right panel thanks to its ejection velocity. The Keplerian rotation of the disk is also present, but fainter. In the bottom-right panel, this rotation is dominating, and only the disk is visible. The top-right panel does not show any sign of structures since the positive and negative velocity components cancel each other out along the line-of-sight.

The 3D structure of a model with $\theta = 45°, \phi = 45°$ is animated in Fig. 2.28 (click on the figure to activate the animation). The animation progressively zooms in and out of the 3D structure, displaying the H_2 density on the left panel and the gas temperature on the right panel. For a better 3D visualisation, it is needed to slightly change some of the parameters of the disk and outflow structures. Therefore, the model presented in these animations is not exactly the same as the one described in Table 2.6, but the idea stays the same. From these animations, one can note that the outflow cavity is clearly defined as well as the proto-planetary disk. All the points surrounding these two structures belong to the envelope model.

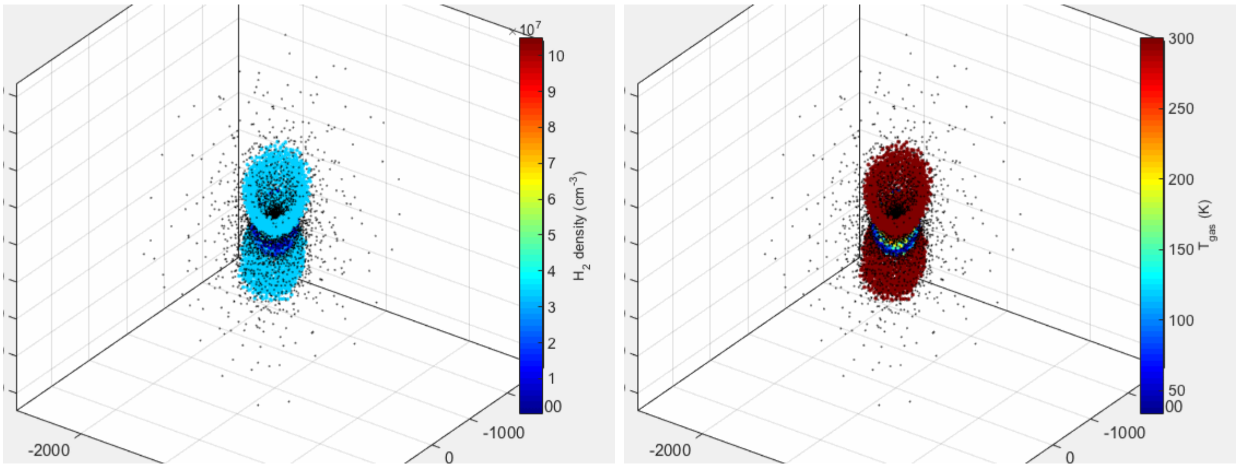

Figure 2.28 – Animation of the 3D density (left) and gas temperature (right) structure of the first example. The outflow and disk structures are clearly recognisable. Click on the figure to activate the movie. Only works with Adobe Acrobat Reader, version ≥ 9 (not greater than 9.4.1 on Linux) or Foxit Reader.

2.7.2 Example 2 - HD 163296

For this second example, the goal is to retrieve the modelling features obtained in the model presented by de Gregorio-Monsalvo et al. (2013) on HD 163296. I do not aim at entirely reproduce their model since it has been done with MCFOST, a 3D Monte Carlo LTE and continuum radiative transfer code (Pinte et al., 2006, 2009, for a more detailed description of the code). MCFOST has been created especially to generate and solve disk modellings, which is not the case of LIME. Proto-planetary disks can be precisely modelled with this code, in a more efficient way than GASS in its current development. Nonetheless, I try to reproduce the disk feature they detect with the CO $J = 3 \rightarrow 2$ emission thanks to GASS and LIME, to demonstrate that the disk description in GASS is valid and can also be used, at first sight, to understand this kind of observations.

The physical properties of HD 163296 determined in Tilling et al. (2012) and de Gregorio-Monsalvo et al. (2013) is used. Since some MCFOST options do not exist in GASS, I tentatively reproduce the disk model using the parameters given in Table 2.7.

Table 2.7 – Physical properties of the model set for HD 163296.

Physical properties	Value
General properties	
Grid min and max radius	$0.003''$, $5''$
N° points	10 000
Distance	120 pc
b−doppler	100 $\mathrm{m\,s^{-1}}$
V_{LSR}	5.71 $\mathrm{km\,s^{-1}}$
Central object mass	2.47 $M_\odot$
HD 163296 disk properties	
ρ_{in}, r_{max}, h_{max}	$0.0035''$, $4.5''$, $5''$
Θ, Φ	−135°, 60°
Temperature profile	
$T_{atm,in}$, $T_{mid,in}$	2000 K, 300 K
Number of regions	3
γ_1, γ_2, γ_3	-0.15, -1, -1.7
$\rho_{1/2}$, $\rho_{2/3}$	100 AU, 150 AU
H_2 density profile	
$n(H_2)_{disk,in}$	1×10^{12} $\mathrm{cm^{-3}}$
Number of regions	2
δ_1, δ_2	-1.5, -8
$\rho_{1/2}$	100 AU
X_{in}(CO) for $T < 27$ K	1.5×10^{-6}
X_{out}(CO) for $T > 27$ K	1.5×10^{-17}

The CO $J = 3 \rightarrow 2$ transition at 345.796 GHz has been modelled with LIME. The output data cube was set with 51 channels and a spectral resolution of 200 $\mathrm{m\,s^{-1}}$ to cover a 10 $\mathrm{km\,s^{-1}}$ band. The spatial resolution is $0.1''$ with 151 pixels to widely cover the radial size of $5''$ of the model. No dust continuum is set in this example. As for the first example, I ran 10 times the same model and averaged them to completely blur out the artefacts due to the gridding process and to obtain a smoothed data cube.

The resulting channels are plotted in Fig. 2.29. The bright CO emission is coming from the front disk surface. de Gregorio-Monsalvo et al. (2013), in their study, also detected a fainter emission coming from the rear disk surface. I have tried to reproduce this emission with GASS but it seems to be difficult since this fainter emission is coming from a region located very close to the inner part of the disk. I did not manage to reproduce exactly the physical model of HD 163296 presented in Tilling et al. (2012), that is likely the reason why the rear emission is not seen in this GASS model. Nevertheless, the front emission and the rotation pattern are successfully reproduced, both are clearly visible between the different channels. To prove that the "missing" emission from the rear disk surface is not due to a caveat in GASS, let us consider the disk model of the first example (with $\theta = 45°, \phi = 45°$) taken alone. With this disk, it is possible to reproduce a signature of both the front and rear emissions. The rotation pattern, presented in Fig. 2.30, clearly reveals the emission of both surfaces of the disk, represented as solid and dashed lines for the front and back surfaces of the gas disk, respectively. The moment 0 map shown in Fig. 2.31 also reveals the front and rear emission of the disk. This disk is larger than HD 163296 and not rotated the same way, it is the reason why both surfaces of the disk are visible in this model. Given the physical parameters of HD 163296, it is much more difficult to reproduce these features with GASS, as explained above.

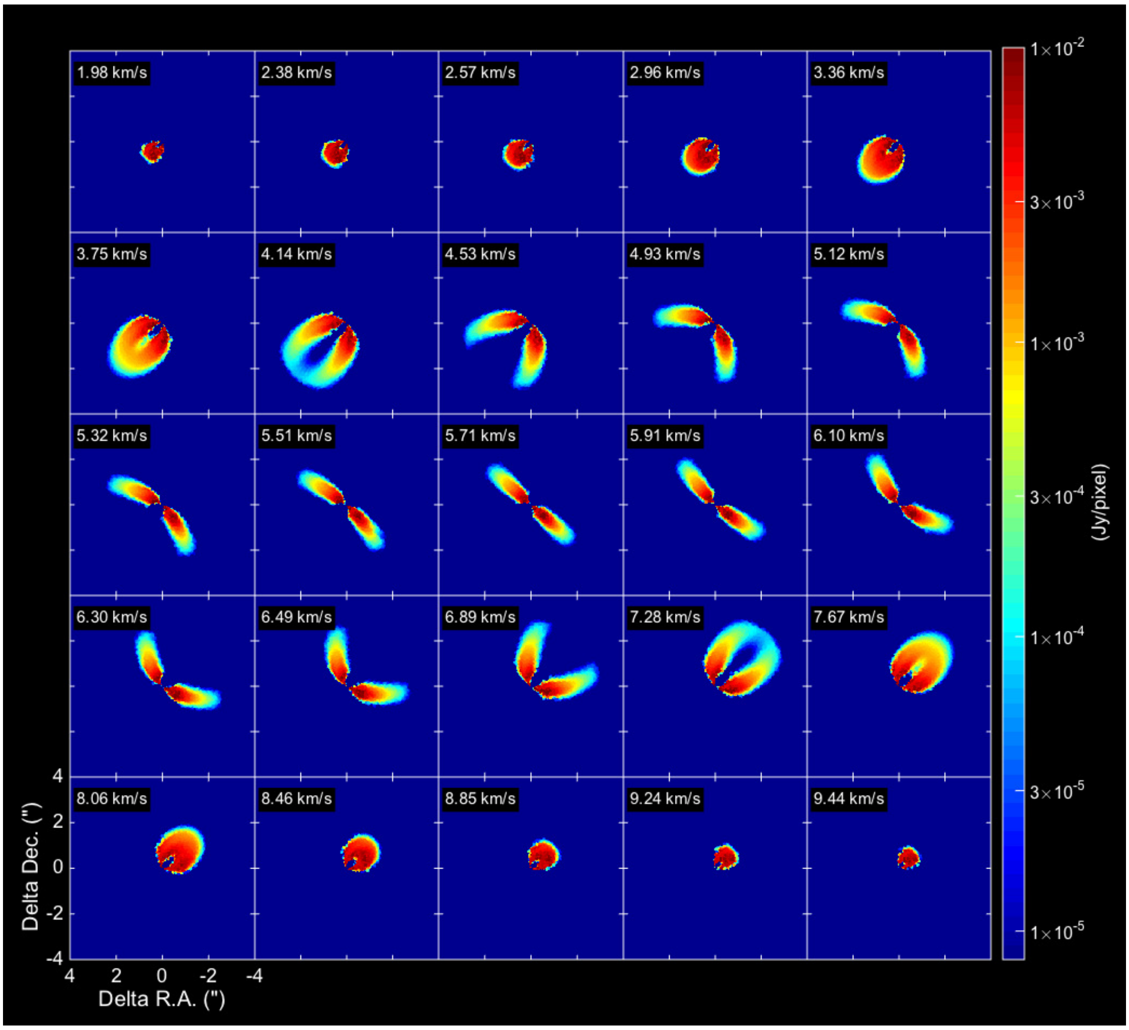

Figure 2.29 – Channel maps of the modelled CO J $= 3 \rightarrow 2$ emission in HD 163296 from 1.98 to 9.44 $\mathrm{km\,s^{-1}}$.

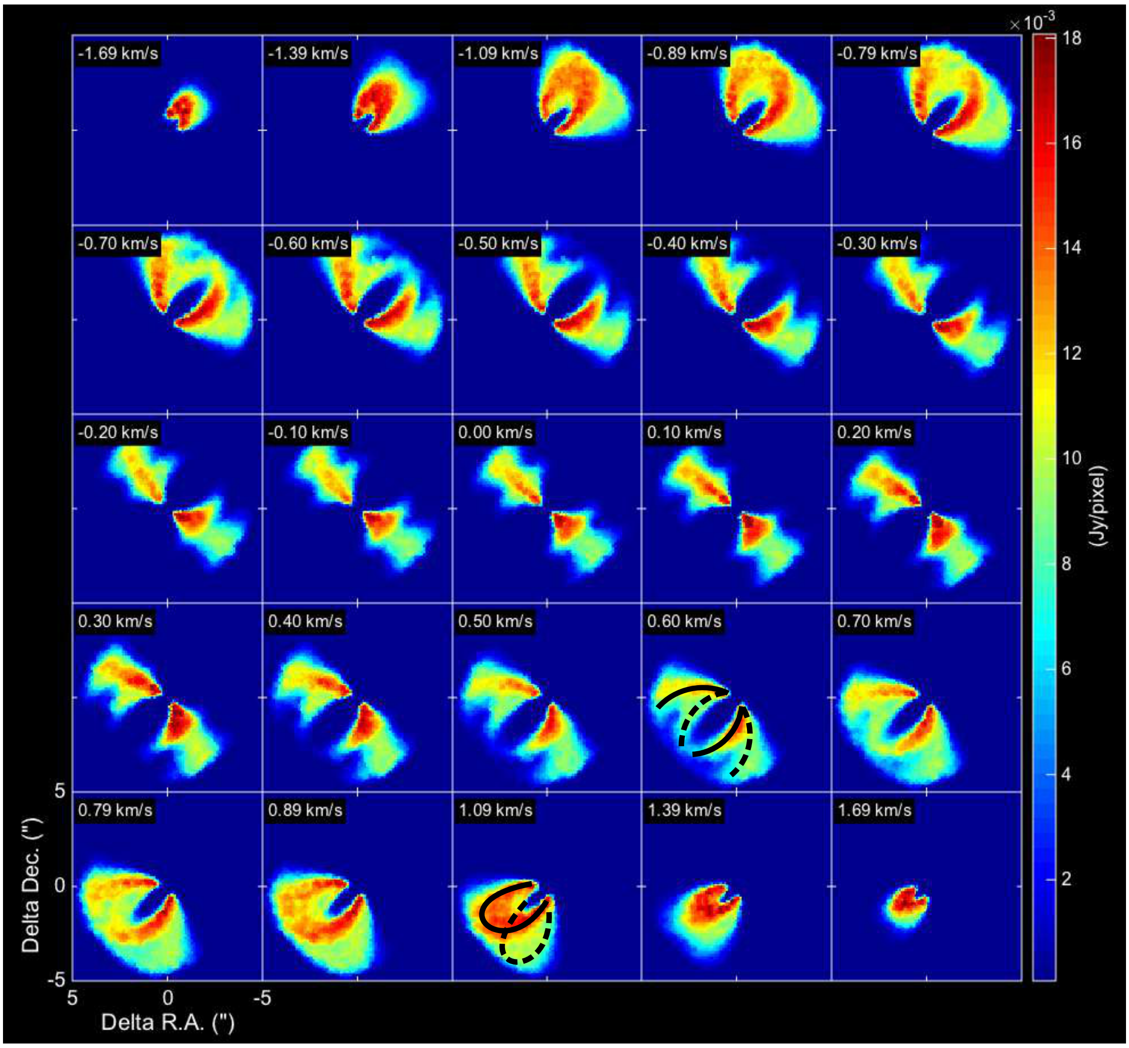

Figure 2.30 – Channel maps of the modelled ^{13}CO J $= 2 \rightarrow 1$ from -1.70 to 1.70 km s^{-1}. The black solid and dotted lines represent the front and back surfaces of the gas disk, respectively.

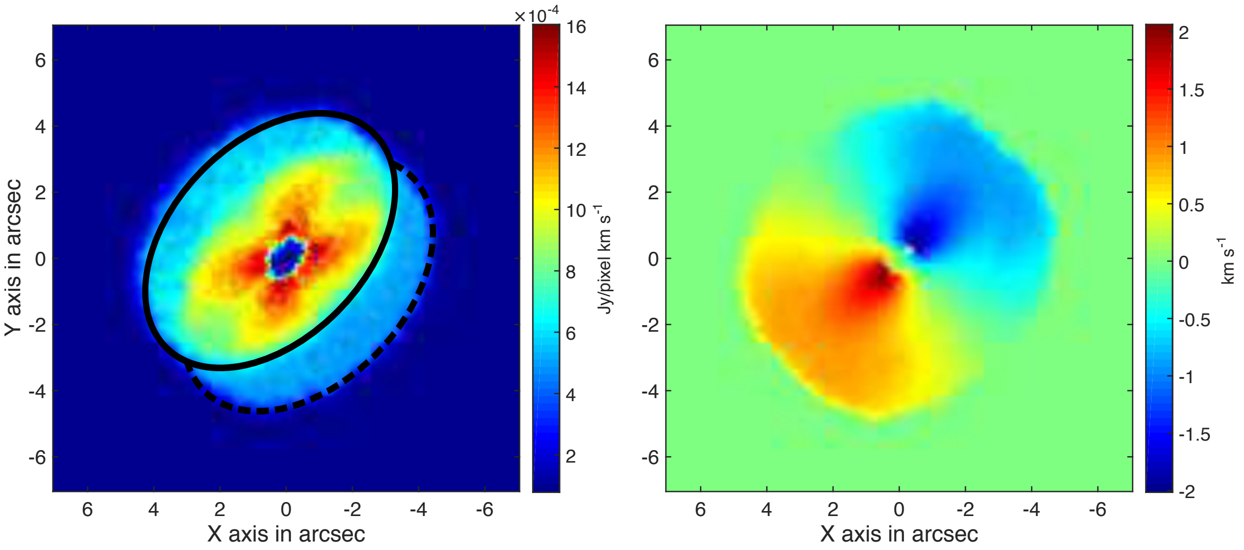

Figure 2.31 – Moment 0 (left) and moment 1 (right) maps calculated over all channels of the data cubes for the disk model only of the first example shown in this section, with $\theta = 45°, \phi = 45°$. The front (black solid line) and rear (black dotted line) surfaces of the gas disk are easily recognisable.

2.8 Concluding remarks

I have developed GASS, a code that allows to easily define the physical structure of different astrophysical structures by creating, manipulating, and mixing several different physical components such as spherical sources, disks, and outflows (see Fig. 2.32). GASS can create input model files for LIME and the output data cubes generated by LIME can be analysed by several post-treatment options in GASS such as plotting spectra, moment maps, or simulating observations. An in-depth benchmarking has been made between LIME and RATRAN. The differences between the two codes on the total integrated intensity over all pixels and channels range from 1% to 3% depending on the physical case. One must take care of LIME input parameters (number of points, pixel size) set for a given physical case since the resulting data cube may not be representative if they are not carefully chosen. I will keep on the development of GASS and, for instance, I expect to improve the GUI or to implement more LIME options in future releases of the code.

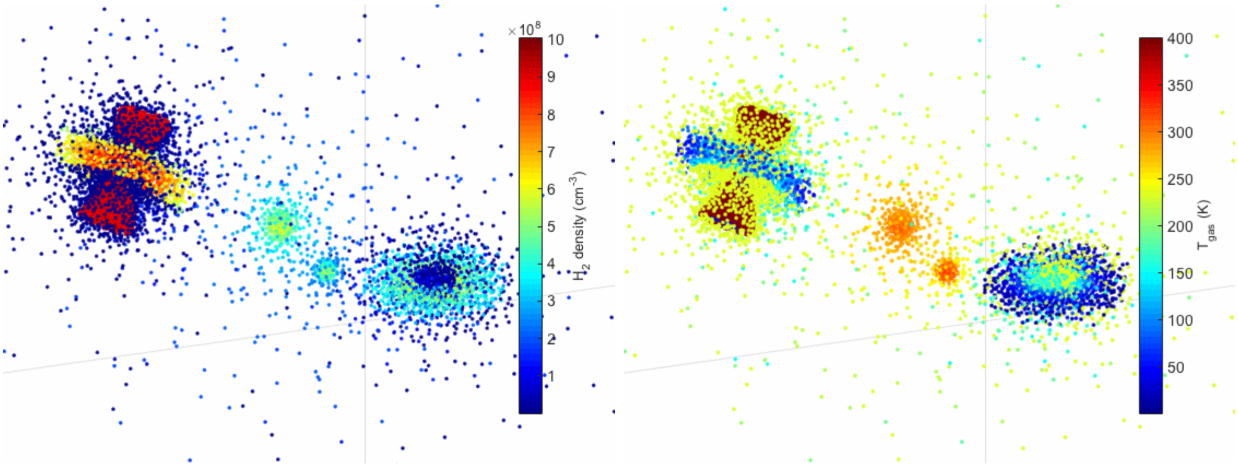

Figure 2.32 – Animation of the 3D density (left) and gas temperature (right) structure of a complex model, containing 2 disks, 2 spherical cores, and 1 outflow. Click on the figure to activate the movie. Only works with Adobe Acrobat Reader, version ≥ 9 (not greater than 9.4.1 on Linux) or Foxit Reader.

“Le commencement de toutes les sciences,
C’est l’étonnement de ce que les choses sont ce qu’elles sont.”

Aristote

Hubble Space Telescope image of the cluster Westerlund 2 and its surroundings.

CHAPTER 3

STUDY OF WATER AND DEUTERATED WATER IN A PRE-STELLAR CORE

Contents

3.1 Water in space

Water is an important molecule not only on Earth but also in space. Indeed, since it is formed by two of the most abundant elements in the Universe that bind in molecules, water governs the chemical composition and the thermal balance of the interstellar dense molecular gas. The latter is also the gas from which stars are formed, so that water influences the whole star formation process at various levels in the different phases (e.g. Caselli and Ceccarelli, 2012). In molecular clouds, icy water is present in large quantities, up to half of the oxygen elemental abundance, and is synthesised on the interstellar grains (e.g. Boogert et al., 2015). In the denser regions inside the molecular clouds, which are the pre-stellar cores that will eventually form stars, water is still mostly icy (Caselli and Ceccarelli, 2012). The same water, formed in those first two stages (see Sect. 1.1), is then released in the gas phase where the dust is warm enough ($\geq$ 100 K) in the hot cores, hot corinos, and proto-stellar molecular shocks (e.g. van Dishoeck et al., 2014). It is then found in proto-planetary disks, where planets form: in the warm and cold zones of these disks, water is present in the gas- and solid-phase, respectively (e.g. Carr and Najita, 2008; Podio et al., 2013). Finally, water is the major component of the volatiles in comets (e.g. Bockelée-Morvan et al., 2014).

In summary, water is seen throughout all the stages of the solar-type star forming process up to the leftovers of this process, represented by comets and meteorites. Nevertheless, its whole history is not fully known: how it evolves from molecular clouds to comet ices and, perhaps, to terrestrial oceans. A crucial aspect in reconstructing the water history is provided by the deuteration of water molecules with one or two deuterium atoms. This is because molecular deuteration is very sensitive to the moment the molecule is formed, the temperature, and also the environment. And since water changes continuously from ice to vapour, it keeps memory of most, if not all, its past formation history (e.g. Ceccarelli et al., 2014). So far, the water deuteration has been measured in only a handful of objects, all of them warm: hot cores, hot corinos, and proto-stellar molecular shocks (e.g. Coutens et al., 2012, 2013, 2014; Taquet et al., 2013a; Persson et al., 2014). In cold molecular clouds, only the upper limits for solid deuterated water exist (Dartois et al., 2003; Parise et al., 2003; Aikawa et al., 2012). In pre-stellar cores, no attempt to measure the abundance of deuterated water has been done so far.

3.2 The pre-stellar core L1544

L1544 is a prototypical starless core in the Taurus molecular cloud complex (d$\sim$140 pc) on the verge of gravitational collapse (Caselli et al., 2002a and references within). It is characterised by high density in its centre (peak density of 2×10^7 cm^{-3}; Keto and Caselli, 2010), low temperature ($\sim$ 7 K; Crapsi et al., 2007), and high CO depletion in its centre, along with a high degree of molecular deuteration (H_2D^+, Caselli et al., 2003; N_2D^+, Crapsi et al., 2005; D_2H^+, DCO^+, Vastel et al., 2006).

Its physical and dynamical structure has recently been reconstructed by Caselli and Ceccarelli (2012) and Keto et al. (2014) using the numerous existing observations towards L1544. Among them, the recent detection of water vapour by the Herschel Space Observatory is spectacular because it represents the very first water detection in a pre-stellar core (Caselli et al., 2010; Caselli and Ceccarelli, 2012). The first of these two Herschel observations was made with the wide-band spectrometer (WBS) with a spectral resolution of 1.1 MHz, and water vapour was detected in absorption against the weak dust continuum radiation ($\sim$ 10 mK) in the cloud. Follow-up observations using the High Resolution Spectrometer (HRS) confirmed the absorption and even detected an inverse P-Cygni emission line profile, too narrow to be seen by the WBS, but which was predicted by theoretical modelling (Caselli et al., 2010).

This detection provided crucial information for reconstructing the physical and chemical structure of L1544. Indeed, this inverse P-Cygni profile, which is characteristic of gravitational con-

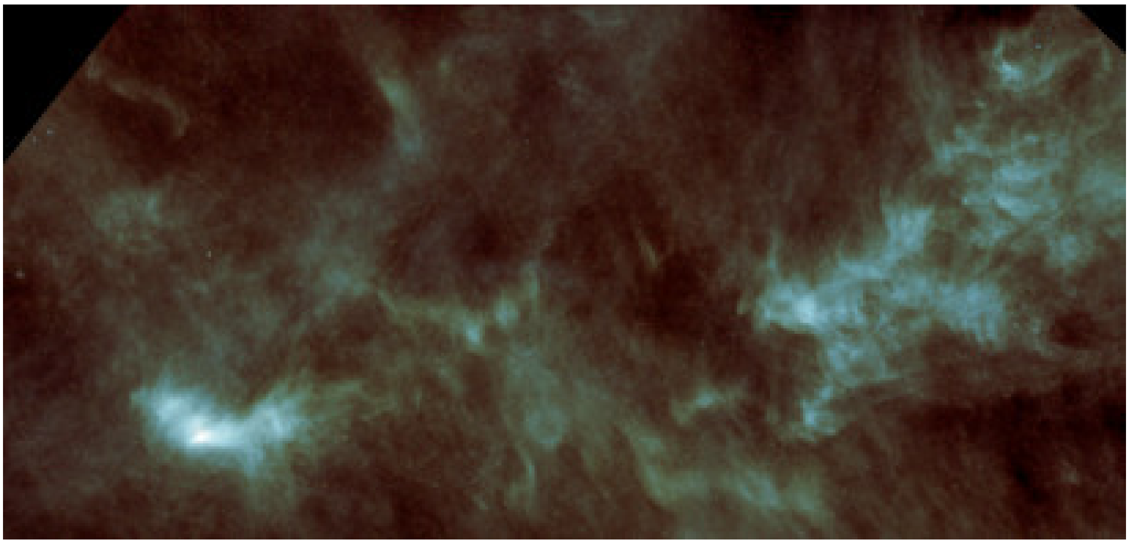

Figure 3.1 – The Taurus Molecular Cloud (TMC) with the bright L1544 pre-stellar core at the bottom left, as seen by Herschel. The image size is approximately 1′ × 2′. Copyright: ESA/Herschel/SPIRE/HIFI.

traction, confirmed that L1544 is on the verge of collapsing. Based on the line shape, Caselli and Ceccarelli (2012) predicted that water is largely frozen into the grain mantles in the interior (≤ 4000 AU) of the L1544 core, where the gaseous H_2O abundance (with respect to H_2) is $< 10^{-9}$. This level of water vapour is believed to be caused by non-thermal desorption processes such as *(a)* the photo-desorption of water molecules from the icy mantles by the far UV photons created locally by the interaction of cosmic rays with H_2 molecules and the far UV starlight, and *(b)* the exothermicity of the grain surface chemical reactions that releases the products (e.g. H_2O and HDO) in the gas phase (Vasyunin and Herbst, 2013; Wakelam et al., 2014). Further away from the centre ($\sim 10^4$ AU), where the density is low enough ($\leq 10^4$ cm^{-3}) for the photo-desorption rate not to be overcome by the freeze-out rate, the gaseous H_2O abundance reaches $\sim 1 \times 10^{-7}$, in agreement with predictions from comprehensive chemical models (Hollenbach et al., 2009).

3.3 Observations

The observation of the ortho-H_2O (1_{10}-1_{01}) line at 556.936002 GHz was taken from Caselli and Ceccarelli (2012). The observation was pointed toward the L1544 coordinates ($\alpha_{2000} = 05^{\rm h}04^{\rm m}17^{\rm s}.21$, $\delta_{2000} = 25^\circ 10' 42''.8$) with Herschel, using simultaneously the wide-band spectrometer (WBS) and high-resolution spectrometer (HRS) of the HIFI instrument. The dust continuum emission flux measured by the WBS at 557 GHz is 10.2 ± 0.2 mK while the rms noise level of the HRS spectrum is 3.8 mK. The half-power beam width (HPBW) of the telescope at this frequency is $40''$.

The HDO fundamental transition $1_{0,1}$–$0_{0,0}$ has been observed on April 16, 17, 28, 29, and 30, 2013 and November 2 and 3, 2013 towards L1544 (same pointing position as for the Herschel data) using the heterodyne instrument (APEX-3) of the APEX observatory. The frequency was centred at 464.92452 GHz to reach the $1_{0,1}$–$0_{0,0}$ ground-state HDO transition, and the RPG eXtended bandwidth Fast Fourier Transform Spectrometer (XFFTS) backend was used to obtain the highest frequency resolution needed for a comparison with the H_2O profile. The HPBW of the telescope at this frequency is $13.4''$. For a better comparison and to be consistent with the H_2O Herschel/HIFI observations, the HDO transition has been mapped within the Herschel/HIFI $40''$ beam. The resulting observation reached an rms of 50 mK in about 0.1 km s^{-1} velocity bin. Weather conditions were excellent between 0.2 and 0.7 mm of precipitable water vapour with system temperatures less than 1000 K. Line intensities are expressed in units of main-beam brightness temperature with a main beam efficiency of 60%[1].

3.4 H_2O modelling

3.4.1 Water molecule modelling issues

The collisional excitation rates for ortho–H_2O are not the same if one consider a collision with ortho–H_2 or para–H_2. In the case of L1544, it is assumed that all the hydrogen is in the para state as required by recent chemical models to produce the high deuterium fraction observed in cold, dense clouds (Flower et al., 2006; Pagani et al., 2007; Troscompt et al., 2009; Sipilä et al., 2013; Kong et al., 2015). I used the o–H_2O – p–H_2 collisional rates value from Dubernet et al. (2009), assuming a H_2O ortho-to-para (hereafter, O/P) ratio of 3 as suggested by previous studies (Keto et al., 2014). Usually, at low temperature, the O/P ratio in thermal equilibrium is very small ($< 1 \times 10^{-4}$ at 20 K). However, when H_2O is formed onto the grain surface, it is formed in the ratio of the available quantum states: ortho:para = 3:1. The ortho and para states of H_2O equilibrate by collisions with H or H_2. If the chemical equilibrium time scale is much shorter than the thermal equilibrium time scale, the O/P ratio will not deviate much from 3:1. Observations generally show ratios close to 3:1 (van Dishoeck et al., 2013). In fact, even though the equilibration of water has not been studied, one can suppose that it follows the same process as the equilibration of the ortho and para states of H_2, which are the following:

- Gas phase H (i.e proton) exchange.
- Gas phase paramagnetic conversion with H_2.
- H (i.e proton) exchange on a grain surface.

Keto et al. (2014) have shown that the rates for these processes in the cold interstellar medium (~ 10 K and $\sim 10^6$ cm^{-3}) have a time scale >1 Gyr, which is much less than the chemical equilibrium time scale. Thus, the hypothesis of a H_2O ortho-to-para ratio of 3 is reasonable.

The large Einstein coefficient (3.45×10^{-3} s^{-1}) of the o–H_2O $1_{1,0}$–$1_{0,1}$ transition results in optical depths across the core up to a thousand, depending on excitation, leading to a very non-linear relationship between the opacity and the column density. This opacity effect slows down the computation of the population level of the line and can lead to a wrong excitation.

3.4.2 Previous studies

While doing a comparison between observations and modellings, conclusions are often based on the line intensity predictions for a particular physical structure (H_2 density, gas and dust temperature, molecular abundances,...). As a consequence, the result relies on the accuracy of the radiative transfer treatment. A previous study of the water emission in L1544, led by Keto et al. (2014), used MOLLIE[2] (Keto, 1990; Keto et al., 2004; Keto and Rybicki, 2010) to fit the Herschel/HIFI water observational data. Initially, MOLLIE is a non-LTE radiative transfer code based on the ALI method, same method used in the RATRAN code (see Sect. 1.4.4.2). For the particular problem of water in L1544, MOLLIE has been modified to treat the radiative transfer with an escape probability method. Caselli and Ceccarelli (2012) and Keto et al. (2014) preferred this method because they did not know if the ALI method is correct to deal with the high optical depth of water lines (up to a few thousands) and if it converges to the right solution. The escape probability method combined with the sub-thermal (or sub-critical density) approximation optimises the calculation for the optically thick, but highly sub-thermally excited H_2O line towards L1544.

---

[1] `http://www.apex-telescope.org/telescope/efficiency/`

[2] `https://www.cfa.harvard.edu/~eketo/mollie/`

The sub-critical (or sub-thermal) assumption consists in considering that the collision rate C_{ul} of a molecule is so slow that every excitation leads immediately to a radiative de-excitation and the production of one photon which escapes the cloud, possibly after many absorptions and re-emissions, before another excitation. As long as $C_{ul} < A_{ul}/\tau$ (Linke et al., 1977) is verified, this assumption is correct, even for high opacities (A_{ul} is the spontaneous emission rate and τ the optical depth). The emission behaves as if the line were optically thin with the line brightness proportional to the column density. Given the density profile of L1544, Keto et al. (2014) have shown that this assumption is valid for this study.

The previous treatment is different from the full non-LTE radiative transfer calculation. Even if the sub-critical excitation approximation is valid, the escape probability method can lead to a wrong calculation, thus to wrong results. LIME has been especially built to deal with high opacities and complex population level calculations (Brinch and Hogerheijde, 2010). Moreover, Daniel et al. (private communication) have made a comparison of radiative transfer codes to treat the particular case of water in L1544. By comparing the results from three non-LTE radiative transfer codes: RATRAN and two private radiative transfer codes (1Dart, Daniel and Cernicharo, 2008, and Eprob), they have shown that an ALI treatment (used by the three codes) is correct for this study, and all of these codes converge to the same result.

Fig. 3.2 shows a comparison of the excitation temperature T_{ex} (see Sect. 1.4.4.1) calculated by MOLLIE and the non-LTE treatment of LIME. It is clearly visible that the calculation of T_{ex} is not the same, revealing that the radiative transfer treatment differs between the two codes. Similar results have been obtained by Daniel et al. (private communication) with the different radiative transfer codes. Further investigations are required to compare these different radiative transfer codes, including a comparison of the results obtained with LIME.

Knowing that the ALI method is valid for this study, it is better to use a full non-LTE radiative transfer code, considering no approximations, to deal with the water modelling. Finally, it is better to model both H_2O and HDO with LIME in order to make a consistent comparison of the results obtained.

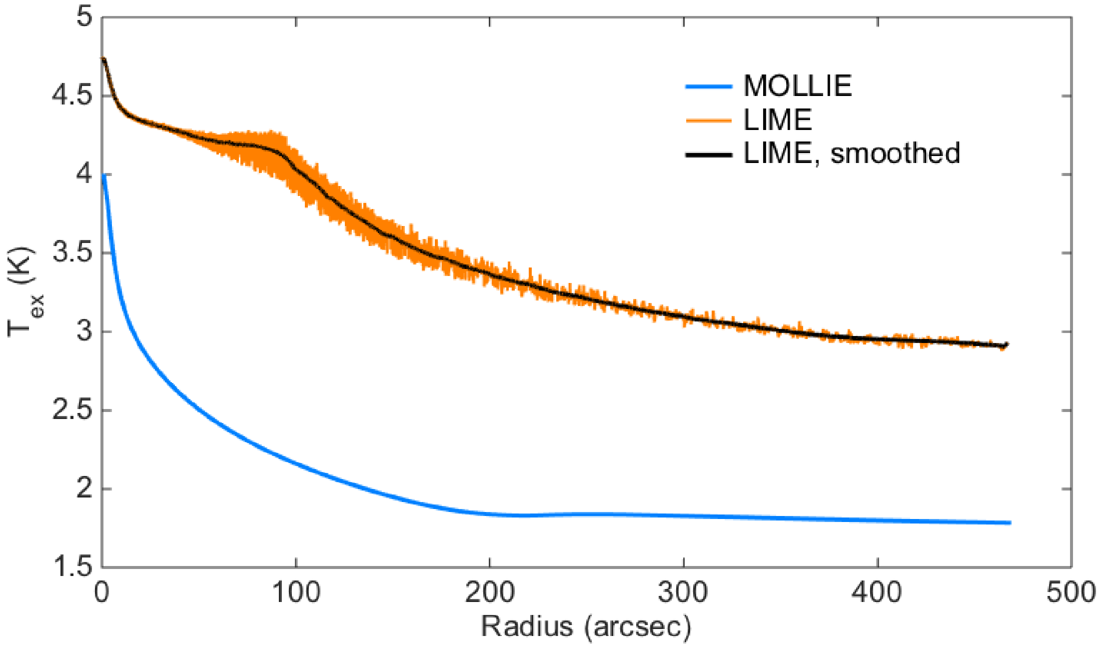

Figure 3.2 – Comparison of the excitation temperature as a function of the radius between MOLLIE and LIME.

3.4.3 H_2O radiative transfer modelling with LIME

I ran several radiative transfer modellings of the water emission using the combination of GASS and LIME, using the physical structure derived by Keto et al. (2014) to solve the molecular excitation of the H_2O transition. Figure 3.3 shows the structure for a slowly contracting cloud in quasi equilibrium. To reproduce the observed line broadening, I considered a Doppler parameter β ranging between 100 and 300 $\mathrm{m\,s^{-1}}$. I found that a value of 200 $\mathrm{m\,s^{-1}}$ gives the best line width fit compared to the observations. This result is consistent with the low gas temperature of L1544.

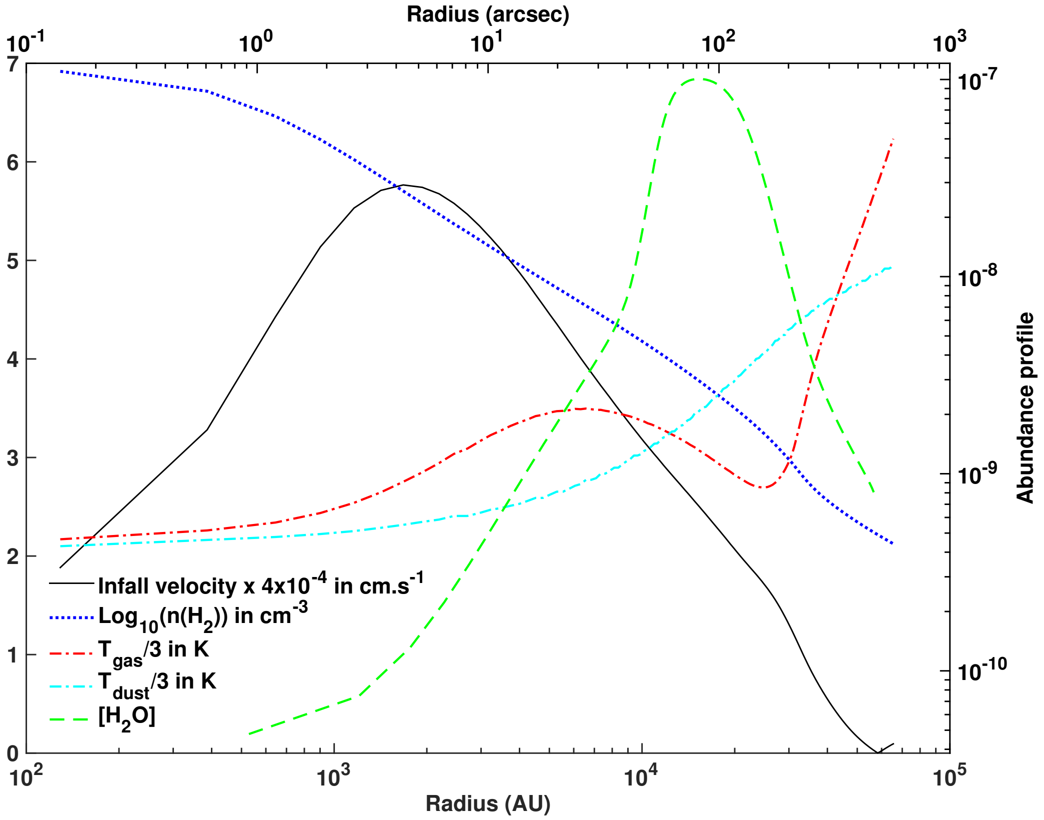

Figure 3.3 – Gas and dust temperature, density, velocity, and water abundance profiles from Keto et al. (2014). The abundance profile is plotted on a logarithmic scale on the right axis of the figure.

Because of the absorption feature in the H_2O observations, it is important to take the continuum value derived from the observations into account and compare its value to the modelling. The LIME code can deal with different input dust opacity files as a function of wavelength such as the tabulated files from Ossenkopf and Henning (1994). The observed continuum value at 557 GHz (or 538.2 μm) is 10.2 ± 0.2 mK (see Caselli and Ceccarelli, 2012), and the best model value found with LIME is 10.0 mK with $\kappa_{557} = 8.41\,\mathrm{cm^2\,g^{-1}}$. Such opacity at this wavelength corresponds to the dust growth model of Ossenkopf and Henning (1994) with no icy mantle and a growth time between 1 and 10 millions years. This does not necessarily means that dust grains in L1544 have no icy mantle since models from Ossenkopf and Henning (1994) are outdated and they may be wrong at some points. In this case, further investigations are needed to derive the grain properties from the dust opacity but it is beyond the scope of this study. Keto and Caselli (2010) based their dust opacity value on the results found by Zucconi et al. (2001) where the authors approximate the grain opacities of Ossenkopf and Henning (1994) by piecewise power laws. Keto and Caselli (2010) derived a value of $\kappa_{557} = 3.83\,\mathrm{cm^2\,g^{-1}}$ thanks to the following equation describing one of these piecewise power laws (see Appendix B of Zucconi et al., 2001):

$$\kappa_\nu = \frac{Q_\nu}{m(H_2)} \times \left(\frac{\lambda_a}{\lambda_{H_2O}}\right)^\alpha \times \left(\frac{m_{gas}}{m_{dust}}\right) , \tag{3.1}$$

with $Q_\nu = 3.3 \times 10^{-26}$ cm^2 H$_2^{-1}$ at $\lambda_a = 1060$ μm, $m(H_2) = 3.35 \times 10^{-24}$ g, and $\alpha = 2.0$. They had to increase the dust opacity value by a factor of four ($\kappa_{557} = 15.3$ cm^2 g^{-1}) to be able to reproduce the low temperatures measured by Crapsi et al. (2007) towards the centre of L1544. Fig. 3.4 shows a comparison between the dust opacity laws presented by Ossenkopf and Henning (1994) and Zucconi et al. (2001) together with the one used by Keto and Caselli (2010) and this study. At 557 GHz, the dust opacity used by Keto and Caselli (2010) is the highest one while the one used in this study is closer to values found by Ossenkopf and Henning (1994) and Zucconi et al. (2001).

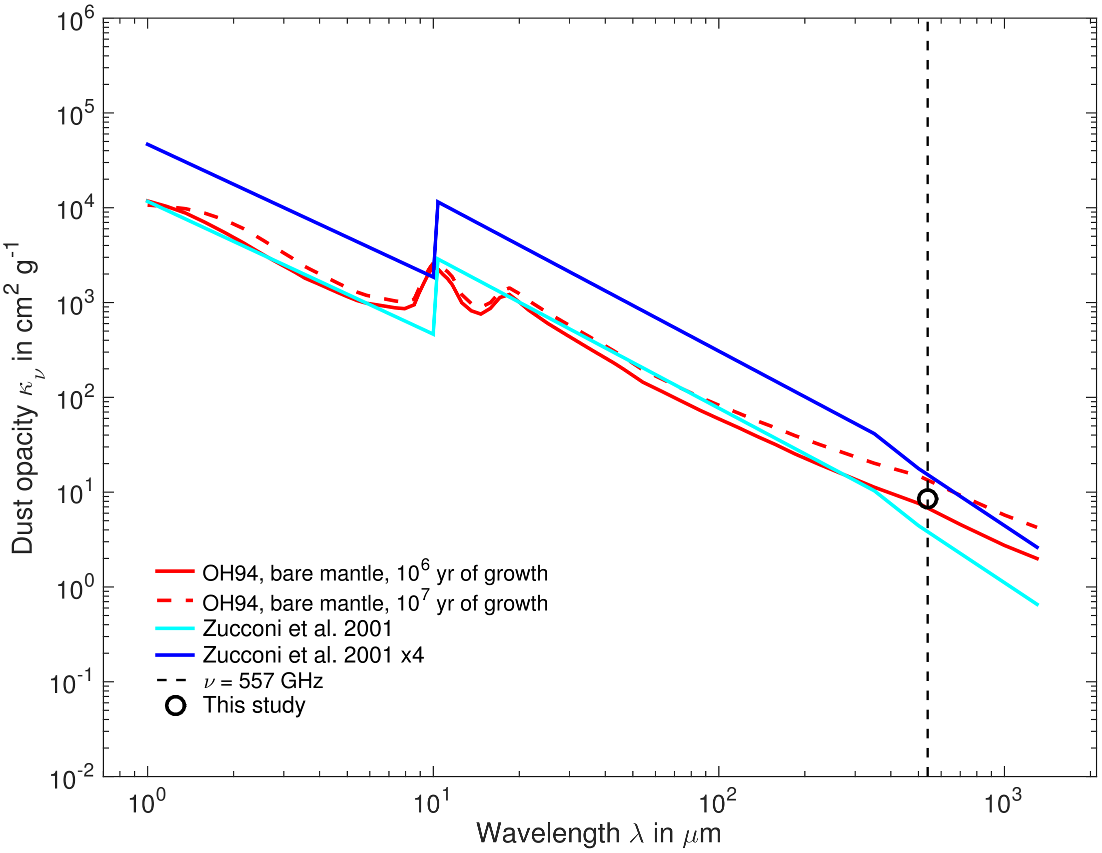

Figure 3.4 – Dust opacity as a function of the wavelength for different dust models. The cyan and blue curves indicate the dust opacity models from Zucconi et al. (2001), multiplied by a factor of four for the blue curve. The red curves display the two Ossenkopf and Henning (1994, or OH94) models approaching the dust opacity derived in this study (black circle): considering a bare mantle with 1 million years of growth (solid red line) and with 10 millions years of growth (dashed red line). The black dashed line shows the position of the studied water transition wavelength.

The result from the LIME modelling with the abundance and structure profile from Keto et al. (2014), coupled with their dust opacity value, is shown in Fig. 3.5. The H_2O emission is overestimated by a factor of ~3.5, and the dust continuum emission is overestimated by a factor of ~2 compared to observations. The latter effect is due to the higher dust opacity ($\kappa_{557} = 15.3$ cm^2 g^{-1}) they used compared to the one found in the best fit ($\kappa_{557} = 8.41$ cm^2 g^{-1}). As discussed above, the difference in the intensity of the line can be explained by the different radiative transfer treatments in MOLLIE and LIME, including different grids describing the same physical structure.

Although I note that Keto and Caselli (2010) and Keto et al. (2014) present a self-consistent model, where a simple chemistry is followed during dynamical and thermal evolution, and where the dynamical evolution is constrained by previous observations of N_2H^+ and CO isotopologues, their analysis nonetheless presents a few issues: approximation in the radiative transfer code, over-

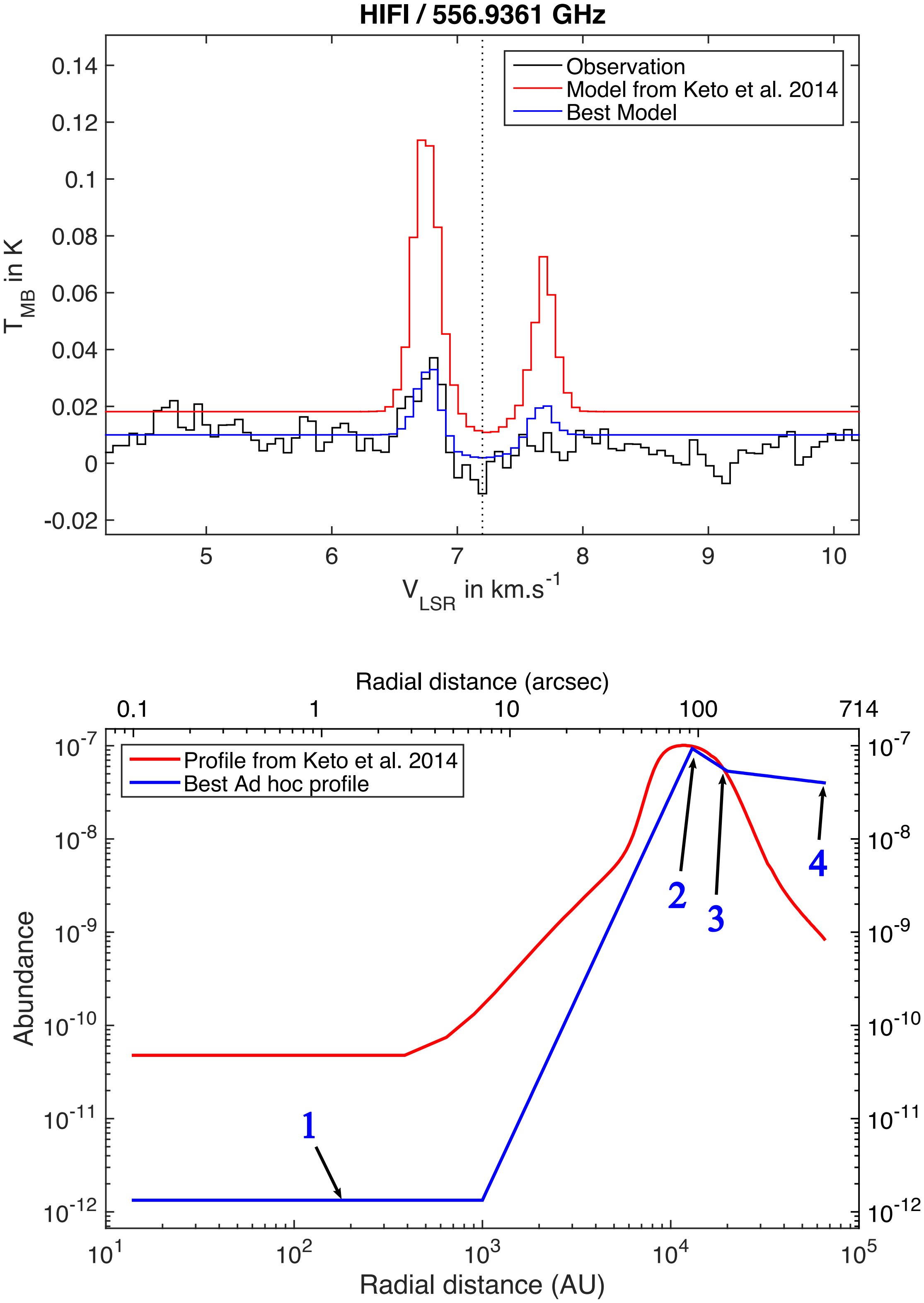

Figure 3.5 – *Top panel:* Comparison between observations and modelling obtained by LIME using the structure and abundance profile from Keto et al. (2014) (in red). The best fit model is shown in blue, using the same structure but an “ad hoc” abundance profile (see text for details). *Bottom panel:* Abundance profile from Keto et al. (2014) in red and best fit “ad hoc” abundance profile in blue as a function of the radial distance from the core in arcsec (top axis) and AU (bottom axis). The arrows marks the different modelled regions for LIME (see text).

estimation of the continuum and line emission when using a full non-LTE code. I therefore decided to explore possibly different water abundance profiles to find a good match to the H_2O observations using LIME. For this purpose, I modified the water abundance profile found by Keto et al. (2014), while using their physical structure constrained with the many data published for many years towards this source. The inverse P-Cygni profile is a combination of blue-shifted emission and red-shifted absorption, split in velocity by the inward gas motion in front and at the rear of the cloud. In L1544, the emission is shifted with respect to the absorption by less than a line width, leading to an asymmetry in the line profile. Therefore, only a complex modelling can tentatively disentangle between the blue-shifted emission and red-shifted absorption. The emission is produced in the inner region of the cloud, where the density approaches the critical density of the transition. Meanwhile the absorption layer is located in the outer part of the cloud, where the water abundance peaks.

The abundance profile from Keto's studies has been arbitrarily divided in four regions (to limit the number of free parameters), and over a hundred of profiles (hereafter referred to as "ad hoc") have been tested through grid calculations to find the best fit shown in Fig. 3.5. To reach this result, I varied the following different parameters located in four distinct regions of the core:

1. The first region is the inner abundance and I found a best fit value of $[H_2O] = 1.3 \times 10^{-12}$ at the centre of the core up to a radius of 1000 AU. Keto et al. (2014) found a value of this inner abundance close to $[H_2O] = 5 \times 10^{-11}$. If the inner abundance is increased to this value, it also changes the slope of the abundance profile (if the second region is already fixed), probing a region where the velocity field is higher. This effect leads to a wider and slightly blue-shifted emission compared to the best fit. Nonetheless, due to the large HIFI beam at 557 GHz, the constraints on the inner abundance are relatively poor. Thus, the contribution of cosmic-ray-induced UV photons responsible for this inner abundance is also poorly constrained, and more detailed observations of this region in particular are needed to develop a deeper analysis of this inner abundance. Cosmic-ray-induced UV photons also appear important for reproducing the observations of CO isotopologues toward L1544 (Keto and Caselli, 2010).

2. The second region defines the peak abundance value of the external layer. I varied the abundance value and the distance from the centres of the core of this region and found a best fit value of $[H_2O] = 9.3 \times 10^{-8}$ at a radius of 13 000 AU.

3. The third region marks the end of the external layer; the abundance value and the distance from the centre of the core are varied. I found a best fit value of $[H_2O] = 5.3 \times 10^{-8}$ at a radius of 20 000 AU.

4. I finally varied the abundance value at the end of the profile, located at the same final radius as that of the physical structure of the core given by Keto et al. (2014). I found a best fit value of $[H_2O] = 4 \times 10^{-8}$. This result may imply that L1544 is well embedded in a relatively large filament in Taurus, so that the extinction A_V is high enough to at least partially shield interstellar UV photons (see Section 3.5).

I decided to first determine the first and second regions at the same time thanks to the grid. I then fixed the third one, which appeared to be independent of the other two. I derived the best fit from these previous models with the help of the standard χ^2 minimisation value for a spectrum, given by Eq. (2.47) in Sect. 2.5.3.

Fig. 3.6 shows a small variation in the peak abundance value at the best fit distance of 13 000 AU from the centre of the core. It is interesting to note that a little variation in the abundance value at this distance can cause a notable difference in the line profile: this is due to more or fewer water molecules being present in the outer envelope and so absorbing more or less emission coming from the central regions. Meanwhile, if the abundance value at the best fit distance of 20 000 AU of the external layer (see Fig. 3.7) is changed, the emission is the same for the three profiles.

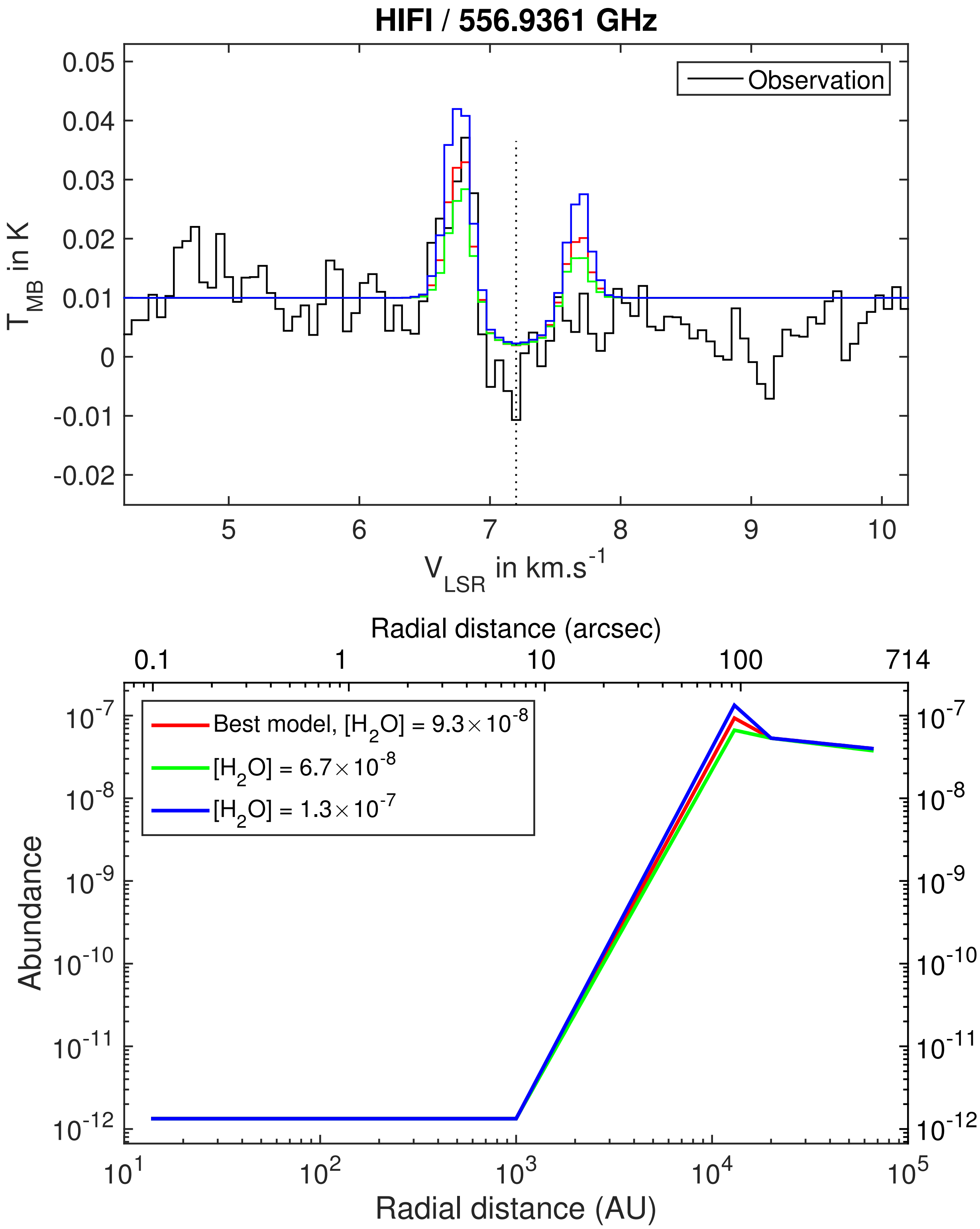

Figure 3.6 – *Top panel:* Modelled versus observed line profile for the o–H_2O $1_{1,0}$–$1_{0,1}$ transition for three different modellings showing how sensitive the line profile is to the peak abundance. The best fit model is shown in red. The abundance value at 13 000 AU varies between 6.7×10^{-8} and 1.3×10^{-7}. *Bottom panel:* H_2O abundance profile used for these respective models as a function of the radial distance from the core in arcsec (top axis) and AU (bottom axis).

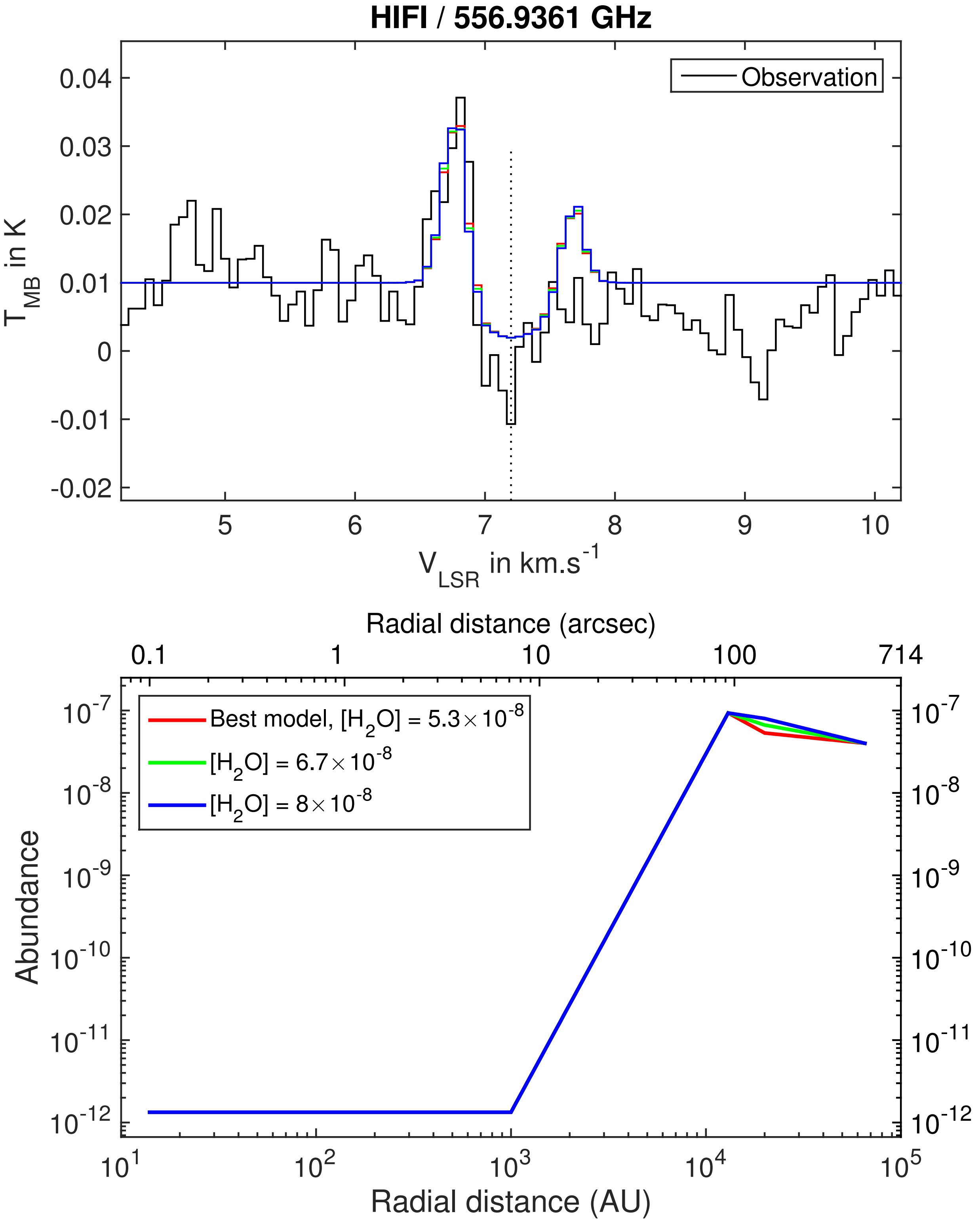

Figure 3.7 – *Top panel:* Modelled versus observed line profile for the o–H_2O $1_{1,0}$–$1_{0,1}$ transition for three different modellings showing the lack of sensitivity of the line profile with respect to abundance value in the external layer. The best fit model is shown in red. The abundance value at 20 000 AU varies between 5.3×10^{-8} and 8×10^{-8}. *Bottom panel:* H_2O abundance profile used for these respective models as a function of the radial distance from the core in arcsec (top axis) and AU (bottom axis).

In fact, emission from a molecule like water with high critical densities is only possible in regions with sufficiently high H_2 densities. In L1544, this region corresponds to the back part of the core approaching the centre (thus moving towards us) and revealing infall through an inverse P-Cygni profile (emission in the blue-shifted part of the line). A peak in the abundance profile of water at a distance of 13 000 AU is consistent with the detection of methanol and complex organic molecules (COMs) at radii of about 10 000 AU from the centre (Vastel et al., 2014; Bizzocchi et al., 2014). Indeed, water, methanol, and COMs have to be present in the gas phase at such radii (Vastel et al., 2014; Bizzocchi et al., 2014), but, water at the volume densities present in the outer envelope can only absorb, while methanol and other complex molecules can emit more easily (as their critical densities are not as high). If the water abundance value at the edge of the core is lower than $[H_2O] \simeq 1 \times 10^{-8}$, the absorption feature will not be deep enough.

3.5 Chemical modelling of H_2O and HDO

To reproduce the water abundance profile deduced by the LIME radiative transfer study, the GRAINOBLE astrochemical model has been used (Taquet et al., 2012, 2014). Briefly, GRAINOBLE couples the gas phase and grain surface chemistries with the rate equation approach introduced by Hasegawa et al. (1992) during the static contraction of a starless core. The abundance profiles of both standard and deuterated water in L1544 have been modelled.

The gas-phase chemical network has been taken from the KIDA database and has been extended to include the spin states of H_2, H_2^+, H_3^+, and the deuterated isotopologues of hydrogenated species with four or fewer atoms alongside with species involved in the gas phase chemical network of water, ammonia, formaldehyde, and methanol. A more detailed description of the chemical network is presented in Taquet et al. (2014). The following gas-grain processes (Langmuir-Hinshelwood mechanism, see Sect. 1.2.1) have also been considered:

1. Accretion of gas phase species on the surface of spherical grains with a fixed diameter a_d assumed to be equal to $0.1\,\mu$m.

2. Diffusion of adsorbed species via thermal hopping, exponentially depending on the diffusion-to-binding energy ratio $E_\mathrm{d}/E_\mathrm{b}$, fixed to 0.65 following previous studies.

3. Reactions between two particles.

4. Desorption of adsorbed species into the gas phase by thermal evaporation, interstellar plus cosmic-ray induced heating of grains, chemical evaporation, and UV photolysis. The thermal evaporation exponentially depends on the binding energy of each species E_b relative to the substrate (see Taquet et al., 2014 for a list of binding energies used in the model). The cosmic-ray-induced heating of grains follows the approach by Hasegawa and Herbst (1993a) and is adapted to the binding energies considered in this work. The approach adopted for the UV photolysis follows the method described in Taquet et al. (2013b).

The multi-layer approach developed by Hasegawa and Herbst (1993b) is used to follow the multi-layer formation of interstellar ices; this approach considered three sets of differential equations: one for gas-phase species, one for surface species, and one for bulk species. The equations governing chemical abundances on the surface and in the bulk are linked by an additional term that is proportional to the rate of growth or loss of the grain mantle.

The formation and the deuteration of the main ice species are tracked following the surface chemical network developed by Taquet et al. (2013b), which is based on laboratory experiments showing the efficient formation of interstellar ice analogues at low temperatures. Transmission probabilities for key reactions involved in the water chemical network have been estimated through quantum chemistry.

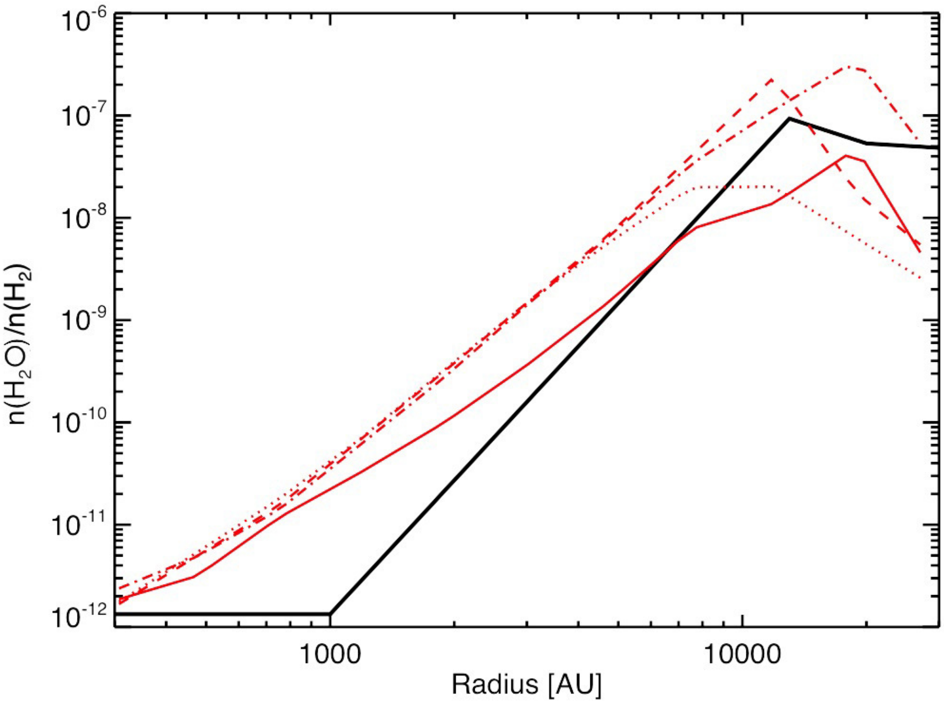

Figure 3.8 – Water abundance profiles in L1544 modelled with GRAINOBLE (red curves) compared with the observed profile based on LIME radiative transfer simulations (black). Dashed-dotted line: $G_0 = 1$, $A_{\mathrm{V,ext}} = 2$, $t_{\mathrm{c}} = 7.5 \times 10^5$ yr; dashed line: $G_0 = 1$, $A_{\mathrm{V,ext}} = 1$, $t_{\mathrm{c}} = 7.5 \times 10^5$ yr; dotted line: $G_0 = 0.1$, $A_{\mathrm{V,ext}} = 1$, $t_{\mathrm{c}} = 7.5 \times 10^5$ yr; solid line: $G_0 = 1$, $A_{\mathrm{V,ext}} = 2$, $t_{\mathrm{c}} = 1.5 \times 10^6$ yr.

The gas-grain chemistry is followed during the static contraction of a dense core starting from a homogeneous translucent sphere with an initial density $n_{\mathrm{H,ini}} = 3 \times 10^3$ cm^{-3} and a maximal radius of 3×10^4 AU. During the static contraction, the core keeps a Plummer-like density profile:

$$n_{\mathrm{H}} = \frac{n_{\mathrm{H},0}}{(1 + (r/R_{\mathrm{f}})^2)^{\eta/2}}, \tag{3.2}$$

where $n_{\mathrm{H},0}$ is the central density, and R_{f} the characteristic radius inside which the density is uniform. The contraction ends when the density profile reaches the observed profile of L1544, with the following parameters: $n_{\mathrm{H},0} = 1.8 \times 10^7$ cm^{-3}, $R_{\mathrm{f}} = 450$ AU, and $\eta = 2.1$. Since R_{f} is given by the product of the sound speed and the free-fall time of the central density, R_{f} decreases with $1/\sqrt{n_{\mathrm{H},0}}$. Intermediate central densities, and the associated timescale needed to reach them, have been chosen to have a total contraction timescale of about one million years, following observational estimates of molecular cloud cores (e.g. Brünken et al., 2014).

The radiative transfer code DUSTY (Ivezić and Elitzur, 1997) has been employed to compute the temporal evolution of the dust temperature profile of the contracting core by assuming that gas and dust temperatures are coupled. As shown in Fig. 3.3, the dust and gas temperatures are decoupled and can differ by up to 4 K. It has been checked *a posteriori* that variations in gas phase temperatures of 4 K only induce small variations (30% at most) in the abundances of gaseous species. The thermal structure of the core is derived from a slab geometry in which the core is irradiated by the interstellar radiation field (ISRF) with a spectrum taken from Evans et al. (2001) and assuming a fixed temperature at the edge of the core of 13 K following the observed temperature profile of L1544.

As discussed in Taquet et al. (2013b, 2014), the abundance and the deuteration of the main ice components like water are known to depend on various physical and chemical parameters that are either poorly constrained or that show distributions of values. To reproduce the water abundance profile deduced by the LIME radiative transfer study, the values of three poorly constrained physical

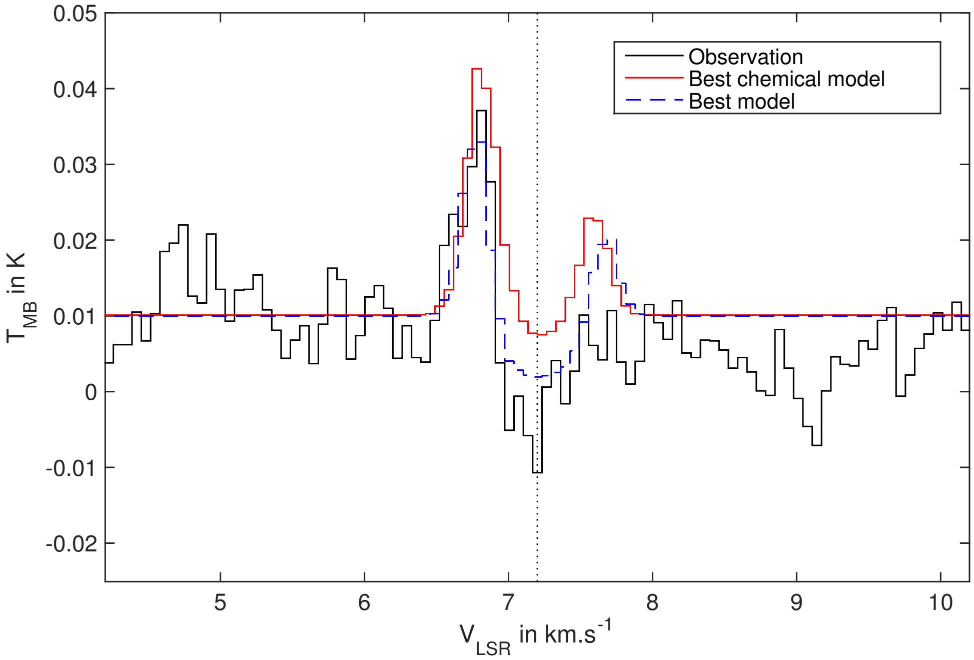

Figure 3.9 – Modelled versus observed (in black) line profiles of the o–H_2O $1_{1,0}$–$1_{0,1}$ transition. The line profile (red line) resulting of the abundance derived by the chemical model that best fit the LIME-deduced water abundance profile ($G_0 = 1$, $A_{\mathrm{V,ext}} = 2$, and $t_c = 1.5 \times 10^6$ yr) is compared to the line profile (dashed blue line) resulting of the best LIME-deduced water abundance profile.

parameters that are thought to have a strong impact on the abundance of gaseous water have been varied:

1. The external visual extinction $A_{\mathrm{V,ext}}$ that influences the radius where the water abundance reaches its maximal value. As shown in Fig. 3.8, decreasing $A_{\mathrm{V,ext}}$ from two to one magnitude enhances the photodissociation of water at the edge of the core, shifting its maximal abundance toward the core centre from 1.8×10^4 to 1.2×10^4 AU.

2. The external ISRF (interstellar radiation field) G_0. The photo-desorption rate of water increases with the flux of external UV photons, which is proportional to G_0. The maximal abundance of water starts to increase with G_0 at low G_0 and then decreases when the photodissociation of gaseous water overcomes its photo-desorption. Decreasing G_0 from 1 to 0.1 decreases the maximum water abundance from 2×10^{-7} to 2×10^{-8}.

3. The contraction timescale t_c. The core contraction timescale impacts the total number of particles that freeze-out on grains at the centre of the dense core but also the number of particles that are photo-evaporated at lower densities and visual extinctions in the outer shells. The increase in the core contraction timescale between 7.5×10^5 and 1.5×10^6 years decreases the water abundance in the dense part of the core, due to higher depletion, but also slightly increases the water abundance towards the edge because of the higher total number of photo-evaporated water molecules.

The parameters of the chemical model that best fit the LIME-deduced water abundance profile are $G_0 = 1$, $A_{\mathrm{V,ext}} = 2$, and $t_c = 1.5 \times 10^6$ yr for a fixed diameter of grain a_d assumed to be equal to 0.1 μm (see Fig. 3.8). The resulting line profile for the o–H_2O $1_{1,0}$–$1_{0,1}$ transition using this abundance profile is shown in Fig. 3.9. One can note that the absorption feature of the line profile is not correctly reproduced, compared to the best fit model. This is mainly due to the low abundance of water at the edge of the core, which is one decade lower than the one used with the

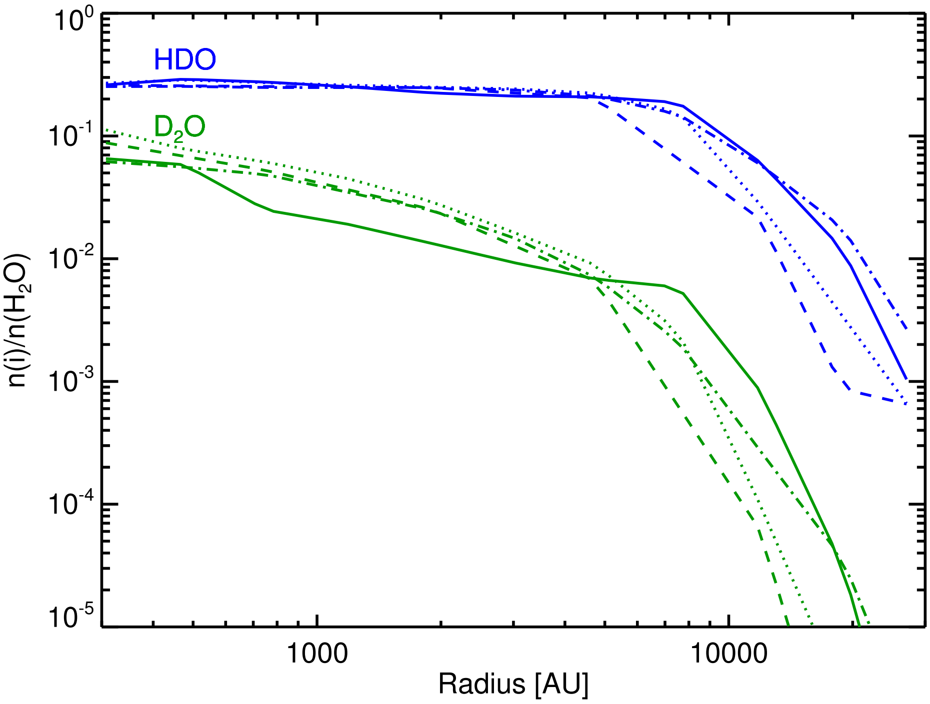

Figure 3.10 – [HDO]/[H_2O] (blue) and [D_2O]/[H_2O] (green) deuteration profiles in L1544 modelled with GRAINOBLE. Dashed-dotted line: $G_0 = 1$, $A_{\mathrm{V,ext}} = 2$, $t_{\mathrm{c}} = 7.5 \times 10^5$ yr; dashed line: $G_0 = 1$, $A_{\mathrm{V,ext}} = 1$, $t_{\mathrm{c}} = 7.5 \times 10^5$ yr; dotted line: $G_0 = 0.1$, $A_{\mathrm{V,ext}} = 1$, $t_{\mathrm{c}} = 7.5 \times 10^5$ yr; solid line: $G_0 = 1$, $A_{\mathrm{V,ext}} = 2$, $t_{\mathrm{c}} = 1.5 \times 10^6$ yr.

best fit abundance profile (see Fig. 3.8), affecting the depth of the absorption as discussed in Sect. 3.4.3.

Based on the water abundance profiles obtained for the four sets of the three parameters (see Fig. 3.8), the deuteration of water have been deduced (see Fig. 3.10). This deuteration will help me derive the deuterated water abundance profile to predict the emission of HDO in L1544 with LIME.

From Fig. 3.10, one can note that the water deuteration weakly depends on the physical parameters: the [HDO]/[H_2O] and [D_2O]/[H_2O] abundance ratios tend to increase towards the centre of the core up to $\sim$ 25 % and $\sim$ 8 %, respectively. As comprehensively studied in previous analyses (Roberts et al., 2004; Flower et al., 2006; Taquet et al., 2014; Sipilä et al., 2015), the increase in the deuteration both in the gas phase and on ices toward the core centre is due to the decrease in both the CO gas phase abundance and the H_2 ortho-to-para ratio, the two main parameters involved in the deuterium chemistry, with the increase in the total density and the decrease in the temperature.

As also discussed in Taquet et al. (2014), the gas phase deuteration of water obtained at the centre of dense cores is higher by more than one order of magnitude than the overall deuteration predicted in interstellar ices.The gas phase D/H abundance ratio of water reflects : (i) the gas phase chemistry, and (ii) the surface chemistry in the outermost layers, in interaction with the gas phase, both of which occurring in dense and cold conditions. The low deuteration of water ice is due to its early formation in the molecular cloud phase when the CO abundance and the H_2 ortho/para ratio were high.

3.6 HDO radiative transfer modelling with LIME

Coutens et al. (2012) have shown that the [HDO]/[H_2O] ratio is about 0.2-2.2% and ~4.8% re-

Table 3.1 – Intensity of the emission and absorption feature of the two transitions with respect to their continuum level.

D/H ratio (in %)	HDO ($1_{0,1}$–$0_{0,0}$) 464.914 GHz		HDO ($1_{1,1}$–$0_{0,0}$) 893.639 GHz	
	absorption (in mK)[b]	emission (in mK)	absorption (in mK)[b]	emission (in mK)
variable[a]	1.9	2.9	5.4	1.5
75%	9.9	42.1	9.0	4.8
22.5%	8.8	10.6	8.7	1.5
7.5%	6.9	1.4	7.7	1.3
2.25%	2.5	0.04	5.5	0.04
0.75%	0.8	0.007	2.6	0.002

[a] D/H ratio as a function of the radius, derived from the dotted astro-chemical modelling shown in Fig. 3.10.

[b] Absorption with respect to the continuum value of 18.9 mK at 464.914 GHz and 10.4 mK at 893.639 GHz.

spectively in the outer part and in the external layer of the envelope of the low-mass proto-star IRAS16293-2422. This layer can be associated to the parental cloud, a remnant of the initial pre-stellar core of the proto-star. Therefore, these [HDO]/[H_2O] ratios can be considered as possible values for L1544. However, observed D/H ratios for other gaseous species, as well as astrochemical models of starless cores, suggest higher values, ranging from 7.5% to 22.5%. I chose to consider six different cases for the D/H ratio:

- constant ratios of 0.75% and 2.25%, in agreement with the [HDO]/[H_2O] ratios found by Coutens et al. (2012) in the outer envelope of IRAS16293-2422, a low-mass proto-star.
- constant ratios of 7.5% and 22.5%, in agreement with other observed D/H ratios in molecules, such as HCO^+, N_2H^+, and H_2CO in pre-stellar cores (e.g. Bacmann et al., 2003; Pagani et al., 2007; Kong et al., 2015).
- variable as a function of the radius. I took the D/H profile found by the chemical modelling performed in Sect. 3.5, with $G_0 = 0.1$, $A_{\rm V,ext} = 1$, and $t_{\rm c} = 7.5 \times 10^5\,{\rm yr}$ (dotted line in Fig. 3.10). This D/H model has been chosen in particular because it represents well the mean value of the D/H ratio found with the chemical modelling, compared to the other three profiles (see Fig. 3.10), especially in the outer part of the core.
- constant ratio of 75% to consider an extreme case where the [HDO]/[H_2O] ratio is very high.

Based on the best fit ad hoc H_2O abundance profile, I derived the HDO abundance profile for the cases listed above and modelled the HDO $1_{0,1}$–$0_{0,0}$ transition at 464.914 GHz and the $1_{1,1}$–$0_{0,0}$ transition at 893.639 GHz. The APEX observation of the 464.914 GHz transition does not show any detection of HDO towards the source (as seen in the upper panel of Fig. 3.11), and the 893.639 GHz transition has not been observed. The predicted continuum value at 464.914 GHz and 893.639 GHz are 18.9 mK and 10.4 mK, respectively. The predicted continuum value is lower at a higher frequency, which is consistent with a cold pre-stellar core such as L1544. The two middle panels of Fig. 3.11 show the spectra of the $1_{0,1}$–$0_{0,0}$ and $1_{1,1}$–$0_{0,0}$ transition derived from the output brightness map of the six different models, and the lower panel displays the related HDO abundance profile. The upper panel compares the APEX observations of the 464.914 GHz transition and the HDO/H_2O = 0.75 model. Table 3.1 shows the intensity of the emission and absorption feature for every model with respect to the continuum level of the line.

I used the observing time calculator of APEX[3] for the APEX-3 instrument to estimate the total time required to detect the emission feature of the HDO line at 464.914 GHz at 3σ, considering

---

[3] `http://www.apex-telescope.org/heterodyne/calculator/`

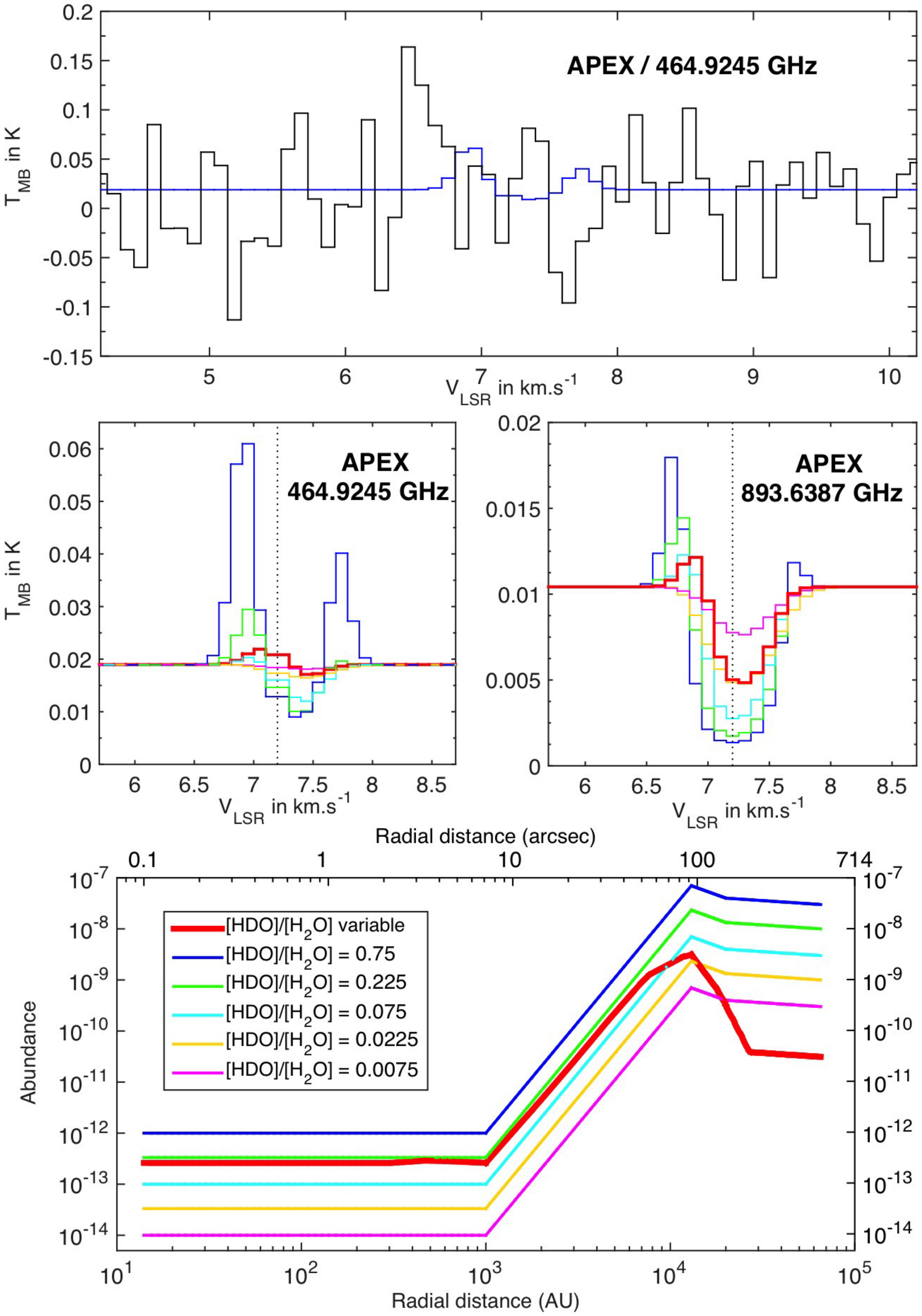

Figure 3.11 – *Top panel:* HDO $1_{0,1}$–$0_{0,0}$ line profile of the HDO/H_2O = 0.75 model (in blue) versus APEX observation (in black). *Middle panels:* HDO $1_{0,1}$–$0_{0,0}$ (left panel) and $1_{1,1}$–$0_{0,0}$ (right panel) line profiles for the six different D/H ratios. *Bottom panel:* HDO abundance profiles as a function of the D/H ratio (see text, Section 3.6) used for these models as a function of the radial distance from the core in arcsec (top axis) and AU (bottom axis).

the D/H ratio of 75%. The intensity of the emission is 42.1 mK, hence a *rms* of about 14 mK is required. According to the calculator, with a precipitable water vapour (pwv) of 0.1 mm, a total time of ∼120 h is needed to detect HDO (∼380 h with pwv = 0.3 mm). This result clearly shows the limits of detectability for deuterated water with single-dish telescopes such a APEX, even if a very high and unrealistic ratio of 75% is considered.

By looking at the brightness map of any of the previous models, one can note that the absorption feature of the HDO lines only shows up within a region of 50″ radius around the centre of the model (see Fig. 3.12). To date, only the ALMA interferometer is sensitive enough at the frequency of the HDO $1_{0,1}$–$0_{0,0}$ transitions to try to detect it: ∼ 2 mK at 464.914 GHz and ∼ 5 mK at 893.639 GHz.

I therefore tried to model a detection of the HDO $1_{0,1}$–$0_{0,0}$ transition at 464.914 GHz (Band 8) with the Common Astronomy Software Applications package (CASA) to simulate ALMA observations with the brightness map of the model derived from LIME. I used the ALMA interferometer in

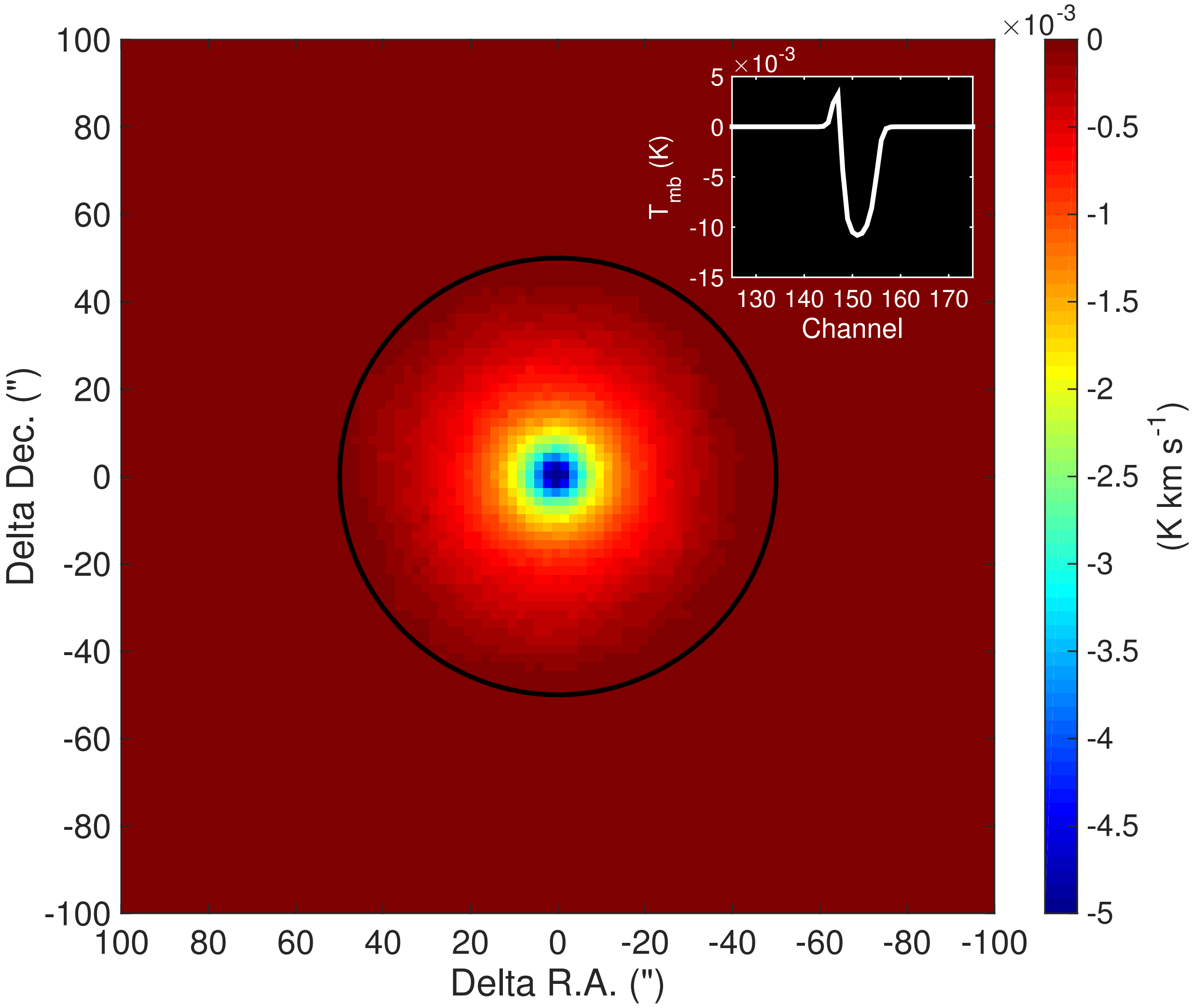

Figure 3.12 – Mean intensity (main beam temperature) map of the HDO $1_{1,1}$–$0_{0,0}$ transition at 893.639 GHz integrated over channels featuring absorption (channels 148 to 160) for the D/H = 22.5% model. The black circle shows the radius of 50″ in which the absorption of HDO is predicted. The top right vignette displays the line profile of the central pixel as an example. For a better visualisation, the continuum has been subtracted in this vignette.

the most compact Cycle 3 configuration of ALMA (C36-1) with a longest baseline of 160.5 m. The antenna beam size is $\sim 12.5''$ and $\sim 6.5''$ at the frequency of the two HDO transitions. I used the Cycle 3 ALMA Observing Tool to derive the integration time it would need to expect a detection (based on results obtained with the HDO modellings) and the sensitivity calculator derived an integration time of approximately three hours.

It is impossible to entirely map L1544 in a convenient number of pointings due to the size of the core (radius of $\sim$ 65 000 AU, which means $\sim 460''$ at 140 pc): it represents more than 150 pointings (respecting the minimum Nyquist sampling). Even if the absorption feature is only considered (radius of $\sim 50''$), it would require at least 17 pointings, which is still a high value regarding the required sensitivity to detect HDO. The ALMA interferometer is not optimum here to detect a very extended emission. I have also tested the possibility to use ACA observations to detect HDO but, even with this compact configuration, the(u,v)-coverage of the plane of the sky is not good enough to detect the line.

I conclude that only a single-dish telescope can give a convenient beam size to cover at least the absorption feature of L1544, but, right now, such low sensitivities ($\sim$ 2 mK at 464.914 GHz and $\sim$ 5 mK at 893.639 GHz) cannot be reached with ground-based observatories, and no space observatory is foreseen in the future.

3.7 Concluding remarks

Based on the recent detection of the $1_{1,0}$–$1_{0,1}$ water transition using the Herschel/HIFI instrument, I used the APEX observatory to constrain the water fractionation in the L1544 pre-stellar core. I used LIME to model the $1_{1,0}$–$1_{0,1}$ H_2O and $1_{0,1}$–$0_{0,0}$ HDO line profiles towards L1544 with a full radiative transfer treatment in 3D.

Keto et al. (2014) derived the density, temperature, and velocity profile of the source. However, using LIME instead of MOLLIE, I found that their abundance profile leads to a predicted line emission that is 3.5 times stronger than the observation; also using their deduced dust opacity, LIME predicts a continuum emission at 557 GHz about two times stronger than the observed value.

These results point to the need for a detailed comparison between these codes for the specific case of water in pre-stellar cores. I have found an ad hoc abundance profile that fits the Herschel/HIFI H_2O observation better using LIME. I also found a new estimation of the dust opacity to reproduce the observed continuum of $\sim$ 10.2 mK.

A detailed chemical modelling using both gas-phase and grain-surface chemistry has been used to roughly reproduce the water abundance profile (compared to the LIME-deduced abundance profile) and predict its subsequent deuterated water abundance profile ($G_0 = 1$, $A_{\mathrm{V,ext}} = 2$, $t_{\mathrm{c}} = 1.5 \times 10^6$ yr, $a_{\mathrm{d}} = 0.1$ μm). I have used this chemical HDO abundance profile, but also constant D/H ratios (up to 75%), to predict the HDO line profile. These predictions of emission have been compared to the APEX observation, without any detection, mainly due to a lack of sensitivity in the data. In this study, I have shown the limit of detectability for deuterated water in pre-stellar cores using ground-based facilities with single-dish telescopes but also interferometric antennas.

This work has been partly published in Quénard et al. (2016) (see Appendix B).

“Sans l’astronomie, l’homme ignore la place qu’il occupe.”

Aristote

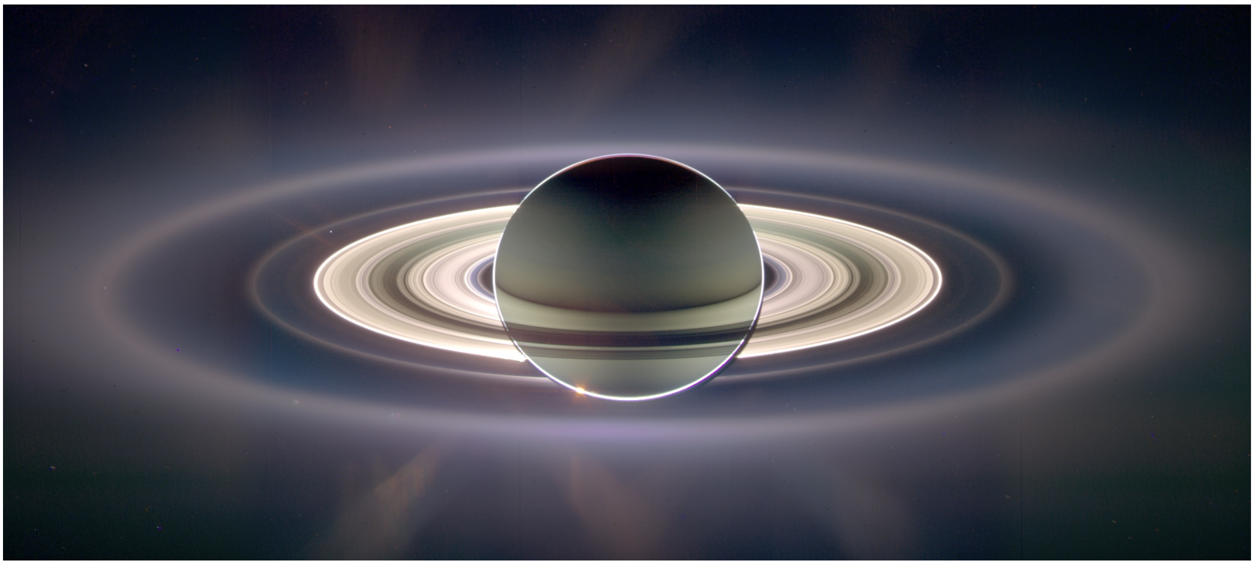

Saturn illuminated by the Sun, as seen by the Cassini spacecraft. The tiny bright dot between the rings on the left is the Earth.

CHAPTER 4

IRAS16293-2422 : A PROTO-SOLAR PROTOTYPE

Contents

4.1 Presentation of the source

IRAS16293-2422 (hereafter IRAS16293) is a typical Class 0 solar-type low-mass proto-star embedded in the LDN1689N cloud within the ρ Ophiuchus complex. This object has been discovered by the IRAS satellite[1]. Located at 120 pc (Loinard et al., 2008), this object is well-studied due to its molecular richness, high deuterium fractionation, and the high intensity of its emission lines (Mundy et al., 1992; Blake et al., 1994; van Dishoeck et al., 1995). Considered to be similar to the Sun during its formation, the mass of IRAS16293 is estimated to be $\sim 1\,\mathrm{M}_{\odot}$ (Coutens et al., 2012) and it is a very luminous object with $\sim 22\,\mathrm{L}_{\odot}$ (Crimier et al., 2010).

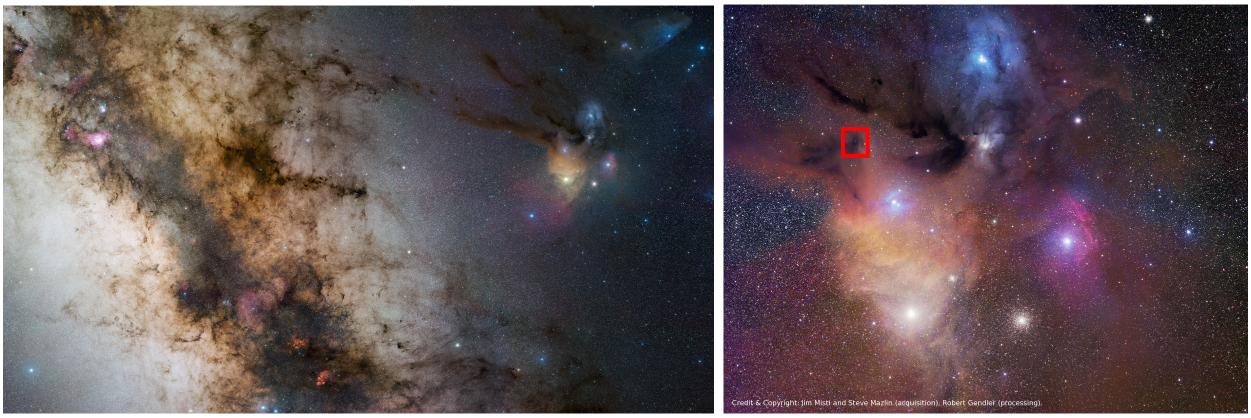

Credit & Copyright: Jim Misti and Steve Mazlin (acquisition), Robert Gendler (processing).

Figure 4.1 – *Left:* The Milky Way centre, spanning the Sagittarius and Scorpius constellations. Credit: ESO/S. Guisard. *Right:* The ρ Ophiuchus cloud within the Scorpius and Ophiuchus constellations. Antares (α Scorpii) and the ρ Ophiuchi stars are visible in the lower left and the top part of this picture, respectively. The red rectangle shows the position of IRAS16293. This image spans about 6 degrees on the sky.

It is also important to note that IRAS16293 is in reality a double system, or even a triple one. In fact the first available interferometric observations of the VLA[2] has allowed Wootten (1989) and Mundy et al. (1992) to resolve two distinct sources: IRAS16293 A in the south-east and IRAS16293 B in the north-west separated by 600 AU (or $\sim 5''$ at 120 pc). The source A is itself composed of two different centimetric objects: A1 and A2 (Wootten, 1989; Loinard et al., 2009) and two submillimetric sources: Aa and Ab (Chandler et al., 2005). Nonetheless, the size of the beam of most observations made using single-dish telescopes does not allow to disentangle the emission coming from these different objects, thus the emission arising from the source A is often considered to come from only one object. Several outflows have also been detected in this source and traced at multiple scales (Castets et al., 2001; Stark et al., 2004; Chandler et al., 2005; Yeh et al., 2008; Loinard et al., 2012; Girart et al., 2014). Fig. 4.2 displays a sketch showing the structure of the source.

Several studies have attempted to determine the physical and chemical parameters of IRAS16293 and thus to establish the density, temperature, and molecular abundance profiles as a function of the distance from the forming star (Ceccarelli et al., 2000a; Schöier et al., 2002, 2004). Ceccarelli et al. (2000a) used water and oxygen lines to get the density and temperature of the gas and dust using an inside-out model of Shu (1977). Schöier et al. (2002) used the dust continuum emission to get the physical structure of the envelope surrounding the proto-star. These two methods obtained roughly the same result regarding the overall structure of IRAS16293: a) an infalling envelope following the inside-out description of Shu (1977) and b) a region of $\sim$300 AU in diameter where the icy mantle of dust grain sublimate: the *hot corino*. The hot corino of IRAS16293 is the first one to be observed (Ceccarelli et al., 2000c; Cazaux et al., 2003; Bottinelli et al., 2004) and this term is derived from the hot cores detected around high-mass proto-stars (e.g. Turner, 1991).

---

[1] InfraRed Astronomical Satellite, launched in 1983.

[2] Very Large Array, *New Mexico, USA*

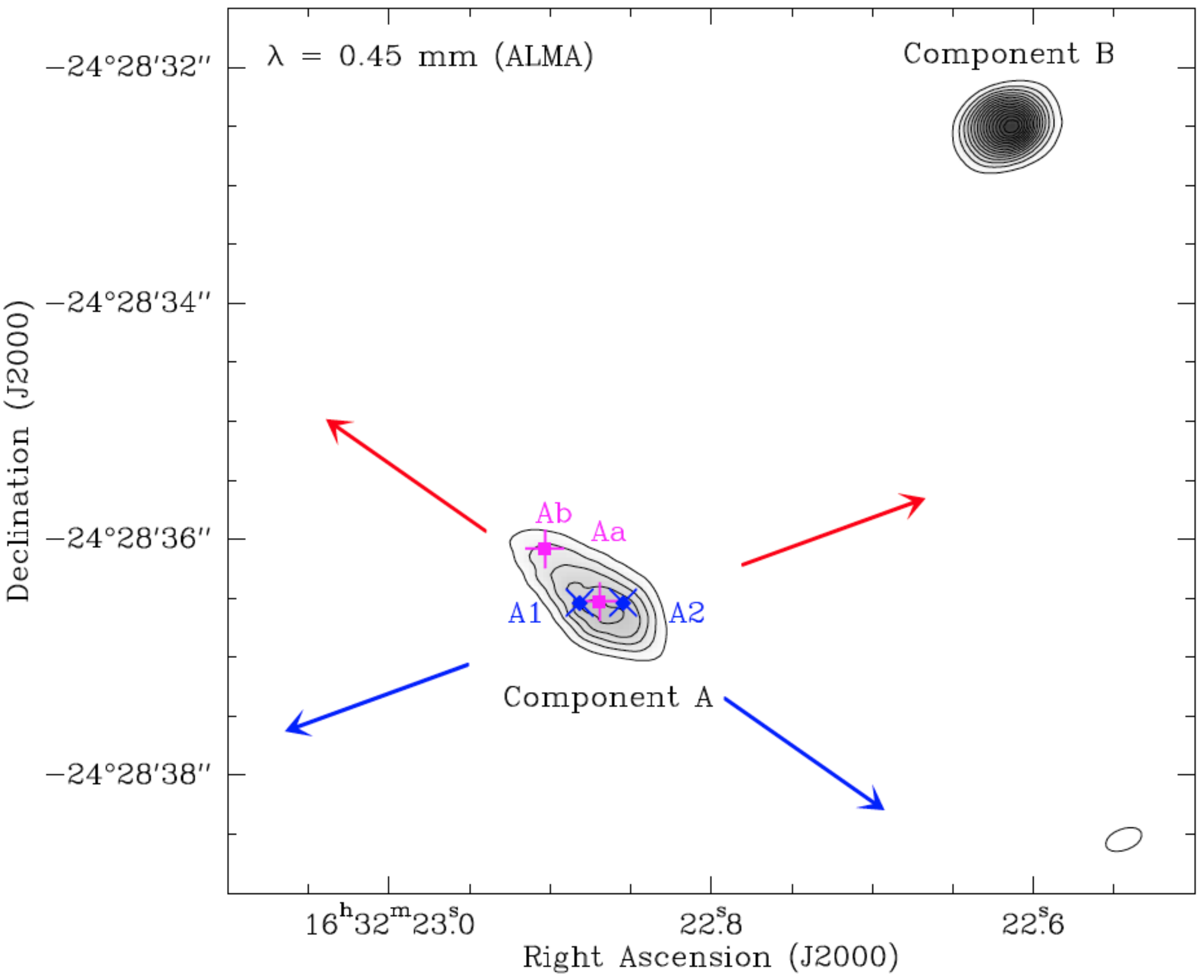

Figure 4.2 – Sub-millimetre continuum image of IRAS16293 obtained with the ALMA interferometer. The direction and position of the outflows produced by the source A (red and blue arrows) as well as the sub-millimetre peaks Aa and Ab (Chandler et al., 2005) and centimetre sources A1 and A2 are indicated. Source: Loinard et al. (2012).

From interferometric observations, Schöier et al. (2004) and Jørgensen et al. (2005) proposed the presence of a cavity of respectively 800 AU and 1200 AU inside the envelope. This cavity would have been carved by the outflowing material, pushing away the envelope material of the proto-star. These authors also suggested that an UV-induced radiation field would arise from the interaction between the shocks and the quiescent envelope. Combined with the UV radiation field of the young proto-star, it would heat up the edge of the cavity and could actively participate in the molecular chemistry of the source, increasing the ionisation in this region.

Crimier et al. (2010) re-analysed all the data available and they used continuum measurement to derive the physical structure of the source (H_2 density, gas and dust temperature profiles of the envelope) from 22 AU to 6000 AU. Shortly, they used available single-dish and interferometric continuum map emission from JCMT, CSO (SHARC I and II), Spitzer (IRS), and IRAM Plateau de Bure, ranging from 23.7 μm to 1300 μm. They used DUSTY (Ivezić and Elitzur, 1997) to derive the dust temperature and H_2 density profile. They considered two different types of density profiles: *(a)* a Shu-like profile (Shu, 1977), assimilated to a double power-law profile with indices of 1.5 and 2, broken at a radius r_{inf}; *(b)* a single power-law profile with an index α. They varied several input parameters such as the index α of the single power-law, the inner and outer radii of the envelope, the infall radius r_{inf} of the Shu-like model, and the initial density $n(T_{dust} = 100\,\mathrm{K})$. They found that the Shu-like profile best fits the SED with $n(T_{dust} = 100\,\mathrm{K}) = 2{\times}10^8\,\mathrm{cm}^{-3}$ and

r_{inf} = 1280 AU. From the derived dust temperature and H_2 density profiles, they obtained the gas temperature profile from the heating (gas compression due to collapse, dust-gas collisions if $T_{dust}>T_{gas}$, photo-pumping of H_2O and CO) and cooling (line emission of H_2O, CO, and O, dust-gas collisions), following the technique described in Ceccarelli et al. (1996). This profile has been used in several physical and chemical studies of the source (e.g. Hily-Blant et al., 2010; Vastel et al., 2010; Coutens et al., 2012; Bottinelli et al., 2014; Jaber et al., 2014; Wakelam et al., 2014; López-Sepulcre et al., 2015; Majumdar et al., 2016). One must note that the presence of multiple sources and hypothetical proto-planetary disks in the core of the envelope (hot corinos) has not been taken into account in the DUSTY model of Crimier et al. (2010). Thus, the inner structure of the source ($<$ 600 AU) is still open to discussions (see Sect. 4.3.3).

4.2 Observations of ions in the source

In this work, I mainly used data coming from two unbiased spectral surveys, *i)* The IRAS16293 Millimetre And Sub-millimetre Spectral Survey, performed at the IRAM-30m (80 – 265 GHz) and JCMT-15m (330 – 370 GHz) telescopes between January 2004 and August 2006, and APEX-12m (265–330 GHz) telescope between June 2011 and August 2012 (TIMASSS, Caux et al., 2011) and *ii)* the HIFI guaranteed time Key Program CHESS (Ceccarelli et al. 2010). The HIFI data presented are part of a full spectral coverage of bands 1a (480–560 GHz; obsid 1342191499), 1b (560–640 GHz; obsid 1342191559), 2a (640 – 720 GHz; obsid 1342214468), 2b (720 – 800 GHz; obsid 1342192332), 3a (800 – 880 GHz; obsid 1342214308), 3b (880 – 960 GHz; obsid 1342192330), 4a (960 – 1040 GHz; obsid 1342191619), 4b (1040 – 1120 GHz; obsid 1342191681), and 5a (1120 – 1200 GHz; obsid 1342191683) which was performed between March 2010 and April 2011. The HIFI Spectral Scan Double Beam Switch (DBS) observing mode with optimisation of the continuum was used with the HIFI acousto-optic Wide Band Spectrometer (WBS), providing a spectral resolution of 1.1 MHz ($\sim$0.6 km s^{-1} at 500 GHz and $\sim$0.3 km s^{-1} at 1 THz) over an instantaneous bandwidth of 4×1 GHz (Roelfsema et al., 2012).

For the TIMASSS survey, the observed coordinates were $\alpha_{2000} = 16^{\rm h}32^{\rm m}22^{\rm s}.6$, $\delta_{2000} = -24°28'33''$ while they were $\alpha_{2000} = 16^{\rm h}32^{\rm m}22^{\rm s}.75$, $\delta_{2000} = -24°28'34.2''$ for the HIFI observations. The differences in the targeted position have been carefully taken into account in this work. For both surveys, the DBS reference positions were situated at least $3'$ apart from the source. Tables 4.1 to 4.8 summarise the observation parameters of both detected and undetected transitions. The spectral resolution ranged between 0.3 and 1.25 MHz, corresponding to velocity resolutions between $\sim$0.51 and $\sim$2.25 km s^{-1}. The data processing of the TIMASSS survey has been extensively described in Caux et al. (2011).

The HIFI data have been processed using the standard HIFI pipeline up to frequency and intensity calibrations (level 2) with the ESA-supported package HIPE 12 (Ott, 2010). Using a routine developed within the HIFI ICC (Instrument Control Center), *flagTool*, spurs not automatically detected by the pipeline have been tagged and removed. Next, the HIPE tasks *fitHifiFringe* and *fitBaseline* were used to remove standing waves and to fit a low-order polynomial baseline to line-free channels. Finally, sideband deconvolution was performed with the dedicated HIPE task *doDeconvolution*.

The spectra observed in both horizontal and vertical polarisation were of similar quality, and averaged to lower the noise in the final spectrum, since polarisation is not a concern for the presented analysis. The continuum values obtained from running *fitBaseline* are well fitted by polynomials of order 3 over the frequency range of the whole band. The single side band continuum derived from the polynomial fit at the considered frequencies (see Tables 4.1 to 4.8) was added to the spectra. Intensities were then converted from antenna to main-beam temperature scale using a forward efficiency of 0.96 and the (frequency-dependent) beam-efficiency taken from the HIFI Beam release note[3] and reported in Tables 4.1 to 4.8 together with the spectroscopic and observing parameters

---

[3] The HIFI Beam: Release #1 found in the official Herschel website (HIFI documentation)

of the transitions used in this work. In these Tables, the V_{LSR}, FWHM, main beam temperature (T_{mb}) as well as the flux of the line ($\int T_{mb}dv$) have been determined using the Gaussian fitting tool of CASSIS.

For both spectral surveys, in this study, the calibration is taken to be 15% for each detected transition. Indeed, considering the upper limit of the calibration error budget given in Roelfsema et al. (2012) and taking into account the recent calibration release, a calibration error of 15% seems reasonable. This value is also adequate for the IRAM-30m, JCMT, and APEX transitions (Caux et al., 2011) because of bad weather conditions. The error in velocities shown in the following tables takes into account both the statistical error made by Gaussian fitting tool of CASSIS and the frequency accuracy budget of the telescopes.

From all the detected molecules in IRAS16293, I have especially focused on ionised species. Ions and electrons, following the magnetic field of the forming star, interact with neutral species, slowing down the gravitational collapse towards the central proto-star. Thus, studying ions allows to understand the gravitational collapse timescale of a given proto-star and its evolution with time. Moreover, ionised species can also help to create and destroy big molecules such as Complex Organic Molecules (COMs), thus they are involved in the chemistry that takes place in the source (Bergin and Langer, 1997).

Only 4 different ionised species are clearly detected in IRAS16293 with the IRAM-30m, JCMT, APEX, and Herschel telescopes:

1. HCO^+ (11 transitions) and 3 of its isotopologues : $H^{13}CO^+$ (7 transitions), $HC^{18}O^+$ (5 transitions), and $HC^{17}O^+$ (1 transition). Unfortunately the $HC^{17}O^+$ transition is not detected at a 3σ level thus it is not used in this study. The deuterated counterparts of HCO^+ and $H^{13}CO^+$ are also detected : DCO^+ (5 transitions) and $D^{13}CO^+$ (3 transitions).

2. N_2H^+ (4 transitions including 1 of them showing a hyper-fine structure) and its deuterated isotopologue, N_2D^+ (3 transitions including 2 of them showing a hyper-fine structure).

3. HCS^+ (6 transitions).

4. CH^+ (1 absorption line).

A total of 46 transitions are available for modelling process but HCO^+ is the most predominant species in the source with a total of 31 transitions detected over 5 different isotopologues (HCO^+, $H^{13}CO^+$, $HC^{18}O^+$, DCO^+, and $D^{13}CO^+$). N_2H^+ (4 transitions and 3 for N_2D^+) and HCS^+ (6 transitions) can also be modelled. Only one transition (absorption line) is detected for CH^+ thus it is difficult to give strong constraints on the physical parameters of this species. Bottinelli et al. (2014) already studied the emission of CH in IRAS16293 thus one can expect that the emission of CH^+ comes from the same region. Therefore, this study is focused on the HCO^+ and N_2H^+ species.

Table 4.1 – Parameters for the observed HCO^+ and $H^{13}CO^+$ lines.

Molecule	Transition $J_{up} - J_{low}$	Freq. (GHz)	E_{up}/k_B (K)	A_{ij} (s^{-1})	rms[1] (mK)	V_{LSR} ($km\,s^{-1}$)	FWHM ($km\,s^{-1}$)	T_{mb} (K)	$\int T_{mb} dv$ ($K\,km\,s^{-1}$)	Telescope	Beam size ($''$)
HCO^+	1 – 0	89.189	4	4.19×10^{-5}	8.4	4.2 ± 0.1	4.0 ± 0.3	4.5 ± 0.7	15.3 ± 2.3[2]	IRAM	27.8
	3 – 2	267.558	26	1.45×10^{-3}	79.7	3.8 ± 0.1	2.3 ± 0.1	25.2 ± 3.8	44.4 ± 6.7[2]	APEX	23.5
	4 – 3	356.734	43	3.57×10^{-3}	18.9	3.6 ± 0.1	3.0 ± 0.1	28.3 ± 4.2	67.6 ± 10.1[2]	JCMT	13.9
	6 – 5	535.062	90	1.25×10^{-2}	9.0	3.5 ± 0.1	2.4 ± 0.1	7.7 ± 1.2	21.1 ± 3.2	HIFI	39.7
	7 – 6	624.208	120	2.01×10^{-2}	9.0	3.5 ± 0.1	2.6 ± 0.1	7.9 ± 1.2	21.6 ± 3.2	HIFI	34.0
	8 – 7	713.341	154	3.02×10^{-2}	18.8	3.6 ± 0.1	2.9 ± 0.1	6.5 ± 1.0	20.1 ± 3.0	HIFI	29.7
	9 – 8	802.458	193	4.33×10^{-2}	24.0	3.7 ± 0.1	3.5 ± 0.1	5.3 ± 0.8	17.9 ± 2.7	HIFI	26.4
	10 – 9	891.557	235	5.97×10^{-2}	22.8	3.8 ± 0.1	3.9 ± 0.1	4.4 ± 0.7	15.6 ± 2.3	HIFI	23.8
	11 – 10	980.636	282	7.98×10^{-2}	25.9	3.9 ± 0.1	4.3 ± 0.1	3.6 ± 0.5	12.4 ± 1.9	HIFI	21.6
	12 – 11	1069.694	334	1.04×10^{-1}	35.1	3.9 ± 0.1	4.4 ± 0.1	2.6 ± 0.4	9.2 ± 1.8	HIFI	19.8
	13 – 12	1158.727	389	1.33×10^{-1}	78.5	4.0 ± 0.1	4.8 ± 0.1	2.1 ± 0.3	8.3 ± 1.7	HIFI	18.3
$H^{13}CO^+$	1 – 0	86.754	4	3.85×10^{-5}	6.8	4.2 ± 0.1	2.1 ± 0.1	1.9 ± 0.3	4.1 ± 0.6	IRAM	28.5
	2 – 1	173.507	12	3.70×10^{-4}	29.0	4.5 ± 0.1	2.1 ± 0.1	3.7 ± 0.6	7.7 ± 1.2	IRAM	14.3
	3 – 2	260.255	25	1.34×10^{-3}	15.2	3.6 ± 0.1	3.0 ± 0.1	3.2 ± 0.5	10.0 ± 1.5	IRAM	9.50
	4 – 3	346.998	42	3.29×10^{-3}	16.2	3.5 ± 0.1	2.4 ± 0.1	3.5 ± 0.5	7.7 ± 1.2	JCMT	14.3
	6 – 5	520.460	87	1.15×10^{-2}	7.3	4.0 ± 0.1	3.2 ± 0.1	0.4 ± 0.1	1.0 ± 0.2	HIFI	40.8
	7 – 6	607.175	117	1.85×10^{-2}	8.3	4.0 ± 0.1	3.0 ± 0.2	0.2 ± 0.1	0.7 ± 0.1	HIFI	35.0
	8 – 7	693.876	150	2.78×10^{-2}	15.2	4.2 ± 0.1	3.3 ± 0.3	0.1 ± 0.1	0.3 ± 0.1	HIFI	30.6
	9 – 8	780.563	187	3.99×10^{-2}	17.7	–	–	–	< 0.2	HIFI	27.2
	10 – 9	867.232	229	5.50×10^{-2}	30.6	–	–	–	< 0.4	HIFI	24.5
	11 – 10	953.883	275	7.35×10^{-2}	52.7	–	–	–	< 0.7	HIFI	22.2
	12 – 11	1127.121	379	1.22×10^{-1}	53.1	–	–	–	< 0.8	HIFI	18.8
	13 – 12	1213.704	437	1.53×10^{-1}	96.5	–	–	–	< 1.4	HIFI	17.5

---

[1] The rms is computed for a spectral resolution of $1\,km\,s^{-1}$ for all transitions.

[2] Lines showing a strong self-absorption profile.

Table 4.2 – Parameters for the observed HC^{18}O$^+$, and HC^{17}O$^+$ lines.

Molecule	Transition $J_{up} - J_{low}$	Freq. (GHz)	E_{up}/k_B (K)	A_{ij} (s^{-1})	rms[1] (mK)	V_{LSR} (km s^{-1})	FWHM (km s^{-1})	T_{mb} (K)	$\int T_{mb}dv$ (K km s^{-1})	Telescope	Beam size ($''$)
HC^{18}O$^+$	1 – 0	85.162	4	3.64×10^{-5}	6.3	4.2 ± 0.1	2.0 ± 0.1	0.2 ± 0.1	0.4 ± 0.1	IRAM	29.1
	2 – 1	170.323	12	3.50×10^{-4}	26.0	4.3 ± 0.1	1.7 ± 0.1	0.4 ± 0.1	0.7 ± 0.1	IRAM	14.5
	3 – 2	255.479	25	1.27×10^{-3}	10.5	3.6 ± 0.3	2.4 ± 0.7	0.1 ± 0.1	0.3 ± 0.1	IRAM	9.7
	4 – 3	340.631	41	3.11×10^{-3}	12.0	4.0 ± 0.1	3.1 ± 0.2	0.4 ± 0.1	1.2 ± 0.2	JCMT	14.5
	6 – 5	510.910	86	1.09×10^{-2}	8.5	4.3 ± 0.1	2.3 ± 0.3	0.06 ± 0.01	0.1 ± 0.1	HIFI	41.6
	7 – 6	596.034	114	1.75×10^{-2}	10.2	–	–	–	< 0.1	HIFI	35.8
	8 – 7	681.145	147	2.63×10^{-2}	15.4	–	–	–	< 0.2	HIFI	31.1
	9 – 8	766.242	184	3.77×10^{-2}	18.6	–	–	–	< 0.2	HIFI	27.7
	10 – 9	851.322	225	5.20×10^{-2}	14.5	–	–	–	< 0.2	HIFI	24.9
	11 – 10	936.384	270	6.95×10^{-2}	21.4	–	–	–	< 0.3	HIFI	22.6
	12 – 11	1021.426	319	9.06×10^{-2}	24.1	–	–	–	< 0.3	HIFI	20.8
	13 – 12	1106.446	372	1.15×10^{-1}	33.6	–	–	–	< 0.5	HIFI	19.2
	14 – 13	1191.443	429	1.45×10^{-1}	75.3	–	–	–	< 1.1	HIFI	17.8
HC^{17}O$^+$	1 – 0	87.058	4	3.89×10^{-5}	6.6	3.9 ± 0.7	6.5 ± 1.8	0.02 ± 0.01	0.09 ± 0.01[2]	IRAM	28.4

---

[1] The rms is computed for a spectral resolution of 1 km s^{-1} for all transitions.

[2] Flux $\approx 2\sigma$ ($< 3\sigma$, flux at $1\sigma < 0.05$ K.km.s^{-1})

Table 4.3 – Parameters for the observed DCO^+ and $D^{13}CO^+$ lines.

Molecule	Transition $J_{up} - J_{low}$	Freq. (GHz)	E_{up}/k_B (K)	A_{ij} (s^{-1})	rms[1] (mK)	V_{LSR} ($km\,s^{-1}$)	FWHM ($km\,s^{-1}$)	T_{mb} (K)	$\int T_{mb}dv$ ($K\,km\,s^{-1}$)	Telescope	Beam size ($''$)
DCO^+	2 – 1	144.077	10	2.12×10^{-4}	19.8	4.3 ± 0.1	1.4 ± 0.1	3.6 ± 0.5	5.5 ± 0.8	IRAM	17.2
	3 – 2	216.113	21	7.66×10^{-4}	21.0	4.4 ± 0.1	2.9 ± 0.1	1.8 ± 0.3	5.7 ± 0.9	IRAM	11.5
	4 – 3	288.144	35	1.88×10^{-3}	7.1	4.2 ± 0.1	2.2 ± 0.1	1.2 ± 0.2	2.9 ± 0.4	APEX	21.8
	5 – 4	360.170	52	3.76×10^{-3}	15.1	3.9 ± 0.1	2.5 ± 0.1	1.2 ± 0.2	2.6 ± 0.4	JCMT	13.7
	7 – 6	504.200	97	1.06×10^{-2}	8.8	4.0 ± 0.1	3.0 ± 0.2	0.08 ± 0.01	0.2 ± 0.1	HIFI	42.1
	8 – 7	576.202	124	1.59×10^{-2}	6.9	–	–	–	< 0.4[2]	HIFI	36.8
	9 – 8	648.193	156	2.28×10^{-2}	11.4	–	–	–	< 0.1	HIFI	32.7
	10 – 9	720.172	190	3.15×10^{-2}	11.8	–	–	–	< 0.1	HIFI	29.4
	11 – 10	792.138	228	4.21×10^{-2}	20.9	–	–	–	< 0.3	HIFI	26.8
	12 – 11	864.089	270	5.48×10^{-2}	25.1	–	–	–	< 0.3	HIFI	24.5
	13 – 12	936.024	315	6.99×10^{-2}	22.2	–	–	–	< 0.3	HIFI	22.7
	14 – 13	1007.941	363	8.75×10^{-2}	31.1	–	–	–	< 0.4	HIFI	21.0
	15 – 14	1079.840	415	1.08×10^{-1}	34.9	–	–	–	< 0.5	HIFI	19.6
	16 – 15	1151.719	470	1.31×10^{-1}	70.6	–	–	–	< 1.0	HIFI	18.4
$D^{13}CO^+$	2 – 1	141.465	10	2.00×10^{-4}	17.0	4.4 ± 0.1	1.8 ± 0.2	0.2 ± 0.1	0.3 ± 0.1	IRAM	17.5
	3 – 2	212.194	20	7.25×10^{-4}	7.8	4.4 ± 0.3	2.7 ± 0.6	0.08 ± 0.01	0.2 ± 0.1	IRAM	11.7
	4 – 3	282.920	34	1.78×10^{-3}	5.7	4.6 ± 0.2	3.1 ± 0.3	0.07 ± 0.01	0.2 ± 0.1	APEX	22.2
	5 – 4	353.640	51	3.56×10^{-3}	19.9	–	–	–	< 0.2	JCMT	14.0
	7 – 6	495.061	95	1.00×10^{-2}	8.5	–	–	–	< 0.1	HIFI	42.8
	8 – 7	565.758	122	1.51×10^{-2}	9.6	–	–	–	< 0.1	HIFI	37.5
	9 – 8	636.445	153	2.16×10^{-2}	16.7	–	–	–	< 0.2	HIFI	33.3
	10 – 9	707.121	187	2.98×10^{-2}	16.7	–	–	–	< 0.2	HIFI	30.0
	11 – 10	777.783	224	3.98×10^{-2}	21.2	–	–	–	< 0.31	HIFI	27.3
	12 – 11	848.432	265	5.19×10^{-2}	17.0	–	–	–	< 0.2	HIFI	25.0
	13 – 12	919.065	309	6.62×10^{-2}	20.8	–	–	–	< 0.3	HIFI	23.1
	14 – 13	989.682	356	8.28×10^{-2}	23.2	–	–	–	< 0.3	HIFI	21.4
	15 – 14	1060.280	407	1.02×10^{-1}	38.4	–	–	–	< 0.5	HIFI	20.0
	16 – 15	1130.860	461	1.24×10^{-1}	59.6	–	–	–	< 0.9	HIFI	18.8
	17 – 16	1201.419	519	1.49×10^{-1}	91.0	–	–	–	< 1.3	HIFI	17.6

---

[1] The rms is computed for a spectral resolution of $1\,km\,s^{-1}$ for all transitions.

[2] Transition blended with CO ($J = 5 \rightarrow 4$).

Table 4.4 – Parameters for the observed N_2H^+ and N_2D^+ lines.

Molecule	Transition $J_{up} - J_{low}$	Freq. (GHz)	E_{up}/k_B (K)	A_{ij} (s^{-1})	rms[1] (mK)	V_{LSR} ($km\,s^{-1}$)	FWHM ($km\,s^{-1}$)	T_{mb} (K)	$\int T_{mb}dv$ ($K\,km\,s^{-1}$)	Telescope	Beam size ($''$)
N_2H^+	$1_1 - 0_1$	93.172	4	3.63×10^{-5}	4.7	4.0 ± 0.1	2.0 ± 0.1	2.4 ± 0.4	5.0 ± 0.8	IRAM	26.6
	$1_2 - 0_1$	93.174	4	3.63×10^{-5}	4.7	4.1 ± 0.1	2.3 ± 0.1	3.2 ± 0.5	7.4 ± 1.1	IRAM	26.6
	$1_0 - 0_1$	93.176	4	3.63×10^{-5}	4.7	3.8 ± 0.1	1.7 ± 0.1	1.2 ± 0.2	2.2 ± 0.3	IRAM	26.6
	$3 - 2$	279.512	27	1.35×10^{-3}	5.2	4.0 ± 0.2	≈ 1.7	≈ 1.5	5.3 ± 0.8	APEX	22.5
	$6 - 5$	558.967	94	1.16×10^{-2}	10.0	3.8 ± 0.1	2.2 ± 0.1	0.2 ± 0.1	0.3 ± 0.1	HIFI	37.9
	$7 - 6$	652.096	125	1.87×10^{-2}	14.4	3.7 ± 0.2	2.3 ± 0.3	0.06 ± 0.01	< 0.16	HIFI	32.5
	$8 - 7$	745.210	161	2.81×10^{-2}	17.1	–	–	–	< 0.2	HIFI	28.5
	$9 - 8$	838.307	201	4.03×10^{-2}	13.5	–	–	–	< 0.2	HIFI	25.3
	$10 - 9$	931.386	246	5.56×10^{-2}	24.2	–	–	–	< 0.3	HIFI	22.8
	$11 - 10$	1024.443	295	7.43×10^{-2}	25.5	–	–	–	< 0.3	HIFI	20.7
	$12 - 11$	1117.477	349	9.68×10^{-2}	56.6	–	–	–	< 0.6	HIFI	19.0
	$13 - 12$	1210.486	407	1.23×10^{-1}	88.2	–	–	–	< 1.3	HIFI	17.5
N_2D^+	$2_1 - 1_1$	154.217	11	1.20×10^{-4}	21.9	7.3 ± 0.1	1.4 ± 0.1	0.6 ± 0.1	0.8 ± 0.1	IRAM	16.0
	$2_2 - 1_1$	154.217	11	1.20×10^{-4}	21.9	4.0 ± 0.1	1.4 ± 0.1	1.4 ± 0.2	2.0 ± 0.3	IRAM	16.0
	$2_0 - 1_1$	154.217	11	1.20×10^{-4}	21.9	-1.4 ± 0.1	1.1 ± 0.1	0.3 ± 0.1	0.4 ± 0.1	IRAM	16.0
	$3_1 - 2_1$	231.322	22	4.38×10^{-4}	13.1	17.1 ± 0.1	2.9 ± 0.6	0.1 ± 0.1	0.8 ± 0.1	IRAM	10.7
	$3_2 - 2_1$	231.322	22	4.38×10^{-4}	13.1	4.5 ± 0.1	2.7 ± 2.1	0.4 ± 0.1	1.2 ± 0.2	IRAM	10.7
	$3_0 - 2_1$	231.322	22	4.38×10^{-4}	13.1	-7.5 ± 0.2	2.9 ± 0.6	0.1 ± 0.1	0.6 ± 0.1	IRAM	10.7
	$4 - 3$	308.422	37	1.10×10^{-3}	14.2	4.5 ± 0.1	1.5 ± 0.1	0.6 ± 0.1	0.9 ± 0.2[2]	APEX	20.4
	$7 - 6$	539.682	104	6.68×10^{-3}	7.6	–	–	–	< 0.08	HIFI	39.3
	$8 - 7$	616.750	133	1.04×10^{-2}	7.2	–	–	–	< 0.08	HIFI	34.4
	$9 - 8$	693.806	167	1.56×10^{-2}	13.7	–	–	–	< 0.2	HIFI	30.6
	$10 - 9$	770.849	204	2.25×10^{-2}	19.3	–	–	–	< 0.2	HIFI	27.5
	$11 - 10$	847.877	244	3.17×10^{-2}	18.9	–	–	–	< 0.2	HIFI	25.0
	$12 - 11$	924.889	289	4.37×10^{-2}	20.8	–	–	–	< 0.3	HIFI	22.9
	$13 - 12$	1001.883	337	5.93×10^{-2}	22.0	–	–	–	< 0.3	HIFI	21.2
	$14 - 13$	1078.858	388	7.93×10^{-2}	38.3	–	–	–	< 0.5	HIFI	19.7
	$15 - 14$	1155.813	444	1.05×10^{-1}	73.9	–	–	–	< 1.1	HIFI	18.3
	$16 - 15$	1232.745	503	1.38×10^{-1}	94.4	–	–	–	< 1.4	HIFI	17.2

---

[1] The rms is computed for a spectral resolution of $1\,km\,s^{-1}$ for all transitions.

[2] Blended with HDCO.

Table 4.5 – Parameters for the observed HCS^+, CH^+, CD^+, and $^{13}CD^+$ lines.

Molecule	Transition $J_{up} - J_{low}$	Freq. (GHz)	E_{up}/k_B (K)	A_{ij} (s^{-1})	rms[1] (mK)	V_{LSR} ($km\,s^{-1}$)	FWHM ($km\,s^{-1}$)	T_{mb} (K)	$\int T_{mb}dv$ ($K\,km\,s^{-1}$)	Telescope	Beam size ($''$)
HCS^+	2 – 1	85.348	6	1.11×10^{-5}	8.1	4.0 ± 0.1	2.3 ± 0.2	0.07 ± 0.01	0.2 ± 0.1	IRAM	29.0
	4 – 3	170.692	20	9.86×10^{-5}	31.5	3.6 ± 0.1	2.5 ± 0.2	0.2 ± 0.1	0.5 ± 0.1	IRAM	14.5
	5 – 4	213.361	31	1.97×10^{-4}	8.7	3.5 ± 0.1	4.2 ± 0.2	0.3 ± 0.1	1.1 ± 0.2	IRAM	11.6
	6 – 5	256.027	43	3.46×10^{-4}	14.7	3.8 ± 0.1	4.1 ± 0.3	0.4 ± 0.1	1.5 ± 0.2	IRAM	9.7
	7 – 6	298.690	57	5.55×10^{-4}	4.5	3.5 ± 0.1	4.1 ± 0.1	0.2 ± 0.1	1.0 ± 0.2	APEX	21.0
	8 – 7	341.350	74	8.35×10^{-4}	17.9	3.6 ± 0.1	3.3 ± 0.2	0.4 ± 0.1	1.4 ± 0.2	JCMT	14.5
	12 – 11	511.943	160	2.87×10^{-3}	8.7	–	–	–	0.3 ± 0.1[2]	HIFI	41.4
CH^+	1 – 0	835.138	40	6.36×10^{-3}	17.1	4.2 ± 0.2	4.5 ± 0.1	-0.7 ± 0.1	3.9 ± 0.6[3]	HIFI	25.4
$^{13}CH^+$	1 – 0	830.216	40	6.38×10^{-3}	20.6	–	–	–	< 0.3	HIFI	25.5
CD^+	2 – 1	906.752	65	5.98×10^{-3}	21.2	–	–	–	< 0.3	HIFI	23.4
$^{13}CD^+$	2 – 1	896.793	65	6.12×10^{-3}	21.7	–	–	–	< 0.3[4]	HIFI	23.6

---

[1] The rms is computed for a spectral resolution of $1\,km\,s^{-1}$ for all transitions.

[2] Flux at $3\sigma < 0.08\,K\,km\,s^{-1}$.

[3] Absorption line.

[4] Transition blended with o-H_2CO ($J = 12_{1,11} \rightarrow 11_{1,10}$) but no detection.

Table 4.6 – Parameters for the observed SO^+, p-H_2D^+, o-H_2D^+, p-D_2H^+, o-D_2H^+, and H_3O^+ lines.

Molecule	Transition $J_{up} - J_{low}$	Freq. (GHz)	E_{up}/k_B (K)	A_{ij} (s^{-1})	rms[1] (mK)	$\int T_{mb}dv$ (K km s^{-1})	Telescope	Beam size ($''$)
SO^+	$4_{-1,7/2}$ - $3_{1,5/2}$	162.199	17	2.13×10^{-5}	22.8	< 0.2	IRAM	15.3
	$4_{1,7/2}$ - $3_{-1,5/2}$	162.574	17	2.14×10^{-5}	18.7	< 0.1	IRAM	15.2
	$5_{1,9/2}$ - $4_{-1,7/2}$	208.590	27	4.70×10^{-5}	11.4	< 0.07	IRAM	11.9
	$5_{-1,9/2}$ - $4_{1,7/2}$	208.965	27	4.72×10^{-5}	11.5	< 0.07	IRAM	11.8
	$6_{-1,11/2}$ - $5_{1,9/2}$	254.978	39	8.77×10^{-5}	13.3	< 0.1	IRAM	9.7
	$6_{1,11/2}$ - $5_{-1,9/2}$	255.353	39	8.81×10^{-5}	9.8	< 0.07	IRAM	9.7
	$7_{1,13/2}$ - $6_{-1,11/2}$	301.362	54	1.47×10^{-4}	9.0	< 0.09	APEX	20.8
	$7_{-1,13/2}$ - $6_{1,11/2}$	301.737	54	1.48×10^{-4}	12.5	< 0.1	APEX	20.8
	$8_{-1,15/2}$ - $7_{1,13/2}$	347.740	70	2.28×10^{-4}	16.4	< 0.2	JCMT	14.2
	$8_{1,15/2}$ - $7_{-1,13/2}$	348.115	70	2.28×10^{-4}	20.0	< 0.2	JCMT	14.2
p-H_2D^+	$2_{2,0}$ - $2_{2,1}$	155.987	322	1.00×10^{-5}	20.9	< 0.1	IRAM	15.9
	$3_{2,1}$ - $3_{2,2}$	646.430	541	3.12×10^{-4}	17.7	< 0.1	HIFI	32.8
	$4_{0,4}$ - $3_{2,1}$	795.551	580	3.87×10^{-6}	21.7	< 0.2	HIFI	26.7
	$3_{0,3}$ - $2_{2,0}$	826.306	362	7.27×10^{-6}	21.1	< 0.2	HIFI	25.7
o-H_2D^+	$2_{1,1}$ - $2_{1,2}$	1111.505	167	9.58×10^{-4}	41.6	< 0.6	HIFI	19.1
p-D_2H^+	$4_{1,4}$ - $3_{2,1}$	635.679	406	5.33×10^{-6}	13.3	< 0.1	HIFI	33.4
	$1_{1,0}$ - $1_{0,1}$	691.660	33	4.55×10^{-4}	14.6	< 0.2	HIFI	30.7
o-D_2H^+	$3_{1,3}$ - $2_{2,0}$	538.683	288	4.67×10^{-6}	8.8	< 0.09	HIFI	39.4
	$2_{1,1}$ - $2_{0,2}$	1038.673	196	1.17×10^{-3}	78.5	< 1.1	HIFI	20.4
H_3O^+	$3_{2,0}$ - $2_{2,1}$	364.797	140	2.79×10^{-4}	19.6	< 0.2	JCMT	13.6
	$0_{0,1}$ - $1_{0,0}$	984.709	55	2.30×10^{-2}	22.2	< 0.3	HIFI	21.5
	$4_{3,0}$ - $3_{3,1}$	1031.300	232	5.15×10^{-3}	26.4	< 0.4	HIFI	20.6
	$4_{2,0}$ - $3_{2,1}$	1069.828	269	9.85×10^{-3}	33.4	< 0.5	HIFI	19.8
	$4_{1,0}$ - $3_{1,1}$	1092.518	291	1.31×10^{-2}	37.4	< 0.5	HIFI	19.4

---

[1] The rms is computed for a spectral resolution of 1 km s^{-1} for all transitions.

Table 4.7 – Parameters for the observed OH^+, OH^-, OD^-, and HOC^+ lines.

Molecule	Transition $J_{up} - J_{low}$	Freq. (GHz)	E_{up}/k_B (K)	A_{ij} (s^{-1})	rms[1] (mK)	$\int T_{mb}dv$ ($K\,km\,s^{-1}$)	Telescope	Beam size ($''$)
OH^+	$1_{0,1/2}$ - $0_{1,1/2}$	909.045	44	5.23×10^{-3}	21.0	< 0.3	HIFI	23.3
	$1_{0,1/2}$ - $0_{1,3/2}$	909.159	44	1.05×10^{-2}	20.2	< 0.3	HIFI	23.3
	$1_{2,5/2}$ - $0_{1,3/2}$	971.804	47	1.82×10^{-2}	22.4	< 0.3	HIFI	21.8
	$1_{2,3/2}$ - $0_{1,1/2}$	971.805	47	1.52×10^{-2}	22.3	< 0.3	HIFI	21.8
	$1_{2,3/2}$ - $0_{1,3/2}$	971.919	47	3.04×10^{-3}	20.8	< 0.3	HIFI	21.8
	$1_{1,1/2}$ - $0_{1,1/2}$	1032.998	50	1.41×10^{-2}	23.5	< 0.3	HIFI	20.5
	$1_{1,3/2}$ - $0_{1,1/2}$	1033.004	50	3.53×10^{-3}	23.6	< 0.3	HIFI	20.5
	$1_{1,1/2}$ - $0_{1,3/2}$	1033.112	50	7.03×10^{-3}	22.4	< 0.3	HIFI	20.5
	$1_{1,3/2}$ - $0_{1,3/2}$	1033.119	44	1.76×10^{-2}	22.2	< 0.3	HIFI	20.5
OH^-	1 – 0	1123.101	54	5.95×10^{-3}	47.3	< 0.7	HIFI	18.9
OD^-	1 – 0	598.596	29	9.00×10^{-4}	13.6	< 0.1	HIFI	35.4
	2 – 1	1196.792	86	8.63×10^{-3}	84.8	< 1.2	HIFI	17.7
HOC^+	$1_{0,0}$ - $0_{0,0}$	89.487	4	2.13×10^{-5}	3.2	< 0.02	IRAM	27.7
	$3_{0,0}$ - $2_{0,0}$	268.451	26	7.41×10^{-4}	18.8	< 0.1	IRAM	9.2
	$4_{0,0}$ - $3_{0,0}$	357.923	43	1.82×10^{-3}	16.5	*blended*	JCMT	13.8
	$6_{0,0}$ - $5_{0,0}$	536.828	90	6.38×10^{-3}	8.3	< 0.08	HIFI	39.5
	$6_{0,0}$ - $5_{0,0}$	536.828	90	6.38×10^{-3}	8.3	< 0.08	HIFI	39.5
	$7_{0,0}$ - $6_{0,0}$	626.258	120	1.02×10^{-2}	8.5	< 0.09	HIFI	33.9
	$8_{0,0}$ - $7_{0,0}$	712.668	155	1.54×10^{-2}	16.9	< 0.2	HIFI	29.8
	$9_{0,0}$ - $8_{0,0}$	805.056	193	2.21×10^{-2}	19.5	< 0.2	HIFI	26.3
	$10_{0,0}$ - $9_{0,0}$	894.420	236	3.05×10^{-2}	18.9	< 0.2	HIFI	23.7
	$11_{0,0}$ - $10_{0,0}$	983.757	283	4.07×10^{-2}	23.6	< 0.3	HIFI	21.6
	$12_{0,0}$ - $11_{0,0}$	1073.063	335	5.30×10^{-2}	30.9	< 0.4	HIFI	19.8
	$13_{0,0}$ - $12_{0,0}$	1162.337	391	6.76×10^{-2}	73.3	< 1.1	HIFI	18.2

---

[1] The rms is computed for a spectral resolution of $1\,km\,s^{-1}$ for all transitions.

Table 4.8 – Parameters for the observed CO$^+$, CF$^+$ lines.

Molecule	Transition $\mathrm{J_{up} - J_{low}}$	Freq. (GHz)	E_{up}/k_B (K)	A_{ij} ($\mathrm{s^{-1}}$)	rms[1] (mK)	$\int T_{mb}dv$ ($\mathrm{K\,km\,s^{-1}}$)	Telescope	Beam size ($''$)
CO$^+$	$2_{3/2}$ - $1_{1/2}$	235.790	17	3.45×10^{-4}	18.2	< 0.1	IRAM	10.5
	$2_{3/2}$ - $1_{3/2}$	235.380	17	6.87×10^{-5}	13.4	< 0.1	IRAM	10.5
	$2_{5/2}$ - $1_{3/2}$	236.063	17	4.16×10^{-4}	20.6	*blended*	IRAM	10.5
	$3_{5/2}$ - $2_{5/2}$	353.059	34	1.46×10^{-5}	21.1	< 0.2	JCMT	14.0
	$3_{5/2}$ - $2_{3/2}$	353.741	34	2.06×10^{-4}	19.8	*blended*	JCMT	14.0
	$3_{7/2}$ - $2_{5/2}$	354.014	34	2.21×10^{-4}	18.6	*blended*	JCMT	14.0
	$5_{9/2}$ - $4_{9/2}$	588.371	85	2.39×10^{-5}	9.8	< 0.1	HIFI	36.0
	$5_{9/2}$ - $4_{7/2}$	589.599	85	1.06×10^{-3}	9.5	< 0.1	HIFI	36.0
	$5_{11/2}$ - $4_{9/2}$	589.872	85	1.09×10^{-3}	11.1	< 0.1	HIFI	35.9
	$6_{11/2}$ - $5_{11/2}$	705.995	119	2.86×10^{-5}	15.3	< 0.2	HIFI	30.0
	$6_{11/2}$ - $5_{9/2}$	707.496	119	1.87×10^{-3}	13.9	< 0.2	HIFI	30.0
	$6_{13/2}$ - $5_{11/2}$	707.769	119	1.90×10^{-3}	16.9	< 0.2	HIFI	30.0
	$7_{13/2}$ - $6_{13/2}$	823.592	158	3.33×10^{-5}	17.2	< 0.2	HIFI	25.7
	$7_{13/2}$ - $6_{11/2}$	825.366	158	3.02×10^{-3}	16.5	< 0.2	HIFI	25.7
	$7_{15/2}$ - $6_{13/2}$	825.639	159	3.06×10^{-3}	16.4	< 0.2	HIFI	25.7
	$8_{15/2}$ - $7_{15/2}$	941.157	204	3.81×10^{-5}	19.2	< 0.3	HIFI	22.5
	$8_{15/2}$ - $7_{13/2}$	943.204	204	4.56×10^{-3}	24.5	< 0.3	HIFI	22.5
	$8_{17/2}$ - $7_{15/2}$	943.477	204	4.60×10^{-3}	25.9	< 0.3	HIFI	22.5
	$9_{17/2}$ - $8_{17/2}$	1058.686	255	4.28×10^{-5}	54.2	< 0.8	HIFI	20.0
	$9_{17/2}$ - $8_{15/2}$	1061.006	255	6.54×10^{-3}	41.9	< 0.6	HIFI	20.0
	$9_{19/2}$ - $8_{17/2}$	1061.279	255	6.59×10^{-3}	40.4	< 0.6	HIFI	20.0
	$10_{19/2}$ - $9_{19/2}$	1176.173	311	4.75×10^{-5}	92.9	< 1.4	HIFI	18.0
	$10_{19/2}$ - $9_{17/2}$	1178.766	311	9.03×10^{-3}	83.5	< 1.2	HIFI	18.0
	$10_{21/2}$ - $9_{19/2}$	1179.039	311	9.08×10^{-3}	98.6	< 1.4	HIFI	18.0
CF$^+$	1_0 - 0_0	102.588	5	4.82×10^{-6}	6.4	< 0.05	IRAM	24.1
	2_0 - 1_0	205.171	15	4.62×10^{-5}	≈ 6.0	*blended*	IRAM	41.3
	5_0 - 4_0	512.846	74	8.21×10^{-4}	8.1	< 0.08	HIFI	41.3
	6_0 - 5_0	615.366	103	1.44×10^{-3}	7.3	< 0.08	HIFI	34.5
	7_0 - 6_0	717.857	138	2.31×10^{-3}	11.3	< 0.1	HIFI	29.5
	8_0 - 7_0	820.317	177	3.48×10^{-3}	15.7	< 0.2	HIFI	25.8
	9_0 - 8_0	922.741	221	4.98×10^{-3}	21.6	< 0.3	HIFI	23.0
	10_0 - 9_0	1025.123	271	6.87×10^{-3}	29.2	< 0.4	HIFI	20.7
	11_0 - 10_0	1127.460	325	9.17×10^{-3}	56.5	< 0.8	HIFI	18.8
	12_0 - 11_0	1229.747	384	1.19×10^{-2}	89.9	< 1.3	HIFI	17.2

---

[1] The rms is computed for a spectral resolution of $1\,\mathrm{km\,s^{-1}}$ for all transitions.

4.3 Study of the emission of HCO^+ and N_2H^+

HCO^+ (or formyl cation) has been detected as an unidentified line for the first time by Buhl and Snyder (1970) toward the high-mass star-forming regions W3(OH), Orion, Sgr A, W51, and toward the dark cloud L134 using the 11 m NRAO telescope. Klemperer (1970) suggested that this line is associated to the ground state of HCO^+ based on structure considerations. Woods et al. (1975) proved this hypothesis thanks to the laboratory measurement of the HCO^+ spectrum. One year later, Snyder et al. (1976) reported the first detection of interstellar $H^{13}CO^+$ close to the predicted frequencies. They also used the NRAO 11 m telescope and they detected this isotopologue in many sources (DR21, DR21(OH), NGC 2264, NGC 7538, Orion A, Sgr B2(OH), W3(OH), W49, W51, and W75N). The same year, Hollis et al. detected DCO^+ using the NRAO 11 m telescope toward DR21(OH), L134, and NGC 2264. The first detection of $HC^{18}O^+$ has been reported in Sgr B2 by Guelin and Thaddeus (1979) (again with the NRAO 11 m telescope). The same authors studied the distribution of five isotopologues of HCO^+ in several sources and detected for the first time $D^{13}CO^+$ in TMC-1 and L183 (Guelin et al., 1982a). They also detected $HC^{17}O^+$ for the first time toward Sgr B2 (Guelin et al., 1982b). Since then, HCO^+ and its isotopologues have been detected in many different kind of sources: star-forming regions (e.g. Orion, W3(OH), W51, DR21), diffuse medium of extra-galactic sources (e.g. Lucas and Liszt, 1994), circumstellar envelope of evolved stars (e.g. Ziurys et al., 2009) and carbon-rich AGB stars (e.g. Pulliam et al., 2011). More recent studies have also detected HCO^+ maser (Hakobian and Crutcher, 2012). In star-forming regions, HCO^+ is very abundant by the relative simplicity of its formation. It is a very good tracer of dense gas ($\geq 10^5\,\mathrm{cm}^{-3}$) and degree of ionisation of a cloud because it probes the electron density (Caselli et al., 2002b).

N_2H^+ (or protonated nitrogen, or diazenylium) was first reported as an unidentified triplet line at 93.174 GHz by Turner (1974) using the NRAO 11-metre telescope. On the basis of *ab initio* quantum chemical calculations, Green et al. (1974) proposed that the line was likely due to protonated N_2. Confirmation of the species detection was reported by Thaddeus and Turner (1975) in the Orion Molecular Cloud 2 (OMC-2) using the same telescope. The deuterated form, N_2D^+, was first observed by Snyder et al. (1977). The species has also been detected in a number of extragalactic sources (Mauersberger and Henkel, 1991) thanks to the IRAM-30m telescope. N_2H^+ is most often used for probing dense interstellar molecular clouds since it is one of the last molecule to freeze out onto dust grains when the density of the cloud increases at the centre. Bergin et al. (2002) have carried out a study in several dense cores and they showed that N_2H^+ is an ideal tracer for the chemistry of dense pre-stellar cores.

4.3.1 Radiative transfer modelling

I have employed the 3D radiative transfer code LIME (see Sect. 1.4.4.3 and Chapter 2, Brinch and Hogerheijde, 2010) in order to derive the line profile of the studied molecular transitions as well as the continuum emission of the source. I have used GASS (cf. Chapter 2) to describe the input 3D physical model of IRAS16293 and set the different parameters of LIME. I chose to generate a grid of 100,000 cells with GASS to be sure that the result given by LIME has correctly converged. The LIME output hyper-spectral cube is in Kelvin units and it has been post-processed with GASS. For single-dish observations, the treatment consists in convolving the cube with the beam size of the desired telescope and to plot the predicted spectrum in main beam temperature as a function of the velocity for each observed frequency. The cube is built with a better spectral resolution (set to $100\,\mathrm{m\,s}^{-1}$ for all models) than the observations but the predicted spectra are resampled at the same spectral resolution as that of the observations. I carefully take into account the different telescopes source pointings in the convolution: observations coming from IRAM-30m and JCMT are pointed toward the source B whereas the Herschel beam is directed in the middle of sources A and B.

All HCO^+ and its isotopologues (except $D^{13}CO^+$) collision files have been taken from the LAMDA database. For each molecule, I have updated the spectroscopic values implemented in these collisions files with the newest spectroscopic data taken from the CDMS database. The collisional rates are taken from Flower (1999) and were calculated for temperatures in the range from 10 to 400 K including energy levels up to $J = 20$ for collisions with H_2. Since the $D^{13}CO^+$ file does not exist, I have created it from the CDMS database by considering that the collisional rates are the same as for DCO^+.

For N_2H^+, two different files are available: one for the hyperfine structure (HFS) transitions and another one for the non-HFS transitions. The N_2H^+ HFS collisional rates are only available for $J \leq 4$ transitions therefore I also used the non-HFS file. Both files are coming from the LAMDA database and I have updated their spectroscopic parameters with those from the CDMS database. In the non-HFS file, the collisional rates given by the LAMDA database are taken to be the same as for HCO^+. The HFS ones are taken from Daniel et al. (2005) for collisions with He and they have been scaled to H_2 by multiplying all collisional rates by a factor of 1.37. In fact, collisional rates vary as a function of $1/\sqrt{\mu}$, where μ is the reduced mass of the colliding system:

$$\mu = \left(\sum_{i=1}^{n} \frac{1}{m_i} \right)^{-1} . \tag{4.1}$$

In our case, $m_{N_2H^+} = 29\,u$, $m_{He} = 4\,u$, and $m_{H_2} = 2\,u$, thus $\mu_{N_2H^+-He} \simeq 3.52\,u$ and $\mu_{N_2H^+-H_2} \simeq 1.87\,u$. Therefore the ratio is:

$$\sqrt{\frac{\mu_{N_2H^+-He}}{\mu_{N_2H^+-H_2}}} \simeq \sqrt{\frac{3.52}{1.87}} \simeq 1.37. \tag{4.2}$$

As $D^{13}CO^+$, the N_2D^+ file does not exist so I created it from the N_2H^+ HFS file (I only need to model HFS N_2D^+ transitions). The N_2H^+ and N_2D^+ hyperfine transitions are not completely the same and some of the N_2D^+ transitions do not exist for N_2H^+. Thus, no collisional rates have been calculated for these transitions and, while creating the N_2D^+ file, I had to ignore these transitions. It has an impact in the calculations of the models and I foresee to get a different N_2D^+ emission than expected.

4.3.2 Physical and chemical structure

The physical structure of IRAS16293 is very complex with multiple outflows, multiple sources, and an envelope. To reproduce the observed HCO^+ and N_2H^+ emission and line profiles I have modelled in 3D the different structures that contribute to its emission. For that, I define the physical structure of each component and their respective HCO^+ and N_2H^+ abundance profiles, as described in the following sub-sections.

4.3.2.1 The envelope model

The physical structure used in this study is based on the definition given by Crimier et al. (2010). The envelope is supposed to be spherical in the 3D model, thus, for this study, I have used Crimier's profiles extrapolated for radii smaller than 22 AU for the sake of the radiative transfer modelling. The resulting gas and dust temperature profiles are shown in Fig. 4.3. The Shu-like density distribution described by Crimier et al. (2010) is:

$$n(r) = n(r_{in}) \times \left(\frac{r_{in}}{r} \right)^{1.5} \text{ if } r < r_{inf}, \tag{4.3}$$

$$n(r) = n(r_{in}) \times \left(\frac{r_{in}}{r} \right)^{2} \text{ if } r \geq r_{inf}, \tag{4.4}$$

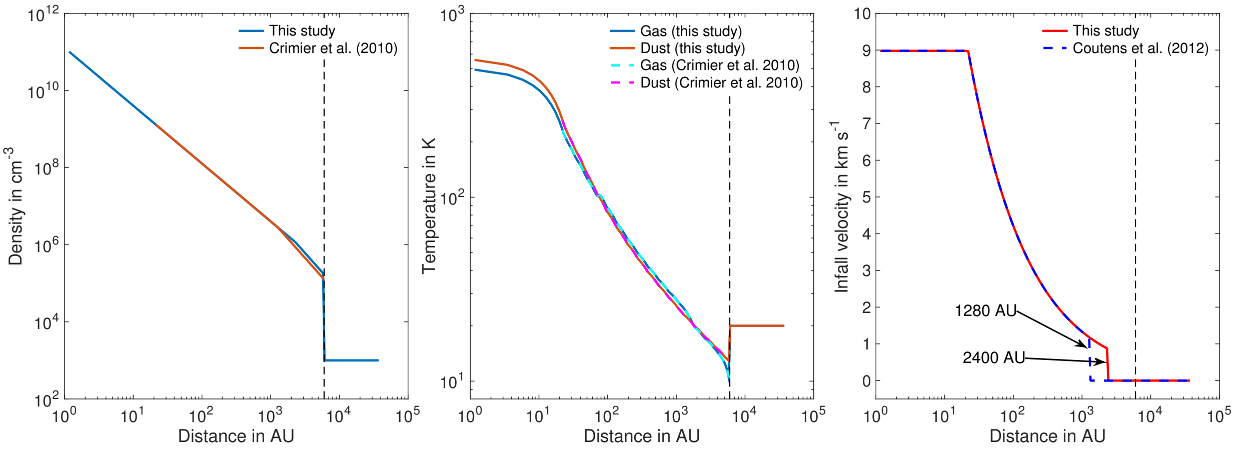

Figure 4.3 – *Left panel:* Density profile (blue) of IRAS16293 used in this study as a function of the radius, compared to Crimier's radial profile (red). *Middle panel:* Gas (blue) and dust (red) temperature profiles of IRAS16293 used in this study as a function of the radius, compared to the gas (cyan) and dust (magenta) Crimier's radial profiles. *Right panel:* Absolute value of the radial infall velocity as a function of the radius used in this study (red line) compared to the profile used by Coutens et al. (2012) (blue dashed line). In all panels, the vertical black dashed line shows the R = 6000 AU limit of the foreground cloud.

where $n(r_{in})$ is the density at r_{in}, the inner radius of the envelope, and r_{inf} refers to the radius where the envelope begins to collapse, marking a change in the slope of the density profile. From their best result, Crimier et al. (2010) derived $r_{inf} = 1280\,\mathrm{AU}$, $r_{in} = 22\,\mathrm{AU}$ and $n(r_{in}) = 1.23\times10^{9}\,\mathrm{cm}^{-3}$. r_{inf} is likely poorly constrained and to best reproduce the line profiles of the HCO^{+} and particularly the N_2H^{+} transitions, I need to set $r_{inf} = 2400\,\mathrm{AU}$. With this new value, the density profile is multiplied by at most a factor of 1.35 (at radius $> 1280\,\mathrm{AU}$, see left panel of Fig. 4.3) which is not a significant change considering the high density of H_2 in the concerned region ($10^{5} - 10^{6}\,\mathrm{cm}^{-3}$).

The velocity field of the source is defined through the standard infall law (Shu, 1977), in which the envelope is free-falling inside r_{inf}, and considered to be static outside (thus the infall velocity is set to 0). Hence, the velocity field is described by the following equations:

$$V_{\mathrm{inf}}(r) = \sqrt{\frac{2\,G\,M_{\star}}{r}} \text{ if } r < r_{inf}, \tag{4.5}$$

$$V_{\mathrm{inf}}(r) = 0 \text{ if } r \geq r_{inf}, \tag{4.6}$$

where V_{inf} is the infall velocity, G the gravitational constant, $M_{\star}$ the mass of the central object, and r the distance from the central object (see right panel of Fig. 4.3). For IRAS16293, the mass of the source A dominates the system, hence I took $M_{\star} = 1\,M_{\odot}$ (Coutens et al., 2012, and references therein); a variation of the mass between 0.8 and 1.5 solar masses changes the line width by 10%. For smaller or larger value, the modelled HCO^{+} lines are too narrow or too broad, respectively. The envelope is supposed to be centred on IRAS16293 A since it is the more massive component of the binary system.

I have modelled the dust continuum with LIME by using different dust opacity values for the observed frequency range and the physical structure described above. A gas-to-dust mass ratio of 100 is assumed.

The radial abundance profile of HCO^{+} and N_2H^{+} in the envelope of IRAS16293 has been estimated using the chemical model Nautilus (e.g. Ruaud et al., 2016). Nautilus is a chemical model that computes the evolution of the species abundances as a function of time in the gas-phase and on grain surfaces. The code has been used for a variety of environments such as dense clouds (Loison et al., 2014), low-mass proto-stellar envelopes (Bottinelli et al., 2014) and the outer re-

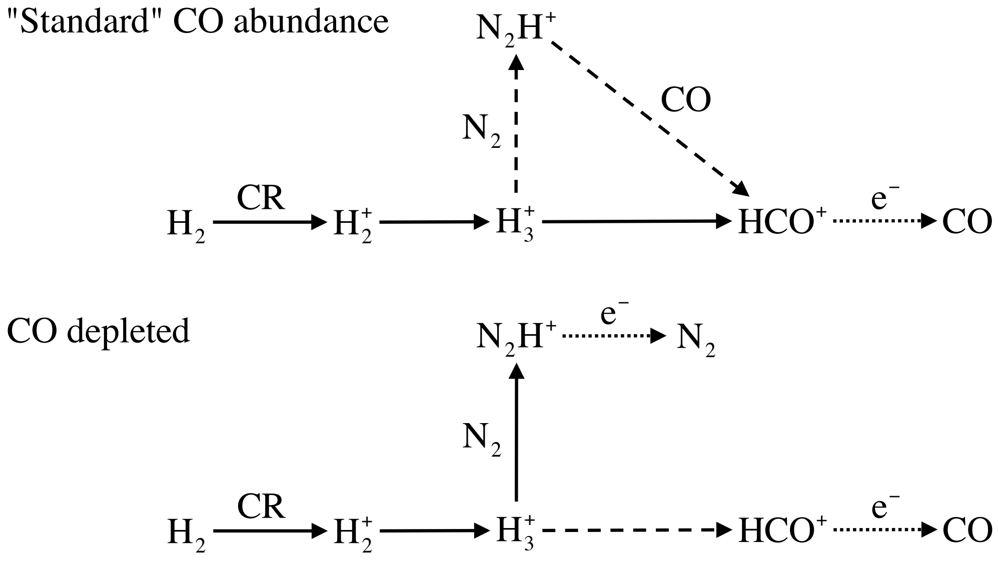

Figure 4.4 – Formation and destruction pathways of HCO$^+$ and N$_2$H$^+$ for a standard CO abundance (1×10^{-4}) and a low abundance (i.e. depletion). Main and secondary reactions are plotted respectively in full and dashed lines. Dissociative recombination are shown in dotted lines. Figure adapted from the Fig. 16 of Jørgensen et al. (2004).

gions of proto-planetary disks (Dutrey et al., 2011). A large number of gas-phase processes are included in the network: bimolecular reactions (between neutral species, between charged species and between neutral and charged species) and unimolecular reactions, i.e. photo-reactions with direct UV photons and UV photons produced by the de-excitation of H$_2$ excited by cosmic-ray particles (Pratap & Tarafdar mechanism), photo-desorption, and direct ionisation and dissociation by cosmic-ray particles. The interactions of the gas phase species with the interstellar grains are: sticking of neutral gas-phase species to the grain surfaces, evaporation of the species from the surfaces due to the temperature, the cosmic-ray heating and the exothermicity of the reactions at the surface of the grains (a.k.a chemical desorption). The species can diffuse and undergo reactions using the rate equation approximation at the surface of the grains (Hasegawa et al., 1992). Details on the processes included in the model can be found in Ruaud et al. (2016). Note that I have used Nautilus in its 2-phase model, meaning that there is no distinction between the surface and the bulk of the mantle of the grains. The gas-phase and grain surfaces reactions are based on the `kida.uva.2014` network[4] (see Wakelam et al., 2015) while the surface network is based on Garrod and Herbst (2006). The full network contains 736 species (488 in the gas-phase and 248 at the surface of the grains) and 10466 reactions (7552 pure gas-phase reactions and 2914 reactions of interactions with grains and reactions at the surface of the grains). For this study I adopted the initial atomic abundances (with respect to the total proton density $n_{\rm H}$) given in Hincelin et al. (2011) with an additional atomic abundance of $6.68{\times}10^{-9}$ for fluorine (Neufeld et al., 2005). The carbon and oxygen abundances are respectively $1.7{\times}10^{-4}$ and $3.3{\times}10^{-4}$ leading to a C/O ratio of $\sim$0.5.

The chemical reaction network of HCO$^+$ and N$_2$H$^+$ depends strongly on H$_3^+$ since their primary formation routes involve this ion (see Eq. 4.7 and 4.8). Indeed HCO$^+$ is formed essentially via:

$$\mathrm{H_3^+ + CO \longrightarrow HCO^+ + H_2}. \tag{4.7}$$

while its destruction is dominated by dissociative recombination:

$$\mathrm{HCO^+ + e^- \longrightarrow CO + H} \tag{4.8}$$

---

[4] `http://kida.obs.u-bordeaux1.fr/networks.html`

for a standard X(CO) = $n(\mathrm{CO})/n(\mathrm{H_2})$ abundance of 1×10^{-4} in the gas phase (all following abundances in this chapter are defined with respect to $n(\mathrm{H_2})$). When CO becomes depleted into the icy grain surfaces at temperatures lower than ~27 K, reaction (4.7) becomes less important and $\mathrm{H_3^+}$ will preferentially react with $\mathrm{N_2}$:

$$\mathrm{H_3^+ + N_2 \longrightarrow N_2H^+ + H_2}. \tag{4.9}$$

An important removal mechanism of $\mathrm{N_2H^+}$ when the CO abundance is $\sim 10^{-4}$ leads to the formation of $\mathrm{HCO^+}$:

$$\mathrm{N_2H^+ + CO \longrightarrow HCO^+ + N_2} \tag{4.10}$$

otherwise $\mathrm{N_2H^+}$ is destroyed by dissociative recombination:

$$\mathrm{N_2H^+ + e^- \longrightarrow N_2 + H}. \tag{4.11}$$

$\mathrm{H_3^+}$ is formed from $\mathrm{H_2}$ and strongly depends on the cosmic ray ionisation rate ζ:

$$\mathrm{H_2 + CR \longrightarrow H_2^+ + e^-}, \tag{4.12}$$

$$\mathrm{H_2^+ + H_2 \longrightarrow H_3^+ + H}. \tag{4.13}$$

In Sect. 4.3.3.1 I show the significance of the cosmic ray ionisation rate in the abundance profiles, thus in the contribution of the envelope to the $\mathrm{HCO^+}$ emission.

This chemical network, gathering CO, $\mathrm{HCO^+}$, and $\mathrm{N_2H^+}$ has been well described by Jørgensen et al. (2004, 2011) and is summarised in Fig. 4.4.

Proto-stellar envelopes are by nature dynamical objects and the time scale of collapse may change the chemical composition of the envelopes (see Aikawa et al., 2008; Wakelam et al., 2014). The $\mathrm{HCO^+}$ and $\mathrm{N_2H^+}$ emissions however seem to originate from the outer part of the envelope ($\gtrsim$1000 AU), where the physical conditions are evolving much more slowly. For this reason and in order to have more flexibility on the parameters to vary, I have used the static model derived by Crimier et al. (2010) to derive the $\mathrm{HCO^+}$ and $\mathrm{N_2H^+}$ abundances with Nautilus in the envelope rather than the dynamical structure of Aikawa et al. (2008). Moreover, as said above, the chemistry of both $\mathrm{HCO^+}$ and $\mathrm{N_2H^+}$ is mainly driven by the cosmic ray ionisation rate, which does not change with time.

4.3.2.2 The foreground cloud

IRAS16293 is embedded in the remnants of its parental cloud, forming a foreground layer in the line of sight. Recently, this cloud has been studied by Coutens et al. (2012) and Wakelam et al. (2014) to analyse the deuteration in the source, and Bottinelli et al. (2014) to investigate CH in absorption. Based on these studies, I have supposed this cloud to be cold ($\mathrm{T_{kin}} \sim 10 - 30\,\mathrm{K}$) and not very dense ($n_\mathrm{H} \sim 10^3 - 10^5\,\mathrm{cm^{-3}}$) with an A_V of 1−4, similar to the physical conditions found in diffuse or translucent clouds (Hartquist and Williams, 1998). For the low A_V (0.5 to 1.5) regime, the expected range of the $\mathrm{HCO^+}$ abundance is a few $10^{-10} - 10^{-8}$, depending on the temperature and on the degree of ionisation of the cloud.

Hartquist and Williams (1998) and Savage and Ziurys (2004) suggested in their studies that the chemistry of $\mathrm{HCO^+}$ in photon-dominated regions is dominated by the reaction described in Eq. (4.7) at high A_V ($\gtrsim 1.5$) where CO is self-shielded. In the low A_V (0.5 to 1.5) regime, the formation of $\mathrm{HCO^+}$ is still possible through the $\mathrm{CO^+}$ chemistry following:

$$\mathrm{C^+ + OH \longrightarrow CO^+ + H}, \tag{4.14}$$

$$\mathrm{C^+ + O_2 \longrightarrow CO^+ + O}. \tag{4.15}$$

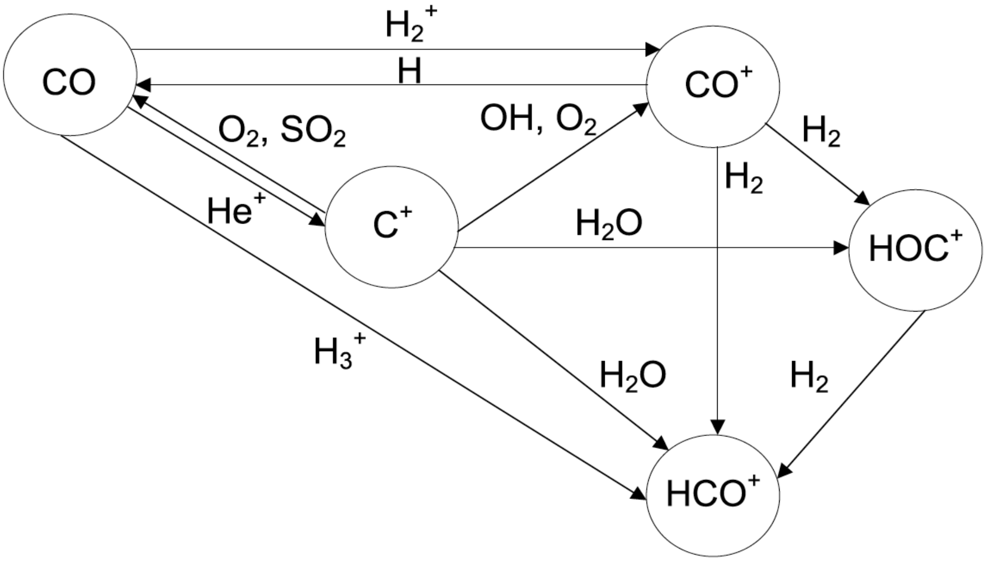

Figure 4.5 – Chemical network that may be involved in the formation of HCO$^+$ in diffuse or translucent clouds. Source: Fig. 8 of Savage and Ziurys (2004).

Then HCO$^+$ is formed by reaction with H_2O or H_2:

$$C^+ + H_2O \longrightarrow HCO^+ + H, \tag{4.16}$$

$$CO^+ + H_2 \longrightarrow HCO^+ + H. \tag{4.17}$$

These two different pathways explain that the HCO$^+$ abundance is relatively constant in diffuse or translucent clouds. A more complete description of the chemistry involved in such clouds is shown in Fig. 4.5. For the low A_V (0.5 to 1.5) regime, the expected range of the HCO$^+$ abundance is a few $10^{-10} - 10^{-8}$, depending on the temperature and the degree of ionisation of the cloud (Hartquist and Williams, 1998; Savage and Ziurys, 2004).

Regarding N_2H^+, it is not expected to be present in such a cloud since dense regions are needed to transform the nitrogen in N_2, required to form N_2H^+ (Hartquist and Williams, 1998).

4.3.2.3 The outflow model

In the case of HCO$^+$, the observed line shapes and intensities cannot be explained only with the contribution of the envelope of the source, particularly for high upper energy level transitions (e.g. $J_{up}>9$). Rawlings et al. (2000) and Rollins et al. (2014) have shown that young outflows can lead to an enhancement of the HCO$^+$ abundance in a short period of time. Briefly, the interaction between the jet and/or the outflowing material and the surrounding quiescent (or infalling) gas is eroding the icy mantle of dust grains, desorbing the molecular materials in the gas phase (e.g. H_2O, CO, H_2CO, CH_3OH). Thanks to the photo-chemical processing induced by the shock-generated radiation field, this sudden enrichment of the gas-phase molecular abundances leads to the formation of many other molecules, such as HCO$^+$. HCO$^+$ will be then destroyed by dissociative recombination or by interaction with water (Doty et al., 2002). Thus, a high HCO$^+$ abundance is not expected in old outflows but rather in young ones ($<$ few hundred years old, Rawlings et al. (2000)) such as the NW-SE outflow detected in IRAS16293.

This young NW-SE outflow ($\sim 400\,$yr) has been traced with H^{13}CO$^+$, SiO, and CO emission (Rao et al., 2009; Girart et al., 2014) using the SMA interferometer. According to Rao et al. (2009), the H^{13}CO$^+$ emission would arise from rotating material around IRAS16293 A rather than the outflow. The direction of this rotating material is roughly the same as the NW-SE outflow,

Table 4.9 – Physical properties of the outflow taken from Rao et al. (2009) and Girart et al. (2014)

Physical properties	Value
$n(\mathrm{H_2})$	$\sim 1 \times 10^7\,\mathrm{cm^{-3}}$
$\mathrm{T_{kin}}$	$\sim 400\,\mathrm{K}$
$\mathrm{V_{outflow}}$	$15\,\mathrm{km\,s^{-1}}$
Outflow extent	$8''$
P.A.	$145°$
Inclination^{5}1	$44°$
Age	$\sim 400\,\mathrm{yr}$
Outflow cavity	No

therefore it is more probable that the $\mathrm{H^{13}CO^+}$ emission they observed is coming from it and is due to the recent enhancement of its abundance. I have included this outflow in the 3D model together with the envelope.

I have considered a hourglass-like geometry for the outflow, as used by Rawlings et al. (2004) in their study of $\mathrm{HCO^+}$. This model is based on the mathematical definition given in Visser et al. (2012) implemented in GASS (see Sect. 2.3.3 for more details on the outflow modelling). Rao et al. (2009) and Girart et al. (2014), using SMA interferometric observations, derived the maximum extent of this outflow ($8''$), its inclination ($44°$), dynamical age ($\sim 400\,\mathrm{yr}$), position angle ($145°$), and velocity ($\mathrm{V_{outflow}} = 15\,\mathrm{km\,s^{-1}}$). Density and temperature are not really well constrained but, based on their SiO (8−7) emission, Rao et al. (2009) suggested that this outflow is dense ($n(\mathrm{H_2}) \sim 1 \times 10^7\,\mathrm{cm^{-3}}$) and hot ($\mathrm{T_{kin}} \sim 400\,\mathrm{K}$). I aim at giving better constraints on the latter two outflow physical properties using all the $\mathrm{HCO^+}$ observations, thus I choose to only vary the gas temperature, the $\mathrm{H_2}$ density, as well as the $\mathrm{HCO^+}$ abundance, all three considered to be constant as a function of the radius.

This outflow is quite young, collimated, and its low velocity suggests that the surrounding envelope is being pushed by the outflowing material. This kind of outflow-envelope interaction has already been observed and studied by Arce and Sargent (2005, 2006) for similar objects. Such interaction between the outflow and the envelope implies that there is no outflow cavity, as suggested by the interferometric observations, so I did not set it in the models.

Table 4.9 summarises the physical parameters of the outflow taken into account in the modelling while Fig. 4.6 shows a sketch of the outflow orientation and position with respect to sources A and B.

The $\mathrm{HCO^+}$ enhancement in the young NW-SE outflow may be explained by the following chemical network, initiated by the sublimation of mantle ices from the solid (s.) to the gas (g.) phase (Rawlings et al., 2000; Viti et al., 2002):

$$\mathrm{CO_{(s.)}} \longrightarrow \mathrm{CO_{(g.)}}, \tag{4.18}$$

$$\mathrm{H_2O_{(s.)}} \longrightarrow \mathrm{H_2O_{(g.)}}. \tag{4.19}$$

The shock-driven radiation field will photo-dissociate the desorbed CO and photo-ionise the newly produced C:

$$\mathrm{CO} + \mathrm{h}\nu \longrightarrow \mathrm{C} + \mathrm{O}, \tag{4.20}$$

$$\mathrm{C} + \mathrm{h}\nu \longrightarrow \mathrm{C^+} + \mathrm{e^-}. \tag{4.21}$$

$\mathrm{HCO^+}$ is then formed by:

$$\mathrm{C^+} + \mathrm{H_2O} \longrightarrow \mathrm{HCO^+} + \mathrm{H}. \tag{4.22}$$

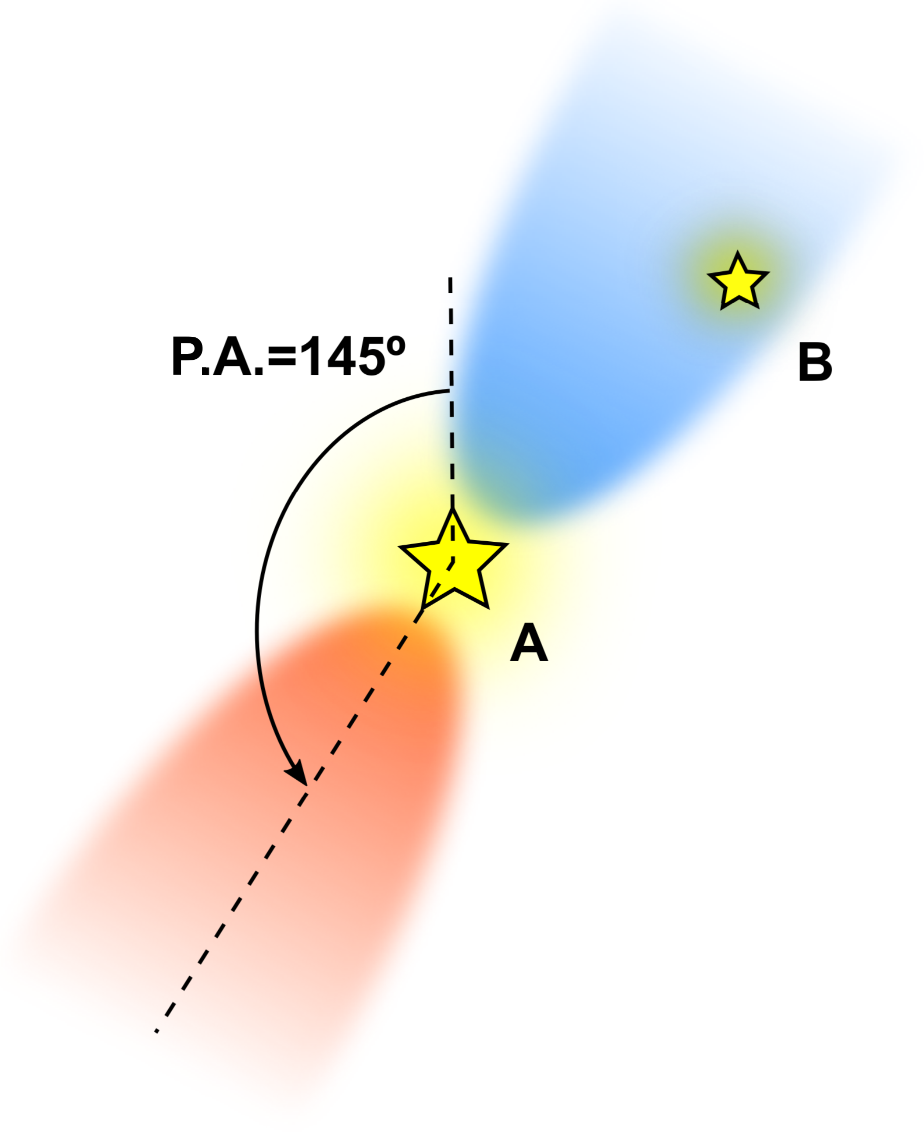

Figure 4.6 – Sketch of the blueshifted (in blue) and redshifted (in red) NW-SE outflow emission. Both sources A and B (separated by 5″) are drawn but only source A is considered in the modelling.

This chemical network is limited by the amount of CO (thus C^+) and H_2O liberated from the dust grains, therefore it can only occur for a certain period of time. Moreover, H_2O can also be photo-dissociated, limiting the formation of HCO^+. The main destruction route of HCO^+ is recombination (see reaction (4.8)) but if the water abundance becomes too high, the following reaction becomes competitive (Doty et al., 2002):

$$\mathrm{HCO^+ + H_2O \longrightarrow H_3O^+ + CO.} \tag{4.23}$$

Other possible formation and destruction routes have been explored by Rollins et al. (2014).

Concerning N_2H^+, it is not expected to be produced in the outflow, thus the latter is not expected to play a role in the emission of this molecule. By setting the abundance of N_2H^+ and its isotopologues to a very low value (1×10^{-15}) in the outflow model, I have verified that no emission is coming from the outflow for this species.

4.3.2.4 Fractionation

This study takes into account N_2H^+, N_2D^+, and numerous isotopologues of HCO^+: $H^{13}CO^+$, $HC^{18}O^+$, DCO^+, and $D^{13}CO^+$. At low temperature, a significant enhancement of these different isotopologues can occur, initiated by various isotope exchange reactions. For instance, ^{13}C can be incorporated preferentially in various molecules through exchange reactions such as (Watson et al., 1976; Smith and Adams, 1980):

$$^{13}C^+ + {}^{12}CO \longrightarrow {}^{12}C^+ + {}^{13}CO + \Delta E, \tag{4.24}$$

with $\Delta E/k = 35\,K$. This isotope exchange reaction is also possible directly with HCO^+ leading to a lower exothermicity (Smith and Adams, 1980):

$$^{13}C^+ + H^{12}CO \longrightarrow {}^{12}C^+ + H^{13}CO + \Delta E, \tag{4.25}$$

with $\Delta E/k = 17\,K$. Multiple other isotope reactions implying $C^{18}O$ lead to the formation of $HC^{18}O^+$. These reactions have been well studied recently by Mladenović and Roueff (2014) who accurately revisited the $^{12}C/^{13}C$ and $^{16}O/^{18}O$ balance. They updated many exothermicity and rate coefficients, taken from recent laboratory measurements.

I am also interested in the deuteration (fractionation of deuterium) that drives the abundance of N_2D^+, DCO^+, and $D^{13}CO^+$, starting by the following reactions (Dalgarno and Lepp, 1984):

$$H_3^+ + HD \longrightarrow H_2D^+ + H_2 + \Delta E, \tag{4.26}$$

with $\Delta E/k = 227\,K$. The newly produced H_2D^+ will then react with CO or N_2:

$$H_2D^+ + CO \longrightarrow DCO^+ + H_2. \tag{4.27}$$

$$H_2D^+ + N_2 \longrightarrow N_2D^+ + H_2. \tag{4.28}$$

The above reactions are the preferred formation routes of DCO^+ and N_2D^+ but not the only ones. At low temperature ($T < 30\,K$) and low densities ($n(H_2) < 10^5\,cm^{-3}$), DCO^+ is enhanced by the following reaction (Dalgarno and Lepp, 1984; Roberts and Millar, 2000):

$$D + HCO^+ \longrightarrow DCO^+ + H, \tag{4.29}$$

increasing rapidly the fractionation of DCO^+. The study of Mladenović and Roueff (2014) also includes the fractionation of DCO^+ and they have shown that considering the higher exothermicity of deuterated isotopologues reactions, the isotopic ^{13}C ratio is lower than the hydrogenic counterpart. Thus, I expect a $D^{12}CO^+/D^{13}CO^+$ ratio lower than the $H^{12}CO^+/H^{13}CO^+$ ratio in the external part of the envelope or in the foreground cloud.

4.3.3 Results and discussions

The analysis process is very complex due to the large number of parameters (11), the size of the data (a few gigabytes for only one modelling) and hence the memory needed to work with several modellings at the same time. As an example, to vary 3 parameters with an excursion of only 3 values for each, it requires 27 different models. For HCO^+, each model contains 31 files (one file for each of the 31 detected transitions), weighting a total of 1.2 GB (38 MB per file). The 27 different models weigh 32.4 GB. Therefore it is really complicated to vary several parameters at the same time, with a large range of different values. Thus, the standard χ^2 minimisation approach is not conceivable here. As a matter of fact, I decided to use a pragmatic approach and so to vary the different parameters of the envelope, foreground cloud, and outflow separately. Doing this, more than 5 000 models have been calculated. One of the strengths of this study resides in the use of the data from the unbiased spectral surveys TIMASSS and CHESS (Sect. 4.2), which provides us with a large number of transitions, spanning a wide range of upper energy levels ($4 - 389\,\mathrm{K}$). This allowed us to constrain each structure with a specific set of transitions. For instance, the HCO^+ low $J = 1 \rightarrow 0$ transition ($E_{\mathrm{up}} = 4\,\mathrm{K}$) strongly constrains the absorption feature created by the cold foreground cloud. The $J_{\mathrm{up}} \gtrsim 8$ transitions ($E_{\mathrm{up}} \gtrsim 154\,\mathrm{K}$) of the same molecule strongly constrain the outflow parameters, but very poorly the envelope since the latter is not contributing much to the total emission of these lines. The N_2H^+ emission only results from the contribution of the envelope, thus this species gives better constraints of this region. I would also like to point out that this study has been performed by considering all the transitions of a species (HCO^+ or N_2H^+) **at the same time**.

For the foreground cloud and the outflow, I only varied three different parameters and the pragmatic approach used is the following one:

1. Based on the results of previous studies, I first define for each parameter of the structure a range of value I test. The goal of this first step is to roughly constrain the different parameters and to get a finer grid of tested value. For each parameter, I define between 5 and 7 values for a total of about 300 models per structure, generated with GASS (representing a total of 360 GB of data). The range of parameters is shown in Table 4.10.

2. Once the output fits files are produced by LIME, I calculate the integrated flux of each predicted line and compare it with the integrated flux of the observed line (given in Sect. 4.2). For a given model, if the difference between observed and modelled flux is above 30% for at least one line, then this model is discarded. Note that I initially made this comparison by setting a limit of 20%, but this value was too restrictive and not enough models were kept to be able to perform the next step.

3. The selected models are used to define new, reduced, ranges for all parameters. I still define 5-7 values in each new range, so that this finer grid has the same size as the large one, *i.e.* about 300 models, generated with GASS. With this method I obtain a reliable range of constraints for each physical parameter I choose to vary. These constraints are shown in Table 4.10.

4. I calculate again the difference in percent of all the predicted lines fluxes compared to the observations and I plot this difference as contour plots with contours at 5%, 10%, 20%, and 30%. The best fit model is also determined here and its parameters are presented in Table 4.10.

For the envelope, varying 5 different parameters at the same time is not feasible for the reason evoked above, so this time, the approach is the following: I varied the parameters one by one, fixing the other four to a constant value. This value is taken in the middle of the tested range (see Table 4.10) to start with. Doing this for all parameters provides me with a pseudo "best fit" value for each parameter. I then repeat the process, setting the constant value equal to the pseudo "best fit" value found in the previous iteration. When convergence is reached, I then perform the same calculation as in item 2 above to derive the constraints shown it Table 4.10. Doing so, I also managed to obtain the best model presented in the same table. Note that the contribution of the envelope to the line emission is not sufficient to derive good constraints on the chemical and physical parameters used to predict the HCO^+ abundance profile.

Figure 4.7 shows a comparison between the observations and the best fit model for all the studied transitions of HCO^+. The particular case of N_2H^+ is discussed in Sect. 4.3.3.5.

Table 4.10 – Range of physical properties varied in this study. *Top panel:* Parameters of the envelope. *Middle panel:* Parameters of the foreground cloud. *Bottom panel:* Parameters of the outflow.

Physical properties	Tested range	Best fit value	Constraints
Age of the parental cloud	$10^5 - 10^6$ yr	1×10^5 yr	$\leqslant 3 \times 10^5$ yr
$n(H_2)_{\mathrm{init,envelope}}$	$1 \times 10^4 - 3 \times 10^5\,\mathrm{cm^{-3}}$	$3 \times 10^4\,\mathrm{cm^{-3}}$	$\leqslant 1 \times 10^5\,\mathrm{cm^{-3}}$
$T_{\mathrm{init,\ envelope}}$	$5 - 15\,\mathrm{K}$	$10\,\mathrm{K}$	None
$\zeta_{\mathrm{envelope}}$	$1 \times 10^{-17} - 1 \times 10^{-16}\,\mathrm{s^{-1}}$	$1 \times 10^{-16}\,\mathrm{s^{-1}}$	$\geqslant 5 \times 10^{-17}\,\mathrm{s^{-1}}$
Age of the proto-star	up to 10^5 yr	4×10^4 yr	$\geqslant 2 \times 10^4$ yr
$n(H_2)_{\mathrm{foreground}}$	$5 \times 10^2 - 3 \times 10^5\,\mathrm{cm^{-3}}$	$2 \times 10^3\,\mathrm{cm^{-3}}$	$5 \times 10^2 - 1 \times 10^4\,\mathrm{cm^{-3}}$
$T_{\mathrm{kin,\ foreground}}$	$10 - 30\,\mathrm{K}$	$20\,\mathrm{K}$	$10 - 30\,\mathrm{K}$
$X(HCO^+)_{\mathrm{foreground}}$	$5 \times 10^{-11} - 1 \times 10^{-6}$	1×10^{-8}	$1 \times 10^{-9} - 1 \times 10^{-7}$
$n(H_2)_{\mathrm{outflow}}$	$1 \times 10^6 - 1 \times 10^8\,\mathrm{cm^{-3}}$	$5.5 \times 10^6\,\mathrm{cm^{-3}}$	$(4 - 7) \times 10^6\,\mathrm{cm^{-3}}$
$T_{\mathrm{kin,\ outflow}}$	$100 - 500\,\mathrm{K}$	$200\,\mathrm{K}$	$180 - 220\,\mathrm{K}$
$X(HCO^+)_{\mathrm{outflow}}$	$1 \times 10^{-10} - 1 \times 10^{-7}$	4×10^{-9}	$(3 - 5) \times 10^{-9}$

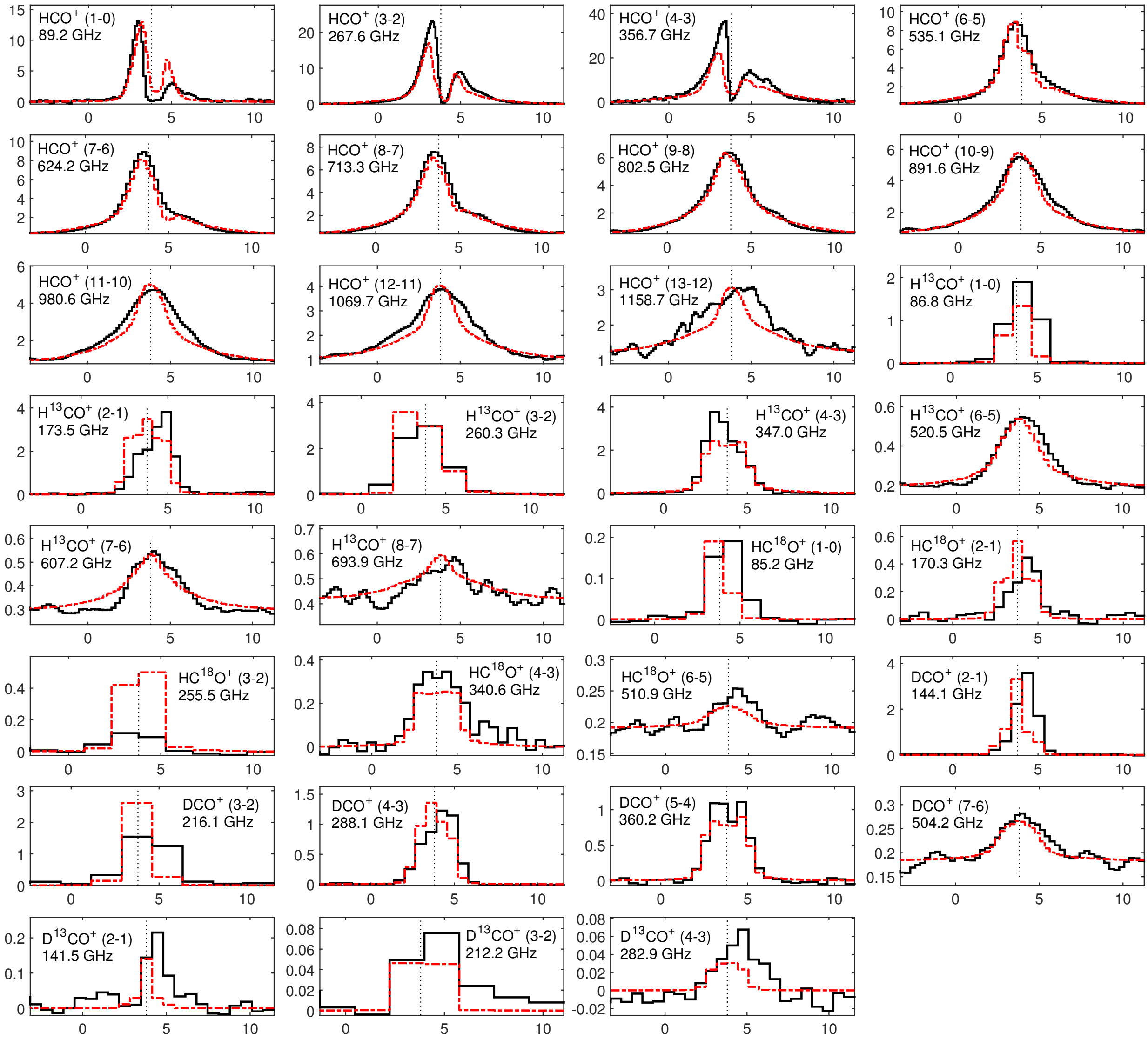

Figure 4.7 – Main beam temperature (in K) of HCO^+, $H^{13}CO^+$, $HC^{18}O^+$, DCO^+, $D^{13}CO^+$, N_2H^+, and N_2D^+ observed transitions (in black) compared to the best fit model (in red) as a function of the velocity (in $\mathrm{km\,s^{-1}}$). The continuum is shown for all transitions. The vertical black dotted line shows the supposed $V_{\mathrm{LSR}} = 3.8\,\mathrm{km\,s^{-1}}$ of IRAS16293.

The contribution of the envelope and the outflow to the total emission of the HCO$^+$ (8–7) transition is shown in Fig. 4.8, considering the physical parameters of the best fit model. From this figure, it is clear that the contribution of the envelope (in green) to the total emission of HCO$^+$ transitions is rather small (especially for high-J transitions). The outflow contribution (in red) clearly dominates the total emission (shown in blue).

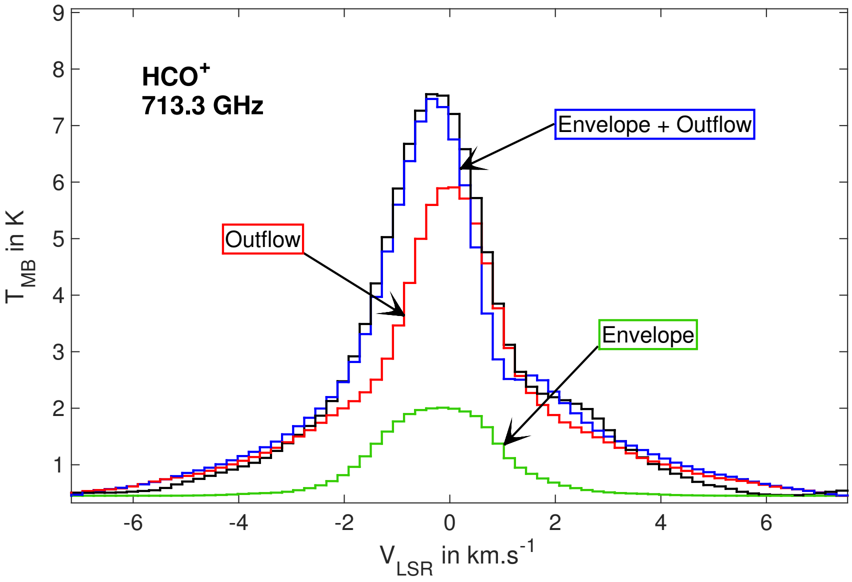

Figure 4.8 – Line profile of the HCO$^+$ (8–7) transition for the best fit parameters of the envelope (in green) and the outflow (in red) structure and for the envelope + outflow together (in blue). The observed line profile is plotted in black. The continuum is shown for this transition.

4.3.3.1 Chemistry of the envelope

For the envelope, the impact of the chemical modelling input parameters on the radial abundance profile of HCO$^+$ was studied. Five different parameters have been separately varied (age, temperature, and density of the parental cloud, cosmic ray ionisation rate, and age of the proto-star) to discriminate their respective effect on the abundance profile and to obtain the best model compared to the observations.

The chemical modelling of the envelope initially starts by considering a static 0D parental cloud extended up to $r = 4 \times 10^4$ AU with an initial gas temperature $T_{\rm kin} = 10\,$K and a high visual extinction to prevent any photo-dissociation to occur.

The next step of the chemical modelling consists in taking the resulting abundances obtained after the parental cloud stage as an input for the static modelling. The 1D physical structure of the envelope is now considered and the abundance as a function of the radius is obtained for different ages of the proto-star, up to 1×10^5 yr. The cosmic ray ionisation rate ζ is supposed to be the same as the one used for the parental cloud step. The visual extinction in the envelope is a function of the atomic hydrogen column density $N_{\rm H}$ (Bohlin et al., 1978; Frerking et al., 1982):

$$A_V = \frac{N_{\rm H}}{1.88 \times 10^{21}\,{\rm cm}^{-2}}. \tag{4.30}$$

To take into account the additional extinction from the foreground cloud in which we assume that the object is embedded, the A_V has been increased by 1.2 (see last paragraph of Sect. 4.3.3.2).

Fig. 4.9 shows the effect of the variation of these chemical parameters on the radial abundance profile of HCO$^+$ and Fig. 4.10 the resulting line profile of the HCO$^+$ (8–7) transition. Among all

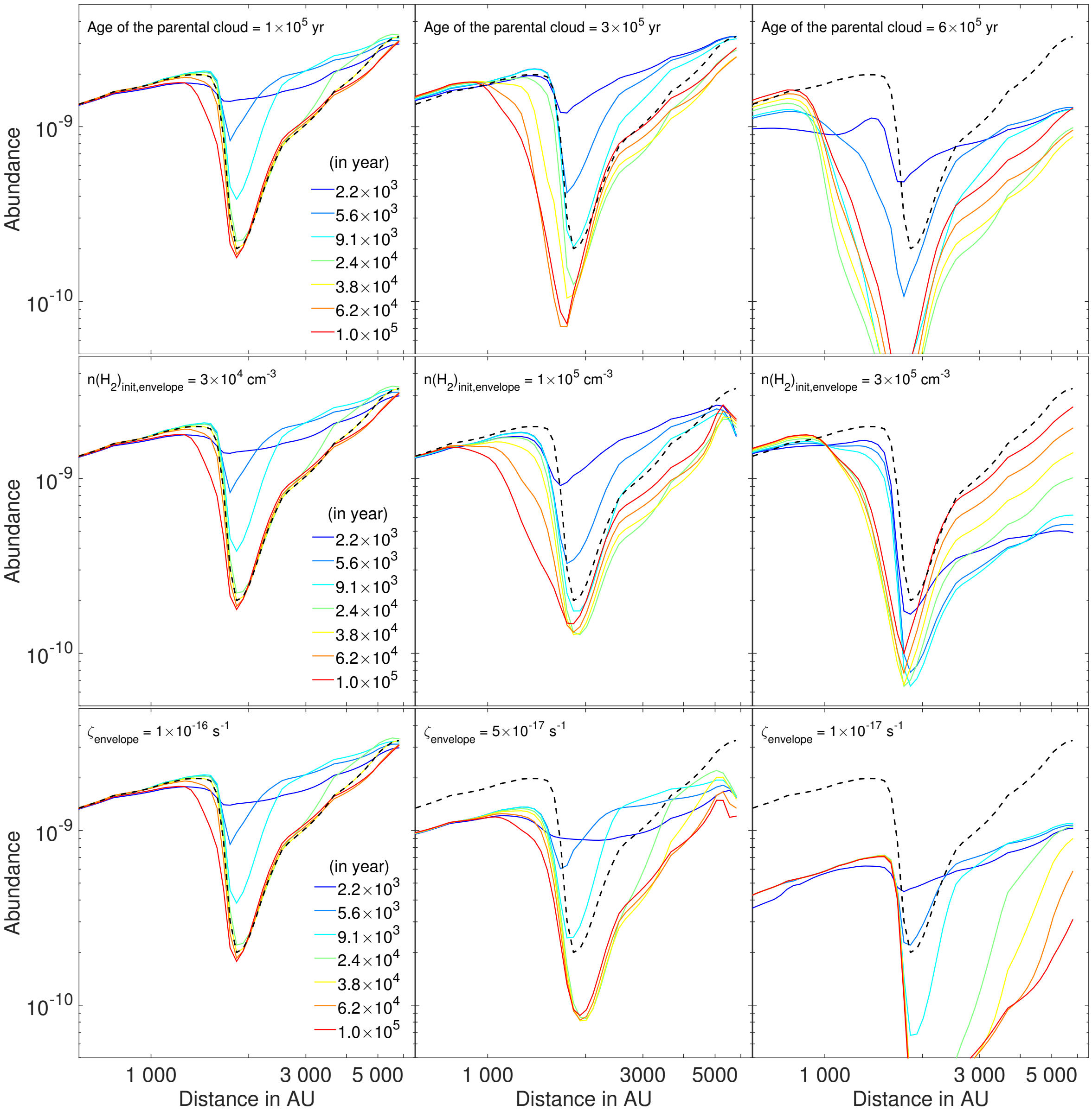

Figure 4.9 – Variation of the abundance profile of HCO^+ determined by Nautilus as a function of the radius for different ages of the proto-star and different set of input chemical parameters. The best fit (age of the parental cloud = 1×10^5 yr, $n(H_2) = 3 \times 10^4\,cm^{-3}$, cosmic ray ionisation rate = $1\times10^{-16}\,s^{-1}$, and age of the proto-star = 3.8×10^4 yr) is shown in black dashed lines. While varying one of the following parameters, the others are set to the best fit value. *Top panels:* Variation of the age of the parental cloud (from left to right): 1×10^5, 3×10^5, and 6×10^5 yr. *Middle panels:* Variation of the initial H_2 density in the parental cloud (from left to right): 3×10^4, 1×10^5, and $3 \times 10^5\,cm^{-3}$. *Bottom panels:* Variation of the cosmic ray ionisation rate (from left to right): 1×10^{-16}, 5×10^{-17}, and $1 \times 10^{-17}\,s^{-1}$.

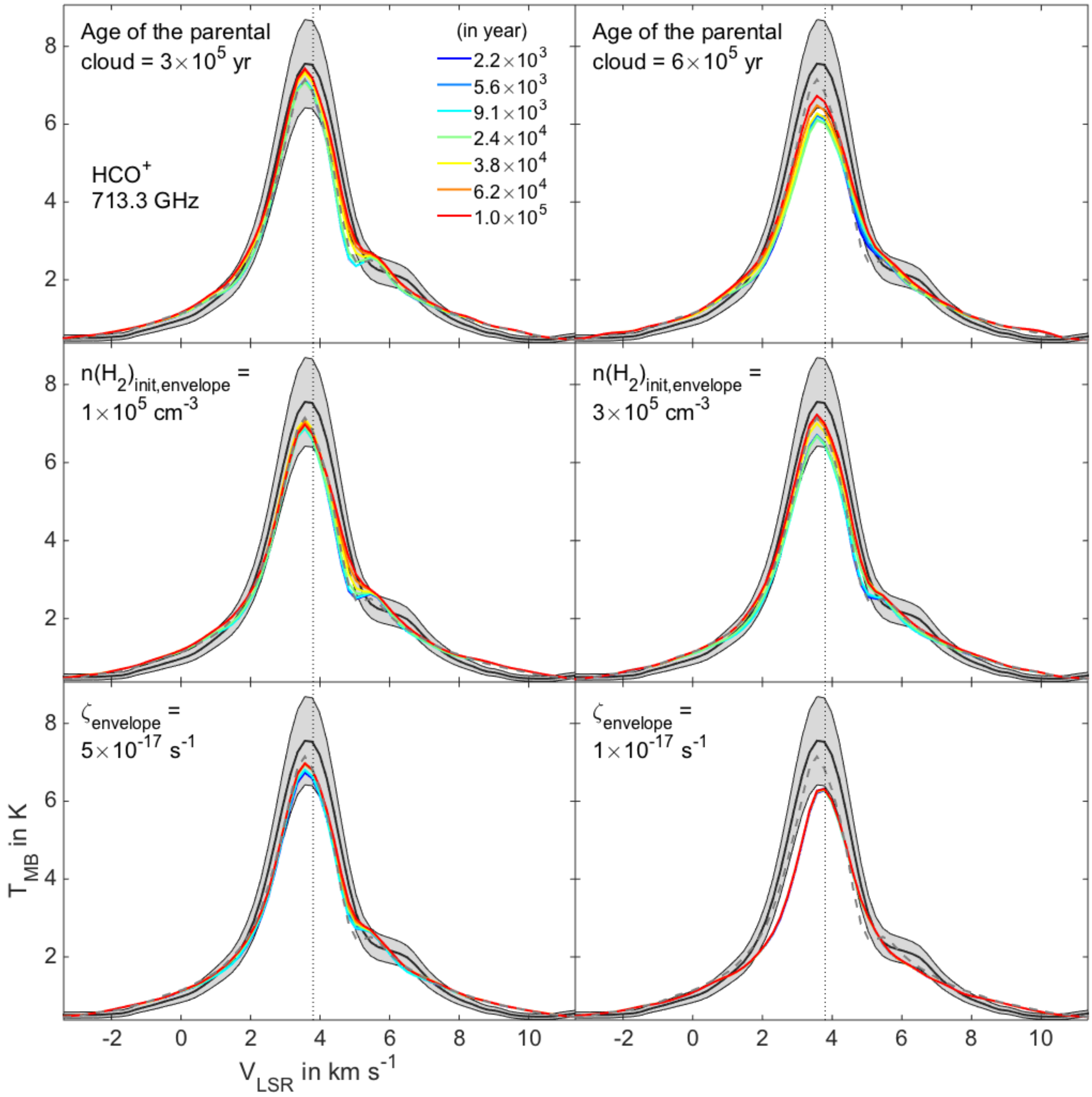

Figure 4.10 – Line profiles of the HCO$^+$ (8–7) transition (for the sake of clarity, only this relevant transition is shown) for different abundance profiles determined by Nautilus for different ages of the proto-star and different set of input chemical parameters (shown in middle and right panels of Fig. 4.9). The best fit model (age of the parental cloud = 1×10^5 yr, $n(H_2) = 3 \times 10^4$ cm^{-3}, cosmic ray ionisation rate = $1{\times}10^{-16}$ s^{-1}, and age of the proto-star = 3.8×10^4 yr) is shown in grey dashed lines. While varying one of the following parameters, the others are set to the best fit value. *Top panels:* Variation of the age of the parental cloud (from left to right): 3×10^5, and 6×10^5 yr. *Middle panels:* Variation of the initial H$_2$ density in the parental cloud (from left to right): 1×10^5, and 3×10^5 cm^{-3}. *Bottom panels:* Variation of the cosmic ray ionisation rate (from left to right): 5×10^{-17}, and 1×10^{-17} s^{-1}. The grey area shows the 20% percent error area with respect to the observation (black solid line). The vertical black dotted line shows the supposed V$_{LSR}$ = 3.8 km s^{-1} of IRAS16293.

the HCO^+ transitions, the latter is the most sensitive to the variation of the envelope abundance profile.

Even if the constraints displayed in Table 4.10 have been obtained using all the HCO^+ transitions, the effect of the HCO^+ abundance profile on line profiles is noticeable using this transition in particular.

Age of the parental cloud. It is well constrained to be $\leqslant 3\times10^5$ yr since for older ages the amount of HCO^+ drops drastically (see top panels of Fig. 4.9) therefore the predicted HCO^+ emission is weaker by more than 20% compared to the observations (see top panels of Fig. 4.10).

H_2 density of the parental cloud. It is poorly constrained but one can note that a higher value of the H_2 density leads to a lower abundance in the external part of the envelope (see middle panels of Fig. 4.9). Less abundance in this part of the envelope reduces the self-absorption of the low upper energy transitions ($J_{up} < 4$) therefore it affects their line profiles. If the density is not too high ($\leqslant 1 \times 10^5\,cm^{-3}$), the HCO^+ abundance does not seem to vary a lot (less than $\sim 10\%$ at 2000 AU) and resulting models giving an integrated flux under a difference of 20% can be found among the different proto-star ages (see middle panels of Fig. 4.10).

Kinetic temperature of the parental cloud. A variation of T_{kin} does not change significantly the resulting abundance so it was arbitrarily fixed to 10 K, according to constraints given by previous studies (Bottinelli et al., 2014; Wakelam et al., 2014, e.g.).

Cosmic ray ionisation rate. The ionisation rate is strongly constrained by the chemical modelling since it affects the amount of H_3^+. A lower cosmic ray ionisation rate reduces the amount of HCO^+ (see bottom panels of Fig. 4.9) produced throughout the source as well as the intensity of the line profiles (see bottom panels of Fig. 4.10). A rate larger than $\sim 5 \times 10^{-17}\,s^{-1}$ is necessary, otherwise intensities of the modelled lines are too small by a factor of 20%. The rate is higher than the standard value of $1.3\times10^{-17}\,s^{-1}$ found in the solar neighbourhood but the ρ Ophiuchus cloud complex is known for its high cosmic ray rate (Hunter et al., 1994). This value is also consistent with previous studies reported for IRAS16293 (e.g. Doty et al., 2004 and Bottinelli et al., 2014).

Age of the proto-star. I have noted that more models are compatible with the observations for higher proto-star ages than lower ones, constrained by the drop of $X(HCO^+)$ arising at a radius of $\sim$ 2000 AU for old ages that leads to weaker self-absorption of high-J lines. One can note that the chemistry does not evolve much after $\sim 2 \times 10^4$ yr, limiting the constraints I can give on the age of the source.

The contribution of the envelope to the emission of HCO^+ clearly does not dominate (see Fig. 4.8), therefore it is difficult to constrain some of the chemical input parameters, such as the density and temperature of the parental cloud and the age of the proto-star. Nonetheless, some of them, such as the cosmic ray ionisation rate or the age of the parental cloud, have an important impact on the abundance profile of HCO^+, thus on the resulting line profile, and it is possible to constrain their value. For the density and temperature of the parental cloud as well as the age of the proto-star, no conclusion can be made because their effects are poorly constrained by the observations.

The best model gives a parental cloud evolving for 1×10^5 yr with an initial gas density $n(H_2) = 3\times10^4\,cm^{-3}$, and a cosmic ray ionisation rate of $1\times10^{-16}\,s^{-1}$ with the age of the proto-star estimated to be 3.8×10^4 yr.

4.3.3.2 Physical parameters of the foreground cloud

Fig. 4.11 shows, for the emission of the HCO^+ $(1-0)$ transition, different radiative transfer modellings within the foreground cloud parameters constraints. One can note that the emission is clearly sensitive to the foreground cloud density and abundance, even for the short range of tested values. The temperature, density, and abundance of the foreground cloud are not independent therefore not all possible sets of parameters of the given range of parameter constraints lead to an acceptable model. For instance, for a high H_2 density, a low HCO^+ abundance is needed to correctly reproduce the observations and vice versa. In Fig. 4.11, the reference model (in red) is the foreground cloud best fit parameters (see Table 4.10) and for each panel I vary one of the parameters only and I fix the other two to the best fit value. These figures are not fully representative of the parameter space of acceptable models but they demonstrate the influence of each parameter on the resulting line emission.

Fig. 4.12 presents the contour plot of the difference (in percent) of all the predicted lines fluxes, compared to the observations, for the foreground cloud H_2 density as a function of the HCO^+ abundance. All the parameters of these models are taken within the range of the constraints values. One can note that there is an anti-correlation density-abundance, clearly marked by the 5% and 10% contours. I did not explore density lower than $5 \times 10^2\,\mathrm{cm^{-3}}$, in agreement with constraints given by previous studies (see Sect. 4.3.2.2), explaining why contours are not closed for lower densities.

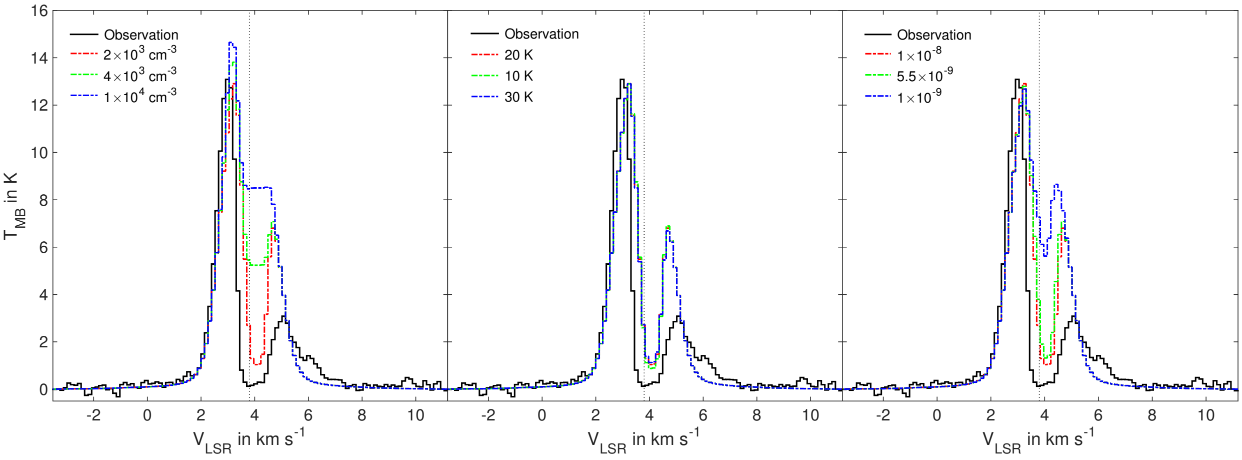

Figure 4.11 – Main beam temperature of the observed HCO^+ $(1-0)$ transition (black line) as a function of the velocity (for the sake of clarity, only this relevant transition is shown). The vertical black dotted line shows the supposed $V_{LSR} = 3.8\,\mathrm{km\,s^{-1}}$ of IRAS16293. The reference model (in red) is the best fit with $n(H_2)_{\mathrm{foreground}} = 2 \times 10^3\,\mathrm{cm^{-3}}$, $T_{\mathrm{kin,\,foreground}} = 20\,\mathrm{K}$, and $X(HCO^+)_{\mathrm{foreground}} = 1 \times 10^{-8}$. While varying one of the following parameters, the others are set to the best fit value. *Left panel:* Variation of the H_2 density of the foreground cloud. *Middle panel:* Variation of the kinetic temperature of the foreground cloud. *Right panel:* Variation of the HCO^+ abundance of the parental cloud.

H_2 density of the foreground cloud. I have tried several densities ranging from $\sim 1 \times 10^3$ to $\sim 1 \times 10^5\,\mathrm{cm^{-3}}$ as suggested by Coutens et al. (2012) for this region combined to several kinetic temperature and molecular abundances. The density I derive ($n(H_2)_{\mathrm{foreground}} = 2 \times 10^3\,\mathrm{cm^{-3}}$) is lower than the one used by Bottinelli et al. (2014) for CH and Wakelam et al. (2014) for the deuteration ($n(H_2)_{\mathrm{foreground}} = 1 \times 10^4\,\mathrm{cm^{-3}}$) but these authors only tested two different densities ($n(H_2)_{\mathrm{foreground}} = 1 \times 10^4$ and $1 \times 10^5\,\mathrm{cm^{-3}}$). I have found that for a density higher than $n(H_2)_{\mathrm{foreground}} = 1 \times 10^4\,\mathrm{cm^{-3}}$, the HCO^+ $J = 1 \rightarrow 0$ transition is not self-absorbed enough (absorption depth higher by a factor of 20% compared to the observations). This strongly constrains the density of the foreground cloud and its visual extinction.

Kinetic temperature of the foreground cloud. The line profiles do not change significantly (less than 5% compared to one another) in the range of tested values ($10-30\,\mathrm{K}$). I therefore arbitrarily set the best model value to 20 K, and I cannot give better constraints than the result obtained by

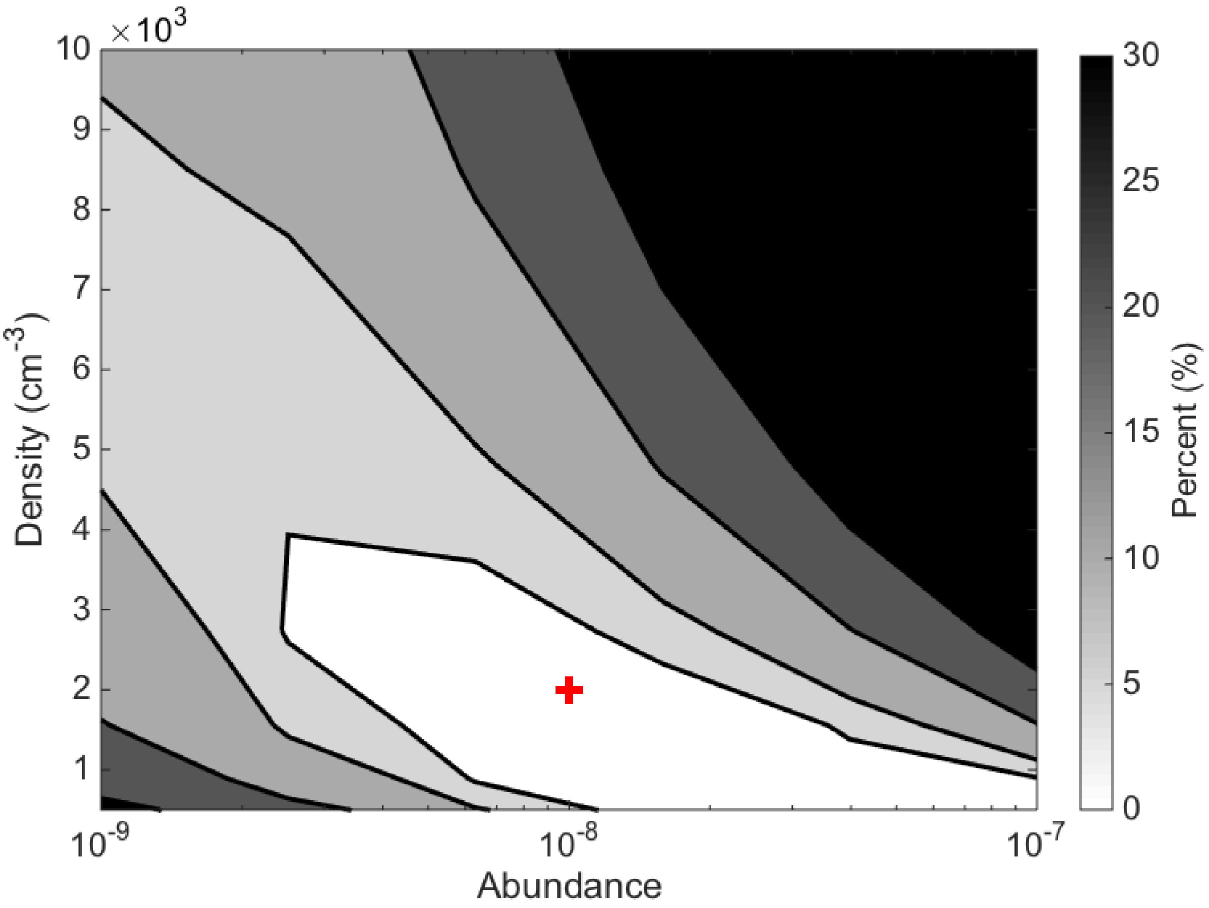

Figure 4.12 – Contour plot of the difference (in percent) of all the predicted lines fluxes compared to the observations for the foreground cloud H_2 density as a function of the HCO^+ abundance. Contours at 5%, 10%, 20%, and 30% are shown. The best fit model is the red cross.

Bottinelli et al. (2014) for CH and Wakelam et al. (2014) for the deuteration where they needed the temperature to be lower than 30 K in order to reproduce their observations.

Abundance of the foreground cloud. The HCO^+ abundance of 1×10^{-8} (with respect to H_2) I get is consistent with the results predicted by Hartquist and Williams (1998) and Savage and Ziurys (2004) at low A_V for diffuse or translucent clouds. An anti-correlation between the H_2 density and the HCO^+ abundance occurs, as seen in Fig. 4.12. This effect limits the constraints I can give on the HCO^+ abundance.

I have found a best model for the foreground cloud with $n(H_2)_{\rm foreground} = 2 \times 10^3\,{\rm cm}^{-3}$, $T_{\rm kin,\,foreground} = 20\,K$, and $X(HCO^+)_{\rm foreground} = 1 \times 10^{-8}$. Using Eq. (4.30), I derive $A_V \simeq 1.2$ for a supposed foreground cloud size of 30 000 AU. The production of HCO^+ is possible in this regime where CO is not self-shielded, as shown in Sect. 4.3.2.2.

4.3.3.3 Physical parameters of the outflow

Fig. 4.13 shows, for the emission of the HCO^+ $(10-9)$ transition, different radiative transfer modellings for values within the outflow parameters constraints (see right column of Table 4.10). As for the foreground cloud, one can note that the emission is clearly sensitive to the outflow density and abundance, even for the short range of tested values. Comments made in the first paragraph of the previous section (§4.3.3.2) also apply to the Fig. 4.13 in which the reference model (in green) is the outflow best fit parameters.

Fig. 4.14 presents the contour plot of the difference (in percent) of all the predicted lines fluxes, compared to the observations, for the outflow H_2 density as a function of the HCO^+ abundance. All the parameters of these models are taken within the range of the constraints values. The contour at 5% (in white) is closed and rather small, proving that the outflow density and abundance are well constrained. As for the foreground cloud, an anti-correlation density-abundance is noticeable, since a white contour also appears in the top-left contour of the figure. The contour at 10% also indicates this trend. This anti-correlation is limited by the outflow density, constrained by other studies (Rao et al., 2009; Girart et al., 2014) to be around $10^7\,\mathrm{cm}^{-3}$ (see Sect. 4.3.2.3). I cannot explore too much the density-abundance parameters space since it would require many models (Fig. 4.14 is already made of 294 models) to extend the range of densities and abundances tested. Therefore, I decided to stay close to the best fit model (red cross in the figure) and maintain the constraints obtained around this value.

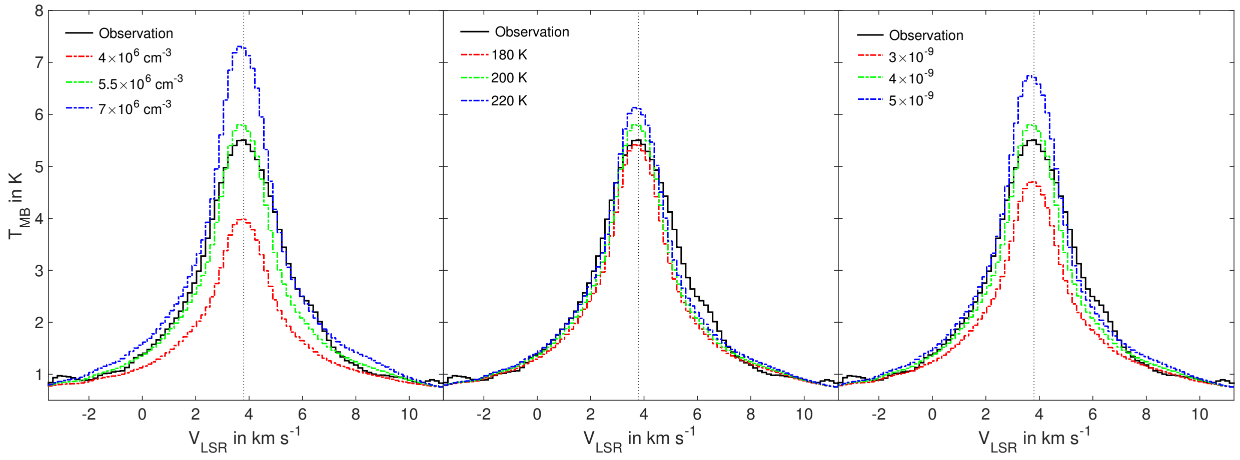

Figure 4.13 – Main beam temperature of the observed HCO^+ $(10-9)$ transition (black line) as a function of the velocity (for the sake of clarity, only this relevant transition is shown). The vertical black dotted line shows the supposed $V_{LSR} = 3.8\,\mathrm{km\,s^{-1}}$ of IRAS16293. The reference model (in green) is the best fit with $n(H_2)_{\mathrm{outflow}} = 5.5 \times 10^6\,\mathrm{cm}^{-3}$, $T_{\mathrm{kin,\ outflow}} = 200\,\mathrm{K}$, and $X(HCO^+)_{\mathrm{outflow}} = 4 \times 10^{-9}$. While varying one of the following parameters, the others are set to the best fit value. *Left panel:* Variation of the H_2 density of the outflow. *Middle panel:* Variation of the kinetic temperature of the outflow. *Right panel:* Variation of the HCO^+ abundance of the outflow.

H_2 density of the outflow. For the density, the constraints I give are limited by the density-abundance anti-correlation and constraints are dominated by local minima. Nonetheless, I notice that densities and abundances are strongly sensitive around these local minima as seen in Fig. 4.14. A little variation of the density by a factor of 10% around the local minima at $5.5 \times 10^6\,\mathrm{cm}^{-3}$ leads to a difference of $\gtrsim 10\%$ in the predicted line fluxes compared to the observations.

Kinetic temperature of the outflow. A lower kinetic temperature ($< 180\,\mathrm{K}$) decreases by ~6% the emission of high upper energy level lines since the gas is not hot enough to excite these transitions. At the opposite, a higher kinetic temperature ($> 220\,\mathrm{K}$) will increase by the same factor the emission of these lines. This effect is even more visible for J_{up} transitions higher than the HCO^+ $(10-9)$ transition shown in Fig. 4.13. For instance, for these lines, the factor can reach a value up to $\sim 50\%$.

Abundance of the outflow. As for the density, the HCO^+ abundance is strongly constrained only around local minima. However, the high HCO^+ abundance ($\sim 4 \times 10^{-9}$ around the best fit) needed to reproduce the observed lines is consistent with the expected strong enhancement described in Sect. 4.3.2.3. The abundance of HCO^+ derived with the chemical modelling of the envelope is al-

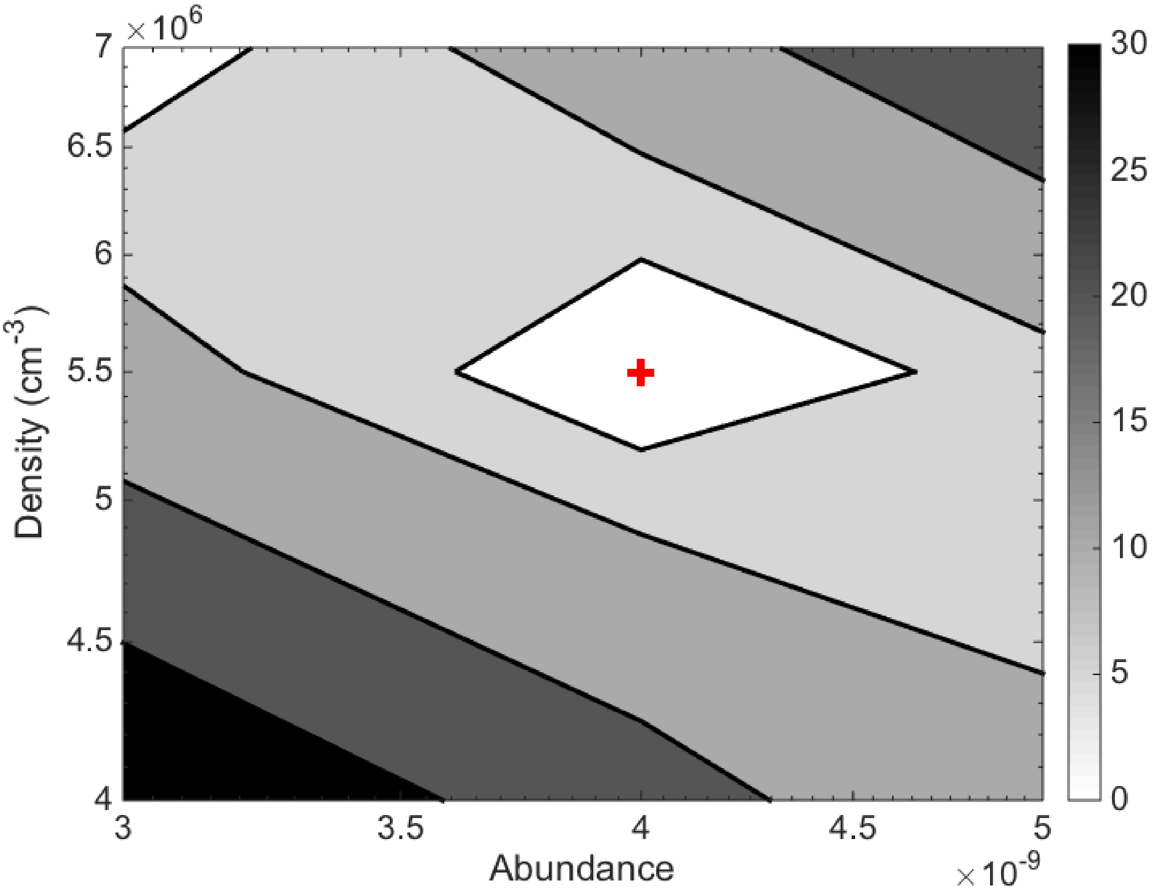

Figure 4.14 – Contour plot of the difference (in percent) of all the predicted lines fluxes, compared to the observations, for the outflow H_2 density as a function of the HCO^+ abundance. Contours at 5%, 10%, 20%, and 30% are shown. The best fit model is the red cross.

ways lower than this value, particularly in the inner region ($< 8''$) where the outflow is completely dominating. This clearly shows that the outflow largely contributes to the emission in a region where it cannot be produced by the envelope.

The ranges of outflow density and temperature are consistent, within a factor of two, with values derived by Rao et al. (2009) and Girart et al. (2014) using only one SiO ($8-7$) transition (see Table 4.9). Fitting several HCO^+ transitions, I provide a better estimation of the outflow properties, particularly the kinetic temperature is strongly constrained. The H_2 density and HCO^+ abundances are only constrained to local minima because of their anti-correlation. Nonetheless, the best fit model for the outflow gives $n(H_2)_{\mathrm{outflow}} = 5.5 \times 10^6\,\mathrm{cm}^{-3}$, $T_{\mathrm{kin,\,outflow}} = 200\,K$, and $X(HCO^+)_{\mathrm{outflow}} = 4 \times 10^{-9}$.

4.3.3.4 Fractionation

I varied the different isotopic ratios with a step of 50 for $^{16}O/^{18}O$ and a step of 5 for $^{12}C/^{13}C$, starting from typical local ISM values (Wilson and Rood, 1994; Bensch et al., 2001). The $^{12}C/^{13}C$ and $^{16}O/^{18}O$ best ratios I derived in this study are consistent with values found in the ISM (Wilson and Rood, 1994) and for the ρ Ophiuchus cloud (Bensch et al., 2001). The following error bars are given for a 20% difference between the modelled and observed line fluxes.

A constant $^{16}O/^{18}O = 500 \pm 50$ ratio is sufficient to reproduce the $HC^{18}O^+$ observations within a difference of 20% on line fluxes. This ratio is in good agreement with the typical ratio of 560 observed in the local ISM (Wilson and Rood, 1994). The $HC^{18}O^+$ transition at 255.5 GHz has been ignored in the error calculation due to a bad calibration of the IRAM-30m observations, as suggested by Caux et al. (2011).

Recently, Mladenović and Roueff (2014) have theoretically studied the fractionation of DCO^+ and they have shown that considering the higher exothermicity of deuterated isotopologues reactions, the isotopic ^{13}C ratio is lower than the hydrogenic counterpart. Thus, I expect a $D^{12}CO^+/D^{13}CO^+$ ratio lower than the $H^{12}CO^+/H^{13}CO^+$ ratio in the external part of the envelope or in the foreground cloud, where the temperature is low. I derive $H^{12}CO^+/H^{13}CO^+ = 50 \pm 5$ and $D^{12}CO^+/D^{13}CO^+ = 40^{+5}_{-10}$, consistent with the results of Mladenović and Roueff (2014).

At low temperature (T $<$ 30K) and low densities ($n(H_2) < 10^5\,cm^{-3}$), DCO^+ is enhanced, increasing rapidly the fractionation of DCO^+ (Dalgarno and Lepp, 1984; Roberts and Millar, 2000). Therefore, the HCO^+/DCO^+ ratio I use is not constant throughout the model but it follows an *ad hoc* law based on a linear decrease of the ratio between 22 and 6000 AU. The resulting HCO^+, $H^{13}CO^+$, DCO^+, and $D^{13}CO^+$ are plotted in Fig. 4.15.

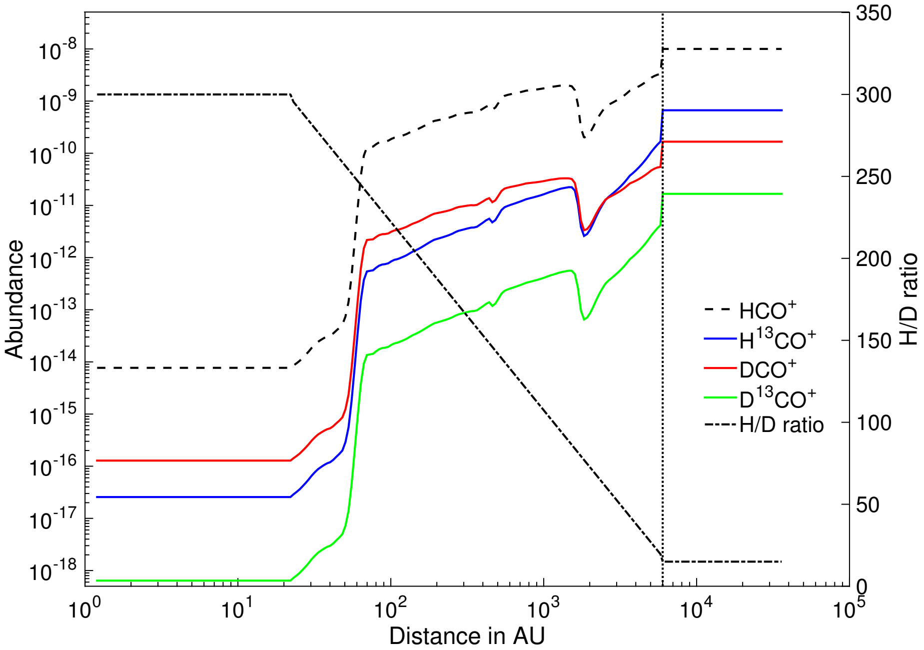

Figure 4.15 – *Left axis:* Abundance profile of HCO^+ (black dashed line) as a function of the radius compared to the $H^{13}CO^+$ (blue), DCO^+ (red), and $D^{13}CO^+$ (green) one. *Right axis:* D/H ratio used in this study (black dash-dotted line). The vertical black dotted line shows the R = 6000 AU limit of the foreground cloud.

The inner H/D ratio of 300 is larger than the H_2O/HDO ratio of ~ 30 ($HDO/H_2O = 3.4\%$ for the hot corino) derived by Coutens et al. (2012) but Persson et al. (2013, 2014) derived a higher value for the hot corino of IRAS16293 (up to 1000) and other low-mass proto-stars. In any case, it will not play an important role in this study since the abundance in the inner part of the envelope is really small ($< 10^{-13}$). The outer H/D ratio of 15 I use for the external part of the envelope is in agreement with the ratio of 20 obtained by Coutens et al. (2012) for the foreground cloud ($HDO/H_2O \sim 4.8\%$). At radii lower than 22 AU and higher than 6000 AU, I suppose that the H/D ratio is constant and equal to 300 and 15 respectively. The outflow H/D ratio is considered to be 300 as well.

4.3.3.5 The case of N_2H^+

As said above, the N_2H^+ emission seems to arise only from the contribution of the envelope. I have used the best astrochemical model I derived for HCO^+ at the same age ($\sim 4 \times 10^4$ yr, orange thick line in Fig. 4.16) and one can note that the resulting spectra for the N_2H^+ transitions highly overestimate (factor of $\sim 2-3$) the observed emission (see Fig. 4.17). The modelled emission is very high and does not reproduce at all the observations.

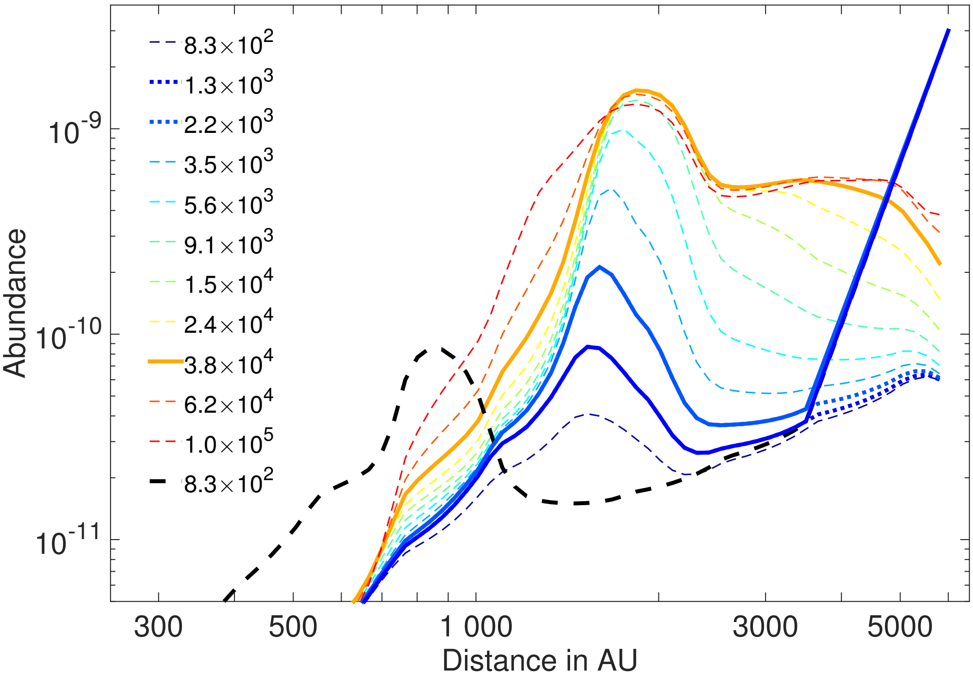

Figure 4.16 – Variation of the abundance profile of N_2H^+ determined by Nautilus as a function of the radius for different ages of the proto-star. The orange line highlights the N_2H^+ abundance profile corresponding to the same chemical parameters than HCO^+. The two blue lines highlight the abundance profiles I need to use to have a better fit to the observations, corresponding to lower proto-star ages and a modified abundance in the outer part of the envelope (original profile shown in dotted lines of respective colours). The black dashed line indicates the artificially shifted model.

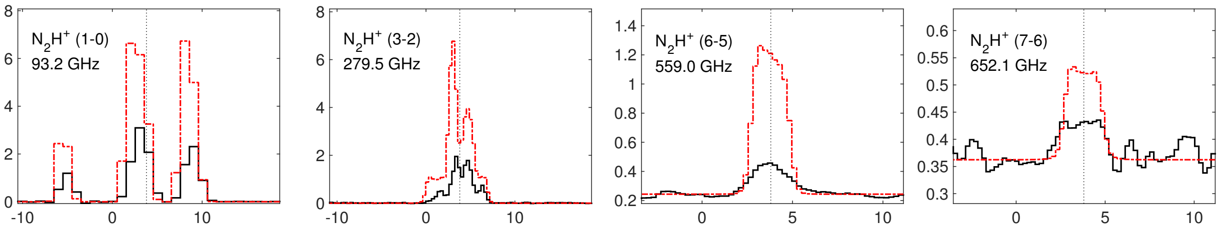

Figure 4.17 – Main beam temperature (in K) of N_2H^+ and N_2D^+ as a function of the velocity (in $\mathrm{km\,s^{-1}}$) for the observed transitions (in black) compared to the predicted model (in red) considering the same best chemical model parameters as HCO^+. The continuum is shown for all transitions. The vertical black dotted line shows the supposed $V_{LSR} = 3.8\,\mathrm{km\,s^{-1}}$ of IRAS16293.

With the same chemical modelling as HCO^+ but for an age between $(1-2) \times 10^3$ yrs (blue thick lines in Fig. 4.16), I obtain a line profile that better reproduces all the N_2H^+ transitions (see Fig. 4.18). However, to do so, I had to artificially increase the N_2H^+ abundance in the outer parts of the envelope, otherwise the emission of the $J = 1 \rightarrow 0$ transition was underestimated by a factor of ~ 3. To determine the abundance profile at large radii, I varied two different parameters: *(a)*

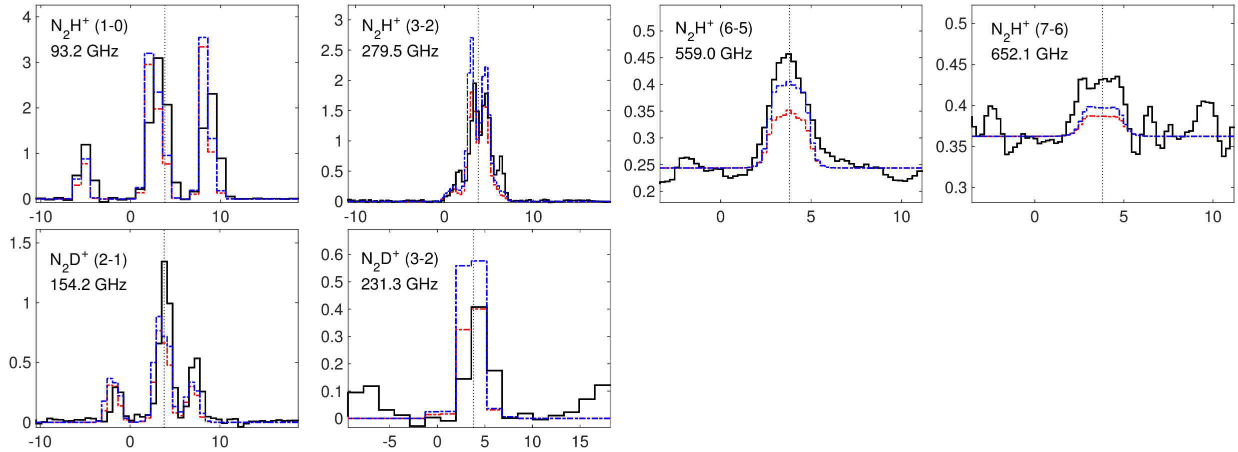

Figure 4.18 – Main beam temperature (in K) of N_2H^+ and N_2D^+ as a function of the velocity (in km s^{-1}) for the observed transitions (in black) compared to the predicted model for lower proto-star ages of 1×10^3 yrs (red dashed line) and 2×10^3 yrs (blue dashed line) and increased abundance on the external edge (see text and blue solid lines in Fig. 4.16). The continuum is shown for all transitions. The vertical black dotted line shows the supposed $V_{LSR} = 3.8$ km s^{-1} of IRAS16293.

the distance at which I choose to stop the abundance profile predicted by Nautilus and *(b)* the abundance value at the edge of the envelope. The best fit model gives a distance of 3500 ± 500 AU with an abundance of $(3 \pm 1) \times 10^{-9}$ at the edge of the envelope as seen in Fig. 4.16. Without this amount of abundance at the edge of the envelope it is not possible to reproduce the observed emission of the N_2H^+ fundamental transition. There is a discrepancy between the predicted model given by Nautilus and the observations that I cannot explain at the moment. I have tried to modify several input parameters of the chemical code without success for retrieving such features at the edge of the envelope.

In addition, one can note that the predicted best fit model does not perfectly reproduce all the observed transitions, especially the N_2H^+ (7-6) transition with $E_{up} = 125$ K. I have explored different parameters of the chemical model to obtain a better agreement. In the previous model, the amount of abundance in the inner regions (where the temperature is higher) is too low, which explains the low intensity of this line. I have shifted the abundance profile of N_2H^+ in the inner region of the envelope by changing the radius at which it peaks. I have tried several radii and a good fit gives a radius of ~ 900 AU instead of ~ 1600 AU for the same proto-star age (see black dashed line in Fig. 4.16). The resulting line profiles are displayed in Fig. 4.19.

This abundance profile is consistent with recent work led by Jørgensen et al. (2011) in which they have shown from SMA interferometric maps that the peak emission of N_2D^+ is located between $5 - 10''$ ($600 - 1200$ AU) away from source A position. One must be careful because their map only shows the peak emission of N_2D^+, the fainter and extended being resolved-out by the interferometric observations. This test demonstrates that another N_2H^+ abundance profile can give better results than the predicted profile given by Nautilus. Further investigations are required to better understand the impact of all the the chemical modelling input parameters on the output abundance profile. Overall, the N_2H^+ abundance profile always possesses the same shape, with a peak abundance in the cold outer part of the envelope.

To reproduce N_2D^+, I derived a constant N_2H^+/N_2D^+ ratio of 9 ± 1 in all the envelope. For (lower) greater values, the N_2D^+ emission becomes to (weak) strong. Emprechtinger et al. (2009) have deduced that a N_2D^+/N_2H^+ ratio above 0.15 signifies that the proto-star is in a stage shortly after the beginning of collapse. In fact, with time and due to the collapse of the envelope, the temperature increases and the deuterium fractionation decreases until it reaches a value of ~ 0.03 at the Class 0/I borderline. In this study, I derived a N_2D^+/N_2H^+ ratio of ~ 0.11 ($N_2H^+/N_2D^+ = 9$)

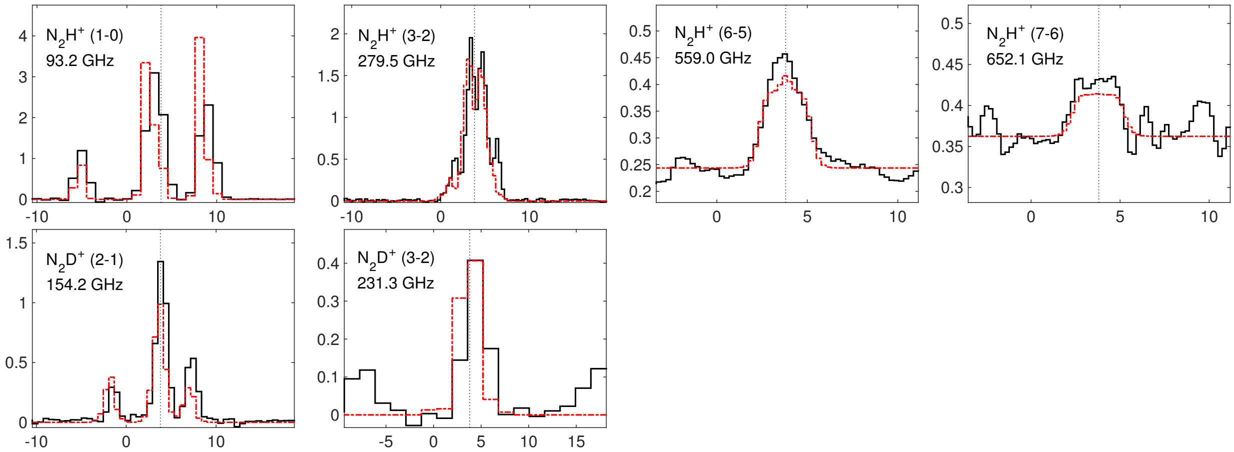

Figure 4.19 – Main beam temperature (in K) of N_2H^+ and N_2D^+ observed transitions (in black) compared to the best fit model (in red) as a function of the velocity (in $\mathrm{km\,s^{-1}}$). The N_2H^+ abundance profile used to perform this modelling is the Nautilus profile for a protostar age of 1×10^3 yrs, shifted towards the centre and with an increased abundance on the external edge (see text and black dashed line in Fig. 4.16). The continuum is shown for all transitions. The vertical black dotted line shows the supposed $V_{LSR} = 3.8\,\mathrm{km\,s^{-1}}$ of IRAS16293.

suggesting that IRAS16293 is at the beginning of the Class 0 stage. One can note that the N_2D^+ transitions at 154.2 GHz is lacking emission but it may be due to the missing collisional rates in the N_2D^+ collision file, as discussed in Sect. 4.3.1.

4.3.4 Concluding remarks

I have used a large number of HCO^+ and N_2H^+ transitions, spanning a wide range of upper energy levels ($4 - 389\,\mathrm{K}$) to reproduce the observed emission. This study gives better constraints on the physical parameters of the outflow and I derived $T_{kin} = 200\,\mathrm{K}$ and $n(H_2) = 5.5 \times 10^6\,\mathrm{cm^{-3}}$ with $X(HCO^+) = 4 \times 10^{-9}$. The emission coming from the outflow is responsible for all the $J_{up} \geqslant 8$ emission and it participates a lot to other transitions. I have also demonstrated that the foreground cloud causes the deep self-absorption seen for $J_{up} \leqslant 4$ HCO^+ lines. This is only possible if this cloud is cold ($\leqslant 30\,\mathrm{K}$) and not dense ($n(H_2) \leqslant 1 \times 10^4\,\mathrm{cm^{-3}}$). I have used the chemical code Nautilus to estimate the HCO^+ abundance of the envelope and, combined with the outflow and the foreground cloud contributions, I have been able to reproduce correctly the observations. By using multiple isotopologues, I also derived several fractionated ratio such as $^{16}O/^{18}O = 500 \pm 50$. I have shown that the $H^{12}CO^+/H^{13}CO^+ = 50 \pm 5$ ratio is slightly higher than the $D^{12}CO^+/D^{13}CO^+ = 40^{+5}_{-10}$ as predicted by recent theoretical works.

The N_2H^+ emission can also be reproduced with the same Nautilus model but for lower protostar ages than HCO^+. Moreover, a better fit is possible if I slightly shift the abundance in the inner warmer region of the envelope. Further investigations are required to understand this effect and it may be difficult to match the chemical predictions of HCO^+ and N_2H^+. This may indicate an issue in the chemical network for these species.

I have studied the deuterium fractionation of both species and I need a HCO^+/DCO^+ ratio varying from 15 (outer region) to 300 (inner region) depending on the distance from the center. For N_2H^+, I only need a constant N_2H^+/N_2D^+ ratio of 9 ± 1 to reproduce the observations.

The structure of IRAS16293, as revealed by the numerous interferometric observations, is in reality much more complicated because it is not homogeneously distributed and peak emissions of some species may occur in a specific region of the source and it can be hardly modelled, even in 3D. This effect has already been observed by e.g. Jørgensen et al. (2011) and it can play an important role in the emission seen with single-dish telescopes. It can explain the difference I get between the predicted model and the observation for optically thin molecules such as $HC^{18}O^+$ or $D^{13}CO^+$. Such effects can also explain the excess in emission seen at red velocities for the $J = 1 \rightarrow 0$ HCO^+ transition that I never managed to correctly reproduce.

This work has been partly submitted in A&A (see Appendix B).

"Deux choses sont infinies : l'univers et la bêtise humaine;
En ce qui concerne l'univers, je n'en ai pas acquis la certitude absolue."

Albert Einstein

NASA's New Horizons spacecraft captured this high-resolution enhanced color view of Pluto on July 14, 2015.

CHAPTER 5

Conclusions and Perspectives

Contents

5.1 The need for 3D modellings. . .

At the beginning, the only goal of GASS (which was not an interface at all) was to generate two spherical sources in interaction. I was interested in the formaldehyde (H_2CO) emission in the low-mass proto-star IRAS16293. From the line profiles, I quickly concluded that both sources A and B contribute to the line emission of this species. These two sources are separated by $\sim 5''$ and show a completely different small scale structure, as revealed by interferometers. Therefore, to tentatively reproduce the emission using LIME (recently available for the community at this time), I began to develop what would become GASS in the future.

Now, GASS is a complete interface to 3D radiative transfer codes and it allows to easily define the physical structure of different astrophysical structures by creating, manipulating, and mixing several different physical components such as spherical sources, disks, and outflows. The main goal of GASS is the generation of 3D physical structures and the easy post-treatment of hyper-spectral data cubes using several analysis tools such as: plotting spectra or moment maps, or simulating interferometric observations. GASS is freely available for the community upon request (website in construction) as a standalone application for Mac OS X, Windows, and any Unix-based operating systems. A scripted MatLab version is also available.

I will keep on developing GASS and, for instance, I expect to improve the GUI or to implement more LIME options in future releases of the code. I also expect to extend the capabilities of GASS to other radiative transfer codes such as RADMC-3D or MC3D for instance. Within the STOP project, it is planned to implement GASS as a Virtual Observatory (VO) web-service applications available for the community.

5.2 . . . to understand star-forming regions

With the development of GASS, I have been able to work with different objects involved in the star formation process, from pre-stellar cores to proto-planetary disks.

5.2.1 The pre-stellar core L1544: detectability of HDO

A 3D modelling is not compulsory to study pre-stellar cores since they are supposed to be roughly spherical, nonetheless, I have shown that a 3D approach is relevant. Using the existing physical structure of this core (Keto et al., 2014), I carried out a new modelling of the recently detected $1_{1,0}$–$1_{0,1}$ water transition (Herschel/HIFI instrument) toward this pre-stellar core. It was the first time a water line is observed in such a young object. Previous studies of this water transitions were made with an LVG approach, leading to a different result compared to a full non-LTE radiative transfer treatment. In fact, the physical structure derived from the LVG approach gives a different line (3.5 times higher) and continuum (2 times higher) emission when applied to a full radiative transfer method. I found a new estimation of both the water abundance profile and the dust opacity to reproduce the observed line and continuum emission.

This study has been coupled to a detailed chemical modelling using both gas-phase and grain-surface chemistry. The result of this chemical study is double: *(1)* I managed to roughly reproduce the newly LIME-estimated water abundance profile and *(2)* I derived a deuterated water abundance profile. I used the latter and several other abundance profiles (derived from the water profile coupled with constant D/H ratios) to predict, with GASS and LIME, the line emission of the $1_{0,1}$–$0_{0,0}$ HDO transition. I compared it to the observed transition obtained with APEX, but the emission is too weak compared to the sensitivity of the observations in any case. In addition, I have shown that observations carried out with existing single-dish telescopes or interferometric antennas cannot detect this transition (considering a reasonable observing time), limiting the detectability of deuterated water in pre-stellar cores.

5.2.2 The low-mass proto-star IRAS16293: study of ions

A Class 0 proto-star like IRAS16293 definitely requires a 3D modelling to correctly predict the line emission of most species. Indeed, this proto-star is composed of multiple sources and multiple bipolar outflows. To take into account these different structures simultaneously, a precise 3D modelling is needed. In this source, I have been focusing on the ionisation since it plays an important role in the chemistry involved in the proto-star. To do so, I have studied HCO^+ and N_2H^+ since a large number of transitions, spanning a wide range of upper energy levels ($4-389\,K$) is available.

From previous LTE and LVG results obtained before the beginning of this thesis, I already knew that an important part of the emission of HCO^+ is coming from one of the outflows. From that, I decided to implement a 3D outflow model in GASS, in order to correctly describe the physical structure of the outflow responsible for the majority of the HCO^+ emission. This study aimed at giving better constraints on the physical parameters of the outflow and I derived $T_{kin} = 200\,K$ and $n(H_2) = 5.5 \times 10^6\,cm^{-3}$ with $X(HCO^+) = 4 \times 10^{-9}$.

I combined this outflow structure with a foreground cloud, responsible for the absorption feature seen for some of the transitions, and an envelope structure, responsible for only a minority of the total emission. The foreground cloud is found to be cold ($\leqslant 30\,K$) and not dense ($n(H_2) \leqslant 1 \times 10^4\,cm^{-3}$). The envelope structure is already determined at large scale by previous studies (Crimier et al., 2010), and I have used the chemical code Nautilus to estimate both the HCO^+ and N_2H^+ abundance profiles inside this envelope, varying several parameters, including the cosmic ionisation rate. The latter is found to be higher ($\geqslant 5 \times 10^{-17}\,s^{-1}$) that the standard solar neighbourhood value of $1.3{\times}10^{-17}\,s^{-1}$, but the ρ Ophiuchus cloud complex is known for its high cosmic ray ionisation rate (Hunter et al., 1994; Doty et al., 2004; Bottinelli et al., 2014).

The study of multiple isotopologues in this source also allowed me to derive several fractionated ratios such as $^{16}O/^{18}O = 500 \pm 50$, $H^{12}CO^+/H^{13}CO^+ = 50 \pm 5$ and $D^{12}CO^+/D^{13}CO^+ = 40^{+5}_{-10}$ as well as to investigate the deuteration of both HCO^+ and N_2H^+.

5.3 Ongoing works

5.3.1 The low-mass proto-star IRAS16293: source B small scale structure

GASS and LIME are not only powerful to study line emission, but also to investigate continuum emission. In the near future, I will concentrate on such a study, which I already started, as I explain below. Thanks to the numerous interferometric observations directed toward this object, it has been clearly proven that the small scale structures of both source A and B are in reality extremely complicated. I began to study the small scale structure of source B using several interferometric continuum images coming from the VLA, SMA, and ALMA. The goal is to constrain the physical properties (temperature and H_2 density) of this source at small scales ($<100\,AU$). I have been focusing especially on the source B because of its spherical shape and its very strong continuum emission. This source has no outflows thus there is no free-free emission that contaminates the spectral energy distribution (SED) of the dust continuum at low frequencies. Once the spherical model of the source is generated with GASS and the radiative transfer done with LIME, I compare the output result with the interferometric observations. The fitted parameters are the total flux, the peak emission and the size of the dust continuum emission. This comparison is directly made within GASS thanks to its post-treatment tools. Once the best fit is found, I used the derived temperature and H_2 density profile of the source to predict the emission of $H^{13}CN$ around source B. The ring-like emission of this species coupled to a strong absorption profile at the centre is a result of the very high dust opacity in the innermost regions of the source. The combination of dust continuum and line emission associated with both the spatial and spectral profile of the source will lead to strong constraints on the small scale physical structure of this particular object. This study is still in progress and is part of a larger project on source B, in collaboration with L. Loinard et al. (UNAM, Mexico). I will lead the first paper studying the physical structure of this object.

These two studies, involving IRAS16293, demonstrate that the combination of GASS and LIME is a strong tool to study both large and small scales physical structures. GASS is already involved in several other projects in this source, helping to study many other molecules (NO, CN, HCl, H_2CO, HC_3N,. . .) observed with the different spectral surveys (e.g. TIMASSS and CHESS).

5.3.2 The proto-planetary disks: photo-evaporation disks and embryo of proto-planets

During this thesis, thanks to the development of GASS, I have been involved in the study of two different proto-planetary disks: the massive disk Gomez's Hamburger (IRAS18059-3211; hereafter GoHam) and the "proplyd" 203–506. As for the outflow, I had to improve GASS to be able to deal with (proto-planetary) disks model. This has been a great leap forward for GASS, since it is now able to model the main structures found during the star formation process: the spherical, the outflow, and the disk structures. In the future, I plan to improve the proto-planetary disk model available in GASS by incorporating, for instance, several other options to better describe the disk physical properties, especially at small scales. The two following works have been done jointly with Olivier Berné and Jason Champion at the institute.

5.3.2.1 A planetary embryo in GoHam

The goal of this investigation is the prediction of molecular emission around this evolved proto-planetary disk. It is located around an A type star and is oriented nearly edge-on. Recent studies (Bujarrabal et al., 2009; Berné et al., 2015) have derived from ^{13}CO SMA and VLT/VIZIR maps that a dense object is located in the southern part of the disk. This "clump" is supposed to be the embryo of a proto-planet but a better spatial resolution is needed to give a better constraint on its size and shape.

As part of an ALMA Cycle 4 proposal, we have predicted the emission of ^{13}CO, HCN, and $H^{13}CN$ in this source. These molecules are good tracers of the dense gas thus they can well disentangle whether the emission is coming from the disk or from the clump, helping us to determine, for instance, the mass and the size of the clump. The physical structure (Bujarrabal et al., 2008) of the disk has been modelled, taking into account the clump-like spherical structure, with GASS and the resulting emission is given by LIME. We use the *rms* noise predicted by the ALMA observing tool (AOT) and an angular resolution of $0.2''$. The predicted ALMA observation of the aforementioned species is shown as an animated simulation in Fig. 5.1 and as integrated maps in Fig. 5.2.

5.3.2.2 The photo-evaporation of HCO^+ in 203–506

When proto-planetary disks are irradiated by UV or X-ray photons originating from their central star or nearby massive stars, their surface can be heated to high temperatures allowing the gas to escape from the gravitational field. This process, called photo-evaporation, is believed to be of major importance in the dynamical evolution of proto-planetary disks (Alexander et al., 2014). "Proplyds" are a class of disks where photo-evaporation is dominated by far-UV photons. During ALMA Cycle 1 observations of the Orion Bar, the proplyd 203–506 has been serendipitously detected by its intense HCO^+ (4-3) emission. This disk has unique properties since molecular emission is not expected in proplyds (Eisner et al., 2016). Another surprising aspect of 203–506 is the HCO^+ line profile: since the disk is observed almost perfectly edge-on, one would expect to observe a double-peaked line due to Keplerian rotation, while the observed line is single-peaked. It is likely that the HCO^+ line emanates from warm molecular gas, and that this gas is not gravitationally bound to the star and is situated at the base of a photo-evaporation flow, where it is escaping

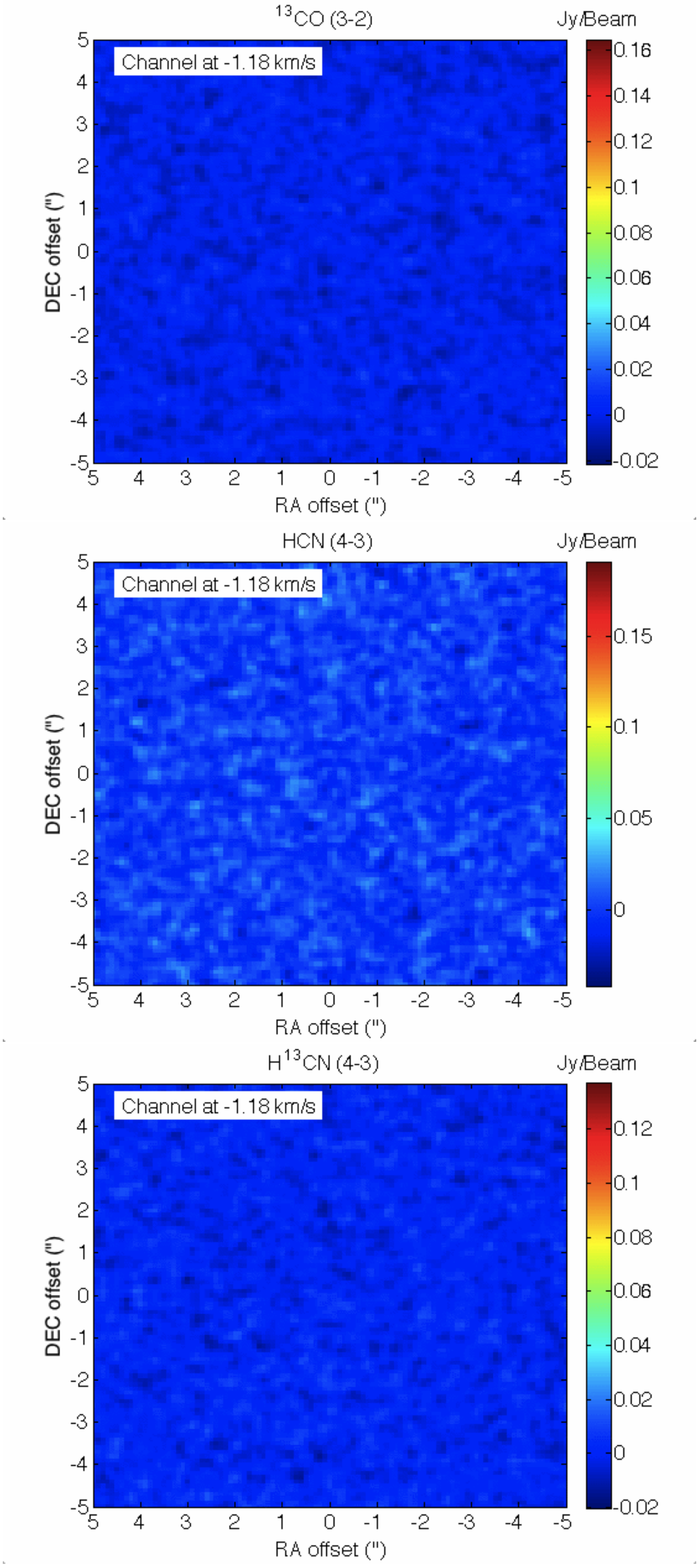

Figure 5.1 – Animation of the emission of ^{13}CO (top panel), HCN (middle panel), and H^{13}CN (bottom panel). Click on the figure to activate the movie. Only works with Adobe Acrobat Reader, version ≥ 9 (not greater than 9.4.1 on Linux) or Foxit Reader.

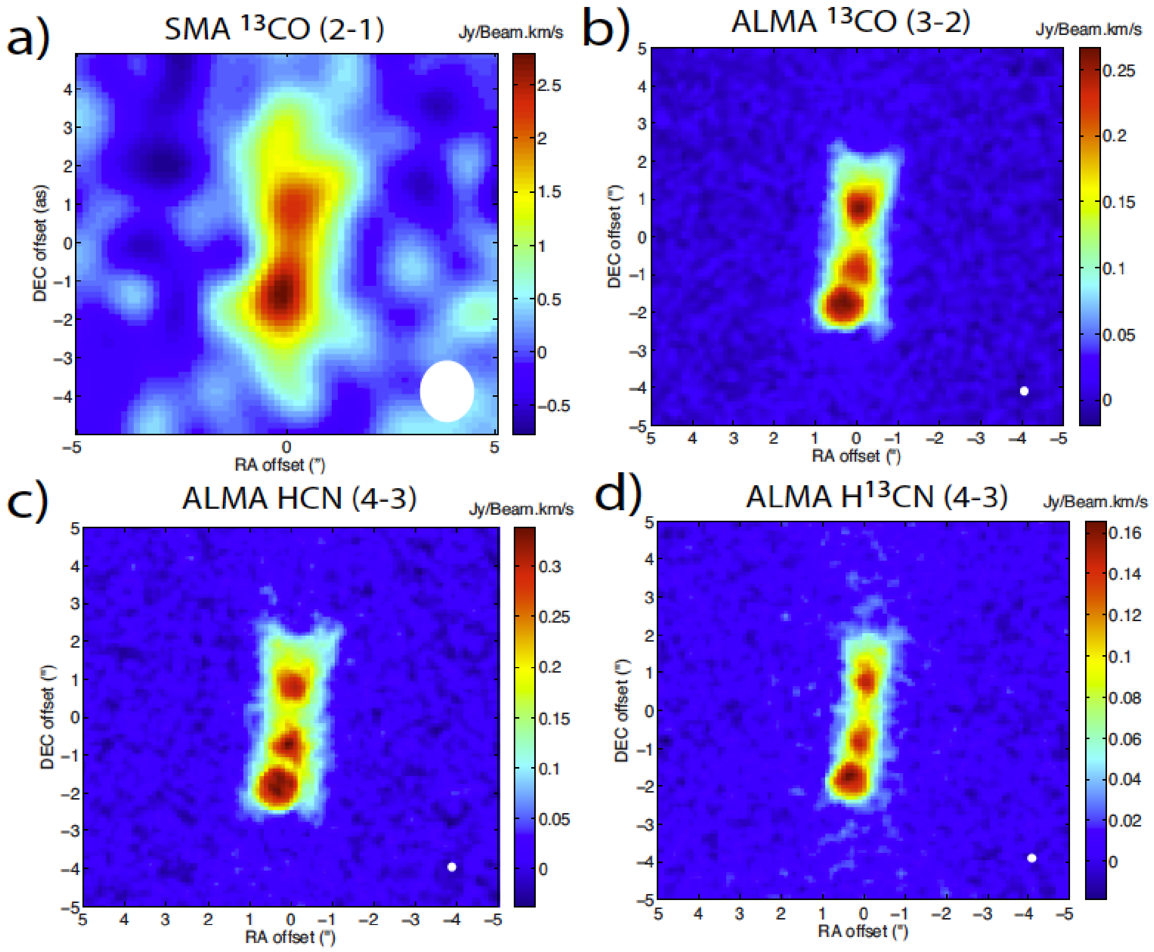

Figure 5.2 – **a)** Velocity integrated ^{13}CO (2-1) map observed with SMA of GoHam (data from Bujarrabal et al., 2009). Excess of emission in the South is due to the clump. **b) c) d)** ALMA band 7 predicted velocity integrated maps (using the combination of GASS and LIME) of GoHam including a molecular clump of 1.5 Jupiter mass, density of 5×10^7 cm^{-3} at 50 K, providing the best fit to the SMA observations of ^{13}CO (2-1). For all maps, the ALMA beam sizes are shown as white ellipses

perpendicularly from the disk surface at a low velocity.

In order to gain further insights into the properties of 203–506 and on the physics of external photo-evaporation, this proplyd is the subject of an ALMA Cycle 4 proposal. Our goals are: *(1)* to spatially and spectrally resolve the photo-evaporation flow and determine its density and velocity and *(2)* to determine the mass of the star and of the disk. We have predicted the emission of HCO$^+$ coming from both the photo-evaporation flow and the disk itself, using GASS and LIME. Within GASS, this proplyd has been modelled in 3D using a combination of the disk and the outflow structure, showing again that GASS is able to deal with complicated 3D structures. The predicted ALMA observation of HCO$^+$ is shown in Fig. 5.3 and as a animated simulation in Fig. 5.4. We use the *rms* noise predicted by the ALMA observing tool (AOT) and an angular resolution of 0.1″.

Supported by the ALMA observations, this study will provide robust constraints on the dynamical evolution of externally illuminated disks and on their lifetime. If this latter value is short (10^{4-5} years), we will be able to confirm that proplyds are transient objects, where planet formation should be fast, if it occurs.

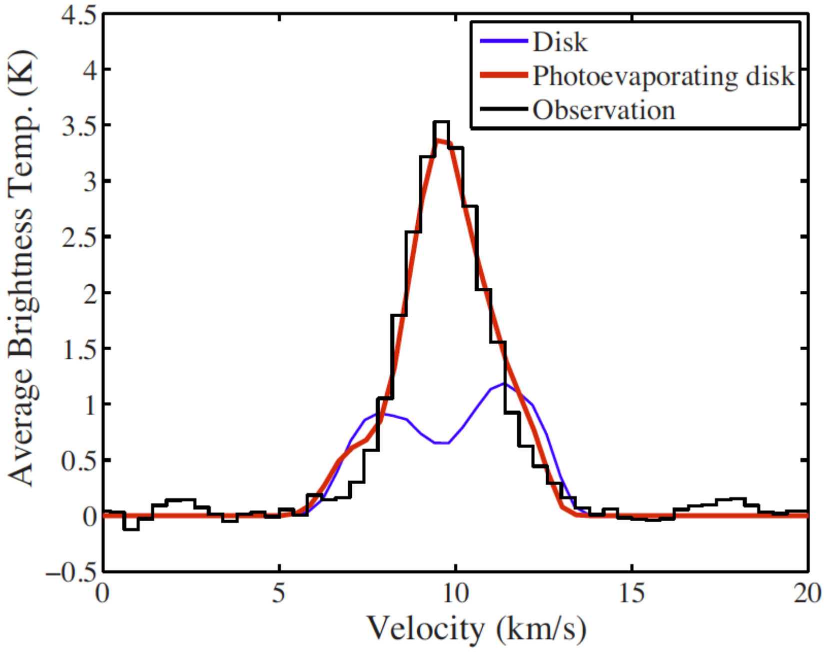

Figure 5.3 – The HCO$^+$ line observed with ALMA during Cycle 1 is shown in black. The red line shows the result of the best radiative transfer model. The blue line is the same model but without a photo-evaporation flow

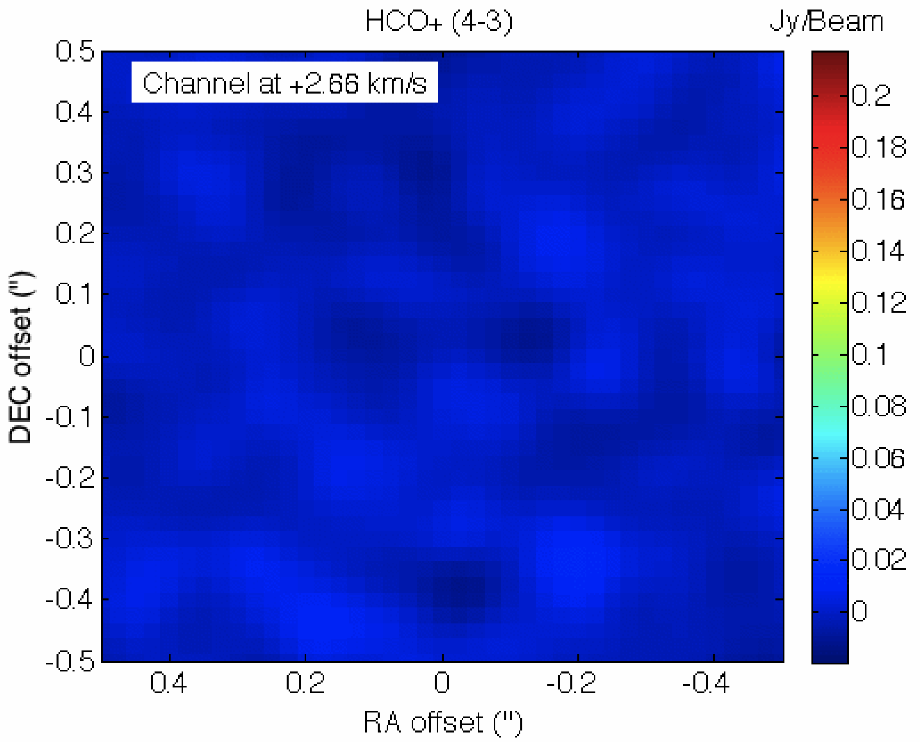

Figure 5.4 – Animation of the emission of HCO$^+$ in 203–506. The 7.6 and 12.2 km s^{-1} channels are dominated by the blue and red contributions from the Keplerian disk. The central (10.2 km s^{-1}) channel is dominated by the emission from the photo-evaporation flow. Click on the figure to activate the movie. Only works with Adobe Acrobat Reader, version ≥ 9 (not greater than 9.4.1 on Linux) or Foxit Reader.

5.3.3 The first galaxies

One of the main advantages of 3D modelling is the wide range of fields to which it can be applied, from star formation to cosmology. I have been involved in the study of two of the most distant galaxies currently known, selected from near-infrared images: Abell2744_Y1 (Laporte et al., 2014) and COSY-0237620370 (Roberts-Borsani et al., 2016). These galaxies have emitted light when the Universe was only 700 million years old (in terms of redshift: $z \sim 7.5$, see Fig. 5.5). The major question in extra-galactic physics is to understand the role played by the first galaxies during the re-ionisation process, when the neutral hydrogen was ionised by the UV photons they produced (for a review see Bromm and Yoshida, 2011). The arrival of radio interferometers, such as ALMA, opened a new window to explore these systems at the frontiers of the observable Universe.

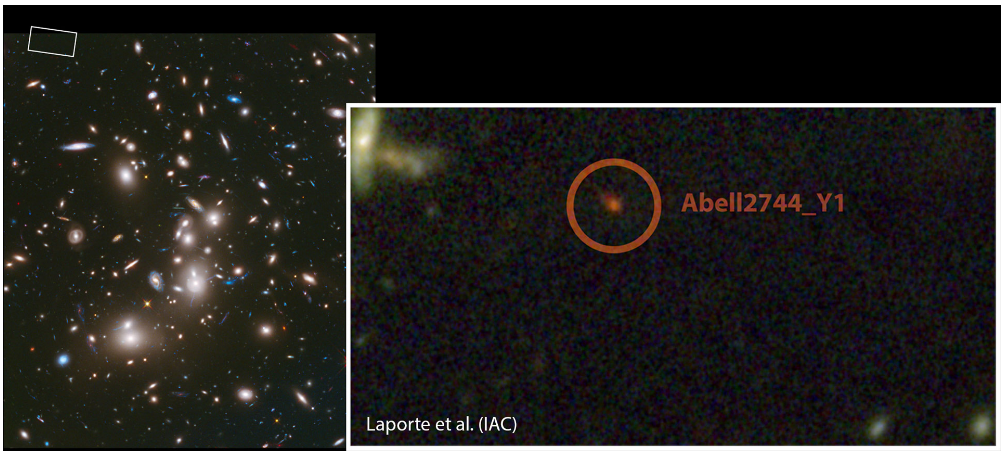

Figure 5.5 – Colour image of Abell2744_Y1, a very distant galaxy selected from the *Hubble Frontier Fields* data, for which GASS and LIME estimated the dust continuum that will be observed by ALMA in band 7. Credits: NASA press release 2014-041.

The capabilities of ALMA are crucial to constrain the dust content and the gas metallicity of galaxies at such epochs, currently completely unknown. It can be achieved by studying redshifted emission lines or the dust continuum emission within the observable radio band of ALMA. The detection of a dust continuum will confirm early metal production and allow estimates of both the dynamical (Venemans et al., 2016) and ISM masses (see appendix of Scoville et al., 2016).

I contributed to estimate the continuum flux of these two galaxies in the ALMA band 6 and 7 using the combination of GASS and LIME. We compared these results with the estimates computed by the SED-fitting and previous very high-z 1.2 mm detections with ALMA (Capak et al., 2015; Willott et al., 2015). We used several dust mass absorption coefficients published in the literature (e.g. Watson et al., 2015), dust properties expected in Combes (2010) and physical properties of our target deduced from SED-fitting as input parameters. We found a minimum flux of $\approx 180\,\mu$Jy and 95 μJy depending on the dust opacity respectively for COSY-0237620370 and Abell2744_Y1, consistent with what is deduced from photo-ionisation modellings and SED-fitting.

Therefore, a 3D modelling approach using GASS and LIME can be used to estimate the flux of an object at the edges of the Universe. Two ALMA proposals have been submitted: *(1)* an accepted proposal for Cycle 3 (2015.1.00594S - PI: N. Laporte, F. Boone, D. Quénard) to observe Abell2744_Y1 (to be performed by the end of June 2016), and *(2)* a submitted proposal for Cycle 4, aiming to observe COSY-0237620370. These observations will help to improve the accuracy of the estimates given by the modellings at such high-redshift.

Afterword

Our knowledge of the interstellar medium and star-forming regions has made a great leap forward in the past decades. We are at the beginning of our understanding about the birth of stars and the chemical complexity that occurs in their environment at different evolutionary stages. From prestellar cores to evolved proto-planetary disks, we have traced this molecular richness. The legacy of *Herschel* left us with questions that have to be answered and a large amount of data to analyse and understand. The complexity and the amount of observational data available is increasing very quickly and current instruments and interferometers such as ALMA and NOEMA are pushing the limits of spatial resolution and sensitivity (e.g. HL Tau proto-planetary disk, Brogan et al., 2015). Numerical simulations and modelling are more and more complex, trying to understand and reproduce as faithfully as possible the more and more accurate observations.

The future *Square Kilometre Array* (SKA) will be available to the scientific community around 2020. One of the major goals of SKA is the search for life and planets. Its impressive spatial resolution ($< 0.1''$ at 1.4 GHz) will allow us to precisely look inside the disk formation and detect the presence of giants proto-planets through the gaps they left in the disk material while orbiting the central star. Moreover, the frequency range of SKA1 LOW (50 - 350 MHz) and SKA1 MID (350 MHz - 14 GHz) coupled with its high sensitivity will help us in our search for pre-biotic molecules and complex organic molecules (both emitting at these frequencies) around forming star. SKA will open a new era in the data treatment (Big Data project) and this huge amount of information has to be analysed with powerful astrochemical and radiative transfer codes. At long-term, the combination of powerful instruments, telescopes, and modelling resources will open a new window to study the origin of life. I strongly intend to help opening this window, with tools such as GASS.

CONCLUSION

Au commencement, l'unique but de GASS (qui n'était alors pas du tout une interface) était de générer deux sources sphériques en interaction. Je me suis intéressé dans un premier temps à l'émission de formaldehyde (H_2CO) dans la proto-étoile de faible masse IRAS16293-2422. À partir du profil des raies, je me suis aperçu que les deux sources A et B contribuent à l'émission des raies de cette espèce. Ces deux sources, séparées de $\sim 5''$, ont une structure à petite échelle complètement différente, comme le montrent les observations interférométriques. Par conséquent, afin de reproduire l'émission du formaldéhyde avec LIME (alors récemment disponible pour la communauté), j'ai commencé à développer ce qui sera GASS dans le futur.

Aujourd'hui, GASS est une interface complète pour les codes de transfert radiatif 3D et il permet de facilement définir la structure physique de différents objets astrophysiques en créant, manipulant, et mélangeant plusieurs composantes physiques telles que des sources sphériques, des disques et des jets moléculaires. Le but premier de GASS est la production de structures physiques en 3D et de simplifier le post-traitement des cubes hyper-spectraux en utilisant les différents outils d'analyse tels que: l'affichage des spectres ou des cartes de flux intégrés, ou encore la simulation d'observations interférométriques. GASS est gratuitement mis à disposition, sur demande, à la communauté scientifique (site internet en construction) comme une application autonome pour Mac OS X, Windows et, de manière générale, n'importe quel système d'exploitation basé sur le noyau Unix. Une version "script" de MatLab est aussi disponible.

Après cette thèse, je poursuivrai le développement de GASS et, par exemple, j'ai pour objectifs d'améliorer l'interface graphique (GUI) ou d'implémenter plus d'options de LIME dans une future version du code. Je prévois également d'étendre les possibilités de GASS à d'autres codes de transfert radiatif tel que RADMC-3D ou MC3D par exemple. Au sein du projet STOP, il est prévu d'implémenter GASS en tant qu'Observatoire Virtuel (OV) intégré à un service web disponible à la communauté.

Avec le développement de GASS, j'ai pu travailler sur différent types d'objets impliqués dans le processus de formation d'étoiles, des cœurs pré-stellaires aux disques proto-planétaires. En ce qui concerne les cœurs pré-stellaires, une modélisation 3D n'est pas obligatoire pour les étudier vu qu'ils sont supposés être approximativement sphériques, néanmoins, j'ai montré lors de ma thèse qu'une approche 3D peut tout aussi être appropriée pour ce genre d'objet. En partant de la structure physique déjà existante du cœur pré-stellaire L1544 (Keto et al., 2014), j'ai réalisé une nouvelle modélisation de la raie de l'eau $1_{1,0}$–$1_{0,1}$ récemment détectée (par Herschel/HIFI) en direction de cet objet. C'est la première fois qu'une transition de l'eau est observée dans un objet aussi jeune. Les premières études de cette raie de l'eau ont été faites avec une approche LVG, mais un résultant différent est obtenu avec une méthode complète de transfert radiatif non-ETL. En effet, la structure physique obtenue par l'approche LVG donne une émission de raies (3.5 fois plus grande) et du continuum (2 fois plus grande) différente de celle obtenue en utilisant la même structure mais avec un traitement de transfert radiatif complet. J'ai donc trouvé une nouvelle estimation du profil d'abondance de l'eau et de l'opacité de la poussière afin de correctement reproduire les observations de l'émission des raies et du continuum.

Cette étude a été couplée à une modélisation chimique détaillée utilisant à la fois la phase gazeuse et la chimie à la surface des grains. Le résultat de cette étude chimique est double: *(1)* nous sommes parvenus à reproduire approximativement le profil de l'abondance de l'eau nouvellement estimé avec LIME et *(2)* un profil de l'abondance de l'eau deutérée a été obtenu à partir de cette chimie. J'ai utilisé ce dernier ainsi que d'autres profils d'abondance (dérivés du profil de l'eau associé à plusieurs rapports D/H constants) pour prédire, avec GASS et LIME, l'émission de la raie $1_{0,1}$–$0_{0,0}$ de HDO. Je l'ai comparée à la transition observée avec APEX, mais tous les modèles prédisent une émission trop faible par rapport à la sensibilité des observations. En outre, j'ai montré que des observations réalisées avec des télescopes à antenne unique ou des interféromètres ne peuvent pas détecter cette transition (en considérant un temps d'observation raisonnable), limitant ainsi la détectabilité de l'eau deutérée dans les cœurs pré-stellaires.

Contrairement aux cœurs pré-stellaires, une proto-étoile de Classe 0 comme IRAS16293 nécessite une modélisation 3D pour prédire correctement l'émission des raies de la plupart des espèces. En effet, cette proto-étoile est composée de multiples sources et de multiples jets bipolaires. Pour tenir compte de ces différentes structures simultanément, une modélisation 3D précise est nécessaire. Dans cette source, je me suis concentré sur l'ionisation car elle joue un rôle important dans la chimie de l'environnement proto-stellaire. Pour ce faire, j'ai beaucoup étudié HCO^+ et N_2H^+ car un grand nombre de transitions, couvrant un large éventail de niveaux d'énergie ($4 - 389\,K$), est disponible.

À partir de précédents résultats ETL et LVG obtenus avant le début de ma thèse, je savais déjà qu'une partie importante de l'émission de HCO^+ venait d'un des jets moléculaires. De là, j'ai décidé d'implémenter dans GASS un modèle 3D d'outflow, afin de décrire correctement la structure physique de l'outflow responsable de la majorité de l'émission de HCO^+. Cette étude vise à donner de meilleures contraintes sur les paramètres physiques de l'outflow et j'obtiens $T_{kin} = 200\,K$ et $n(H_2) = 5.5 \times 10^6\,cm^{-3}$ avec $X(HCO^+) = 4 \times 10^{-9}$.

J'ai combiné cette structure d'outflow avec un nuage en avant-plan, responsable de l'absorption observée pour certaines transitions, et une structure d'enveloppe, responsable uniquement d'une partie mineure de l'émission totale. Le nuage en avant-plan est froid ($\leqslant 30\,K$) et peu dense ($n(H_2) \leqslant 1 \times 10^4\,cm^{-3}$). La structure de l'enveloppe à grande échelle a déjà été déterminée par des études précédentes (Crimier et al., 2010), mais j'ai utilisé le code chimique Nautilus pour estimer les profils d'abondance de l'enveloppe, à la fois pour HCO^+ et N_2H^+ , en faisant varier plusieurs paramètres, dont le taux d'ionisation par rayon cosmique. Ce dernier est plus élevé ($\geqslant 5 \times 10^{-17}\,s^{-1}$) que la valeur standard au voisinage solaire de $1.3 \times 10^{-17}\,s^{-1}$, mais le nuage complexe de ρ Ophiuchus est connu pour son haut taux d'ionisation par rayons cosmiques (Hunter et al., 1994; Doty et al., 2004; Bottinelli et al., 2014).

L'étude de multiples isotopologues dans cette source a aussi permis d'obtenir divers taux de fractionnement tel que $^{16}O/^{18}O = 500 \pm 50$, $H^{12}CO^+/H^{13}CO^+ = 50 \pm 5$ et $D^{12}CO^+/D^{13}CO^+ = 40^{+5}_{-10}$ mais également d'étudier le taux de deutération de HCO^+ et de N_2H^+.

Grâce aux nombreuses observations interférométriques en direction de cet objet, il est clairement prouvé que la structure à petite échelle, à la fois de la source A et de la source B, est en réalité extrêmement compliquée. J'ai commencé à étudier la structure à petite échelle de la source B en utilisant plusieurs images interférométriques du continuum provenant du VLA, SMA et ALMA. L'objectif est de contraindre les propriétés physiques (température et densité de H_2) de cette source à petite échelle ($< 100\,AU$). Je me suis concentré en particulier sur la source B en raison de sa forme sphérique et de sa très forte émission du continuum. Cette source n'a pas d'outflows, il n'y a donc pas d'émission free-free qui contamine la distribution spectrale d'énergie (SED) du continuum de la poussière à basses fréquences. Une fois le modèle sphérique de la source généré avec GASS et le transfert radiatif résolu avec LIME, je compare le résultat avec les observations interférométriques. Les paramètres ajustés sont le flux total, l'intensité au pic et la taille de l'émission du continuum. Cette comparaison est directement faite dans GASS grâce à ses outils de post-traitement. Une fois que le meilleur ajustement est trouvé, j'ai utilisé le profil de température et de densité de H_2 obtenu pour la source afin de prédire l'émission de $H^{13}CN$ autour de la source B. L'émission de cette espèce, en forme d'anneau couplée à une forte absorption au centre de la source, résulte de l'opacité de la poussière très élevée dans la région la plus interne de la source. La combinaison de continuum de la poussière et de l'émission de la raie, associée à la fois au profil spatial et spectral de la source, va permettre d'obtenir de fortes contraintes sur la structure physique à petite échelle de cette source particulière. Cette étude est toujours en cours et elle fait partie d'une étude approfondie en collaboration avec L. Loinard et al. (UNAM, Morelia, Mexique). Je dirigerai le premier article étudiant la structure physique de cet objet.

Ces études démontrent que la combinaison de GASS et de LIME est un outil puissant pour étudier à la fois la structure physique à petite échelle et à grande échelle des proto-étoiles.

Au cours de ma thèse, grâce au développement de GASS, j'ai été impliqué dans l'étude de deux disques proto-planétaires différents : le disque massif du Hamburger de Gomez (IRAS18059-3211; ci-après GoHam) et le "proplyd" 203–506. Comme pour les outflows, j'ai dû améliorer GASS pour qu'il soit en mesure de créer des modèles de disques proto-planétaires. Cela a été un grand bond en avant pour GASS, car le code était désormais en mesure de modéliser les principales structures que l'on peut trouver au cours du processus de formation des étoiles: des structures sphériques, des outflows et des structures de disque. Prochainement, je prévois d'améliorer le modèle de disque proto-planétaire de GASS en incorporant, par exemple, plusieurs autres options pour mieux décrire les propriétés physiques des disques, en particulier à petites échelles. Les deux travaux suivants ont été effectués en collaboration avec Olivier Berné et Jason Champion de l'IRAP.

Le premier travail est l'étude d'un embryon planétaire dans le disque GoHam. Le but de cette étude est la prédiction de l'émission moléculaire autour de ce disque proto-planétaire évolué. Il est situé autour d'une étoile de type A et est quasiment orienté sur la tranche ("edge-on"). Des études récentes (Bujarrabal et al., 2009; Berné et al., 2015) ont déterminé, grâce aux cartes d'émission de ^{13}CO observées par le SMA et le VLT/VIZIR, qu'un objet dense est situé dans la partie sud du disque. Ce "clump" est supposé être l'embryon d'une proto-planète, mais une meilleure résolution spatiale est nécessaire pour donner une meilleure contrainte sur sa taille et sa forme.

Dans le cadre d'une demande de temps ALMA Cycle 4, nous avons prédit l'émission de ^{13}CO, HCN et $H^{13}CN$ dans cette source. Ces molécules sont de bons traceurs du gaz dense donc elles peuvent bien différencier l'émission provenant du disque ou du clump, aidant ainsi à déterminer, par exemple, la masse et la taille du clump. La structure physique du disque (Bujarrabal et al., 2008) a été modélisée avec GASS en tenant compte de la structure (supposée) sphérique du clump; l'émission résultante est donnée par LIME. Nous utilisons le bruit *rms* prédit par l'outil d'observation d'ALMA (AOT) et une résolution angulaire de $0.2''$. Les cartes simulées de l'émission des précédentes espèces observées par ALMA sont représentées sur la Fig. 5.6.

La deuxième étude concerne la photo-évaporation de HCO^+ dans le disque 203–506. Quand les disques proto-planétaires sont irradiés par un rayonnement UV ou X provenant de leur étoile centrale ou des étoiles massives à proximité, leur surface peut être chauffée à des températures élevées, permettant au gaz de sortir du champ gravitationnel. Ce processus, appelé photo-évaporation, est d'une importance majeure pour comprendre l'évolution dynamique des disques proto-planétaires (Alexander et al., 2014). Les "proplyds" sont une classe de disques pour lesquels la photo-évaporation est dominée par des photons UV. Pendant les observations ALMA Cycle 1 de la Barre d'Orion, le proplyd 203–506 a été détecté par chance grâce à son intense émission de la raie

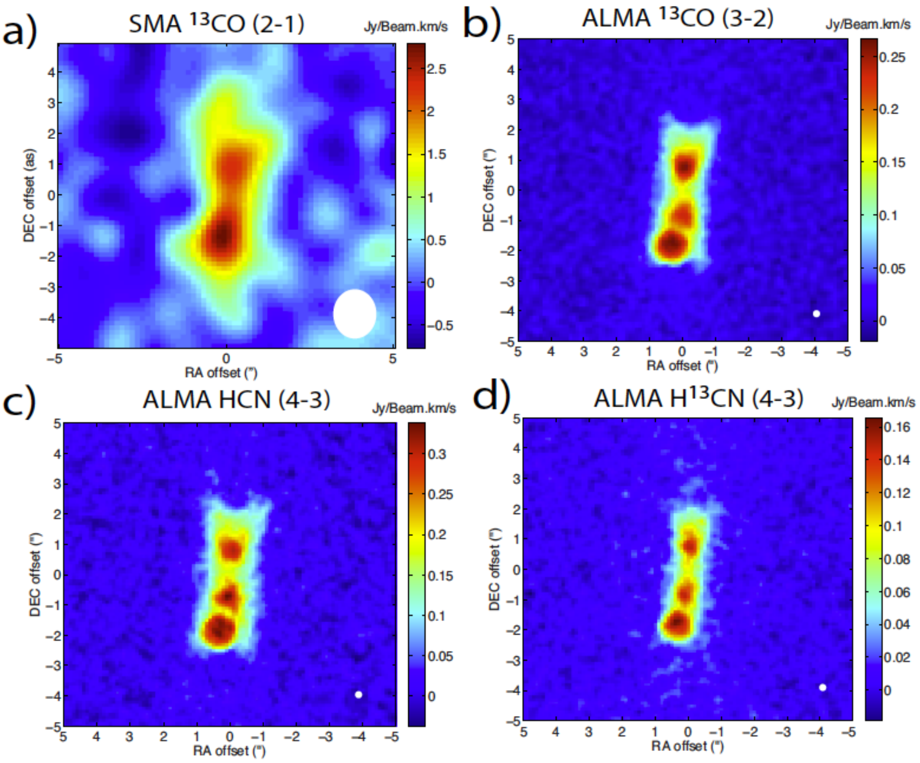

Figure 5.6 – **a)** Carte intégrée en vitesse du ^{13}CO (2-1) dans GoHam, observé par le SMA (tiré de Bujarrabal et al., 2009). L'excès d'émission au Sud est causé par la présence de GoHam b. **b) c) d)** Cartes intégrées en vitesse des raies modélisées (en utilisant la combinaison de GASS et de LIME) dans GoHam en incluant un clump moléculaire de 1.5 masses de Jupiter avec une densité de 5×10^7 cm^{-3} et une température de 50 K. Ce modèle est le meilleur ajustement de ^{13}CO (2-1) comparé aux observations SMA. Dans chaque carte, la taille du lobe est indiquée par une ellipse blanche.

HCO$^+$ (4-3). Ce disque possède des propriétés uniques vu que l'émission de raies moléculaires n'est pas prévue pour les proplyds (Eisner et al., 2016). Un autre aspect surprenant de 203–506 est le profil de la raie de HCO$^+$: vu que le disque est observé presque parfaitement par la tranche, on s'attendrait à observer un double pic dû à la rotation Képlérienne, tandis que la raie observée possède un unique pic. Il est probable que la raie de HCO$^+$ émane du gaz moléculaire chaud et que ce gaz ne soit pas gravitationnellement lié à l'étoile. Ce HCO$^+$ se trouverait à la base d'un flot de photo-évaporation qui s'échappe lentement du disque, perpendiculairement à la surface de ce dernier.

Afin d'obtenir de nouvelles informations sur les propriétés de 203–506 et sur la physique de photo-évaporation externe, ce proplyd fait l'objet d'une proposition ALMA Cycle 4. Nos objectifs sont: *(1)* de résoudre spatialement et spectralement le flot de photo-évaporation et déterminer sa densité et sa vitesse et *(2)* de déterminer la masse de l'étoile et du disque. Nous avons prédit l'émission de HCO$^+$ provenant à la fois du flot de photo-évaporation et du disque lui-même, en utilisant GASS et LIME. Dans GASS, ce proplyd a été modélisé en 3D en utilisant une combinaison du modèle de structure de disque et du modèle de structure d'outflow, ce qui montre (à nouveau) que GASS est capable de traiter des structures 3D complexes. L'observation de HCO$^+$ prédite pour ALMA est représentée sur la Fig. 5.7. Nous utilisons le bruit *rms* prédit par l'outil d'observation ALMA (AOT) et une résolution angulaire de 0.1″.

Aidée par les observations ALMA, cette étude fournira des contraintes robustes sur l'évolution dynamique des disques irradiés par un champ de radiation externe et sur leur durée de vie. Si cette dernière valeur est courte (10^{4-5} ans), nous serons en mesure de confirmer que les proplyds sont des objets transitoires, où la formation planétaire devrait être rapide, si elle se produit.

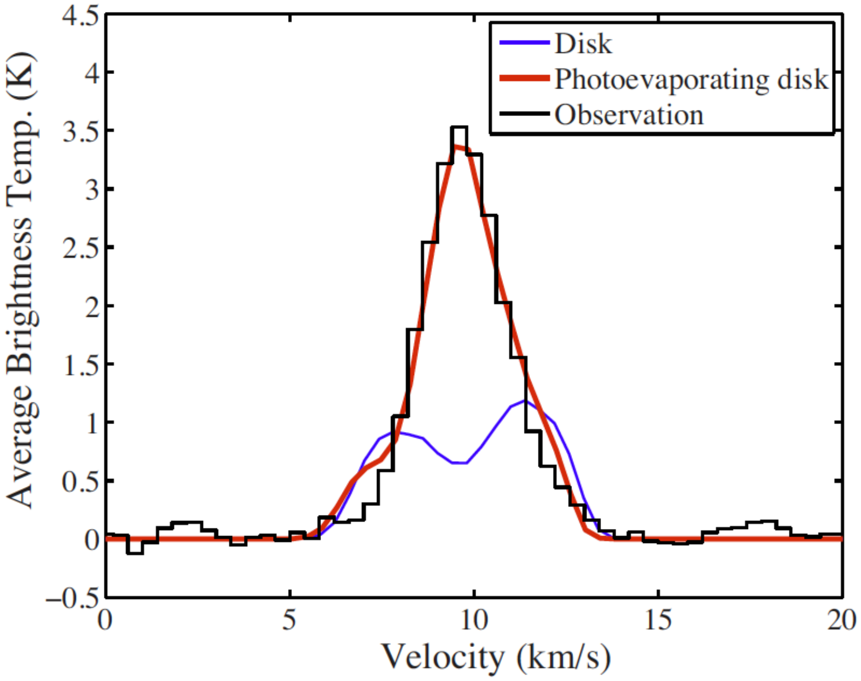

Figure 5.7 – Raie de HCO$^+$ observé par ALMA pendant le Cycle 1 (en noir). La courbe rouge montre le résultat du meilleur ajustement du modèle de transfert radiatif. La courbe bleue représente le même modèle mais sans le flot de photo-évaporation.

Notre connaissance du milieu interstellaire et des régions de formation d'étoiles a fait un grand bond en avant au cours des dernières décennies. Nous sommes au début de notre compréhension de la naissance des étoiles et de la complexité chimique qui se produit dans leur environnement à différents stades d'évolution. Des cœurs pré-stellaires aux disques proto-planétaires évolués, nous avons suivi cette richesse moléculaire. L'héritage de *Herschel* nous a laissé beaucoup de questions sans réponses et beaucoup de données à analyser et à comprendre. La complexité et la masse de données d'observations disponibles augmentent très rapidement et les instruments et les interféromètres actuels comme ALMA et NOEMA repoussent les limites de la résolution spatiale et de la sensibilité (e.g. le disque proto-planétaire HL Tau, Brogan et al., 2015). Les modélisations et simulations numériques sont de plus en plus complexes, essayant toujours de comprendre et de reproduire le plus fidèlement possible des observations de plus en plus précises.

Le futur *Square Kilometre Array* (SKA) sera disponible à la communauté scientifique autour de 2020. L'un des principaux objectifs de SKA est la recherche des planètes et de la vie. Sa résolution spatiale impressionnante ($< 0.1''$ at 1.4 GHz) nous permettra de regarder précisément à l'intérieur de la formation des disques et de détecter la présence de proto-planètes géantes à travers les gaps qu'elles laissent dans le disque, en orbitant autour de l'étoile centrale. En outre, la gamme de fréquences de SKA1 LOW (50–350 MHz) et SKA1 MID (350 MHz–14 GHz) couplée à sa haute sensibilité va nous aider dans notre recherche des molécules pré-biotiques et des molécules organiques complexes (toutes deux ayant des raies émettant à ces fréquences) autour d'étoiles en formation. SKA va ouvrir une nouvelle ère dans le traitement des données (projet Big Data) et cette énorme masse d'information doit être analysée avec de puissants codes astrochimiques et de transfert radiatif. À long terme, la combinaison de puissants instruments, de télescopes, et de modélisation ouvrira une nouvelle fenêtre pour étudier l'origine de la vie.

APPENDIX A

THE GRAPHICAL USER INTERFACE OF GASS

The Graphical User Interface of GASS is shown in this appendix. It is composed of several tabs, each one of them having a particular purpose and reflecting a function of GASS. They are made of several buttons, pop-up menus, radio buttons,... allowing to set the different parameters. In addition, warnings and progress bars are implemented to inform the user during the execution of the code. Key figures are displayed to ease the visualisation of the 3D models. The GUI of GASS is subjected to recurrent changes since it is in constant evolution to match the need of the users. The figures displayed below may become obsolete in the future.

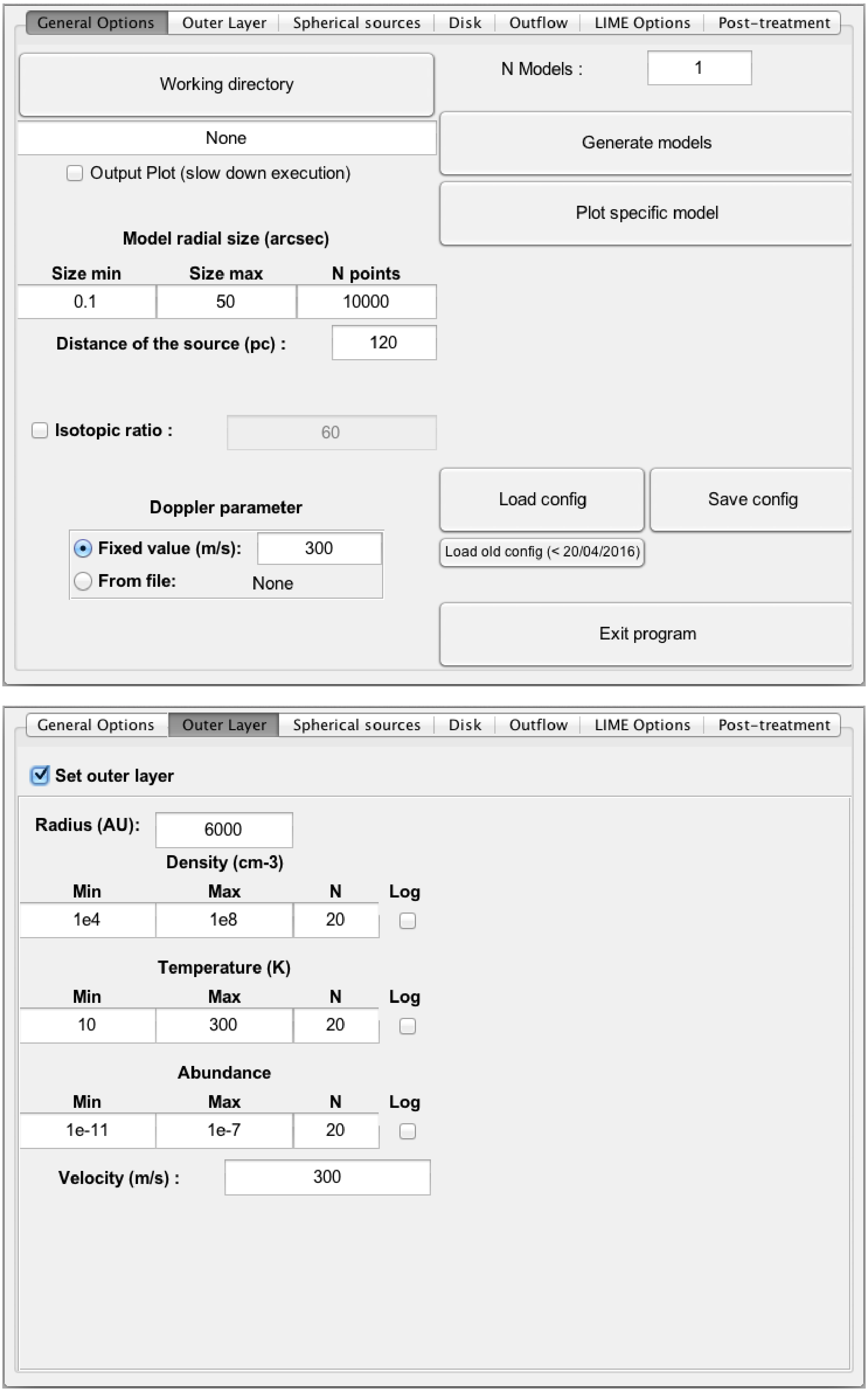

Working directory: None

N Models : 1

☐ Output Plot (slow down execution)

Model radial size (arcsec)

Size min	Size max	N points
0.1	50	10000

Distance of the source (pc) : 120

☐ **Isotopic ratio :** 60

Doppler parameter

● **Fixed value (m/s):** 300

○ **From file:** None

☑ **Set outer layer**

Radius (AU): 6000

Density (cm-3)

Min	Max	N	Log
1e4	1e8	20	☐

Temperature (K)

Min	Max	N	Log
10	300	20	☐

Abundance

Min	Max	N	Log
1e-11	1e-7	20	☐

Velocity (m/s) : 300

Figure A.1 – *Top panel:* General options of GASS. *Bottom panel:* Outer layer options of GASS.

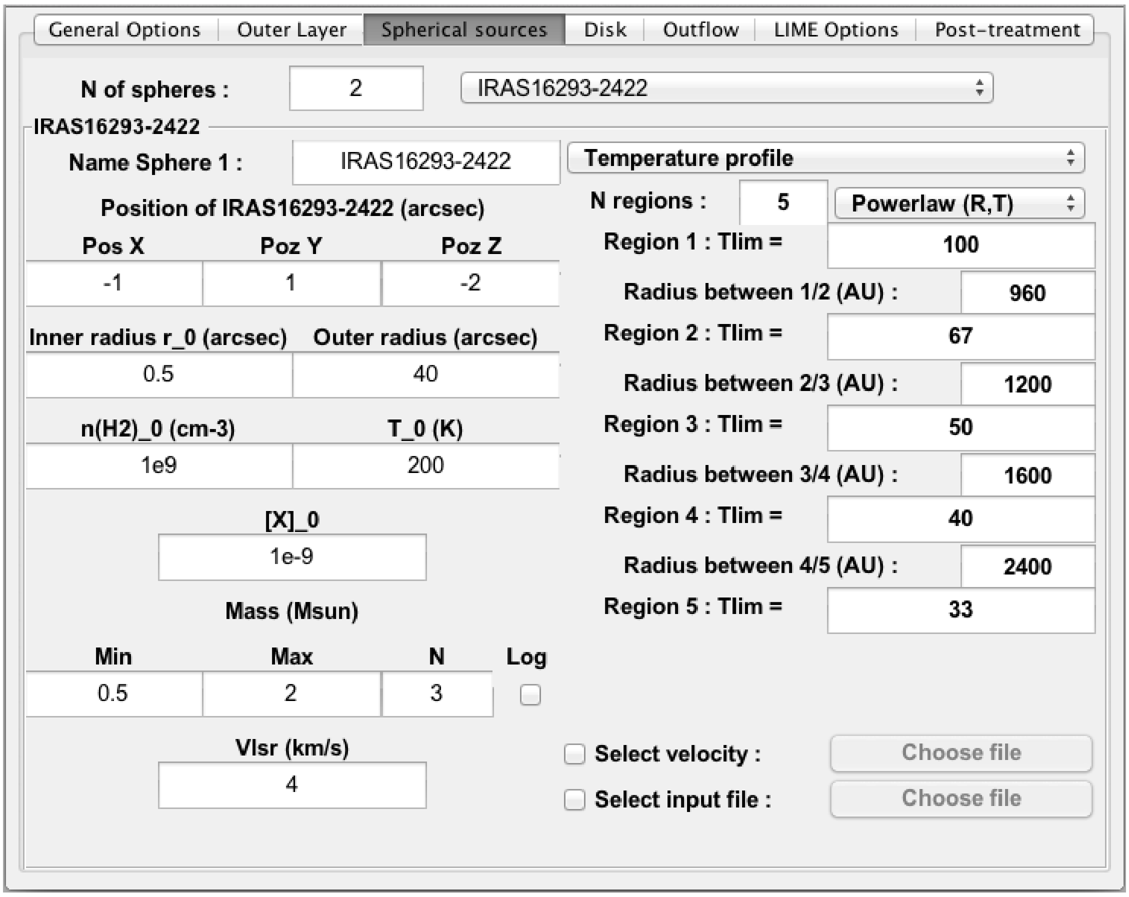

N of spheres : 2 — IRAS16293-2422

IRAS16293-2422

Name Sphere 1 : IRAS16293-2422

Position of IRAS16293-2422 (arcsec)

Pos X	Poz Y	Poz Z
-1	1	-2

Inner radius r_0 (arcsec)	Outer radius (arcsec)
0.5	40

n(H2)_0 (cm-3)	T_0 (K)
1e9	200

[X]_0: 1e-9

Mass (Msun)

Min	Max	N	Log
0.5	2	3	☐

Vlsr (km/s): 4

Temperature profile

N regions : 5 — Powerlaw (R,T)

Region 1 : Tlim = 100

Radius between 1/2 (AU) : 960

Region 2 : Tlim = 67

Radius between 2/3 (AU) : 1200

Region 3 : Tlim = 50

Radius between 3/4 (AU) : 1600

Region 4 : Tlim = 40

Radius between 4/5 (AU) : 2400

Region 5 : Tlim = 33

☐ Select velocity :

☐ Select input file :

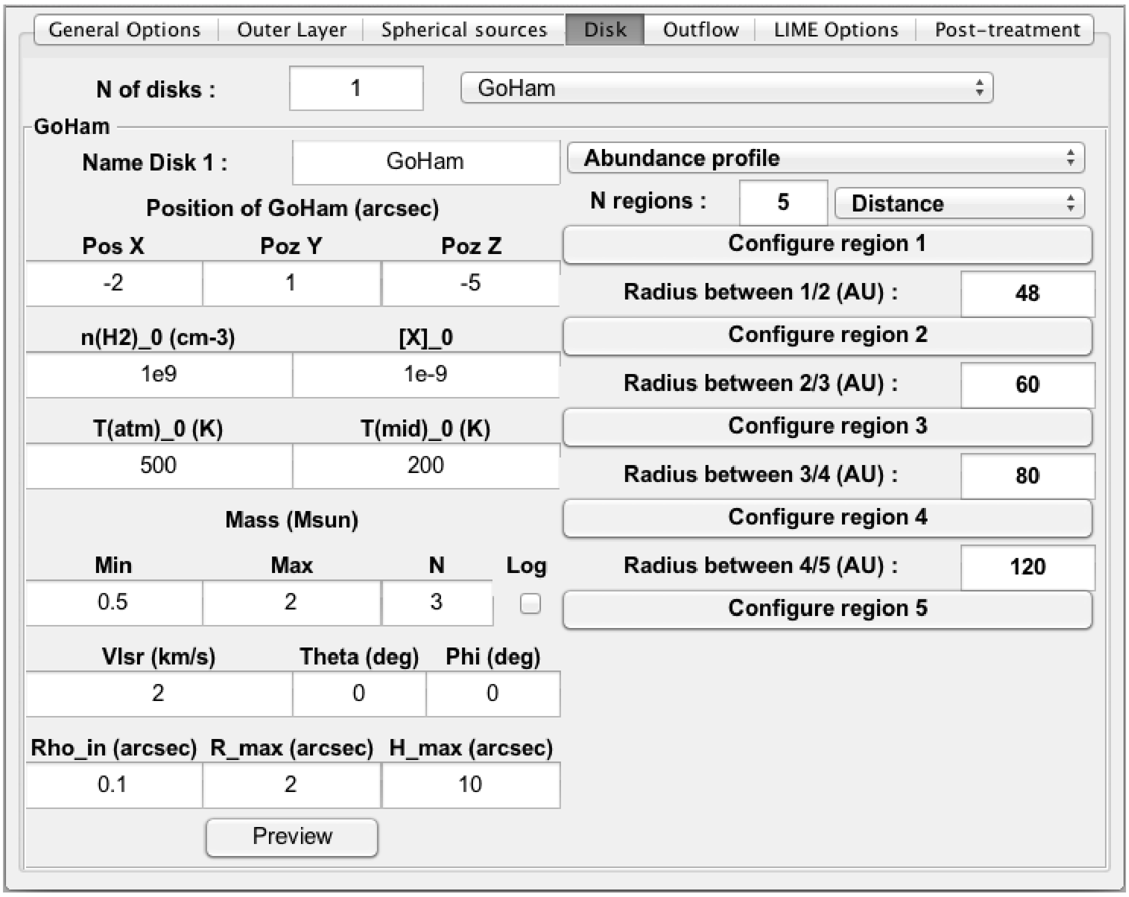

N of disks : 1 — GoHam

GoHam

Name Disk 1 : GoHam

Position of GoHam (arcsec)

Pos X	Poz Y	Poz Z
-2	1	-5

n(H2)_0 (cm-3)	[X]_0
1e9	1e-9

T(atm)_0 (K)	T(mid)_0 (K)
500	200

Mass (Msun)

Min	Max	N	Log
0.5	2	3	☐

Vlsr (km/s)	Theta (deg)	Phi (deg)
2	0	0

Rho_in (arcsec)	R_max (arcsec)	H_max (arcsec)
0.1	2	10

Abundance profile

N regions : 5 — Distance

Radius between 1/2 (AU) : 48

Radius between 2/3 (AU) : 60

Radius between 3/4 (AU) : 80

Radius between 4/5 (AU) : 120

Figure A.2 – *Top panel:* Spherical sources options of GASS. *Bottom panel:* Disks options of GASS.

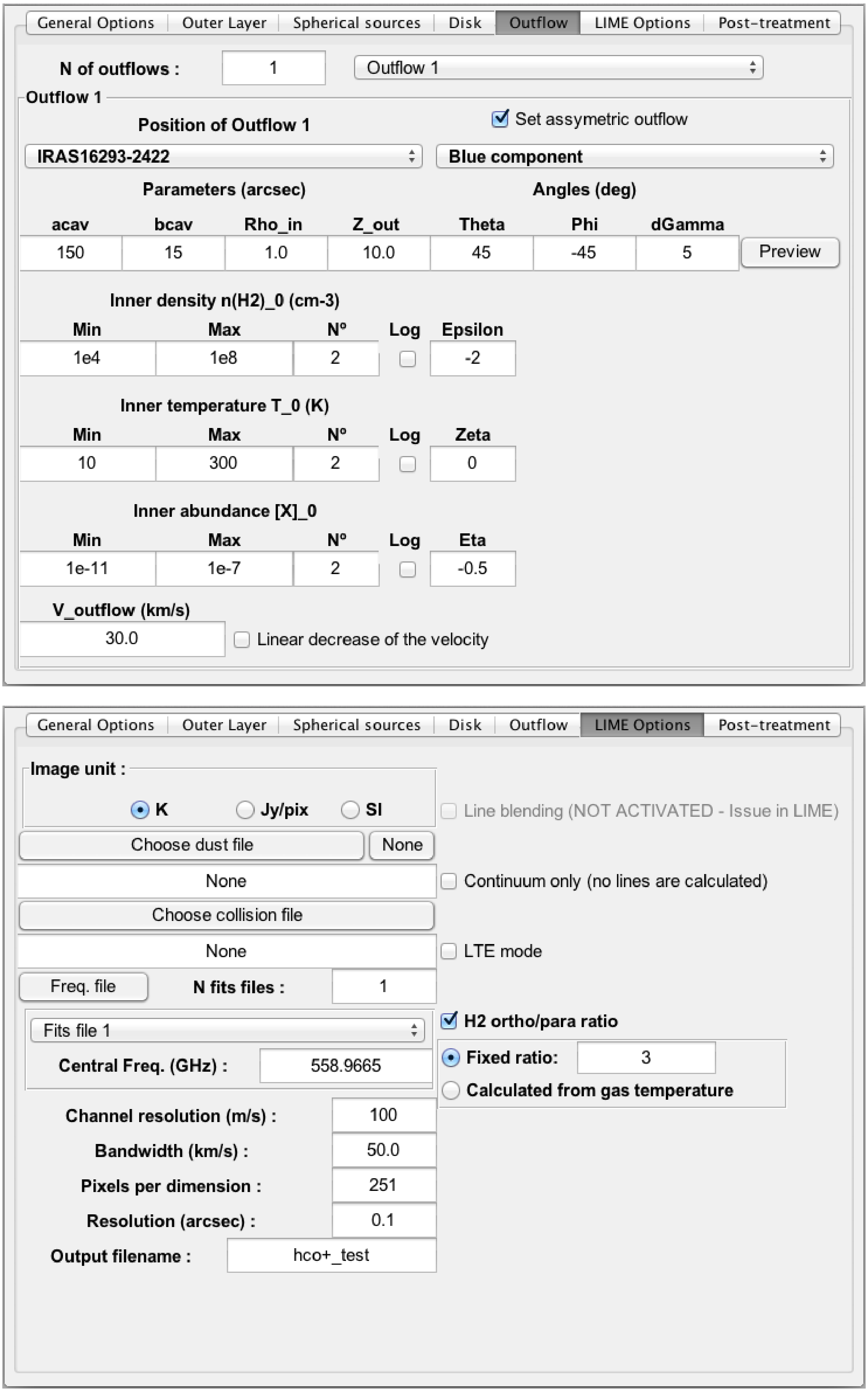

N of outflows : 1

Outflow 1

Outflow 1

Position of Outflow 1: IRAS16293-2422

☑ Set assymetric outflow

Blue component

Parameters (arcsec)

Angles (deg)

acav	bcav	Rho_in	Z_out	Theta	Phi	dGamma
150	15	1.0	10.0	45	-45	5

Inner density n(H2)_0 (cm-3)

Min	Max	Nº	Log	Epsilon
1e4	1e8	2	☐	-2

Inner temperature T_0 (K)

Min	Max	Nº	Log	Zeta
10	300	2	☐	0

Inner abundance [X]_0

Min	Max	Nº	Log	Eta
1e-11	1e-7	2	☐	-0.5

V_outflow (km/s): 30.0

☐ Linear decrease of the velocity

Image unit : ● K ○ Jy/pix ○ SI

☐ Line blending (NOT ACTIVATED - Issue in LIME)

None

☐ Continuum only (no lines are calculated)

None

☐ LTE mode

N fits files : 1

Fits file 1

Central Freq. (GHz) : 558.9665

☑ H2 ortho/para ratio

● Fixed ratio: 3

○ Calculated from gas temperature

Channel resolution (m/s) : 100

Bandwidth (km/s) : 50.0

Pixels per dimension : 251

Resolution (arcsec) : 0.1

Output filename : hco+_test

Figure A.3 – *Top panel:* Outflow options of GASS. *Bottom panel:* LIME options of GASS.

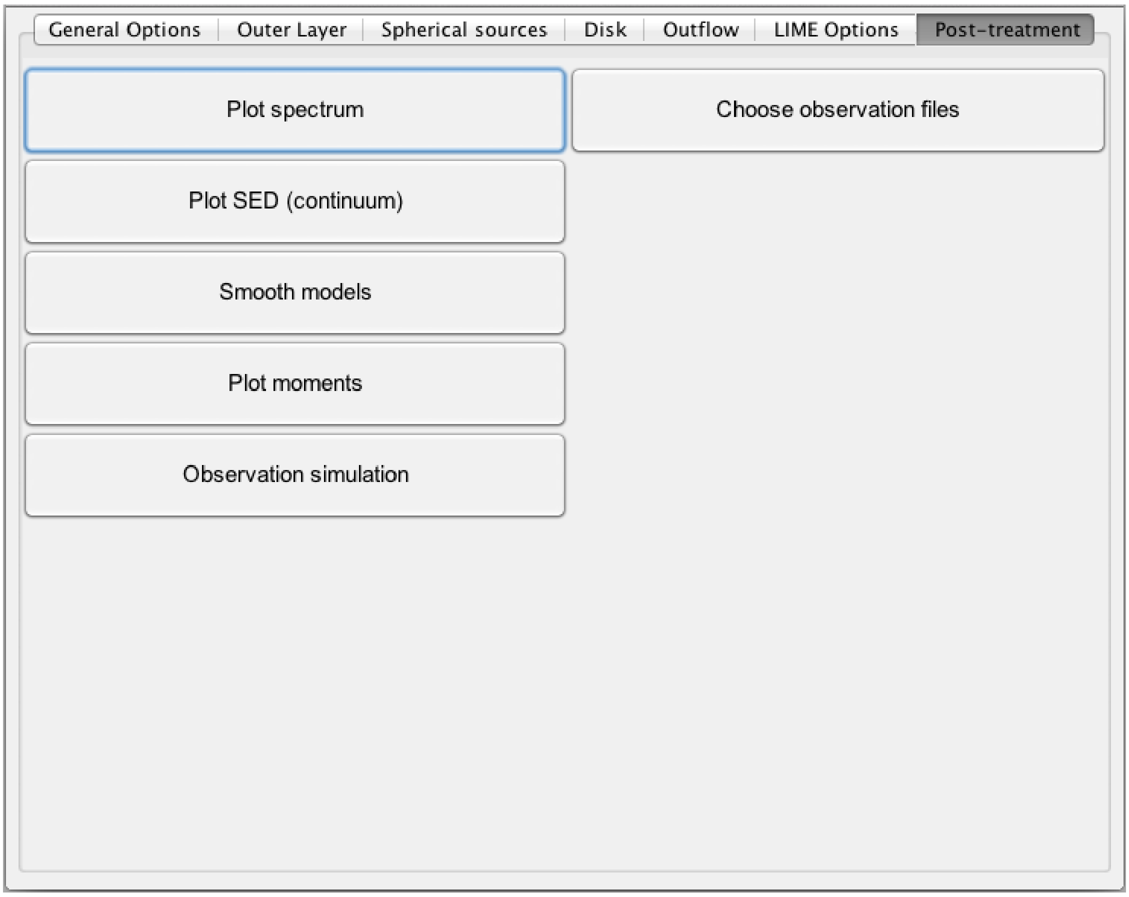

Figure A.4 – Post-treatment options of GASS.

APPENDIX B

PUBLICATIONS RELATED TO THIS THESIS

In this appendix are presented the different publications related to this thesis:

1. *Detectability of deuterated water in pre-stellar cores*, **Quénard, D.**, Taquet, V., Vastel, C., Caselli, P., and Ceccarelli, C.; 2016, A&A 585, A36
2. *3D modelling of* HCO^+ *and its isotopologues in the low-mass proto-star IRAS16293-2422*, **Quénard, D.**, Bottinelli S., Caux, E.; submitted to A&A.
3. *Modelling the 3D physical structure of astrophysical sources with GASS*, **Quénard, D.**, Bottinelli S., Caux, E.; in prep., to be submitted before the end of the thesis.

A&A 585, A36 (2016)
DOI: 10.1051/0004-6361/201527008

Astronomy & Astrophysics

Detectability of deuterated water in prestellar cores*

D. Quénard[1,2], V. Taquet[3], C. Vastel[1,2], P. Caselli[4], and C. Ceccarelli[5,6]

[1] Université de Toulouse, UPS-OMP, IRAP, 31028 Toulouse Cedex 4, France
e-mail: dquenard@irap.omp.eu
[2] CNRS, IRAP, 9 Av. colonel Roche, BP 44346, 31028 Toulouse Cedex 4, France
[3] Leiden Observatory, Leiden University, PO Box 9513, 2300 RA Leiden, The Netherlands
[4] Max-Planck Institute for Extraterrestrial Physics, Giessenbachstrasse 1, 85748 Garching, Germany
[5] Université Grenoble Alpes, IPAG, 38000 Grenoble, France
[6] CNRS, IPAG, 38000 Grenoble, France

Received 20 July 2015 / Accepted 23 October 2015

ABSTRACT

Context. Water is an important molecule in the chemical and thermal balance of dense molecular gas, but knowing its history throughout the various stages of the star formation is a fundamental problem. Its molecular deuteration provides us with a crucial clue to its formation history. H_2O has recently been detected for the first time towards the prestellar core L1544 with the *Herschel* Space Observatory with a high spectral resolution (HIFI instrument).

Aims. Prestellar cores provide the original reservoir of material from which future planetary systems are built, but few observational constraints exist on the formation of water and none on its deuteration before the collapse starts and a protostar forms at the centre. We report on new APEX observations of the ground state $1_{0,1}$–$0_{0,0}$ HDO transition at 464 GHz towards the prestellar core L1544. The line is undetected, and we present an extensive study of the conditions for its detectability in cold and dense cloud cores.

Methods. The water and deuterated water abundances have been estimated using an advanced chemical model simplified for the limited number of reactions or processes that are active in cold regions (<15 K). In this model, water is removed from the gas phase by freezing onto dust grains and by photodissociation. We use the LIME radiative transfer code to compute the expected intensity and profile of both H_2O and HDO lines and compare them with the observations.

Results. The predicted H_2O line intensity of the LIME model using an abundance and structure profile, coupled with their dust opacity, is over-estimated by a factor of ~3.5 compared to the observations. We present several ad hoc profiles that best-fit the observations and compare the profiles with results from an astrochemical modelling, coupling gas phase and grain surface chemistry. The water deuteration weakly depends on the external visual extinction, the external ISRF, and contraction timescale. The [HDO]/[H_2O] and [D_2O]/[H_2O] abundance ratios tend to increase towards the centre of the core up to 25% and ~8%, respectively.

Conclusions. Our comparison between observations, radiative transfer, and chemical modelling shows the limits of detectability for singly deuterated water, through the ground-state transitions $1_{0,1}$–$0_{0,0}$ and $1_{1,1}$–$0_{0,0}$ at 464.9 and 893.6 GHz, respectively, with both single-dish telescope and interferometric observations. This study also highlights the need of a detailed benchmark amongst different radiative transfer codes for this particular problem of water in prestellar cores.

Key words. ISM: abundances – astrochemistry – line: identification – ISM: molecules – ISM: individual objects: L1544

1. Introduction

Water is an important molecule not only on Earth but also in space. Indeed, since it is formed by the two most abundant elements in the Universe that bind in molecules, water governs the chemical composition and the thermal balance of the interstellar dense molecular gas. This is also the gas from which stars are formed, so that water influences the whole star formation process at various levels in the different phases (e.g. Caselli & Ceccarelli 2012). In molecular clouds, iced water is present in large quantities, up to half the oxygen elemental abundance, and is synthesised on the interstellar grains (e.g. Boogert et al. 2015). In the denser regions inside the molecular clouds, which are the prestellar cores that will eventually form stars, water is still mostly iced (Caselli et al. 2012). The same water, formed in those first two stages, is then found in the gas phase where the dust is warm enough (≥100 K) in the hot cores, hot corinos, and protostellar molecular shocks (e.g. van Dishoeck et al. 2014). It is then again iced and gaseous in the different warm and cold, respectively, zones of the protoplanetary disks, where planets form (e.g. Carr & Najita 2008; Podio et al. 2013). Finally, water is the major component of the volatiles in comets (e.g. Bockelée-Morvan et al. 2014).

In summary, we see water throughout all the stages of the solar-type star forming process up to the leftovers of this process, represented by comets and meteorites. Nevertheless, we do not fully know its whole history: how it evolves from molecular clouds to comet ices and, perhaps, to terrestrial oceans. A crucial aspect in reconstructing the water history is provided by its deuteration by water molecules with one or two deuterium atoms. This is because molecular deuteration is very sensitive to the moment the molecule is formed, the temperature, and also the environment. And since water changes continuously from ice to vapour, it keeps memory of most, if not all, its past formation history (e.g. Ceccarelli et al. 2014). So far, the water deuteration has been measured in only a handful of objects, all of them warm: hot cores, hot corinos, and protostellar molecular

---

* Molecular line data (FITS cube) are only available at the CDS via anonymous ftp to cdsarc.u-strasbg.fr (130.79.128.5) or via http://cdsarc.u-strasbg.fr/viz-bin/qcat?J/A+A/585/A36

shocks (e.g. Coutens et al. 2012, 2013, 2014; Taquet et al. 2013b; Persson et al. 2014). In cold molecular clouds, only the upper limits of the iced deuterated water exist (Dartois et al. 2003; Parise et al. 2003; Aikawa et al. 2012). In prestellar cores, no attempt to measure the deuterated water has been published so far.

This article presents the first upper limit on HDO/H_2O in a prestellar core, L1544 (Sect. 2), by combining *Herschel* observations (Caselli et al. 2012) with new observations obtained at the APEX telescope (Sect. 3). We also report a radiative transfer and chemical study of the ortho-H_2O and HDO fundamental lines in L1544 (Sects. 4 and 5, respectively), and show that the two HDO fundamental lines at 464 and 893 GHz lines are not observable with the present facilities. A final section (Sect. 6) summarises the results.

2. The prestellar core L1544

L1544 is a prototypical starless core in the Taurus molecular cloud complex ($d \sim 140$ pc) on the verge of gravitational collapse (Caselli et al. 2002a and references within). It is characterised by high density in its centre (peak density of 2×10^7 cm^{-3}; Keto & Caselli 2010), low temperature (~7 K; Crapsi et al. 2007), and high CO depletion in its centre, accompanied by a high degree of molecular deuteration (Caselli et al. 2003; Crapsi et al. 2005; Vastel et al. 2006).

Its physical and dynamical structure has recently been reconstructed by Caselli et al. (2012) and Keto et al. (2014) using the numerous existing observations towards L1544. Among them, the recent detection of water vapour by the *Herschel* Space Observatory is spectacular because it represents the very first water detection in a prestellar core (Caselli et al. 2010, 2012). The first of these two *Herschel* observations was made with the wide-band spectrometer (WBS) with a spectral resolution of 1.1 MHz, and water vapour was detected in absorption against the weak dust continuum radiation (~10 mK) in the cloud. Follow-up observations using the High Resolution Spectrometer (HRS) confirmed the absorption and even detected an inverse P-Cygni emission line profile, too narrow to be seen by the WBS, which was predicted by theoretical modelling (Caselli et al. 2010).

This detection provided crucial information for reconstructing the physical and chemical structure of L1544. Indeed, this inverse P-Cygni profile, which is characteristic of gravitational contraction, confirmed that L1544 is on the verge of collapsing. Based on the line shape, Caselli et al. (2012) predict that water is largely frozen into the grain mantles in the interior (≤4000 au) of the L1544 core, where the gaseous H_2O abundance (with respect to H_2) is $<10^{-9}$. This level of water vapour is believed to be caused by non-thermal desorption processes such as (a) the photo-desorption of water molecules from the icy mantles by the far UV photons created locally by the interaction of cosmic rays with H_2 molecules and the far UV starlight; and (b) the exothermicity of the grain surface chemical reactions that releases the products (e.g. H_2O and HDO) in the gas phase (Vasyunin & Herbst 2013; Wakelam et al. 2014). Farther away from the centre (~10^4 AU), where the density is low enough ($\leq 10^4$ cm^{-3}) for the photo-desorption rate not to be overcome by the freeze-out rate, the gaseous H_2O abundance reaches $\sim 1 \times 10^{-7}$, in agreement with predictions from comprehensive chemical models (Hollenbach et al. 2009).

3. Observations

We observed the HDO fundamental transition $1_{0,1}$–$0_{0,0}$ on April 16, 17, 28, 29, and 30, 2013 and November 2 and 3, 2013 towards L1544 ($\alpha_{2000} = 05^h04^m17.21^s$, $\delta_{2000} = 25°10'42.8''$) using the heterodyne instrument (APEX-3) of the APEX observatory. The frequency was centered at 464.92452 GHz to reach the $1_{0,1}$–$0_{0,0}$ ground-state HDO transition, and the RPG eXtended bandwidth Fast Fourier Transform Spectrometer (XFFTS) backend was used to obtain the highest frequency resolution needed for a comparison with the H_2O profile. To be consistent with the H_2O *Herschel*/HIFI observations, we mapped the HDO transition within the *Herschel*/HIFI 40″ beam and reached an rms of 50 mK in about 0.1 km s^{-1} velocity bin, averaging all positions in order to compare both observations. Weather conditions were excellent between 0.2 and 0.7 mm of precipitable water vapour with system temperatures less than 1000 K. Line intensities are expressed in units of main-beam brightness temperature with a main beam efficiency of 60%[1]. The ortho-H_2O (1_{10}–1_{01}) line observation was taken from Caselli et al. (2012) and was observed with *Herschel*/HIFI. The dust continuum emission flux at 557 GHz is 10.2 ± 0.2 mK and the rms noise level is 3.8 mK in the spectrum.

4. H_2O modelling

4.1. LIME radiative transfer model

We ran several radiative transfer modellings of the water emission using LIME, a 3D radiative transfer code (Brinch & Hogerheijde 2010) based on ALI (accelerated lambda iteration) calculations. Created from RATRAN-1D (Hogerheijde & van der Tak 2000), LIME does a full radiative transfer treatment in two steps. The first one is to compute the population level of every molecular transition found in the input collision file of the desired molecule. The collisional excitation rates for ortho-H_2O are not the same if we consider a collision with ortho-H_2 or para-H_2. In the case of L1544, we assume that all the hydrogen is in the para state as required by recent chemical models to produce the high deuterium fraction observed in cold, dense clouds (Flower et al. 2006; Pagani et al. 2007; Troscompt et al. 2009; Sipilä et al. 2013; Kong et al. 2015). We used the o-H_2O - p-H_2 collision value from Dubernet et al. (2009), and we assumed a H_2O ortho-to-para ratio of 3.

To calculate the population level, LIME needs the 3D structure of the source defined in each point of a model as a function of its Cartesian coordinates (X, Y, Z). The source model is usually defined by a few thousand points distributed randomly among a desired radius. Each point is the centre of a 3D cell, and LIME defines the physical properties of the model in each 3D cells (density, temperature, velocity profile, etc.). At least 10 000 points are required to construct the model in order to prevent undersampling. Below 10 000 points, neighbouring 3D cells will be created with different sizes, and non-homogeneous effects will appear in the resulting image after the *ray-tracing*. Thanks to its random distribution, each one of the 10 000 points is located at a unique radius, thus uniquely defined by its physical property. The distribution of points across the model as a function of the radius follows a power law type distribution. This leads to an increasing number of model points per unit volume towards the centre of the cloud, since a finer sampling is needed where the volume densities are higher.

In the second steps, LIME performs a ray-tracing to output the desired image, depending on the user choice of spatial and spectral resolution and of the number of channels, for instance. As a result, a hyper-spectral cube is created for each chosen line

---

[1] `http://www.apex-telescope.org/telescope/efficiency/`

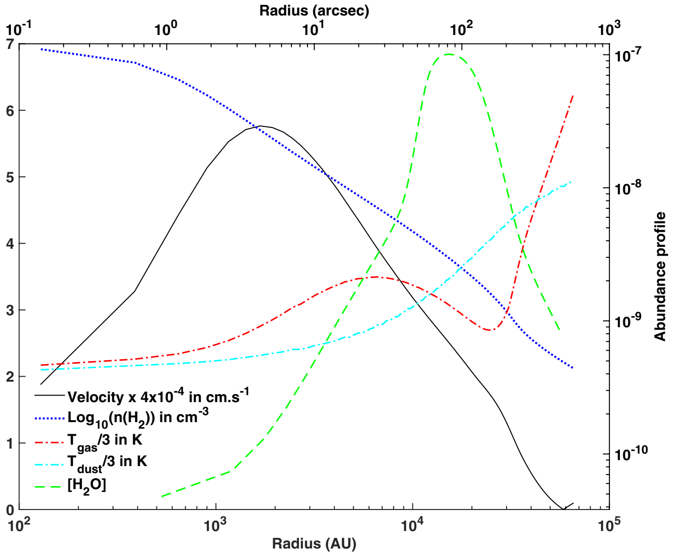

Fig. 1. Gas and dust temperature, density, velocity, and water abundance profiles from Keto et al. (2014). The abundance profile is plotted on a logarthmic scale on the right axis of the figure.

transition. To finish, this cube can be convolved with the beam of the telescope to obtain the spectrum.

The large Einstein coefficient (3.45×10^{-3} s^{-1}) of the H_2O $1_{1,0}$–$1_{0,1}$ transition results in optical depths across the core up to a thousand, depending on excitation, leading to a very non-linear relationship between the opacity and the column density. This opacity effect slows down the computation of the population level of the line and can lead to a wrong excitation. Keto et al. (2014) used MOLLIE (Keto 1990; Keto & Rybicki 2010) to fit their *Herschel*/HIFI data. For the particular problem of water in L1544, MOLLIE has been modified to treat the radiative transfer with an escape probability method. This method optimises the calculation for the optically thick, but highly subthermally excited H_2O line towards L1544. Therefore, LIME and MOLLIE are two distinct ways to treat the water modelling problem, and it is necessary to model both H_2O and HDO with LIME in order to make a consistent comparison. More information about the differences between MOLLIE and a full radiative transfer code such as LIME will be discussed in a dedicated paper.

4.2. Grid results

We used the physical structure as derived by Keto et al. (2014) to solve the molecular excitation of the H_2O transition. Figure 1 shows the structure for a slowly contracting cloud in quasi equilibrium. To reproduce the observed line broadening, we considered a Doppler parameter β ranging between 100 and 300 m s^{-1}. We found that a value of 200 m s^{-1} gives the best line width fit compared to the observations. This result is consistent with the low gas temperature of L1544.

Because of the absorption feature in the H_2O observation, it is important to take the continuum value derived from the observations into account and compare its value to the modelling. The LIME code can deal with different input dust opacity files as a function of wavelength such as the tabulated files from Ossenkopf & Henning (1994). The observed continuum value at 557 GHz (or 538.2 μm) is 10.2 ± 0.2 mK (see Caselli et al. 2012), and the best model value found with LIME is 10.0 mK with $\kappa_{557} = 8.41$ cm^2 g^{-1}. Keto & Caselli (2010) based their dust opacity value on the results found by Zucconi et al. (2001) where the authors approximate the grain opacities of Ossenkopf & Henning (1994) by piecewise power laws. Keto & Caselli (2010) derived a value of $\kappa_{557} = 3.83$ cm^2 g^{-1} thanks to the following equation describing one of these piecewise power laws (see Appendix B of Zucconi et al. 2001):

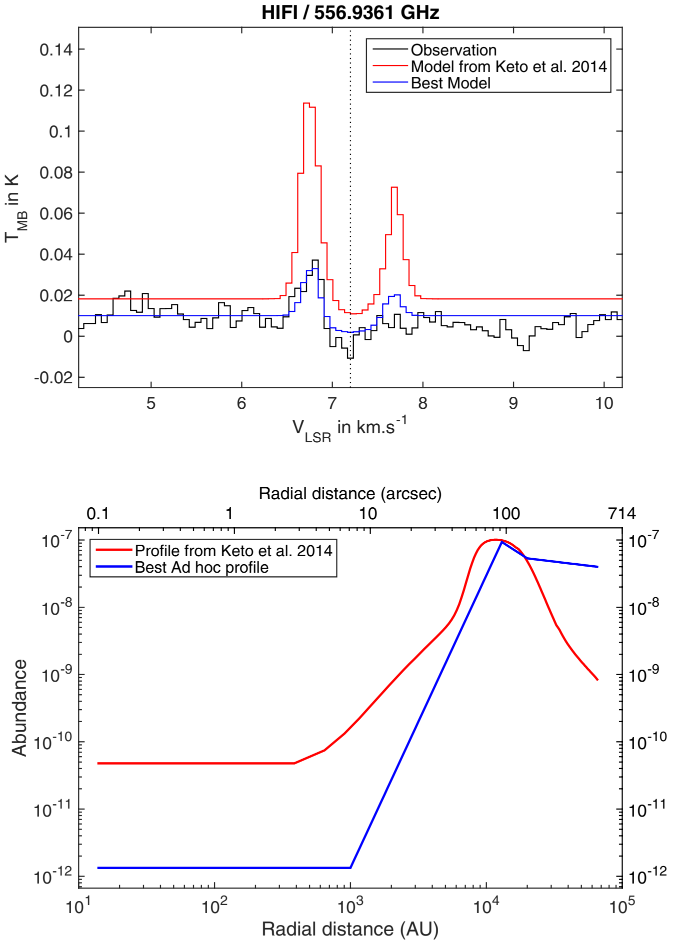

Fig. 2. *Top panel*: comparison between observations and modelling obtained by LIME using the structure and abundance profile from Keto et al. (2014; in red). The best fit model is shown in blue, using the same structure but an ad hoc abundance profile. *Bottom panel*: abundance profile from Keto et al. (2014) in red and best fit ad hoc abundance profile in blue as a function of the radial distance from the core in arcsec (top axis) and AU (bottom axis).

$$\kappa_\nu = \frac{Q_\nu}{m(H_2)} \times \left(\frac{\lambda_a}{\lambda_{H_2O}}\right)^\alpha \times \left(\frac{m_{gas}}{m_{dust}}\right), \qquad (1)$$

with $Q_\nu = 3.3 \times 10^{-26}$ cm^2 H_2^{-1} at $\lambda_a = 1060\,\mu$m, $m(H_2) = 3.35 \times 10^{-24}$ g, and $\alpha = 2.0$. They had to increase the dust opacity value by a factor of four ($\kappa_{557} = 15.3$ cm^2 g^{-1}) to be able to reproduce the low temperatures measured by Crapsi et al. (2007) towards the centre of L1544.

The result from the LIME modelling with the abundance and structure profile from Keto et al. (2014), coupled with their dust opacity value, is shown in Fig. 2. The H_2O emission is over-estimated by a factor of ~3.5, and the dust continuum emission is overestimated by a factor of ~2 compared to observations. The latter effect is due to the higher dust opacity ($\kappa_{557} = 15.3$ cm^2 g^{-1}) they used compared to the one we found in our best fit ($\kappa_{557} = 8.41$ cm^2 g^{-1}). As discussed above, the difference in the intensity of the line can be explained by the different radiative transfer treatments in MOLLIE and LIME, including different grids describing the same physical structure, which will be investigated in a forthcoming paper.

Although we note that Keto & Caselli (2010) and Keto et al. (2014) present a self-consistent model, where a simple chemistry is followed during dynamical and thermal evolution, and where the dynamical evolution is constrained by previous observations of N_2H^+ and CO isotopologues, we decided here to explore possibly different water abundance profiles to find a good match to the H_2O observations using LIME. For this purpose, we modified the water abundance profile found by Keto et al. (2014), while using their physical structure constrained with the many data published for many years towards this source. The inverse P-Cygni profile is a combination of blue-shifted emission and red-shifted absorption, split in velocity by the inward gas motion in front and at the rear of the cloud. In L1544, the emission is shifted with respect to the absorption by less than a line width, leading to an asymmetry in the line profile. Therefore, only a complex modelling can tentatively disentangle between the blue-shifted emission and red-shifted absorption. The emission is produced in the inner region of the cloud, where the density approaches the critical density of the transition. Meanwhile the absorption layer is located in the outer part of the cloud, where the water abundance peaks.

Several ad hoc profiles have been tested through grid calculations to find the best fit shown in Fig. 2, varying the following different parameters located in four distinct regions of the core:

1. The first region is the inner abundance and we found a best fit value of $[H_2O] = 1.3\times10^{-12}$ at the centre of the core until a radius of 1000 AU. Keto et al. (2014) found a value of this inner abundance close to $[H_2O] = 5 \times 10^{-11}$. If we increase the inner abundance to this value, we also change the slope of the abundance profile, probing a region where the velocity field is higher. This effect leads to a wider and slightly blue-shifted emission compared to our best fit. Nonetheless, due to the large HIFI beam at 557 GHz, the constraints on the inner abundance are relatively poor. Thus, the contribution of cosmic-ray-induced UV photons responsible for this inner abundance is also poorly constrained, and a proper benchmark between LIME and other radiative transfer codes is needed to develop a deeper analysis of this inner abundance. Cosmic-ray-induced UV photons also appear important for reproducing the observations of CO isotopologues toward L1544 (Keto & Caselli 2010).
2. The second region defines the peak abundance value of the external layer. We varied the abundance value and the distance from the centres of the core of this region. We found a best fit value of $[H_2O] = 9.3\times10^{-8}$ at a radius of 13 000 AU.
3. The third region marks the end of the external layer and, along with the first region, we varied the abundance value and the distance from the centre of the core. We found a best fit value of $[H_2O] = 5.3 \times 10^{-8}$ at a radius of 20 000 AU.
4. We finally varied the abundance value at the end of the profile, located at the same final radius of the physical structure of the core given by Keto et al. (2014). We found a best fit value of $[H_2O] = 4\times10^{-8}$. This result may imply that L1544 is well embedded in a relatively large filament in Taurus, so that the extinction A_V is high enough to at least partially shield interstellar UV photons (see Sect. 4.3).

We decided to first determine the first and second regions at the same time thanks to the grid. We then fixed the third one, which appeared to be independent of the other two. We derived the best fit from these previous models with the help of the standard χ^2 minimization value for a spectrum of N points, given by the equation (Coutens et al. 2012):

$$\chi^2 = \sum_{j=1}^{N} \frac{(I_{\mathrm{obs},j} - I_{\mathrm{model},j})^2}{\mathrm{rms}^2 + (\mathrm{cal} \times I_{\mathrm{obs},j})^2}, \tag{2}$$

where I_{obs} and I_{model} are the observed and the modelling intensity, cal_i is the calibration factor of the spectrum, and N is the total number of points of the spectrum. In the left-hand panels of Fig. 3 we show a small variation in the peak abundance value at the best fit distance of 13 000 AU from the centre of the core. It is interesting to note that a little variation in the abundance value at this distance can cause a notable difference in the line profile. Meanwhile, if we change the abundance value at the best fit distance of 20 000 AU of the external layer (see right panels of Fig. 3), the emission is the same for the three profiles.

In fact, emission from a molecule like water with high critical densities is only possible in regions with sufficiently high H_2 densities. In L1544, this region corresponds to the back part of the core approaching the centre (thus moving towards us) and revealing infall through an inverse P-Cygni profile (emission in the blue-shifted part of the line). We are seeing differences in the height of the blue peak by changing the abundance of water around 13 000 AU owing to more or fewer water molecules being present in the outer envelope to be able to absorb the emission coming from the central regions. This results does not contradict the detection of methanol and complex organic molecules (COMs) at radii of about 10 000 AU from the centre (Vastel et al. 2014; Bizzocchi et al. 2014), because water, methanol, and COMs have to be present in the gas phase at such radii. However, water at the volume densities present in the outer envelope can only absorb, while methanol and other complex molecules can emit more easily (as their critical densities are not as high). If the water abundance value at the edge of the core is lower than $[H_2O] \simeq 1 \times 10^{-8}$, the absorption feature will not be deep enough.

4.3. Chemical modelling of H_2O and HDO

We modelled the abundance profile of standard and deuterated water in L1544 using the GRAINOBLE astrochemical model, described in Taquet et al. (2012, 2014). Briefly, GRAINOBLE couples the gas phase and grain surface chemistry with the rate equation approach introduced by Hasegawa et al. (1992) during the static contraction of a starless core. The gas-phase chemical network was taken from the KIDA database and has been extended to include the spin states of H_2, H_2^+, H_3^+, and the deuterated isotopologues of hydrogenated species with four or fewer atoms among with species involved in the gas phase chemical network of water, ammonia, formaldehyde, and methanol. A more detailed description of the chemical network is presented in Taquet et al. (2014). We also considered the following gas-grain processes:

1. Accretion of gas phase species on the surface of spherical grains with a fixed diameter a_d assumed to be equal to 0.1 μm.
2. Diffusion of adsorbed species via thermal hopping, exponentially depending on the diffusion-to-binding energy ratio E_d/E_b. We set $E_d/E_b = 0.65$, following our previous studies.
3. Reaction between two particles via the Langmuir-Hinshelwood mechanism.

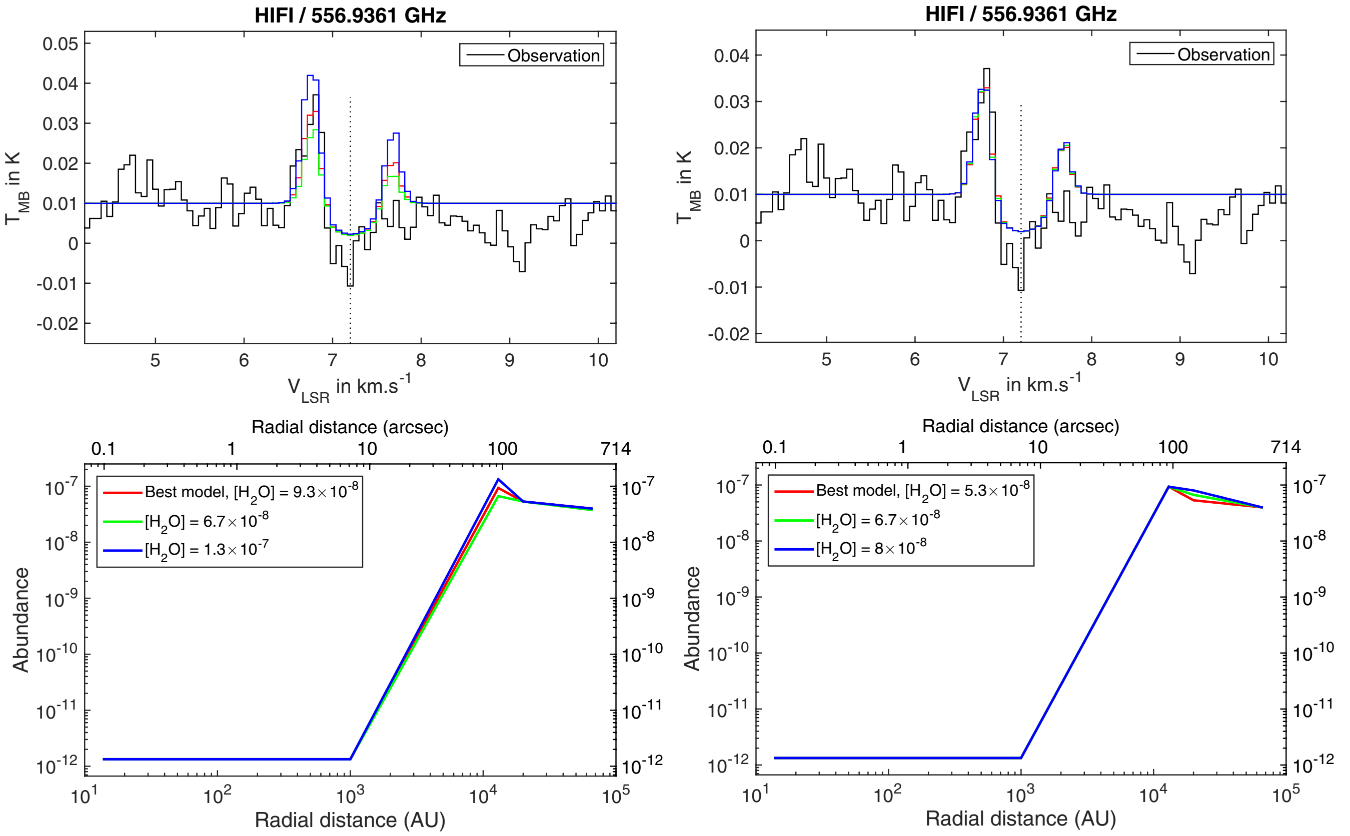

Fig. 3. *Top panels*: line profile versus observation for three different modellings. The best fit model is shown in red. In the *left panel*, the abundance value at 13 000 AU varies between 6.7×10^{-8} and 1.3×10^{-7} and for the *right panel*, the abundance value at 20 000 AU varies between 5.3×10^{-8} and 8×10^{-8}. *Bottom panel*: H_2O abundance profile used for these respective models as a function of the radial distance from the core in arcsec (top axis) and AU (bottom axis).

4. Desorption of adsorbed species into the gas phase by thermal evaporation, interstellar plus cosmic-ray induced heating of grains, chemical evaporation, and UV photolysis. The thermal evaporation exponentially depends on the binding energy of each species E_b relative to the substrate (see Taquet et al. 2014, for a list of binding energies used in the model). The cosmic-ray-induced heating of grains follows the approach by Hasegawa & Herbst (1993a) and is adapted to the binding energies considered in this work. The approach adopted for the UV photolysis follows the method described in Taquet et al. (2013a).

We used the multi-layer approach developed by Hasegawa & Herbst (1993b) to follow the multi-layer formation of interstellar ices and considered three sets of differential equations: one for gas-phase species, one for surface species, and one for bulk species. The equations governing chemical abundances on the surface and in the bulk are linked by an additional term that is proportional to the rate of growth or loss of the grain mantle. As a consequence, surface species are continuously trapped in the bulk because of the accretion of new particles.

We followed the formation and the deuteration of the main ice species following the surface chemical network developed by Taquet et al. (2013a), which is based on laboratory experiments showing the efficient formation of interstellar ice analogues at low temperatures. Transmission probabilities for key reactions involved in the water chemical network have been estimated through quantum chemistry.

The gas-grain chemistry is followed during the static contraction of a dense core starting from a homogeneous translucent sphere of a initial density $n_{\rm H,ini} = 3\times10^3$ cm^{-3} and a maximal radius of 3×10^4 AU. During the static contraction, the core keeps a Plummer-like density profile:

$$n_{\rm H} = \frac{n_{\rm H,0}}{(1 + (r/R_{\rm f})^2)^{\eta/2}}, \tag{3}$$

where $n_{\rm H,0}$ is the central density, and $R_{\rm f}$ the characteristic radius inside which the density is uniform. The contraction ends when the density profile reaches the observed profile of L1544, with the following parameters: $n_{\rm H,0} = 1.8 \times 10^7$ cm^{-3}, $R_{\rm f} = 450$ AU, and $\eta = 2.1$. Since $R_{\rm f}$ is given by the product of the sound speed and the free-fall time of the central density, $R_{\rm f}$ decreases with $1/\sqrt{n_{\rm H,0}}$. Intermediate central densities, and the associated timescale needed to reach them, have been chosen to have a total contraction timescale of about one million years, following observational estimates of molecular cloud cores (e.g. Brünken et al. 2014).

We used the radiative transfer code DUSTY (Ivezic & Elitzur 1997) to compute the temporal evolution of the dust temperature profile of the contracting core by assuming that gas and dust temperatures are coupled. As shown in Fig. 1, the dust and gas temperatures are decoupled and can differ by up to 4 K. We checked at posteriori that variations in gas phase temperatures of 4 K only induce small variations in abundances of gaseous species by 30% at most. The thermal structure of the core is derived from a slab geometry in which the core is irradiated by the interstellar radiation field (ISRF) with a spectrum taken from Evans et al. (2001) and assuming a fixed temperature at the edge of core of 13 K following the observed temperature profile of L1544.

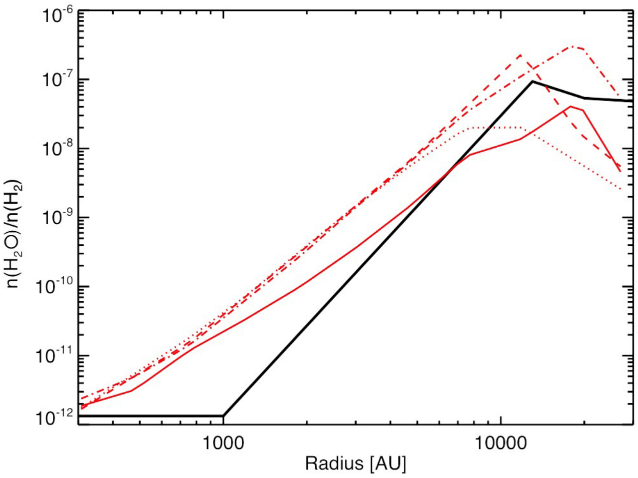

Fig. 4. Water abundance profile in L1544 modelled with GRAINOBLE (red curves) compared with the observed profile based on LIME radiative transfer simulations (black). Dashed-dotted line: $G_0 = 1$, $A_{\rm V,ext} = 2$, $t_c = 7.5 \times 10^5$ yr; dashed line: $G_0 = 1$, $A_{\rm V,ext} = 1$, $t_c = 7.5 \times 10^5$ yr; dotted line: $G_0 = 0.1$, $A_{\rm V,ext} = 1$, $t_c = 7.5 \times 10^5$ yr; solid line: $G_0 = 1$, $A_{\rm V,ext} = 2$, $t_c = 1.5 \times 10^6$ yr.

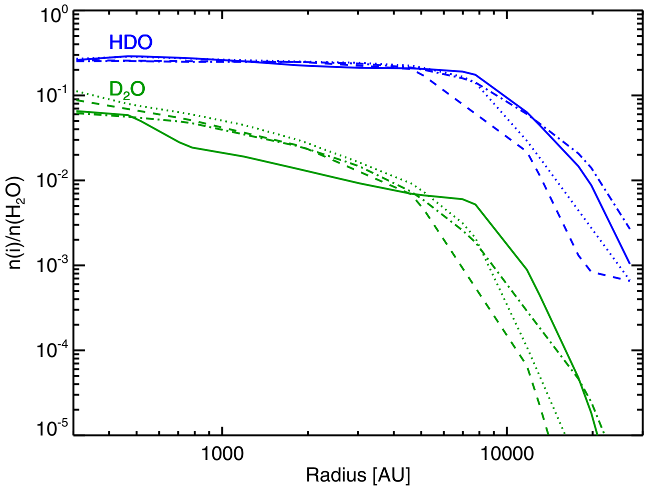

Fig. 5. [HDO]/[H_2O] (blue) and [D_2O]/[H_2O] (green) deuteration profile in L1544 modelled with GRAINOBLE. Dashed-dotted line: $G_0 = 1$, $A_{\rm V,ext} = 2$, $t_c = 7.5 \times 10^5$ yr; dashed line: $G_0 = 1$, $A_{\rm V,ext} = 1$, $t_c = 7.5 \times 10^5$ yr; dotted line: $G_0 = 0.1$, $A_{\rm V,ext} = 1$, $t_c = 7.5 \times 10^5$ yr; solid line: $G_0 = 1$, $A_{\rm V,ext} = 2$, $t_c = 1.5 \times 10^6$ yr.

As discussed in Taquet et al. (2013a, 2014), the abundance and the deuteration of the main ice components like water are known to depend on various physical and chemical parameters that are either poorly constrained or that show distributions of values. To reproduce the water abundance profile deduced by the LIME radiative transfer study, we varied the values of three poorly constrained physical parameters that are thought to have a strong impact on the abundance of gaseous water:

1. The external visual extinction $A_{\rm V,ext}$ that influences the radius where the water abundance reaches its maximal value. As shown in Fig. 4, decreasing $A_{\rm V,ext}$ from two to one magnitude enhances the photodissociation of water at the edge of the core, shifting its maximal abundance toward the core centre from 1.8×10^4 to 1.2×10^4 AU.
2. The external ISRF (interstellar radiation field) G_0. The photo-desorption rate of water increases with the flux of external UV photons, which is proportional to G_0. The maximal abundance of water starts to increase with G_0 at low G_0 and then decreases when the photo-dissociation of gaseous water overcomes its photo-desorption. Decreasing G_0 from 1 to 0.1 decreases the maximun water abundance from 2×10^{-7} to 2×10^{-8}.
3. The contraction timescale t_c. The core contraction timescale impacts the total number of particles that freeze-out on grains at the centre of the dense core but also the number of particles that are photo-evaporated at lower densities and visual extinctions in the outer shells. The increase in the core contraction timescale between 7.5×10^5 and 1.5×10^6 yr decreases the water abundance in the dense part of the core, owing to higher depletion, but also slightly increases the water abundance towards the edge because of the higher total number of photo-evaporated water molecules.

The water deuteration profiles obtained for the three sets of parameters used to model the water abundance profile in Fig. 4 are shown in Fig. 5. The water deuteration weakly depends on the physical parameters: the [HDO]/[H_2O] and [D_2O]/[H_2O] abundance ratios tend to increase towards the centre of the core up to ~25% and ~8%, respectively. As comprehensively studied in previous analyses (Roberts et al. 2004; Flower et al. 2006; Taquet et al. 2014; Sipilä et al. 2015), the increase in the deuteration both in the gas phase and on ices toward the core centre is due to the decrease in both the CO gas phase abundance and the H_2 ortho/para ratio, the two main parameters limiting the deuterium chemistry, with the increase in the total density and the decrease in the temperature. As also discussed in Taquet et al. (2014), the gas phase deuteration of water obtained at the centre of dense cores is higher by more than one order of magnitude than the overall deuteration predicted in interstellar ices. The gas phase D/H abundance ratio of water reflects the gas phase chemistry and surface chemistry in the outermost ice layers, in interaction with the gas phase, that are occurring in dense and cold conditions. The low deuteration of water ice is due to its early formation in the molecular cloud phase when the CO abundance and the H_2 ortho/para ratio were high.

Finally, the parameters of the chemical model that best fit the LIME-deduced water abundance profile are $G_0 = 1$, $A_{\rm V,ext} = 2$, and $t_c = 1.5 \times 10^6$ yr for a fixed diameter of grain a_d assumed to be equal to 0.1 μm (see Fig. 4).

5. HDO modelling with LIME

Coutens et al. (2012) have shown that in the outer part of the envelope of the low-mass protostar IRAS 16293-2422, the [HDO]/[H_2O] ratio is about 0.2–2.2% and ~4.8% in the external layer. This layer can be associated to the parental cloud, a remnant of the initial prestellar core of the protostar. Thus, we can say that an expected realistic [HDO]/[H_2O] ratio in L1544 may be close to these values. Nonetheless, observed D/H ratios for other gaseous species, as well as astrochemical models of starless cores, suggest much higher values, ranging from 7.5% to 22.5%. We chose to consider six different D/H ratios:

- 0.75% and 2.25%, in agreement with the [HDO]/[H_2O] ratios found by Coutens et al. (2012) in the external layer of IRAS 16293-2422, a low-mass protostar.
- 7.5% and 22.5%, in agreement with other observed D/H ratios in molecules, such as HCO^+, N_2H^+, and H_2CO in

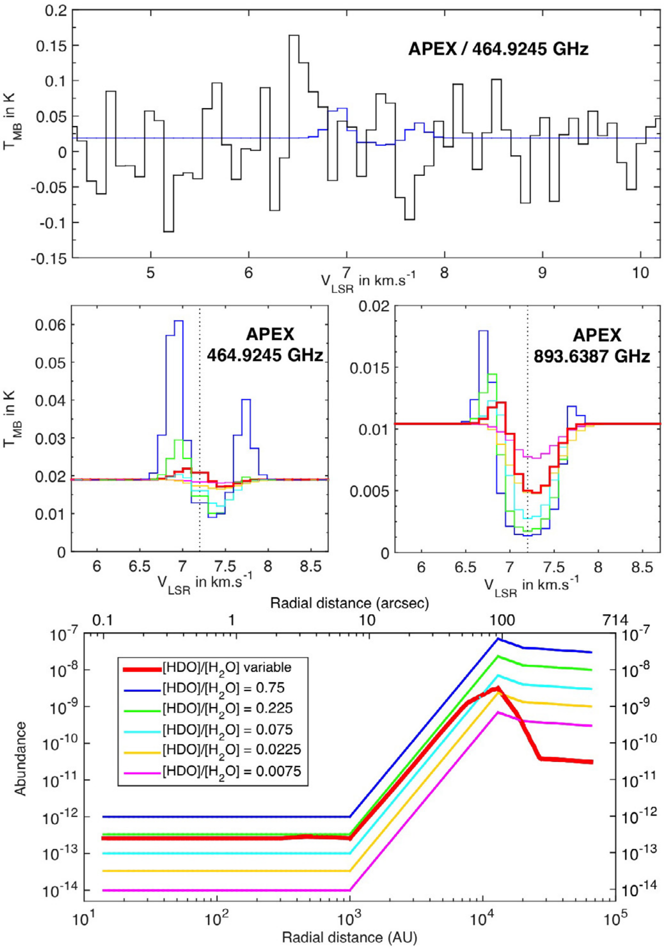

Fig. 6. *Top panel*: HDO $1_{0,1}$–$0_{0,0}$ line profile of the D/H = 1 model (in blue) versus APEX observation (in black). *Middle panels*: HDO $1_{0,1}$–$0_{0,0}$ (*left panel*) and $1_{1,1}$–$0_{0,0}$ (*right panel*) line profiles for the six different D/H ratios. *Bottom panel*: HDO abundance profiles as a function of the D/H ratio (see text, Sect. 5) used for these models as a function of the radial distance from the core in arcsec (top axis) and AU (bottom axis).

Table 1. Intensity of the emission and absorption feature of the two transitions with respect to their continuum level.

D/H ratio (in %)	HDO ($1_{0,1}$–$0_{0,0}$) 464.914 GHz		HDO ($1_{1,1}$–$0_{0,0}$) 893.639 GHz	
	absorption (in mK)[b]	emission (in mK)	absorption (in mK)[b]	emission (in mK)
variable[a]	1.9	2.9	5.4	1.5
75%	9.9	42.1	9.0	4.8
22.5%	8.8	10.6	8.7	1.5
7.5%	6.9	1.4	7.7	1.3
2.25%	2.5	0.04	5.5	0.04
0.75%	0.8	0.007	2.6	0.002

Notes. (a) D/H ratio as a function of the radius, derived from the dotted astro-chemical modelling shown in Fig. 5. (b) Absorption with respect to the continuum value of 18.9 mK at 464.914 GHz and 10.4 mK at 893.639 GHz.

prestellar cores (e.g. Bacmann et al. 2003; Pagani et al. 2007; Kong et al. 2015).

- variable as a function of the radius. We took the D/H ratio found by the dotted astro-chemical modelling plotted in Fig. 5. This chemical modelling corresponds to $G_0 = 0.1$, $A_{\mathrm{V,ext}} = 1$, and $t_c = 7.5 \times 10^5$ yr.
- 75% to consider an extreme case where the [HDO]/[H_2O] ratio is very high.

Based on our best-fit ad hoc H_2O abundance profile, we derived the abundance profile for the six previous different D/H ratios we consider. We modelled the HDO $1_{0,1}$–$0_{0,0}$ transition at 464.914 GHz and the $1_{1,1}$–$0_{0,0}$ transition at 893.639 GHz. The APEX observation of the 464.914 GHz transition does not show any detection of HDO towards the source (as seen in the upper panel of Fig. 6), and the 893.639 GHz transition has not been observed. The predicted continuum value at 464.914 GHz and 893.639 GHz are 18.9 mK and 10.4 mK, respectively. The predicted continuum value is lower at a higher frequency, which is consistent with a cold prestellar core such as L1544. The two middle panels of Fig. 6 show the spectra of the $1_{0,1}$–$0_{0,0}$ and $1_{1,1}$–$0_{0,0}$ transition derived from the output brightness map of the six different models, and the lower panel displays the related HDO abundance profile. The upper panel compares the APEX observations of the 464.914 GHz transition and the D/H = 1 model. This comparison clearly shows the limits of detectability for deuterated water with single-dish telescopes such a APEX, even if we consider a very high and unrealistic ratio. Table 1 shows the intensity of the emission and absorption feature for every model with respect to the continuum level of the line.

By looking at the brightness map of any of the previous models, one can note that the absorption feature of the HDO lines only shows up on a 50″ scale around the centre of the model. If we consider the most compact Cycle 3 configuration of ALMA (C36-1), it is impossible to entirely map L1544 in a convenient number of pointings owing to the size of the core (~20 000 AU, which means ~143″ at 140 pc), and even if we consider only the absorption feature (~50″), it would still require too many pointings since the antenna beamsize of the C36-1 configuration is ~12.5″ and ~6.5″ for the two HDO transitions. The ALMA interferometer is not optimum here to detect a very extended emission, and complementary ACA observations will not be sufficient to cover the missing (*u*, *v*)-plane observations. Only a single-dish telescope can give a convenient beam size to cover at least the absorption feature of L1544, but right now, such low sensitivities (~2 mK at 464.914 GHz and ~5 mK at 893.639 GHz) cannot be reached with ground-based observatories, and no space observatory is foreseen in the future.

6. Conclusions

Based on the recent detection of the $1_{1,0}$–$1_{0,1}$ water transition using the *Herschel*/HIFI instrument, we used the APEX observatory to constrain the water fractionation in the L1544 prestellar core. We used LIME to model the $1_{1,0}$–$1_{0,1}$ H_2O and $1_{0,1}$–$0_{0,0}$ HDO line profiles towards L1544 with a full radiative transfer treatment in 3D. Keto et al. (2014) derived the density, temperature, and velocity profile of the source. However, using LIME instead of MOLLIE, we found that their abundance profile predicts an emission that is 3.5 times stronger than the observation while using their deduced dust opacity, LIME predicts a continuum emission at 557 GHz about two times stronger than the observed value.

This result points to the need for a detailed comparison between these codes for the specific case of water in prestellar cores. We have found an ad hoc abundance profile that fits the *Herschel*/HIFI H_2O observation better using LIME. We also found a new estimation of the dust opacity to reproduce the observed continuum of ~10.2 mK. We used a detailed chemical modelling using both gas-phase and grain-surface chemistry to reproduce the water profile and predict its subsequent deuterated water profile. The resulting profile ($G_0 = 1$, $A_{\rm V,ext} = 2$, $t_{\rm c} = 1.5 \times 10^6$ yr, $a_{\rm d} = 0.1$ μm) has then been compared with our APEX observations. Our study shows the limit of detectability for deuterated water in prestellar cores using ground-based facilities with both single-dish telescopes and interferometric antennas.

Acknowledgements. The authors are grateful to Carlos De Breuck for his help during the APEX observations. C.C. acknowledges the financial support by the French Space Agency CNES. P.C. acknowledges the financial support of the European Research Council (ERC; project PALs 320620).

References

Aikawa, Y., Wakelam, V., Hersant, F., Garrod, R. T., & Herbst, E. 2012, ApJ, 760, 40
Bacmann, A., Lefloch, B., Ceccarelli, C., et al. 2003, ApJ, 585, L55
Bizzocchi, L., Caselli, P., Spezzano, S., & Leonardo, E. 2014, A&A, 569, A27
Bockelée-Morvan, D., Biver, N., Crovisier, J., et al. 2014, A&A, 562, A5
Boogert, A., Gerakines, P., & Whittet, D. 2015, ARA&A, 53, 541
Brinch, C., & Hogerheijde, M. R. 2010, A&A, 523, A25
Brünken, S., Sipilä, O., Chambers, E. T., et al. 2014, Nature, 516, 219
Carr, J. S., & Najita, J. R. 2008, Science, 319, 1504
Caselli, P., & Ceccarelli, C. 2012, A&ARv, 20, 56
Caselli, P., Walmsley, C. M., Zucconi, A., et al. 2002, ApJ, 565, 331
Caselli, P., van der Tak, F. F. S., Ceccarelli, C., & Bacmann, A. 2003, A&A, 403, L37
Caselli, P., Keto, E., Pagani, L. et al. 2010, A&A, 521, L29
Caselli, P., Keto, E., Bergin, E. A., et al. 2012, ApJ, 759, L37
Ceccarelli, C., Caselli, P., Bockelée-Morvan, D., et al. 2014, Protostars and Planets VI, 859
Coutens, A., Vastel, C., Caux, E., et al. 2012, A&A, 539, A132
Coutens, A., Vastel, C., Cabrit, S., et al. 2013, A&A, 560, A39
Coutens, A., Vastel, C., Hincelin, U., et al. 2014, MNRAS, 445, 1299
Crapsi, A., Caselli, P., Walmsley, C. M., et al. 2005, ApJ, 619, 379
Crapsi, A., Caselli, P., Walmsley, M. C., & Tafalla, M. 2007, A&A, 470, 221
Dartois, E., Thi, W.-F., Geballe, T. R., et al. 2003, A&A, 399, 1009
van Dishoeck, E. F., Bergin, E. A., Lis, D. C., & Lunine, J. I. 2014, Protostars and Planets VI, 835
Dubernet, M.-L., Daniel, F., Grosjean, A., & Lin, C. Y. 2009, A&A, 497, 911
Evans, N. J., II, Rawlings, J. M. C., Shirley, Y. L., & Mundy, L. G. 2001, ApJ, 557, 193
Flower, D. R., Pineau Des Forêts, G., & Walmsley, C. M. 2006, A&A, 449, 621
Hasegawa, T. I., & Herbst, E. 1993a, MNRAS, 261, 83
Hasegawa, T. I., & Herbst, E. 1993b, MNRAS, 263, 589
Hasegawa, T. I., Herbst, E., & Leung, C. M. 1992, ApJS, 82, 167
Hogerheijde, M., & van der Tak, F. 2000, Astrophysics Source Code Library, 0008.002
Hollenbach, D., Kaufman, M. J., Bergin, E. A., & Melnick, G. J. 2009, ApJ, 690, 1497
Ivezic, Z., & Elitzur, M. 1997, MNRAS, 287, 799
Keto, E. R. 1990, ApJ, 355, 190
Keto, E., & Caselli, P. 2010, MNRAS, 402, 1625
Keto, E., & Rybicki, G. 2010, ApJ, 716, 1315
Keto E., Rawlings J., Caselli P. 2014, MNRAS, 440, 2616, 301
Kong, S., Caselli, P., Tan, J. C., Wakelam, V., & Sipilä, O. 2015, ApJ, 804, 98
Ossenkopf, V., & Henning, T. 1994, A&A, 291, 943
Pagani, L., Bacmann, A., Cabrit, S., & Vastel, C. 2007, A&A, 467, 179
Parise, B., Simon, T., Caux, E., et al. 2003, A&A, 410, 897
Persson, M. V., Jørgensen, J. K., van Dishoeck, E. F., & Harsono, D. 2014, A&A, 563, A74
Podio, L., Kamp, I., Codella, C., et al. 2013, ApJ, 766, L5
Roberts, H., Herbst, E., & Millar, T. J. 2004, A&A, 424, 905
Sipilä, O., Caselli, P., & Harju, J. 2013, A&A, 554, A92
Sipilä, O., Caselli, P., & Harju, J. 2015, A&A, 578, A55
Taquet, V., Ceccarelli, C., & Kahane, C. 2012, A&A, 538, A42
Taquet, V., Peters, P. S., Kahane, C., et al. 2013a, A&A, 550, A127
Taquet, V., López-Sepulcre, A., Ceccarelli, C., et al. 2013b, ApJ, 768, L29
Taquet, V., Charnley, S. B., & Sipilä, O. 2014, ApJ, 791, 1
Troscompt, N., Faure, A., Maret, S., et al. 2009, A&A, 506, 1243
Vastel, C., Caselli, P., Ceccarelli, C., et al. 2006, ApJ, 645, 1198
Vastel, C., Ceccarelli, C., Lefloch, B., & Bachiller, R. 2014, ApJ, 795, LL2
Vasyunin, A. I., & Herbst, E. 2013, ApJ, 769, 34
Wakelam, V., Vastel, C., Aikawa, Y., et al. 2014, MNRAS, 445, 2854
Zucconi, A., Walmsley, C. M., & Galli, D. 2001, A&A, 376, 650

Astronomy & Astrophysics manuscript no. ions_paper
May 3, 2016

3D modelling of HCO^+ and its isotopologues in the low-mass proto-star IRAS16293−2422

D. Quénard[1,2], S. Bottinelli[1,2], E. Caux[1,2], and V. Wakelam[3,4]

[1] Univ. Toulouse, UPS-OMP, Institut de Recherche en Astrophysique et Planétologie (IRAP), UMR 5277, Toulouse, France

[2] CNRS, IRAP, UMR 5277, 9 Av. Colonel Roche, BP 44346, F-31028, Toulouse Cedex 4, France

[3] Univ. Bordeaux, LAB, UMR 5804, F-33270, Floirac, France

[4] CNRS, LAB, UMR 5804, F-33270, Floirac, France

Written February 1, 2016

ABSTRACT

Context. Ions and electrons play an important role in various stages of the star formation process. By following the magnetic field of their environment and interacting with neutral species, they slow down the gravitational collapse of the matter towards the central proto-star. Ionised species also help to create and destroy big molecules such as Complex Organic Molecules (COMs), thus they are involved in the chemistry that takes place in the proto-stellar environment.

Aims. Low-mass proto-stars are particularly well-studied for their similarity with the young Sun during its formation but their structure is complex, often mixing multiple components, disks, outflows, and jets. We present a study of HCO^+ and its isotopologues ($H^{13}CO^+$, $HC^{18}O^+$, DCO^+, and $D^{13}CO^+$) in IRAS16293−2422, combining the observations of two spectral surveys. The HCO^+ emission arises from the contribution of the envelope, the young outflow, and the foreground cloud. We aim at constraining the physical parameters of these different structures using all the observed transitions.

Methods. We use the GASS code to generate the 3D physical structure of the source, combined with the LIME radiative transfer code to compute the expected intensity and profile of the lines and compare them with the observations. The HCO^+ abundance of the envelope have been estimated using Nautilus, a gas-grain chemical model. Fitting a large range of upper energy level transitions and different isotopologues at the same time gives strong limits of the input physical parameters for all these structures.

Results. We provide better constraints on the physical parameters of the outflow and we derive $T_{kin} = 200\,K$ and $n(H_2) = 5.5 \times 10^6\,cm^{-3}$ with an HCO^+ abundance of 4×10^{-9}. We also demonstrate that the foreground cloud is cold ($\leqslant 30\,K$) and not dense ($n(H_2) \leqslant 1 \times 10^4\,cm^{-3}$) as suggested by previous studies. The HCO^+ abundance predicted by Nautilus for the envelope coupled with the contribution of the outflow and the foreground cloud allow us to reproduce the observations.

Conclusions. The young outflow clearly dominates the emission of HCO^+ in IRAS16293−2422 and the foreground cloud is responsible for the self-absorption seen for some of the transitions. The envelope is only contributing partially for the overall emission of this species. We also show that the $H^{12}CO^+/H^{13}CO^+$ ratio is slightly higher than the $D^{12}CO^+/D^{13}CO^+$ as predicted by recent theoretical results.

Key words. astrochemistry – methods: numerical – radiative transfer – ISM: individual objects: IRAS16293−2422 – ISM: molecules – ISM: abundances

1. Introduction

IRAS16293−2422 (hereafter IRAS16293) is a typical solar-type low-mass proto-star located at 120 pc (Loinard et al. 2008) embedded in the LDN1689N cloud within the ρ Ophiuchus complex. It is composed of two distinct cores IRAS16293 A and IRAS16293 B separated by ~5″ (Wootten 1989; Mundy et al. 1992). Several outflows have also been detected in this source and traced at multiple scales (Castets et al. 2001; Stark et al. 2004; Chandler et al. 2005; Yeh et al. 2008; Loinard et al. 2013; Girart et al. 2014). This source is well-studied due to its strong emission lines and its high deuterium fractionation. This Class 0 proto-star is the first source in which a hot corino has been discovered (Ceccarelli et al. 2000; Cazaux et al. 2003; Bottinelli et al. 2004).

HCO^+ (or formyl cation) has been detected as an unidentified line for the first time by Buhl & Snyder (1970) toward the high-mass star-forming regions W3(OH), Orion, Sgr A, and W51 and toward the dark cloud L134 using the 11 m NRAO telescope. Klemperer (1970) suggested that this line is associated to ground state of HCO^+ based on structure considerations, Woods et al. (1975) proved this hypothesis thanks to the laboratory measurement of the HCO^+ spectrum. One year later, Snyder et al. (1976) reported the first detection of interstellar $H^{13}CO^+$ close to the predicted frequencies. They also used the NRAO 11 m telescope and they detected this isotopologue in many sources (DR21, DR21(OH), NGC 2264, NGC 7538, Orion A, Sgr B2(OH), W3(OH), W49, W51, and W75N). The same year, Hollis et al. detected DCO^+ using the NRAO 11 m telescope toward DR21(OH), L134, and NGC 2264. The first detection of $HC^{18}O^+$ has been reported in Sgr B2 by Guélin & Thaddeus (1979) (again with the NRAO 11 m telescope). The same authors studied the distribution of five isotopologues of HCO^+ in several sources and detected for the first time $D^{13}CO^+$ in TMC-1 and L183 (Guélin et al. 1982a). They also detected $HC^{17}O^+$ for the first time toward Sgr B2 (Guélin et al. 1982b). Since then, HCO^+ and its isotopologues have been detected in many different kind of sources: star-forming regions (e.g. Orion, W3(OH), W51, DR21), diffuse medium of extra-galactic sources (e.g. Lucas & Liszt 1994), circumstellar envelope of evolved stars (e.g. Ziurys et al. 2009) and carbon-rich AGB stars (e.g. Pulliam et al. 2011). More recent studies have also detected HCO^+ maser (Hakobian & Crutcher 2012). In star-forming regions, HCO^+ is very abundant by the relative simplicity of its formation. It is a very good tracer of dense gas ($\geq 10^5\,\mathrm{cm}^{-3}$) and degree of ionisation of a cloud because it probes the electron density (Caselli et al. 2002).

The goal of this paper is to reproduce the HCO^+ (and its isotopologues $H^{13}CO^+$, $HC^{18}O^+$, DCO^+, and $D^{13}CO^+$) observed emission (described in Sect. 2) by comparing with results of 3D radiative transfer modellings (see Sect. 3). The 3D physical structure of the object is described in Sect. 4 as well as the HCO^+ abundance we consider. Results are presented in Sect. 5 together with discussions on the parameters used in this study. Concluding remarks are given in Sect. 6.

2. Observations

In this work, we mainly used data coming from two unbiased spectral surveys, *i)* The IRAS16293 Millimetre And Submillimetre Spectral Survey, performed at the IRAM-30m (80 – 265 GHz) and JCMT-15m (330 – 370 GHz) telescopes between January 2004 and August 2006, and APEX-12m (265–330 GHz) telescope between June 2011 and August 2012 (TIMASSS, Caux et al. 2011) and *ii)* the HIFI guaranteed time Key Program CHESS (Ceccarelli et al. 2010). The HIFI data presented in this article are part of a full spectral coverage of bands 1a (480 – 560 GHz; obsid 1342191499), 1b (560 – 640 GHz; obsid 1342191559), 2a (640 – 720 GHz; obsid 1342214468), 2b (720 – 800 GHz; obsid 1342192332), 3a (800 – 880 GHz; obsid 1342214308), 3b (880 – 960 GHz; obsid 1342192330), 4a (960 – 1040 GHz; obsid 1342191619), 4b (1040 – 1120 GHz; obsid 1342191681), and 5a (1120 – 1200 GHz; obsid 1342191683) which was performed between March 2010 and April 2011. The HIFI Spectral Scan Double Beam Switch (DBS) observing mode with optimisation of the continuum was used with the HIFI acousto-optic Wide Band Spectrometer (WBS), providing a spectral resolution of 1.1 MHz (~0.6 km s^{-1} at 500 GHz and ~0.3 km s^{-1} at 1 THz) over an instantaneous bandwidth of 4×1 GHz (Roelfsema et al. 2012).

For the TIMASSS survey, the observed coordinates were $\alpha_{2000} = 16^h32^m22^s.6$, $\delta_{2000} = -24°28'33''$ while they were $\alpha_{2000} = 16^h32^m22^s.75$, $\delta_{2000} = -24°28'34.2''$ for the HIFI observations. The differences of the aimed position have been carefully taken into account in this work. For both surveys, the DBS reference positions were situated at least 3′ apart from the source. Table 1 summarises the observation parameters.

The data processing of the TIMASSS survey has been extensively described in Caux et al. (2011). The HIFI data have been processed using the standard HIFI pipeline up to frequency and intensity calibrations (level 2) with the ESA-supported package HIPE 12 (Ott 2010). Using a routine developed within the HIFI ICC (Instrument Control Center), *flagTool*, spurs not automatically detected by the pipeline have been tagged and removed. Then, the HIPE tasks *fitHifiFringe* and *fitBaseline* were used to remove standing waves and to fit a low-order polynomial baseline to line-free channels. Finally, sideband deconvolution was performed with the dedicated HIPE task *doDeconvolution*.

The spectra observed in both horizontal and vertical polarisation were of similar quality, and averaged to lower the noise in the final spectrum, since polarisation is not a concern for the presented analysis. The continuum values obtained from running *fitBaseline* are well fitted by polynomials of order 3 over the frequency range of the whole band. The single side band continuum derived from the polynomial fit at the considered frequencies (Table 1) was added to the spectra. Intensities were then converted from antenna to main-beam temperature scale using a forward efficiency of 0.96 and the (frequency-dependent) beam-efficiency taken from the HIFI Beam release note[1]. Intensities are reported in Table 1 together with the spectroscopic and observing parameters of the transitions used in this work.

3. Radiative transfer modelling

In order to derive the line profile of the studied molecular transitions and the continuum emission, we have used LIME, a 3D non-LTE radiative transfer code (Brinch & Hogerheijde 2010). LIME is based on the Monte Carlo method and it includes elements of the accelerated Lambda iteration process. LIME works in two steps:

1. The first step consists in solving the radiative transfer equations to obtain the population level density of all the collisional transitions of a given species. To do this, LIME requires an input 3D description of the physical structure of the source (H_2 density, gas and dust temperature profiles, velocity field,. . .) as well as other parameters such as dust opacity tables, doppler broadening, and distance of the source for instance.
2. The second step consists in propagating photons in the model to obtain a hyper-spectral cube of the brightness at different frequencies. LIME has several input parameters that allows the user to correctly define the properties of the output cube.

We have used GASS (Generator of Astrophysical Sources Structures, Quénard et al. in prep.) to describe the input 3D physical model of IRAS16293 and set the different parameters of LIME. GASS is a user friendly interface that allows to create, manipulate, and mix one or several different physical structures such as spherical sources, disks, and outflows. The functioning of GASS is divided into different parts: the grid generation, the model creation, and the post-treatment options, everything wrapped into a Graphical User Interface (GUI). Multiple graphical outputs help the user to visualise the physical model in 3D. GASS is fully adapted to LIME and it produces output models than can be directly read by LIME.

Briefly, GASS generates a grid of cells randomly distributed as a function of the molecular density. Thus, an increasing number of points are located in a region where the volume density is higher. Each cell contains a fixed value of all the physical parameters. The minimal number of points required by LIME to correctly sample a grid is a few thousands. We choose to generate a grid of 100,000 cells with GASS to be sure that the result given by LIME has correctly converged. A complete description of the procedure that creates the different structures of the physical model is given in Quénard et al. (in prep.).

The LIME output hyper-spectral cube is in Kelvin units and it has been post-processed with GASS. For single-dish observations, the treatment consists in convolving the cube with the

---

[1] The HIFI Beam: Release #1

Table 1: Parameters for the observed HCO^+, $H^{13}CO^+$, $HC^{18}O^+$, DCO^+, and $D^{13}CO^+$ lines.

Molecule	Transition $J_{\rm up} - J_{\rm low}$	Freq. (GHz)	$E_{\rm up}/k_B$ (K)	A_{ij} (s^{-1})	rms (mK)	Vlsr (km s^{-1})	FWHM (km s^{-1})	T_{mb} (K)	$\int T_{\rm mb}dv$ (K km s^{-1})	Telescope	Beam size (″)
HCO^+	1 – 0	89.189	4	4.19×10^{-5}	8.1	4.20 ± 0.20	3.97 ± 0.33	4.45 ± 0.10	15.3 ± 1.69[1]	IRAM	27.8
	3 – 2	267.558	26	1.45×10^{-3}	55.8	3.76 ± 0.01	2.29 ± 0.02	25.2 ± 0.3	44.4 ± 4.44[1]	APEX	23.5
	4 – 3	356.734	43	3.57×10^{-3}	26.1	3.64 ± 0.02	3.06 ± 0.05	28.3 ± 0.5	67.6 ± 6.76[1]	JCMT	13.9
	6 – 5	535.062	90	1.25×10^{-2}	11.5	3.52 ± 0.03	2.43 ± 0.08	7.73 ± 0.20	21.1 ± 2.11	HIFI	39.7
	7 – 6	624.208	120	2.01×10^{-2}	12.4	3.48 ± 0.02	2.55 ± 0.04	7.85 ± 0.11	21.6 ± 2.16	HIFI	34.0
	8 – 7	713.341	154	3.02×10^{-2}	27.7	3.55 ± 0.02	2.86 ± 0.04	6.50 ± 0.08	20.1 ± 2.01	HIFI	29.7
	9 – 8	802.458	193	4.33×10^{-2}	37.5	3.70 ± 0.02	3.46 ± 0.04	5.28 ± 0.05	17.9 ± 2.69	HIFI	26.4
	10 – 9	891.557	235	5.97×10^{-2}	37.5	3.83 ± 0.01	3.88 ± 0.03	4.42 ± 0.03	15.6 ± 2.34	HIFI	23.8
	11 – 10	980.636	282	7.98×10^{-2}	44.6	3.88 ± 0.01	4.27 ± 0.03	3.63 ± 0.02	12.4 ± 1.86	HIFI	21.6
	12 – 11	1069.694	334	1.04×10^{-1}	63.3	3.87 ± 0.02	4.41 ± 0.05	2.64 ± 0.02	9.20 ± 1.84	HIFI	19.8
	13 – 12	1158.727	389	1.33×10^{-1}	147.2	4.04 ± 0.04	4.77 ± 0.11	2.13 ± 0.04	8.29 ± 1.66	HIFI	18.3
$H^{13}CO^+$	1 – 0	86.754	4	3.85×10^{-5}	6.5	4.17 ± 0.01	2.13 ± 0.02	1.91 ± 0.02	4.13 ± 0.45	IRAM	28.5
	2 – 1	173.507	12	3.70×10^{-4}	22.1	4.48 ± 0.03	2.05 ± 0.06	3.74 ± 0.10	7.73 ± 1.31	IRAM	14.3
	3 – 2	260.255	25	1.34×10^{-3}	14.2	3.61 ± 0.02	3.04 ± 0.04	3.19 ± 0.02	9.98 ± 1.70	IRAM	9.50
	4 – 3	346.998	42	3.29×10^{-3}	22.1	3.52 ± 0.03	2.36 ± 0.06	3.52 ± 0.04	7.65 ± 1.38	JCMT	14.3
	6 – 5	520.460	87	1.15×10^{-2}	9.2	4.02 ± 0.02	3.21 ± 0.05	0.35 ± 0.01	1.02 ± 0.10	HIFI	40.8
	7 – 6	607.175	117	1.85×10^{-2}	11.2	4.06 ± 0.06	3.00 ± 0.14	0.24 ± 0.01	0.67 ± 0.10	HIFI	35.0
	8 – 7	693.876	150	2.78×10^{-2}	22.0	4.18 ± 0.11	3.31 ± 0.27	0.14 ± 0.01	0.29 ± 0.09	HIFI	30.6
	9 – 8	780.563	187	3.99×10^{-2}	27.2	–	–	–	< 0.210	HIFI	27.2
$HC^{18}O^+$	1 – 0	85.162	4	3.64×10^{-5}	5.9	4.17 ± 0.05	1.96 ± 0.13	0.18 ± 0.02	0.35 ± 0.04	IRAM	29.1
	2 – 1	170.323	12	3.50×10^{-4}	19.6	4.34 ± 0.05	1.66 ± 0.12	0.42 ± 0.03	0.70 ± 0.12	IRAM	14.5
	3 – 2	255.479	25	1.27×10^{-3}	9.7	3.57 ± 0.27	2.43 ± 0.71	0.11 ± 0.02	0.28 ± 0.15	IRAM	9.7
	4 – 3	340.631	41	3.11×10^{-3}	16.2	3.96 ± 0.08	3.11 ± 0.21	0.36 ± 0.02	1.12 ± 0.20	JCMT	14.5
	6 – 5	510.910	86	1.09×10^{-2}	10.6	4.27 ± 0.11	2.31 ± 0.27	0.06 ± 0.02	0.12 ± 0.06	HIFI	41.6
	7 – 6	596.034	114	1.75×10^{-2}	13.7	–	–	–	< 0.106	HIFI	35.8
DCO^+	2 – 1	144.077	10	2.12×10^{-4}	13.7	4.32 ± 0.01	1.42 ± 0.01	3.57 ± 0.02	5.45 ± 0.93	IRAM	17.2
	3 – 2	216.113	21	7.66×10^{-4}	17.8	4.41 ± 0.03	2.91 ± 0.09	1.74 ± 0.03	5.67 ± 0.97	IRAM	11.5
	4 – 3	288.144	35	1.88×10^{-3}	8.90	4.20 ± 0.03	2.24 ± 0.06	1.24 ± 0.04	2.87 ± 0.57	APEX	21.8
	5 – 4	360.170	52	3.76×10^{-3}	20.9	3.86 ± 0.04	2.51 ± 0.10	1.16 ± 0.02	2.57 ± 0.46	JCMT	13.7
	7 – 6	504.200	97	1.06×10^{-2}	10.9	4.02 ± 0.09	3.03 ± 0.22	0.08 ± 0.01	0.22 ± 0.05	HIFI	42.1
	8 – 7	576.202	124	1.59×10^{-2}	9.1	–	–	–	< 0.396[2]	HIFI	36.8
$D^{13}CO^+$	2 – 1	141.465	10	2.00×10^{-4}	11.7	4.38 ± 0.07	1.27 ± 0.16	0.21 ± 0.04	0.27 ± 0.05	IRAM	17.5
	3 – 2	212.194	20	7.25×10^{-4}	6.6	4.43 ± 0.26	2.69 ± 0.61	0.08 ± 0.02	0.22 ± 0.04	IRAM	11.7
	4 – 3	282.920	34	1.78×10^{-3}	7.10	4.55 ± 0.14	3.05 ± 0.34	0.07 ± 0.01	0.21 ± 0.04	APEX	22.2
	5 – 4	353.640	51	3.56×10^{-3}	27.3	–	–	–	< 0.211	JCMT	14.0

Notes. (1) Lines showing a strong self-absorption profile. (2) Transition blended with CO (J = 5 → 4).

beam size of the desired telescope and to plot the predicted spectrum in main beam temperature as a function of the velocity for each observed frequency. The cube is built with a better spectral resolution (set to $100\,\mathrm{m\,s^{-1}}$ for all models) than the observations but the predicted spectra are resampled at the same spectral resolution as the observations. We carefully take into account the different telescopes source pointings in the convolution: observations coming from IRAM-30m and JCMT are pointed toward the source B whereas the *Herschel* beam is directed in the middle of sources A and B.

4. Physical and chemical structure

The physical structure of IRAS16293 is very complex with multiple outflows, multiple sources, and an envelope. To reproduce the observed HCO^+ emission and line profiles we have modelled in 3D the different structures that contribute to its emission. For that, we define the physical structure of each component and their respective HCO^+ abundance, as described in the following sub-sections.

4.1. The envelope model

Thanks to continuum measurements, Crimier et al. (2010) have derived the physical structure of the source (H_2 density, gas and dust temperature profiles of the envelope) from 22 AU to 6000 AU. To derive the density profile, they used a Shu-like model (Shu 1977) assimilated to a double power-law profile with indices of 1.5 and 2. This physical profile has been used in several physical and chemical studies of the source (e.g. Hily-Blant et

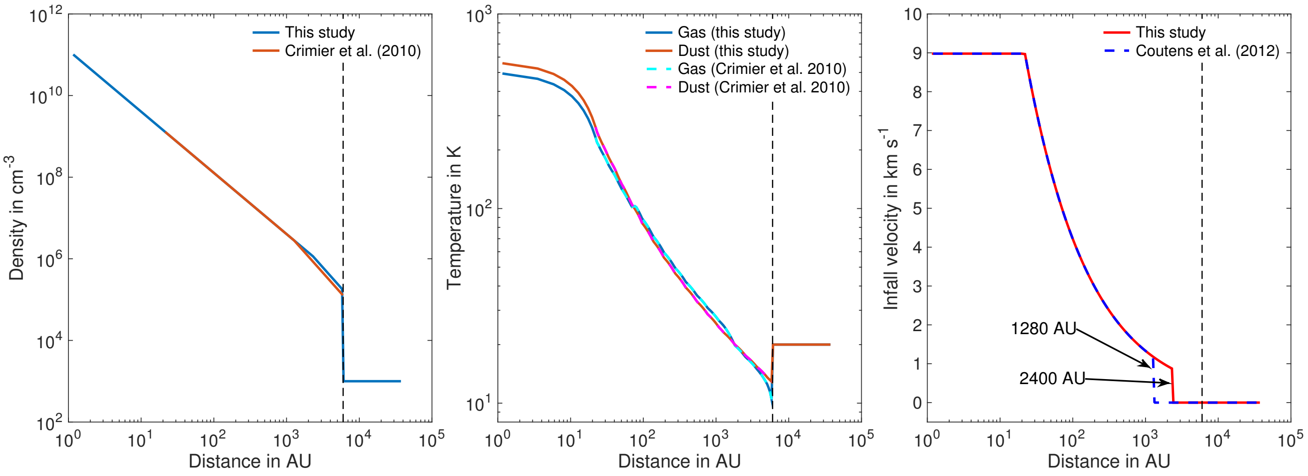

Fig. 1: *Left panel:* Density profile (blue) of IRAS16293 used in this study as a function of the radius, compared to Crimier's radial profile (red). *Middle panel:* Gas (blue) and dust (red) temperature profiles of IRAS16293 used in this study as a function of the radius, compared to the gas (cyan) and dust (magenta) Crimier's radial profiles. In both panels, the black dotted line shows the R = 6000 AU limit of the foreground cloud. *Right panel:* Absolute value of the radial infall velocity as a function of the radius used in this study (red line) compared to the profile used by Coutens et al. (2012) (blue dashed line).

al. 2010; Vastel et al. 2010; Coutens et al. 2012; Bottinelli et al. 2014; Jaber et al. 2014; Wakelam et al. 2014; López-Sepulcre et al. 2015; Majumdar et al. 2016) and we base our physical structure on the same definition. One must note that the presence of multiple sources and hypothetical proto-planetary disks in the core of the envelope (hot corinos) has not been taken into account in the study of Crimier et al. (2010). Thus, the inner structure of the source (< 600 AU) is still open to discussions.

The envelope is supposed to be spherical in the 3D model, thus, for our study, we have used Crimier's profiles extrapolated for radii smaller than 22 AU for the sake of the radiative transfer modelling. The resulting gas and dust temperature profiles are shown in Fig. 1. The Shu-like density distribution described by (Crimier et al. 2010) is:

$$n(r) = n(r_{in}) \times \left(\frac{r_{in}}{r}\right)^{1.5} \text{ if } r < r_{inf}, \tag{1}$$

$$n(r) = n(r_{in}) \times \left(\frac{r_{in}}{r}\right)^{2} \text{ if } r \geq r_{inf}, \tag{2}$$

where $n(r_{in})$ is the density at r_{in}, the inner radius of the envelope. From their best result, Crimier et al. (2010) derived $r_{inf} = 1280\,\mathrm{AU}$, $r_{in} = 22\,\mathrm{AU}$ and $n(r_{in}) = 1.23 \times 10^9\,\mathrm{cm}^{-3}$. r_{inf} refers to the radius where the envelope begins to collapse, marking a change in the slope of the density profile. For $r > r_{inf}$, the envelope is supposed to be static, thus the infall velocity is set to 0 (see Eq. (4)). r_{inf} is likely poorly constrained and to correctly reproduce the line profiles of the HCO$^+$ transitions, we need to set $r_{inf} = 2400\,\mathrm{AU}$. The implied differences on the density and velocity profiles are not significant (see left and right panels of Fig. 1). The velocity field of the source is defined through the standard infall law (Shu 1977):

$$V_{\mathrm{inf}}(r) = \sqrt{\frac{2\,G\,M_\star}{r}} \text{ if } r < r_{inf}, \tag{3}$$

$$V_{\mathrm{inf}}(r) = 0 \text{ if } r \geq r_{inf}, \tag{4}$$

where V_{inf} is the infall velocity, G the gravitational constant, $M_\star$ the mass of the central object, and r the distance from the central object. For IRAS16293, $M_\star = 1\,M_\odot$ (Coutens et al. 2012, and references therein) and our study confirms that the modelled HCO$^+$ lines are too broad for higher central masses. The envelope is supposed to be centred on IRAS16293 A since it is the more massive component of the binary system.

We have modelled the dust continuum with LIME by using different dust opacity values for our observed frequency range and the physical structure described above. A gas-to-dust mass ratio of 100 is assumed.

The radial abundance profile of HCO$^+$ in the envelope of IRAS16293 has been estimated using the chemical model Nautilus (e.g. Ruaud et al. 2016). Nautilus is a chemical model that computes the evolution of the species abundances as a function of time in the gas-phase and on grain surfaces. The code has been used for a variety of environments such as dense clouds (Loison et al. 2014), low-mass proto-stellar envelopes (Bottinelli et al. 2014) and the outer regions of proto-planetary disks (Dutrey et al. 2011). A large number of gas-phase processes are included in the network: bimolecular reactions (between neutral species, between charged species and between neutral and charged species) and unimolecular reactions, i.e. photo-reactions with direct UV photons and UV photons produced by the de-excitation of H_2 excited by cosmic-ray particles (Pratap & Tarafdar mechanism), photo-desorption, and direct ionisation and dissociation by cosmic-ray particles. The interactions of the gas phase species with the interstellar grains are: sticking of neutral gas-phase species to the grain surfaces, evaporation of the species from the surfaces due to the temperature, the cosmic-ray heating and the exothermicity of the reactions at the surface of the grains (a.k.a chemical desorption). The species can diffuse and undergo reactions using the rate equation approximation at the surface of the grains (Hasegawa et al. 1992). Details on the processes included in the model can be found in Ruaud et al. (2016). Note that we have used Nautilus in its 2-phase model, meaning that there is no distinction between the surface and the bulk of the mantle of the grains. The gas-phase reactions are based on the `kida.uva.2014` network[2] (see Wakelam et al. 2015) while the surface network is based on Garrod & Herbst (2006). The full network contains 736 species (488 in the gas-phase and 248 at the surface of the grains) and 10466 reactions

---

[2] `http://kida.obs.u-bordeaux1.fr/networks.html`

(7552 pure gas-phase reactions and 2914 reactions of interactions with grains and reactions at the surface of the grains). For this study we adopted the initial atomic abundances (with respect to the total proton density n_H) given in Hincelin et al. (2011) with an additional atomic abundance of 6.68×10^{-9} for fluorine (Neufeld et al. 2005). The carbon and oxygen abundances are respectively 1.7×10^{-4} and 3.3×10^{-4} leading to a C/O ratio of ~0.5.

The chemical reaction network of HCO^+ depends strongly on H_3^+ since its primary formation route is:

$$H_3^+ + CO \longrightarrow HCO^+ + H_2. \tag{5}$$

H_3^+ is formed from H_2 and strongly depends on the cosmic ray ionisation rate ζ:

$$H_2 + CR \longrightarrow H_2^+ + e^-, \tag{6}$$

$$H_2^+ + H_2 \longrightarrow H_3^+ + H. \tag{7}$$

In Sect. 5.1 we show the significance of the cosmic ray ionisation rate in the abundance profiles, thus in the contribution of the envelope in the HCO^+ emission.

Proto-stellar envelopes are by nature dynamical objects and the time scale of collapse may change the chemical composition of the envelopes (see Aikawa et al. 2008; Wakelam et al. 2014). The HCO^+ emission however seems to originate from the outer part of the envelope ($\gtrsim$ 1000 AU), where the physical conditions are evolving much slowly. For this reason and in order to have more flexibility on the parameters to vary, we have used the static model derived by Crimier et al. (2010) to derive the HCO^+ abundance with Nautilus in the envelope rather than the dynamical structure of Aikawa et al. (2008). Moreover, as said above, the chemistry of HCO^+ is mainly driven by the cosmic ray ionisation rate, which does not change with time.

4.2. The foreground cloud

IRAS16293 is embedded in the remnants of its parental cloud, forming a foreground layer in the line of sight. Recently, this cloud has been studied by Coutens et al. (2012) and Wakelam et al. (2014) to analyse the deuteration in the source, and Bottinelli et al. (2014) to investigate CH in absorption. Based on these studies, we have supposed this cloud to be cold ($T_{kin} \sim 10–30$ K) and not very dense ($n(H_2) \sim 10^3 - 10^5$ cm^{-3}) with an A_V of 1–4, similar to the physical conditions found in diffuse or translucent clouds (Hartquist & Williams 1998). For the low A_V (0.5 to 1.5) regime, the expected range of the HCO^+ abundance is a few $10^{-10} - 10^{-8}$ (all abundances are defined with respect to $n(H_2)$), depending on the temperature and on the degree of ionisation of the cloud (Hartquist & Williams 1998; Savage & Ziurys 2004).

4.3. The outflow model

The observed line shapes and intensities cannot be explained only with the contribution of the envelope of the source, particularly for high upper energy level transitions (e.g. $J_{up}>9$). Rawlings et al. (2000) and Rollins et al. (2014) have shown that young outflows can lead to an enhancement of the HCO^+ abundance in a short period of time. Briefly, the interaction between the jet and/or the outflowing material and the surrounding quiescent (or infalling) gas is eroding the icy mantle of dust grains, desorbing the molecular materials in the gas phase (e.g. H_2O, CO, H_2CO, CH_3OH). Thanks to the photo-chemical processing induced by the shock-generated radiation field, this sudden enrichment of the gas-phase molecular abundances leads to the formation of many other molecules, such as HCO^+. HCO^+ will be then destroyed by dissociative recombination or by interaction with water. Thus, we do not expect a high HCO^+ abundance in old outflows bur rather in young ones (< few hundred years old, Rawlings et al. (2000)) such as the NW-SE outflow detected in IRAS16293.

Table 2: Physical properties of the outflow taken from Rao et al. (2009) and Girart et al. (2014)

Physical properties	Value
$n(H_2)$	$\sim 1 \times 10^7$ cm^{-3}
T_{kin}	~ 400 K
$V_{outflow}$	15 km s^{-1}
Outflow extent	8″
P.A.	145°
Inclination[a]	44°
Age	~ 400 yr

Notes. [a] with respect to the plane of the sky.

This young NW-SE outflow (~400 yr) has been traced with $H^{13}CO^+$, SiO, and CO emission (Rao et al. 2009; Girart et al. 2014) using the SMA interferometer. According to Rao et al. (2009), the $H^{13}CO^+$ emission would arise from rotating material around IRAS16293 A rather than the outflow. The direction of this rotating material is roughly the same as the NW-SE outflow, therefore it is more probable that the $H^{13}CO^+$ emission they observed is coming from it and is due to the recent enhancement of its abundance. We have included this outflow in our 3D model together with the envelope.

We have considered a hourglass-like geometry for the outflow, as used by Rawlings et al. (2004) in their study of HCO^+. Our model is based on the mathematical definition given in Visser et al. (2012) implemented in GASS (Quénard et al. in prep. for more details on the outflow modelling). Its physical properties are not really well constrained but, based on their SiO (8−7) emission, Rao et al. (2009) suggested that this outflow is dense ($n(H_2) \sim 1 \times 10^7$ cm^{-3}) and hot ($T_{kin} \sim 400$ K). Girart et al. (2014) derived the maximum extent of this outflow (~ 8″), its inclination (~ 44°), dynamical age (~ 400 yr), and velocity ($V_{outflow} \sim 15$ km s^{-1}). We choose to only vary the gas temperature, the H_2 density, and the HCO^+ abundance, all three considered to be constant to find a good fit of our observations and better constrain the outflow physical properties. This outflow is quite young, collimated, and its low velocity suggests that the surrounding envelope is being pushed by the outflowing material. This kind of outflow-envelope interaction has already been observed and studied by Arce & Sargent (2005) and Arce & Sargent (2006) for similar objects. Table 2 summarises the physical parameters of the outflow we take into account in our modelling while Fig. 2 shows a sketch of the outflow orientation and position with respect to sources A and B.

5. Results and discussions

We have calculated several models, varying the different parameters of the envelope, foreground cloud, and outflow separately. One of the strengths of this study resides in the use of the data from the unbiased spectral surveys TIMASSS and CHESS (Sect. 2), which provides us with a large number of transitions, spanning a wide range of upper energy levels (4 − 389 K). This al-

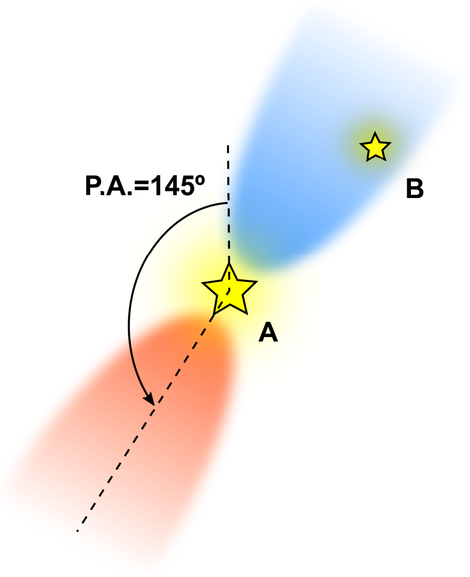

Fig. 2: Sketch of the blueshifted (in blue) and redshifted (in red) NW-SE outflow emission. Both sources A and B (separated by 5″) are drawn but only source A is considered in the modelling.

lowed us to constrain each structure with a specific set of transitions. For instance, the low $J = 1 \rightarrow 0$ transition ($E_{up} = 4$ K) strongly constrains the absorption feature created by the cold foreground cloud. The $J_{up} \gtrsim 8$ transitions ($E_{up} \gtrsim 154$ K) strongly constrain the outflow parameters, but very poorly the envelope since it is not contributing much to the total emission of these lines. For each structure, we have run several radiative transfer models and we have found the best fit parameters using a standard χ^2 minimisation. We give in Table 3 the range of parameters we have tested and the corresponding best value we derived alongside the constraints we give for these parameters. Figure 3 shows a comparison between the observations and the best fit model for all the studied transitions.

5.1. Chemistry of the envelope

For the envelope, we studied the impact of the chemical modellings input parameters on the radial abundance profile of HCO^+. We have varied five different parameters separately (age, temperature, and density of the parental cloud, cosmic ray ionisation rate, and age of the proto-star) to discriminate their respective effect on the abundance profile and to obtain the best model compared to the observations.

We initially start the chemical modelling of the envelope by considering a static 0D parental cloud extended up to $r = 4 \times 10^4$ AU with an initial gas temperature $T_{kin} = 10$ K and a high visual extinction to prevent any photo-dissociation to occur.

The next step of the chemical modelling consists in taking the resulting abundances obtained after the parental cloud stage as an input for the static modelling. We now consider the 1D physical structure of the envelope and we obtain the abundance as a function of the radius for different ages of the proto-star, up to 1×10^5 yr. The cosmic ray ionisation rate ζ is supposed to be the same as the one we use for the parental cloud step. The visual extinction in the envelope is a function of the hydrogen column density N_H:

$$A_V = \frac{N_H}{1.59 \times 10^{21}\ \mathrm{cm^{-2}}}. \quad (8)$$

To take into account the additional extinction from the foreground cloud in which we assume that the object is embedded, the A_V has been increased by 1.2 (see last paragraph of Sect. 5.2). Fig. 4 shows the effect of the variation of these chemical parameters on the radial abundance profile of HCO^+.

Age of the parental cloud. It is well constrained to be $< 3 \times 10^5$ yr since for older ages the amount of HCO^+ drops drastically (see top panels of Fig. 4) therefore the predicted HCO^+ emission is too small.

H_2 density of the parental cloud. It is poorly constrained but one can note that a higher value of the H_2 density leads to a lower abundance in the external part of the envelope (see middle panels of Fig. 4). Less abundance in this part of the envelope reduces the self-absorption of the low upper energy transitions ($J_{up} < 4$) therefore it affects their line profiles. If the density is not too high ($\leqslant 1 \times 10^5\ \mathrm{cm^{-3}}$), the HCO^+ abundance does not seem to vary a lot and acceptable models can be found among the different proto-star ages.

Kinetic temperature of the parental cloud. A variation of T_{kin} does not change significantly the resulting abundance so it was let fixed to 10 K.

Cosmic ray ionisation rate. The ionisation rate ($\geqslant 8 \times 10^{-17}\ \mathrm{s^{-1}}$) is strongly constrained by the chemical modelling since it affects the amount of H_3^+ (thus HCO^+, see bottom panels of Fig. 4) produced through the source. It is higher than the standard value of $1.3 \times 10^{-17}\ \mathrm{s^{-1}}$ found in the solar neighbourhood but the ρ Ophiuchus cloud complex is known for its high cosmic ray rate (Hunter et al. 1994). This value is also consistent with previous studies reported for IRAS16293 (e.g. Doty et al. 2004 and Bottinelli et al. 2014).

Age of the proto-star. It is constrained by the drop of $X(HCO^+)$ arising at a radius ~ 2000 AU for old ages that leads to lower self-absorption of $J_{up} <= 7-10$ lines. One can note that the chemistry does not evolve much after $\sim 2 \times 10^4$ yr, limiting the constraints we can give on the age of the source.

The contribution of the envelope to the emission of HCO^+ clearly does not dominate, therefore it is difficult to constrain some of the chemical input parameters. Nonetheless, some of them have an important impact on the abundance profile of HCO^+, thus on the resulting line profile, and it is possible to constrain their value.

The best model gives a parental cloud evolving for 1×10^5 yr with an initial gas density $n(H_2) = 3 \times 10^4\ \mathrm{cm^{-3}}$, and a cosmic ray ionisation rate of $1 \times 10^{-16}\ \mathrm{s^{-1}}$ with the age of the proto-star estimated to be 3.8×10^4 yr.

5.2. Physical parameters of the foreground cloud

Fig. 5 shows, for the emission of the HCO^+ (1−0) transition, different radiative transfer modellings within the foreground cloud parameters constraints. One can note that the emission is clearly sensitive to the foreground cloud density and abundance, even for the short range of tested values. The temperature, density, and abundance of the foreground cloud are not independent therefore not all possible sets of parameters of the given range of parameter constraints lead to an acceptable model. For instance, for a high H_2 density, a low HCO^+ abundance is needed to correctly reproduce the observations and vice versa. In Fig. 5, the reference model (in red) is the foreground cloud best fit parameters

Table 3: Range of physical properties varied in this study

Physical properties	Tested range	Best fit value	Constraints
Age of the parental cloud	$10^5 - 10^6$ yr	1×10^5 yr	$\leqslant 3 \times 10^5$ yr
$n(H_2)_{\mathrm{init,envelope}}$	$1 \times 10^4 - 3 \times 10^5$ cm^{-3}	3×10^4 cm^{-3}	$\leqslant 1 \times 10^5$ cm^{-3}
$T_{\mathrm{init,\ envelope}}$	$5 - 15$ K	10 K	None
$\zeta_{\mathrm{envelope}}$	$1 \times 10^{-17} - 1 \times 10^{-16}$ s^{-1}	1×10^{-16} s^{-1}	$\geqslant 8 \times 10^{-17}$ s^{-1}
Age of the proto-star	up to 10^5 yr	4×10^4 yr	$\geqslant 2 \times 10^4$ yr
$n(H_2)_{\mathrm{foreground}}$	$5 \times 10^2 - 3 \times 10^5$ cm^{-3}	2×10^3 cm^{-3}	$1 \times 10^3 - 1 \times 10^4$ cm^{-3}
$T_{\mathrm{kin,\ foreground}}$	$10 - 30$ K	20 K	None
$X(HCO^+)_{\mathrm{foreground}}$	$5 \times 10^{-11} - 1 \times 10^{-8}$	1×10^{-8}	$\geqslant 1.5 \times 10^{-9}$
$n(H_2)_{\mathrm{outflow}}$	$1 \times 10^6 - 1 \times 10^8$ cm^{-3}	5.5×10^6 cm^{-3}	$(4 - 7) \times 10^6$ cm^{-3}
$T_{\mathrm{kin,\ outflow}}$	$100 - 500$ K	200 K	$180 - 220$ K
$X(HCO^+)_{\mathrm{outflow}}$	$1 \times 10^{-10} - 1 \times 10^{-7}$	4×10^{-9}	$(3 - 5) \times 10^{-9}$

Notes. *Top panel:* Parameters of the envelope. *Middle panel:* Parameters of the foreground cloud. *Bottom panel:* Parameters of the outflow.

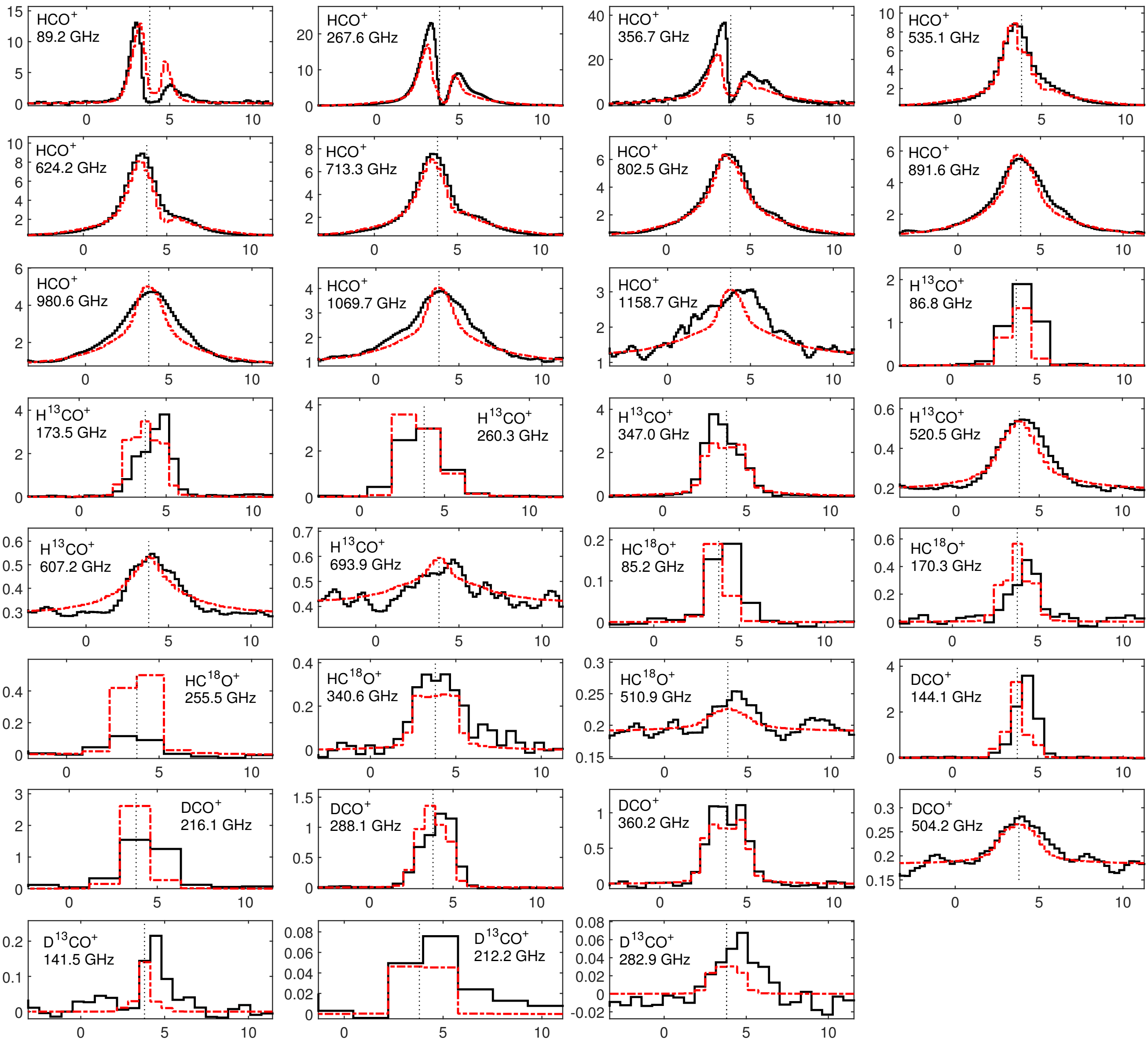

Fig. 3: Main beam temperature (in K) of HCO$^+$, H^{13}CO$^+$, HC^{18}O$^+$, DCO$^+$, and D^{13}CO$^+$ observed transitions (in blue) compared to the best fit model (in red) as a function of the velocity (in km s^{-1}). The continuum is shown for all transitions. The vertical black dotted line shows the $V_{\mathrm{LSR}} = 3.8$ km s^{-1} of IRAS16293.

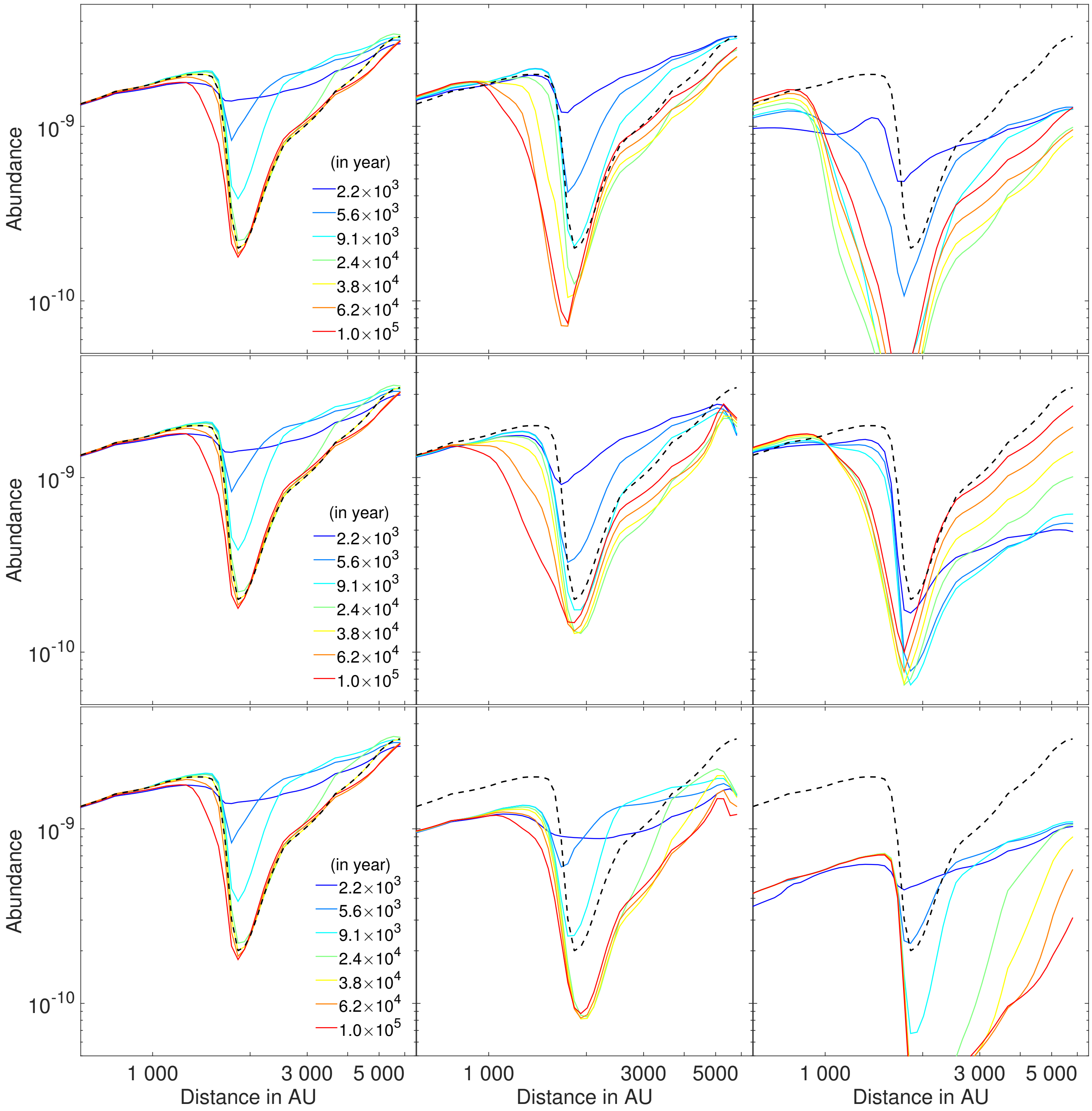

Fig. 4: Variation of the abundance profile of HCO^+ determined by Nautilus as a function of the radius for different ages of the proto-star and different set of input chemical parameters. The best fit is shown in black dashed lines. *Top panels:* Variation of the age of the parental cloud (from left to right): 1×10^5, 3×10^5, and 6×10^5 yr. *Middle panels:* Variation of the initial H_2 density in the parental cloud (from left to right): 6×10^4, 2×10^5, and 6×10^5 cm^{-3}. *Bottom panels:* Variation of the cosmic ray ionisation rate (from left to right): 1×10^{-16}, 5×10^{-17}, and 1×10^{-17} s^{-1}.

(see Table 3) and for each panel we vary one of the parameters only and we fix the other two to the best fit value. These figures are not fully representative of the parameter space of acceptable models but they demonstrate the influence of each parameter on the resulting line emission.

H_2 density of the foreground cloud. We have tried several densities ranging from $\sim 1 \times 10^3$ to $\sim 1 \times 10^5\,cm^{-3}$ as suggested by Coutens et al. (2012) for this region combined to several kinetic temperature and molecular abundances. The density we derive ($n(H_2)_{foreground} = 2 \times 10^3\,cm^{-3}$) is lower than the one used by Bottinelli et al. (2014) for CH and Wakelam et al. (2014) for the deuteration ($n(H_2)_{foreground} = 1 \times 10^4\,cm^{-3}$) but these authors only tested two different densities ($n(H_2)_{foreground} = 1 \times 10^4$ and $1 \times 10^5\,cm^{-3}$). We have found that for a density higher than $n(H_2)_{foreground} = 1 \times 10^4\,cm^{-3}$, the HCO^+ $J = 1 \rightarrow 0$ transition is not self-absorbed enough. This strongly constrains the density of the foreground cloud and its visual extinction.

Kinetic temperature of the foreground cloud. The line profiles do not change significantly in the range of tested values (10 − 30 K). We therefore used the best model value of 20 K,

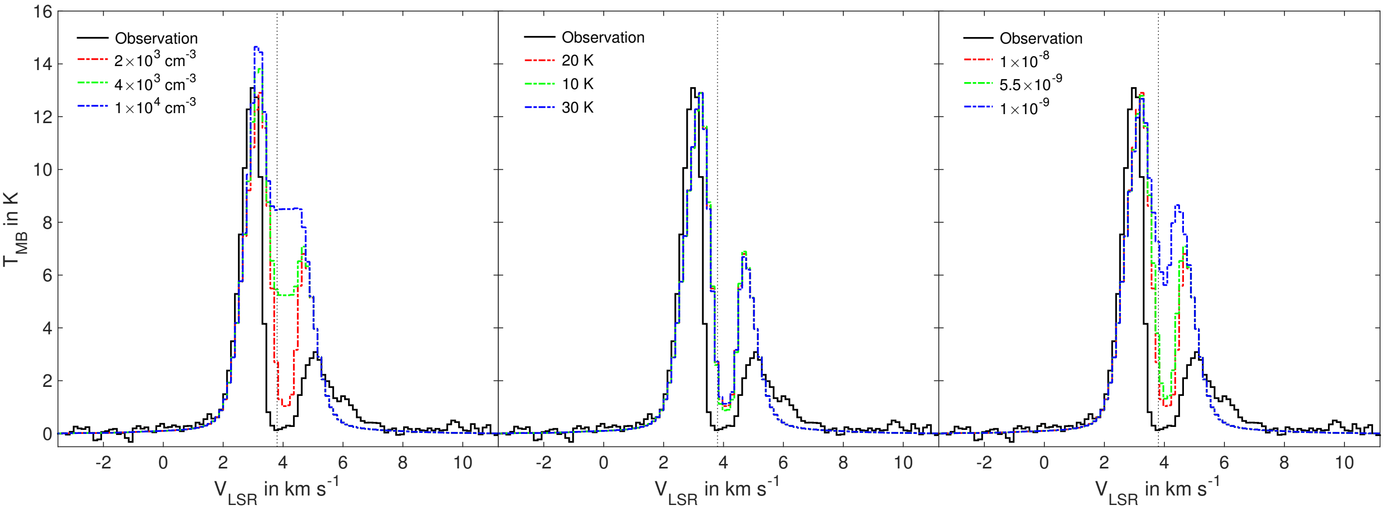

Fig. 5: Main beam temperature of the observed HCO^+ $(1-0)$ transition (black line) as a function of the velocity. The vertical black dotted line shows the $V_{LSR} = 3.8\,km\,s^{-1}$ of IRAS16293. The reference model (in red) is the best fit with $n(H_2)_{foreground} = 2\times10^3\,cm^{-3}$, $T_{kin,\,foreground} = 20\,K$, and $X(HCO^+)_{foreground} = 1\times10^{-8}$. *Left panel:* Variation of the H_2 density of the foreground cloud. *Middle panel:* Variation of the kinetic temperature of the foreground cloud. *Right panel:* Variation of the HCO^+ abundance of the parental cloud.

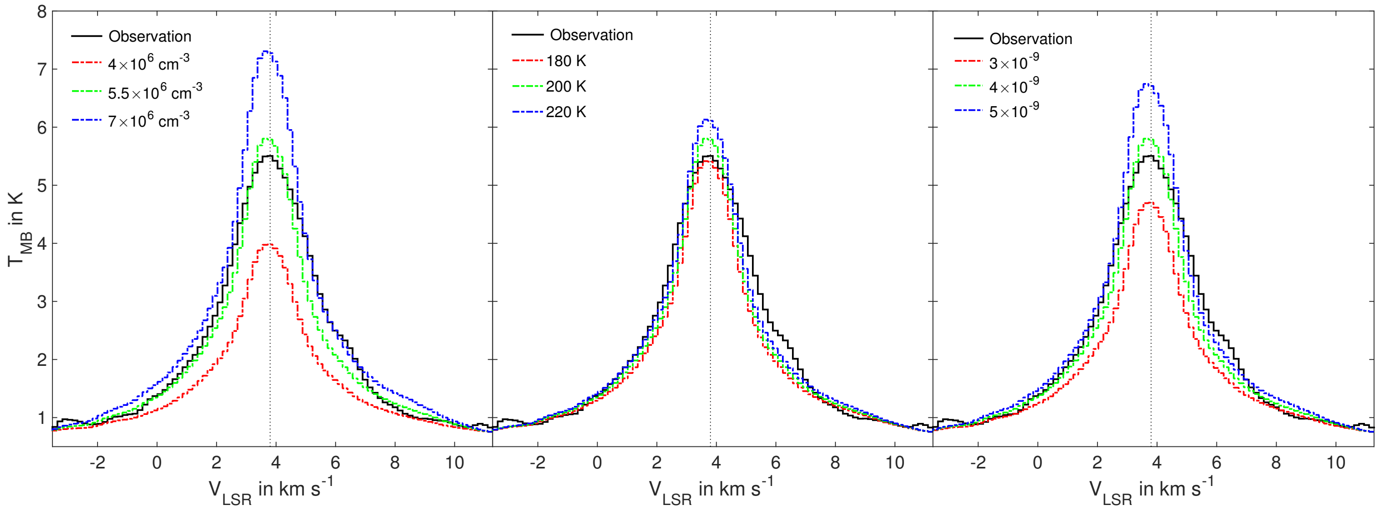

Fig. 6: Main beam temperature of the observed HCO^+ $(10-9)$ transition (black line) as a function of the velocity. The vertical black dotted line shows the $V_{LSR} = 3.8\,km\,s^{-1}$ of IRAS16293. The reference model (in green) is the best fit with $n(H_2)_{outflow} = 5.5\times10^6\,cm^{-3}$, $T_{kin,\,outflow} = 200\,K$, and $X(HCO^+)_{outflow} = 4\times10^{-9}$. *Left panel:* Variation of the H_2 density of the outflow. *Middle panel:* Variation of the kinetic temperature of the outflow. *Right panel:* Variation of the HCO^+ abundance of the outflow.

and we cannot give better constraints than the result obtained by Bottinelli et al. (2014) for CH and Wakelam et al. (2014) for the deuteration where they needed the temperature to be lower than 30 K in order to reproduce their observations.

Abundance of the parental cloud. The HCO^+ abundance of 1×10^{-8} (with respect to H_2) we get is consistent with the results predicted by Hartquist & Williams (1998) and Savage & Ziurys (2004) at low A_V for diffuse or translucent clouds. If we increase the H_2 density, the HCO^+ abundance has to drop in order not to get the foreground cloud emitting rather than absorbing, constraining the value we can consider for the HCO^+ abundance.

We have found a best model for the foreground cloud with $n(H_2)_{foreground} = 2\times10^3\,cm^{-3}$, $T_{kin,\,foreground} = 20\,K$, and $X(HCO^+)_{foreground} = 1\times10^{-8}$. Using Eq. (8), we derive $A_V \simeq 1.2$ for a supposed foreground cloud size of 30 000 AU.

5.3. Physical parameters of the outflow

Fig. 6 shows, for the emission of the HCO^+ $(10-9)$ transition, different radiative transfer modellings within the outflow parameters constraints. As for the foreground cloud, one can note that the emission is clearly sensitive to the outflow density and abundance, even for the short range of tested values. Comments made in the first paragraph of the previous section (§5.2) also apply to the Fig. 6 in which the reference model (in green) is the outflow best fit parameters.

H_2 density of the outflow. For the density, a lower value than $4\times10^6\,cm^{-3}$ leads to an important decrease in the emission, even for a very high HCO^+ abundance $(10^{-8}-10^{-7})$. A value higher than $7\times10^6\,cm^{-3}$ leads to an important increase of the emission, even for a very low abundance $(10^{-11}-10^{-10})$.

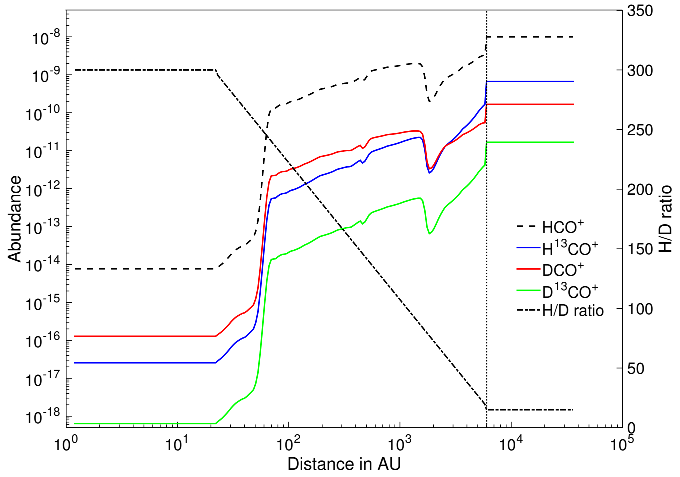

Fig. 7: *Left axis:* Abundance profile of HCO^+ (black dashed line) as a function of the radius compared to the $H^{13}CO^+$ (blue), DCO^+ (red), and $D^{13}CO^+$ (green) one. *Right axis:* D/H ratio used in our study (black dash-dotted line). The vertical black dotted line shows the R = 6000 AU limit of the foreground cloud.

Kinetic temperature of the outflow. A lower kinetic temperature (< 180 K) will decrease the emission of high upper energy level lines since the gas is not hot enough to excite these transitions. At the opposite, a higher kinetic temperature (> 220 K) will increase too much the emission of these lines. This effect is even more visible for higher J_{up} transitions than the HCO^+ (10 − 9) transition shown in Fig. 6.

The ranges of outflow density and temperature are in good agreement with values derived by Rao et al. (2009) and Girart et al. (2014) using only one SiO (8 − 7) transition (see Table 2). Fitting several upper energy level HCO^+ transitions, we provide a better estimation of the outflow properties, particularly the H_2 density and the kinetic temperature are strongly constrained.

Abundance of the outflow. The high HCO^+ abundance (4×10^{-9}) needed to reproduce the observed lines is consistent with the expected strong enhancement described in Sect. 4.3. The abundance of HCO^+ derived with the chemical modelling of the envelope is always lower than this value, particularly in the inner region (<8″) where the outflow is completely dominating. This clearly shows that the outflow largely contributes to the emission in a region where it cannot be produced by the envelope.

The best fit model for the outflow gives $n(H_2)_{\rm outflow} = 5.5 \times 10^6$ cm^{-3}, $T_{\rm kin,\ outflow} = 200\,K$, and $X(HCO^+)_{\rm outflow} = 4 \times 10^{-9}$.

5.4. Fractionation

The $^{12}C/^{13}C$ and $^{16}O/^{18}O$ ratios we used in this study are consistent with values found in the ISM (Wilson & Rood 1994) and for the ρ Ophiuchus cloud (Bensch et al. 2001). A constant $^{16}O/^{18}O = 500$ ratio is sufficient to reproduce our $HC^{18}O^+$ observations. Recently, Mladenović & Roueff (2014) have theoretically studied the fractionation of DCO^+ and they have shown that considering the higher exothermicity of deuterated isotopologues reactions, the isotopic ^{13}C ratio is lower than the hydrogenic counterpart. Thus, we expect a $D^{12}CO^+/D^{13}CO^+$ ratio lower than the $H^{12}CO^+/H^{13}CO^+$ ratio in the external part of the envelope or in the foreground cloud, where the temperature is low. We derive $H^{12}CO^+/H^{13}CO^+ = 50$ and $D^{12}CO^+/D^{13}CO^+ = 40$, consistent with the results of Mladenović & Roueff (2014).

At low temperature (T < 30K) and low densities ($n(H_2)<10^5$ cm^{-3}), DCO^+ is enhanced, increasing rapidly the fractionation of DCO^+ (Dalgarno & Lepp 1984; Roberts & Millar 2000). Therefore, the HCO^+/DCO^+ ratio we use is not constant throughout the model but it follows an *ad hoc* law based on a linear decrease of the ratio between 22 and 6000 AU. The resulting HCO^+, $H^{13}CO^+$, DCO^+, and $D^{13}CO^+$ are plotted in Fig. 7. The inner H/D ratio of 300 is consistent with the H_2O/HDO ratio derived by Coutens et al. (2012). Persson et al. (2013, 2014) derived a higher value for the hot corino of IRAS16293 (up to 1000) and other low-mass proto-stars but it will no play an important role in our study since the abundance in the inner part of the envelope is really small ($< 10^{-13}$). The outer H/D ratio of 15 we use for the external part of the envelope is in agreement with the results obtained by Coutens et al. (2012). At radii lower than 22 AU and higher than 6000 AU, we suppose that the H/D ratio is constant and equal to 300 and 15 respectively. The outflow H/D ratio is considered to be 300 as well.

6. Conclusions

We have used a large number of HCO^+ transitions, spanning a wide range of upper energy levels (4 – 389 K) to reproduce the observed emission. This study gives better constraints on the physical parameters of the outflow and we derived $T_{\rm kin} = 200$ K and $n(H_2) = 5.5 \times 10^6$ cm^{-3} with $X(HCO^+) = 4 \times 10^{-9}$. The emission coming from the outflow is responsible for all the $J_{\rm up} \geqslant 8$ emission and it participates a lot to other transitions. We have also demonstrated that the foreground cloud causes the deep self-absorption seen for $J_{\rm up} \leqslant 4$ lines. This is only possible if this cloud is cold ($\leqslant$ 30 K) and not dense ($n(H_2) \leqslant 1{\times}10^4$ cm^{-3}). We have used the chemical code Nautilus to estimate the HCO^+ abundance of the envelope and, combined with the outflow and the foreground cloud contributions, we have been able to reproduce correctly the observations. By using multiple isotopologues, we also derived several fractionated ratio ($^{12}C/^{13}C = 40 - 50$, $^{16}O/^{18}O = 500$, and H/D= 15 to 300 depending on the radius). We have shown that the $H^{12}CO^+/H^{13}CO^+ = 50$ ratio is slightly higher than the $D^{12}CO^+/D^{13}CO^+ = 40$ as predicted by recent theoretical results.

Acknowledgements. V.W. thanks the French CNRS/INSU programme PCMI and the ERC Starting Grant (3DICE, grant agreement 336474) for their funding.

References

Aikawa, Y., Wakelam, V., Sakai, N., et al. 2008, Organic Matter in Space, 251, 129
Arce, H. G., & Sargent, A. I. 2005, ApJ, 624, 232
Arce, H. G., & Sargent, A. I. 2006, ApJ, 646, 1070
Bensch, F., Pak, I., Wouterloot, J. G. A., Klapper, G., & Winnewisser, G. 2001, ApJ, 562, L185
Bottinelli, S., Ceccarelli, C., Neri, R., et al. 2004, ApJ, 617, L69
Bottinelli, S., Wakelam, V., Caux, E., et al. 2014, MNRAS, 441, 1964
Brinch, C., & Hogerheijde, M. R. 2010, A&A, 523, AA25
Buhl, D., & Snyder, L. E. 1970, Nature, 228, 267
Caselli, P., Walmsley, C. M., Zucconi, A., et al. 2002, ApJ, 565, 344
Castets, A., Ceccarelli, C., Loinard, L., Caux, E., & Lefloch, B. 2001, A&A, 375, 40
Caux, E., Kahane, C., Castets, A., et al. 2011, A&A, 532, A23
Cazaux, S., Tielens, A. G. G. M., Ceccarelli, C., et al. 2003, ApJ, 593, L51
Ceccarelli, C., Loinard, L., Castets, A., Tielens, A. G. G. M., & Caux, E. 2000, A&A, 357, L9
Chandler, C. J., Brogan, C. L., Shirley, Y. L., & Loinard, L. 2005, ApJ, 632, 371
Coutens, A., Vastel, C., Caux, E., et al. 2012, A&A, 539, AA132
Crimier, N., Ceccarelli, C., Maret, S., et al. 2010, A&A, 519, AA65
Dalgarno, A., & Lepp, S. 1984, ApJ, 287, L47
Doty, S. D., Schöier, F. L., & van Dishoeck, E. F. 2004, A&A, 418, 1021

Dutrey, A., Wakelam, V., Boehler, Y., et al. 2011, A&A, 535, A104
Garrod, R. T., & Herbst, E. 2006, A&A, 457, 927
Girart, J. M., Estalella, R., Palau, A., Torrelles, J. M., & Rao, R. 2014, ApJ, 780, L11
Guélin, M., & Thaddeus, P. 1979, ApJ, 227, L139
Guélin, M., Langer, W. D., & Wilson, R. W. 1982, A&A, 107, 107
Guélin, M., Cernicharo, J., & Linke, R. A. 1982, ApJ, 263, L89
Hakobian, N. S., & Crutcher, R. M. 2012, ApJ, 758, L18
Hartquist, T. W., & Williams, D. A. 1998, The molecular astrophysics of stars and galaxies, by T.W. Hartquist and D.A. Williams, D. A.. International Series in Astrononmy and Astrophysics, Vol. 4, Oxford University Press. 1999. 560 pages; 112 line illus. ISBN13: 978-0-19-850158-9, 4,
Hasegawa, T. I., Herbst, E., & Leung, C. M. 1992, ApJS, 82, 167
Hily-Blant, P., Maret, S., Bacmann, A., et al. 2010, A&A, 521, L52
Hincelin, U., Wakelam, V., Hersant, F., et al. 2011, A&A, 530, A61
Hollis, J. M., Snyder, L. E., Lovas, F. J., & Buhl, D. 1976, ApJ, 209, L83
Hunter, S. D., Digel, S. W., de Geus, E. J., & Kanbach, G. 1994, ApJ, 436, 216
Jaber, A. A., Ceccarelli, C., Kahane, C., & Caux, E. 2014, ApJ, 791, 29
Klemperer, W. 1970, Nature, 227, 1230
Loinard, L., Torres, R. M., Mioduszewski, A. J., & Rodríguez, L. F. 2008, ApJ, 675, L29
Loinard, L., Zapata, L. A., Rodríguez, L. F., et al. 2013, MNRAS, 430, L10
Loison, J.-C., Wakelam, V., Hickson, K. M., Bergeat, A., & Mereau, R. 2014, MNRAS, 437, 930
López-Sepulcre, A., Jaber, A. A., Mendoza, E., et al. 2015, MNRAS, 449, 2438
Lucas, R., & Liszt, H. 1994, A&A, 282, L5
Majumdar, L., Gratier, P., Vidal, T., et al. 2016, MNRAS,
Mladenović, M., & Roueff, E. 2014, A&A, 566, A144
Mundy, L. G., Wootten, A., Wilking, B. A., Blake, G. A., & Sargent, A. I. 1992, ApJ, 385, 306
Neufeld, D. A., Wolfire, M. G., & Schilke, P. 2005, ApJ, 628, 260
Ossenkopf, V., & Henning, T. 1994, A&A, 291, 943
Ott, S. 2010, Astronomical Data Analysis Software and Systems XIX, 434, 139
Persson, M. V., Jørgensen, J. K., & van Dishoeck, E. F. 2013, A&A, 549, L3
Persson, M. V., Jørgensen, J. K., van Dishoeck, E. F., & Harsono, D. 2014, A&A, 563, A74
Pulliam, R. L., Edwards, J. L., & Ziurys, L. M. 2011, ApJ, 743, 36
Rao, R., Girart, J. M., Marrone, D. P., Lai, S.-P., & Schnee, S. 2009, ApJ, 707, 921
Rawlings, J. M. C., Taylor, S. D., & Williams, D. A. 2000, MNRAS, 313, 461
Rawlings, J. M. C., Redman, M. P., Keto, E., & Williams, D. A. 2004, MNRAS, 351, 1054
Roberts, H., & Millar, T. J. 2000, A&A, 361, 388
Roelfsema, P. R., Helmich, F. P., Teyssier, D., et al. 2012, A&A, 537, A17
Rollins, R. P., Rawlings, J. M. C., Williams, D. A., & Redman, M. P. 2014, MNRAS, 443, 3033
Ruaud, M., Wakelam, V., & Hersant, F. 2016, MNRAS,
Savage, C., & Ziurys, L. M. 2004, ApJ, 616, 966
Shu, F. H. 1977, ApJ, 214, 488
Snyder, L. E., Hollis, J. M., Lovas, F. J., & Ulich, B. L. 1976, ApJ, 209, 67
Stark, R., Sandell, G., Beck, S. C., et al. 2004, ApJ, 608, 341
Vastel, C., Ceccarelli, C., Caux, E., et al. 2010, A&A, 521, L31
Visser, R., Kristensen, L. E., Bruderer, S., et al. 2012, A&A, 537, AA55
Wakelam, V., Vastel, C., Aikawa, Y., et al. 2014, MNRAS, 445, 2854
Wakelam, V., Loison, J.-C., Herbst, E., et al. 2015, ApJS, 217, 20
Wilson, T. L., & Rood, R. 1994, ARA&A, 32, 191
Woods, R. C., Dixon, T. A., Saykally, R. J., & Szanto, P. G. 1975, Physical Review Letters, 35, 1269
Wootten, A. 1989, ApJ, 337, 858
Yeh, S. C. C., Hirano, N., Bourke, T. L., et al. 2008, ApJ, 675, 454
Ziurys, L. M., Tenenbaum, E. D., Pulliam, R. L., Woolf, N. J., & Milam, S. N. 2009, ApJ, 695, 1604

Astronomy & Astrophysics manuscript no. LimeServer_paper
November 18, 2015

Modelling the 3D physical structure of astrophysical sources with GASS

D. Quénard[1,2], S. Bottinelli[1,2], and E. Caux[1,2]

[1] Université de Toulouse, UPS-OMP, IRAP, Toulouse, France

[2] CNRS, IRAP, 9 Av. colonel Roche, BP 44346, 31028 Toulouse Cedex 4, France

Written April 10, 2015

ABSTRACT

Context. The era of interferometric observations leads to the need of a more and more precise description of physical structures and dynamics of star-forming regions, from pre-stellar cores to proto-planetary disks.
Aims. The molecular emission can be traced in multiple physical components such as infalling envelopes, outflows, and proto-planetary disks. To compare with the observations, a precise and complex radiative transfer modelling of these regions is needed.
Methods. We present GASS, a code that allows to generate the 3D physical structure model of astrophysical sources. From the GASS graphical interface, the user easily creates different components such as spherical envelopes, outflows, and disks. The physical properties (molecular density, temperature, velocity field, etc.) of these components are modelled thanks to multiple graphical interfaces that display various figures to ease and help the user. For each component, the code randomly generates points in a three dimensional grid with a sample probability weighted by the molecular density.
Results. The created models can be used as the physical structure input for 3D radiative transfer codes to predict the molecular line or continuum emission. An analysis of the output hyper-spectral cube given by such radiative transfer code can be made directly in GASS using the various post-treatment options implemented. This paper is focused on the results given by LIME, a 3D radiative transfer code, and a benchmarking is made between this code and RATRAN.
Conclusions. Because of the complex geometry observed in star-forming regions, GASS is well-suited to model and analyse both interferometric and single-dish data.

Key words. astrochemistry – methods: numerical – radiative transfer – ISM: molecules

1. Introduction

The ability to predict line emission is crucial in order to make a comparison with observations. Different modelling approximations and hypothesis can be considered depending on the complexity of the problem. From LTE to full radiative transfer codes, the goal is always to predict the physical properties of the source the most accurately possible. Non-LTE calculations can be very time consuming but are often needed in most of the cases since many studied regions are far from LTE. A few freely usable codes are available such as RATRAN[1] (Hogerheijde & van der Tak 2000) a 1D radiative transfer code, LIME (Brinch & Hogerheijde 2010) a 3D one, MC3D[2], and RADMC-3D[3].

Among the choice of 3D radiative transfer code available to date, LIME is the only one doing a full non-LTE ALI (accelerated lambda iteration) continuum and gas line radiative transfer treatment. Other available codes only offer a LTE or LVG gas line radiative transfer (RADMC-3D) or a dust continuum radiative transfer (MC3D and RADMC-3D). LIME is based on RATRAN and a benchmarking of the two codes has been made by Brinch & Hogerheijde (2010). LIME is well-suited for the treatment of most physical problems due to its performance and its flexible use: proper treatment of line blending, multiple species input, multi-line raytracing, and multi-core parallelisation.

We have developed a user-friendly interface, GASS (Generator of Astrophysical Sources Structure), in order to easily define the physical structure of a star-forming region and create input models for LIME. Thanks to its interface, GASS allows to create, manipulate, and mix one or several different physical components such as spherical sources (see Section 3.1), disks (see Section 3.2), and outflows (see Section 3.3).

The outline of this paper is the following. Section 2 presents the griding process used to create the model with GASS, Section 3 describes how the physical properties of each of the structure is generated by the code, Section 4 provides an in-depth comparison between {GASS + LIME} and RATRAN, Section 5 gives an example of the 3D modelling capabilities of GASS, and finally, conclusions are given in Section 6.

2. Grid generation

In order to work in LIME, models need to be set in a cartesian grid that can be defined by two means: (a) from a script called *model.c* included directly in the code that allows to define the physical properties very basically, for instance as a function of the radius without any complexe 3D structure; (b) from an input model parameter file of the source in which the physical parame-

---

[1] `http://www.sron.rug.nl/~vdtak/ratran/`

[2] `http://www.astrophysik.uni-kiel.de/~star/index.php?seite=mc3d`

[3] `http://www.ita.uni-heidelberg.de/~dullemond/software/radmc-3d/`

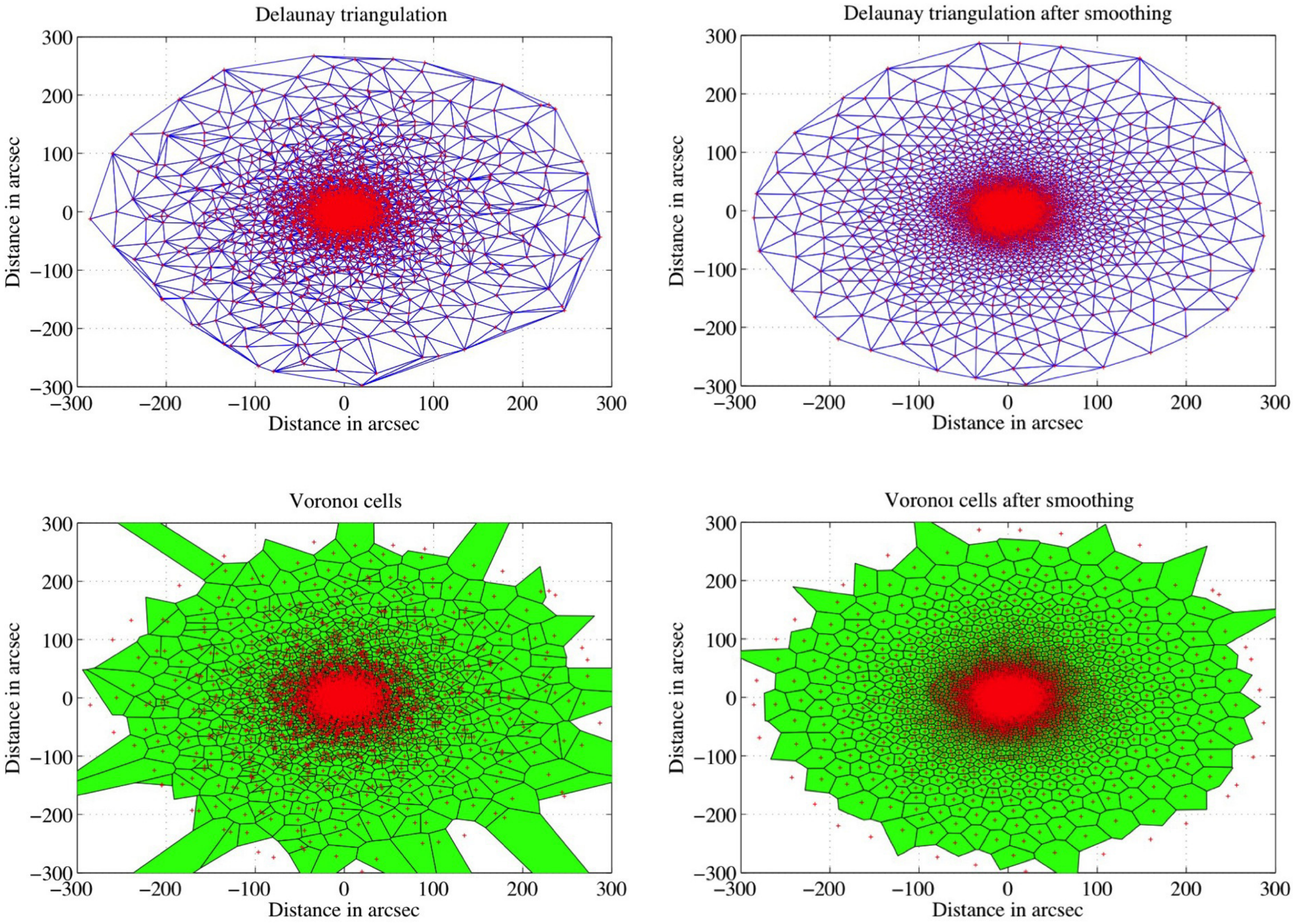

Fig. 2: The Delaunay triangulation (top panels) and Voronoï cells (bottom panels) before (left) and after (right) the smoothing process with the Lloyd algorithm. The grid points are shown in red.

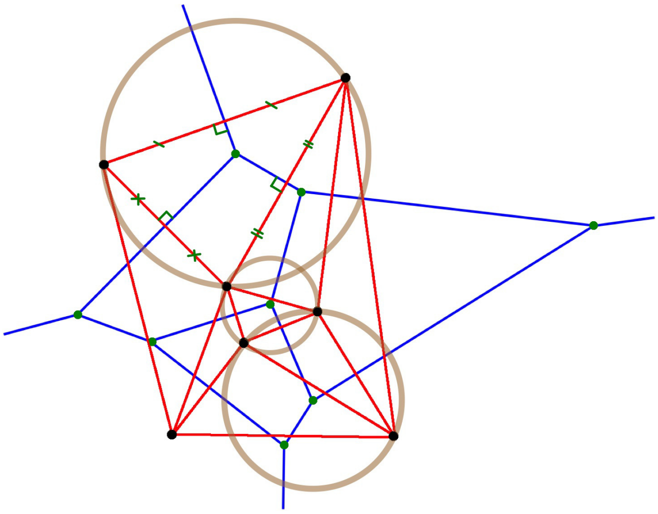

Fig. 1: Example of the Voronoï cells building. The black dots are the grid points and the red lines show the Delaunay triangulation from which we derive the Voronoï cells in blue. Three examples of the Delaunay triangle circumcircle are plotted in brown. We also display one example of the three bisector construction in one Delaunay triangle.

ters (temperature, density, abundance, . . .) are described at each point of the cartesian grid. It is important to keep in mind that an input file is a huge gain in time since the model is created before giving it to LIME. Otherwise, LIME will generate its own grid as a function of the desired number of point and this step can be very time consuming.

The model generation is entirely managed by GASS and the procedure is the following:

1. Creation of the random grid as a function of the number of points. In order to have a good convergence of the calculations, the advice is to use at least a few thousands points for the grid (Brinch & Hogerheijde 2010). Each point is randomly distributed among the desired radius of the grid, and in the spherical source case, the distribution of grid points follows the density profile. Such a distribution leads to an increasing number of grid points per unit volume toward the centre to follow the distribution of the volume density across the spherical source. In the disk and outflow cases, considering their specific geometries, we decided to distribute the point equally all over their structure.
2. From this random grid, a Delaunay triangulation (Delaunay 1934) is generated by connecting three neighbouring points. These points defines the Delaunay circle and no other points of the grid lies in the circle.
3. From the Delaunay grid we can construct the Voronoï cells (Voronoï 1908). Fig. 1 shows a sketch of how the Voronoï diagram is built from the Delaunay triangulation of the black

dots. The three bisectors (in blue) of each Delaunay triangle (in red) define the centre of the circumcircle (in brown) of each triangle. This centre defines a vertex (green points) of the Voronoï diagram. Thus, each bisector of a Delaunay triangle is an edge of a Voronoï cell. By construction, two given points of the grid can thus be created much closer or further apart than desired. This leads to a very irregular Delaunay grid and an insufficient number of points in the grid will produce non-homogenous effect induced by the different sizes and shapes of the Voronoï cells. A few thousands points is the minimum required to avoid this effect.

4. The final step consists in smoothing the grid to reduce even more the previous effect. We based our smoothing on the Lloyd algorithm (Lloyd 1982; Springel 2010), which consists in moving every point in the centre of mass of its Voronoï cell. From the new points positions we re-create the Delaunay grid and we repeat the process (bullets 3. and 4.). We choose to limit the iteration number at 10 to keep the randomness of the distribution. A great number of iterations will tend to completely smooth the grid and form a regular grid.

Fig. 2 displays the Delaunay triangulation and the Voronoï diagram before and after smoothing of a 2D grid. The points of the grid are plotted in red. The comparison between the two figures shows the impact of the smoothing algorithm after 10 iterations: the size of the Voronoï cells is more homogeneous at a given radius but the grid points are still distributed randomly.

To illustrate the different point distribution and smoothing effect according to the different structures, we simulated them and the results are shown in Fig. 3 where the cumulated number of points in the grid as a function of the radius in arcsec are plotted. The blue and red curves are the distribution of points before and after smoothing respectively. In the top panel, a spherical source located at 120 pc generated with 10,000 points distributed over a $50''$ grid was considered. In this plot, one can notice that the smoothing process only moves the points in the 3D grid without affecting the distribution as a function of the radius. During the smoothing process, some of the points will be moved inside and outside of the inner and outer edges of the grid (in this example: $0.1''$ for the inner edge and $50''$ for the outer one), and these points are not included in the model anymore. To be sure that the minimum number of points will be at least 10,000 points, 2.5% more points are arbitrary added (total of 10,250 points) during the creation of the grid. In this example, 239 points have been rejected after the smoothing process.

The case of the disk grid generation is slightly different since we also have to consider the inner cylindrical and outer spherical radius (ρ_{in} and r_{max}) and the maximum height (h_{max}) of the disk (see Fig. 4 and Section 3.2). This results in a different distribution of points compared to the envelope. Indeed, grid points are generated over the entire volume of the cube defining the size of the modelled region, whereas the disk is a flattened structure, resulting in a lot of points being generated outside of the edges. The Lloyd algorithm will then reject more points outside of the grid and to avoid this effect we limit the number of iteration to five and 5% more points are added in this case. The middle panel of Fig. 3 displays a simulation of a disk grid generation by setting a total number of 5,000 points, an inner and outer radii of $1''$ and $10''$ respectively. The maximum height of the disk is set to $2''$. One can note from this figure that the Lloyd algorithm moves many points according to the different shape of the distribution before and after the smoothing process.

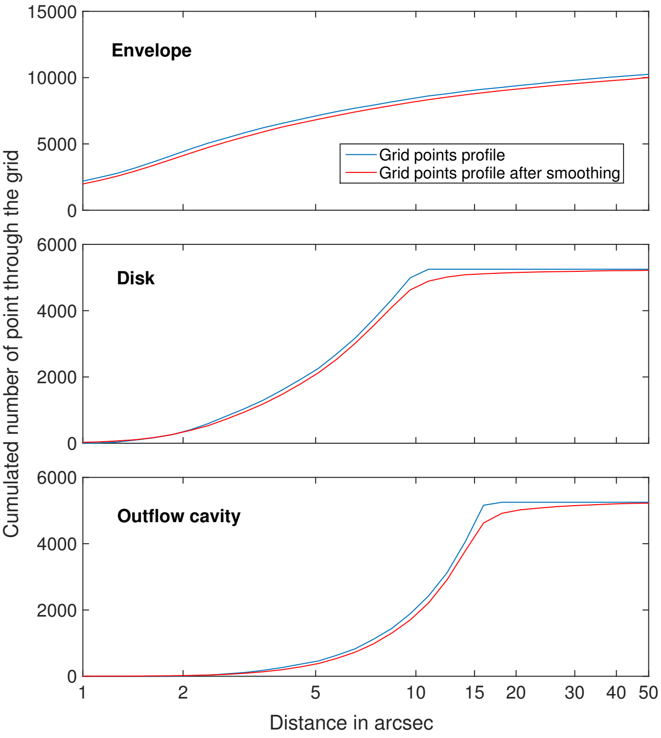

Fig. 3: Cumulated number of points through the grid as a function of the radial distance in arcsec for the three different type of structure. The distribution of points is shown before (in blue) and after (in red) the smoothing process.

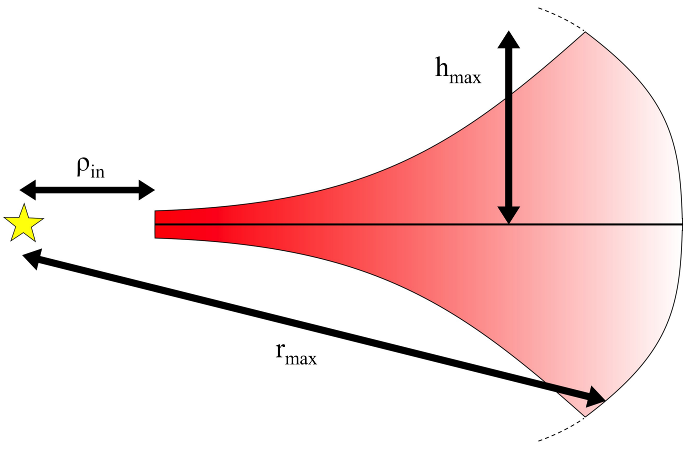

Fig. 4: Sketch showing the different parameters that define the structure of the disk. ρ_{in} is the inner cylindrical radius of the disk while r_{max} is its outer spherical radius, shown by the dotted lines. h_{max} is taken from the mid-plane of the disk.

The outflow model is always considered attached either to an envelope or a disk and cannot be created alone. Nonetheless, for the outflow the points generation is performed as it is for the disk (see bottom panel of Fig. 3). In the outflow case we consider the inner cylindrical radius ρ_{in} and the maximum height z_{out} of the outflow (see Fig. 5). The cavity angle $\tan \gamma_{cav} = z_{outflow}/\rho_{outflow}$ is defined as the angle between the points and the mid-plane (see Fig. 5). Each point of the grid is generated between γ_{cav} and

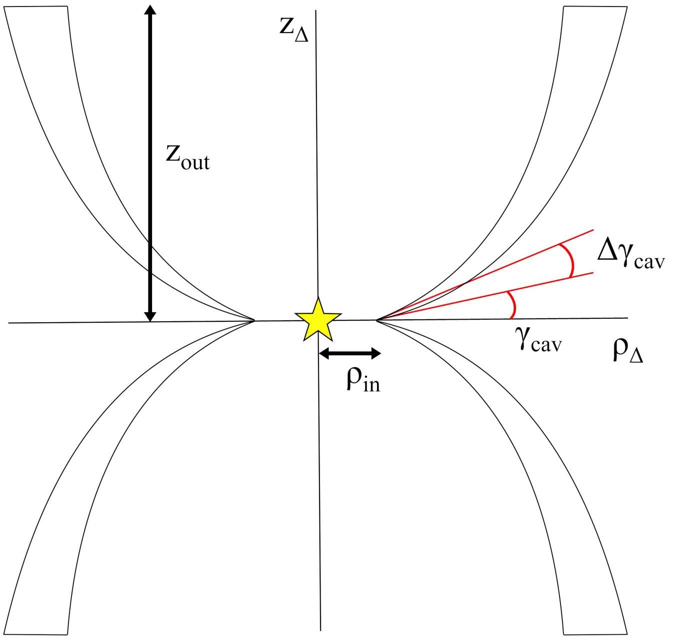

Fig. 5: Sketch showing the different parameters that define the structure of the outflow. ρ_{in} is the inner cylindrical radius of the outflow while z_{out} is the maximum height that the outflow can reach. ρ_Δ and z_Δ define the cylindrical axes of the outflow. $\Delta\gamma_{cav}$ defines the width of the cavity walls.

$\gamma_{cav} + \Delta\gamma$ where $\Delta\gamma$ is set by the user and define the width of the cavity wall (see Section 3.3 for more details about the cavity walls). The smoothing process is here also limited to five iterations to avoid a great number of points to be moved outside of the model and 5% more points are added as in the disk generation process. The bottom panel of Fig. 3 displays a simulation of an outflow cavity grid generation by setting a total number of 5,000 points, an inner and outer radii of 1″ and 15″ respectively with $a_{outflow} = 150''$, $b_{outflow} = 15''$, and $\Delta\gamma = 5°$. The shape and the clear limit at 15″ of the outflow cavity can be identified in this plot. Visser et al. (2012) have used the same kind of outflow cavity walls griding process. We do not consider the same angle constraints than Visser et al. (2012) since the outflow is always created with another structure (envelope or disk).

3. Creation of the model

3.1. Spherical sources generation

Each Voronoï cell created will be defined by a constant value for each of the physical parameters we consider: gas temperature, dust temperature, H_2 density, molecular abundance, velocity field and doppler parameter. The given value for each cell is determined through an interpolation of the physical profile defined in input for each of these parameters. Since the grid is distributed randomly, each one of the Voronoï cells is situated at a different radius, thus it is uniquely defined by its physical properties. Both the density and temperature profiles can be defined with a variable number of regions N_{temp} and N_{dens} respectively as a function of the radial distance from the central object by:

1. Multiple power law profiles: for each temperature region i, a power law coefficient α_i and a temperature $T_{env,i}$ value is set for a given radius $r_{0,i}^{temp}$ and for each density region j a power law coefficient β_j and a density $n(H_2)_{env,j}$ value is set for a given radius $r_{0,j}^{dens}$. The total physical profile is then defined as
$$T_{env} = \sum_{i}^{N_{temp}} T_{env,i} \left(\frac{r_i}{r_{0,i}^{temp}} \right)^{\alpha_i}, \quad (1)$$
$$n(H_2)_{env} = \sum_{j}^{N_{dens}} n(H_2)_{env,j} \left(\frac{r_j}{r_{0,j}^{dens}} \right)^{\beta_j}. \quad (2)$$
where r_i and r_j are all the radii that define the regions i and j respectively. Thus, the final temperature or density value of a region becomes the first temperature or density value of the following regions, ensuring the continuity of the physical profile.
2. Multiple temperature or density steps: for each region, a temperature or a density is set for a given radius. The code interpolates the temperature linearly and the density logarithmically between the two points. As above, different radii can be set for the temperature and the density profile.

The abundance profile can only be defined in multiple regions N_{abund} as a function of the radius or the temperature. The interpolation process is the same as of the temperature or the density profile but the user can choose a constant or logarithmic abundance within the region. Each abundance value in each region can be gridded to calculate multiple models at the same time.

In the case that more than one structure (spherical source or disk) is used, the problem is to take into account their different contribution over the entire grid. This is only done for the spherical sources meanwhile outflows and disks impose their own physical properties in the region where they are defined, without considering the presence of the spherical sources (see Section 3.3). In any case, the outflow structure always prevails over other structures. For each point of the grid, the density of each source is added following the equation:

$$n_{cell} = \sum_{i}^{N} n_i, \quad (3)$$

where n_{cell} is the total H_2 density of the cell, n_i the H_2 density contribution of the spherical structure i and N the number of different spherical structures. For the gas temperature we consider the ideal gas law equation of state $P = nk_BT$, where P is the pressure of the gas, n the number density, k_B the Boltzmann constant, and T the absolute temperature. Since we consider a polyatomic species, each cell contains a total energy of

$$U_{cell} = \frac{5}{2} k_B T_{cell} n_{cell} = \sum_{i}^{N} \frac{5}{2} k_B T_i n_i, \quad (4)$$

where U_{cell} is the internal energy of the cell, T_{cell} the total temperature and n_{cell} the total number density. The previous equation combined with Eq. (3) leads to

$$T_{cell} = \frac{1}{\sum_i^N n_i} \times \sum_{i}^{N} T_i n_i. \quad (5)$$

The dust temperature can be defined separately but it can also be considered to be equal to the gas temperature. The molecular abundance $[X]$ can be defined as

$$[X] = \frac{n_X}{n}, \quad (6)$$

where n_X is the number density of the species. Considering the contribution of all the spherical sources, the abundance in each cell is

$$[X_{cell}] = \frac{n_{X,cell}}{n_{cell}} = \frac{1}{\sum_i^N n_i} \times \sum_i^N [X]_i n_i, \tag{7}$$

where $[X_{cell}]$ is the total molecular abundance in the cell and $n_{X,cell}$ is the total number density of the species.

To calculate the radiative transfer one need to define the total Doppler broadening, often called the $b-$doppler parameter:

$$b = v_D = \sqrt{v_{th}^2 + v_{turb}^2}, \tag{8}$$

where v_{turb} is the (micro-)turbulence velocity which operates on length scales shorter than the photon mean free path. The thermal velocity, v_{th}, is the random motion of molecules due to the kinetic temperature of the gas:

$$v_{th} = \sqrt{\frac{2\,k_B\,T}{\mu\,m_H}}, \tag{9}$$

Considering a Gaussian profile, the FWHM due to the Doppler broadening is:

$$\mathrm{FWHM}_D = 2\,\sqrt{\ln(2)} \times v_D, \tag{10}$$

where FWHM_D is the spectral line full width at half maximum. Eq. 10 can also be written as

$$b = \frac{1}{2\,\sqrt{\ln(2)}} \times \mathrm{FWHM}_D = 0.60 \times \mathrm{FWHM}_D. \tag{11}$$

In the current GASS version, the $b-$doppler parameter is considered constant throughout the grid and its value is defined by the user in the interface. The velocity field of the spherical source is determined by adding the different projections on the cartesian coordinates (X, Y, Z) of each velocity field induced by each structure included in the model. The intensity of the velocity field for each point of the grid for the spherical model is defined as an infall model (Shu 1977) by:

$$V_{inf}(r) = \sqrt{\frac{2\,G\,M_\star}{r}}, \tag{12}$$

where V_{inf} is the infall velocity, G the gravitational constant, $M_\star$ the mass of the central object, and r the distance from the central object. The projections on each cartesian coordinates are calculated by:

$$r = \sqrt{(X - X_\star)^2 + (Y - Y_\star)^2 + (Z - Z_\star)^2}, \tag{13}$$

$$\theta = \arctan\left(\frac{\sqrt{(X - X_\star)^2 + (Y - Y_\star)^2}}{Z - Z_\star}\right), \tag{14}$$

$$\phi = \arctan\left(\frac{(Y - Y_\star)}{(X - X_\star)}\right), \tag{15}$$

where $X_\star$, $Y_\star$, and $Z_\star$ are the coordinates of the central object. This leads to the following equations for the projection of the velocity vector:

$$\left\{\begin{array}{lcl} \mathbf{V}_x &=& -r\sin\theta\cos\phi\;\mathbf{e}_x, \\ \mathbf{V}_y &=& -r\sin\theta\sin\phi\;\mathbf{e}_y, \\ \mathbf{V}_z &=& -r\cos\theta\;\mathbf{e}_z, \end{array}\right. \tag{16}$$

where $\mathbf{e}_x$, $\mathbf{e}_y$, and $\mathbf{e}_z$ are the unit vectors. The velocity vector for each cell is then defined from the velocity of each structure i by:

$$\left\{\begin{array}{lcl} \mathbf{V}_{x,cell} &=& \sum_i^N \mathbf{V}_{x,i}, \\ \mathbf{V}_{y,cell} &=& \sum_i^N \mathbf{V}_{y,i}, \\ \mathbf{V}_{z,cell} &=& \sum_i^N \mathbf{V}_{z,i}. \end{array}\right. \tag{17}$$

3.2. Disk generation

The main difference between the spherical source model and the disk model is the number of symmetries. In the spherical case, every physical parameter can be defined as a function of the radius. In the disk model there is only one symmetry around the rotational axis of the disk. The physical properties are therefore defined as a function of both the radius ρ and the height z. One must take care of the difference between r and ρ: r is the spherical radial distance and ρ is the cylindrical radial distance. The link between the two radii is given by $r = \sqrt{\rho^2 + z^2}$. As said above, we have to consider the inner and outer radius (ρ_{in} and r_{max}) and the maximum height (h_{max}) of a disk. Every point of the grid must be included between these values and they must also be at a smaller height than the pressure scale height h_0, which is defined as follow (Brinch & Hogerheijde 2010):

$$h_0 = \sqrt{\frac{2\,T_{mid}\,k_B\,\rho^3}{G\,M_\star\,m_H}}, \tag{18}$$

with T_{mid} the mid-plane temperature of the disk, k_B the Boltzmann constant, G the gravitational constant, $M_\star$ the mass of the central object, and m_H the hydrogen atom mass. To calculate this value we need to define the mid-plane temperature gradient across the disk. This temperature can be defined by a power law (Williams & Best 2014):

$$T_{mid} = T_{mid,0}\left(\frac{\rho}{\rho_{in}}\right)^\gamma, \tag{19}$$

where $T_{mid,0}$ is the mid-plane temperature at the radius ρ_{in}. We also define the atmosphere temperature profile of a disk as the temperature profile at a specific height $z = 4\,h_0$ of the disk (see Williams & Best 2014). We set the atmosphere temperature the same way the mid-plane temperature is defined, by a power law

$$T_{atm} = T_{atm,0}\left(\frac{\rho}{\rho_{in}}\right)^\gamma, \tag{20}$$

with $T_{atm,0}$ is the atmosphere temperature at the radius ρ_{in}. All the characteristic value ($T_{mid,0}$, $T_{atm,0}$, ρ_{in}, and γ) can be set in the GASS user interface and plots are made to ease the visualisation of the results. The resulting temperature $T(\rho, z)$ in each cell of the disk as a function of ρ and z is (Williams & Best 2014):

$$T(\rho, z) = \begin{cases} T_{mid} + (T_{atm} - T_{mid})\left[\sin\left(\frac{\pi z}{4\,h_0}\right)\right]^4 & \text{if } z < 4\,h_0 \\ T_{atm} & \text{if } z \geqslant 4\,h_0 \end{cases}. \tag{21}$$

The density distribution is based on the profile from Brinch & Hogerheijde (2010) and defined by

$$n_{H_2}(\rho, z) = n_0\left(\frac{\rho}{\rho_{in}}\right)^\delta \exp\left[-\left(\frac{z}{h_0}\right)^2\right], \tag{22}$$

with n_0 the H_2 density at ρ_0. As for the temperature profile, n_0 and δ can be set in the interface. The way GASS deals with the abundance profile generation is the same as for the envelope. The abundance profile can be defined as a function of the cylindrical radial distance ρ or as a function of the total temperature profile $T(\rho, z)$ of the disk. Thus, according to the choice of these two options, the abundance profile will depend on the disk height z.

The cylindrical axis Δ of the disk model can be rotated as a function of two angles, Θ and Φ, thanks to the rotation matrix

$$R_{(\Theta,\Phi)} = \begin{pmatrix} \cos(\Phi) & 0 & -\sin(\Phi) \\ \sin(\Theta)\sin(\Phi) & \cos(\Theta) & \sin(\Theta)\cos(\Phi) \\ \cos(\Theta)\sin(\Phi) & -\sin(\Theta) & \cos(\Theta)\cos(\Phi) \end{pmatrix}, \tag{23}$$

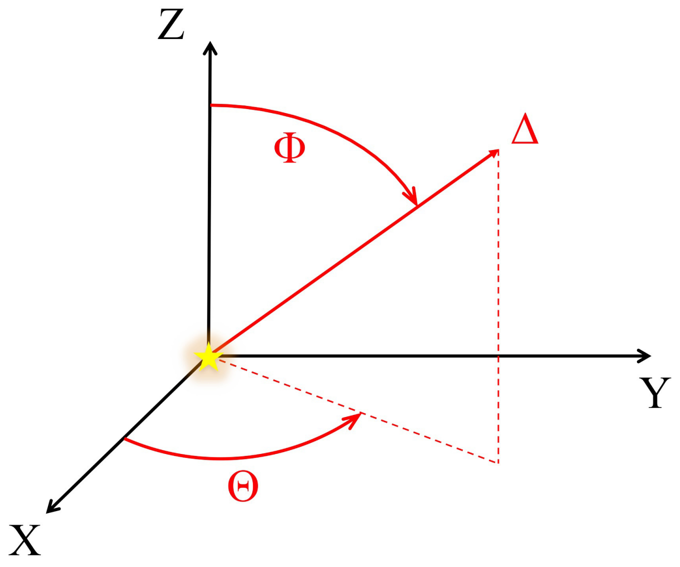

Fig. 6: Sketch showing the different angles that are used by the code to rotate the disk and the outflow models. Δ represents the axis on which the model is constructed.

where Θ is the angle between the axis Δ and the z-axis and Φ is the angle between the x-axis and projection of the axis Δ in the (X, Y) plane (see Fig. 6).

Fig. 7 shows a disk located at 300 pc generated with 10,000 points with $\rho_{in} = 0.7''$, $r_{max} = 7''$, $\Theta = 45°$, and $\Phi = 45°$. In this figure is also displayed the velocity field, supposed to follow the Keplerian rotation with the equation

$$V_{rot}(\rho, z) = \sqrt{\frac{G\, M_\star}{(\rho^2 + z^2)^{1/2}}}. \tag{24}$$

Fig. 8 shows the resulting positions of the grid points in cylindrical coordinates plotted with the pressure scale height h_0. This plot verifies that the program correctly rejects as disk points any point higher than the pressure scale height.

GASS also computes the total gas mass of the disk by adding the mass contribution of every cell i identified to belong to the disk model. Considering the total number of disk points N_{disk}, one can write

$$M^{gas}_{disk} = \frac{m_{H_2}}{M_\odot} \times \sum_{i}^{N_{disk}} 2\pi\, \rho_i\, d\rho_i\, dz_i\, n(H_2)_i, \tag{25}$$

with m_{H_2} the mass of H_2, ρ_i the cylindrical distance of the cell i, $d\rho_i$ and dz_i its size, and $n(H_2)_i$ its H_2 density.

3.3. Outflow generation

To date, one can consider three distinct types of outflows driven by jets or winds and a summary of their properties has been given in Arce et al. (2007):

1. The wind-driven shell model, with a wide-angle radial wind and a thin shell interacting with the envelope.
2. The turbulent jet model, with Kelvin-Helmholtz instabilities along the jet/environmental boundary leading to a turbulent viscous layer.

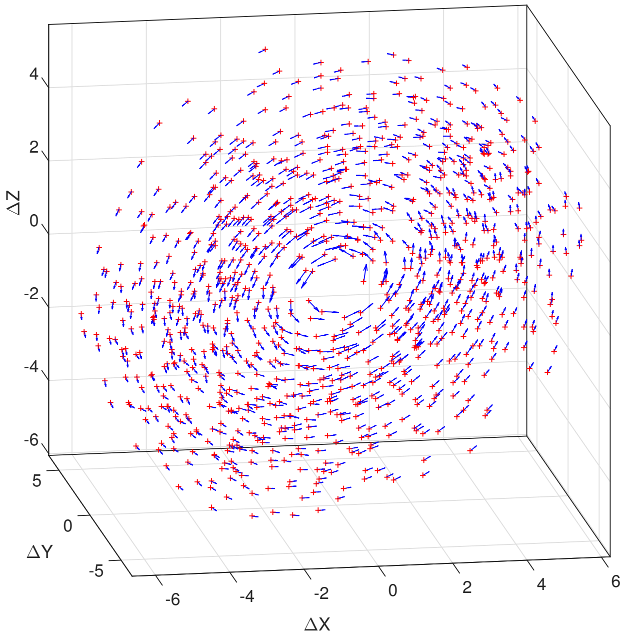

Fig. 7: Grid points distribution (red crosses) over the described model. The inner radius ρ_{in} is clearly visible as well as the two rotation angles Θ and Φ. The velocity vectors are plotted in blue and show the Keplerian rotation of the disk.

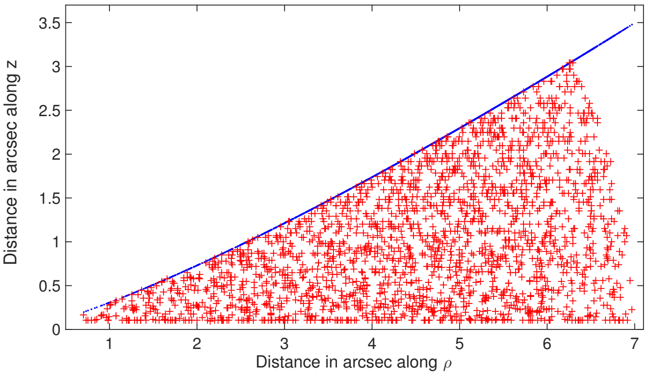

Fig. 8: Disk profile in cylindrical coordinates (ρ, z). Grid points are shown in red whereas the specific pressure scale height h_0 is plotted in blue. GASS automatically rejects any point above this height. The inner cylindrical and outer spherical radii (ρ_{in} and r_{out}) can be identified as well.

3. The jet bow-shock model with a highly collimated jet blowing the envelope away and creating a thin outflow shell (cavity walls) around the jet.

Arce & Sargent (2006) and Arce et al. (2007) have shown that in reality these different kinds of outflows are probing different outflow ages, thus probing different protostars stages (Cantó et al. 2008). Young outflows tend to be associated to the outflow type *(3)* with highly collimated jets and a faint wind. As the protostar evolves, the loss of surrounding materials leads to a less dense environment around the jet. The outflow becomes wider and the wind stronger, now associated to the type *(1)* of outflows. This trend can be used to estimate the age of a low-mass protostar (see Arce & Sargent 2006, especially their discussion section and Fig. 8).

GASS can deal with both the wind-driven shell model *(1)* and the jet bow-shock outflow model *(3)* by setting the appropriate value of the parameters $a_{outflow}$, $b_{outflow}$, and $\Delta\gamma$ (see Fig. 5).

The outflow model is based on the mathematical definition given by Visser et al. (2012) and assimilated to an ellipse (or a part of an ellipse) centred on a central object with $a_{outflow}$ and $b_{outflow}$ the ellipse parameters. The outflow is modelled around an axis Δ (first superimposed to the z-axis) and the height of the outflow z_Δ is defined as a function of the cylindrical radial distance ρ_Δ from Δ by:

$$z_\Delta = b_{outflow}\sqrt{1-\left(\frac{\rho_\Delta}{a_{outflow}}-1\right)^2}. \qquad (26)$$

The model is considered to be bipolar and symmetric with respect to the (X, Y) plane but the user can choose only one part of the outflow in the interface if needed. In our models, outflows are always associated to a spherical structure or a proto-planetary disk and cannot be modelled alone. Thus, there is always a central object which defines the centre coordinates of the outflow. The axis Δ can be rotated in the model as a function of the two angles Θ and Φ thanks to the rotation matrix described in the previous section. The size of the outflow is limited by an inner radius r_{in} and a maximum height z_{out} determined by the user in the interface. The code will then identify which points belong to the outflow structure, thus no points are added to the model.

In its region of influence, the outflow imposes its physical parameters as if its gas blows away the spherical envelope when it forms. The H_2 density n_{H_2}, the gas temperature T_{gas}, and the abundance $[X]$ are defined using a power law as a function of the cylindrical radial distance ρ from the central object:

$$\left\{n_{H_2}, T_{gas}, [X]\right\} = \{n_0, T_0, [X]_0\}\left(\frac{\rho}{\rho_{in}}\right)^{\{\epsilon,\zeta,\eta\}}, \qquad (27)$$

where n_0, T_0, and $[X]_0$ are respectively the density, temperature, and abundance value at ρ_{in}. ϵ, ζ, and η are the power-law indices associated to each of this parameter respectively. The velocity field is defined along the shape of the outflow with a constant value, taking into account that the velocity vector is always parallel to the Δ axis. Since the outflow gas is still subject to the gravitational field of the central object, the velocity vector of the outflow is added to the spherical model one. Fig. 9 shows the grid points that are assimilated to an outflow model located at 120 pc. The outflow parameters are: $\rho_{in} = 1''$, $\rho_{out} = 15''$, $a_{outflow} = 150''$, $b_{outflow} = 15''$, $\Theta = 45°$, and $\Phi = -45°$.

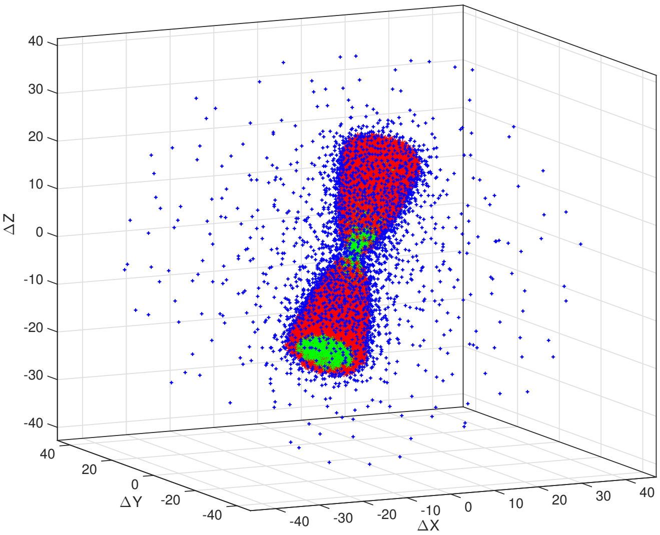

Fig. 9: All the points have been generated by the outflow grid process. The red points have been identified among these points as the outflow cavity structure and now belongs to its model. All the other points have been rejected, the blue and green ones are respectively outside and inside the cavity walls of the outflow.

3.4. Post-LIME treatment

Once the models have been calculated by LIME, GASS offers several functionalities to deal with the output fits file, depending on the observations in hands of the user or depending on the processing he wants to perform with the models. A smoothing tool allows the user to smooth a certain number of model. Even if a smoothing process is already done through the Lloyd algorithm (see Section 2), averaging several runs allows to reduce the initial number of points in the grid. Each model is built with a different grid, thus the average of these runs minimises the artifacts due to the grid. The total execution time of a run in LIME depends a lot on this initial number of points, thus it is faster and more efficient to run ten models with 10,000 points at the same time and average them rather than doing a single run with 100,000 points. The smooth option in GASS does this automatically and creates a resulting smoothed fits file for each transition.

The moment 0 and 1 of a given data cube can be calculated by the program, using the following equations:

$$M_0 = \int I(v)\,dv, \qquad (28)$$

$$M_1 = \frac{\int I(v)\,v\,dv}{\int I(v)\,dv} = \frac{\int I(v)\,v\,dv}{M_0}, \qquad (29)$$

where the integral is calculated over the desired number of channels. The graphical interface allows the user to choose the channels over which s/he wants to calculate the moments and plot the results.

Another tool allows to plot the resulting spectra of each transition in order to compare them to single-dish observations. The user gives in input a formatted file containing the information about the observations such as the name of the telescope (or the size of the antenna), the rms and a table of frequencies and intensities for each spectra. The code reads each data cube (fits files) produced by LIME and the graphical interface allows the user to choose the desired pointing position of the telescope in the output map. The best fit model is then calculated over all the models, following the standard χ^2 minimisation value for N_{spec} spectra of N points, given by the equation :

$$\chi^2 = \sum_{i=1}^{N_{spec}} \chi_i^2 \quad \text{and} \quad \chi_i^2 = \sum_{j=1}^{N} \frac{(I_{obs,j} - I_{model,j})^2}{rms^2 + (cal_i \times I_{obs,j})^2}, \qquad (30)$$

where I_{obs} and I_{model} are respectively the observed and the modelled intensity, cal_i is the calibration factor of the spectrum and N is the total number of points of the spectrum.

In the case of interferometric observations, the analysis is more complicated. GASS possesses a tool that helps the comparison between the observations and the models. A 2D Gaussian tool allows to convolve the data cube with the observed beam of the interferometric data by giving the major and minor axes of the beam and its position angle. It is also possible to add a white noise to the data cube before the convolution to reproduce the observed rms. From the graphical interface, the user can display the moment 0 of the original data cube as well as the convolved data cube + noise. The input data cube must be in Jy/pixel and GASS can write an output fits file with the final results in Jy/beam. It is then possible to read this output fits file in the Common Astronomy Software Applications package (CASA) to perform further analysis of the model (position-velocity diagram for instance). One can also use directly the output hyper-spectral cube created by {GASS + LIME} to produce observation simulations with the *simobserve* and *simanalyze* CASA tasks. An example of all these tools is shown in Section 5.

4. Benchmarking

Considering a 1D collapse model, Brinch & Hogerheijde (2010) performed a benchmarking between LIME and RATRAN, focused on the convergence of the population level between the two codes. In this section we extended this benchmarking to test different critical physical output parameters between the two codes:

1. The population density of the energy levels as a function of the radius.
2. The shape and intensity of the line profile across different beam positions and sizes in the map.
3. The value of the predicted continuum level.

In this benchmarking, the RATRAN version used is that of March 2013, and the LIME version is 1.5.

Since RATRAN is a 1D code, we consider a spherical model of a collapsing envelope around a central object located at 120 pc. To perform this benchmarking, we use a source having the physical structure of IRAS16293-2422 as derived by Crimier et al. (2010), and we compute the emission of HCO^+ from $J = 1 \rightarrow 0$ to $J = 13 \rightarrow 12$.

LIME and RATRAN have different input parameters needed to be set. For this benchmark, these parameters are defined in Table 1. We use variable gas and dust temperatures and H_2 density profiles as a function of the radius (see Fig. 10) and set a constant abundance and b−doppler value all over the model of 5×10^{-12} and 200 $\mathrm{m\,s^{-1}}$, respectively. By construction, in the two codes, the velocity field plays an important role in the resulting data cubes. Since RATRAN is built with spherical shells, the value of the radial velocity field is the same between two given radii. In LIME, every cell is located at a different radius and thus possess a different value of the velocity field, not always considered radial (depending on the 3D structure of the model). This effect strongly affect the calculated opacity since a larger column density of gas have the same velocity in RATRAN. Therefore, in order to avoid any difference between the two calculations, the velocity field was set to zero in this benchmarking. The only line broadening process considered is the b−doppler parameter.

Table 1: Benchmark model properties.

Number of channels	71
Channel resolution	100 $\mathrm{m\,s^{-1}}$
Image size	171 x 171
Pixel size	0.2″
Outer radius	6000 au (50″ at 120 pc)
Gas-to-dust ratio	100
RATRAN shell numbers	191
LIME number of points	101992

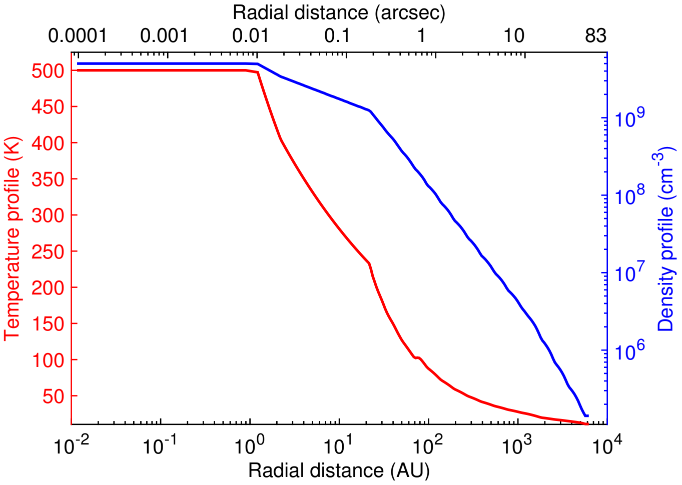

Fig. 10: Gas and dust temperatures (in red) and H_2 density (in blue) as a function of the radius.

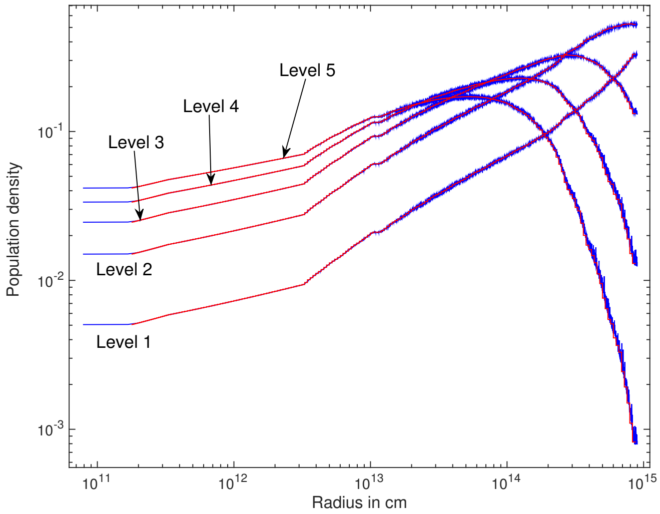

Fig. 11: Population density of the first 5 levels of HCO^+ as a function of the radius. The blue curves corresponds to LIME and the red one to RATRAN.

RATRAN and LIME are both doing first the calculation of the population density of the different energy levels of the molecule. Fig. 11 shows a good agreement between RATRAN and LIME for the calculation of the population density of the first five levels of HCO^+. One can note that the LIME curves become a bit ratty at large radii, this is due to the cell density becoming smaller in the outer part of the model. This effect does not affect the resulting images since the mean value stay very close to the RATRAN ones.

An illustration of the comparison between the outputs of RATRAN and LIME is shown in Fig. 12 for three transitions among all the calculated ones. Figures 12a, 12b, and 12c display the $J = 1 \rightarrow 0$, $J = 6 \rightarrow 5$, and $J = 13 \rightarrow 12$ transitions respectively. These transitions span a wide range of upper energy levels, E_{up} ($\sim$ 4 K to $\sim$ 400 K), and give a good sample to trace the differences between the two codes. Figures 12d shows the results for the $J = 13 \rightarrow 12$ transition, but with a different

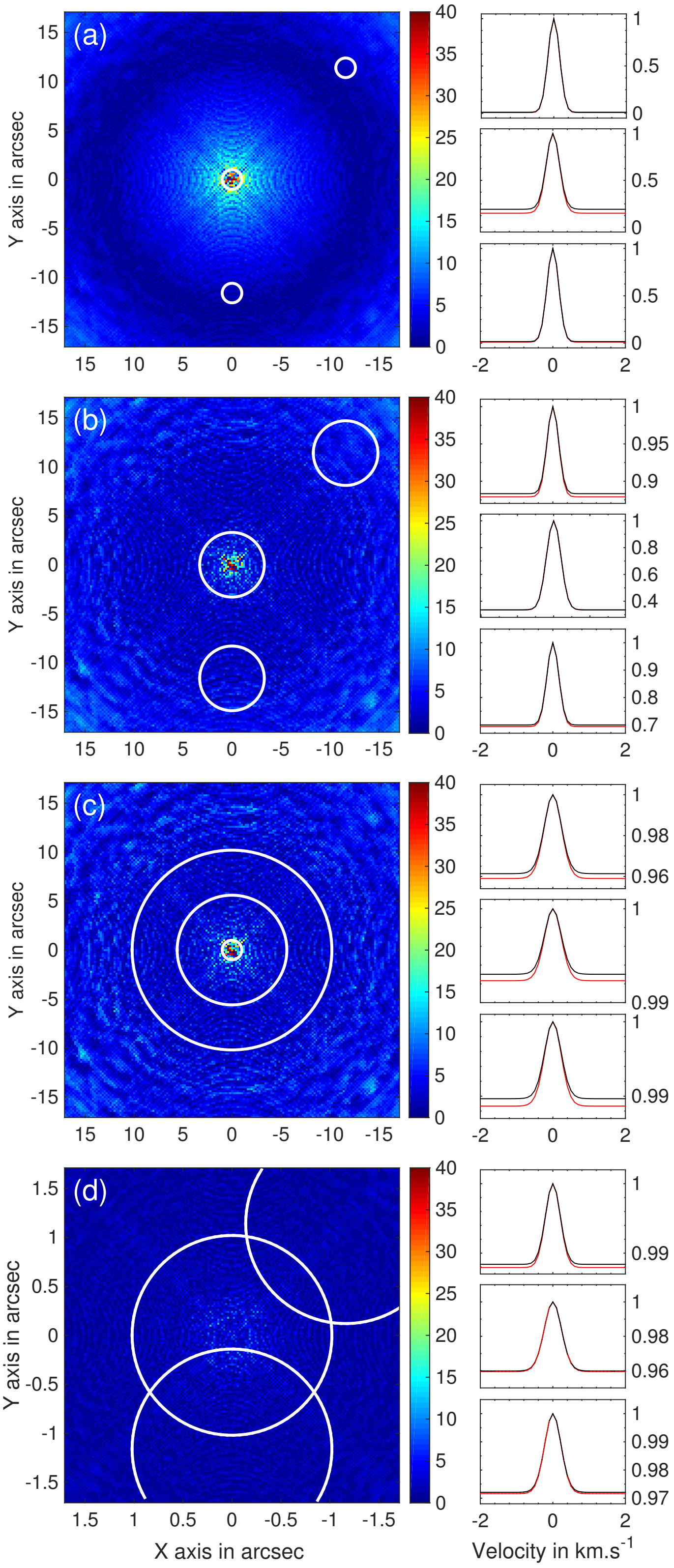

Fig. 12: *Left panels:* Comparison in % between the output cubes of RATRAN and LIME for the HCO$^+$ $J = 1 \rightarrow 0$, $J = 6 \rightarrow 5$, and $J = 13 \rightarrow 12$ transitions. The white circles show the positions and the size of the beams used to compute the spectra. Panel (a): [0,0]", [0,-11.6]", [-11.6,11.4]" and R = 1", panel (b): same positions, R = 3.3", panel (c): [0,0]" and R = 1", 5.6" and 10.2", panel (d): [0,0]", [0,-1.16]", [-1.16,1.14]" and R = 1.02". *Right panels:* Resulting spectra (in K) are plotted in black for RATRAN and in red for LIME.

pixel size. In each of the four figures, the left panel shows the resulting image of the difference in percent between the run of RATRAN and the run of LIME. For each beam drawn on these images, a spectrum is computed as the mean value of all the pixels contained in that beam. All computed spectra of a given transition are plotted in the right panels of the corresponding figure.

The total flux of a given transition is obtained by integrating the map over all channels and all pixels. The difference between RATRAN and LIME on this total flux is ~3% for all the transitions calculated. Examining the maps in details (see Fig. 12a, b, and c), one can note that the innermost part of the image (R ~ 3″) shows a pixel-to-pixel difference larger than those of the outer part of the image. In this region the difference can reach a value up to 40% in contrast to the mean value of ~3% obtained anywhere else. This effect is filtered out when we look at the spectrum averaged over a certain number of pixels. Figure 13 shows the impact on the flux differences for each transition and each beam as a function of the beam position in the map or as a function of the beam radius. The left panel shows a clear trend depending on the distance from the centre of the map. This is in direct correlation with the difference seen in the innermost part of the image. In the right panel, the size of the beam also affects the difference between the maps, the more are the pixels averaged the more the differences are filtered out between the spectra, especially when the beam is on the centre of the map. One can also note that the difference is larger for the $J = 1 \rightarrow 0$ transition compared to other transitions, which is also noticeable on the map (left panel of Fig. 12a). This can be explained by the different continuum level calculated by RATRAN and LIME, visible in the spectra plotted in the right panel of Fig. 12a (one must take care of the different Y-axis scales between the spectra). This is due to opacity effects resulting from the different griding process between the two codes. Since the $J = 1 \rightarrow 0$ transition of HCO$^+$ is the most optically thick line among the others, this trend is therefore enhanced for this line.

The spectra plotted in the right panels of Fig. 12a, b, and c show a remaining difference from the continuum calculation as well. This is due to another effect induced by the pixel size used (0.2″). The physical properties of the model described are varying a lot in a region that corresponds to the size of only one pixel, and particularly the temperature profile. Since the dust emission is strongly dependent on this profile, the pixel-to-pixel difference is larger with a larger pixel size. Fig. 12d displays the $J = 13 \rightarrow 12$ transition modelled with a pixel size of 0.02″. The number of pixels is the same, thus only an inner map of the previous $J = 13 \rightarrow 12$ map (shown in Fig. 12c) is output. In this zoomed map, the previous difference seen in the centre of the map does not appear anymore. The resulting spectra (right panel of Fig. 12) show a better agreement for the continuum level (1% vs 6% previously) considering the same beam size and position.

To summarise, depending on the physical problem treated, one must take care of some input properties that can be set in LIME:

1. If too few points are set in the model, the population density will not be calculated correctly and the spatial coverage of the model will not be smooth enough. This will result in visible and non-desired structure in the output image.
2. A pixel size much larger than the mean scale of variation of the physical properties set in the model will lead to a wrong continuum calculation. Since the pixel is too large, it will not

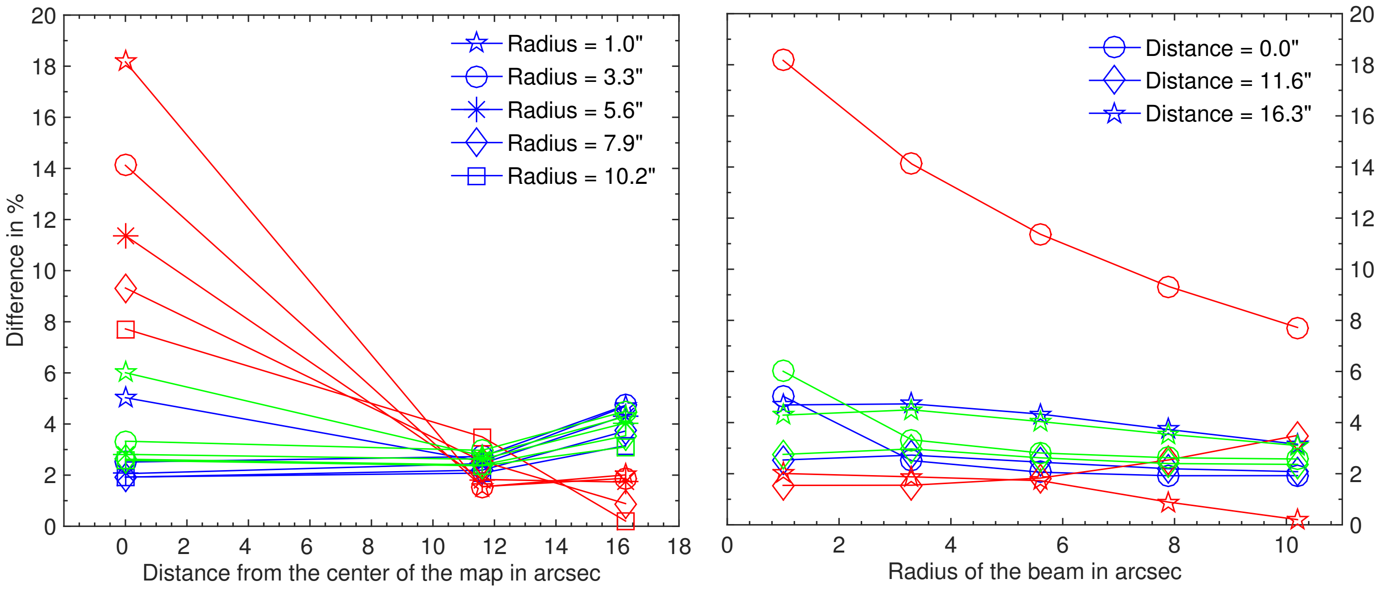

Fig. 13: For both panels, the red line refers to the $J = 1 \rightarrow 0$ transition, the blue line refers to the $J = 6 \rightarrow 5$ transition, and the green line refers to the $J = 13 \rightarrow 12$ transition. *Left panel:* Difference in % between the LIME and RATRAN maps as a function of the distance of the beam from the centre of the map in arcsec. Different marker styles refer to different beam sizes. *Right panel:* Difference in % between the LIME and RATRAN map as a function of the beam size in arcsec. Different marker styles refer to different beam distances from the centre of the map.

probe correctly the physics occurring in the region it covers and the pixel intensity will only reflect an average value of what is going on on a smaller scale.

Finally, one can note that if the size of the data cube is too large (large number of pixel and/or channel), LIME will take a long time to create it, leading to a long calculation time while running a grid of models.

5. Example

In this section, the ^{13}CO $J = 2 \rightarrow 1$ emission of an object composed of a spherical source (assimilated to a proto-stellar envelope), a proto-planetary disk, and a bipolar outflow, was considered. Table 2 summarises the physical properties set in this example, which does not correspond to any specific case. All the structures are located in the centre (0, 0, 0) of the model and the resulting velocity field given by these structures is taken into account.

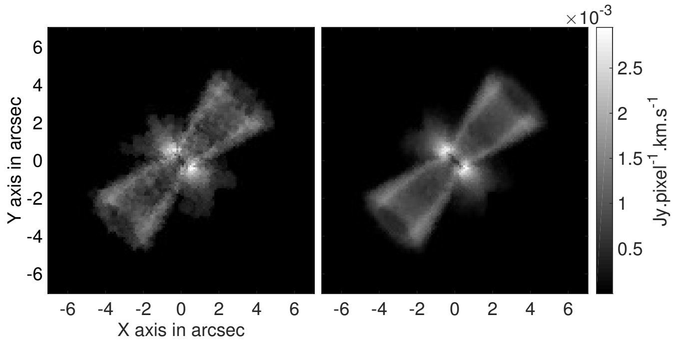

Fig. 14: Moment 0 map over all channels for the ^{13}CO $J = 2 \rightarrow 1$ transition. *Left panel:* One model only. *Right panel:* Ten smoothed models.

Table 2: Physical properties of the model set for the example section.

Physical properties	Value
General properties	
Grid min, max radius	0.1″, 7″
N° points	10,000
Distance	300 pc
b–doppler	200 m.s^{-1}
V$_{LSR}$	0 km.s^{-1}
Central object mass	3 M$_\odot$
Envelope properties	
T$_{env,max}$	200 K ($\alpha = -0.5$)
n(H$_2$)$_{env,max}$	1×10^9 cm^{-3} ($\beta = -1.5$)
X$_{in}$(^{13}CO), X$_{out}$(^{13}CO)	1.5×10^{-13}, 7.5×10^{-11}
Protoplanetary disk properties	
ρ_{in}, r_{max}, h_{max}	0.7″, 4.5″, 5″
Θ, Φ	45°, −70°
T$_{atm}$, T$_{mid}$	500 K, 50 K ($\gamma = -0.5$)
n(H$_2$)$_{disk}$	6.5×10^7 cm^{-3} ($\delta = -1.0$)
X$_{in}$(^{13}CO) for T < 27 K	1.5×10^{-6}
X$_{out}$(^{13}CO) for T > 27 K	1.5×10^{-17}
Outflow properties	
$a_{outflow}$, $b_{outflow}$, ρ_{in}, z_{out}	150″, 8″, 0.5″, 5″
V$_{outflow}$	10 km.s^{-1}
Θ, Φ, $\Delta\gamma$	45°, −70°, 15°
T$_{outflow}$	100 K
n(H$_2$)$_{outflow}$	5×10^6 cm^{-3}
X(^{13}CO)	1.5×10^{-6}

The output data cube was set with 151 channels and a spectral resolution of 100 m.s^{-1}. The spatial resolution is 0.1″ with 141 pixels to cover the radial size of 7″ of the model. From the

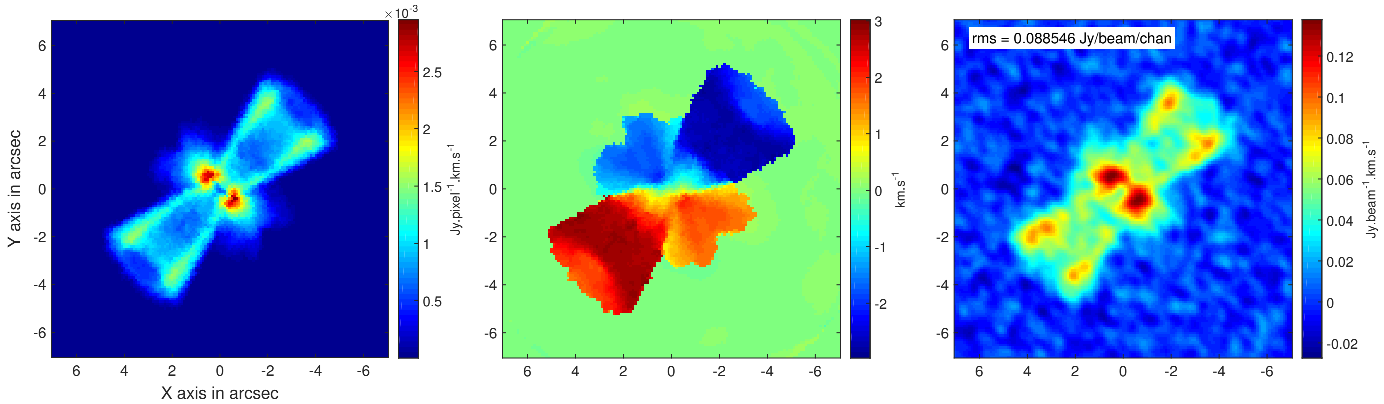

Fig. 15: *Left panel:* Moment 0 map over all channels for ^{13}CO $J = 2 \rightarrow 1$. *Middle panel:* Moment 1 map over all channels for the same transition. *Right panel:* Moment 0 map resulting of the convolution between the data cube and a beam with $b_{min} = 0.4''$, $b_{maj} = 0.5''$, $PA = -40°$, and a white noise of 0.6 Jy/beam per channel.

previous section, one can note that the pixel size is small enough to cover the physical variation of the example since no dust continuum emission is set. The same physical case considering the dust continuum emission would have required a pixel size of 0.01″.

Thanks to GASS, we ran ten times the same model and smoothed them as described in Section 3.4 in order to completely blur out the artifacts due to the griding process. The integrated intensity over all channels is shown in the Fig. 14 for one model compared to the smoothed one.

From the fits file of the smoothed data cube, we have plotted in Fig. 15 the resulting moment 0 and moment 1 maps over all channels. In the moment 0 map (left panel), the outflow cavity emission is clearly seen as well as the disk emission at the centre of the image. The depletion of ^{13}CO onto dust grains in the inner part of the disk, where the temperature drops below 27 K, is well marked. In the moment 1 map (middle panel), the outflow is clearly identified (thanks to its ejection velocity) as well as the Keplerian rotation of the disk.

The data cube computed by LIME has been written in Jy/pixel in order to work with the observation simulation tool of GASS. The input file is the smoothed data cube and the simulated beam properties are $b_{min} = 0.4''$, $b_{maj} = 0.5''$, and $PA = -40°$. A white noise of 0.6 Jy/beam per channel is also added before the convolution. After the convolution, GASS produces a map with the intensity in Jy/beam. The final rms is $\sim 8.9 \times 10^{-2}$ Jy/beam/channel and the result is shown in the right panel of Fig. 15.

GASS creates output fits files with the convolved data cube with the beam shape written in the header. These files can be read with data cube analysis packages (CASA, GILDAS, DS9, etc.) to proceed any further analysis.

6. Conclusions

We have developed GASS, a code that allows to easily define the physical structure of a star-forming region by creating, manipulating, and mixing several different physical components such as spherical sources, disks, and outflows. GASS can create input model files for LIME and the output data cubes generated by LIME can be analyzed by several post-treatment options in GASS such as plot spectra, moments, or simulate observations. An in-depth benchmarking has been made between LIME and RATRAN and the remaining difference between the two codes of the total integrated intensity over all pixels and channels ranges from 1% to 3% depending on the physical case. One must take care of LIME input parameters (number of points, pixel size) set for a given physical case since the resulting data cube may differ if they are not well settle.

Acknowledgements. The authors would like to thank Olivier Berné for very useful discussions about the disk modelling. We also acknowledge Christian Brinch who gave precisions about the griding process in LIME. We acknowledge Michiel Hogerheijde and Ian Stewart for their advices about the benchmarking between LIME and RATRAN.

References

Arce, H. G., & Sargent, A. I. 2006, ApJ, 646, 1070
Arce, H. G., Shepherd, D., Gueth, F., et al. 2007, Protostars and Planets V, 245
Brinch, C., & Hogerheijde, M. R. 2010, A&A, 523, AA25
Cantó, J., Raga, A. C., & Williams, D. A. 2008, Rev. Mexicana Astron. Astrofis., 44, 293
Crimier, N., Ceccarelli, C., Maret, S., et al. 2010, A&A, 519, AA65
Delaunay, B. 1934, Bulletin de l'Académie des Sciences de l'URSS. Classe des sciences mathématiques et naturelles, Issue 6, 793-800
Hogerheijde, M. R., & van der Tak, F. F. S. 2000, A&A, 362, 697
Lloyd, S. P. 1982, Ieee T Inform Theory, 28, 129
Ossenkopf, V., & Henning, T. 1994, A&A, 291, 943
Shu, F. H. 1977, ApJ, 214, 488
Springel, V. 2010, MNRAS, 401, 791
Visser, R., Kristensen, L. E., Bruderer, S., et al. 2012, A&A, 537, AA55
Voronoï, G. 1908, Journal für die reine und angewandte Mathematik, 133, 97-178
Williams, J. P., & Best, W. M. J. 2014, ApJ, 788, 59

List of Figures

List of Tables

BIBLIOGRAPHY

Adams, F. C., Lada, C. J., and Shu, F. H.: 1987, *The Astrophysical Journal* **312**, 788

Aikawa, Y., Wakelam, V., Garrod, R. T., and Herbst, E.: 2008, *The Astrophysical Journal* **674**, 984

Aikawa, Y., Wakelam, V., Hersant, F., Garrod, R. T., and Herbst, E.: 2012, *The Astrophysical Journal* **760**, 40

Alexander, R., Pascucci, I., Andrews, S., Armitage, P., and Cieza, L.: 2014, *Protostars and Planets VI* pp 475–496

Andre, P.: 1994, p. 179

Andre, P. and Montmerle, T.: 1994, *The Astrophysical Journal* **420**, 837

Andre, P., Ward-Thompson, D., and Barsony, M.: 1993, *The Astrophysical Journal* **406**, 122

Arce, H. G. and Sargent, A. I.: 2005, *The Astrophysical Journal* **624**, 232

Arce, H. G. and Sargent, A. I.: 2006, *The Astrophysical Journal* **646**, 1070

Arce, H. G., Shepherd, D., Gueth, F., Lee, C.-F., Bachiller, R., Rosen, A., and Beuther, H.: 2007, *Protostars and Planets V* pp 245–260

Bacmann, A., Lefloch, B., Ceccarelli, C., Steinacker, J., Castets, A., and Loinard, L.: 2003, *The Astrophysical Journal Letters* **585**, L55

Bada, J. L.: 2013, *Chemical Society Reviews* **42(5)**, 2186

Bensch, F., Pak, I., Wouterloot, J. G. A., Klapper, G., and Winnewisser, G.: 2001, *The Astrophysical Journal Letters* **562**, L185

Bergin, E. A., Alves, J., Huard, T., and Lada, C. J.: 2002, *The Astrophysical Journal Letters* **570**, L101

Bergin, E. A. and Langer, W. D.: 1997, *The Astrophysical Journal* **486**, 316

Berné, O., Fuente, A., Pantin, E., Bujarrabal, V., Baruteau, C., Pilleri, P., Habart, E., Ménard, F., Cernicharo, J., Tielens, A. G. G. M., and Joblin, C.: 2015, *Astronomy and Astrophysics* **578**, L8

Bizzocchi, L., Caselli, P., Spezzano, S., and Leonardo, E.: 2014, *Astronomy and Astrophysics* **569**, A27

Blake, G. A., van Dishoeck, E. F., Jansen, D. J., Groesbeck, T. D., and Mundy, L. G.: 1994, *The Astrophysical Journal* **428**, 680

Bockelée-Morvan, D., Biver, N., Crovisier, J., Lis, D. C., Hartogh, P., Moreno, R., de Val-Borro, M., Blake, G. A., Szutowicz, S., Boissier, J., Cernicharo, J., Charnley, S. B., Combi, M., Cordiner, M. A., de Graauw, T., Encrenaz, P., Jarchow, C., Kidger, M., Küppers, M., Milam, S. N., Müller, H. S. P., Phillips, T. G., and Rengel, M.: 2014, *Astronomy and Astrophysics* **562**, A5

Bohlin, R. C., Savage, B. D., and Drake, J. F.: 1978, *The Astrophysical Journal* **224**, 132

Boogert, A. C. A., Gerakines, P. A., and Whittet, D. C. B.: 2015, *Annual Review of Astronomy and Astrophysics* **53**, 541

Bottinelli, S., Ceccarelli, C., Lefloch, B., Williams, J. P., Castets, A., Caux, E., Cazaux, S., Maret, S., Parise, B., and Tielens, A. G. G. M.: 2004, *The Astrophysical Journal* **615**, 354

Bottinelli, S., Wakelam, V., Caux, E., Vastel, C., Aikawa, Y., and Ceccarelli, C.: 2014, *Monthly Notices of the Royal Astronomical Society* **441(3)**, 1964

Brinch, C. and Hogerheijde, M. R.: 2010, *Astronomy & Astrophysics* **523**, A25

Brogan, C. L., Pérez, L. M., Hunter, T. R., Dent, W. R. F., Hales, A. S., Hills, R. E., Corder, S., Fomalont, E. B., Vlahakis, C., Asaki, Y., and others: 2015, *The Astrophysical Journal Letters* **808(1)**, L3

Bromm, V. and Yoshida, N.: 2011, *Annual Review of Astronomy and Astrophysics* **49**, 373

Brünken, S., Sipilä, O., Chambers, E. T., Harju, J., Caselli, P., Asvany, O., Honingh, C. E., Kamiński, T., Menten, K. M., Stutzki, J., and Schlemmer, S.: 2014, *Nature* **516**, 219

Buhl, D. and Snyder, L. E.: 1970, *Nature* **228**, 267

Bujarrabal, V., Young, K., and Castro-Carrizo, A.: 2009, *Astronomy and Astrophysics* **500(3)**, 1077

Bujarrabal, V., Young, K., and Fong, D.: 2008, *Astronomy and Astrophysics* **483(3)**, 839

Burke, D. J., Puletti, F., Brown, W. A., Woods, P. M., Viti, S., and Slater, B.: 2015, *Monthly Notices of the Royal Astronomical Society* **447**, 1444

Callahan, M. P., Smith, K. E., Cleaves, H. J., Ruzicka, J., Stern, J. C., Glavin, D. P., House, C. H., and Dworkin, J. P.: 2011, *Proceedings of the National Academy of Science* **108**, 13995

Cantó, J., Raga, A. C., and Williams, D. A.: 2008, *Revista Mexicana de Astronomia y Astrofisica* **44**, 293

Capak, P. L., Carilli, C., Jones, G., Casey, C. M., Riechers, D., Sheth, K., Carollo, C. M., Ilbert, O., Karim, A., Lefevre, O., Lilly, S., Scoville, N., Smolcic, V., and Yan, L.: 2015, *Nature* **522**, 455

Carr, J. S. and Najita, J. R.: 2008, *Science* **319**, 1504

Caselli, P. and Ceccarelli, C.: 2012, *Astronomy and Astrophysics Review* **20**, 56

Caselli, P., Keto, E., Pagani, L., Aikawa, Y., Yı ldız, U. A., van der Tak, F. F. S., Tafalla, M., Bergin, E. A., Nisini, B., Codella, C., van Dishoeck, E. F., Bachiller, R., Baudry, A., Benedettini, M., Benz, A. O., Bjerkeli, P., Blake, G. A., Bontemps, S., Braine, J., Bruderer, S., Cernicharo, J., Daniel, F., di Giorgio, A. M., Dominik, C., Doty, S. D., Encrenaz, P., Fich, M., Fuente, A., Gaier, T., Giannini, T., Goicoechea, J. R., de Graauw, T., Helmich, F., Herczeg, G. J., Herpin, F., Hogerheijde, M. R., Jackson, B., Jacq, T., Javadi, H., Johnstone, D., Jørgensen, J. K., Kester, D., Kristensen, L. E., Laauwen, W., Larsson, B., Lis, D., Liseau, R., Luinge, W., Marseille, M., McCoey, C., Megej, A., Melnick, G., Neufeld, D., Olberg, M., Parise, B., Pearson, J. C., Plume, R., Risacher, C., Santiago-García, J., Saraceno, P., Shipman, R., Siegel, P., van Kempen, T. A., Visser, R., Wampfler, S. F., and Wyrowski, F.: 2010, *Astronomy and Astrophysics* **521**, L29

Caselli, P., van der Tak, F. F. S., Ceccarelli, C., and Bacmann, A.: 2003, *Astronomy and Astrophysics* **403**, L37

Caselli, P., Walmsley, C. M., Zucconi, A., Tafalla, M., Dore, L., and Myers, P. C.: 2002a, *The Astrophysical Journal* **565**, 331

Caselli, P., Walmsley, C. M., Zucconi, A., Tafalla, M., Dore, L., and Myers, P. C.: 2002b, *The Astrophysical Journal* **565(1)**, 344

Castets, A., Ceccarelli, C., Loinard, L., Caux, E., and Lefloch, B.: 2001, *Astronomy and Astrophysics* **375(1)**, 40

Caux, E., Kahane, C., Castets, A., Coutens, A., Ceccarelli, C., Bacmann, A., Bisschop, S., Bottinelli, S., Comito, C., Helmich, F. P., Lefloch, B., Parise, B., Schilke, P., Tielens, A. G. G. M., van Dishoeck, E., Vastel, C., Wakelam, V., and Walters, A.: 2011, *Astronomy and Astrophysics* **532**, A23

Cazaux, S., Tielens, A. G. G. M., Ceccarelli, C., Castets, A., Wakelam, V., Caux, E., Parise, B., and Teyssier, D.: 2003, *The Astrophysical Journal Letters* **593**, L51

Ceccarelli, C., Caselli, P., Bockelée-Morvan, D., Mousis, O., Pizzarello, S., Robert, F., and Semenov, D.: 2014, *arXiv preprint arXiv:1403.7143*

Ceccarelli, C., Castets, A., Caux, E., Hollenbach, D., Loinard, L., Molinari, S., and Tielens, A. G. G. M.: 2000a, *Astronomy and Astrophysics* **355**, 1129

Ceccarelli, C., Hollenbach, D. J., and Tielens, A. G. G. M.: 1996, *The Astrophysical Journal* **471**, 400

Ceccarelli, C., Loinard, L., Castets, A., Faure, A., and Lefloch, B.: 2000b, *Astronomy and Astrophysics* **362**, 1122

Ceccarelli, C., Loinard, L., Castets, A., Tielens, A. G. G. M., and Caux, E.: 2000c, *Astronomy and Astrophysics* **357**, L9

Chandler, C. J., Brogan, C. L., Shirley, Y. L., and Loinard, L.: 2005, *The Astrophysical Journal* **632(1)**, 371

Collings, M. P., Anderson, M. A., Chen, R., Dever, J. W., Viti, S., Williams, D. A., and McCoustra, M. R. S.: 2004, *Monthly Notices of the Royal Astronomical Society* **354**, 1133

Combes, F.: 2010, in D. J. Whalen, V. Bromm, and N. Yoshida (eds.), *American Institute of Physics Conference Series*, Vol. 1294 of *American Institute of Physics Conference Series*, pp 9–16

Coutens, A., Vastel, C., Cabrit, S., Codella, C., Kristensen, L. E., Ceccarelli, C., van Dishoeck, E. F., Boogert, A. C. A., Bottinelli, S., Castets, A., Caux, E., Comito, C., Demyk, K., Herpin, F., Lefloch, B., McCoey, C., Mottram, J. C., Parise, B., Taquet, V., van der Tak, F. F. S., Visser, R., and Yı ldız, U. A.: 2013, *Astronomy and Astrophysics* **560**, A39

Coutens, A., Vastel, C., Caux, E., Ceccarelli, C., Bottinelli, S., Wiesenfeld, L., Faure, A., Scribano, Y., and Kahane, C.: 2012, *Astronomy and Astrophysics* **539**, A132

Coutens, A., Vastel, C., Hincelin, U., Herbst, E., Lis, D. C., Chavarría, L., Gérin, M., van der Tak, F. F. S., Persson, C. M., Goldsmith, P. F., and Caux, E.: 2014, *Monthly Notices of the Royal Astronomical Society* **445**, 1299

Crapsi, A., Caselli, P., Walmsley, C. M., Myers, P. C., Tafalla, M., Lee, C. W., and Bourke, T. L.: 2005, *The Astrophysical Journal* **619**, 379

Crapsi, A., Caselli, P., Walmsley, M. C., and Tafalla, M.: 2007, *Astronomy and Astrophysics* **470**, 221

Crimier, N., Ceccarelli, C., Maret, S., Bottinelli, S., Caux, E., Kahane, C., Lis, D. C., and Olofsson, J.: 2010, *Astronomy and Astrophysics* **519**, A65

Dalgarno, A. and Lepp, S.: 1984, *The Astrophysical Journal Letters* **287**, L47

Daniel, F. and Cernicharo, J.: 2008, *Astronomy and Astrophysics* **488**, 1237

Daniel, F., Dubernet, M.-L., Meuwly, M., Cernicharo, J., and Pagani, L.: 2005, *Monthly Notices of the Royal Astronomical Society* **363**, 1083

Dartois, E., Thi, W.-F., Geballe, T. R., Deboffle, D., d'Hendecourt, L., and van Dishoeck, E.: 2003, *Astronomy and Astrophysics* **399**, 1009

de Graauw, T., Helmich, F. P., Phillips, T. G., Stutzki, J., Caux, E., Whyborn, N. D., Dieleman, P., Roelfsema, P. R., Aarts, H., Assendorp, R., Bachiller, R., Baechtold, W., Barcia, A., Beintema, D. A., Belitsky, V., Benz, A. O., Bieber, R., Boogert, A., Borys, C., Bumble, B., Caïs, P., Caris, M., Cerulli-Irelli, P., Chattopadhyay, G., Cherednichenko, S., Ciechanowicz, M., Coeur-Joly, O., Comito, C., Cros, A., de Jonge, A., de Lange, G., Delforges, B., Delorme, Y., den Boggende, T., Desbat, J.-M., Diez-González, C., di Giorgio, A. M., Dubbeldam, L., Edwards, K., Eggens, M., Erickson, N., Evers, J., Fich, M., Finn, T., Franke, B., Gaier, T., Gal, C., Gao, J. R., Gallego, J.-D., Gauffre, S., Gill, J. J., Glenz, S., Golstein, H., Goulooze, H., Gunsing, T., Güsten, R., Hartogh, P., Hatch, W. A., Higgins, R., Honingh, E. C., Huisman, R., Jackson, B. D., Jacobs, H., Jacobs, K., Jarchow, C., Javadi, H., Jellema, W., Justen, M., Karpov, A., Kasemann, C., Kawamura, J., Keizer, G., Kester, D., Klapwijk, T. M., Klein, T., Kollberg, E., Kooi, J., Kooiman, P.-P., Kopf, B., Krause, M., Krieg, J.-M., Kramer, C., Kruizenga, B., Kuhn, T., Laauwen, W., Lai, R., Larsson, B., Leduc, H. G., Leinz, C., Lin, R. H., Liseau, R., Liu, G. S., Loose, A., López-Fernandez, I., Lord, S., Luinge, W., Marston, A., Martín-Pintado, J., Maestrini, A., Maiwald, F. W., McCoey, C., Mehdi, I., Megej, A., Melchior, M., Meinsma, L., Merkel, H., Michalska, M., Monstein, C., Moratschke, D., Morris, P., Muller, H., Murphy, J. A., Naber, A., Natale, E., Nowosielski, W., Nuzzolo, F., Olberg, M., Olbrich, M., Orfei, R., Orleanski, P., Ossenkopf, V., Peacock, T., Pearson, J. C., Peron, I., Phillip-May, S., Piazzo, L., Planesas, P., Rataj, M., Ravera, L., Risacher, C., Salez, M., Samoska, L. A., Saraceno, P., Schieder, R., Schlecht, E., Schlöder, F., Schmülling, F., Schultz, M., Schuster, K., Siebertz, O., Smit, H., Szczerba, R., Shipman, R., Steinmetz, E., Stern, J. A., Stokroos, M., Teipen, R., Teyssier, D., Tils, T., Trappe, N., van Baaren, C., van Leeuwen, B.-J., van de Stadt, H., Visser, H., Wildeman, K. J., Wafelbakker, C. K., Ward, J. S., Wesselius, P., Wild, W., Wulff, S., Wunsch, H.-J., Tielens, X., Zaal, P., Zirath, H., Zmuidzinas, J., and Zwart, F.: 2010, *Astronomy and Astrophysics* **518**, L6

de Gregorio-Monsalvo, I., Ménard, F., Dent, W., Pinte, C., López, C., Klaassen, P., Hales, A., Cortés, P., Rawlings, M. G., Tachihara, K., Testi, L., Takahashi, S., Chapillon, E., Mathews, G., Juhasz, A., Akiyama, E., Higuchi, A. E., Saito, M., Nyman, L.-Å., Phillips, N., Rodón, J., Corder, S., and Van Kempen, T.: 2013, *Astronomy and Astrophysics* **557**, A133

Delaunay, B.: 1934, *Izv. Akad. Nauk SSSR, Otdelenie Matematicheskii i Estestvennyka Nauk* **7(793-800)**, 1

Doty, S. D., Schöier, F. L., and van Dishoeck, E. F.: 2004, *Astronomy and Astrophysics* **418**, 1021

Doty, S. D., van Dishoeck, E. F., van der Tak, F. F. S., and Boonman, A. M. S.: 2002, *Astronomy and Astrophysics* **389(2)**, 446

Dubernet, M.-L., Daniel, F., Grosjean, A., and Lin, C. Y.: 2009, *Astronomy and Astrophysics* **497**, 911

Dutrey, A., Wakelam, V., Boehler, Y., Guilloteau, S., Hersant, F., Semenov, D., Chapillon, E., Henning, T., Piétu, V., Launhardt, R., Gueth, F., and Schreyer, K.: 2011, *Astronomy and Astrophysics* **535**, A104

Eisner, J. A., Bally, J. M., Ginsburg, A., and Sheehan, P. D.: 2016, *ArXiv e-prints* **1604**, arXiv:1604.03134

Emprechtinger, M., Caselli, P., Volgenau, N. H., Stutzki, J., and Wiedner, M. C.: 2009, *Astronomy and Astrophysics* **493**, 89

Evans, II, N. J.: 1999, *Annual Review of Astronomy and Astrophysics* **37**, 311

Evans, II, N. J., Rawlings, J. M. C., Shirley, Y. L., and Mundy, L. G.: 2001, *The Astrophysical Journal* **557**, 193

Fayolle, E. C., Balfe, J., Loomis, R., Bergner, J., Graninger, D., Rajappan, M., and ÃŰberg, K. I.: 2016, *The Astrophysical Journal Letters* **816**, L28

Flower, D. R.: 1999, *Monthly Notices of the Royal Astronomical Society* **305**, 651

Flower, D. R., Pineau Des Forêts, G., and Walmsley, C. M.: 2006, *Astronomy and Astrophysics* **449**, 621

Fraser, H. J., Collings, M. P., McCoustra, M. R. S., and Williams, D. A.: 2001, *Monthly Notices of the Royal Astronomical Society* **327**, 1165

Frerking, M. A., Langer, W. D., and Wilson, R. W.: 1982, *The Astrophysical Journal* **262**, 590

Garrod, R. T. and Herbst, E.: 2006, *Astronomy and Astrophysics* **457**, 927

Gilbert, W.: 1986, *Nature* **319**, 618

Girart, J. M., Estalella, R., Palau, A., Torrelles, J. M., and Rao, R.: 2014, *The Astrophysical Journal Letters* **780(1)**, L11

Goldsmith, P. F. and Langer, W. D.: 1999, *The Astrophysical Journal* **517**, 209

Green, S., Montgomery, Jr., J. A., and Thaddeus, P.: 1974, *The Astrophysical Journal Letters* **193**, L89

Guelin, M., Cernicharo, J., and Linke, R. A.: 1982a, *The Astrophysical Journal Letters* **263**, L89

Guelin, M., Langer, W. D., and Wilson, R. W.: 1982b, *Astronomy and Astrophysics* **107**, 107

Guelin, M. and Thaddeus, P.: 1979, *The Astrophysical Journal Letters* **227**, L139

Hakobian, N. S. and Crutcher, R. M.: 2012, *The Astrophysical Journal Letters* **758**, L18

Hartquist, T. W. and Williams, D. A.: 1998, *The molecular astrophysics of stars and galaxies, by T.W. Hartquist and D.A. Williams, D. A.. International Series in Astrononmy and Astrophysics, Vol. 4, Oxford University Press. 1999. 560 pages; 112 line illus. ISBN13: 978-0-19-850158-9* 4

Hasegawa, T. I. and Herbst, E.: 1993a, *Monthly Notices of the Royal Astronomical Society* **261**, 83

Hasegawa, T. I. and Herbst, E.: 1993b, *Monthly Notices of the Royal Astronomical Society* **263**, 589

Hasegawa, T. I., Herbst, E., and Leung, C. M.: 1992, *The Astrophysical Journal Supplement Series* **82**, 167

Hildebrand, R. H.: 1983, *Quarterly Journal of the Royal Astronomical Society* **24**, 267

Hily-Blant, P., Maret, S., Bacmann, A., Bottinelli, S., Parise, B., Caux, E., Faure, A., Bergin, E. A., Blake, G. A., Castets, A., Ceccarelli, C., Cernicharo, J., Coutens, A., Crimier, N., Demyk, K., Dominik, C., Gerin, M., Hennebelle, P., Henning, T., Kahane, C., Klotz, A., Melnick, G., Pagani, L., Schilke, P., Vastel, C., Wakelam, V., Walters, A., Baudry, A., Bell, T., Benedettini, M., Boogert, A., Cabrit, S., Caselli, P., Codella, C., Comito, C., Encrenaz, P., Falgarone, E., Fuente, A., Goldsmith, P. F., Helmich, F., Herbst, E., Jacq, T., Kama, M., Langer, W., Lefloch, B., Lis, D., Lord, S., Lorenzani, A., Neufeld, D., Nisini, B., Pacheco, S., Phillips, T., Salez, M., Saraceno, P., Schuster, K., Tielens, X., van der Tak, F., van der Wiel, M. H. D., Viti, S., Wyrowski, F., and Yorke, H.: 2010, *Astronomy and Astrophysics* **521**, L52

Hincelin, U., Wakelam, V., Hersant, F., Guilloteau, S., Loison, J. C., Honvault, P., and Troe, J.: 2011, *Astronomy and Astrophysics* **530**, A61

Hogerheijde, M. R. and van der Tak, F. F.: 2000, *arXiv preprint astro-ph/0008169*

Hollenbach, D., Kaufman, M. J., Bergin, E. A., and Melnick, G. J.: 2009, *The Astrophysical Journal* **690**, 1497

Hollis, J. M., Pedelty, J. A., Snyder, L. E., Jewell, P. R., Lovas, F. J., Palmer, P., and Liu, S.-Y.: 2003, *The Astrophysical Journal* **588**, 353

Hollis, J. M., Snyder, L. E., Lovas, F. J., and Buhl, D.: 1976, *The Astrophysical Journal Letters* **209**, L83

Hunter, S. D., Digel, S. W., de Geus, E. J., and Kanbach, G.: 1994, *The Astrophysical Journal* **436**, 216

Ivezić, Z. and Elitzur, M.: 1997, *Monthly Notices of the Royal Astronomical Society* **287**, 799

Jaber, A. A., Ceccarelli, C., Kahane, C., and Caux, E.: 2014, *The Astrophysical Journal* **791**, 29

Jiménez-Serra, I., Testi, L., Caselli, P., and Viti, S.: 2014, *The Astrophysical Journal Letters* **787**, L33

Jørgensen, J. K., Bourke, T. L., Nguyen Luong, Q., and Takakuwa, S.: 2011, *Astronomy & Astrophysics* **534**, A100

Jørgensen, J. K., Lahuis, F., Schöier, F. L., Van Dishoeck, E. F., Blake, G. A., Boogert, A. A., Dullemond, C. P., Evans II, N. J., Kessler-Silacci, J. E., and Pontoppidan, K. M.: 2005, *The Astrophysical Journal Letters* **631(1)**, L77

Jørgensen, J. K., Schöier, F. L., and van Dishoeck, E. F.: 2004, *Astronomy and Astrophysics* **416**, 603

Kelly, B. C., Shetty, R., Stutz, A. M., Kauffmann, J., Goodman, A. A., and Launhardt, R.: 2012, *The Astrophysical Journal* **752**, 55

Keto, E. and Caselli, P.: 2010, *Monthly Notices of the Royal Astronomical Society* **402**, 1625

Keto, E., Rawlings, J., and Caselli, P.: 2014, *Monthly Notices of the Royal Astronomical Society* **440**, 2616

Keto, E. and Rybicki, G.: 2010, *The Astrophysical Journal* **716**, 1315

Keto, E., Rybicki, G. B., Bergin, E. A., and Plume, R.: 2004, *The Astrophysical Journal* **613**, 355

Keto, E. R.: 1990, *The Astrophysical Journal* **355**, 190

Klemperer, W.: 1970, *Nature* **227**, 1230

Kong, S., Caselli, P., Tan, J. C., Wakelam, V., and Sipilä, O.: 2015, *The Astrophysical Journal* **804**, 98

Koshland, D. E.: 2002, *Science* **295(5563)**, 2215

Kuan, Y.-J., Charnley, S. B., Huang, H.-C., Tseng, W.-L., and Kisiel, Z.: 2003, *The Astrophysical Journal* **593**, 848

Lampton, M., Margon, B., and Bowyer, S.: 1976, *The Astrophysical Journal* **208**, 177

Laporte, N., Streblyanska, A., Clement, B., Pérez-Fournon, I., Schaerer, D., Atek, H., Boone, F., Kneib, J.-P., Egami, E., Martínez-Navajas, P., Marques-Chaves, R., Pelló, R., and Richard, J.: 2014, *Astronomy and Astrophysics* **562**, L8

Linke, R. A., Goldsmith, P. F., Wannier, P. G., Wilson, R. W., and Penzias, A. A.: 1977, *The Astrophysical Journal* **214**, 50

Lloyd, S. P.: 1982, *IEEE TRANSACTIONS ON INFORMATION THEORY* **IT-28(2)**, 129

Loinard, L., Rodriguez, L., Pech, G., Chandler, C., Brogan, C., Ho, P., and Wilner, D.: 2009, in *American Astronomical Society Meeting Abstracts #213*, Vol. 41 of *Bulletin of the American Astronomical Society*, p. 296

Loinard, L., Torres, R. M., Mioduszewski, A. J., and Rodríguez, L. F.: 2008, *The Astrophysical Journal Letters* **675**, L29

Loinard, L., Zapata, L. A., Rodríguez, L. F., Pech, G., Chandler, C. J., Brogan, C. L., Wilner, D. J., Ho, P. T., Parise, B., Hartmann, L. W., and others: 2012, *Monthly Notices of the Royal Astronomical Society: Letters* p. sls038

Loison, J.-C., Wakelam, V., Hickson, K. M., Bergeat, A., and Mereau, R.: 2014, *Monthly Notices of the Royal Astronomical Society* **437**, 930

López-Sepulcre, A., Jaber, A. A., Mendoza, E., Lefloch, B., Ceccarelli, C., Vastel, C., Bachiller, R., Cernicharo, J., Codella, C., Kahane, C., Kama, M., and Tafalla, M.: 2015, *Monthly Notices of the Royal Astronomical Society* **449**, 2438

Lovelock, J. E.: 1965, *Nature* **207**, 568

Lucas, R. and Liszt, H.: 1994, *Astronomy and Astrophysics* **282**, L5

Majumdar, L., Gratier, P., Vidal, T., Wakelam, V., Loison, J.-C., Hickson, K. M., and Caux, E.: 2016, *Monthly Notices of the Royal Astronomical Society* **458**, 1859

Mauersberger, R. and Henkel, C.: 1991, *Astronomy and Astrophysics* **245**, 457

Mautner, M. N.: 2009, *Bioethics* **23(8)**, 433

McKay, C. P.: 2004, *PLoS Biology* **2(9)**, e302

McKee, C. F. and Ostriker, E. C.: 2007, *Annual Review of Astronomy and Astrophysics* **45**, 565

Miller, S. L.: 1953, *Science* **117**, 528

Miller, S. L. and Urey, H. C.: 1959, *Science* **130**, 245

Mladenović, M. and Roueff, E.: 2014, *Astronomy and Astrophysics* **566**, A144

Müller, H. S. P., Schlöder, F., Stutzki, J., and Winnewisser, G.: 2005, *Journal of Molecular Structure* **742**, 215

Müller, H. S. P., Thorwirth, S., Roth, D. A., and Winnewisser, G.: 2001, *Astronomy and Astrophysics* **370**, L49

Mundy, L. G., Wootten, A., Wilking, B. A., Blake, G. A., and Sargent, A. I.: 1992, *The Astrophysical Journal* **385**, 306

Neufeld, D. A., Wolfire, M. G., and Schilke, P.: 2005, *The Astrophysical Journal* **628**, 260

Ossenkopf, V. and Henning, T.: 1994, *Astronomy and Astrophysics* **291**, 943

Osterbrock, D. E.: 1974, *Astrophysics of gaseous nebulae*

Ott, S.: 2010, *ASP Conference Series* **434**, 139

Pagani, L., Bacmann, A., Cabrit, S., and Vastel, C.: 2007, *Astronomy and Astrophysics* **467**, 179

Parise, B., Simon, T., Caux, E., Dartois, E., Ceccarelli, C., Rayner, J., and Tielens, A. G. G. M.: 2003, *Astronomy and Astrophysics* **410**, 897

Persson, M. V., Jørgensen, J. K., and van Dishoeck, E. F.: 2013, *Astronomy and Astrophysics* **549**, L3

Persson, M. V., Jørgensen, J. K., van Dishoeck, E. F., and Harsono, D.: 2014, *Astronomy and Astrophysics* **563**, A74

Pickett, H. M., Poynter, R. L., Cohen, E. A., Delitsky, M. L., Pearson, J. C., and Müller, H. S. P.: 1998, *Journal of Quantitative Spectroscopy and Radiative Transfer* **60**, 883

Pinte, C., Harries, T. J., Min, M., Watson, A. M., Dullemond, C. P., Woitke, P., Ménard, F., and Durán-Rojas, M. C.: 2009, *Astronomy and Astrophysics* **498**, 967

Pinte, C., Ménard, F., Duchêne, G., and Bastien, P.: 2006, *Astronomy and Astrophysics* **459**, 797

Podio, L., Kamp, I., Codella, C., Cabrit, S., Nisini, B., Dougados, C., Sandell, G., Williams, J. P., Testi, L., Thi, W.-F., Woitke, P., Meijerink, R., Spaans, M., Aresu, G., Ménard, F., and Pinte, C.: 2013, *The Astrophysical Journal Letters* **766**, L5

Pulliam, R. L., Edwards, J. L., and Ziurys, L. M.: 2011, *The Astrophysical Journal* **743**, 36

Quénard, D., Taquet, V., Vastel, C., Caselli, P., and Ceccarelli, C.: 2016, *Astronomy and Astrophysics* **585**, A36

Rao, R., Girart, J. M., Marrone, D. P., Lai, S.-P., and Schnee, S.: 2009, *The Astrophysical Journal* **707(2)**, 921

Rawlings, J. M. C., Redman, M. P., Keto, E., and Williams, D. A.: 2004, *Monthly Notices of the Royal Astronomical Society* **351(3)**, 1054

Rawlings, J. M. C., Taylor, S. D., and Williams, D. A.: 2000, *Monthly Notices of the Royal Astronomical Society* **313**, 461

Roberts, H., Herbst, E., and Millar, T. J.: 2004, *Astronomy and Astrophysics* **424**, 905

Roberts, H. and Millar, T. J.: 2000, *Astronomy and Astrophysics* **361**, 388

Roberts-Borsani, G. W., Bouwens, R. J., Oesch, P. A., Labbe, I., Smit, R., Illingworth, G. D., van Dokkum, P., Holden, B., Gonzalez, V., Stefanon, M., Holwerda, B., and Wilkins, S.: 2016, *The Astrophysical Journal* **823**, 143

Roelfsema, P. R., Helmich, F. P., Teyssier, D., Ossenkopf, V., Morris, P., Olberg, M., Shipman, R., Risacher, C., Akyilmaz, M., Assendorp, R., Avruch, I. M., Beintema, D., Biver, N., Boogert, A., Borys, C., Braine, J., Caris, M., Caux, E., Cernicharo, J., Coeur-Joly, O., Comito, C., de Lange, G., Delforge, B., Dieleman, P., Dubbeldam, L., de Graauw, T., Edwards, K., Fich, M., Flederus, F., Gal, C., di Giorgio, A., Herpin, F., Higgins, D. R., Hoac, A., Huisman, R., Jarchow, C., Jellema, W., de Jonge, A., Kester, D., Klein, T., Kooi, J., Kramer, C., Laauwen, W., Larsson, B., Leinz, C., Lord, S., Lorenzani, A., Luinge, W., Marston, A., Martín-Pintado, J., McCoey, C., Melchior, M., Michalska, M., Moreno, R., Müller, H., Nowosielski, W., Okada, Y., Orleański, P., Phillips, T. G., Pearson, J., Rabois, D., Ravera, L., Rector, J., Rengel, M., Sagawa, H., Salomons, W., Sánchez-Suárez, E., Schieder, R., Schlöder, F., Schmülling, F., Soldati, M., Stutzki, J., Thomas, B., Tielens, A. G. G. M., Vastel, C., Wildeman, K., Xie, Q., Xilouris, M., Wafelbakker, C., Whyborn, N., Zaal, P., Bell, T., Bjerkeli, P., de Beck, E., Cavalié, T., Crockett, N. R., Hily-Blant, P., Kama, M., Kaminski, T., Leflóch, B., Lombaert, R., De Luca, M., Makai, Z., Marseille, M., Nagy, Z., Pacheco, S., van der Wiel, M. H. D., Wang, S., and Yı ldız, U.: 2012, *Astronomy & Astrophysics* **537**, A17

Rollins, R. P., Rawlings, J. M. C., Williams, D. A., and Redman, M. P.: 2014, *Monthly Notices of the Royal Astronomical Society* **443(4)**, 3033

Ruaud, M., Wakelam, V., and Hersant, F.: 2016, *Monthly Notices of the Royal Astronomical Society* p. stw887

Ruiz-Mirazo, K., Briones, C., and de la Escosura, A.: 2014, *Chem. Rev.* **114(1)**, 285

Ruiz-Mirazo, K., Peretó, J., and Moreno, A.: 2004, *Origins of Life and Evolution of the Biosphere* **34(3)**, 323

Rybicki, G. B. and Hummer, D. G.: 1991, *Astronomy and Astrophysics* **245**, 171

Savage, C. and Ziurys, L. M.: 2004, *The Astrophysical Journal* **616**, 966

Schöier, F. L., Jørgensen, J. K., van Dishoeck, E. F., and Blake, G. A.: 2002, *Astronomy and Astrophysics* **390**, 1001

Schöier, F. L., Jørgensen, J. K., van Dishoeck, E. F., and Blake, G. A.: 2004, *Astronomy and Astrophysics* **418**, 185

Schöier, F. L., van der Tak, F. F. S., van Dishoeck, E. F., and Black, J. H.: 2005, *Astronomy and Astrophysics* **432**, 369

Scoville, N., Sheth, K., Aussel, H., Vanden Bout, P., Capak, P., Bongiorno, A., Casey, C. M., Murchikova, L., Koda, J., Álvarez-Márquez, J., Lee, N., Laigle, C., McCracken, H. J., Ilbert, O., Pope, A., Sanders, D., Chu, J., Toft, S., Ivison, R. J., and Manohar, S.: 2016, *The Astrophysical Journal* **820**, 83

Shalabiea, O. M. and Greenberg, J. M.: 1994, *Astronomy and Astrophysics* 290

Shu, F. H.: 1977, *The Astrophysical Journal* **214**, 488

Sipilä, O., Caselli, P., and Harju, J.: 2013, *Astronomy and Astrophysics* **554**, A92

Sipilä, O., Caselli, P., and Harju, J.: 2015, *Astronomy and Astrophysics* **578**, A55

Smith, D. and Adams, N. G.: 1980, *The Astrophysical Journal* **242**, 424

Snyder, L. E., Hollis, J. M., Lovas, F. J., and Ulich, B. L.: 1976, *The Astrophysical Journal* **209**, 67

Snyder, L. E., Lovas, F. J., Hollis, J. M., Friedel, D. N., Jewell, P. R., Remijan, A., Ilyushin, V. V., Alekseev, E. A., and Dyubko, S. F.: 2005, *The Astrophysical Journal* **619**, 914

Snyder, L. E., Watson, W. D., Hollis, J. M., and Buhl, D.: 1977, *The Astrophysical Journal Letters* **218**, L61

Sobolev, V. V.: 1960, *Moving envelopes of stars*

Springel, V.: 2010, *Monthly Notices of the Royal Astronomical Society* **401(2)**, 791

Stark, R., Sandell, G., Beck, S. C., Hogerheijde, M. R., van Dishoeck, E. F., van der Wal, P., van der Tak, F. F. S., Schäfer, F., Melnick, G. J., Ashby, M. L. N., and de Lange, G.: 2004, *The Astrophysical Journal* **608**, 341

Sullivan, W. T. and Baross, J.: 2007, *Planets and Life: The Emerging Science of Astrobiology*, Cambridge University Press

Szostak, J. W.: 2009, *Nature* **459**, 171

Taquet, V., Ceccarelli, C., and Kahane, C.: 2012, *Astronomy and Astrophysics* **538**, A42

Taquet, V., Charnley, S. B., and Sipilä, O.: 2014, *The Astrophysical Journal* **791**, 1

Taquet, V., López-Sepulcre, A., Ceccarelli, C., Neri, R., Kahane, C., Coutens, A., and Vastel, C.: 2013a, *The Astrophysical Journal Letters* **768**, L29

Taquet, V., Peters, P. S., Kahane, C., Ceccarelli, C., López-Sepulcre, A., Toubin, C., Duflot, D., and Wiesenfeld, L.: 2013b, *Astronomy and Astrophysics* **550**, A127

Thaddeus, P. and Turner, B. E.: 1975, *The Astrophysical Journal Letters* **201**, L25

Tilling, I., Woitke, P., Meeus, G., Mora, A., Montesinos, B., Riviere-Marichalar, P., Eiroa, C., Thi, W.-F., Isella, A., Roberge, A., Martin-Zaidi, C., Kamp, I., Pinte, C., Sandell, G., Vacca, W. D., Ménard, F., Mendigutía, I., Duchêne, G., Dent, W. R. F., Aresu, G., Meijerink, R., and Spaans, M.: 2012, *Astronomy and Astrophysics* **538**, A20

Troscompt, N., Faure, A., Maret, S., Ceccarelli, C., Hily-Blant, P., and Wiesenfeld, L.: 2009, *Astronomy and Astrophysics* **506**, 1243

Turner, B. E.: 1974, *The Astrophysical Journal Letters* **193**, L83

Turner, B. E.: 1991, *The Astrophysical Journal Supplement Series* **76**, 617

van Cittert, P. H.: 1934, *Physica* **1**, 201

van der Tak, F. F. S., Black, J. H., Schöier, F. L., Jansen, D. J., and van Dishoeck, E. F.: 2007, *Astronomy and Astrophysics* **468(2)**, 627 van Dishoeck, E. F., Bergin, E. A., Lis, D. C., and Lunine, J. I.: 2014, *Protostars and Planets VI* pp 835–858

van Dishoeck, E. F., Blake, G. A., Jansen, D. J., and Groesbeck, T. D.: 1995, *The Astrophysical Journal* **447**, 760

van Dishoeck, E. F., Herbst, E., and Neufeld, D. A.: 2013, *Chemical Reviews* **113**, 9043

Vastel, C., Bottinelli, S., Caux, E., Glorian, J.-M., and Boiziot, M.: 2015, pp 313–316

Vastel, C., Caselli, P., Ceccarelli, C., Phillips, T., Wiedner, M. C., Peng, R., Houde, M., and Dominik, C.: 2006, *The Astrophysical Journal* **645**, 1198

Vastel, C., Ceccarelli, C., Caux, E., Coutens, A., Cernicharo, J., Bottinelli, S., Demyk, K., Faure, A., Wiesenfeld, L., Scribano, Y., Bacmann, A., Hily-Blant, P., Maret, S., Walters, A., Bergin, E. A., Blake, G. A., Castets, A., Crimier, N., Dominik, C., Encrenaz, P., Gérin, M., Hennebelle, P., Kahane, C., Klotz, A., Melnick, G., Pagani, L., Parise, B., Schilke, P., Wakelam, V., Baudry, A., Bell, T., Benedettini, M., Boogert, A., Cabrit, S., Caselli, P., Codella, C., Comito, C., Falgarone, E., Fuente, A., Goldsmith, P. F., Helmich, F., Henning, T., Herbst, E., Jacq, T., Kama, M., Langer, W., Lefloch, B., Lis, D., Lord, S., Lorenzani, A., Neufeld, D., Nisini, B., Pacheco, S., Pearson, J., Phillips, T., Salez, M., Saraceno, P., Schuster, K., Tielens, X., van der Tak, F., van der Wiel, M. H. D., Viti, S., Wyrowski, F., Yorke, H., Cais, P., Krieg, J. M., Olberg, M., and Ravera, L.: 2010, *Astronomy and Astrophysics* **521**, L31

Vastel, C., Ceccarelli, C., Lefloch, B., and Bachiller, R.: 2014, *The Astrophysical Journal Letters* **795**, L2

Vasyunin, A. I. and Herbst, E.: 2013, *The Astrophysical Journal* **769**, 34

Venemans, B. P., Walter, F., Zschaechner, L., Decarli, R., De Rosa, G., Findlay, J. R., McMahon, R. G., and Sutherland, W. J.: 2016, *The Astrophysical Journal* **816**, 37

Visser, R., Kristensen, L. E., Bruderer, S., van Dishoeck, E. F., Herczeg, G. J., Brinch, C., Doty, S. D., Harsono, D., and Wolfire, M. G.: 2012, *Astronomy & Astrophysics* **537**, A55

Viti, S., Natarajan, S., and Williams, D. A.: 2002, *Monthly Notices of the Royal Astronomical Society* **336**, 797

Voronoï, G.: 1908, *Journal für die reine und angewandte Mathematik* **133**, 97

Wakelam, V., Loison, J.-C., Herbst, E., Pavone, B., Bergeat, A., Béroff, K., Chabot, M., Faure, A., Galli, D., Geppert, W. D., Gerlich, D., Gratier, P., Harada, N., Hickson, K. M., Honvault, P., Klippenstein, S. J., Le Picard, S. D., Nyman, G., Ruaud, M., Schlemmer, S., Sims, I. R., Talbi, D., Tennyson, J., and Wester, R.: 2015, *The Astrophysical Journal Supplement Series* **217**, 20

Wakelam, V., Vastel, C., Aikawa, Y., Coutens, A., Bottinelli, S., and Caux, E.: 2014, *Monthly Notices of the Royal Astronomical Society* **445**, 2854

Watanabe, N. and Kouchi, A.: 2002, *The Astrophysical Journal Letters* **571**, L173

Watson, D., Christensen, L., Knudsen, K. K., Richard, J., Gallazzi, A., and Michałowski, M. J.: 2015, *Nature* **519**, 327

Watson, W. D., Anicich, V. G., and Huntress, Jr., W. T.: 1976, *The Astrophysical Journal Letters* **205**, L165

Williams, J. P. and Best, W. M. J.: 2014, *The Astrophysical Journal* **788(1)**, 59

Willott, C. J., Carilli, C. L., Wagg, J., and Wang, R.: 2015, *The Astrophysical Journal* **807**, 180

Wilson, T. L. and Rood, R.: 1994, *Annual Review of Astronomy and Astrophysics* **32**, 191

Woods, R. C., Dixon, T. A., Saykally, R. J., and Szanto, P. G.: 1975, *Physical Review Letters* **35**, 1269

Wootten, A.: 1989, *The Astrophysical Journal* **337**, 858

Yeh, S. C., Hirano, N., Bourke, T. L., Ho, P. T., Lee, C.-F., Ohashi, N., and Takakuwa, S.: 2008, *The Astrophysical Journal* **675(1)**, 454

Zernike, F.: 1938, *Physica* **5**, 785

Zinnecker, H. and Yorke, H. W.: 2007, *Annual Review of Astronomy and Astrophysics* **45**, 481

Ziurys, L. M., Tenenbaum, E. D., Pulliam, R. L., Woolf, N. J., and Milam, S. N.: 2009, *The Astrophysical Journal* **695**, 1604

Zucconi, A., Walmsley, C. M., and Galli, D.: 2001, *Astronomy and Astrophysics* **376**, 650

Abstract

The era of interferometric observations leads to the need of a more and more precise description of the physical structure and dynamics of star-forming regions, from pre-stellar cores to proto-planetary disks. The molecular and dust continuum emission can be described with multiple physical components. To perform a meaningful comparison with the observations, a precise and complex radiative transfer modelling of these regions is required.

I have developed during this thesis a standalone application called GASS (Generator of Astrophysical Sources Structures, Quénard et al., in prep.) for this purpose. Thanks to its interface, GASS allows to create, manipulate, and mix several different physical components such as spherical sources, disks, and outflows. The code is divided into different parts: the interface, the grid generation, the model creation, and the post-treatment options. A benchmarking between the combination of GASS and LIME (a 3D non-LTE radiative transfer code, Brinch and Hogerheijde, 2010) and RATRAN (a 1D counter-part, Hogerheijde and van der Tak, 2000) has been performed.

In this thesis, I used GASS to work on different astrophysical cases and, among them, I studied in details the water and deuterated water emission in the pre-stellar core L1544 and the emission of ions in the low-mass proto-star IRAS16293-2422.

I analysed the water emission in the pre-stellar core L1544 (Quénard et al., 2016) using the combination of GASS and LIME. This work shows that the water abundance profile and the dust opacity estimation in the core are different from the values obtained with previous works. Based on this result, I used an astrochemical gas-grain code to reproduce the new water abundance profile. The HDO/H_2O ratio has also been estimated from this chemical modelling, allowing to predict the line emission of HDO in this core. From this estimate, I showed that it is not possible with current instruments and telescopes (considering a realistic observing time) to detect HDO in pre-stellar cores.

The second work I carried out aims at studying the emission of ions in IRAS16293-2422 (Quénard et al., submitted) also using GASS and LIME. I focused on HCO^+, N_2H^+, and their (fractionated and deuterated) isotopologues since they are the most abundant ions in this source. Moreover, a lot of data are available from the spectral surveys for these species. The HCO^+ emission arises mainly from a young outflow but also from the envelope whereas the N_2H^+ emission is only resulting from the latter. The Nautilus gas-grain chemical code was used to predict the abundance profile of these two ions in the envelope. The results of this work show that a high cosmic ionisation rate ($\geqslant 5 \times 10^{-17}\,\mathrm{s}^{-1}$) is needed to reproduce correctly the line emission and that the presence of a foreground cloud is required to correctly reproduce the absorption and/or emission of some transitions.